Understanding Structure of Pharmaceutical Organic Solids in Confined Media

University of East Anglia

Karol Przemyslaw Nartowski

University of East Anglia
School of Pharmacy
September 2016

Dedicated to my family and friends

Acknowledgements

Throughout my PhD I received the support and guidance from many people both internally within the academia and outside the University, however there are some people who deserve special mention:

I am eternally grateful to my supervisory team, Prof. Yaroslav Khimyak and Dr. László Fábián, for allowing me to undertake an exciting and challenging PhD program and providing me with guidance and support through the last four years. I would like to thank Yaroslav for his strict work ethics and great ability to make things happen, which has allowed me to achieve goals that I would never had thought been possible some time ago. I am also grateful for all the informal chats, musical indoctrination, comments on current world issues and Royal Opera House visits.

I consider myself lucky to have a chance to meet and work alongside all great people in the Khimyak's group and within the Chemistry and Pharmacy Schools. Thanks to them, these were the best four years in the (NMR) basement ever! In Lucy, Sus, Sere, Fabi, Dani and Liz I have found friends for life! Very special thanks go to two very special ladies, Lucy and Sus, for their invaluable help in these last days before submission, your help is very much appreciated. Special thanks go also to Franco, Jacob and Pedro for all the pub entertainment, political and scientific discussions on 'single droplet drying' and physicist perspective to NMR: 'it is an electromagnetic wave, there is energy, there must be a photon involved!'. Khaled deserves separate sentence for being such a great and loyal friend in the last four years, for all the discussions about cars, computers and Middle East's both cuisine and politics. Thank you to all the project students (Jen, Jack, Tori, Pav, Diksha, Susanna) and undergrad students I have had the chance to supervise and teach in the last four years. It was pleasure to work alongside with you in the lab and I wish all of you well in your continued work.

I would also like to thank UEA for the scholarship and provided facilities and all the staff at University of East Anglia. Special note goes to Dr. Colin MacDonald for constant aid when dealing with moody spectrometers and helpful discussions for understanding new pulse programs; Bertrand Lézé for assistance with PXRD and SEM and discussing practicalities of PXRD; and Leo Earl at UEA High Performance Computing facility for technical assistance with CASTEP. I am also grateful to EPSRC Directed Assembly Network for funding some of the projects I was involved in. and for the access to the UK 850 MHz Solid-State NMR Facility at the Warwick University.

I would also like to thank my very close friends in Poland who had always time for me whenever I was back home. Special thanks go to Bartosz and Tomasz for years of friendship, for sharing good moments and helping out always when there was need for that. Special note goes also to Dr hab. Bożena Karolewicz and Dr Artur Owczarek, who encouraged me to undertake this project and were always supportive when things did not go well.

To Kasia, thank you for being by my side in the last three years, for your visits to Norwich and the best 30th birthday ever. Thank you, for everyday Skype conversation and for coping with my complaints, boring experiments and endless nights in the lab, when I just went to change a sample and was back after few hours. Thank you for your continued support throughout the whole of my PhD and for sharing the best moments in last few years. It means a lot.

A special mention is given to my family, in particular my parents, (not so) little sister and brother for putting up with the endless complaining when things were going wrong. For your help and visits to Norwich, for all the phone and Skype calls, for asking: 'why didn't you call us last week...again?'. I am very grateful for all your support throughout my whole life.

When I was eight years old, my father showed me a prism, explained what is a rainbow, and showed me that light is not always white. I am not sure he is aware that this is all his fault.

Abstract

Mesoporous silicas have attracted growing attention in pharmaceutical drug delivery due to their synthetically tailored pore diameters, large pore volume and surface area. The narrow distribution of the pores makes mesoporous silicas exciting as nano-size crystallisation chambers for studies of molecular aggregation and drug polymorphism. Determination and understanding of structure and dynamics of confined solids presents significant analytical challenge due to lack of long range ordering. In this work we demonstrate how solid-state NMR can gain molecular insight into the structures of confined pharmaceuticals which are not accessible with other techniques. Using NMR as a probe for local mobility we demonstrated differences in the molecular dynamics of confined pre-nucleating species as compared to the confined crystals and amorphous molecules embedded in seemingly uniform composites.

Indomethacin, tolbutamide and flufenamic acid were chosen as model systems. These compounds differ significantly in structural flexibility leading to a large number of polymorphs and challenges in controlling the phase transitions. Crystallisation processes from amorphous state into confined solvate and stable form V of indomethacin were monitored inside the pores of *ca.* 30 nm. Using ^{13}C and ^{1}H solid-state NMR we controlled the formation of metastable tolbutamide form V inside the pores of 3 nm, followed by its recrystallisation into the most stable form I^H. Using ^{19}F NMR and ^{19}F T_1 relaxation measurements we were able to gain molecular level insight into the crystallisation mechanisms of confined crystals, as we demonstrated the formation of a liquid-like layer on the silica surface prior to the build-up of confined crystal of flufenamic acid. All findings from NMR measurements were corroborated with PXRD, DSC and N_2 adsorption proving the presence of nano confined crystals.

Combined application of nano-size crystallisation methodology and solid-state NMR spectroscopy is essential in directing molecular aggregation and answering fundamental questions on self-assembly of crystalline solids.

Publications:

1. K.P. Nartowski, D. Malhotra, L.E. Hawarden, J. Sibik, D. Iuga, J.A. Zeitler, L.Fabian, Y.Z. Khimyak: **^{19}F NMR Spectroscopy as a Highly Sensitive Method for the Direct Monitoring of Confined Crystallisation within Nanoporous Materials.**
Angew. Chem. Int. Ed., 2016, 55(31), 8904-8908.

2. D.E. Braun, K.P. Nartowski, Y.Z. Khimyak, K.R. Morris, S.R. Byrn, U.J. Griesser: **Structural Properties, Order–Disorder Phenomena, and Phase Stability of Orotic Acid Crystal Forms.** Mol. Pharm., 2016, 13(3), 1012-1029.

3. K.P. Nartowski, Y.Z. Khimyaka, D.J. Berry: **Tuning the spontaneous formation kinetics of caffeine : malonic acid co-crystals.**
CrystEngComm, 2016, 18(15), 2617-2620.

4. K.P. Nartowski, J. Tedder, D.E. Braun, L. Fabian, Y. Z. Khimyak: **Building solids inside nano-space: from confined amorphous through confined solvate to confined 'metastable' polymorph.** Phys. Chem. Chem. Phys., 2015, 17(38), 24761-24773.

5. I. Sarceviča, L. Orola, K.P. Nartowski, Y.Z. Khimyak, A.N. Round, L. Fábián: **Mechanistic and kinetic insight into spontaneous cocrystallization of isoniazid and benzoic acid.** Mol. Pharm., 2016, 12(8), 2981-2992.

6. A.M. Rashid, S.F.D. Batey, K. Syson, H. Koliwer-Brandl, F. Miah, J. E. Barclay, K.C. Findlay, K.P. Nartowski, Y.Z. Khimyak, R. Kalscheuer, S. Bornemann: **Assembly of α-Glucan by GlgE and GlgB in Mycobacteria and Streptomycetes.**
Biochemistry, 2016, 55, 3270-3284.

7. J. Hellrup, M. Holmboe, K.P. Nartowski, Y.Z. Khimyak, D Mahlin: **Structure and mobility of lactose in lactose/sodium montmorillonite nanocomposites,**
Langmuir, **DOI:** 10.1021/acs.langmuir.6b01967.

Oral presentations:

1. **Controlled crystallisation in porous silicas: NMR insight into structure and self-assembly mechanism of confined organic crystalline phases.** Presented at 2015 NMR DG Postgraduate meeting at University of Manchester

2. **Mesoporous silica materials from amorphous by design to new polymorphs and nano-crystalline drug delivery systems.** Presented at 5th APS International PharmSci 2014 The Science of Medicines at University of University of Hertfordshire, Hatfield

List of Abbreviations

BABA	Back-to-back
BET	Brunauer, Emmet and Teller
BJH	Barrett, Joyner and Halenda
CCDC	The Cambridge Crystallographic Data Centre
CP/MAS	Cross Polarisation Magic Angle Spinning
CRAMPS	Combined Rotations and Multi-Pulse Sequence
CSA	Chemical Shift Anisotropy
CTAB	Cetyltrimethylammonium Bromide
CTACl	Cetyltrimethylammonium Chloride
DUMBO	Decoupling Using Mind Boggling Optimization
FFA	Flufenamic Acid
FID	Free Induced Decay
FS-LG	Frequency Switched Lee Goldburg
HETCOR	Heteronuclear Correlation
IMC	Indomethacin
INEPT	Insensitive Nuclei Enhanced by Polarisation Transfer
IUPAC	International Union for Pure and Applied Chemistry
LCT	Liquid-Crystal Templating
MAS	Magic Angle Spinning
MCM	Mobil Composition of Matter
NMR	Nuclear Magnetic Resonance
NOESY	Nuclear Overhauser Spectroscopy
PMLG	Phase Modulated Lee Goldburg

PSD	Pore Size Distribution
PPM	Parts Per Million
PXRD	Powder X-Ray Diffraction
r f	Radio Frequency
SBA	Santa Barbara Acid
SEM	Scanning Electron Microscopy
TB	Tolbutamide
TEM	Transmission Electron Microscopy
TEOS	Tetraethyl Orthosilicate
TMS	Tetramethylsilane
T_1	Spin-lattice relaxation time, Longitudinal relaxation time
$T_{1\rho}$	Spin-lattice relaxation time in the rotating frame, Longitudinal relaxation time in the rotating frame

Table of Contents

Introduction

Chapter 1

Introduction

Porous materials with high surface areas and large volumes are of importance in material science due to possible applications in catalysis, gas storage, size exclusion chromatography or enzyme immobilisation.[1–6] International Union of Pure and Applied Chemistry classifies porous solids into three groups based on their pore size diameter into:

1. Microporous solids with pore width smaller than *ca.* 2 nm, *e.g.*, zeolites[7], metal organic frameworks (MOF)[8], microporous polymers[9];

2. Mesoporous solids with pore widths between 2 nm and 50 nm, *e.g.*, silica and alumina based materials[10];

3. Macroporous solids, with pore widths exceeding about 50 nm, *e.g.*, silica and alumina based materials, porous glasses[11] and macroporous metal oxide[12].

In the most recent IUPAC classification the micropores are further divided into narrow micropores (ultramicropores) with sizes < 0.7 nm and wide micropores (supermicropores) due to the differences in the physisorption mechanism of gases into narrow micropores.[13]
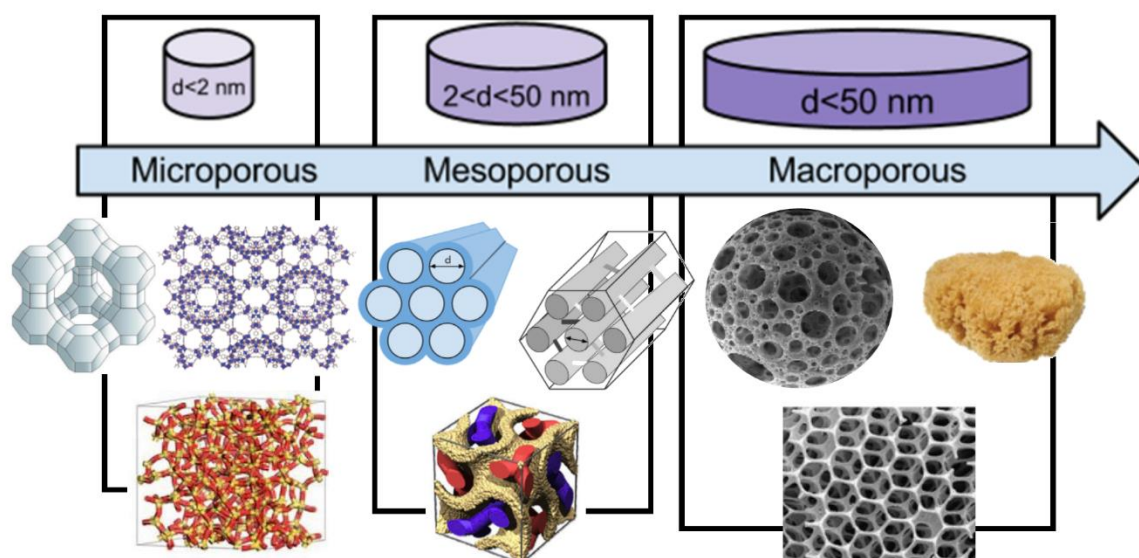
Figure 1-1. IUPAC classification of porous solids. Adapted from [9,14,15]

The application of porous solids in the chemical engineering and catalysis is well recognised with zeolites being the most widely used catalysts in the industrial processes, including oil refinement, synthetic organic chemistry or petrochemistry.[10] These microporous crystalline materials, composed of silicon, aluminium and oxygen organised in three dimensional structure forming

channels and cages in nanometer and subnanometer scale, are of particular importance for small molecules with kinetic diameters below 10 Å.[10,16] Zeolites have recently been reported as drug delivery carriers for encapsulation of small pharmaceuticals (sulphonamide antibiotics[17,18], ketoprofen[7], 5-fluorouracil[19] and α-cyano-4- hydroxycinnamic acid[16]) due to their structural properties, high affinity for guest molecules and low toxicity (for some natural compounds *e.g.*, clinoptilolite)[7,18]. Although the successful incorporation and controlled release of ibuprofen, 5-fluorouracil and indomethacin from microporous MOFs[8,20,14] and zeolitic imidazolate framework[21,22] has been demonstrated recently, application of these materials as drug delivery systems is debatable and more research is required in order to assure their safety.[23] The main drawback for a use of microporous solids for drug encapsulation is the small size of the pores/cages and even smaller diameter of the pores windows and interconnections, which makes encapsulation of large pharmaceutical molecules or biomolecules very difficult.

The discovery of the M41S family of ordered mesoporous silica based materials by Mobil researchers in 1992 with pore sizes between 16-100 Å (and above) extended the possible applications of host-guest chemistry for larger molecules and small proteins.[24,25] The MCM-41 material (Mobil Composition of Matter No. 41) in comparison to highly crystalline microporous zeolites or MOFs is composed of amorphous silica walls, with hexagonally ordered uniform pores, which are synthetically tailored by adjusting the reaction conditions. The unique features of silica based mesoporous scaffolds including high pore volume and high surface area, which can be chemically functionalised due to the presence of the silanol groups, made these materials promising multifunctional candidates for drug delivery systems. The properties of these materials and synthetic procedures, which enable control over the pore size and geometry, are discussed in the following sections.

1.1 Mesoporous silicas

In this work we used four different types of mesoporous silica hosts with different pore size diameter including MCM-41 (*ca.* 3 nm), SBA-15 (*ca.* 7 nm), MCF (*ca.* 29 nm) and CPG (*ca.* 55 nm) materials, therefore in this section we will focus on introducing the structural differences between these scaffolds.
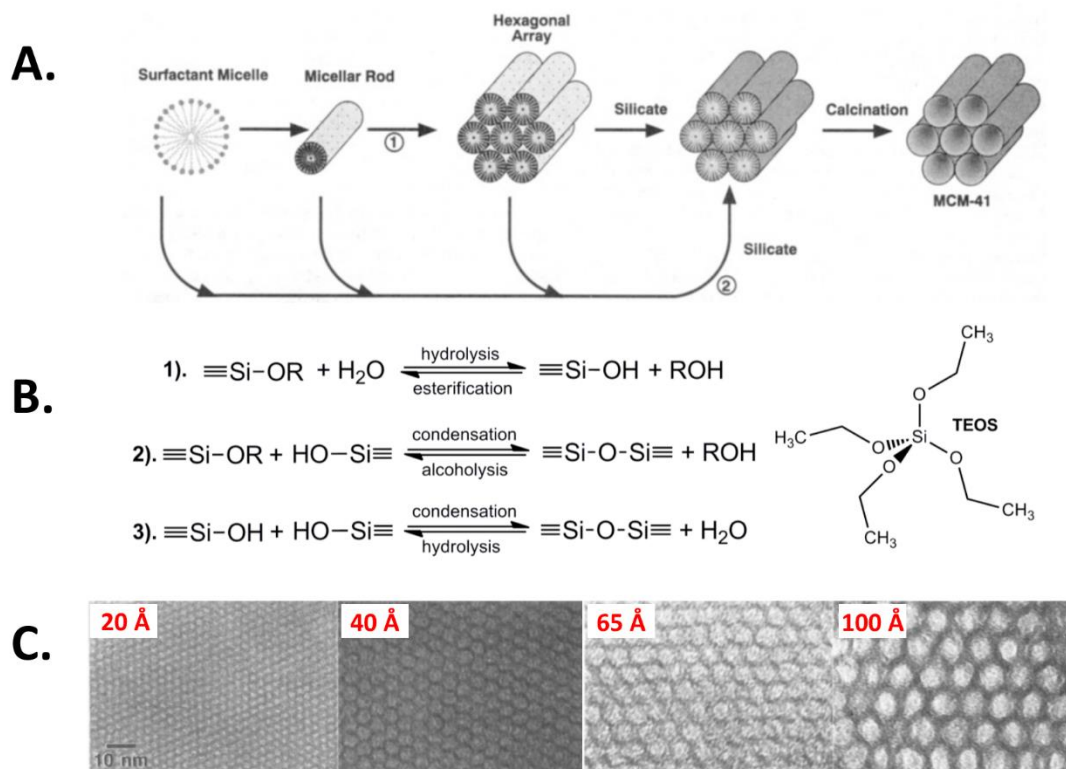
Figure 1-2. **A.** Two possible mechanisms for MCM-41 synthesis: 1) liquid crystal templating initiated; 2) silicate anion initiated; **B.** Series of reactions in sol-gel process: For TEOS: 1) hydrolysis of TEOS yields a silanol group $OH-Si(OC_2H_5)_3$, silanol groups can react (condensation) with each other (3) or with alkoxide (2) forming siloxane bonds, which are the basis for gel network. **C.** TEM images of MCM-41 silicas with different pore sizes. Adapted from [25,26].

The synthesis of MCM-41 mesoporous silica was originally described as occurring *via* liquid crystal templating (LCT) mechanism, where the dissolved surfactant molecules act as the supramolecular template for condensation of the silica source.[24,25] The structure directing agents used as a templates for MCM-41 synthesis are usually quaternary alkylammonium salt cationic surfactants [C_nH_{2n+1} (CH_3)$_3N^+$, where n = 8-16][25], which form micelles in the acidic and basic solutions at room temperature. The length of the alkyl tail of the surfactant determines the size of the pores in the resulting solid, therefore one of the pathways for tuning of the pores diameter is simply to change the size of the micellar template.[25] The analogy of the architecture of the pores, *e.g.* hexagonal (MCM-41), cubic (MCM-48) or laminar (MCM-50),[10] is also determined through the supramolecular structure of the micellar mesophase, which is formed in solution prior to the addition of the silica source, *e.g.*, TEOS, sodium silicate. The silica source in the acidic or basic environments undergoes hydrolysis and assembly around the micellar template followed by the condensation. The condensation of the silicate ion is facilitated by heating the mixture under static conditions and results in gel formation. The removal of the surfactant from the resulting solid is usually carried out through calcination or ion exchange.

The LCT mechanism for MCM-41 formation was developed based on the observation that the structure of resulting solid depends on the initial surfactant to silica molar ratios, *e.g.*, a hexagonal array of the pores (MCM-41) was observed at 0.6, a cubic phase (MCM-48) at 1.0 and a lamellar phase (MCM-50) at 1.3 CTMAOH/TEOS molar ratios.[27,28] In this mechanism micelles form micellar rods, which in the next step will form hexagonal array of micellar rods followed by incorporation of the inorganic phase around the micellar template (mechanism (1) in Figure 1-2A.).[10,25] As the micellar liquid crystals formed in solution are highly sensitive to small changes in the composition, the authors did not exclude that the ordering of the micelles follows the addition of the silicate (mechanism (2) in Figure 1-2B.).[25]
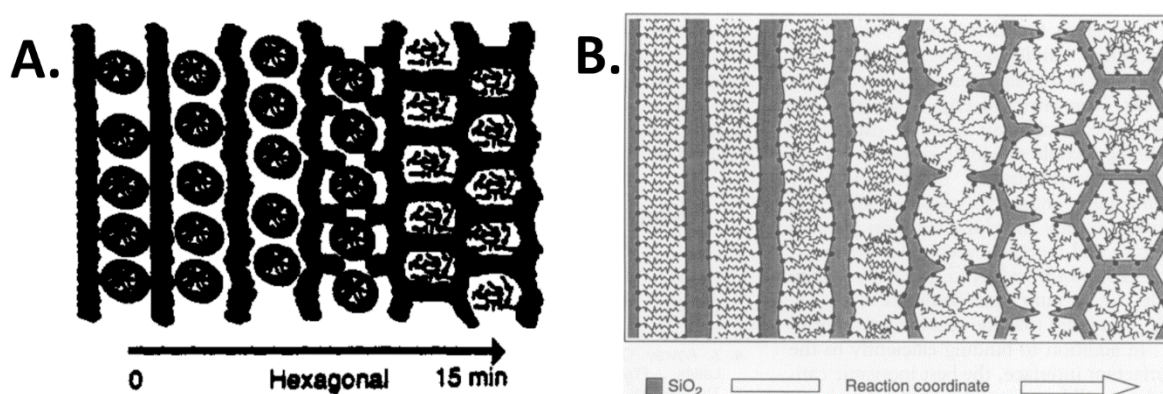
Figure 1-3. A. Modified LCT mechanism proposed by Steel *et al.*; **B.** cooperative formation of inorganic-organic interface proposed by Chmelka and co-workers. Adapted from [29,30].

The LCT mechanism proposed by Beck and co-workers[25] was challenged by Davies *et al.* who concluded, based on *in situ* [14]N NMR, that the surfactant is not arranged into a liquid crystalline phase during the synthesis of MCM-41.[31] This was proven independently using ^{14}N NMR by Steel *et al.* who proposed a modified LCT mechanism in which the template rods are intercalated between layers of silicate, which upon heating collapse forming a hexagonal mesophase.[32] A slight variation of this mechanism was proposed by Chmelka and co-workers based on PXRD results, which indicated the presence of a lamellar phase prior to the formation of a hexagonal silica arrangement.[30] The authors proposed cooperative formation of the silica:surfactant interface prior to silica condensation and subsequent charge density matching between the surfactant and silica.[10,30] This last step implements the curvature in order to balance the differences in the charge distribution between the silica anions and positively charged surfactant head groups.

Although the presented mechanisms show some differences in the detail of the formation of hexagonal array of mesophase all described hypothesis rely on the electrostatic interactions between the silica precursor and positively charged heads of surfactant.
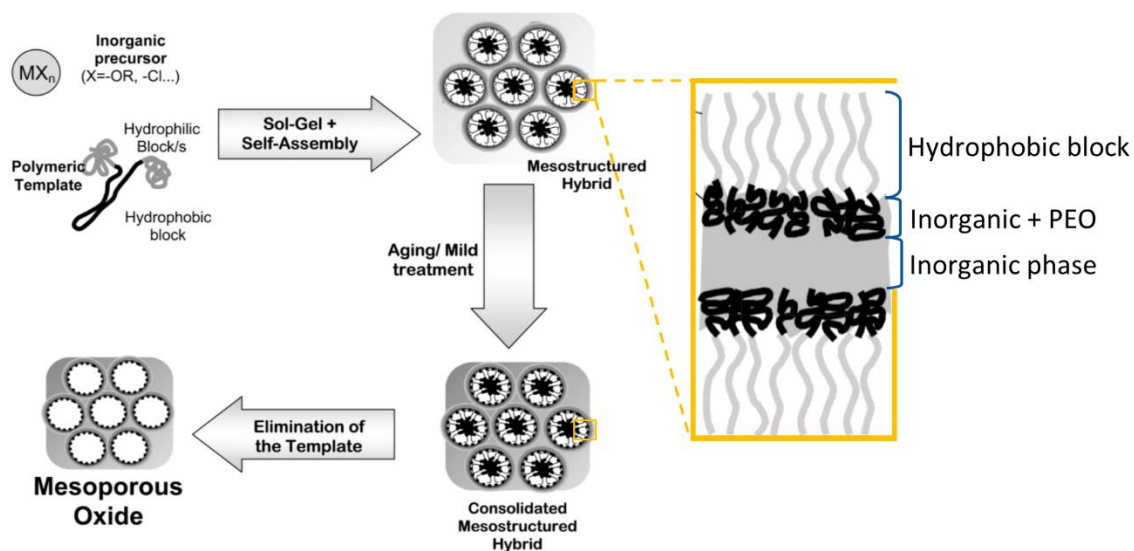
Figure 1-4. The synthetic pathway for mesoporous silica using block copolymer. The yellow frame shows the schematic structure of organic-inorganic interface, where PEO is molecularly mixed with inorganic phase. Adapted from [33,34].

Six years after the discovery of the MCM-41 scaffold, Zhao *et al.* reported the synthesis of a new family of mesoporous silica materials using triblock copolymer poly(ethylene oxide)-poly(propylene oxide)-poly(ethylene oxide) as a template for condensation of silica source.[35] The most frequently used copolymers for synthesis of SBA type materials are Poloxamers P123 ($PEO_{20}PPO_{70}PEO_{20}$) and F127 ($PEO_{101}PPO_{56}PEO_{101}$). The copolymer dispersed in the acidified aqueous solution forms micelles around which the silica source (typically TEOS), self-assembles and condensates in sol-gel processes (Figure 1-4). The resulting product forms two-dimensional, well-ordered hexagonal mesoporous silica material with uniform pore sizes between *ca.* 50 and 300 Å and thick pore walls, resulting in increased hydrothermal stability as compared to the MCM-41 silica.[35] The organic-inorganic interface for PEO-PPO-PEO copolymers and silica is composed of the PEO blocks integrated with silica source as demonstrated by Spiess and co-workers using solid-state NMR.[33,34]

The molecularly mixed interface composed of PEO and silica source results in the presence of micropores in the silica walls. The level of microporosity within the final product can be adjusted through the control of experimental conditions, *i.e.*, the condensation and aging temperature and

time of both processes.[36,37] In general, extended aging time (48 h) and increased temperature of the process (363-373 K) results in a decrease in materials microporosity (Figure 1-5).[33,36,37]
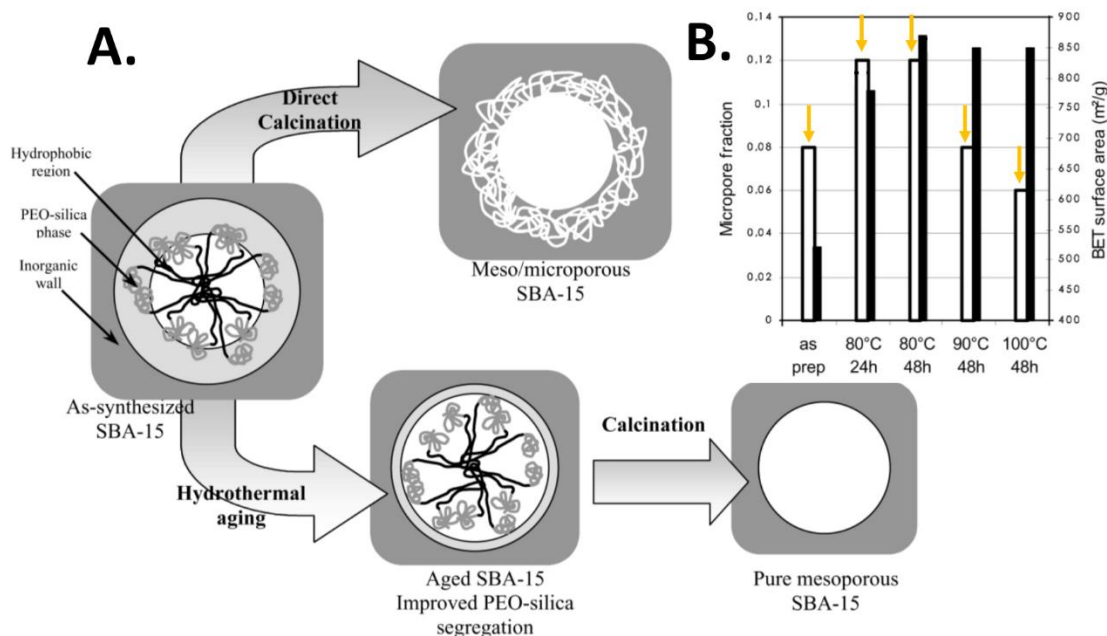
Figure 1-5. A. Changes in the organic-inorganic interphase segregation as a function of aging time SBA-15; **B.** Changes in the micropore fraction (yellow arrows) and BET surface area (black bars) as a function of aging time and temperature. Adapted from [33,36].

Further modifications of the synthetic conditions resulted in formation of new materials within the SBA family of mesoporous solids. For example, SBA-16 porous hosts with ink bottle pores and a three-dimensional cubic cage structure are formed using as a copolymer poloxamer F127.[15]

Increase in the pore size diameter can be achieved using swelling agents (typically 1,3,5-trimethylbenzene, TMB, mesitylene) during the synthesis of SBA-15 materials.[15] The addition of the swelling agent results in the enlargement of the micelles, and formation of a microemulsion as a colloidal template. Therefore this method developed by Stucky and co-workers is called microemulsion templating (Figure 1-6).[38]
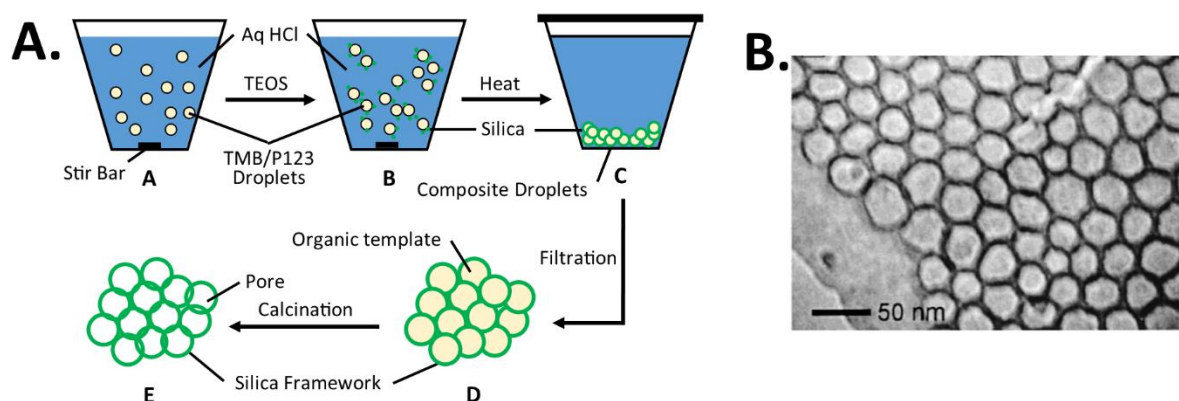
Figure 1-6. A. MCF synthesis mechanism proposed by Stucky and co-workers. The process is described in details in the text. **B.** TEM image of MCF silica with cell sizes between 29 and 34 nm. Adapted from [38].

The synthesis of mesostructured cellular foam (MCF) starts with the formation of oil-in-water microemulsion composed of TMB droplets coated with P123 copolymer dispersed in an aqueous solution of HCl (Figure 1-6). Addition of hydrophobic TEOS results in its hydrolysis at the surface of the droplets and formation of the silica cation and ethanol, which acts as a co-surfactant. The silica cation may begin to condensate and aggregate at the microemulsion template resulting in the composite droplets. Aging in autoclave at higher temperatures results in further ordering and condensation of the silica. The organic phase is removed from the resulting solid through calcination.[38] The final product forms a three-dimensional sponge-like foam composed of large uniform spherical cells (15–50 nm), which are accessible *via* windows (5–20 nm).[15] The size of the windows can be increased synthetically through the addition of NH_4F prior to aging. The morphology and particle size of the material is easily controlled during synthesis.[4,15]

Due to large surface area, synthetically tailored pore sizes, and pore volumes, which enable encapsulation of larger pharmaceutical molecules, mesoporous silicas are promising materials for drug delivery.[39–41] The surface of the scaffolds, covered with silanol groups, is an attractive target for chemical decoration, alongside the modification of synthetic procedures towards incorporation of organic and inorganic functionalities within the framework expands the possible applications of this materials in advanced (bio)catalysis as well as controlled and targeted drug delivery.[2,42]

1.2   Mesoporous silicas for drug delivery

Mesoporous silica materials as promising candidates for drug delivery are frequently investigated for their performance in adsorption and release of drug molecules. Additionally, the possibility to synthesise mesoporous silicas as nanoparticles opened new area of research in nanomedicines,

targeted and intracellular delivery of drugs. These two important and exciting fields of pharmaceutical research are not the focus of this work and comprehensive reviews on both topics can be found elsewhere.[2,3,40,42–48]

Here we discuss the fundamental effect of mesoporous confinement on the physical state of encapsulated molecules in order to understand the host-guest chemistry between the silica pores and pharmaceutical guest molecules. Therefore, the effect of confinement on intercalated pharmaceutical molecules will be discussed regarding the outcome of encapsulation, *i.e.*, stabilisation of amorphous drug or formation of nanocrystalline solids inside the silica pores. The developed models will enable us to predict the phase of confined pharmaceuticals and gain molecular level understanding of aggregation processes on different length scales.

1.3 Amorphous and crystalline Active Pharmaceuticals Ingredients (API) in drug delivery[49]

Knowledge of the physical form of API during formulation and manufacturing process of new drug products is of paramount importance from a regulatory and industrial perspective. For solid-state pharmaceutical formulations one needs to consider whether the drug molecules form an amorphous or crystalline system. The amorphous solid lacks three-dimensional long range ordering of constituent molecules, and therefore can be defined as a disordered, non-crystalline solid. Molecules in amorphous materials have, however, some short range order with their neighbours, but in general are randomly distributed in the solid (Figure 1-7).[50,51] A crystalline solid can be defined as 'a solid body having a characteristic internal structure and enclosed by symmetrically arranged plane surfaces, intersecting at definite and characteristic angles.'[52] A crystal can be thought as infinite 3D lattice of atoms (points) repeating periodically in all three dimensions.[53] Therefore, the molecules in a crystalline API form periodically repeated unit cells, which provide long range structural ordering and physical stability of the material (Figure 1-7).
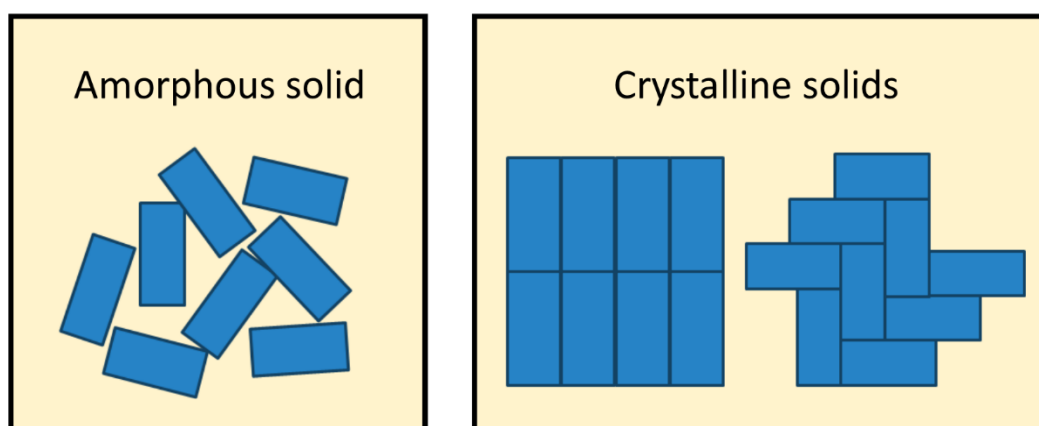
Figure 1-7. Structural differences between amorphous and crystalline solids.

One of the biggest challenges in the development of pharmaceutical solid oral formulations is related to the increasing number of drug candidates defined as having low solubility, estimated as 70 % investigational new drugs.[54,55] These molecules require special manufacturing processes in order to increase their water solubility, including modification of the crystal form, micronisation, complexation, being delivered as lipid formulation or encapsulated in the polymer matrix.[54] It is also possible to formulate poorly water soluble API's in the amorphous form, which greatly enhances dissolution rate and bioavailability.[51,54,56] It was demonstrated by Mullins and Macek early in 1960 that amorphous novobiocin has increased oral bioavailability in dogs as compared to the free acid and its sodium and calcium salts.[57] This observation was further confirmed for numerous API and 1.1 to 1000 fold increase in the apparent dissolution of amorphous API as compared to crystalline drug have been reported.[54] The preparation methods of amorphous API have been recently reviewed[51,55,56] and these includes quenching of melts, rapid precipitation, freeze-drying, spray-drying, introduction of impurities, milling and vapour condensation.[49,51,56] The preparation method for successful amorphisation of pharmaceutical solids and decreased recrystalliation rate is of importance as it changes dynamic and energetic properties of the system. It was shown by Fukuoka *et al.* that amorphous indomethacin prepared by slow cooling of molten drug is stable for 2 years.[58] Yoshioka *et al*. showed later that grinding of amorphous IMC prepared by quench cooling of a melt decreased its physical stability.[59] Recently Karmwar *et al.* compared several methods for preparation of amorphous IMC and found quenched cooled amorphous materials most stable, followed by materials prepared using cryo-milling and spray-drying.[60]

The main drawback of amorphous API formulations is their low stability as compared to crystalline solids due to their Gibbs free energy, which make disordered solids thermodynamically metastable.[50,51,56,61] Therefore, there is much interest towards the development of new ways for stabilisation of amorphous pharmaceuticals including formulation of polymer based amorphous solid dispersions, co-amorphous systems or nanoencapsulation within mesoporous silicas.[41,49,55,62–65] Recent developments in solid-state NMR have enabled a molecular level understanding of structure and dynamics of amorphous drug-polymer solid dispersions, and these methods can be extended for application in other systems including amorphous composites based on mesoporous silica scaffolds.[66–69]

1.4 Stabilisation of amorphous API within mesoporous silica scaffolds

The first application of the MCM-41 silica scaffold as drug delivery carrier for ibuprofen (IBU) was demonstrated by Vallet-Regi *et al.* in 2001 and started a new era of nanoencapsulation in pharmaceutical formulations.[70] The early reports in this new field involved understanding the adsorption and release of drug molecules and there was very little attention paid towards physical

properties of confined molecules.[43,71–73] Babonneau and co-workers demonstrated increased mobility of IBU, benzoic acid[74], lauric acid[75] and benzamide confined within the MCM-41 and amino functionalised MCM-41 hosts compared to bulk drug.[76] The detailed understanding of the physical state of IBU confined within the 3.5 nm and 11.6 nm MCM-41 scaffolds was further developed by the group using advanced solid-state NMR methods. The drug molecules confined within the 3.5 nm MCM-41 were found in a highly mobile state at room temperature and vitrified into a glassy state at 223 K, as demonstrated using ^{1}H-^{13}C CP/MAS NMR.[77] On the other hand, cooling of IBU confined within the 11.6 nm MCM-41 resulted in crystallisation of confined molecules.[77] Increased mobility of confined molecules was also demonstrated by the authors using ^{1}H MAS PFG-NMR.[78] Further understanding of the physical state of IBU confined within the MCM-41 host at high drug loadings was developed by Skorupska et al.[79] and is further discussed in the General Discussion Chapter. The specific interactions between confined IBU and the MCM-41 silica walls and the effect of microsolvation on the system was probed by Delle Piane et al. using DFT calculations. The authors suggested static disorder of adsorbed IBU due to surface heterogeneity and higher affinity of the silica surface for water molecules than for ibuprofen.[80,81]

The promising application of SBA-15 as a carrier for ten poorly soluble drugs was demonstrated by Van Speybroeck et al.[41] The authors demonstrated increased dissolution rate of encapsulated species as compared to the bulk crystalline drug. The authors highlighted lack of the melting peaks and T_g in the DSC analysis of the composites indicating monomolecular adsorption of the drug at the silica surface. The confined molecules were stable in a non-crystalline state for a six month's period of storage at 52 % RH and the performance of the composites was maintained.[41] In another study the authors demonstrated that glibenclamide encapsulated within SBA-15 in a non-crystalline state has four times higher absorption in rats as compared to the reference product.[82]

The effect of the loading method and drug content within the SBA-15 scaffold on the physical state of two model compounds itraconazole (ITZ) and IBU was investigated by Mellaerts et al.[83] The authors demonstrated that encapsulated ITZ molecules at 30 wt. % loadings agglomerated to form glassy plugs inside the silica pores, whilst at low drug loadings monomolecular adsorption of the molecules was observed.[83] Kinnari et al. showed increased stability of amorphous ITZ confined within the mesoporous silicon and non-ordered mesoporous silica particles in an accelerated stability study.[84] The authors confirmed that at ca 30 wt. % loadings the ITZ molecules formed glassy plugs inside the pores due to the presence of a glass transition in DSC thermograms.[84]

Limnell et al. investigated physical stability of amorphous IMC confined within the MCM-41 and SBA-15 porous hosts for three months under stressed conditions (303 K and 56 % RH). The confined molecules stayed amorphous over the storage time, with no detectable traces of crystalline species

in PXRD.[85] Ukmar *et al.* also observed formation of highly mobile amorphous IMC confined within the MCM-41 and SBA-15 scaffolds through the analysis of solid-state NMR analysis and ^{1}H T_1 relaxation measurements.[86,87] It was shown by our group that thermally induced recrystallisation of amorphous IMC could be supressed after encapsulation within 30 nm pores of the MCF silica scaffold at loadings up to 50 wt. % (Chapter 5).[88] More recently, Kiwilsza *et al.* demonstrated 70 times faster dissolution rate of amorphous nimodipine confined inside the MCM-41 and SBA-15 pores as compared to the bulk drug. Using solid-state NMR the authors demonstrated that the API loaded outside is in crystalline phase whilst that encapsulated drug is in highly mobile regime.[89,90] Skorpupska *et al.* has shown recently that it is possible to encapsulate two compounds inside the silica pores using the melting method (present in the bulk in form of co-crystal).[91,92] The encapsulated molecules inside the pores did not recrystallise and remained in highly mobile amorphous state. Furthermore, it was shown that for a mixture of two compounds MCM-41 may work as a molecular sieve selectively encapsulating only compound with lower molecular mass.[92]

In summary, the presented examples demonstrated possible application of MCM-41 and SBA-15 (*ca.* 3-12 nm) mesoporous silicas as new promising carriers for amorphous drug delivery systems. The confined molecules demonstrated increased stability in the amorphous state likely due to molecular adsorption at the silica surface. We will discuss further the possibility of designing amorphous composites based on the mesoporous silicas in Chapter 8 (General discussion and conclusions) with respect to the size of the pores, drug loading level and size of the molecules.

1.5 Polymorphism of crystalline API

Investigation of the physical state of confined molecules requires knowledge of the crystalline forms of API as encapsulated molecules may form confined nanocrystals.[93] It is known that chemical compounds can exist in different molecular arrangements in the solid state leading to variety of crystalline structures, known as polymorphs.[94] According to McCrone's definition 'a polymorph is a solid crystalline phase of a given compound resulting from the possibility of at least two different arrangements of the molecules of that compound in the solid state'.[95] Although over the years many definitions of polymorph and polymorphism were developed, that of McCrone seems to be the most recognised and frequently used by chemists.[96] Identification of a range of experimental crystallisation conditions suitable for production of a specific polymorph is an important challenge in industrial and academic research. Nucleation and crystal growth processes are influenced by crystallisation conditions *i.e.*, nature of solvent, temperature, seeding method, humidity or the presence of additives. Moreover, crystallisation method *e.g.*, solvent evaporation, cooling of supersaturated solution, crystallisation from a melt, high pressure treatment or sublimation may determine the crystallisation outcome.[96–99]

The importance of polymorphism from a pharmaceutical perspective was firstly highlighted by Haleblian and McCrone in 1969. The authors identified several polymorphism related problems in drug delivery, including stability issues in suspensions or differences in bioavailability after administration of API in different crystalline forms.[100] Despite years of studies on pharmaceutical polymorphism, the problems highlighted nearly fifty years ago by Haleblian and McCrone are still relevant from industrial and regulatory perspective and represent large part of pharmaceutical research.[98,101] The crystalline structure of an API determines the physicochemical properties of a solid including dissolution, thermal conductivity or fusion temperature (Table 1-1). These properties may significantly affect manufacturing processes such as filtering, drying or tableting and in turn the final quality of a drug product.[101]

Table 1-1. Properties which can differ between polymorphs.[49,102]

Thermodynamic	Kinetic	Packing	Surface	Mechanical
Melting temperature	Dissolution rate	Density	Surface free energy	Hardness
Enthalpy, entropy, heat capacity	Solid-state reaction rates	Conductivity	Interfacial tensions	Tensile strength
Free energy	Physical/chemical stability	Morphology	Habit	Compactability
	Rate of nucleation		Colour	Flow properties

It is, therefore, fundamentally important to identify possible polymorphs of an API and their relative stability during early stages of development, prior to the manufacturing process. Different thermodynamic properties of these forms can significantly affect the properties of the drug during storage and handling.[101] One well documented example of the effect of lack of understanding of API polymorphism on the drug formulation quality is that of ritonavir, marketed firstly as Norvir by Abbot Laboratories.[103] The occurrence of a new thermodynamically more stable and less soluble crystalline phase of ritonavir (form II) in the marketed formulation of Norvir resulted in decreased bioavailability of the drug. This in turn led to the temporary withdrawal of the product from the market affecting the supply chain of the lifesaving drug.[103,104] The company had to prepare new formulation of the drug using ritonavir form II as the previously used phase (form I) could not be stabilised within the formulation.[103,104]

The transitions between different polymorphs occur to increase the stability of the system through the decrease of the Gibbs free energy. Thermodynamically, the relationship between two phases can be either monotropic or enantiotropic. For an enantiotropic system, reversible phase transition

between two phase is possible through the changes of temperature of the system. In monotropic system any transition from one polymorph to another is irreversible below the melting point.[101] The pharmaceutical processing (*e.g.*, wet granulation or milling) may trigger the polymorphic transition between different crystalline phases of API. It is therefore important to understand relative stability of different phases during development process and identify the candidate which demonstrates a compromise between desirable properties and physical stability in the formulation.[101] Although polymorphism is not a recently discovered phenomenon, the controllable and predictable formation of polymorphs is a broad and challenging field of the interest in chemical and pharmaceutical sciences.

1.6   Thermal behaviour of confined solids

The phase behaviour of small molecules (gases, organic liquids, water), polymers and metals constrained in the nanosize spaces have been widely studied since the first observation of the pore size dependent decrease of glass transition temperature of confined liquids by Jackson and McKenna in 1991.[105–109] Although much work has been done to understand the phase behaviour of nanoencapsulated materials, there is still a lack of molecular level understanding of the impact of mesoscopic confinement and surface chemistry on phase transition, formation of clusters and specific molecular alignment inside the mesopores.[106–109] Understanding of such complex heterogeneous systems requires combined application of analytical methods, which enable probing of both structure and dynamics of confined molecules at the molecular level.

The phase behaviour of encapsulated materials is different to that of the bulk size species mostly due to the changes in the surface-to-volume ratio of the nanosize confined solids.[93,106,110] This phenomenon is the most noticeable in the melting point depression, which is correlated with the size of the crystal (Figure 1-8 A. C.).[93,110,111] The melting point depression of a nanocrystal in relation to the melting temperature of a bulk phase is described by the Gibbs-Thomson equation (Eq. 1-1):

$$\frac{\Delta T_m}{T_{m,bulk}} = -\frac{2M}{\Delta H^{fus}\rho r}\gamma_{nl}\cos\theta \qquad\qquad \text{(Eq. 1-1)}$$

where M is the molecular mass of the chemical compound, ρ is the particle density, r is the particle radius (assuming spherical shape), γ_{nl} is the specific interfacial energy (surface tension) between the solid phase and the surrounding it fluid, θ is the interfacial angle between the nucleating condensed phase and the contacting surface, ΔH^{fus} is the molar heat of fusion of the bulk solid phase, ΔT_m is the change in the melting temperature between bulk and the solid with radius (r) and $T_{m,bulk}$ is the melting temperature of the bulk solid (r→∞).[93,110] The equation predicts the change in

the melting point ΔT_m as a linear function of inverse particle radius (1/r), assuming that other parameters are constant and size independent.[93,110] For the practical use of the (Eq. 1-1) the contact angle of 180° is assumed, indicating that the confined nuclei are homogenous and do not wet the surface of the pore.[93,110] Therefore, the equation (Eq. 1-1) simplifies to the form given in (Eq. 1-2):

$$\frac{\Delta T_m}{T_{m,bulk}} = -\frac{2M}{\Delta H^{fus}\rho r}\gamma_{nl} \qquad \text{(Eq. 1-2)}$$

It was hypothesised that confined materials form a liquid-like non-freezing layer of the thickness of one or two molecules at the pore surface prior to the formation of solid in the centre of the pore.[107] This layer effectively changes the diameter of frozen or crystalline material inside the pores and may change the phase behaviour of confined molecules likely due to changes of energy of the system. Furthermore, the presence of a molecular liquid-like layer may be reason for enhanced mobility of confined molecules and a decreased average enthalpy of melting of confined crystals.[107] This may also explain observed increased mobility of amorphous pharmaceuticals confined within MCM-41 and SBA-15 silicas[77,79,90,112]

To encompass the dependence of the melting point on the interfacial energies between the nucleus, and surrounding liquid and surface one may combine the Young equation (Eq. 1-3) with the simplified Gibbs-Thomson equation (Eq. 1-2) equation leading to (Eq. 1-4) (Figure 1-8 C.):

$$\gamma_{ns} - \gamma_{sl} = \gamma_{nl}\cos\theta \qquad \text{(Eq. 1-3)}$$

$$\frac{\Delta T_m}{T_{m,bulk}} = -\frac{2M(\gamma_{ns}-\gamma_{sl})}{\Delta H^{fus}\rho r} \qquad \text{(Eq. 1-4)}$$

where γ_{ns} is the interfacial energy between the particle and surface, γ_{sl} is the interfacial energy between the surface and liquid and γ_{nl} is the interfacial energy between the particle and liquid.
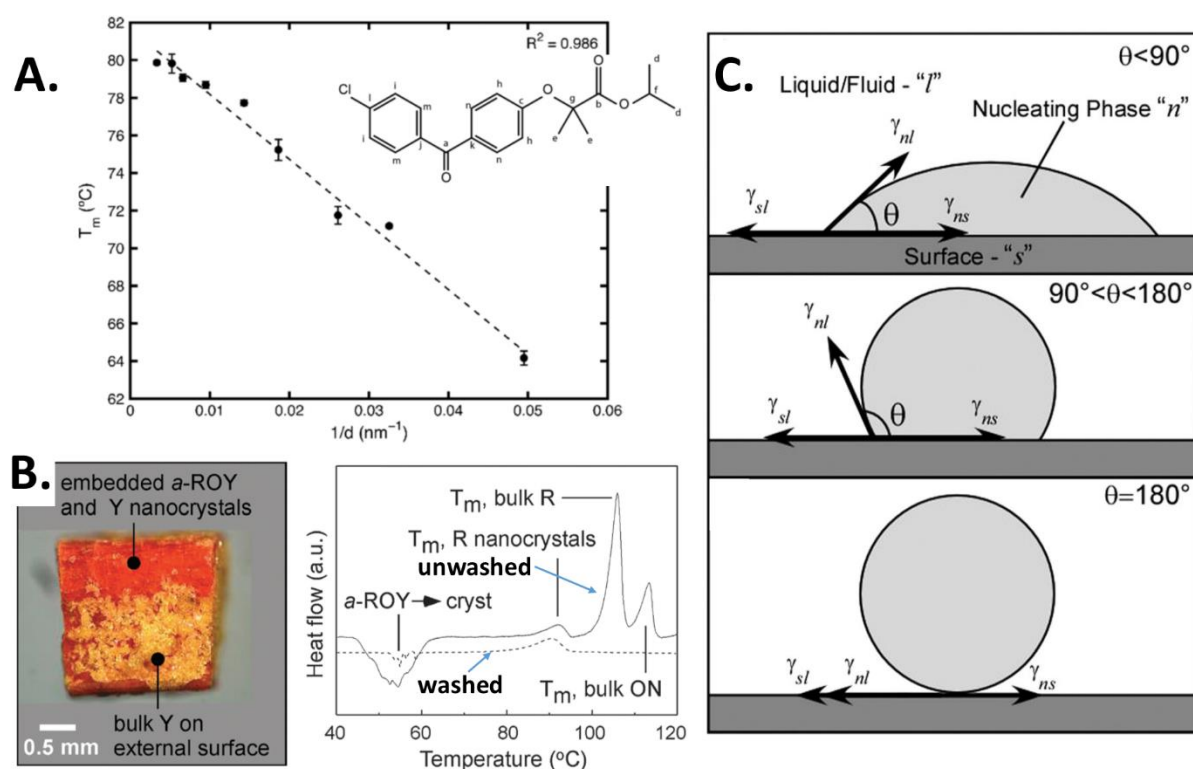
Figure 1-8. A. Linear inverse relationship between melting point of confined fenofibrate and pore size diameter; **B.** Use of the melting point depression to distinguish between bulk and confined crystals of ROY (5-methyl-2-[(2-nitrophenyl)amino]-3-thiophenecarbonitrile). Washed composites shows only melting point of confined species; **C.** Illustration of the static equilibrium described by the Young equation: **Top:** favourable surface-nucleus interactions, (wetting of the surface), **Middle:** unfavourable surface-nucleus interactions 90° < θ < 180° (poor wetting), **Bottom:** absence of surface wetting – assumption for simplified Gibbs-Thomson equation. Adapted from [93,110,111]

The decrease of the melting point of confined nanocrystals is an important indicator, which enables distinguishing between bulk and encapsulated crystalline phase (Figure 1-8 B.). It has been used in confined crystallisation studies to confirm the formation of encapsulated crystals.[113–115] This fundamental property of nanosize crystals was used in this study to assess the extent of the loading of the drug within the silica pores and to distinguish drug molecules loaded outside the pores of the scaffold from encapsulated crystalline pharmaceuticals.

1.7 Formation of nanocrystalline solids inside mesoporous silicas

The crystallisation outcome is determined very early during nucleation and strongly depends on the size of critical nuclei formed during crystal nucleation.[94] Therefore, it is possible to control the crystallisation outcome through the control of the size of critical nucleus by encapsulation of the molecules inside nanopores, which are of the size of critical nuclei.[93,110,114,116]

Investigation of crystallisation processes of organic molecules within mesoscopic confinement of CPG (controlled pore glasses) materials, polymeric monoliths and AAO membranes (anodic aluminium oxide) was started by Ward *et al.* and Beiner *at al.* [113–115,117–119] and recently reviewed by Ward *et. al.*[93,110] Ha *et al.* demonstrated selective crystallisation of a metastable polymorph of anthranilic acid within 7.5 nm pores of CPG host.[116] Using a well-known polymorphic model compound ROY [5-methyl-2-[(2-nitrophenyl)-amino]-3-thiophenecarbonitrile] confined inside 30 nm pores of polymer monolith the authors were able to exclusively obtain red prisms of the compound.[116] Interestingly, crystallisation of ROY inside smaller pores of 20 nm was successively suppressed indicating critical size effects.[116] In another study, Ward and co-workers obtained new polymorphs of pimelic acid, suberic acid and coumarine encapsulated in the CPG and polymer monoliths with pores size diameter smaller than 23 nm and 40 nm respectively.[115] Additionally, the authors noted that enantiotropic phase behaviour of glutaric acid and suberic acid in the bulk is switched to monothropic upon the confinement in CPG and p-PCHE monoliths.[115] Beiner *et al.* demonstrated selective crystallisation of metastable polymorph of paracetamol inside the pores of CPG between 22 and 103 nm and stabilisation of amorphous drug inside the pores smaller than 10 nm.[113,114]

The controlled crystallisation of organic molecules inside the mesoporous materials is a growing and attractive area of crystal engineering as it enables discoveries of new crystalline phases and stabilisation of metastable polymorphs inside the nanopores. Despite the increasing amount of research in the field, the effect of the pore size and surface properties on the confined crystallisation outcome is poorly understood and largely unpredictable. Therefore, there is a need for systematic studies of drug-silica systems to gain full understanding of these complex heterogeneous materials. The application of solid-state NMR due to its sensitivity to local environment of atoms may help to gain an insight into molecular aggregation processes on the nanoscale and role of the interface in directing crystallisation towards new or metastable polymorphs.

1.8 Aims of the project

Despite the increasing amount of published research on mesoporous silicas for drug delivery, there is still a lack of molecular level understanding of host-guest chemistry between the silica scaffold and encapsulated molecules. The understanding of the physical stability and possible phase transitions of confined molecules is of importance for knowledge based design of new functional porous materials, which can be used as drug carriers. Further developments in this field, for example tuning the surface properties through the incorporation of additional functionalities, or encapsulation of complex biomolecules require an in-depth understanding of the host-guest interactions in model materials.

As molecules intercalated in the mesopores can be frequently found in the amorphous state, the detailed structural analysis of silica-drug composite solids using methods sensitive to long range ordering is limited. Confined nanocrystalline solids pose significant analytical challenge due to the broadening of the PXRD peaks and decrease and broadening of the melting point. These limitations of more traditional methods used in formulation science encourage us to exploit the huge potential of solid-state NMR towards molecular level understanding of structure and dynamics of pharmaceutical molecules encapsulated within the mesoporous silicas.

Therefore, the project aims are divided into synthetic and analytical categories. Firstly, we will develop synthetic procedures for encapsulation of model pharmaceuticals (IMC, FFA, TB), with different structural and physicochemical properties within the pores of model mesoporous silicas, namely MCM-41, SBA-15, MCF and CPG, which differ in the pore size diameter and available surface area and pore volume for drug adsorption. Synthesis of homogenous composites, with different loading levels and all drug molecules encapsulated inside the pores of silica is not trivial and requires development of control methods and efficient screening techniques prior to advanced characterisation using solid-state NMR. Due to this we aim to develop a multi technique approach in order to assure unequivocally the deposition of the drug molecules exclusively in the silica pores. This will employ the combined use of nitrogen physisorption together with diffraction (PXRD), thermal (DSC, TGA), microscopic (SEM) methods.

Secondly, through the combined application of the ^{1}H-^{13}C excitation methods, which are sensitive to different molecular motions and ^{1}H $T_{1(\rho)}$ relaxation measurements we aim to investigate local structure and dynamics of molecules confined within mesoporous silicas and identify species in different environments. By using materials with different pore sizes and different levels of drug content within the pores we aim to investigate molecular aggregation in confined geometries to develop models for better understanding of crystallisation processes at different length scales. Through the application of variable temperature studies and relaxation measurement we are going

to obtain clearer information on the dynamics of confined molecules alongside development of *in situ* methods NMR for monitoring the phase transitions of encapsulated molecules. Finally, the physical stability of the confined species in contact with organic solvents or atmospheric moisture will be investigated through an accelerated stability study at 75 % RH. This will determine the performance of the materials during long term storage and further enable us to gain an insight into microsolvation of confined species during early stages of drug dissolution and release, which is of importance from industrial perspective.

Finally, we aim to develop combined computational and solid-state NMR approach, to determine the conformation of indomethacin molecules in two low crystallinity polymorphs and use this information in crystal structure prediction. In order to achieve this goal, we will perform calculation of ^{1}H and ^{13}C chemical shifts of IMC molecules isolated from different crystal structures available in the CSD using the CASTEP code, and identify ^{1}H and ^{13}C sites sensitive to major conformational changes. This information will be further applied for comparison of experimental and calculated chemical shifts of both investigated materials to determine the spatial position of structurally important motifs.

Characterisation Techniques

Chapter 2

2.1 Nuclear Magnetic Resonance (NMR)

Nuclear Magnetic Resonance (NMR) spectroscopy relies on the interaction of nuclei placed in an external magnetic field under the application of oscillating radiofrequency electromagnetic field, and is used to study structure and dynamics of a variety of materials, from solutions, through semi-solids and soft materials to solid materials. Full understanding of the NMR phenomenon and advanced methodology requires bringing together quantum mechanics and the product operator formulism, nevertheless semi-classical approach can be used to some extent to explain NMR concepts.

2.1.1 Basic NMR principles[120–123]

Nucleus, composed of protons and neutrons, with intrinsic properties including charge, mass and spin angular momentum ($\vec{I}$), give rise to a magnetic moment ($\vec{\mu}$) in an analogy to an electric charge, which creates magnetic field when rotating. The magnetic moment is proportional to the spin quantum number (I) and the gyromagnetic ratio, a constant characteristic for a particular nucleus. Only nuclei with spin quantum number I ≠ 0 are magnetically active (*e.g.*, $\frac{1}{2}, 1, \frac{3}{2}, 2, \frac{5}{2} \dots$). The magnetic moment of the nucleus is given as:

$$\vec{\mu} = \gamma \hbar \vec{I}$$
(Eq. 2-1)

where γ is the gyromagnetic ratio of a given nucleus, ħ is the reduced Planck's constant and $\vec{I}$ is the spin angular momentum.

The spin quantum number is related to the spin angular momentum, being a vector quantity through an equation:

$$\vec{I}^2 = (I(I + 1)\hbar^2)$$
(Eq. 2-2)

Without the application of strong external magnetic field, all 2I+1 orientations of $\vec{I}$ have the same energy. When a strong external magnetic field is applied (B_0), arbitrarily chosen to be oriented along the *z* axis, the magnetic moments will align either with (spin-up) or against (spin-down) the applied field. The energy associated with a magnetic moment can be considered as:

$$E = -\vec{\mu} B_0$$
(Eq. 2-3)

When a strong magnetic field oriented along the *z* axis is considered, the quantisation coincides with applied field B_0, and can be given as:

$$E = -\mu_z B_0 = -m\hbar\gamma B_0 \qquad \text{(Eq. 2-4)}$$

where m is the magnetic quantum number, taking 2I+1 values in integer steps between +I and −I with a selection rule $\Delta m = \pm 1$. The nuclear spin energy levels are now split into 2I+1 non-degenerate levels, which are separated by ΔE proportional to the applied field and the gyromagnetic ratio, and therefore different for each nucleus (Figure 2-1). This effect is known as Zeeman interaction or Zeeman splitting.

$$\Delta E = \hbar\gamma B_0 \qquad \text{(Eq. 2-5)}$$
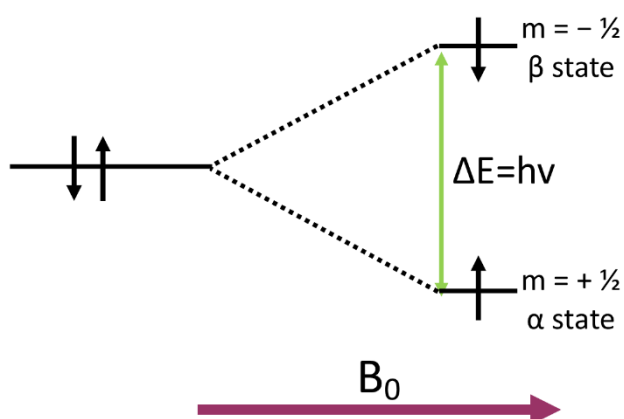
Figure 2-1. Relative energy levels and two magnetic a spin states (α and β) of spin ½ nucleus with increasing strength of external field B_0. Adapted from [120–122]

2.1.1.1 *Larmor precession*[120–123]

The overall net magnetisation of a nuclear spin is the result of its magnetic moment and the angular momentum of the spin. A nucleus placed in the external magnetic field B_0 experiences a torque, which acts on the magnetic moment and aligns it perpendicular to the field. The angular velocity (ω_0) of this motion is given by equation:

$$\omega_0 = -\gamma B_0 \, , \qquad \text{(Eq. 2-6)}$$

This motion is specific to each type of nucleus and is known as the Larmor frequency (v_0):

$$v_0 = \left|\frac{\gamma}{2\pi}\right| B_0 \qquad\qquad \text{(Eq. 2-7)}$$

If we assume a ^{1}H nucleus is placed in an external field of 9.4 T, its Larmor frequency is equal to 400 MHz. This is in the radiofrequency range of the electromagnetic spectrum and corresponds to the wavelength of 75 cm. When compared (Eq. 2-7) with (Eq. 2-5) it is evident that the energy difference between α and β spin states is proportional to the gyromagnetic ratio of the nucleus and applied external magnetic field, *i.e.,* Larmor frequency. Therefore, to induce NMR transitions radiofrequency radiation (radiofrequency (*rf*) pulses) close to that of Larmor frequency is required.

2.1.1.2 *Bulk magnetisation*[120–124]

In real samples we measure the interactions of large number of spins with the external magnetic field at the same time. In the case of multiple nuclear spins being placed in an external magnetic field (B_0) at temperature (T) thermal equilibrium is achieved according to the Boltzman distribution:

$$\frac{N_U}{N_L} = e^{\frac{-\Delta E}{kT}} \qquad\qquad \text{(Eq. 2-8)}$$

Where ΔE is the energy difference between spin states, k is the Boltzman constant, T is the absolute temperature and N is the population of spins in lower (L) and upper (U) states. Let us consider ^{1}H nuclei placed in a 9.4 T magnet at temperature T = 300 K. Based on (Eq. 2-8), the energy difference ΔE between two spin states equals 2.65×10^{-25} J and kT = 4.14×10^{-21} J, hence $\Delta E/kT = 6.4 \times 10^{-5}$. Therefore, for 1 million spins, an extremely small population difference of *ca.* 32 spins in the α state is observed as compared to the β state. This small difference of spins in α state forms a net magnetisation aligned along *z* axis which is called bulk magnetisation (M_0).
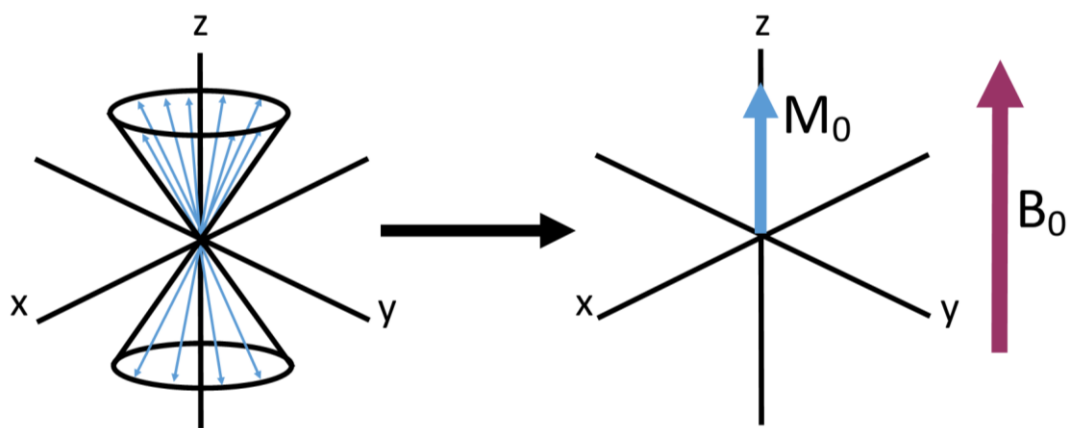
Figure 2-2. Vector model of bulk magnetisation for spin ½ nuclei, where differences in population of spins in both states give rise to bulk magnetisation M_0 aligned with B_0. Adapted from [124].

As mentioned in the previous section, to satisfy the energy difference between α and β spin states radiofrequency pulses close to the Larmor frequency can be used to induce NMR transitions. This is simply done by passing current *via* a coil surrounding the sample, which in turn produces a magnetic field of the applied *rf* field denoted B_1. The introduced magnetic field B_1 is oscillating at the Larmor frequency of the spin in the transverse plane, perpendicular to B_0 (*z* axis). To aid visualisation of the effects of *rf* pulses on the bulk magnetisation, the concept of a rotating frame of reference was introduced (Figure 2-3).
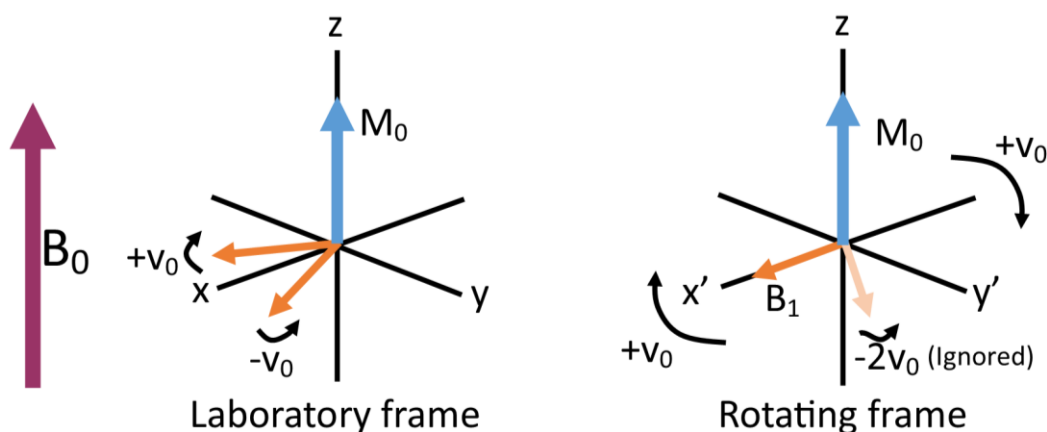
Figure 2-3. Representation of laboratory and rotating frame of reference. Adapted from [124]

In the laboratory frame x, y, z coordinates are viewed as static, while the rotating frame of reference uses coordinates x', y' which are rotating with the frequency of nuclear precession. The magnetic field introduced by the *rf* pulse oscillates in the transverse plane with a nuclear precession (for NMR

condition to be satisfied), represented by $\pm v_0$ in Figure 2-3. In the rotating frame of reference one of the *rf* field vectors is now static and the second rotates with $2v_0$ in opposite (-) direction far from resonance and can be ignored. Therefore, in the rotating frame, time dependency of the *rf* field is removed and both M_0 and B_1 are seen as static and perpendicular to each other.

2.1.1.3 Chemical shift[120–123]

As discussed in the previous sections the resonance frequency of a particular nucleus depends on its gyromagnetic ratio (γ) and applied external field B_0. If only one resonance frequency was observed for a particular nucleus, NMR would be a rather limited analytical technique. In reality, one can observe a spared of the resonance frequencies for each nucleus in the NMR spectrum. This is due to the NMR frequency being sensitive to the local environment of the nucleus in the molecule, which in turn is affected not only by the external magnetic field but also by the surrounding electrons.

Electrons circulating in their orbitals can be seen in a similar way as current passing through the wire producing small (local) magnetic field in the opposite direction to B_0. This secondary field which adds to the field felt by nucleus, is called the shielding interaction, and depends on the chemical environment of the nuclei giving rise to the chemical shift (δ).

The effective (local) magnetic field (B) felt by the nucleus is slightly smaller than the applied external magnetic field (B_0) and is given by the equation:

$$B = B_0 - B' = B_0(1 - \sigma) \qquad \text{(Eq. 2-9)}$$

where σ is the shielding constant.

The electron density around atoms in molecules is rather complex and depends on several factors including formation of bonds, presence of electronegative nuclei in close proximity, unpaired electrons or through space interactions within molecular clusters. Experimentally, chemical shift (γ) is measured as a frequency difference of the analysed nucleus (v) with respect to the reference nucleus (v_{ref}) of known frequency and presented on the ppm (parts per million) scale:

$$\delta = 10^6 \left(\frac{v - v_{ref}}{v_{ref}} \right) \qquad \text{(Eq. 2-10)}$$

For different nuclei there are different reference compounds used as standards *e.g.,* TMS (tetramethylsilane) being a reference for ^{1}H, ^{29}Si, ^{13}C chemical shift or 1 M NaCl solution as a reference for ^{23}Na chemical shift.

2.1.2 Solid-state NMR[125,126]

Nuclear spin interactions in solid state have very different effect on the spectrum compared to the same interactions in solution state. Nuclear spins of dissolved molecules interacting with external magnetic field average most of their interactions due to fast molecular tumbling, leading to narrow isotropic (orientation independent) chemical shifts. In solid state, due to significantly decreased molecular motions, orientation dependent nuclear spin interactions are no longer averaged as in solution state, leading to broadening of the NMR peaks.

The energy of different types of interactions of nuclear spin with local magnetic field can be described in quantum mechanical terms using Hamiltonian operators ($\hat{H}$):

$$\hat{H} = \vec{I} \cdot A \cdot \vec{B} \, , \qquad\qquad\qquad \text{(Eq. 2-11)}$$

where *A* is the orientation dependence of the NMR interaction with respect to the *x, y, z* axes and $\vec{B}$ represents the external magnetic field. The quantum mechanical description of the energy of nuclear spin interactions, which may contribute to the observed line widths in the NMR spectrum, are implemented in the spin Hamiltonian equation:

$$\hat{H}_{TOTAL} = \hat{H}_z + \hat{H}_{CSA} + \hat{H}_D + \hat{H}_Q + \hat{H}_J \qquad \text{(Eq. 2-12)}$$

Where $\hat{H}_z$ is the Zeeman interaction Hamiltonian, $\hat{H}_{CSA}$ is the chemical shift anisotropy Hamiltonian, $\hat{H}_D$ is the dipolar coupling Hamiltonian, $\hat{H}_Q$ is the quadrupolar coupling Hamiltonian (observed only if I > 1) and $\hat{H}_J$ is the J-coupling Hamiltonian.

The above equation for molecules undergoing significant molecular motions, *i.e.*, for isotropic liquid, is simplified and only the Zeeman interaction ($\hat{H}_Z$), the isotropic chemical shift interaction ($\hat{H}_{CS}$) and the spin-spin (J-coupling) interaction ($\hat{H}_J$) are observed.

2.1.3 Nuclear magnetic interactions[125,126]

In solid-state NMR orientation dependant interactions contribute to significant broadening of the resonances, therefore several methodologies have been developed to overcome CSA interactions,

dipolar coupling interactions and quadrupolar coupling interactions (not observed in this research). Zeeman interactions are of the same order of magnitude in solid and solution state, and J-coupling interactions in solid-state NMR are considerably smaller compared than the anisotropic interactions. Therefore, only chemical shift anisotropy and dipolar interactions will be discussed in the following sections.

2.1.3.1 Chemical shift anisotropy[125,126]

The chemical shift originates from the effect of the external magnetic field B_0 on the electrons of the nuclei circulating in its electronic cloud. An electron in motion produces a small magnetic field which in turn can add or subtract to the local field felt by a nucleus. The orientation dependence of this interaction is due to the fact that atoms in molecules rarely possess spherical and symmetrical electronic clouds. More often an electronic cloud can be seen as an ellipsoid which elongates in the direction of hydrogen bonds or bonding orbitals. As molecules in solution state are in the fast motional regime this interaction are isotropic; solid powdered materials, however, may adopt several different orientations with respect to the external magnetic field B_0. As the chemical shielding interaction felt by the nucleus is slightly different in all three dimensions, the distribution of chemical shifts is observed. This in turn leads to line broadening in the solid-state NMR spectra.
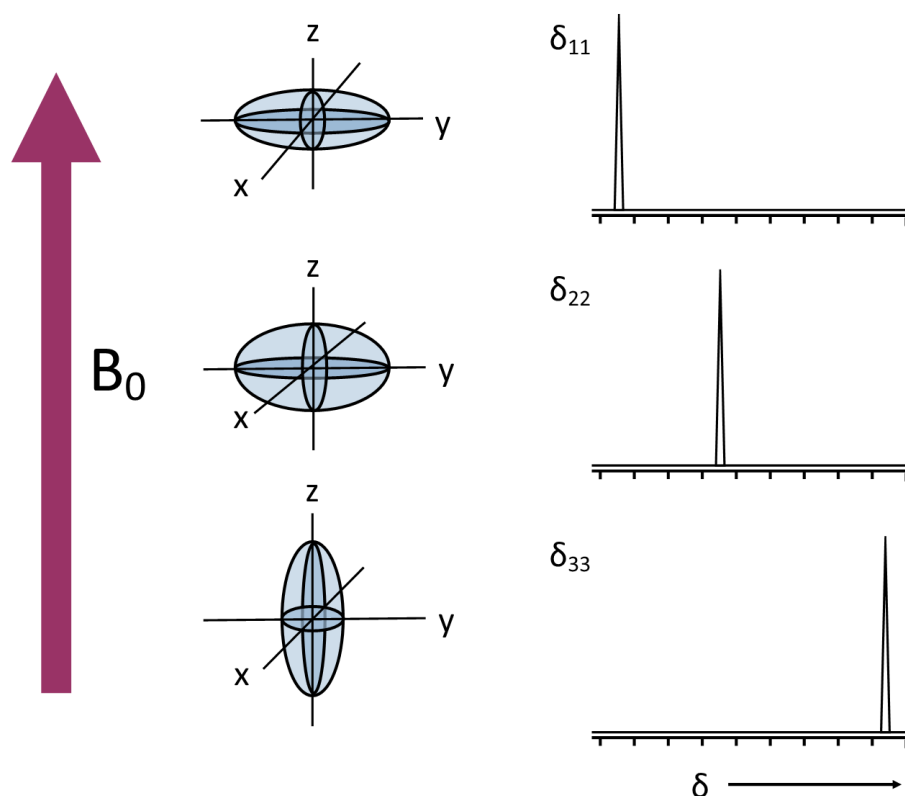
Figure 2-4. Principal values of the chemical shift tensor (δ_{11}, δ_{22}, δ_{33}) and its orientation dependence with respect to the external magnetic field. Adapted from [125].

For better understanding of the chemical shift Hamiltonian one can divide it into isotropic and anisotropic components. For a shielding tensor with axial symmetry, $\delta_{XX} = \delta_{YY}$, so that the ellipsoid will look like a symmetrical cigar in Figure 2-4, the chemical shift Hamiltonian equation is simplified to:

$$\widehat{H}_{CS} = \gamma B_0 I_z \left[\delta_{iso} + \frac{1}{2}\delta_{CSA}(3cos^2\theta - 1) \right] \qquad \text{(Eq. 2-13)}$$

where Θ describes the molecular orientation with respect to the external magnetic field, δ_{iso} is the isotropic chemical shielding factor, δ_{CSA} is the magnitude of CSA; using Haeberlen conventions for shielding parameters both the latter can be described through the equations :

$$\text{Isotropic shielding, } \delta_{iso} = \frac{1}{3}(\delta_{XX} + \delta_{YY} + \delta_{ZZ}) \qquad \text{(Eq. 2-14)}$$

$$\text{Anisotropy, } \zeta = \delta_{ZZ} - \delta_{iso} \qquad \text{(Eq. 2-15)}$$

The isotropic part of the Hamiltonian is simply an average of all three principal components of the chemical shift tensor, while the magnitude of the anisotropy is related to the isotropic chemical shift minus that of the widest part of the electronic cloud aligned with the external magnetic field B_0.

In real powder samples, molecules are aligned with all possible orientations, therefore a distribution of the chemical shifts is observed in the spectrum with the characteristic shape called powder pattern (Figure 2-5).
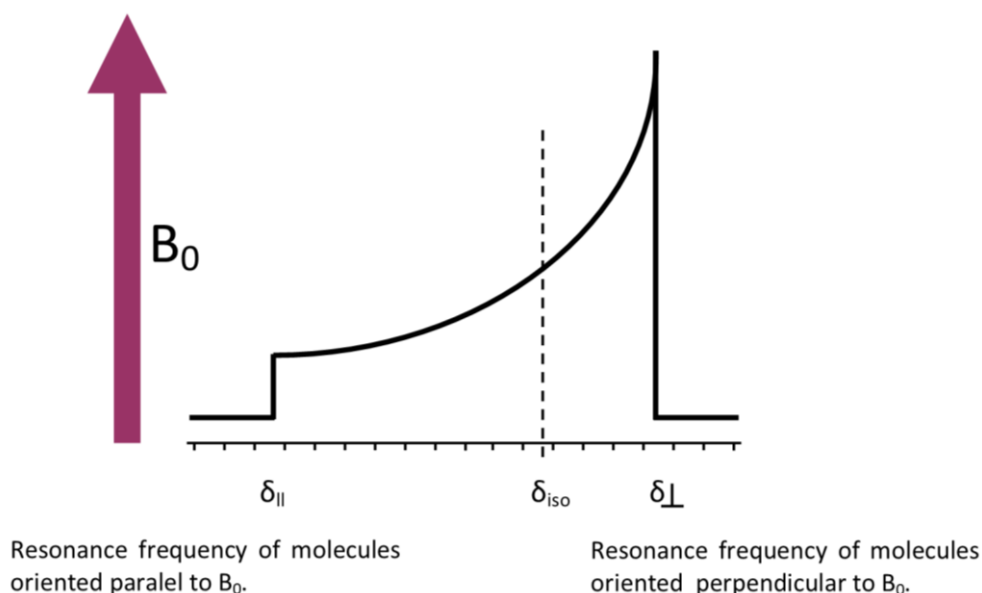
Figure 2-5. Static powder pattern of molecule having axial symmetry with respect to B_0. Adapted from[126].

The anisotropic component of the chemical shift Hamiltonian has a geometric component ($3cos^2\Theta-1$), which means that at a particular well-chosen axis this component of the chemical shift Hamiltonian can be eliminated. Techniques to eliminate CSA by using its geometrical dependence on the orientation angle with respect to static magnetic field will be discussed in section 2.1.4.1.

2.1.3.2 Dipolar coupling[125,126]

The dipolar coupling is a through space interaction between nuclear magnetic moments of two spins. It can either occur between two like spins (homonuclear, I-I) or two spins of different nuclei (heteronuclear, I-S). In solid-state NMR dipolar interactions can lead to significant line broadening, therefore experimental techniques which are used to overcome dipolar interactions are described in section 2.1.4.

A. Homonuclear dipolar couplings

The homonuclear dipolar coupling is an interaction between the magnetic moment of like spins which are close in space and the energy of this interaction for a two spin system can be described using the Hamiltonian:

$$\hat{H}_D^{homo} = -\left(\frac{\mu_0}{4\pi}\right)\left(\frac{\gamma_{I_1}\gamma_{I_2}\hbar}{r_{I_1I_2}^3}\right)\frac{1}{2}\left(3cos^2\Theta_{I_1I_2}-1\right)\left[2I_{1z}I_{2z}-\frac{1}{2}(I_1^+I_2^-+I_1^-I_2^+)\right] \quad \text{(Eq. 2-16)}$$

where I_1 and I_2 are like spins, $r_{I_1I_2}$ is the distance between both like spins, μ_0 is the permeability of free space and γ is the gyromagnetic ratio of each spin.

Despite its complexity, the dipolar Hamiltonian can be divided in three general terms, *i.e.*, the dipolar constant term labelled in green, the geometric term labelled in yellow and the spin term labelled in blue. The individual analysis of each of the three components of the dipolar Hamiltonian equation enables a better understanding of its effect on the NMR spectrum.

From the dipolar constant component it is evident that the dipolar interactions are directly proportional to the gyromagnetic ratio of interacting spins, and inversely proportional to the third power of the distance between two like spins. Therefore, it is evident that for abundant nuclei, with high gyromagnetic ratio, dipolar interactions are extremely strong (^{1}H-^{1}H in the range of 100 kHz), while for pairs of nuclei with low gyromagnetic ratio and low natural abundance (^{13}C-^{13}C or ^{29}Si-^{29}Si) these are almost negligible.

The geometric component of the equation describes the orientation dependence of the interaction and, as seen previously in CSA, it can be eliminated by alignment of the interacting spins along a particular axis with respect to the external magnetic field. This will be further discussed in section 2.1.4.1.

Finally, the spin term of the equation describes the energy conserving 'flip-flop' transition of two like spins with similar resonance frequencies. In this interaction one spin can 'flip' up to the higher energy state, while at the same time the second spin is 'flipping' down to the lower energy state. This interaction is commonly known as spin diffusion (Figure 2-6). The 'flip-flop' transition of two spins is given in the equation by two operators: I$^+$ (rising operator) and I$^-$ (lowering operator), which increase (I$^+$) or decrease (I$^-$) the angular momentum leading to transitions between two energy levels.
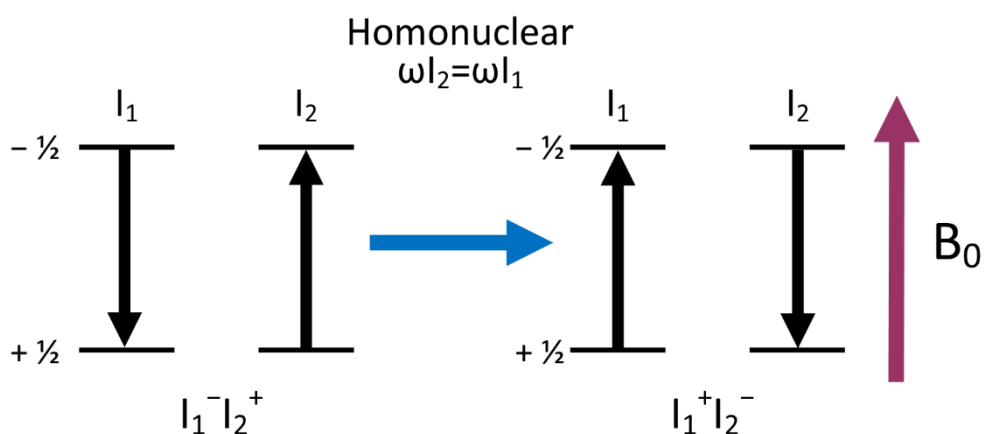
Figure 2-6. Schematic representation of 'flip-flop' transition of two like spins I$_1$ and I$_2$. Adapted from [125].

B. Heteronuclear dipolar couplings

The heteronuclear dipolar coupling is an interaction between the magnetic moments of two unlike spins being in close proximity to each other. In NMR terms two unlike spins can be labelled I (for abundant nuclei like ^1H or ^{19}F) and S (for rare nuclei like ^{13}C or ^{29}Si). In the presence of the external magnetic field both spins I and S undergo the Zeeman interaction and align themselves either with (spin up) or against (spin down) the external magnetic field (B_0). As each of the spins possesses nuclear magnetic moment they can be seen as small magnets with a local magnetic field. Therefore, if spin I is in close proximity to spin S its local magnetic field will be affected by the local magnetic field of spin S and vice versa. The energy of the interaction is described using the dipolar Hamiltonian:

$$\hat{H}_D^{hetero} = -\left(\frac{\mu_0}{4\pi}\right)\left(\frac{\gamma_I\gamma_S\hbar}{r_{IS}^3}\right)(3cos^2\Theta_{IS} - 1)I_zS_z \qquad \text{(Eq. 2-17)}$$

The heteronuclear dipolar coupling Hamiltonian has a similar form to the homonuclear dipolar Hamiltonian, however its spin component is significantly reduced. This is due to the energy conserving 'flip-flop' transition being only possible between two spins with similar resonance frequencies (Figure 2-7). The strength of the dipolar interaction between unlike spins, similarly to like spins, depends on the gyromagnetic ratio of interacting spins, the distance between them and their orientation with respect to the external magnetic field.
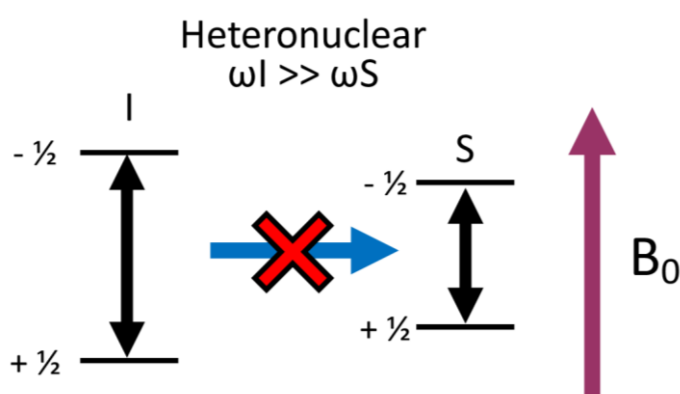
Figure 2-7. For two spins I and S with different frequencies energy conserving 'flip-flop' transitions cannot occur. Adapted from [125]

The effect of the heteronuclear dipolar coupling between two spins I and S on the NMR spectrum of a polycrystalline powder sample, where all crystallites have random orientation with respect to

the external magnetic field, is represented by Pake pattern (Figure 2-8). The observed Pake doublet is a result of the orientation dependence of the two spin states (α and β) with respect to the external magnetic field, where Ө is between 0° and 90°. The maximum intensity of the 'horn' is observed when molecules are aligned perpendicularly with respect to B_0. The splitting of Pake doublet is equal to the dipolar coupling constant (D). When the sample is placed at an angle Ө=54.74° the resonance frequency is not dependant of the heteronuclear dipolar constant, as the geometric term of the Hamiltonian is averaged out, $(3\cos^2Ө – 1) = 0$. This angle is known in solid-state NMR as the 'magic angle' and, as it will be shown in next sections, alignment along this axis can effectively reduce or totally remove geometry dependence of the nuclear spin interactions.
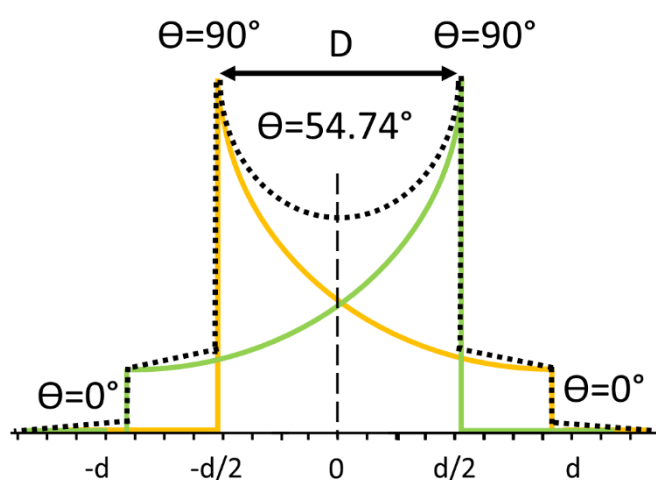
Figure 2-8. Powder pattern (Pake doublet) resulting from heteronuclear dipolar interactions between two unlike (I and S) spin ½ nuclei. Adapted from [26,125,126].

2.1.4   Experimental techniques in solid-state NMR

The complexity of nuclear spins interactions with the external magnetic field and with each other makes NMR spectroscopy challenging to apply in solid samples. As the field of solid-state NMR has been further developed, several experimental techniques have been proposed and successfully implemented in commercially available spectrometers to either compensate or selectively extract the most important interactions of interacting spins, gaining molecular level information of solid materials. The most frequently used experimental methodologies are described in the following sections.

2.1.4.1   *Magic angle spinning (MAS)*[125,126]

The orientation dependence of the spin-spin interactions described by the term $(3\cos^2Ө-1)$ in CSA and dipolar coupling Hamiltonians can be eliminated assuming the analysed material is spun at an

angle of 54.74° with respect to the external magnetic field (Figure 2-9). By spinning a sample at the 'magic angle' conditions, the geometric term ($3cos^2\Theta-1$) is averaged to 0 and the anisotropy of the interactions is eliminated, resulting in an isotropic chemical shift. This was firstly proposed by Andrew *et al*. in 1958 for a single crystal of sodium chloride and revolutionised the field of solid-state NMR.[127]
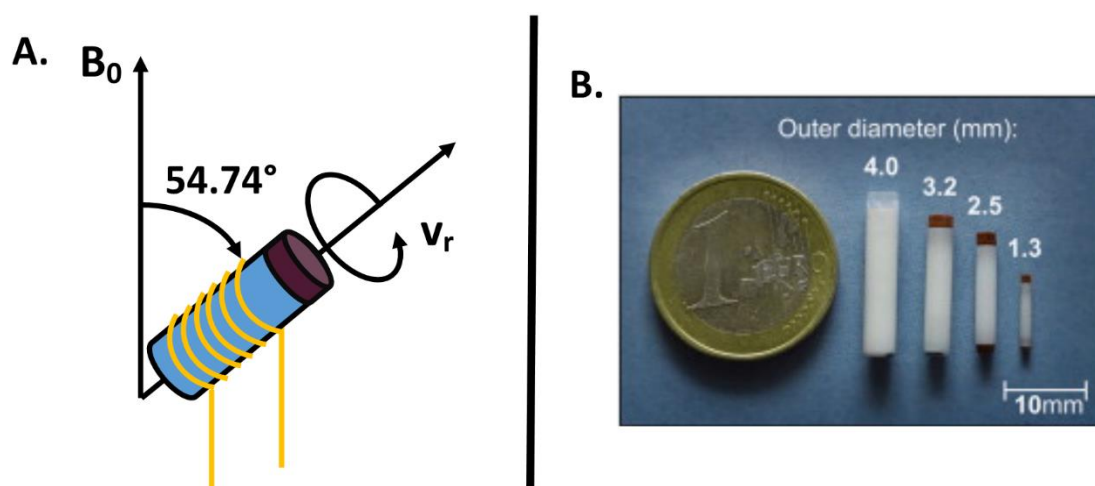
Figure 2-9. A. Schematic representation of the NMR rotor aligned at a 'magic angle' with respect to the external magnetic field. **B.** Variety of NMR rotor sizes available to reach different MAS rates. Adapted from[128]

To effectively eliminate the geometric term of the spin-spin interaction described by the Hamiltonians, MAS rates need to be at least three times higher than the strength of the interactions. For example, the ^{1}H-^{13}C heteronuclear dipolar coupling can be successfully eliminated by the application of an MAS rate of 10-15 kHz. Much stronger interactions (in the range of *ca.* 80 kHz) are frequently observed in solid-state NMR for the homonuclear dipolar couplings of high abundance, high gyromagnetic ratio nuclei (^{1}H, ^{19}F). Although in such cases the application of ultrafast MAS rates of 120 kHz is now possible with currently developed solid-state NMR probes, the dipolar interactions cannot be fully averaged and are still present in the spectrum.

2.1.4.2 Decoupling and rf pulses[125,126]

As seen in the previous section, MAS is an effective technique to eliminate CSA, however it shows limitations when applied to systems with strong homo- and heteronuclear dipolar couplings. Therefore, to further improve the resolution of solid-state NMR spectra of such materials, decoupling techniques using complex *rf* pulses were developed. Through the analysis of the dipolar Hamiltonian (section 2.1.3.2) one can see differences in the spin term of the equation when like or

unlike spin couples are considered. Due to differences in homo- and heteronuclear decoupling, such schemes will be discussed separately in next two sections.

A. Heteronuclear decoupling

Let us consider a pair of spins, abundant (I) and dilute (S), being in close proximity such that dipolar interactions are possible, leading to significant broadening of the spectral lines (*e.g.*, directly bounded ^{1}H to ^{13}C with a dipolar interaction equal 30 kHz). Based on the heteronuclear dipolar Hamiltonian one can think of eliminating the dipolar interaction in two ways: either by the application of MAS to average the geometrical term of the Hamiltonian, or by the manipulation of the spin part of the Hamiltonian equation in such a way that the effect of the abundant spin I on the dilute spin S averages to 0 over time. This can be achieved through the application of continuous high power irradiation at a frequency close to the frequency of the abundant spin (I) during FID acquisition of the dilute spin (S). This method, called continuous wave (CW) spin decoupling,[129] results in continuous exchange of spins between high and low energy states at a rate determined by the decoupling power. As the continuous application of decoupling *rf* pulses during long acquisition periods may lead to sample (and probe) overheating, CW decoupling method is not frequently used as more robust, and material (probe) friendly, decoupling techniques were developed.

The most frequently used pulse sequence for heteronuclear dipolar decoupling is the two pulse phase modulation (TPPM)[130] which consist of two high power pulses $P = 165° + \varphi$ and $\bar{P} = 165° - \varphi$ with a phase shift (φ) of 10 to 70°. This pulse sequence was further employed to build supercycles of high decoupling efficiency known as SPINAL-X[131] (where X is number of P or $\bar{P}$ pulses in the supercycle *i.e.*, 16, 32, 64 or 128).

B. Homonuclear decoupling

Homonuclear dipolar coupling interactions are much more difficult to overcome due to the complexity of the spin term in the Hamiltonian equation. Similarly to the heteronuclear dipolar coupling Hamiltonian the geometric term of the equation can be eliminated by the application of 'magic angle' spinning, however the spin term is much more difficult to overcome as the magnetisation of two interacting like nuclei cannot be manipulated independently. Many pulse sequences have been developed to average the spin term of the homonuclear dipolar Hamiltonian with two main decoupling methods based on multi-pulse or phase modulated sequences.
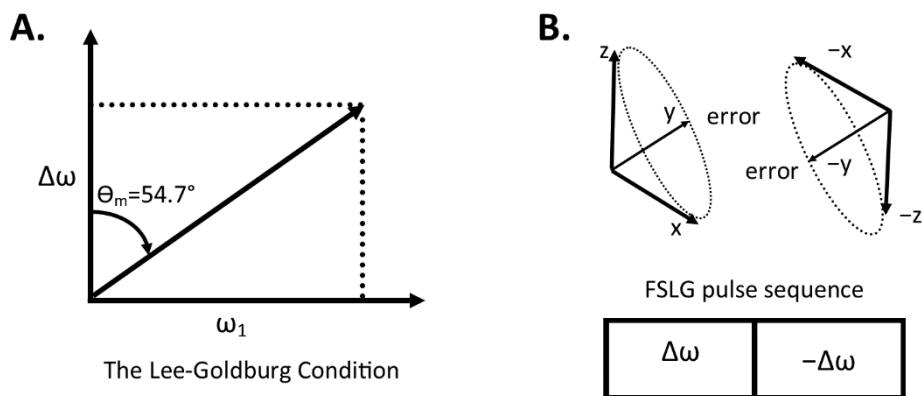
Figure 2-10. A. Schematic representation of LG conditions. An effective magnetic field is created along the 'magic angle' axis when the *rf* offset ($\Delta\omega$) and pulse amplitude (ω_1) is set in the way it coincides with the 'magic angle' ($\Delta\omega = \omega_1\sqrt{2}$). **B.** FSLG pulse sequence for compensation of errors in magnetisation rejections by frequency switch. Adapted from [26,125].

In the frequently used multi-pulse sequence based on Lee-Goldburg (LG)[132] condition, *i.e.,* Frequency-Switched-Lee-Goldburg (FSLG),[133] an off-resonance *rf* pulse is applied with the offset value:

$$\Delta\omega = \omega_1 \tan\theta_m \qquad\qquad (Eq.\ 2\text{-}18)$$

where $\Delta\omega$ is a LG offset and θ_m is the 'magic angle'.

The applied rf pulse creates an effective rf field in the rotating frame which is aligned at the 'magic angle' with respect to the laboratory frame (B_0). The efficiency of the LG sequence was further improved by the application of frequency switch from positive to negative ($\Delta\omega$; $-\Delta\omega$) to average out pulse imperfections.

As simultaneous phase and frequency jumps were difficult to apply in many commercial spectrometers at the time of the development of the FSLG sequence, next generation of pulse sequences based on discrete phase modulation of on-resonance pulses were developed (PMLG[134] – phase modulated Lee-Goldburg, DUMBO[135] – decoupling using mind boggling optimisation). The homonuclear decoupling pulse sequences like PMLG and DUMBO show very good performance at relatively low MAS rates. At increased spinning speeds the decoupling performance of both pulse sequences diminishes, as the *rf* pulse cycling gets closer to the rotor periods. Both Lee-Goldburg based (FSLG[133] and PMLG[134]) homonuclear decoupling sequences were used throughout this work

to record high resolution ^{1}H spectra of pharmaceutical polymorphs and in HETeronuclear CORelation experiments as a decoupling scheme within the indirect dimension. Furthermore, we were able to compare the decoupling performance of fast MAS (75 kHz) at 20.0 T with the PMLG pulse sequence used at 9.4 T and 6.8 kHz spinning speed, which happened to be extremely robust when properly optimised (Chapter 4).

2.1.5 Cross polarisation (CP)[125,126,136,137]

Cross polarisation is a double-resonance technique which is frequently used in solid-state NMR to increase sensitivity of dilute spins like ^{29}Si (natural abundance (NA) = 4.7 %), ^{13}C (NA = 1.1 %) and ^{15}N (NA = 0.03 %). Furthermore, the application of CP is particularly useful when dilute nuclei have a low gyromagnetic ratio, as the acquisition of good quality spectra of such nuclei is of significant challenge using the Bloch decay experiment. The second problem frequently encountered during the acquisition of spectra of low abundance spin ½ nuclei is their long relaxation time, in the order of tens second for ^{13}C in organic solids and minutes for ^{29}Si in framework materials. As relaxation is highly enhanced by homonuclear dipolar interactions, which are rarely observed for low abundance spins, only much less effective heteronuclear dipolar interactions participate in relaxation processes of dilute spins. The long spin-lattice relaxation times significantly increase the experimental time needed for acquisition of good quality spectra, as their recycle delay needs to be sufficiently long to allow longitudinal relaxation to occur.

Therefore, the application of CP pulse sequence eliminates both problems, as the magnetisation is transferred from high abundant spins to low abundant spins through the cross polarisation step, effectively reducing the number of scans and the recycle delay required to acquire good quality spectrum.

The transfer of magnetisation from high to low abundant spins is driven by dipolar couplings between both nuclei. Therefore, the local environment of the observed nuclei is very important. The principle of the CP experiment can be explained in a simplistic manner using the doubly rotating frame model (Figure 2-12). Within the first frame all I spins are processing at their Larmor frequency about B_0, with all magnetic fields generated by I spins appearing static. Similarly, within the second laboratory frame all S spins rotating at their Larmor frequency about B_0 appear to be static. Let us consider an initial I 90°x on-resonance pulse, which produces initial magnetisation along the -*y* axis in the I rotating frame. In the next step, the on-resonance -y I contact pulse is applied, which locks/holds the magnetisation along the -*y* axis and produces the so called spin lock field $B_1(I)$. When the contact pulse is applied, the spin locking field $B_1(I)$ is the only field acting on I spins so B_0 effects on abundant spins vanishes. At the same time the contact pulse is applied on the S spins producing $B_1(S)$ field in a rotating frame.
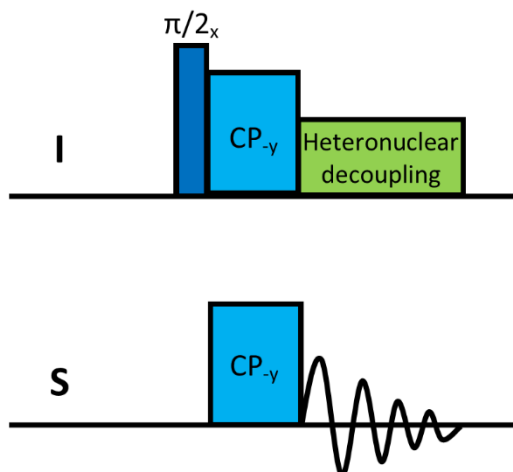
Figure 2-11. The cross polarisation pulse sequence. Full description is given in the text.

In order to transfer the magnetisation from abundant to dilute spins the amplitude of the contact pulses have to be carefully set in order to match the Hartmann-Hahn condition:

$$\gamma_I B_1(I) = \gamma_S B_1(S) \pm n\omega_r \qquad \text{(Eq. 2-19)}$$

where γ_I and γ_S is the gyromagnetic ratio of abundant and dilute nuclei and $B_1(I)$, $B_1(S)$ is the spin locking field in the rotating frame of I and S nuclei, and ω_r is the frequency of MAS respectively.

The Hartmann-Hahn match is met when both spins precess at the same rate in the rotating frame, *i.e.*, when the energy gaps of both spin states of spin I and S is equal (irrespective of their Zeeman energies in the laboratory frame).
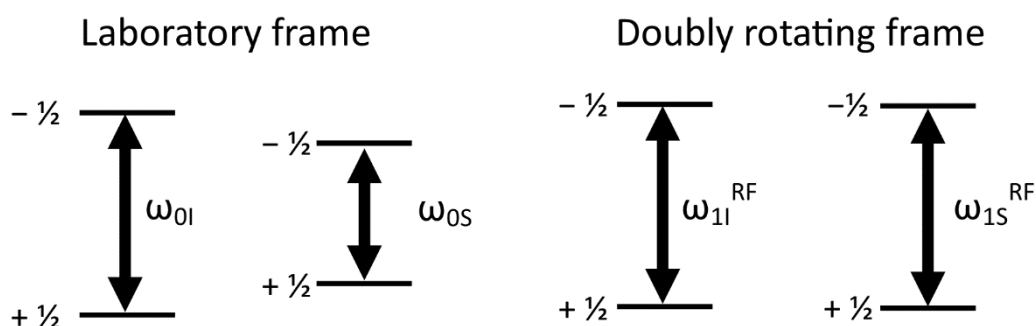
Figure 2-12. Differences in the energy gaps between spins I and S in laboratory and rotating frame when the Hartmann-Hahn condition is met. Adapted from [125].

The cross polarisation experiment can be explained using the dipolar-coupling operator describing the interaction between two spins S and I:

$$\hat{H}_D^{IS} = -\left(\frac{\mu_0}{4\pi}\right)\left(\frac{\gamma_I \gamma_S \hbar}{r_{IS}^3}\right)(3\cos^2\Theta_{IS} - 1)I_z S_z \qquad \text{(Eq. 2-20)}$$

The I_z and S_z operators are not altered by the rotation about the *z* axis only, therefore the heteronuclear dipolar Hamiltonian does not change when transferred in the doubly rotating frame. At this moment, both I and S spins are aligned perpendicularly to the *z* axis in the *xy* plane in their individual rotating frames. At this condition, the dipole-dipole operator cannot affect the net energy of the spin system as it depends on the applied field B_1 and on the magnetisation of spins aligned parallel to the quantisation axis. When the Hartmann-Hahn condition is met, the rotating frame energy gaps of spin I and S are equal, and dipolar interactions are possible. Hence, energy can be transferred between I and S spins in a conserving way that the total energy and polarisation of the system does not change.

2.1.6 Analysis of molecular motions using solid-state NMR spectroscopy

Analysis of molecular motions in solids is of huge interest in materials science as these may determine the properties of the materials, including stress resistance of polymers, physical stability and phase separation of drug-polymer amorphous solid dispersions[49] or understanding of phase transitions and stability of drug polymorphs. Solid-state NMR spectroscopy is a powerful method to probe molecular motions in solid-state at different time- and length scales, as different motional processes have an effect on the nuclear spins system on either the Larmor, spectral or relaxation timescales. These three characteristic timescales depend further on the sample, observed nuclei and physical parameters, *i.e.*, temperature and magnetic field.

There are several methods which can be used to probe dynamics in solid-state NMR. These include analysis of line shape, measurement of different relaxation times, exchange experiments or kinetics of polarisation transfer in CP experiments with different contact times. For better understanding of the experimental techniques that measure motional processes in solid-state NMR, relaxation phenomena are briefly described in this section.

2.1.6.1 Nuclear relaxation

For a particular spin system placed in the external magnetic field (for sufficiently long time) thermal equilibrium between spin populations in higher and lower energy levels is reached and can be predicted according to the Boltzmann distribution. After the application of a *rf* pulse, perturbation

of the distribution in the spin energy levels is observed and the system is no longer in equilibrium. Frequently, *rf* pulse generates spin coherence, which depends on the pulse magnitude, *i.e.*, the $\pi/2$ pulse transfers spins into the *xy* plane, while the π pulse inverts the spin system along the *z* axis.

The perturbed spin system will seek an equilibrium through the nuclear relaxation processes. That occurs either through spin-spin interactions (T_2 relaxation), or through energy (as heat) transfer to the surroundings, known as spin-lattice relaxation (T_1 relaxation).
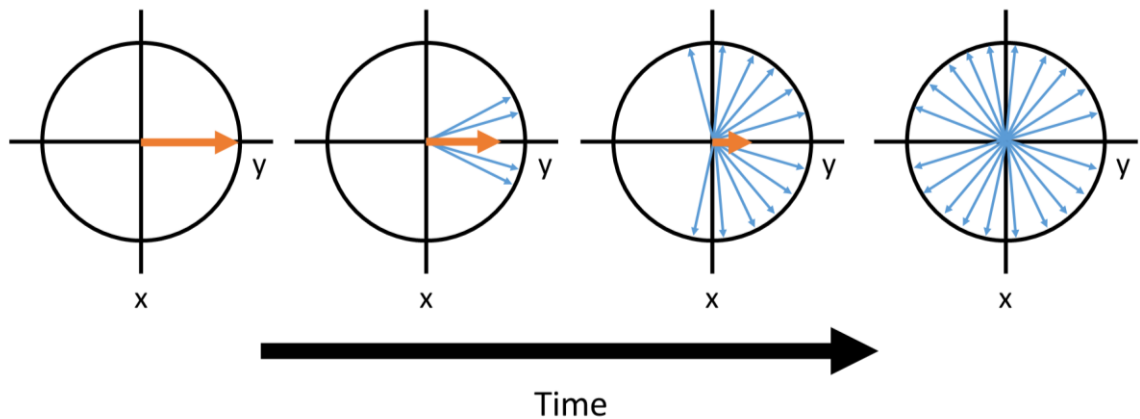
Figure 2-13. Transverse T_2 relaxation. Mutual exchange between spin levels and differences in local field results in loss of phase coherence leading to zero net magnetisation in the *xy* plane. Adapted from [124].

Spin-spin relaxation involves mutual exchange between the spin energy levels (α and β). That results in loss of coherence without change in the net energy of the system (Figure 2-13). Loss of the NMR signal related to T_2 relaxation is due to repetition of the exchange processes, which will randomise the phase. Furthermore, slight inhomogeneities in the magnetic field result in differences in precession frequencies (fanning out) of spins. This, in turn, leads to loss of phase coherence without net energy changes.
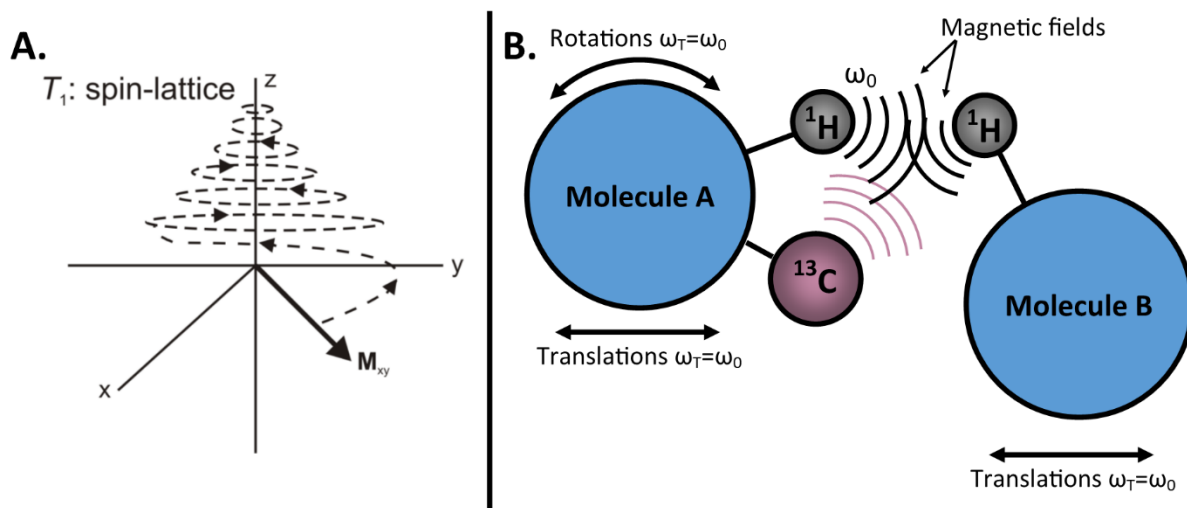
Figure 2-14. A. Re-establishment of magnetisation equilibrium through T_1. **B.** Effect of molecular motions on dipolar interactions between nuclei inducing fluctuations in the local magnetic field. Adapted from [26].

Spin-lattice relaxation (longitudinal relaxation) is a process in which Boltzmann distribution of spins is re-established through loss of heat energy to the surroundings (Figure 2-14). As the energy of the perturbed system is very small, no change in the temperature of the sample is observed due to this relaxation process. The T_1 relaxation is predominately governed by dipolar interactions, however different relaxation mechanisms are also possible, including CSA, quadrupolar interactions and spin-rotation. Dipolar interactions depend on molecular motions leading to fluctuations in the local magnetic field. These fluctuations can be in the order of the Larmor frequency of nucleus of interest, leading to mutual spin flips. As the interacting nuclei are not identical, a change in net energy is observed accompanying spin exchange. This process occurs until equilibrium is re-established with a rate dependent on T_1.

2.1.6.2 *Measurement of spin-lattice relaxation times*

The perturbed spin system goes back to thermal equilibrium following an exponential decay described by the Bloch equation:

$$\frac{dM_z(t)}{dt} = \frac{M_z(t) - M_0}{T_1} \qquad \text{(Eq. 2-21)}$$

where M_0 is the magnetisation at the thermal equilibrium, $M_z(t)$ is the longitudinal magnetisation at time t and T_1 is a time constant. According to Bloch's theory, longitudinal relaxation follows first

order kinetics. Therefore, after application of π/2 pulse z-magnetisation at time *t* can be measured using the following equation:

$$M_z = M_0 \left(1 - e^{\frac{t}{T_1}} \right)$$
(Eq. 2-22)

In this work T_1 relaxation was measured using the inversion recovery pulse sequence (see Chapter 3). The measurement starts with the application of a π pulse, followed by the delay time (τ) during which the system relaxes. After the delay time (τ) a π/2 pulse is applied for detection of the remaining longitudinal magnetisation. During the set of experiments, the delay time (τ) is varied, which enables to plot the remaining z-magnetisation as a function of delay time.

2.1.6.3 *Measurement of spin-lattice relaxation times in the rotating frame*

As T_1 is sensitive to fast motions (usually on the MHz timescale) spin-lattice relaxation in the rotating frame ($T_{1\rho}$) is sensitive to slower motions (usually on the kHz timescale). Measurements of $T_{1\rho}$ are frequently applied in polymer science to determine the movement of backbone polymer chain.[49] We applied $T_{1\rho}$ measurements to detect motions of the aromatic ring in crystalline tolbutamide, which happened to be on the timescale of $T_{1\rho}$.

2.1.7 NMR crystallography for pharmaceutical solids

Structural characterisation of pharmaceutical crystalline solids is of great interest for both academia and pharmaceutical industry as a different arrangement of atoms in the crystal lattice determines physical properties of a solid, including its melting temperature, density, stability, thermal conductivity, dissolution and compressibility. The ability to determine the three-dimensional structure of solids as complex as membrane proteins, virus particles or complex inorganic materials is a key achievement of the last decades in the field of single crystal X-ray diffraction.

In contrast, determination of the atomic level structure for powdered materials is of significant challenge in diffraction studies and frequently requires application of other characterisation methods sensitive to the local environment of atoms, namely NMR spectroscopy. The wide variety of powdered samples including pharmaceutical polymorphs and co-crystals obtained by grinding methods or new low crystallinity phases gained recently much interest, bringing together experimentalists and computational chemists in the emerging field of NMR crystallography.

Solid-state NMR spectroscopy shows advantages over X-ray diffraction based methods due to the wide range of structural information, accessed through the analysis of chemical shifts, or through the use of dipolar couplings in the determination of interatomic distances of crystalline solids.

Moreover, as NMR spectroscopy is sensitive to the local environment of atoms, it enables structural investigation of disordered systems, nanocrystalline solids or mixed composite materials, where amorphous and crystalline domains often coexist. Alongside structural information on the arrangement of atoms/molecules in the crystal, solid-state NMR can probe dynamical processes at different timescales. The analysis of molecular dynamics within the crystal, even if observed through the X-ray diffraction, is artificially modelled to give fractional probabilities for atomic positions. Information on the details of molecular motions in terms of correlation time and activation energy are difficult to obtain from X-ray diffraction studies.[138] These can be assessed accurately using NMR relaxation experiments and observed directly in the spectra as peak splitting or *via* the decrease of the signal intensity through their interference with decoupling.[139,140] In this section we will briefly summarise some advances in NMR crystallography for structural studies of pharmaceutical solids, as some detailed reviews for the combined use of NMR spectroscopy and first principles calculations of chemical shifts are now available for a wide range of materials and nuclei.[138,141–143]

2.1.7.1 The use of chemical shifts[138]

The isotropic chemical shifts are the easiest parameters to obtain from MAS NMR spectra for spin ½ nuclei and they carry information on the position of atoms in the crystalline solid and fine interactions with their surroundings. Even without the application of more advanced solid-state NMR methods for the analysis of intermolecular distances through the dipolar couplings it is possible to gain an insight into the number of molecules in the asymmetric unit or possible hydrogen bonding patterns.

2.1.7.1.1 Determination of the number of molecules in the asymmetric unit

Molecules may form a crystal with more than one molecule in the asymmetric unit. Therefore, each molecule in the crystallographic site is in a different environment, which can be probed using solid-state NMR. For pharmaceutical solids, ^{13}C NMR is frequently used to observe single carbon peaks or peak splitting due to differences in chemical shifts for each ^{13}C if more than one molecule is present in the asymmetric unit. This information is of great value to solve a crystal structure from both single crystal and powder diffraction data. For example, testosterone is known to form two different polymorphs (α- and β-testosterone) which have one (β-testosterone) or two (α-testosterone) molecules in the asymmetric unit. The structure of α-testosterone was investigated by Harris *et al.* using solid-state NMR and computational methods (Figure 2-15 A and B). The authors were able to assign the ^{13}C chemical shifts to individual testosterone molecules present in the asymmetric unit through the application of ^{13}C INADEQUATE and CASTEP calculations. As ^{13}C solid-state NMR is highly sensitive to the local environment of atoms in the structure it can be used to

distinguish between different phases in heterogeneous materials. Nifedipine was shown to have three polymorphs labelled I, II and III according to Burger and Koller.[144,145] Nifedipine form I investigated by Harris *et al.* was shown to have two molecules in the asymmetric unit based on the ^1H-^{13}C CP/MAS spectra. The concomitant presence of nifedipine forms I and II was identified by the authors in the ^1H-^{13}C CP/MAS spectrum during the crystallisation from the melt due to the presence of multiple ^{13}C peaks highlighting the high sensitivity of solid-state NMR towards heterogeneous solids (Figure 2-15 C).
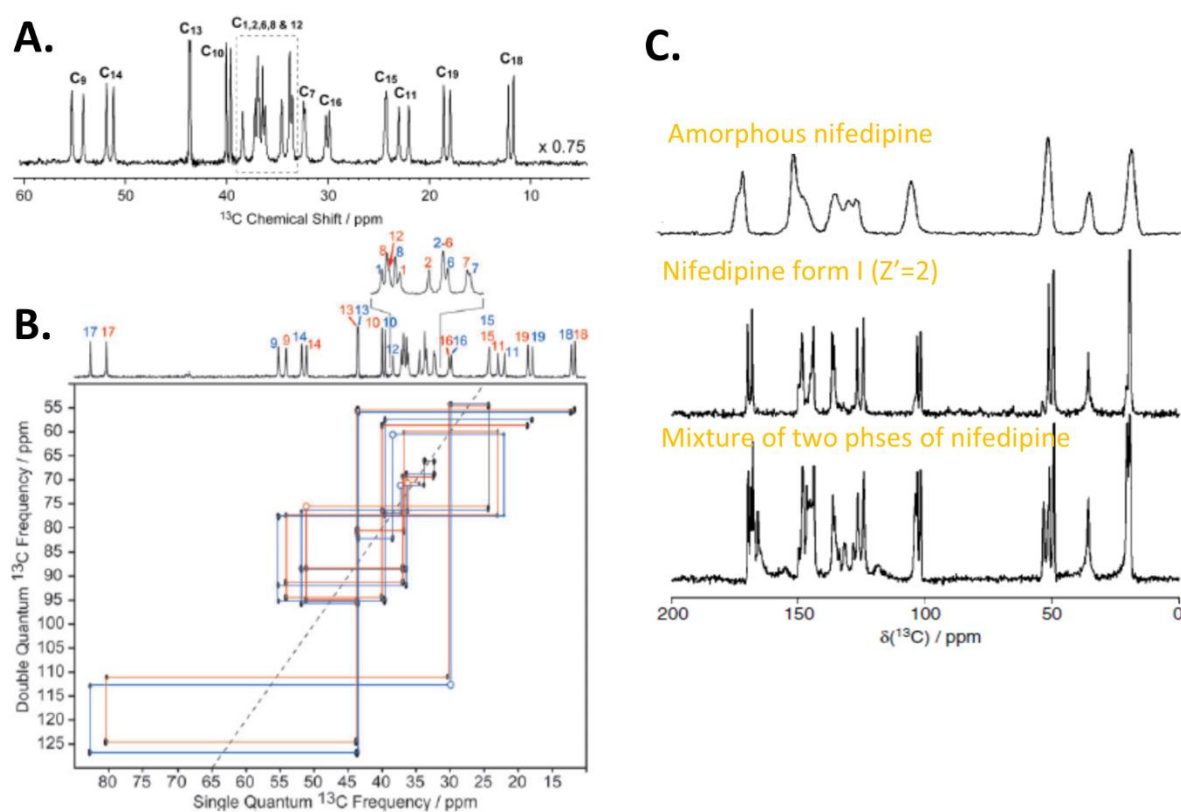
Figure 2-15. Low frequency region of **A.** ^1H-^{13}C CP/MAS spectra of α-testosterone showing two peaks for each carbon due to the presence of two molecules in the asymmetric unit; **B.** INADEQUATE spectrum of α-testosterone, which enables to assign ^{13}C sites from two different molecules (labelled in red and in blue) forming a crystal; **C.** Amorphous and crystalline nifedipine form I, with two molecules in the asymmetric unit. It is possible to distinguish a mixture of different phases in the material due to the high sensitivity of solid-state NMR to the local environment of atoms in the structure, resulting in multiple peaks in the spectra. Adapted from [144,146].

2.1.7.1.2 NMR insight into hydrogen bonding pattern in the crystal

The three dimensional structure of the crystal is frequently stabilised by the framework of hydrogen bonds, which determines molecular packing in the crystal. ^{1}H and ^{13}C chemical shifts are very sensitive to different hydrogen bonding patterns in the crystal, therefore for systems with multiple hydrogen donors and acceptors analysis of peak positions may give vital information on the possible packing scheme.
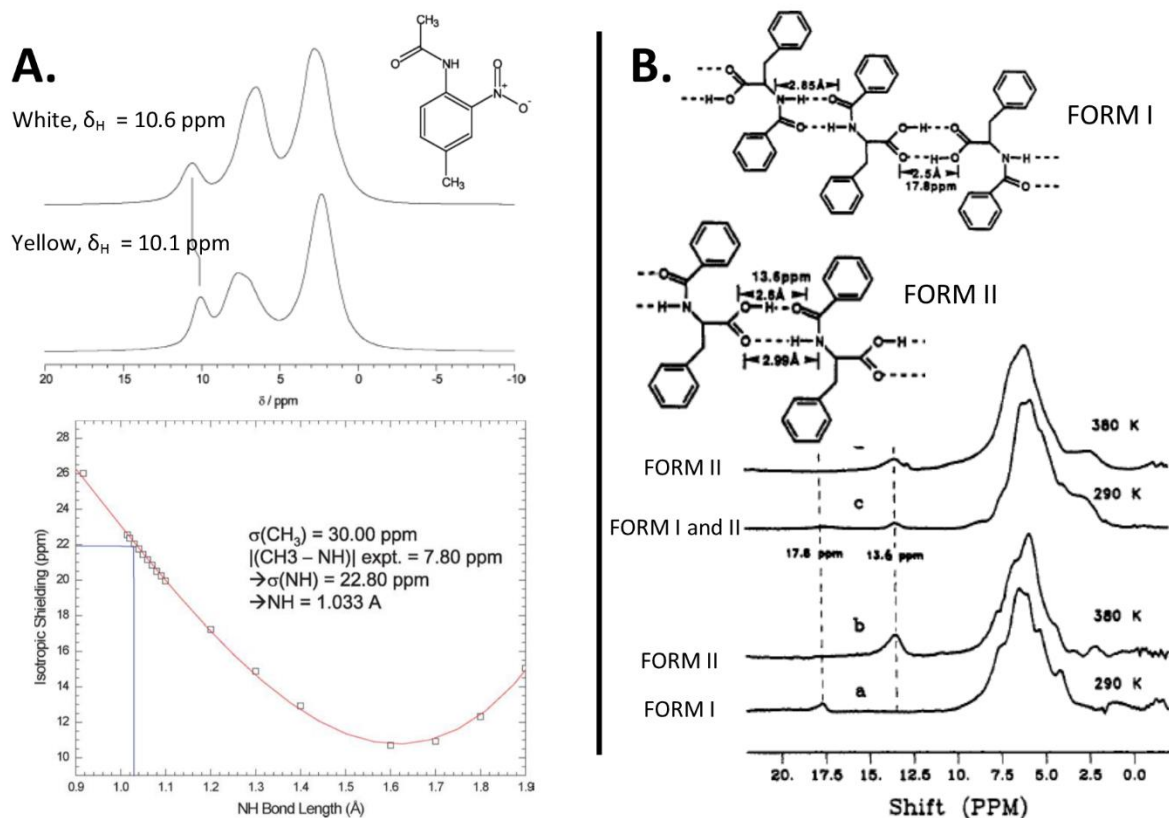
Figure 2-16. **A.** Top: ^{1}H MAS spectra of white and yellow polymorphs of methylnitroacetanilide showing differences in the ^{1}H chemical shifts due to different hydrogen bonding between polymorphs. Bottom: DFT computed isotropic shielding constant (on an absolute scale) of the hydrogen bonded proton in the white form of methylnitroacetanilide, as a function of the N–H distance for the dimer, with all other atoms fixed at the positions given in the published crystal structure. **B.** ^{1}H CRAMPS spectra of different crystalline forms of N-benzoyl-*L*-phenylalanine at 290 K and after subsequent heating to 380 K. The differences in the hydrogen bonds between two forms of the amino acid were determined based on the distinct ^{1}H chemical shifts between the OH groups involved in hydrogen bonds. Adapted from [147,148].

This is also of importance if several polymorphic forms can be present with different hydrogen bonding patterns. For example, Harris *et al.* demonstrated, using ^{1}H MAS NMR, that two polymorphs of methylnitroacetanilide (white and yellow) have distinct hydrogen bonding patterns in the crystal, which are indicated by the small differences in the ^{1}H chemical shifts assigned to the

NH⋯O hydrogen bond.[147] The authors also proved the sensitivity of the ^{1}H chemical shift to the distance between interacting species forming the hydrogen bond. The dependence of the DFT calculated isotropic ^{1}H chemical shifts as a function of N-H distance in methylnitroacetanilide crystal enabled to adjust the hydrogen bonding in the structure of the white polymorph (Figure 2-16A). The sensitivity of ^{1}H chemical shifts to the interatomic distances of interacting species was also shown by Scott and co-workers using ^{1}H CRAMPS spectroscopy for different crystalline forms of N-benzoyl-*L*-phenylalanine. The authors demonstrated that in two crystalline forms of the amino acid two distinct types of -O-H⋯O= bonds are present with different distances between O⋯O atoms. In the symmetrically fused crystal structure (Form I) the O⋯O was determined as 2.5 Å resulting in a ^{1}H peak at 17.8 ppm, whilst in the asymmetrically bounded structure of Form II this distance was determined as 2.6 Å and assigned to the ^{1}H peak at 13.8 ppm.

2.1.7.1.3 Salt or co-crystal: problem of proton migration

In the structural studies of multi component crystal systems the determination of the proton position in the hydrogen bond provides the ability to distinguish between salt or co-crystal. This somehow philosophical question on proton migration in solid state chemistry has its implications in solving the unknown structures using CSP (Crystal Structure Prediction) methods, as the acidic proton position was shown to have a significant effect on the relative energy ordering of different structures.[149,150] Therefore it is of great importance to determine the proton position in multi component systems experimentally prior to computational search. The high sensitivity of ^{15}N chemical shifts towards the position of the acidic proton was shown by Jones and co-workers for model salts and co-crystals of caffeine with dicarboxylic acids, where *ca.* 50 ppm shift of the ^{15}N peaks towards a higher field was observed for protonated nitrogen in caffeine salts as compared to the hydrogen bonded caffeine co-crystals (Figure 2-17).
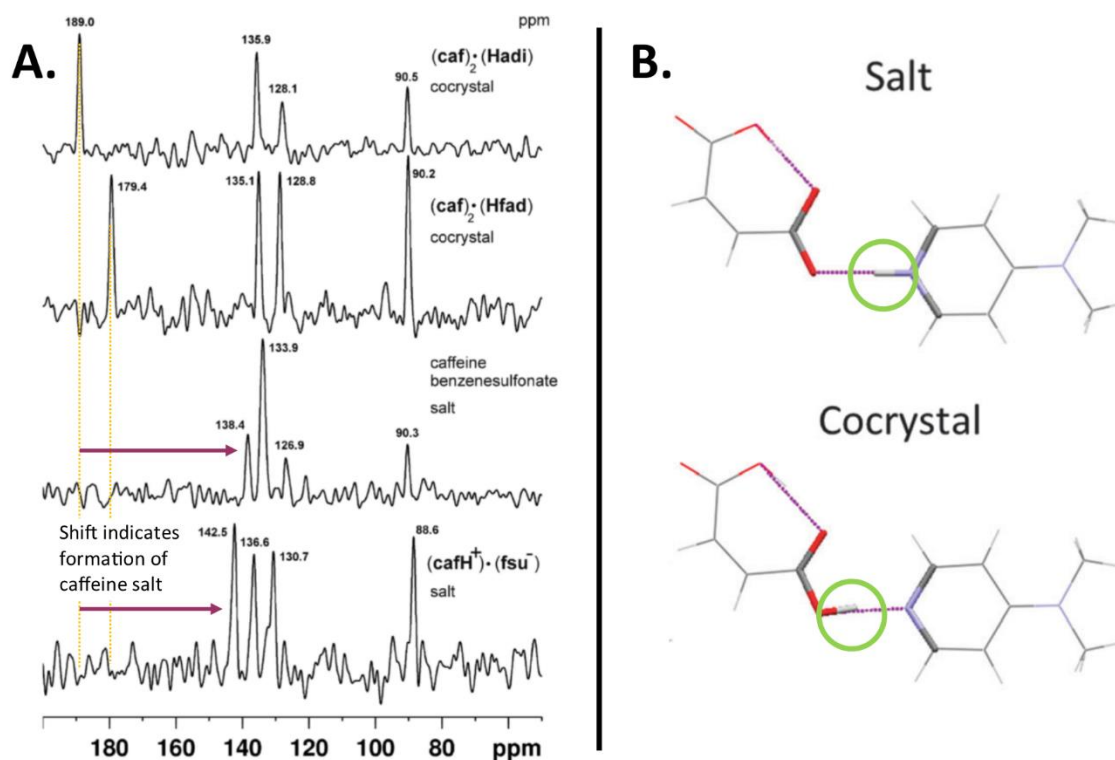
Figure 2-17. A. High sensitivity of ^{15}N chemical shifts in the ^{1}H-^{15}N CP/MAS NMR spectra to proton migration for model salts and co-crystals of caffeine with dicarboxylic acids. **B.** Difference in the position of the proton between salt and co-crystal (indicated with a circle) affects the relative energy ordering between predicted structures using CSP methods. Adapted from [150,151].

2.1.8   First principles of calculations of NMR parameters[141,142]

In order to calculate NMR parameters of a solid it is necessary to determine its total energy, from which the fundamental NMR interaction tensors can be derived. The total energy of the system can be obtained by solving the Schrödinger equation for a particular solid of interest. For a multi body system this requires a tremendous amount of computational effort, hence it is not possible to apply it for a real solid system (at this moment). Therefore, in the Quantum Mechanical model the nonrelativistic electronic Schrödinger equation for system of nuclei and electrons is solved using the Born-Oppenheimer approximation, which assumes that the motion of electrons in a molecule can be separated from motions of atomic nuclei [142]:

$$H(R)\Psi(r;R) = E(R)\Psi(r;R) \qquad\qquad \text{(Eq. 2-23)}$$

where the electronic Hamiltonian H(R) describes the kinetic energy of electrons together with their electrostatic interactions and depends parametrically on the nuclear positions (R). The many-body wave function Ψ(r; R) is a function of the electrons (r) and nuclei (R) coordinates in the system.[142]

To determine the electronic energy of the system one can use the knowledge of its electronic density (so called density functional theory, DFT).[152,153] This approach is used in most QM calculations, where the total ground state electronic energy of the system (E_0) is calculated as a function of the electron density $\rho(r)$:

$$E_0[\rho(r)] = E_{Ne}[\rho(r)] + T_S[\rho(r)] + J[\rho(r)] + E_{XC}[\rho(r)] \qquad \text{(Eq. 2-24)}$$

where the nucleus-electron interactions (E_{Ne}), kinetic energy of non-interacting electrons (T_s) and classical Coulomb interactions between electrons (J) can be efficiently determined and the only unknown factor is the exchange correlation energy (E_{xc}), which needs to be approximated in order to calculate the electronic energy of the system (E_0).

There are many exchange-correlation functionals available to use in DFT calculations, however it is important to know the limitations of each with respect to the material under investigation. For example, LDA functional (local density approximation) considers the electron density to be constant at each spatial coordinate, which is only valid for uniform electron gas.[141] Therefore, LDA is known to overestimate atomisation energies and overbind resulting in short internuclear distances, especially for covalently bonded organic systems and molecular crystals, where hydrogen bonds and short contact interactions generate changes in the electron density.[141] For better approximation of the electron density in these systems GGA functional (general gradient approximation) can be used, which includes a gradient of the electron density, $\nabla\rho(r)$. The commonly used GGA function for molecular crystals is that of Perdew, Burke and Ernzerhof (PBE) and it is used throughout this work.[154]

One of the properties of many solid materials is their periodic structure. This enables performing calculations only for a single unit cell, which in turn reduces significantly computational complexity. The periodicity of the structure allows the application of the Bloch theorem:

$$V(r + L) = V(r) \qquad \text{(Eq. 2-25)}$$

where V(r) is the potential at r and V(r + L) is the potential at r displaced by the lattice vector L. This implies periodicity of the electron density ρ and, therefore, periodicity of the magnitude of the wavefunction $\Psi(r)$. The Bloch theorem, however, does not assumes periodicity of the phase of the

wavefunction, therefore it is said that the wavefunction is quasi-periodic and can be written as follows:

$$\Psi_k(r) = e^{ik \cdot r} u_k(r) \qquad \text{(Eq. 2-26)}$$

where $e^{ik \cdot r}$ is an arbitrary phase factor and $u_k(r)$ is a periodic function.

The DFT codes applicable for calculation of solid-state electronic structures with the GIPAW technique (gauge including projector augmented wave) use planewaves as basis functions:

$$u_k(r) = \sum_G c_{G_k} e^{iG \cdot r} \qquad \text{(Eq. 2-27)}$$

where c_{G_k} are the Fourier coefficients and G are the reciprocal lattice vectors. As the planewaves do not look like atomic or molecular orbitals in order to represent the wavefunction many basis functions are used. Therefore, the quality of planewave DFT calculations depends on two factors: (I) number of k indices (k-points) to sample the first Brillouin zone and (II) number of indices G (G-vectors) for a number of planewave basis functions. Both of these parameters are optimised in the convergence tests in order to achieve the property of interest to be invariant with increasing number of k-points or G-vectors.[141]

A drawback of the planewave basis is its inability to accurately represent the tightly bound core electrons, as a large number of planewave coefficients is required, increasing computational costs significantly. These are overcome by the application of pseudopotentials, which use two approximations to treat the core of atom: (I) the frozen core approximation assumes that electrons close to the core of atom (within a particular radius r_{cut}) do not participate in bonding and therefore their environment is unchanged, and (II) the application of smoothed wavefunction, which is easier to represent by a planewave basis set instead of a valence wave function rapidly oscillating close to the nuclei.[141,142]

The use of pseudopotentials allows accurate and efficient calculation of most properties of the material which relay on valence regions, however, for the calculation of NMR parameters, the electronic structure in close proximity to the nuclei is of high importance. The basis for the calculation of all-electron (AE) wavefunction from pseudo (PS)-wavefunction was provided by van de Walle and Blöchl:

$$\Psi^{AE}(r) = T\Psi^{PS}(r) \qquad\qquad \text{(Eq. 2-28)}$$

where the Projector Augmented Wave (PAW) transformation operator T is generated alongside the pseudopotential. The PAW transformation enables to compute a certain atomic-like state to be computed in a pseudo-wave function and to replace the 'pseudised' component with its all-electron form.[142] Further developments by Pickard and Mauri replaced the transformation operator T with the field-dependent transformation operator T_B, which resolved the 'gauge origin problem' and enabled accurate calculation of the magnetic shielding for periodic systems.[155]

GIPAW methodology enables the calculation of the absolute magnetic shielding tensor **σ**, which is the response of the electrons to an applied external magnetic field B_{ext}.[141] This interaction is described by an effective Hamiltonian:

$$H = -\sum_K \gamma_K I_K (1 - \sigma_K) B_{ext} \qquad\qquad \text{(Eq. 2-29)}$$

where γ and I are the gyromagnetic ratios and the spin angular momentum of K, respectively. Therefore, the response of the electrons to an external magnetic field results in an induced magnetic field B_{ind}, which for a diamagnetic environment is mainly due to orbital currents:

$$B_{ind}(R_K) = -\sigma_K B_{ext} \qquad\qquad \text{(Eq. 2-30)}$$

The relationship between the absolute magnetic shielding tensor σ and the chemical shifts δ is given as follows:

$$\delta = \frac{\sigma_{ref} - \sigma_{sample}}{1 - \sigma_{ref}} \qquad\qquad \text{(Eq. 2-31)}$$

where for all but heavy elements:

$$|\sigma_{ref}| \ll 1 \qquad\qquad \text{(Eq. 2-32)}$$

leading to:

$$\delta \approx \sigma_{ref} - \sigma_{sample}.$$ (Eq. 2-33)

The agreement between the calculated and experimental absolute shielding is made through the use of a reference shielding σ$_{ref}$, which can be determined by comparison of the computed magnetic shielding and the observed experimental chemical shifts. The accuracy of σ$_{ref}$ can be improved by using statistical approach; by plotting the calculated shielding $-\sigma_{iso}^{calc}$ versus the experimental chemical shifts δ_{iso}^{exp} for a series of compounds. Therefore, the calculated chemical shift can be determined through:

$$\delta_{iso}^{calc} = \frac{c - \sigma_{iso}^{calc}}{m},$$ (Eq. 2-34)

Where m and c are the slope and the intercept, respectively. For well-defined systems m ≈ 1 and extrapolation of c to 0 allows to σ$_{ref}$ to be determined. For ^{13}C NMR, the reference shielding was found between 169.2 and 178.9 ppm, which depends on the investigated system.[141] In our studies we used σ$_{ref}$ of 169.5 ppm for ^{13}C in order to compare our results with those published by Brown and co-workers.[156]

2.1.8.1 Structural models for NMR calculations

In order to calculate NMR parameters, a three dimensional model of a structure is required. For molecular crystals of pharmaceutical solids, the structural models can be obtained from diffraction data. It is known that the positions of hydrogens in X-ray diffraction-based structures are not accurate and depend on the temperature of data acquisition and diffraction method – single crystal or PXRD. As DFT calculations are typically performed at 0 K and do not include temperature effects it is recommended to use geometry optimisation for diffraction-based structures prior to the calculation of NMR parameters in order to minimise the energy of the structure. The importance of this procedure has been highlighted in many papers and summarised recently by Ashbrook and McKay[141] and earlier by Harris and co-workers[143].

The structural models determined using diffraction based methods are frequently not available due to difficulties to produce significantly large crystals for single crystal diffraction or due to low crystallinity of the material. In order to generate the starting 3D configuration of atoms in the unit cell it is possible to 'manually' adopt the known structure through substitution of atoms, changes in molecular orientation or cell dimensions and removing parts of the molecule or solvent from the

structure.[141] All these operations significantly change the energy of the system as the positions of the atoms may be far from optimal, therefore they require geometry optimisation prior to NMR calculations.

It is also possible to generate the structure using crystal structure prediction (CSP) methodology. Although this method is computationally expensive for molecular crystals, it is possible to make it feasible by the application of structural constraints (cell size, symmetry, stoichiometry or constraint conformation).[150,157,158] Several examples of combined application of CSP together with GIPAW calculations have been published for structural studies of pharmaceuticals[159–162], or more recently gels and large MOFs.[163,164]

2.2 Powder X-ray Diffraction[53,165,166]

2.2.1 Crystalline solids

Powder X-ray diffraction is a widely used method to characterise materials with a three-dimensional ordered structure, including crystalline pharmaceutical compounds and ordered porous materials (MCM-41, SBA-15). A crystalline solid can be defined as 'a solid body having a characteristic internal structure and enclosed by symmetrically arranged plane surfaces, intersecting at definite and characteristic angles.'[52] A crystal can be thought as infinite 3D lattice of atoms (points) repeating periodically in all three dimensions. Atoms aligned in a particular pattern can be seen as forming small boxes (unit cells) of which the lattice is comprised. There are seven possible shapes of unit cells known as seven crystal systems, described in terms of three translational vectors a, b, c and intervector angles α, β, γ. The crystal systems can be classified into the 14 Bravais lattices based on the number of lattice points per unit cell including simple, body-centred, face-centred and end-centred. The arrangement of atoms or scattering centres in the crystal can be determined through X-ray diffraction, as ordered array of atoms, ions or molecules in the crystal with spatial distribution in the range of 100 pm (1 Å) can be used as diffraction grating for X-rays.

Differences in the arrangement of atoms in the three dimensional space for each crystalline material lead to unique diffraction patterns, characteristic of a particular solid. Two main techniques are employed to access structural information of ordered materials. These are single crystal X-ray diffraction and powder X-ray diffraction. The first is used frequently to obtain precise information about unit cell parameters, position of atoms, bond lengths and angles between them, and can only be applied for materials which are able to form crystals of sufficient size. The second method, which was used in this thesis, enables powdered materials including pharmaceuticals, or confined nanocrystals to be analysed, and allows a characteristic 'fingerprint' of the material to be

observed in the form of a PXRD pattern, where the X-ray intensities are plotted against the scattering angle.
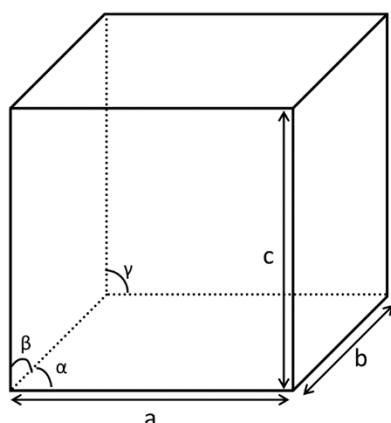
Crystal system	Cell lengths	Cell angles
Cubic	a=b=c	α=β=γ=90°
Tetragonal	a=b≠c	α=β=γ=90°
Orthorhombic	a≠b≠c	α=β=γ=90°
Monoclinic	a≠b≠c	α=γ=90°≠β>90°
Triclinic	a≠b≠c	α≠β≠γ≠90°
Hexagonal	a=b≠c	α=120° β=γ=90°
Rhombohedral	a=b=c	α=β=γ≠90°

Figure 2-18. Seven crystal systems and related cell parameters.

2.2.2   Generation of X-rays and interference

To generate X-rays, the anode is bombarded with electrons emitted by an electrically heated filament (usually tungsten) and accelerated in vacuum by high potential voltage of 20-60 kV. The anode emits a 'white radiation' spectrum with two X-ray peaks (K_α and K_β) superimposed at higher frequency, which depends on the metal used as anode (usually Cu or Mo). The electrons emitted by the filament knock out the electrons from the inner shell (K) of Cu making vacancies for electrons from the outer shell. As electrons from the outer shells descend, energy is emitted in the form of radiation. K_α is emitted by electrons descending from the L shell, while K_β is emitted by electrons descending from the M shell. In practice the K_α and K_β radiation is composed by doublets ($K_{\alpha1}$, $K_{\alpha2}$ and $K_{\beta1}$, $K_{\beta2}$ – these are usually not resolved). The presence of the doublet $K_{\alpha1}$, $K_{\alpha2}$ is due to small splitting (0.020 keV) of L_{II} and L_{III} energy levels of the 2p orbital in copper, leading to two wavelengths of $K_{\alpha1}$= 1.54056 Å and $K_{\alpha2}$= 1.54439 Å.
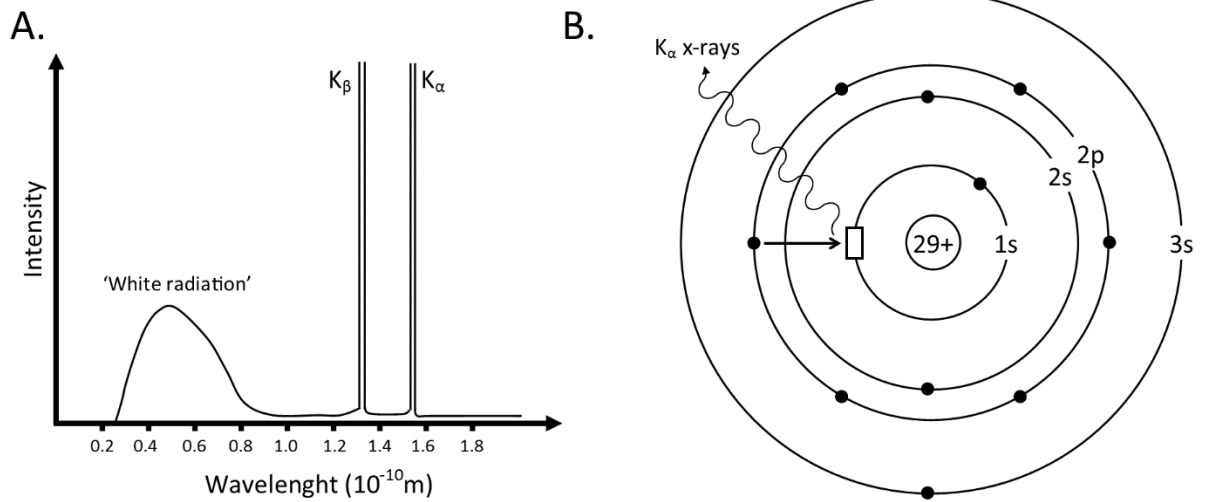
Figure 2-19. A. An X ray emission spectra of Cu. **B.** Generation of X-rays through changes in the electronic structure of Cu. Adapted from [53].

As X-rays are electromagnetic waves they can be classified as sine waves with a wavelength ranging from 0.01-10 nm. They can be scattered by a point object resulting in a new wave of the same frequency (if there is no loss in energy) spreading in all directions. When waves are scattered by two or more points, they all produce waves of the same wavelength which interfere with each other by adding they amplitudes. With two waves present the detected amplitude is not a simple sum of the amplitudes of the individual waves but depends on the phase shift $\delta\phi$. Two waves of the same wavelength can have a phase shift with respect to each other if they are not coincident. This can be described on a linear scale in wavelength units (Δ) or respectively as a phase shift ($\delta\phi$) on an angular scale:

$$\frac{\Delta}{\lambda} = \frac{\delta\varphi}{2\pi} \Rightarrow \delta\varphi = \frac{\Delta}{\lambda}2\pi \qquad \text{(Eq. 2-35)}$$

In two extreme examples, the detected intensity (I) of two sine waves (A_1 and A_2) being either of the same phase ($\delta\phi$=0) or shifted by $\delta\phi$=π constructive or destructive interference is observed, and can be written as:

For $\delta\phi$ = 0 : $I = (A_1 + A_2)^2$ $\qquad$ (Eq. 2-36)

For $\delta\phi$ = π : $I = (A_1 - A_2)^2$ $\qquad$ (Eq. 2-37)

In general terms the above equations for two and more (j) waves can be written as:

$$I = (A_1 + A_2 \exp(i\delta\varphi))^2 \qquad \text{(Eq. 2-38)}$$

$$I = \left[\sum_j A_j exp(i\varphi_j) \right]^2 \qquad \text{(Eq. 2-39)}$$

In X-ray diffraction the measured intensity is the square of sum of the amplitudes of waves scattered by electrons bound to atoms distributed in the three dimensional space. Therefore, the detected waves arrive to the detector with a phase shift, which contains information about relative atomic positions. This feature with the application of Bragg's Law is used to access the structural information of crystalline solids.

2.2.3 Bragg's Law

Bragg's Law treats crystals as built from planes of atoms acting as semi-transparent mirrors. The crystallographic planes are characterised by the Miller indices (hkl) and, if parallel, have the same Miller index and are equally spaced by the distance d_{hkl}.
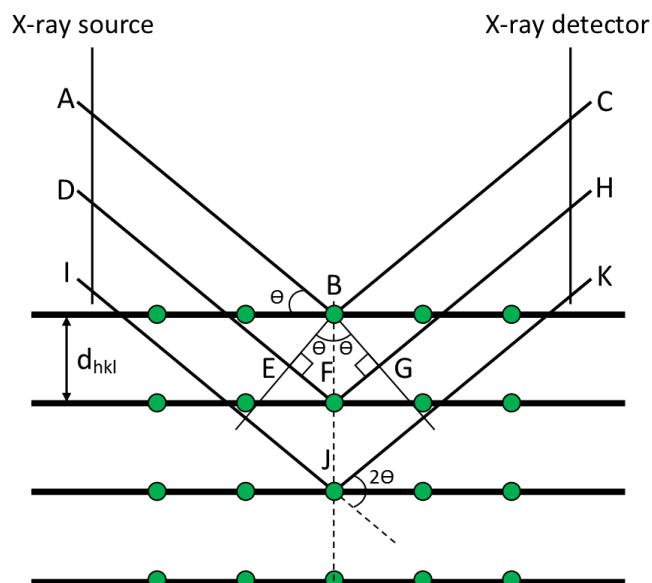
Figure 2-20. Example of X-ray diffraction resulting in reflections at a particular angle θ used to derive Bragg's equation (adapted from [53,165]).

When a monochromatic beam of parallel X-rays (ADI) is directed on a crystal (represented by green dots aligned in planes in Figure 2-20), at Θ_{hkl} the ray A is scattered by atom B, while ray D (and I) penetrates the material and is scattered by atom F (and J). Since both reflected waves (A and D) have the same direction, superposition of both rays occurs. It is evident from Figure 2-20 that ray D travels longer distance (EF) before and (FG) after being reflected. The constructive interference between reflected waves A and I occur only when the difference in distance Δ = EF + FG is a multiple (n) of wavelength (λ):

$$\Delta = EF + FG = n\lambda \qquad \text{and} \qquad EF = FG \qquad \text{(Eq. 2-40)}$$

In geometrical terms (based on **Figure 2-20**):

$$\sin\alpha = \frac{EF}{d_{hkl}} \Rightarrow EF = d_{hkl}\ \sin\alpha \qquad \text{(Eq. 2-41)}$$

$$\Delta = EF + FG = 2d_{hkl}\sin\alpha \qquad \text{(Eq. 2-42)}$$

$$n\lambda = 2d_{hkl}\sin\alpha \qquad \text{(Eq. 2-43)}$$

The above equation is known as Bragg's equation and it relates the spacing between the particular planes (d_{hkl}) with Bragg's angle Θ_{hkl} at which the reflections from those particular planes are observed. The observed reflections in PXRD patterns are usually labelled using Miller indices (100), (110), (111), according to the plane from which they diffract. However, in some geometries systematic absences of reflections are observed due to destructive interferences of reflected waves from particular planes.

2.3 Nitrogen adsorption isotherm analysis[13,167–169]

Nitrogen adsorption at its boiling point at 77 K is a frequently used method for analysis of porous solids as it provides structural information of porous hosts, such as pore size distribution in the range from micro- to macropores, pores volume and surface area. Furthermore, it is a method of choice to confirm the intercalation of the organic phase inside the pores of the mesoporous scaffolds loaded with drug molecules, as a decrease of the total pore volume and surface is observed for the silica-drug composites when compared to the pure host. The measurements are usually performed by the application of volumetric or gravimetric methodology. In the case of

volumetric determination of an adsorption isotherm (as used in this study) a known quantity of gas is admitted to the confined volume containing the adsorbent at constant temperature. As gas is adsorbed at the materials surface the known gas pressure decreases until equilibrium is reached. The adsorbed amount of gas at a particular equilibrium pressure is determined as the difference between the admitted amount of gas and the amount of gas which is required to fill the space around the adsorbent. The shape of the isotherm depends on the structural features of the material under investigation, *i.e.,* textural parameters, pores geometry and its chemical composition. Based on the recent IUPAC publication on physisorption of gases, eight distinct physisorption isotherms were proposed, with only type IV being common for mesoporous materials (highlighted in yellow in Figure 2-21).
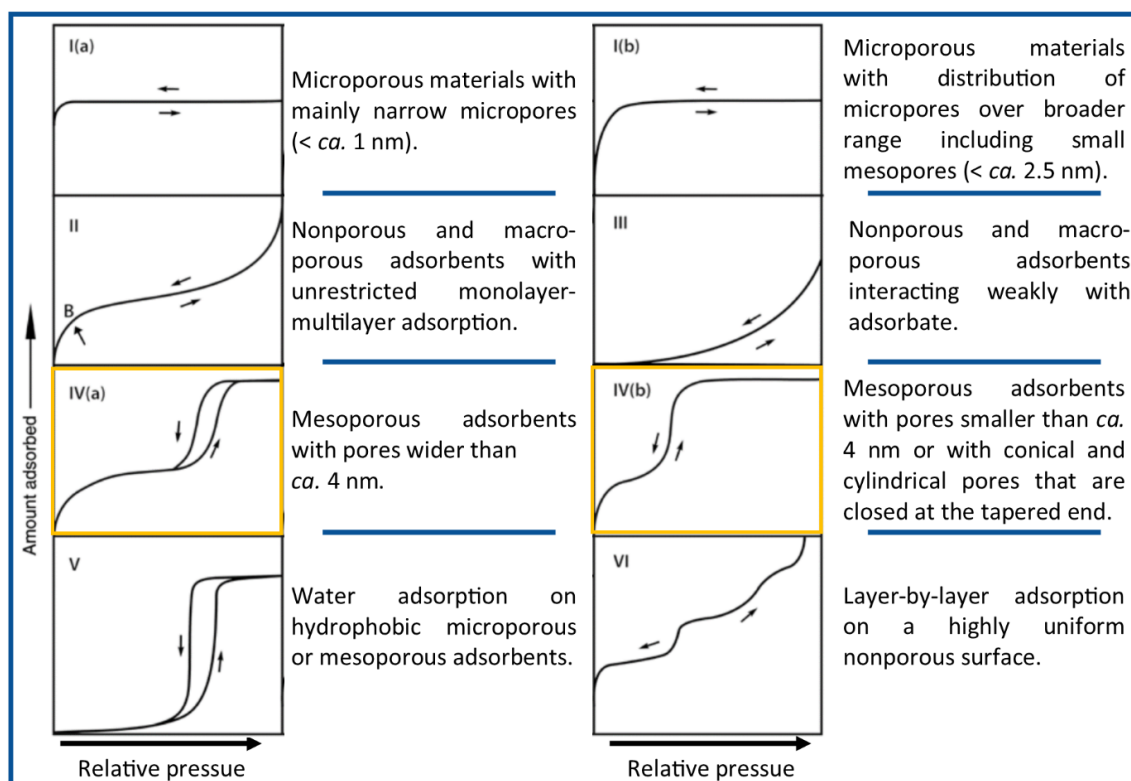
Figure 2-21. Types of nitrogen adsorption isotherms as proposed by IUPAC.

The Type I physisorption isotherm is characteristic of microporous solids with relatively small external surface area, *e.g.*, zeolites, certain porous oxides, microporous polymers or activated carbons. At low relative pressure (P/P_0) steep uptake is observed due to increased interactions of the adsorbate with the micropores of molecular sizes resulting in fast filling of the accessible pores space. Based on the shape of the initial step of the adsorption isotherm, microporous materials can

be further divided into ultramicroporous with pore sizes smaller than 0.7 nm and wide microporous materials with pore sizes wider than 0.7 nm.

Nonporous and macroporous materials display Type II and Type III adsorption isotherms. The shape of the reversible Type II isotherm indicates nonrestricted monolayer-multilayer coverage of the material surface up to relative pressure close to unity, while finite adsorption is observed in the Type III isotherm at high P/P_0. The observed sharp B-point indicates completion of the formation of a monolayer and the start of multilayer adsorption. The overlap of the monolayer formation and multilayer adsorption processes is manifested as less pronounced B-point on the Type II isotherm. In cases of weak adsorbent-adsorbate interactions the B-point is not observed due to clustering of the adsorbate molecules at most favourable surface sites displayed in the Type III isotherm.

Type V isotherm is very similar in shape to the Type III isotherm, due to the relatively weak adsorbate-adsorbent interactions and molecular clustering. At higher P/P_0, pore filling is observed as a steep increase in the adsorbed amount of gas.

Layer-by-layer adsorption of gas molecules at highly uniform nonporous surface is displayed by Type VI isotherm, where the height of the step describes adsorption capacity of each adsorbed layer. The steepness of the step is material and temperature dependent. Stepped adsorption is also possible for ultramicroporous solids with energetically different sites, *e.g.,* zeolites with high crystallinity (Zeolite X) where each step is related to cavity filling.

The Type IV isotherm is characteristic of mesoporous materials including mesoporous silica scaffolds. The adsorption branch of the isotherm at low P/P_0 is similar to Type II isotherm and displays the monolayer-multilayer adsorption of nitrogen at the pore walls, which is followed by pore (capillary) condensation at P lower than P_0. This phenomenon is related to condensation of gas to a liquid-like phase at relative pressure lower than the saturation pressure of the bulk liquid. A characteristic feature of Type IV isotherms is the plateau of the adsorbed amount of gas after the pore condensation step. Type IV isotherms can either show a hysteresis loop (Type IVa) for the mesoporous materials with pores wider than *ca.* 4 nm, or be fully reversible (Type IVb) for mesoporous materials with pores diameter narrower than *ca.* 4 nm. The relationship between the relative pressure at which the condensation step is observed and the size of the formed liquid-like meniscus of condensed gas can be explained by Kalvin equation (Eq. 2-44) and is used for mesopores size calculations.

$$\frac{1}{r_1} + \frac{1}{r_2} = -\frac{RT}{\sigma V} \ln\left(\frac{P}{P_0}\right) \qquad\qquad \text{(Eq. 2-44)}$$

The equation correlates the principal radii of the meniscus curvature (r_1 and r_2) with the relative pressure (P/P_0) at which condensation occurs; σ and V represent the surface tension of the liquid condensate and the molecular volume, respectively. To apply the Kalvin equation to obtain the pore radius or the pore width the pore shape model needs to be chosen and it is necessary to assume that the meniscus curvature is directly related to the pore width. In general, for spherical meniscus $r_1=r_2=r_k$ and the equation can be rearranged:

$$r_k = \frac{2\sigma V}{RTln\left(\frac{P}{P_0}\right)}$$
(Eq. 2-45)

where r_k is termed Kalvin radius.

2.3.1 Desorption hysteresis in porous materials

During the desorption step of an adsorbate from the surface of mesoporous materials a hysteresis loop is frequently observed. The size and shape of the hysteresis loop is related either to adsorption metastability or in more complex pores systems to network effects. In case of open cylindrical pores, for the adsorption branch of the isotherm the thermodynamic equilibrium is shifted towards higher P/P_0 due to the metastability of the adsorption multilayer. As evaporation (desorption) of the liquid-like condensed gas from the pores does not include the nucleation step, the steep part of desorption isotherm reflects a reversible transition from liquid to gas phase, hence thermodynamic equilibration is established on the desorption branch of isotherm. Based on recent studies, IUPAC expanded the classification of hysteresis loops into six different types listed in Figure 2-22.

The H1 type of isotherm is characteristic of materials which display narrow distribution of uniform mesopores including templated silicas (MCM-41, SBA-15), some controlled pore glasses and mesoporous carbons. Similar hysteresis loops can also be obtained for mesoporous materials with ink bottle pores where the neck diameter has a similar width as the diameter of the main pore/cavity.

The H2 (a and b) isotherms are characteristic of more complex, usually interconnected pore systems, and are frequently observed for systems with ink bottle type of pores. The steep desorption branch of H2(a) type of hysteresis loop is related either to pore-blocking/percolation in narrow necks or cavitation-induced evaporation effects. These phenomena are observed for some silica gels, vycor glass or ordered mesoporous silica materials SBA-16 and KIT-5. When the sizes of the pores necks are distributed over wider ranges, the H2(b) loop is observed *e.g.*, mesocellular silica foams.
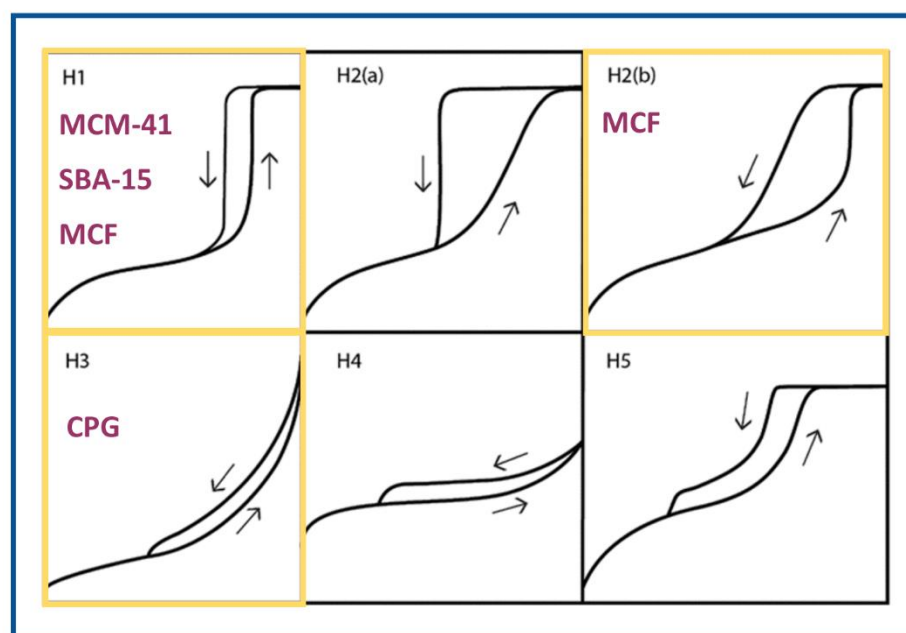
Figure 2-22. Nitrogen adsorption isotherms based on IUPAC classification. The hysteresis loops observed in this study are highlighted in yellow. Adapted from [13]

The H3 and H4 hysteresis loops display similar shape with H3 being characteristic of non-rigid aggregates of plate-like particles characteristic of clay materials. These can also be observed for macroporous or large mesoporous materials which are not completely filled with condensed adsorbate. The steep increase of adsorption at low relative pressure in the H4 loop is associated with micropores filling, hence this type of hysteresis loop is observed for aggregated zeolite crystals, mesoporous zeolites or hierarchical micro-mesoporous carbons. For mesoporous materials with partially blocked pores (*e.g.*, plugged hexagonal templated silicas) type H5 hysteresis loop was recently identified by IUPAC.

2.3.2 Determination of surface area, pores size diameter and pores volume of mesoporous materials

The Brunauer, Emmet and Teller (BET)[170] method developed nearly 80 years ago to evaluate the surface area of porous materials is still widely used, despite of its simplified theoretical model of adsorption. The BET method for surface determination is based on the following assumptions:

A. The heat of adsorption of the first monolayer is constant.

B. The lateral interaction of adsorbed molecules is negligible.

C. The adsorbed molecules can act as a new adsorption surface.

D. The heat of adsorption of all monolayers is the same apart from the first.

The determination of the volume of the monolayer coverage (V_m) and its use in the determination of the surface area (A_s) is based on the (Eq. 2-46):

$$A_s = (V_m/22414)N_A\sigma \qquad\qquad \text{(Eq. 2-46)}$$

Where N_A is the Avogadro number and σ represents the area covered by one nitrogen molecule (the accepted value is 0.162 nm^2). The V_m can be estimated using three parameters BET equation (Eq. 2-47):

$$V_{ads} = V_m \frac{c\frac{P}{P_0}}{1-\frac{P}{P_0}} \frac{1-(n+1)\left(\frac{P}{P_0}\right)^n + n\left(\frac{P}{P_0}\right)^{n+1}}{1+(c-1)\left(\frac{P}{P_0}\right)-c\left(\frac{P}{P_0}\right)^{n+1}} \qquad \text{(Eq. 2-47)}$$

where V_{ads} is the adsorbed volume which depends on the relative pressure (P/P_0), the c parameter which is related to the heat of adsorption of the first adsorbed layer and the n parameter, which describes the number of layers which can be adsorbed at the materials surface. The equation can be simplified to include only two parameters (Eq. 2-48), assuming n→∞:

$$V_{ads} = V_m \frac{c\frac{P}{P_0}}{\left(1-\frac{P}{P_0}\right)\left(1+(c-1)\frac{P}{P_0}\right)} \qquad\qquad \text{(Eq. 2-48)}$$

The BET equation can only be applied to the linear part of the isotherm due to other phenomena being observed at higher relative pressures *e.g.*, pores condensation. The linearity of the adsorption branch of the isotherm is usually observed in the P/P_0 range of 0.05 to 0.3.

The pore size diameter and pore volume can be determined from the adsorption-desorption isotherm, which can be derived from the Kelvin equation (Eq. 2-49). For mesoporous materials which display finite adsorbed amount of the adsorbate the total pores volume can be derived at the relative pressure close to unity, based on the assumption that at $P/P_0 \approx 1$ the pores are filled with condensed liquid adsorbate.

There are several models proposed for the determination of the pore size diameter including the most widely used Barrett, Joyner and Halenda (BJH method)[171]. The BJH method can be applied in the pore condensation region above $P/P_0 > 0.4$ as it is based on the shift of the gas-liquid phase

transition of confined fluid compared to the bulk liquid, and for cylindrical pores it is described using the modified Kelvin equation:

$$ln \frac{P}{P_0} = -\frac{2\gamma V_m}{RT(r_p - t_c)}$$

(Eq. 2-49)

where r_p is the pore radius, t_c is the thickness of the adsorbed multilayer, γ is the surface tension of the bulk liquid and V_m is the molar liquid volume. For materials with pore size diameter below 10 nm the validity of the Kelvin equation is debatable as macroscopic models are no longer valid to described adsorption phenomena. It was shown using highly ordered MCM-41 type of materials with different pores sizes, determined independently using PXRD and transmission microscopy, that adsorption methods based on the Kelvin equation underestimates pore size diameter of *ca.* 20-30 %. For this type of materials, methods based on molecular simulation or DFT are now recommended for use, as they contain both thermodynamic and density information on confined fluids and are able to describe adsorption phenomena on the molecular level. For the small pores MCM-41 material (*ca.* 3.2 nm) synthesised in this study, reliable pore size diameter as corroborated using PXRD could only be obtain using the NLDFT model.

2.4 Thermal analysis[172]

2.4.1 Differential scanning calorimetry

Differential scanning calorimetry (DSC) measures an uptake or release of thermal energy by a material which is subjected to linear heating or cooling, hence it enables to identify thermal transitional events including melting, crystallisation, glass transition or thermal decomposition. The energy uptake of a material closed in a metallic crucible is compared to the energy uptake of an empty reference pan, both placed in high accuracy furnace (Figure 2-23 in the case of heat flux DSC instrument).

The material and the reference pans placed in the furnace are heated with the same linear heating rate. Due to the heat capacity (C_p) of the analysed sample it will heat slower (T_s) as compared to an empty reference pan (T_r), *i.e.*, the temperature of the reference will increase slightly faster than the temperature of the analysed material. When the material melts (t_1) the temperature of the sample T_s does not change until the process is completed, while the temperature of the reference T_r pan is still linearly increasing. As soon as melting is completed (t_2) the temperature of both the reference and the sample increase linearly again. The differential signal ΔT of the two heating curves T_s and T_r gives rise to a peak in the DSC thermogram ($\Delta T = T_s - T_r$), which represents an endothermic

melting process. The area of the peak is related to the heat of transition (enthalpy in J g^{-1}). Example of a DSC thermogram is presented in Figure 2-24.
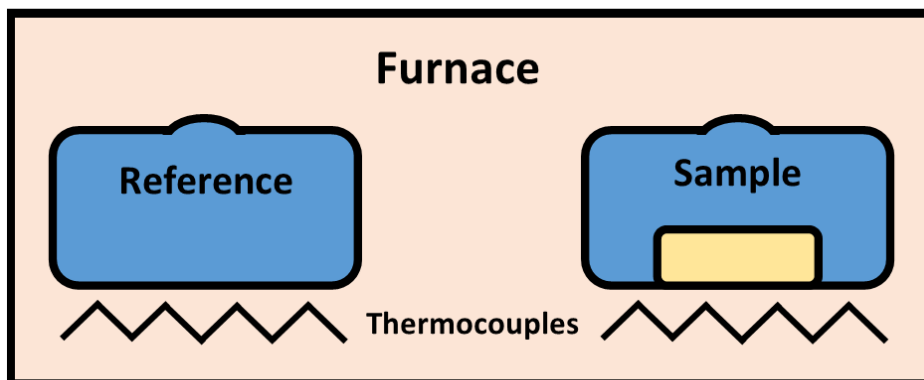
Figure 2-23. Schematic representation of heat flux DSC calorimeter. Adapted from [172].
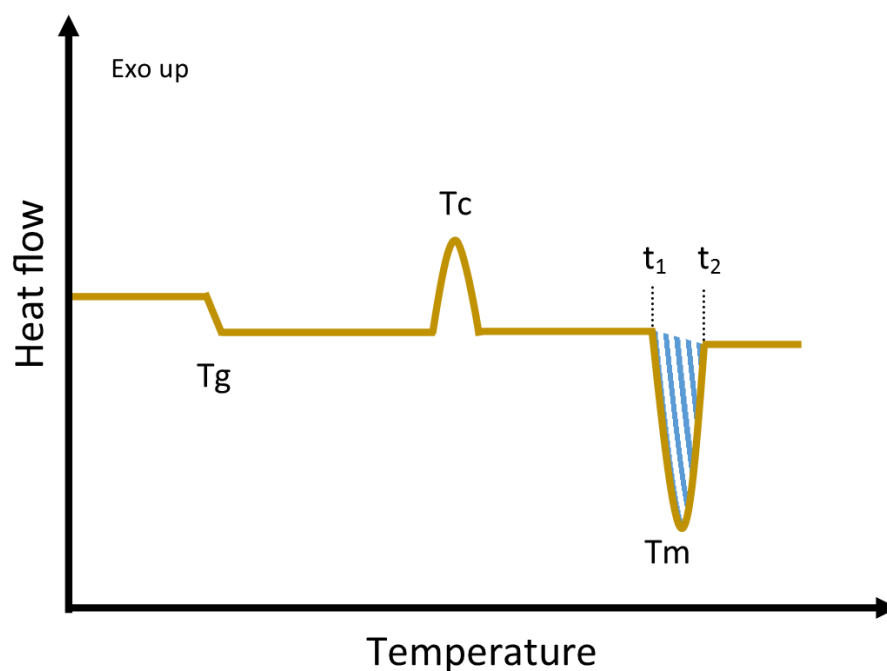
Figure 2-24. Example of a DSC thermogram with highlighted glass transition temperature (T_g), exothermic crystallisation (T_c) and endothermic melting (T_m) events. The points t_1 and t_2 represent the onset and the end of the melting transition, while peak area (shaded in blue) gives information on the heat of transition – detailed description in the text. Adapted from [49].

2.4.2 Thermogravimetric analysis

Thermogravimetric analysis is an experimental method which enables the detection and used changes in mass of the material to describe chemical or physical processes that the reactant undergoes upon heating. The analysed sample placed in a metallic or ceramic crucible (depends on the temperature range) and situated on a microbalance is submitted to linear temperature increase and the resulting changes in the mass are measured as a function of temperature (or time at particular temperature in isothermal studies).

This method has been widely used in studies of chemical processes that the materials undergo upon heating, including accurate measurement of reaction rates. In the pharmaceutical field it is frequently used to measure the loss of water and the temperature range at which dehydration occurs. In the case of pharmaceutical hydrates (or solvates) it enables a determination of the solvent:drug stoichiometry of the material or possible water uptake of pharmaceutical excipients during technological processes. Furthermore, it can be used to determine the composition of materials with significantly different degradation temperatures, *e.g.*, organic-inorganic composite materials, as used in this thesis.
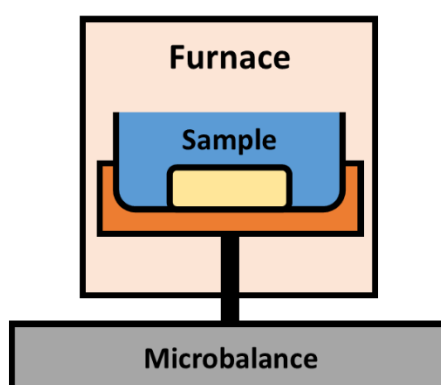
Figure 2-25. Schematic representation of the thermobalance used for thermogravimetric analysis.

Differences in the dehydration temperatures are frequently used to distinguish between surface and the crystalline water. Furthermore, many commercially available instruments enable to analysis to be performed in either inert gas atmosphere or oxidative conditions, which may have a significant impact on the analysed mass loss of the materials (Figure 2-26). It needs to be emphasised that TGA analysis needs to be complemented using other techniques, due to the complexity of the solid state reactions.
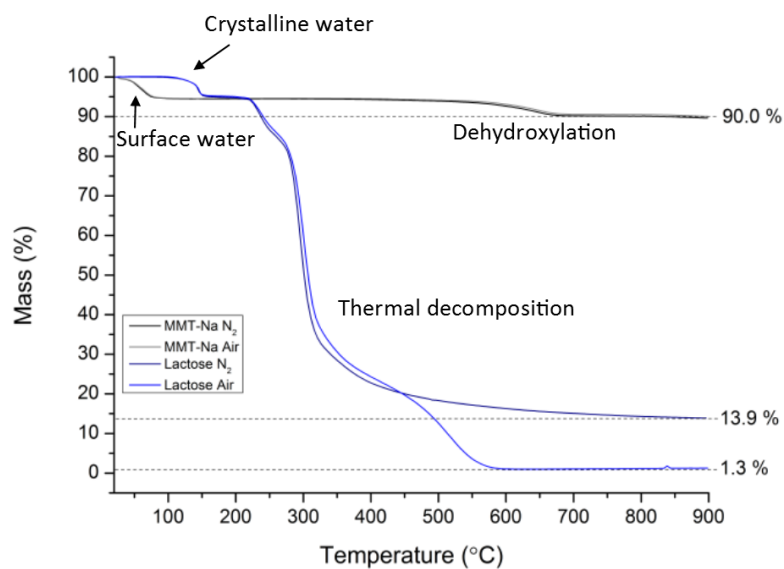
Figure 2-26. Example of the TGA curve of lactose monohydrate and Na-montmorillonite clay analysed under inert (N$_2$) and oxidative (air) atmosphere. Several different phenomena are observed in the thermogram.

Experimental section

Chapter 3

3.1   Materials

Indomethacin (IMC), flufenamic acid (FFA), tolbutamide (Tb), Pluronic P123, n-hexadecyltrimethylammonium bromide 1,2,3-trimethylbenzene, tetraethylorthosilicate (TEOS), ammonium fluoride, sodium chloride, 37 wt. % hydrochloric acid, nitric acid, methanol, ethanol and acetonitrile were purchased from Sigma-Aldrich and used without further purification.

3.2   Synthesis of porous solids

3.2.1   MCM-41 silica host

Spherical submicrometer mesoporous MCM-41 particles were synthesised according to the method previously described by Grün *et al.*[173] In a typical synthesis, 2.5 g of n-hexadecyltrimethylammonium bromide was dissolved in miliQ quality water (50 mL). A solution of ammonia (37 wt. %, 13.2 g) and ethanol (60 g) was mixed with the solution of n-hexadecyltrimethylammonium bromide. The resulting solution was stirred for 15 min and 4.7 g of TEOS was added leading to a synthesis mixture with the following composition: 1 TEOS : 0.3 C16TMABr : 11 NH3 : 144 H2O : 58 EtOH. After stirring for 2 h, a precipitate was formed, filtered and washed using methanol and deionised water. The material was dried at 363 K overnight and calcined at 823 K for 5 h in air atmosphere.

3.2.2   SBA-15 silica host

The SBA-15 porous host was synthesised using the method reported by Zhao *et al.* with the addition of NaCl to obtain a highly ordered and hydrothermally stable material as described by Li *et al.* and Ryoo *et al.*[35,174,175] The triblock copolymer P-123 (2.0 g) and NaCl (5.5 g) were dissolved in 2M HCl aqueous solution (62.5 mL) at room temperature in a 250 mL polypropylene bottle to obtain a clear colourless solution. TEOS (4.23 mL) was then added dropwise and stirred at 313 K for 20 h. The final molar composition of the synthesis mixture was 1 TEOS : 0.017 P123 : 6.16 HCl : 4.6 NaCl : 165 H2O. This mixture was aged in an oven at 363 K for 24 h, filtered, washed with miliQ quality water and dried. The resulting dry white solid was then calcined at 823 K overnight in air atmosphere.

3.2.3   MCF silica host

Spherical particles of Mesostructured Cellular Foam (MCF) were synthesised using the method published by Han *et al.*[4] In a standard synthesis, 4 g of triblock co-polymer Pluronic P123 as a micellar template was dissolved in 75 mL of 1.5 M HCl at room temperature. Subsequently, 4 g of a swelling agent (1,3,5-trimethylbenzene) was added to swell the micelles and the resulting solution was heated to 313 K in a water bath and stirred vigorously for 2 h. Subsequently, 9.2 mL of TEOS as a source of silica was added dropwise to the polymer/1,3,5-trimethylbenzene mixture and stirred for another 5 min. The mixture was then transferred to a PTFE bottle and aged at 313 K for 20 h

without stirring. After that time 46 mg of NH_4F was added to the mixture and further aged at 373 K for another 24 h. The resulting white solid was filtered, washed with miliQ quality water and ethanol and dried in an oven at 313 K for 24 h. The dried powder was then calcined in air at 1173 K for 10 h.

3.2.4 Controlled Pore Glass (CPG)

Controlled Pore Glass (CPG), developed by Haller, is a rigid glass containing a network of interconnected pores.[11] The glass is formed by a phase rearrangement process of alkali borosilicate glasses at elevated temperatures.[176,177] Control of the time and the temperature of the process enables tailoring of the pore size diameter and leads to a narrow distribution of the pores. The product obtained after leaching forms a continuous, silica rich glass with a porous network of specified pore dimensions. The CPG material is used mainly in the exclusion and absorptive chromatography of biomolecules and, due to the possible organofunctionalisation of its internal surfaces, as a support for the immobilisation of bio-reactive molecules.[11] In our study, commercially available (Merck Millipore) CPG material with a pore size of 550 Å served as a nano-size crystallisation chamber for the investigation of IMC phase changes under confinement.

3.3 Drugs loading details

3.3.1 Indomethacin

Loading from the melt. The CPG or the MCF material (200 mg) was mixed with IMC in a glass vial (15 mL) for 3 min using a spatula to obtain host : drug weight ratios of 85-15, 80-20, 75-25, 70-30, 50-50 and put into a vacuum oven (200 mbar) at 438 K for 2 h (*i.e.*, a temperature above the melting point of γ-IMC). The loaded composites were then cooled to an ambient temperature and stored in a desiccator at 277 K. The presence of an amorphous phase was confirmed using DSC, PXRD and solid-state NMR. Composites loaded from the melt were labelled as follows: host–IMC (host is CPG or MCF) and host–guest ratio (*e.g.*, CPG–IMC 85–15).

Phase transformation of amorphous IMC under confinement. Typically, to drive IMC crystallisation from an amorphous phase, 280 mL of methanol were added dropwise to 200 mg of host-IMC composite loaded from the melt. The wetted samples were then mixed promptly and thoroughly with a spatula for 30 s to allow a uniform filling of the pores with the solvent and left on a bench at room temperature in sealed glass vials for 24 h. Subsequently, the materials were dried under vacuum at 313 K for 2 h and stored in a desiccator at 277 K. The volume and solvent addition procedure were carefully optimised. Composites loaded from the melt and subsequently treated with methanol were labelled as follows: host–IMC (CPG or MCF), host guest ratio + 0.28 mL MeOH (*e.g.*, CPG–IMC 85–15 + 0.28 mL MeOH).

Incipient wetness loading method. Indomethacin loading solutions were prepared by dissolving the drug in a vial in hot methanol to obtain concentrations of 150, 200 and 250 mg mL^{-1}. To investigate the effect of the volume and the concentration of the loading solution on the IMC phase formation, 120 mL or 150 mL of the IMC solution was then added dropwise to 200 mg of the CPG host and 160 mL of the same loading solution was added to the MCF material. The loaded host was mixed promptly and thoroughly with a spatula to obtain uniform loading and evaporate any excess of the solvent from the sample.

3.3.2 Flufenamic acid

The mesoporous host (MCM-41, SBA-15 or MCF) was mixed with gently grinded FFA at host:guest ratios of 85-15, 80-20, 75-25, 70-30, 60-40, 50-50 wt. wt.$^{-1}$ inside an amber glass vial with a spatula for 60 s to allow uniform mixing of both compounds. Prepared physical mixtures were heated to 423-428 K for 5 min on the hot plate, *i.e.*, 288-293 K above the melting point of FFA acid (*ca.* 408 K for commercially available FFA form I) and mixed with a spatula. The resulting composite materials were labelled as follows: host name-FFA (host is MCM, SBA or MCF) and host-guest ratio, (*e.g.*, MCM-FFA 85-15).

3.3.3 Tolbutamide

Tolbutamide was loaded into MCM-41 (host) using melt loading method. The drug and the material were mixed together in a glass vial for 3 min using a spatula in host:guest ratios of 85:15, 80:20, 75:25, 70:30, 60:40 and 50:50 (wt. wt.$^{-1}$). The obtained mixture of the powders was heated on a hot plate at 408 K, *i.e.*, above the melting point of TB, and mixed with a spatula for 5 min, ensuring that the drug was adsorbed within the pores *via* capillary action. Once loaded, the samples were cooled to room temperature and stored within a desiccator.

3.4 Preparation methods for reference polymorphic forms

3.4.1 Indomethacin

The indomethacin purchased from Sigma-Aldrich was the γ-IMC (form I[178]). The α-IMC (form II[179]) was formed by dissolving 300 mg of the drug in 40 mL of warm ethanol in a round bottom flask and promoting evaporation of the solvent using a rotary evaporator at 323 K. The resulting powder was then ground in a mortar and stored in the freezer. An IMC:MeOH (1:1) solvate was obtained using the method described by Joshi *et al.*[180] 500 mg of IMC was dissolved in 8 mL of methanol at 353 K and left on the bench at room temperature in a vial covered with parafilm to reduce evaporation. Fine needles were collected after two days and dried using filter paper. The stoichiometric ratio between the solvent and IMC was confirmed using thermogravimetric analysis. A reference sample of IMC form V was obtained by the slow desolvation of the IMC:MeOH (1:1) solvate at room

temperature for two months under a perforated parafilm cover. Indomethacin form IV was prepared by annealing of the intact IMC glass at temperatures from 333-363 K. The IMC glass was prepared by melting γ-IMC *ca.* 10 K above its melting point (γ-IMC m.p. = 433 K) and quench cooling on the cold metal block.

3.4.2 Flufenamic acid

FFA form I is the commercially available form from Sigma-Aldrich. FFA form III was obtained by dissolving 500 mg in 10 mL of ethanol and heating to 358 K until the drug is dissolved. The obtained solution was left on the bench at room temperature to cool down.[181] The FFA form III crystallises as yellow needles after a few days. We further made an attempt to obtain FFA form V using the method described by Lee *et al*. using salt additives to crystallisation solution.[182] In all attempts only FFA form III was obtained.

3.4.3 Tolbutamide

Tolbutamide form I^L is the commercially available form. The phase transition of form I^L to form I^H happens at *ca.* 313 K. The Tb form IV was obtained as white needles on the surface of the crystallisation vial. 300 mg of Tb was dissolved in warm methanol and left on a bench at room temperature to crystallise. The white, fine needles of Tb form IV were formed on the walls of a glass vial. We observed that Tb form IV has a phase transition at 253 K. This form is further labelled Tb form IV^L. The very unstable Tb form V was formed inside the MCM-41 and SBA-15 silicas loaded from the melt. Tb form V normally crystallises from methanol with traces of nitric acid according to Nath *et al.*[183]

3.5 Computational details for chemical shift calculations

All computations were performed using the CASTEP code (ver. 7.03) and on the fly ultrasoft pseudopotentials.[184] Calculations were performed for the crystal structures and isolated molecules of IMC (structure code: INDMET[178], INDMET02[179], BANMUZ[185]), crystal structures of FFA form I and FFA form III (structure code: FPAMCA11[186], FPAMCA[187]) and crystal structures of Tb form I, IV and V (structure code: ZZZPUS02[188], ZZZPUS04[189], ZZZPUS07[189], ZZZPUS10[183]) reported in CCDC. Geometry optimisations were carried out using the Perdew-Burke-Ernzerhof (PBE) generalised gradient approximation (GGA) exchange-correlation density functional[154], ultrasoft pseudopotentials[190], a k-point mp spacing of 0.05 Å^{-1} and a cut-off energy of 800 eV. Geometry optimisation was run with constrained cell dimensions and positions of all heavy atoms.

Calculations of the NMR chemical shieldings were performed using the gauge including projector augmented wave approach (GIPAW) and on the fly pseudopotentials as implemented in CASTEP

code.[155,191] The computed isotropic NMR shieldings were converted to chemical shifts using the following equation:

$$\delta_{calc} = \sigma_{iso} - \sigma_{ref} \qquad \text{(Eq. 3-1)}$$

where σ_{iso} is the isotropic chemical shielding generated from first-principles calculations and σ_{ref} was chosen as the zero intercepts of the fits of the calculated shielding vs. experimental chemical shifts.

3.6 Characterisation conditions

3.6.1 Powder X-ray diffraction

Powder X-ray diffraction patterns were measured using an ARLTM X'TRA Powder Diffractometer (Thermo Fisher Scientific Inc., Waltham, MA, U.S.) employing Cu Kα radiation source (λ = 0.1540562 nm). The patterns were recorded in the range of 2θ from 5 to 36° applying a step size of 0.01° and a scanning rate of 6 s per step for loaded materials and 2 s per step for reference polymorphic forms.

3.6.2 Nitrogen adsorption

Adsorption-desorption isotherms of nitrogen were obtained using a Nova 2200e Surface Area and Pore Size Analyzer (Quantachrome, Hook, UK) at 77 K. All samples were outgassed prior to analysis under high vacuum at 313 K for 12 h. The pore size distribution analysis was performed using the Barrett–Joyner–Halenda (BJH) algorithm using the Broekhoff-de Boer method for the estimation of adsorbed statistical film thickness. The BET specific surface area was calculated using the molecular area of nitrogen of 0.162 nm^2 over a relative pressure range from p/p0=0.05 to 0.20 assuming a monolayer coverage of the material surface. For all three hosts, the size of the pores was calculated from the adsorption branch of the isotherms. The size of the interconnecting pores windows of the MCF host was calculated from the desorption branch of the isotherms.[4,38,192]

3.6.3 Electron microscopy

Scanning electron micrographs were recorded to assess the size and morphology of porous hosts using a JSM 4900 LV (JEOL Ltd, Japan) electron microscope at accelerating voltage of 20 kV. Samples were deposited on an adhesive carbon foil and gold coated prior to the analysis.

3.6.4 Differential scanning calorimetry

Differential scanning calorimetry measurements were performed with a Q 2000 MTDSC instrument (TA Instruments, New Castle, DE, U.S.) using standard crimped TA 100 μL aluminium pans. The sample weight of the loaded materials was 8-10 mg to increase detectability of the crystalline phase, while the sample weight of pure reference crystalline materials was 2-3 mg. The temperature and energy calibration was performed using indium, tin and n-octadecane. A heating rate of 5 K min^{-1} was applied in all the temperature ranges depending on the composite/reference sample under a nitrogen purge of 50 mL min^{-1}. Results were analysed with the TA Instruments Universal Analysis 2000 software (TA Instruments-Waters LLC).

3.6.5 Thermogravimetric analysis

The content of the guest within the loaded materials was determined using a TQ 500 thermogravimetric analyser (TA Instruments, New Castle, DE, U.S.). All samples (5-10 mg) were loaded on platinum pans and heated from room temperature to 383 K with a heating rate of 5 K min^{-1} to remove residual water. Subsequently, the samples were heated from 383 to 873 K using a heating rate of 30 K min^{-1} and left at 873 K for 15 min to ensure total decomposition of the loaded drug. Finally, the analysed samples were heated to 903 K and cooled to 298 K. A sample and balance nitrogen purge flow of 25 mL min^{-1} and 10 mL min^{-1}, respectively, were applied. All results were analysed using the TA Instruments Universal Analysis 2000 software (TA Instruments-Waters LLC).

3.6.6 THz spectroscopy

Terahertz spectroscopy measurements were performed using Advantest TAS7500TS system with a broadband Cherenkov type THz wave source module TAS1130 based on LiNbO$_3$ crystal. 20-50 mg (depending on sample) of sample material was mixed with 300 mg of PTFE powder, pressed into a pellet under 2 tons of pressure and mounted onto a copper sample holder. The copper holder was screwed on the cold finger of a modified continuous flow cryostat (ST-100 FTIR, Janis, Wilmington, MA, USA). The cryostat was operated under vacuum and the temperature was controlled using a temperature controller (Lake ShoreModel 331, Westerville, OH, USA). Samples were annealed for 30 min at approximately 379 K inside the cryostat under vacuum in order to get rid of any adsorbed water vapour. In the next step the cryostat was filled with liquid nitrogen and the samples were cooled to 80 K in approximately 30 min. The system was left to equilibrate for 20 min before the measurements commenced. For all subsequent measurements the samples were heated in 20 K intervals and allowed to equilibrate for 5 min at each heating step. The estimated accuracy in temperature control is 1 K due to the rather robust metal sample holder. The data were analysed using Matlab.[193] The spectra for samples containing crystalline FFA were corrected for a background caused by particle scattering using an asymmetric least squares method with p = 0.008

and $\lambda = 1 \times 10^5$.[194] Background correction was not possible for purely amorphous samples as it was not possible to distinguish between the absorption caused by particle scattering and the absorption caused by molecular interactions.

3.6.7   Solid-state NMR spectroscopy

^{29}Si solid-state NMR spectra were acquired using a Bruker 300 MHz Avance III spectrometer with a double resonance probe operating at frequencies 300.13 MHz for ^{1}H and 59.63 MHz for ^{29}Si. The materials were packed into the 4 mm zirconia rotors and rotated using dry air. The ^{29}Si chemical shifts are given in ppm with respect to external TMS.

 ^{1}H, ^{19}F, ^{13}C and ^{15}N NMR experiments were acquired using a 400 MHz Bruker AVANCE III solid-state NMR spectrometer equipped with a triple resonance probe operating at 400.23 MHz for ^{1}H, 376.57 MHz for ^{19}F, 100.64 MHz for ^{13}C and 40. 57 MHz for ^{15}N. Materials were packed into 4 mm zirconia rotors and rotated using dry air. The ^{1}H and ^{13}C chemical shifts are given in ppm with respect to external TMS, the ^{19}F chemical shifts were recorded with respect to CFCl$_3$ setting PTFE peak to −122.0 ppm and the ^{15}N chemical shifts are quoted with respect to liquid NH$_3$ at 0 ppm by setting reference peak of glycine to 33.4 ppm.[195]

Further ^{1}H, ^{13}C and ^{19}F experiments were performed using a 850 MHz Bruker AVANCE III spectrometer equipped with a triple resonance probe operating at 850.22 MHz for ^{1}H, 799.94 for ^{19}F and 213.81 for ^{13}C. For ^{13}C NMR experiments, materials were packed into 4 mm zirconia rotors and rotated at an MAS rates in the range from 10 to 13 kHz to avoid overlapping of spinning sidebands with ^{13}C peaks. For ^{19}F analysis, all materials were packed into 2.5 mm zirconia rotors and rotated at an MAS rate of 30 kHz. ^{1}H analysis was performed using 1.0 mm double resonance probe operating at 850.22 MHz for ^{1}H, all materials were packed into 1 mm zirconia rotors and rotated at an MAS rate of 78 kHz.

3.6.7.1   *One dimensional single pulse magic angle spinning (MAS)*

All 1D MAS experiments were acquired using a single pulse followed by acquisition of the FID.
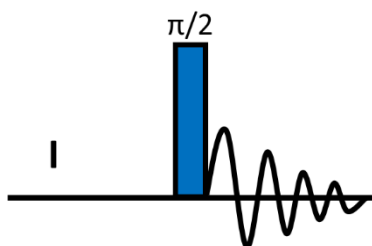
Figure 3-1. Representation of the pulse sequence for 1D MAS NMR experiment.

- ^{1}H MAS NMR spectra were acquired using a ^{1}H $\pi/2$ pulse length of 2.6 μs at an MAS rate of 10 kHz or a ^{1}H $\pi/2$ pulse length of 1.8 μs at an MAS rate of 78 kHz. The recycle delay was set based on the material ^{1}H relaxation times.

- ^{19}F MAS NMR spectra were acquired using a ^{19}F $\pi/2$ pulse length of 3.6 μs at an MAS rate of 10 kHz or a ^{19}F $\pi/2$ pulse length of 4.0 μs at an MAS rate of 30 kHz and a recycle delay of 10 s.

- ^{29}Si MAS NMR spectra were acquired using a ^{29}Si $\pi/2$ pulse length of 4.1 μs at an MAS rate of 4 kHz and recycle delay of 240 s. Usually 2048 transients were acquired for all silica porous hosts.

3.6.7.2   Single pulse ^{13}C with high power decoupling (^{13}C{^{1}H} MAS NMR)

^{13}C{^{1}H} MAS NMR spectra were acquired using a ^{13}C $\pi/2$ pulse length of 3.5 μs at an MAS rate of 10 kHz and recycle delay of 30 s using SPINAL64[131] heteronuclear ^{1}H decoupling during acquisition with a *rf* field of 89 kHz. Typically 1024 scans were acquired with 30 s delay between scans.
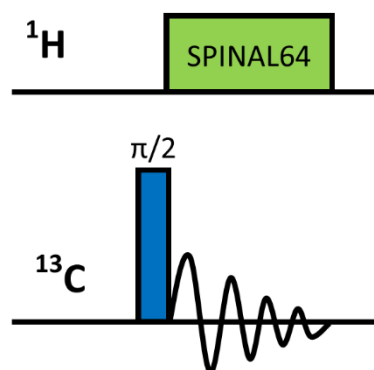
Figure 3-2. Representation of a ^{13}C MAS NMR experiment with ^{1}H high power decoupling (^{13}C{^{1}H} MAS NMR).

3.6.7.3   One dimensional ^{1}H CRAMPS MAS NMR

High resolution ^{1}H spectra were recorded using a PMLG[134] homonuclear decoupling pulse sequence at an MAS spinning rate of 6.8 kHz optimised for best decoupling performance. In ^{1}H 1D CRAMPS, a ^{1}H $\pi/2$ pulse length of 2.5 μs and 32 μs windowed PLMG1 cycle was applied with an effective *rf* decoupling power of 100 kHz. A short acquisition window (10−15 ms) was used in order to acquire a complete data set and to avoid probe overheating. Typically 16-64 transients were acquired with a recycle delay of 10 s.
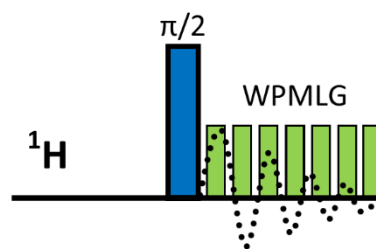
Figure 3-3. Representation of a 1D ^{1}H MAS NMR experiment with WPLMG CRAMPS decoupling.

3.6.7.4 ^{1}H-X Cross-polarisation magic angle spinning (CP/MAS)

All CP/MAS NMR experiments were acquired using ramp amplitude implemented on the ^{1}H channel during the contact step and the SPINAL64[131] heteronuclear dipolar decoupling used during acquisition.
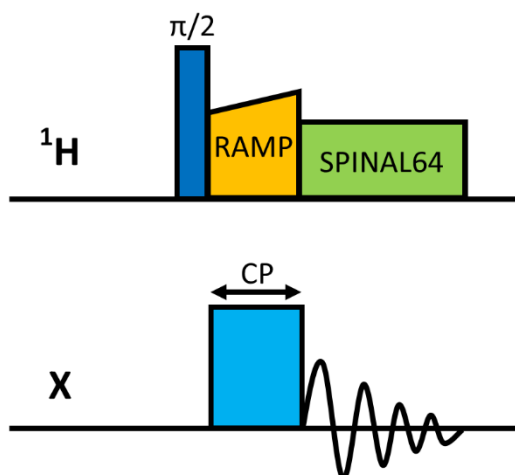
Figure 3-4. Representation of a ^{1}H-^{13}C CP/MAS pulse sequence.

- ^{1}H-^{13}C CP/MAS NMR spectra were acquired using a ^{1}H $\pi/2$ pulse length of 3.2 μs and a CP contact time of 2 ms at an MAS rate of 10 kHz. The Hartman–Hahn conditions were set using hexamethylbenzene (HMB). Typically 1024 transients were acquired for loaded silica composites and 256 transients for reference crystalline materials with a recycle delay of 10 s.

- ^{1}H-^{29}Si CP/MAS NMR spectra were acquired using a ^{1}H $\pi/2$ pulse length of 3.7 μs and a CP contact time of 2 ms at an MAS rate of 4 kHz. The Hartmann–Hahn match was set with kaolinite. Typically 1024 transients were acquired with a recycle delay of 30 s. The ^{1}H-^{29}Si

variable contact time CP/MAS NMR measurements used contact times ranging from 0.05 to 10.0 ms.

- o ^{1}H-^{15}N CP/MAS NMR spectra were acquired using a ^{1}H $\pi/2$ pulse length of 3.2 μs and a CP contact time of 2 ms at an MAS rate of 10 kHz. The Hartmann–Hahn match was set with glycine. Typically 256 transients were acquired with a recycle delay of 10 s.

3.6.7.5   Non-quaternary suppression (Dipolar dephasing) experiment

Distinction between protonated and quaternary carbons can be made using dipolar dephasing ^{1}H-^{13}C CP/MAS NMR pulse sequence, which is a spectral editing method. During the dephasing delay implemented between the CP step and acquisition, ^{13}C bound to the ^{1}H lose their magnetisation due to strong heteronuclear dipolar interactions leading to absence of the signals. This enables to distinguish CH and CH$_2$ functional groups from quaternary carbons. Usually the CH$_3$ carbon peaks do not lose the intensity in the NQS experiment due to the fast mobility of the methyl group which is only slightly affected by heteronuclear dipolar interactions.
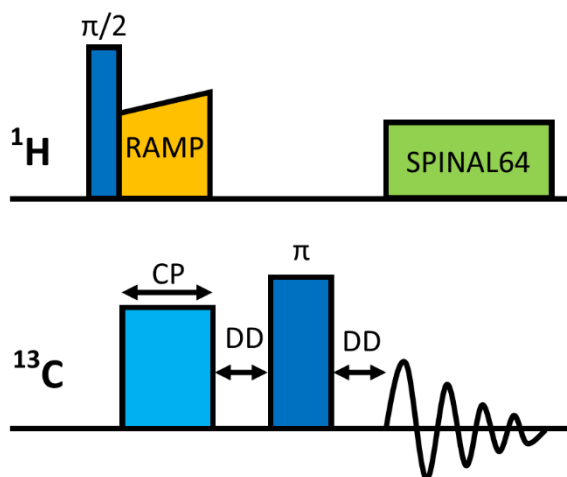
Figure 3-5. Representation of a ^{1}H-^{13}C CP/MAS dipolar dephasing (DD) NMR experiment.

The dephasing delay (DD) used in the experiment was 60 μs. Typically 256 transients were acquired for Z'=1 and Z'=2 structures and 1024 for Z'=3 (α-IMC) for better resolution.

3.6.7.6   One dimensional ^{1}H → ^{13}C J-MAS-INEPT experiment

The enhancement of ^{13}C signal in solids with high mobility is very difficult to achieve using CP based methods due to efficiency loss of the cross polarisation step. For such systems enhancement of the ^{13}C signal can be achieved using transfer of nuclear spin polarisation from ^{1}H spins by application of INEPT[196] pulse sequence under MAS conditions.[197,198] Furthermore, this method can be used to

detect through bond connections between heteronuclei.[197,199] The maximum signal enhancement for two coupled spin ½ nuclei is achieved when τ = 1/4J, assuming $T_2 >> 1/J$.[197,198] It needs to be emphasised that for rigid solids with very short T_2 relaxation times it is not possible to store the magnetisation in the *xy* plane for long enough to obtain sufficient polarisation transfer.[198] For such systems homonuclear dipolar decoupling needs to be applied during the τ evolution times.[198] Hence, we used the J-MAS-INEPT experiment as a probe of heterogenous solid materials which are composed of species with different mobility, which cannot be detect using CP based methods.
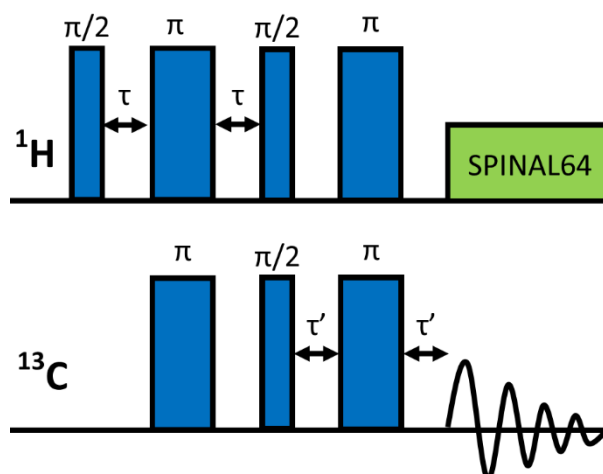
Figure 3-6. Representation of a J-MAS-INEPT pulse sequence.

All J-MAS INEPT experiments were acquired at an MAS rate of 10 kHz using a ^{1}H π/2 pulse length of 3.2 μs and ^{13}C π/2 pulse length of 3.5 μs. The τ and τ′ delays were optimised for best signal enhancement and set to τ = 1.1 ms and τ′ = 0.9 ms. SPINAL64[131] heteronuclear dipolar decoupling was applied during acquisition. Typically 1024 scans were used for drug : silica composites with recycle delay of 10 s.

3.6.7.7 Two dimensional ^{1}H-X heteronuclear correlation (HETCOR)

2D ^{1}H-X HETCOR[200,201] NMR experiment enables to correlate the ^{1}H chemical shifts recorded in the indirect dimension with the X nuclei chemical shifts in the direct dimension. The FSLG[133] homonuclear dipolar decoupling is applied during the t_1 increment which enables ^{1}H magnetisation to evolve only under the chemical shift Hamiltonian. By using short contact times during the CP step it can be assumed that only hydrogens covalently bound to carbons are correlated.
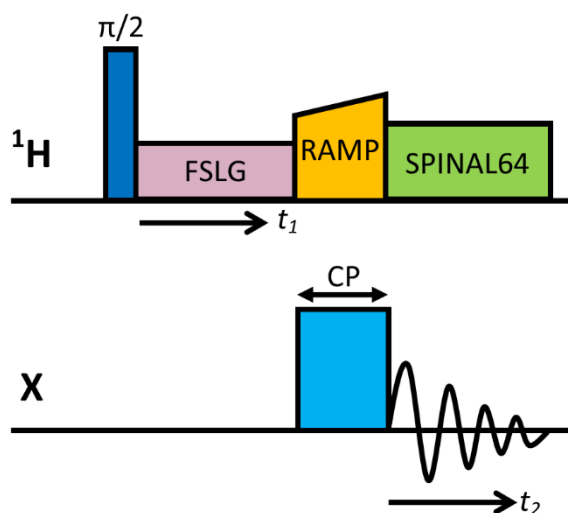
Figure 3-7. Representation of a ^{1}H-X HETCOR pulse program.

2D ^{1}H-^{13}C HETCOR[133,200] MAS NMR spectra were acquired using FSLG[201] homonuclear dipolar decoupling with a ^{1}H *rf* field of *ca.* 92.6 kHz and CP contact time of 50 μs. SPINAL64[131] heteronuclear dipolar decoupling was used during acquisition. A recycle delay of 2 s and an MAS rate of 10 kHz were used. Typically 128 increments were recorded in the indirect dimension with 192 transients per increment.

3.6.7.8   Two dimensional ^{1}H-^{1}H spin diffusion experiment

Close proximities between different ^{1}H sites were probed using 2D ^{1}H-^{1}H spin diffusion experiment with windowed PMLG homonuclear decoupling reported by Leskes *et al*.[134] at 9.4 T and 6.8 kHz MAS rate or phase sensitive NOESY experiment (the same as for solution state spectrometers) at 20 T and 78 kHz. The pulse program is composed by π/2 pulse, creating transverse magnetisation evolving during t_1 followed by another π/2 pulse, which places the magnetisation along the *z* axis where it evolves for a fixed mixing time (t_m). The last π/2 pulse moves back the magnetisation in the *xy* plane for acquisition. WPMLG homonuclear decoupling is used during t_1 evolution and acquisition.
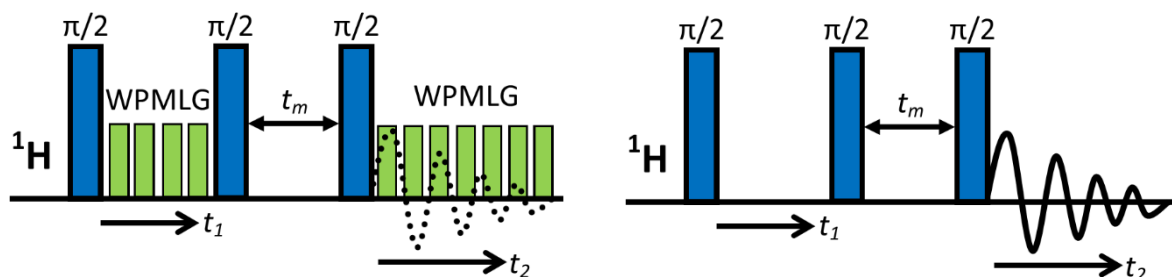
Figure 3-8. Representation of a ^{1}H-^{1}H NOESY experiment acquired with WPLMG decoupling at 9.4 T (left) and without decoupling at 20.0 T (right) spectrometers.

A ^{1}H $\pi/2$ pulse lengths of 2.5 µs at 9.4 T and 1.8 µs at 20.0 T were applied, using recycle delays of 4 and 5 s, respectively. 256 (9.4 T) and 512 (20.0 T) increments were acquired in t_1 with 8 (9.4 T) or 4 (20.0 T) scans per increment. Full build-up curves were constructed when analysing the IMC polymorphs at 9.4 T (from 0 – 2 ms in 20 experiments). Analyses at 20.0 T were performed at two mixing times of 50 and 150 ms.

3.6.7.9   Two dimensional ^{1}H-^{1}H SQ DQ correlation experiment

The high-resolution two-dimensional ^{1}H-^{1}H Double-Quantum CRAMPS NMR experiment at 9.4 T was performed using a pulse sequence previously published by Brown *et al.* (Figure 3-9).[202] The spectra were acquired at an MAS rate of 6.8 kHz optimised for best decoupling efficiency. The POST-C7 pulse sequence was used to obtain double quantum coherences with an effective *rf* field of 7 x MAS rate, *i.e.*, 47.6 kHz and a ^{1}H $\pi/2$ pulse length of 2.5 µs. During the evolution period (t_1) 32 µs windowed DUMBO cycle was applied, while 32 µs windowless DUMBO cycle was applied during the acquisition step, both with an effective *rf* decoupling power of 100 kHz. A short acquisition window (10–15 ms) was applied in order to acquire a complete data set and to avoid probe overheating. A total of 128 increments were acquired in the indirect dimension with 16 scans each.
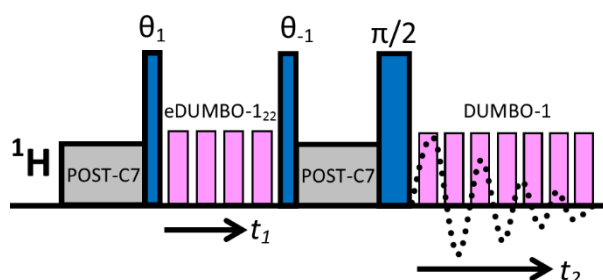
Figure 3-9. Representation of a 2D ^{1}H-^{1}H Double-Quantum CRAMPS experiment with POST-C7 excitation reconversion pulse sequence and DUMBO decoupling.

Application of additional homonuclear dipolar decoupling pulse sequences at high MAS rates (78 kHz) and high field spectrometers (20.0 T) do not improve the resolution of the spectra but may lead to artefacts. In this case for the acquisition of ^{1}H-^{1}H Double-Quantum correlation spectra at 20.0 T and at an MAS rate of 78 kHz we used BABA pulse sequence for excitation and recoupling and a ^{1}H $\pi/2$ pulses of 1.8 µs (Figure 3-10). A total of 400 increments were acquired in the indirect dimension with 16 transients for each increment and a recycle delay of 5 s.
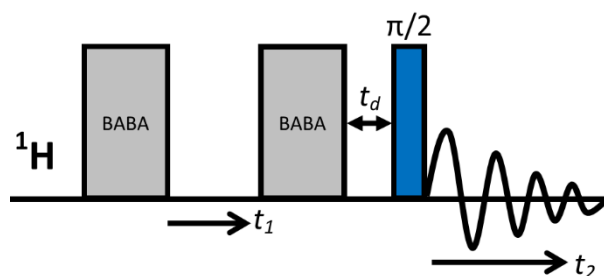
Figure 3-10. Representation of a 2D ^{1}H-^{1}H Double-Quantum pulse sequence using BABA excitation reconversion pulse sequence.

3.6.8 Spin-lattice relaxation

3.6.8.1 Spin-lattice relaxation in the laboratory frame T_1

All T_1 relaxation experiments for both ^{1}H and ^{19}F nuclei were acquired using a standard inversion-recovery (IR) pulse sequence (Figure 3-11).
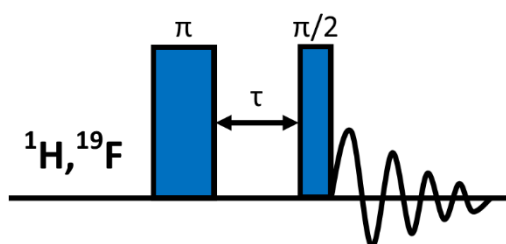
Figure 3-11. Representation of an inversion recovery pulse sequence.

The first π pulse rotates the magnetisation to the −z axis followed by the evolution period τ and the second π/2 pulse rotates the magnetisation back to the −xy plane for detection of the remaining magnetisation. The ^{1}H and ^{19}F π/2 pulses used were 3.4 μs and 3.6 μs long, respectively. Typically, 16 experiments were acquired with a τ delay in the range from 0.001 to 15 s for ^{19}F T_1 relaxation measurements and 0.01 to 30 s for ^{1}H T_1 relaxation measurements. The peaks intensities or integrations were plotted as a function of the delay time τ and fitted with the monoexponential equation (Eq. 3-2):

$$M_z(t) = M_{0z}\left[1 - 2exp\left(-\frac{t}{T_1}\right)\right] \qquad \text{(Eq. 3-2)}$$

where t is the delay time and $M_z(t)$ is remaining net magnetisation after t delay.

3.6.8.2 *Spin-lattice relaxation in the rotating frame $T_{1\rho}{}^H$ and $T_{1\rho}{}^C$*

The modified CP pulse sequence was used to measure $T_{1\rho}{}^H$ and $T_{1\rho}{}^C$. For $T_{1\rho}{}^H$ after the first $\pi/2$ pulse the spin-locking pulse is implemented, which locks the ^1H magnetisation along the y axis for a set time τ between 0.01 and 20 ms. During this time ^1H magnetisation evolves under homonuclear dipolar interactions resulting in decrease of net magnetisation, which depends on the ^1H relaxation efficiency in the rotating frame. The remaining ^1H magnetisation is detected *via* ^{13}C using the standard CP step implemented after the spin-locking pulse (Figure 3-12).

The indirect detection of $T_{1\rho}{}^H$ enables better resolution of different ^1H sites through ^{13}C spectrum. In all experiments a spin-locking power of 78 kHz, a CP contact pulse of 2 ms and a recycle delay of 10 s were used. A total of 12 experiments were acquired varying the length τ of the spin locking pulse. The peak intensities were fitted to the exponential equation (Eq. 3-3):

$$M(t) = M_{0i}\,exp\left(-\frac{t}{T_{1\rho i}}\right),\qquad\qquad \text{(Eq. 3-3)}$$

where *t* is the duration of spin locking pulse and *M(t)* is the peak intensity at time *t*.
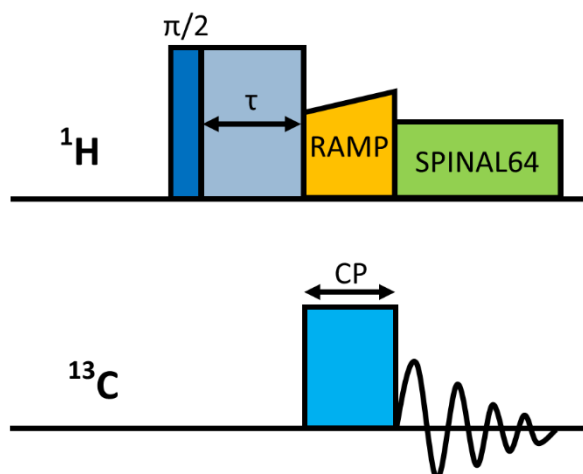
Figure 3-12. Representation of a $T_{1\rho}{}^H$ pulse sequence with spin-locking pulse applied on ^1H channel.

Similarly, it is possible to measure $T_{1\rho}{}^C$ relaxation times. The pulse sequence is composed of a $\pi/2$ pulse followed by a CP step, after which the spin locking pulse is applied on the ^{13}C channel locking the ^{13}C magnetisation along *y* axis for set time (τ) between 0.01 to 20 ms (Figure 3-13). During this time the ^{13}C magnetisation evolves under homonuclear spin-spin interactions resulting in decrease

of the net magnetisation similarly to $T_{1\rho}^H$. A total of 12 experiments with different τ values were acquired. The peak intensities were fitted to the exponential equation (Eq. 3-3). A CP contact time of 2 ms and a recycle delay of 10 s were used. A spin locking *rf* pulse of 72 kHz was applied.
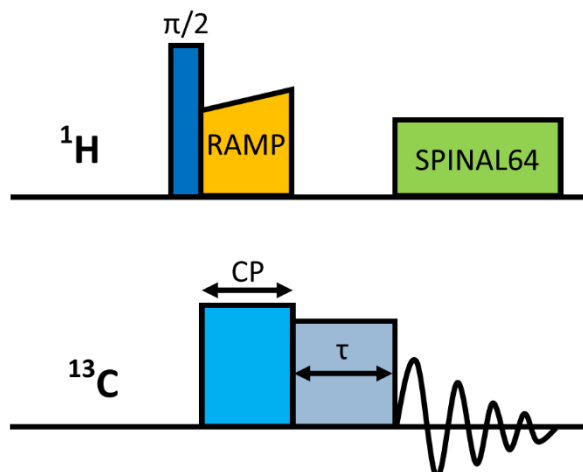
Figure 3-13. Representation of a $T_{1\rho}^C$ pulse sequence with spin-locking pulse applied on ^{13}C channel.

3.6.9 Variable temperature (VT) experiments

Typically, VT measurements were performed in the temperature range from 223 to 353 K in 10 K steps. The temperature control was achieved using the Bruker BCU II chilling unit or through the heating the sample using heater implemented in the probe. The temperature of the sample was stabilised for 5 min at set temperature before starting the measurement.

3.6.10 Data processing

All NMR spectra were acquired and processed using Bruker Topspin 3.1.7 software. Deconvolution of NMR peaks and relaxation data fitting was made using Origin Pro 8.5.1 software.

Indomethacin polymorphism: introducing solid state studies on indomethacin form IV and form V

Chapter 4

4.1 Introduction

Indomethacin (IMC) (2-{1-[(4-Chlorophenyl)carbonyl]-5-methoxy-2-methyl-1*H*-indol-3-yl}acetic acid) is a model pharmaceutical compound used frequently in crystallographic research due to its well-recognised polymorphism and complex phase behaviour.[59,156,179,203–216] The molecular flexibility of the 4-chlorophenyl ring, carboxylic acid motif and methoxy group makes it an interesting system for conformational studies (Figure 4-1 A and B). The conformational flexibility is demonstrated by the arrangement of the IMC molecules in the different crystal structures.
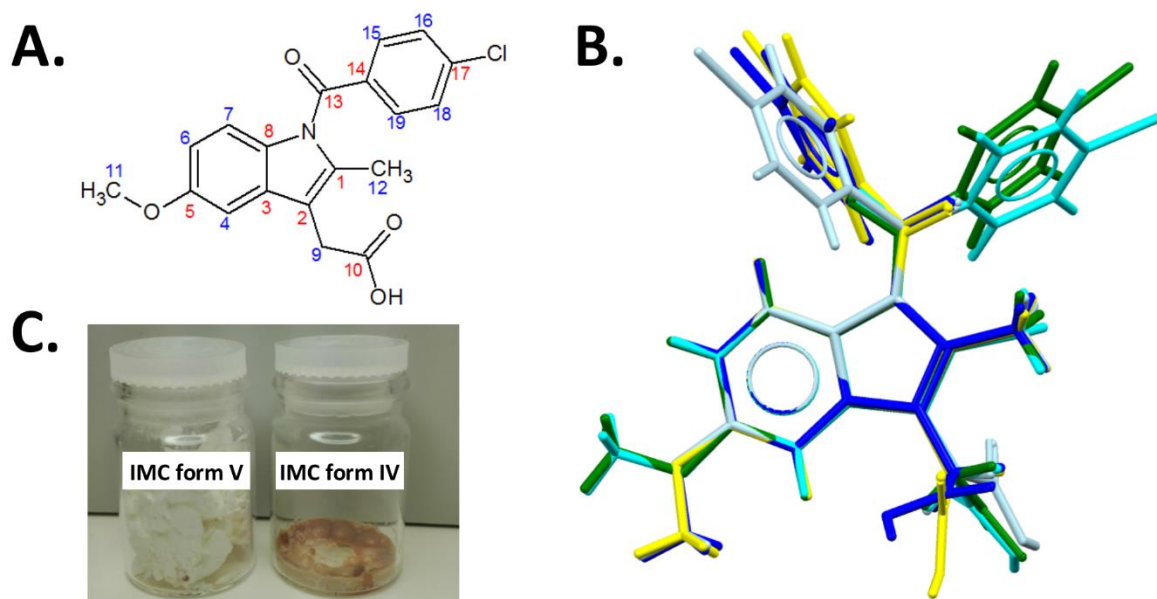
Figure 4-1. **A.** Structure of IMC with numbering of carbon atoms. Red labels indicate quaternary carbons. **B.** Conformation flexibility of IMC in three different crystalline forms; most thermodynamically stable γ-IMC (yellow), IMC MeOH solvate (green) and α-IMC (molecule A – dark blue; molecule B – cyan; molecule C – light blue) structures are overlaid with carbons C5-C7. **C.** Crystals of IMC form IV – obtained by annealing of IMC glass and IMC form V formed after desolvation of MeOH solvate.

Therefore, by looking at molecular conformation in different solvents or in the amorphous state and comparing them with the IMC conformation within the crystal one can gain understanding of aggregation processes at the early stages of crystallisation from a solution or the amorphous state.

The main focus of this chapter is the application of solid-state NMR spectroscopy to clarify molecular level arrangements in different solid forms of IMC, and to investigate structural differences between two polymorphic forms of IMC (Form IV and Form V). These forms have been incorrectly considered to be one crystalline phase (δ-IMC, Figure 4-1C). The story of δ-IMC began 40 years ago, when Borka published the first paper on IMC polymorphism.[203] Due to small differences in the melting points between the two IMC forms (IV and V) (analysed at that time using hot stage microscopy) and poor IR spectroscopic data, the author specified that the crystalline form IV (δ-IMC) can be obtained from warm methanol or annealing of the IMC glass in the range of temperature from 343 to 363 K.[203] Despite a large volume of research published on its crystalline forms (including δ-IMC) there is a lack of understanding of the differences in the structure of these two forms.

This chapter developed from a short study into systematic investigation of different IMC phases due to scientific curiosity to fundamentally understand the self-organisation of molecules from the solution or amorphous state into their solid form, and investigate opportunities to control these processes. IMC form IV and form V are not trivial examples of pharmaceutical polymorphism. The crystal structures of both the forms are yet to be determined, as single crystals are difficult to obtain and low crystallinity of the powders leads to significant broadening of the PXRD peaks. Additionally, the relatively large molecular weight of the compound (357.79 g mol $^{-1}$), significant flexibility and Z'=2 (as determined using solid-state NMR) make the application of CSP methods challenging. IMC form IV and form V are therefore excellent examples of challenging problems to be solved by NMR crystallography. The ultimate goal of this study is to elucidate the structural reorganisation of the IMC methanol solvate upon desolvation, which forms a new crystalline form - IMC form V. Additionally, solid-state NMR methods were employed to obtain information on the conformation of molecules forming low crystallinity IMC form IV (obtained by annealing of IMC glass). This is of importance from a pharmaceutical perspective as IMC crystallisation from the amorphous state is a frequently discussed model in polymorphism and stability of organic glasses.

This chapter is a part of collaboration between Universities in Innsbruck, Cambridge, UCL (London), Riga and Norwich and includes the following researchers: Dr Doris Braun (University of Innsbruck: crystal structure prediction, conformational analysis, indexing of IMC form V), Prof. Chris Pickard (University of Cambridge: crystal structure prediction), Dr Inese Sarcevice (University of Riga: VT PXRD studies).

4.1.1 Solvent mediated crystallisation

The crystal structure of the most stable IMC polymorph (γ-IMC) was determined by Kistenmacher and Marsh in 1972.[178] Two years later, Borka studied the polymorphism of IMC extensively by isolating four forms of IMC including Form I (γ-IMC, m. p. 433 K), Form II (α-IMC, m. p. 427 K), Form III (m. p. 421 K), Form IV (m. p. 407 K) and several solvates, often labelled as β-IMC.[203] Crystallisation of IMC can result in the formation of different polymorphic forms depending on the level of supersaturation, solvent used and crystallisation method. There have been seven studies to date which focus on the crystallisation of IMC from different solvents[180,203,206,207,209,212,217] and one study discussing crystallisation from binary mixtures[218] of the solvents, reporting crystallisation from a total of 25 solvents. Solvents at high IMC supersaturation yield either solvates or α-IMC, indicating kinetically controlled crystallisation. Solvated forms of IMC can be obtained from tert-butanol, cyclohexanone, dichloromethane, chloroform, tetrachloromethane, benzene and tetrahydrofuran. IMC solvates are predominately formed at 0.5:1 solvent:IMC stoichiometric ratio, with only crystallisation from MeOH and tert-butanol yielding structures at 1:1 solvent:IMC stoichiometric ratios.[217] These two examples are the only fully solved crystalline IMC solvate structures to be reported in the CCDC.[185,219] The most thermodynamically stable γ-IMC was obtained at low supersaturation from 15 solvents indicating thermodynamically controlled crystallisation of IMC occurs under these conditions. The solvent mediated crystalline forms of IMC are summarised in Table 4-1.

A hybrid approach to solvent mediated recrystallisation was recently proposed by Surwase *et al.*[220] The authors performed several recrystallisations from amorphous suspensions of IMC in water at different temperatures and pH, isolating and identifying seven different crystalline forms of indomethacin, including three new polymorphs with distinct PXRD, DSC, FTIR and Raman spectroscopic features.[220]

4.1.2 Crystallisation from the amorphous state

There are at least 11 reports on the recrystallisation of IMC from the amorphous state, including isothermal[204,213] and non-isothermal recrystallisation studies[59,208], molecular mobility and stability studies describing the effect of water on amorphous IMC[214,216] and, more recently, a study investigating the effect of preparation methods on stability, dissolution and recrystallisation behaviour of amorphous indomethacin[221,222].

There are several methods for the preparation of amorphous indomethacin including melt quenching, spray drying and cryo- or ball milling.[212,221] The preparation method is known to affect the recrystallisation behaviour and stability of amorphous IMC.[60] It was shown in several studies that the most stable amorphous IMC is obtained by quenching of molten material.[58,59,204,213,221]

Table 4-1. Summary of literature data on crystalline forms of IMC obtained after crystallisation from different solvents. The table includes information from seven studies published on IMC polymorphism.

Solvent	Crystalline form of IMC	Additional notes*
Alcohols		
Methanol	Form I (γ-IMC)[209] Form II (α-IMC)[203,217], solvate[180,203,212,217], Form IV (δ-IMC) [180,203,212],	Solvate of IMC is formed at low supersaturations, while at higher supersaturations form II (α-IMC) or mixture of both forms can be obtained. Form IV (δ-IMC) is a desolvation product of methanol solvate.
Ethanol	Form II (α-IMC)[203,206,207,209,212,217], Form I (γ-IMC)[206,217]	High supersaturation, slow evaporation or precipitation from warm ethanol using water as antisolvent, Low supersaturation
1-Propanol	Solvate[203,209,217] and/or Form II (α-IMC); Form I (γ-IMC)[217]	High supersaturation Low supersaturation
2-Propanol	Solvate and/or Form II (α-IMC); Form I (γ-IMC)[217]	High supersaturation Low supersaturation
tert-Butanol	Solvate[180,212,217]	High and low supersaturation
1-Butanol	Solvate and/or Form II (α-IMC); Form I (γ-IMC)[217]	High supersaturation, Low supersaturation
Isobutanol	Solvate and/or Form II (α-IMC); Form I (γ-IMC)[217]	High supersaturation Low supersaturation
Pentanol	Solvate and/or Form II (α-IMC); Form I (γ-IMC)[217]	High supersaturation Low supersaturation
Isopentanol	Solvate and/or Form II (α-IMC); Form I (γ-IMC)[217]	High supersaturation Low supersaturation
Octan-2-ol	Solvate and/or Form II (α-IMC); Form I (γ-IMC)[217]	High supersaturation Low supersaturation
Cyclohexanol	Solvate and/or Form II (α-IMC); Form I (γ-IMC)[217]	High supersaturation Low supersaturation
Ketones and ethers		
Acetone	Solvate[203,209,217], Form II (α-IMC)[217], Form I (γ-IMC)[217]	High supersaturation Low supersaturation
Butan-2-on	Solvate and/or Form II (α-IMC), Form I (γ-IMC)[217]	High supersaturation Low supersaturation
Cyclohexanone	Solvate[217]	High and low supersaturation
Halogenated solvents		
Dichloromethane	Solvate[203,209,217]	High and low supersaturation
Chloroform	Solvate[203,209,217]	High and low supersaturation
Tetrachloromethane	Solvate[217]	High and low supersaturation
Other		
Benzene	Solvate[203,209,217]	High and low supersaturation
Toluene	Solvate and/or Form II (α-IMC), Form I (γ-IMC)[217]	High supersaturation Low supersaturation
Dimethyl formamide	Form II (α-IMC)[203]	
Glacial acetic acid	Form II (α-IMC)[203]	
Acetonitrile	Form II (α-IMC)[203,207,217] Form I (γ-IMC)[203,206,217],	High supersaturation Low supersaturation
Ethyl acetate	Solvate and/or Form II (α-IMC)[203,217] Form I (γ-IMC)[217]	High supersaturation Low supersaturation
Diethylether	Solvate[203,209,217], Form II (α-IMC)[209,217] Form I (γ-IMC)[203,217]	High supersaturation Low supersaturation
Tetrahydrofuran	Solvate[209,217]	High and low supersaturation
Water	Form II (α-IMC)[203], Form I (γ-IMC)[207,209]	Slow evaporation[207,209]

* Additional notes highlight the crystallisation conditions, preparation methods or observations made by authors. In most studies crystallisation of IMC was carried out using slow evaporation method at high or low supersaturation of the drug in the solvent. Two papers describe antisolvent precipitation as a method to obtain α-IMC.

Furthermore, the cooling rate of molten IMC also determines the stability and recrystallisation behaviour of an amorphous drug.[59,208] The most pronounced effect was observed through the non-isothermal crystallisation of amorphous IMC obtained by slow or quench cooling of molten material, where recrystallisation to either α- or γ-IMC was reported.[59] The processing of amorphous melt, *i.e.*, mortar grinding of IMC glass, compared to un-triturated material, significantly reduced the stability of non-crystalline drug. Glassy IMC was reported to be stable for over 2 years[58], while the 36 hours induction period prior to crystallisation of rapidly cooled, mortar grinded material was reported by Fukuoka *et al.* and later by Yoshioka *et al.*[58,59]

All reports on crystallisation of amorphous IMC demonstrate the formation of either α- or γ-IMC. Kinetic studies of isothermal recrystallisation of amorphous IMC below the glass transition temperature (IMC T_g *ca.* 323 K) show the formation of the most stable γ-IMC, while α-IMC predominately crystallises at temperatures above 323 K.[59,204,213] Interestingly, there have been no further reports on the formation of IMC form IV from amorphous IMC as previously shown by Borka.[203] We therefore hypothesised that IMC form IV can only be formed from rapidly cooled, intact glass, as all previously described studies used ground amorphous drug. This hypothesis was evaluated in numerous experiments where the same isothermal crystallisation of IMC glass was performed in different laboratories at UEA, University of Riga, University of Innsbruck, UCL and University of Warwick.

4.2 Results and discussion

4.2.1 Solid state characterisation of IMC polymorphs and MeOH solvate

4.2.1.1 Powder X-ray diffraction and differential scanning calorimetry studies
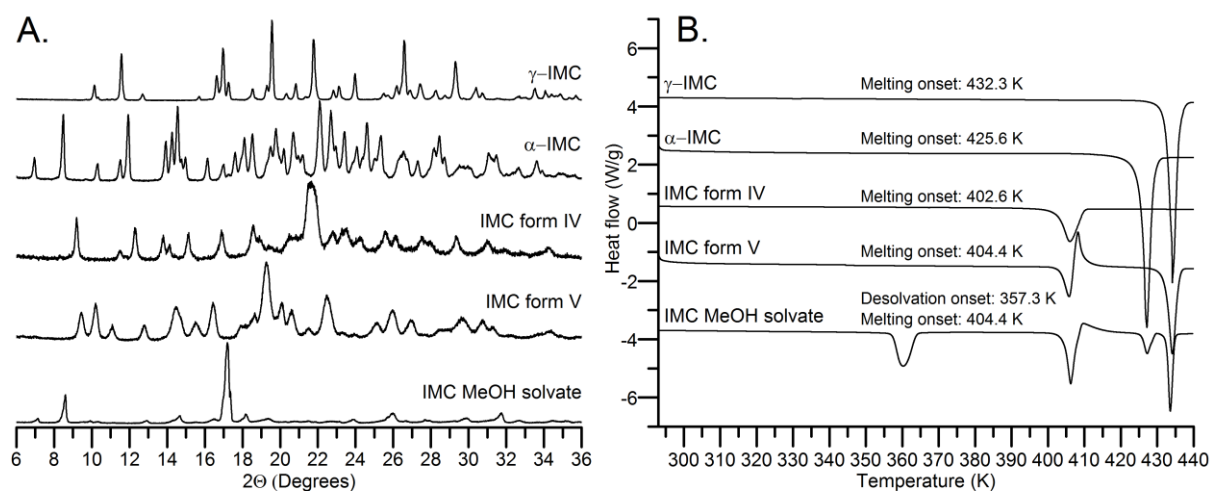

Figure 4-2. A. PXRD traces and **B.** DSC thermograms of IMC polymorphs and MeOH solvate.

The thermodynamically most stable form of indomethacin (γ-IMC) has the space group symmetry $P\bar{1}$ with Z' = 1. The γ-IMC crystal structure is stabilised by centrosymmetric $R_2^2(8)$ hydrogen bonded ring motifs,[223] formed between carboxylic acid groups. γ-IMC shows a melting point between 432.1 to 434.3 K and an enthalpy of fusion of 110 J g^{-1}.[178,207,224] Metastable α-IMC, another frequently occurring polymorph, crystallises in the monoclinic space group $P2_1$ with Z' = 3 and has very different conformations compared to γ-IMC. α-IMC exhibits a melting point between 426.0 to 428.0 K with an enthalpy of fusion of 97.5 J g^{-1}.[207,215] The methanol solvate crystallises in the monoclinic space group $P2_1/n$ (Z' = 1), with a stoichiometric ratio of IMC:MeOH of 1:1 (BANMUZ[185]). The solvate structure is stabilised by hydrogen bonds between the carboxylic acid groups of IMC and the alcohol groups of the methanol molecules, which form a $R_4^4(12)$ ring motif.[185] The solvent molecules are located in channels along the crystallographic b axis, from which they may easily escape during desolvation.[180] The DSC curve (open pan) of IMC methanol solvate shows an endothermic peak at an onset temperature of 357 K, which is in agreement with previous studies and corresponds to the desolvation of the solvate to IMC form V.[180,212] A second endothermic event at 404.4 K is related to the melting of form V and is followed by recrystallisation of the two more stable forms of IMC (α and γ). IMC form V, often incorrectly called δ or form IV, can be obtained *via* slow desolvation of the methanol solvate at room or elevated temperatures, or under vacuum.[180,220] Based on our experience, a slow desolvation process at room temperature may take up to 3 months, but leads to pure form V; while a much faster desolvation at elevated temperatures often leads to a mixture of polymorphs (V, γ, α). The crystal structure of IMC form V is yet to be determined, as this phase is a desolvation product exhibiting low crystallinity. The diffraction pattern of form V was indexed to a monoclinic unit cell (298 K: a = 18.5450 Å, b = 5.4032 Å, c = 18.2967 Å, β = 95.6421°) using the first twenty peaks with DICVOL04 with a space group $P2_1$ based on a statistical assessment of systematic absences, as implemented in the DASH structure solution package.[225,226] From the cell volume it was derived that there are two IMC molecules in the asymmetric unit (Z' = 2). IMC form V shows small needles which melt between 403–404 K followed by recrystallisation directly into γ-IMC or α-IMC or mixture of both.[180] All DSC data of the reference samples are summarised in Figure 4-2B. The PXRD patterns of the reference samples (Figure 4-2A) are in good agreement with the simulated patterns for the IMC structures published in the CSD (Cambridge Structural Database) for structures INDMET (γ-IMC, form I), INDMET02 (α-IMC, form II) and BANMUZ (IMC methanol solvate).[178,179,185,227] The PXRD pattern of IMC:MeOH (1 : 1) solvate shows two strong intensity peaks with d(002) = 10.27 Å and d(004) = 5.15 Å, even after careful grinding, which may be related to preferred orientation of the fine needles. The PXRD pattern of form V IMC is in a good agreement with those published previously.[212,220]
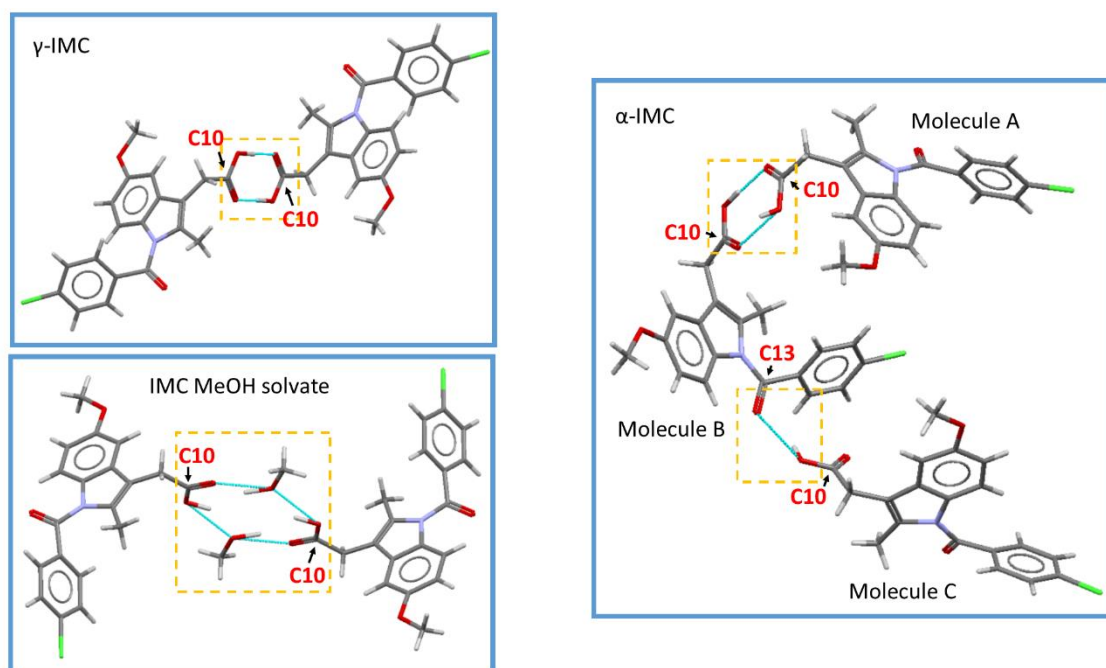
Figure 4-3. Hydrogen bonding patterns in three different IMC crystal structures: γ-IMC, IMC MeOH solvate and α-IMC (CSD ref. INDMET, BANMUZ and INDMET02).

There is only one previous report of IMC form IV (Borka, 1974), which includes only the preparation method and melting point of the material at *ca.* 407 K.[203] IMC form IV was formed from quenched cooled IMC glass after annealing at 343-363 K, which is in agreement with Borka's results. The crystalline phase grows as a brownish opaque chunk from the IMC amorphous glass (Figure 4-1C). Pure IMC form IV was only formed when the IMC glass was fracture-free. Any visible imperfections in the IMC glass always resulted in concomitant crystallisation of IMC form IV and either α- or γ-IMC. The cracks in the glass are easily introduced by quenching at very low temperatures, *e.g.* in an ice bath. The DSC thermogram of IMC form IV shows a broad melting event with an onset at 402.6 K and the fusion enthalpy of *ca.* 66 J g^{-1} (Figure 4-2B). There was no clear single crystal formed during the recrystallisation process. The PXRD pattern of the unground material shows very broad peaks indicating its low crystallinity (Figure 4-4). The crystallinity of the sample increased rapidly by crushing or scratching the surface, as shown in PXRD traces 2 and 3 in Figure 4-4. Unfortunately, indexing of the IMC form IV PXRD pattern was not possible due to low crystallinity of the sample and possible impurities from α-IMC (See Figure 4-4 traces 4, 6 and 7). There was no further increase in the crystallinity of the material after ball milling. Instead, the sample became amorphous, which is typical for all IMC polymorphs.[60,212] Further exposure of the amorphous material to the EtOH vapour led to formation of α-IMC.
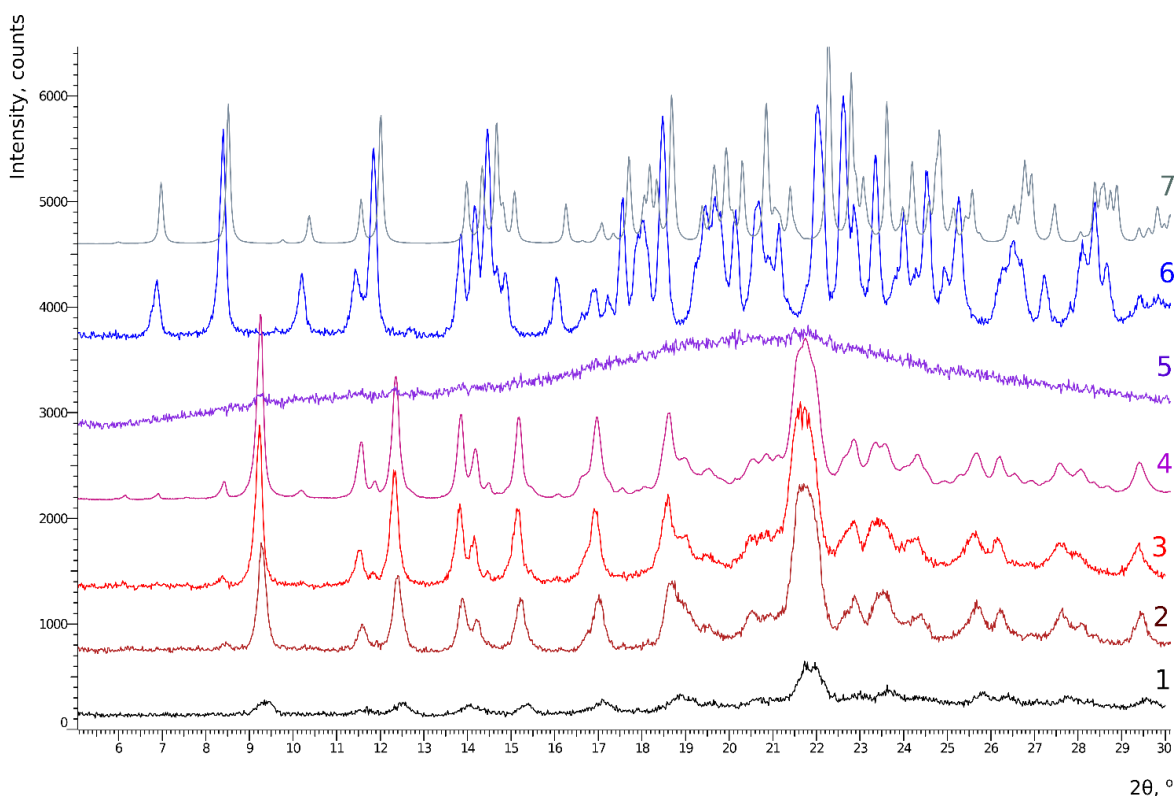
Figure 4-4. PXRD traces of IMC form IV. **1)** Chunk of IMC form IV without grinding; **2)** ground IMC form IV and **3)** sample 2) after 6 hours storage; **4)** ground IMC form IV after overnight acquisition used for indexing; **5)** PXRD of indomethacin IV after milling in ball mills (5 mL milling jars, 10 min, 25 Hz, 1 × 8 mm ball); **6)** material 5) after keeping it under the vapour of EtOH for 1 h; **7)** simulated PXRD of INDMET02[179].

4.2.1.2 Solid-state NMR

Indomethacin has been widely studied using solid-state NMR spectroscopy, as a complementary technique to single crystal structure determination of both the α- and γ-polymorphs. Advanced solid-state NMR methods focusing on detailed analysis of hydrogen bonding patterns and inter- and intramolecular distances within the crystal were supported by first principles calculations.[156,205,215,228] The analysis of the differences in ^{13}C and ^{1}H spectra between crystalline forms of IMC is presented in the following sections, starting with the well described model of γ-IMC to compare our experimental set up with previously published data. Inter- and intramolecular connectivity between nuclei were analysed using ^{1}H-^{1}H SQ-DQ and ^{1}H-^{1}H spin diffusion experiments and compared with available crystal structures in the CSD for γ-IMC, α-IMC and IMC MeOH solvate (INDMET[178], INDMET02[179], BANMUZ[185], respectively). All presented spectra were acquired at both 9.4 and 20.0 T using either fast MAS (78 kHz at 20.0 T) or CRAMPS experiments (6.8 kHz at 9.4 T) with windowed PLMG decoupling (see experimental section for details).

Structural analogies reflected in the changes of ^{13}C and ^{1}H spectra of known IMC polymorphs, due to the conformational differences of molecules in the unit cell, were used to gain structural

information of IMC forms IV and V. The methodology of experimental and computational studies is presented in the following steps:

1. Acquisition of ^{13}C spectra and identification of quaternary and non-quaternary carbons in a set of ^{13}C and [1]H-^{13}C correlation experiments: [1]H-^{13}C CP/MAS, [1]H-^{13}C NQS CP/MAS, [1]H-^{13}C HETCOR at short contact time (50 μs);

2. Calculation of ^{1}H and ^{13}C chemical shifts of geometry optimised structures based on the GIPAW approach and comparison with experimental data;

3. Detailed assignment of ^{1}H spectrum based on GIPAW calculations and [1]H-^{13}C HETCOR spectrum;

4. Acquisition of ^{1}H spectra: [1]H at fast MAS, ^{1}H CRAMPS, and correlation experiments [1]H-^{1}H SQ-DQ and set of [1]H-^{1}H spin diffusion experiments to evaluate molecular proximities between different ^{1}H sites for IMC crystal structures.

This approach was tested on the three known indomethacin structures and further applied to two unknown structures of IMC. Firstly, we focussed on γ-IMC and IMC MeOH solvate (Z'=1) which show significant conformational differences, in order to rationalise structurally related changes in the spectra. This information was used to analyse the more complex structure of α-IMC. Three main regions of the ^{13}C spectrum, *i.e.*, aliphatic region (0-60 ppm), aromatic region (90-145 ppm) and carbonyl and methoxy (C5) motifs (150-190 ppm) can be distinguished. To analyse conformational differences between IMC polymorphs, it is important to rationalise changes in the peak position (^{13}C and ^{1}H) related to the molecular conformation. The structural and spectral details gained from the known structures of IMC were applied to enable evaluation of conformational differences in IMC form IV and IMC form V. As IMC form V was obtained *via* desolvation of the IMC methanol solvate, we focused on changes in the peak positions and intensities for both forms and compared these to previously assigned peaks of the spectrum of γ-IMC. Here we report solid-state NMR spectra of the IMC methanol solvate and forms IV and V of IMC, the application of GIPAW calculations to a pharmaceutical molecule with Z'=3 (α-IMC) and detailed assignment of all ^{13}C sites in the crystal structures of α-IMC and IMC MeOH solvate for the first time.

4.2.1.3   Solid-state NMR of γ-IMC

The most stable form of IMC (γ-IMC) has one molecule in the asymmetric unit which is in agreement with single, narrow peaks found in the ^{1}H-^{13}C CP/MAS NMR spectrum, where each peak corresponds to one ^{13}C site in the IMC structure, in agreement with the spectra published previously (Figure 4-6).[205,210,228,229] The structure of IMC has both quaternary and non-quaternary carbons, which can be identified using the [1]H-^{13}C CP/MAS NQS or [1]H-^{13}C HETCOR experiments, respectively. In the NQS experiment, non-quaternary carbons are supressed due to strong dipolar couplings between ^{13}C and ^{1}H nuclei (see methods chapter for details). Only ^{13}C sites with bound protons

undergoing fast motions (*e.g.*, CH_3 group) are still visible in the spectra due to the decreased strength of ^1H-^{13}C dipolar interactions. The ^1H-^{13}C HETCOR experiment uses dipolar couplings to provide the map of connections between different ^1H and ^{13}C sites. By using the HETCOR experiment at short contact time we were able to only detect ^{13}C nuclei which are directly bound to ^1H nuclei, hence distinguish the presence of quaternary carbons in the spectrum. The presented ^{13}C projection (Figure 4-6) and 2D HETCOR spectrum at short CP contact time (Figure 4-7) is in excellent agreement with the previously published 2D INEPT (insensitive nuclei enhanced by polarisation transfer) spectrum by Bradley *et al.*[156] The distinction between quaternary (red) and non-quaternary (blue) carbons in the ^1H-^{13}C CP/MAS spectrum of γ-IMC can be easily observed (Figure 4-6). By acquisition of the ^1H-^{13}C CP/MAS spectrum at high field (20 T) alongside application of the chemical shift calculations, we were able to gain sufficient separation of different ^{13}C sites for complete assignment of the spectrum. With the exception of overlapping peaks for carbons C15, C19 and C2, C6, it was possible to distinguish all ^{13}C sites and correlate them with ^1H sites using ^1H-^{13}C 2D HETCOR experiment (Figure 4-6, Figure 4-7).

Interestingly, there was a large shift and splitting of the C17 peak between the spectra recorded at 9.4 T (δ_{C17}=141.7 ppm) and 20.0 T (δ_{C17}=139.0 ppm). This can be explained by the second-order effects between ^{13}C and ^{35}Cl,^{37}Cl due to large quadrupolar moments of chlorine isotopes. This effect was previously observed by Apperley *et al.* for γ-IMC and described in detail.[144] At high magnetic field (B_0) the C-Cl site is predicted to be a 1:1 doublet composed of two powder patterns in agreement with our ^{13}C spectra recorded at 20.0 T. Using perturbation theory, the authors calculated (C-Cl) the effective dipolar coupling constant (D') of 576 Hz for ^{35}Cl and quadrupole coupling constant (χ) of −67 MHz (assuming positive anisotropy of J in order of 100 Hz).[144] Additionally, at 16.4 T authors observed a splitting of one C17 site, which was explained as J_{CCl} coupling of *ca.* −40 Hz. This value is in agreement with literature data of J_{CCl} in range from −20 to −10 Hz.[230–232] Parameters (D', χ) calculated by Apperley *et al.* are in excellent agreement with values obtained with MagresView[233] for geometry optimised γ-IMC (INDMET[178]) being χ=−67.5 MHz and D'=570 Hz. The effect of chlorine on two other sites of chlorophenyl ring (C16 and C18) was displayed as peak broadening in ^1H-^{13}C CP/MAS spectrum acquired at 9.4 T and in ^1H-^{13}C HETCOR spectrum as clear doublet, likely due to better decoupling efficiency through the use of LG based heteronuclear decoupling pulse sequence in HETCOR experiment (Figure 4-6, Figure 4-7). Similar observation was made for the ^1H-^{13}C CP/MAS and ^1H-^{13}C HETCOR spectra of the IMC MeOH solvate (Figure 4-10, Figure 4-12).
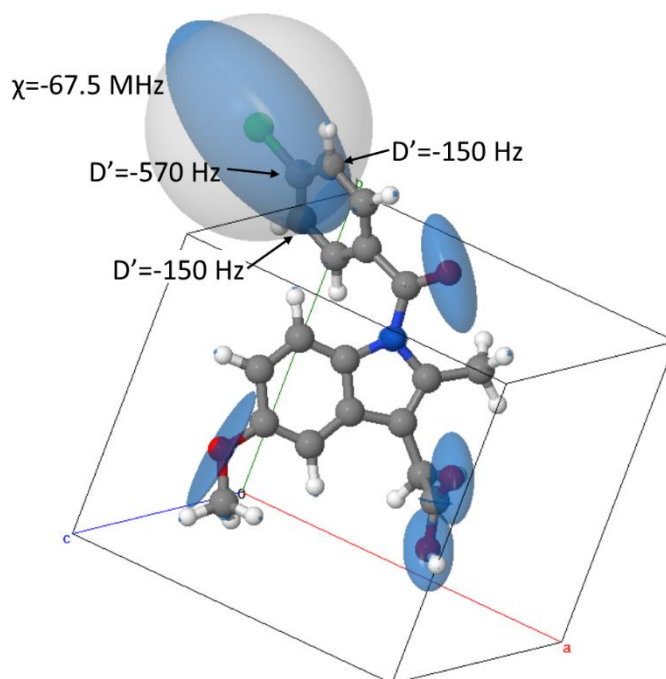
Figure 4-5. Visualisation of EFG (blue ellipsoids) and dipolar couplings for γ-IMC from chlorine to three carbon atoms in the chlorophenyl ring, which are in 3 Å proximity from chlorine (marked as a grey sphere). The strengths of quadrupolar constant and dipolar couplings were calculated using MagresView.[233]
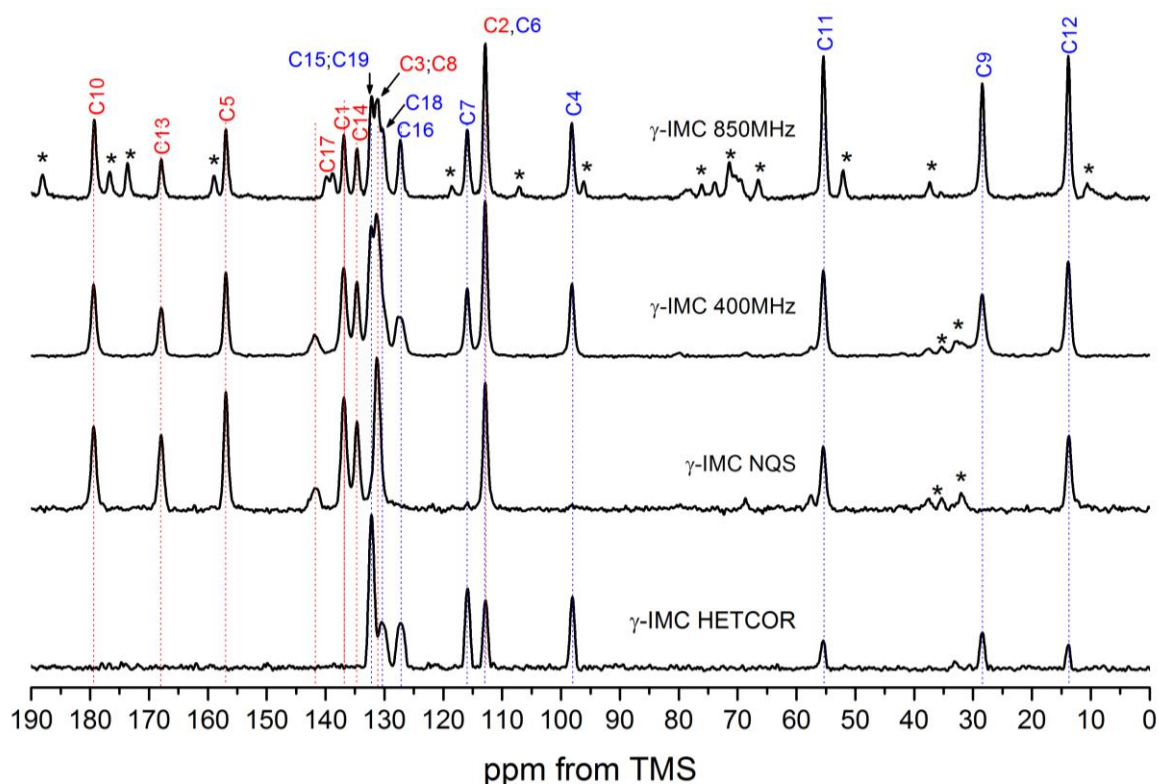
Figure 4-6. From the top: ^{1}H-^{13}C CP/MAS solid-state NMR spectra of γ-IMC acquired at 20.0 and 9.4 T, ^{1}H-^{13}C CP/MAS NQS and ^{13}C projection of ^{1}H-^{13}C HETCOR solid-state NMR spectra of γ-IMC (9.4 T). Spectra acquired at 10 kHz (9.4 T) and 13 kHz (20.0 T). Spinning sidebands are labelled with asterisks. Carbon labelling is based on GIPAW calculations (quaternary carbons are labelled in red and non-quaternary carbons are labelled in blue in agreement with scheme in Figure 4-1A).

There are two published ^{1}H and ^{13}C chemical shift GIPAW calculations of the γ-IMC structure which are in a very good agreement with our calculations (Table 4-2).[228,229] Ukmar *et al.* focused on general computational details, comparing different approaches in geometry optimisation and different types of pseudopotentials used in DFT calculations together with simplified assignment of the ^{1}H and ^{13}C spectra, but included no details on structural analysis.[228] Bradley *et al.* presented the differences in the calculated ^{1}H chemical shifts of a single IMC molecule and full periodic crystal structure of γ-IMC, discussing in detail the effects of CH-π interactions on the differences between them. These authors used quantitative analysis of ^{1}H DQ build-up curves to investigate subtle differences in the [1]H-^{1}H proximities in the crystal structure.[229] Neither group discussed changes in the ^{13}C chemical shifts, which are a rich source of structural information. We therefore evaluated the use of both ^{1}H and ^{13}C chemical shifts to investigate structural relationships between different IMC polymorphs. For the conformational analysis, changes in the position of carbon peaks C4 and C6 (with respect to the position of methoxy group) and carbons C15-C19 (position of chlorophenyl) are of high importance, as these motifs differ significantly between the structures (Figure 4-1). As reported by Bradley *et al.* changes in the ^{1}H chemical shifts can be directly related to CH-π interactions, hydrogen bonds or close interactions to the highly electronegative nuclei. It is important to note that the values of chemical shift of the methyl hydrogens H12 and H11 are calculated as an average of three chemical shifts of three different protons. The motional averaging of the CH_3 motif is not implemented in GIPAW calculations and the calculated chemical shifts differ quite significantly (usually one ^{1}H chemical shift differs *ca.* 1 ppm from the two others depending on its position with respect to the aromatic ring or electronegative nuclei in close proximity). To further evaluate the effect of the molecular conformation on the changes of the chemical shifts, we used geometry optimised isolated molecules of IMC extracted from three different crystal structures (INDMET[178]; INDMET02[179] and BANMUZ[185]) as models.

The ^{1}H CRAMPS spectrum of γ-IMC also agrees with the previously published spectra.[228,229] There are only four peaks in the spectrum making the assignment challenging (Figure 4-8), however combined analysis of the [1]H-[13]C 2D HETCOR experiment and GIPAW calculations enabled the assignment of the different proton sites (Figure 4-7), which is in agreement with previously published data.[228,229] The first peak in the spectrum at *ca.* 2 ppm is assigned to aliphatic protons H9, H11 and H12; while the two peaks at *ca.* 6 and 7 ppm are due to the aromatic protons in the structure. The remaining peak at *ca.* 12 ppm can be assigned to the carboxylic motif. Hydrogen H16, which is a part of the chlorophenyl ring, has a significantly different value of chemical shift (*ca.* 1 ppm) compared to three other protons in the same ring (Figure 4-7), which is due to the aromatic ring current interactions between H16 and the centre of the chlorophenyl ring of the neighbouring IMC molecule, which is in close proximity to H16 (3.42 Å).[156]

The other hydrogens of the chlorophenyl ring (H15; H18; H19) form close contact inter- and intramolecular interactions (*ca.* 2.6 Å) with oxygens, which may have a deshielding effect on the surrounding electronic cloud, leading to downfield shifts of the peaks.

Table 4-2. Experimental (exp) and calculated (calc) ^{13}C and ^{1}H isotropic chemical shifts for γ-IMC. Nonquaternary carbons are labelled in blue.

^{13}C site	δ_{exp}	$\delta_{calc}{}^{a}$	$\delta_{calc}{}^{b}$	$\delta_{calc}{}^{c}$	$\delta_{mol}{}^{b}$	$\delta_{mol}{}^{c}$	^{1}H site	δ_{exp}	$\delta_{calc}{}^{a}$	$\delta_{calc}{}^{b}$	$\delta_{calc}{}^{c}$	$\delta_{mol}{}^{b}$	$\delta_{mol}{}^{c}$
C1	136.7	138.4	140.0	138.1	140.2	138.7							
C2	112.7	111.9	115.2	111.2	114.9	113.8							
C3	131.0	132.0	132.4	131.3	131.5	130.4							
C4	98.0	95.5	95.6	94.4	92.6	91.8	H4	5.4	6.1	5.8	5.8	6.3	6.3
C5	156.8	157.8	158.4	157.9	158.9	158.3							
C6	112.7	114.8	111.1	113.7	111.3	111.1	H7	5.9	6.2	5.9	5.8	5.8	5.8
C7	115.8	115.0	115.4	114.2	113.6	112.9	H6	6.1	6.5	6.1	6.0	5.8	5.8
C8	131.0	131.5	131.0	130.9	130.4	130.8							
C9	28.3	28.1	25.6	24.7	22.2	21.7	H9	1.8	1.9; 2.1	1.4; 1.7	1.5; 1.7	3.3; 3.6	3.3; 3.5
C10	179.1	177.0	180.2	178.0	171.8	169.4							
C11	55.2	54.9	54.4	52.9	51.7	50.4	H11	2.4	2.5^	2.3^	2.3^	3.5	3.5
C12	13.7	14.1	11.2	10.5	6.9	6.3	H12	2.1	2.2^	1.8^	1.8^	2.1	2.1
C13	167.8	167.7	169.4	167.6	167.9	166.2							
C14	134.5	134.4	134.0	133.6	135.0	134.3							
C15	132.0	132.3	132.4	132.1	130.6	130.2	H15	7.2	7.5	7.2	7.1	6.8	6.8
C16	127.2	126.6	128.0	126.2	128.6	128.4	H16	5.7	6.2	5.6	5.5	6.6	6.6
C17	141.7	144.0	145.4	143.3	145.6	143.2							
C18	130.3	129.7	130.3	129.3	129.1	126.7	H18	7.1	7.4	7.0	6.9	6.9	6.8
C19	132.0	133.1	134.1	132.9	132.2	131.4	H19	7.2	7.7	7.1	7.2	7.3	7.2
							OH	12.8	14.4	14.4	14.1	7.2	7.3

[a]Ukmar *et al.*[228], [b]Bradley *et al.*,[156] [c]our calculations,
^average of three calculated ^{1}H chemical shifts for CH_3 groups
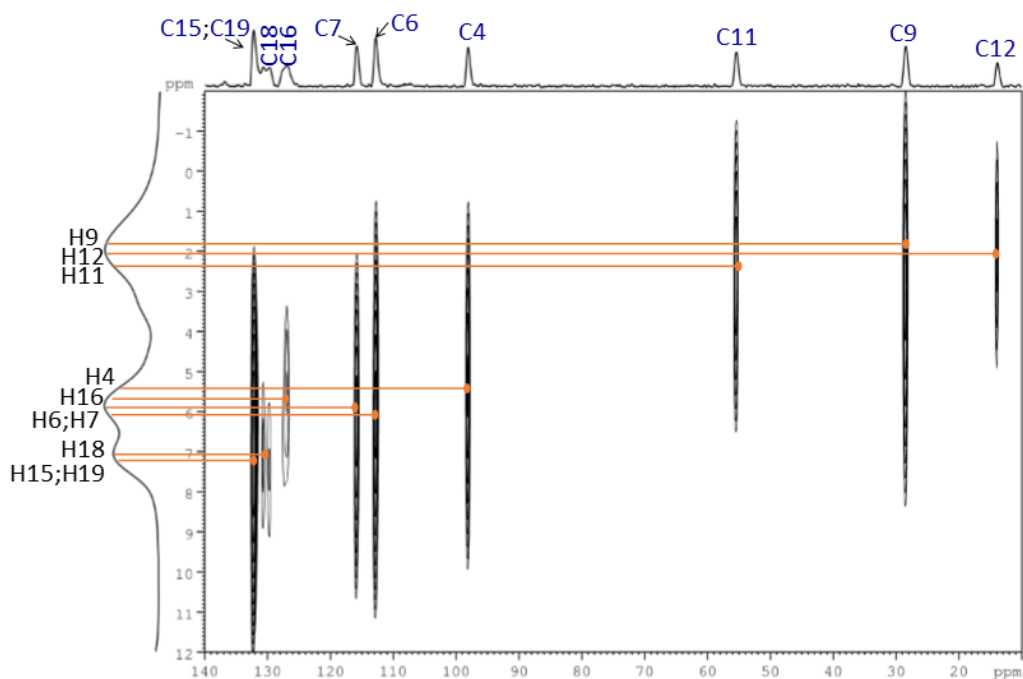
Figure 4-7. ^1H-^{13}C HETCOR spectrum of γ-IMC (9.4 T) acquired at 10 kHz. Cross-peaks between ^1H and ^{13}C enable to assignment of ^1H spectra.

Qualitative (and quantitative) information on the close proximities between different ^1H sites in the crystal structure can be elucidated from both ^1H SQ-^1H DQ correlation and ^1H-^1H NOESY experiments in solid-state NMR. Spectral resolution is a highly important factor and determines the usefulness of ^1H data in qualitative and quantitative analysis. Two approaches can be used to improve the resolution of ^1H spectra; for "medium" field spectrometers moderate spinning rates and well optimised pulse sequences with CRAMPS decoupling gave excellent results (in our case 9.4 T and 6.8 kHz spinning speed), while for high field spectrometers application of fast MAS probes eliminates the need for use multipulse sequences as CSA and dipolar interactions are partly overcome by MAS (in our case 20.0 T with 78 kHz spinning speed). We used both approaches; firstly, collecting the complete dataset at lower field using CRAMPS decoupling based pulse sequences and then validating the data using the UK 850 MHz Solid-State NMR Facility.
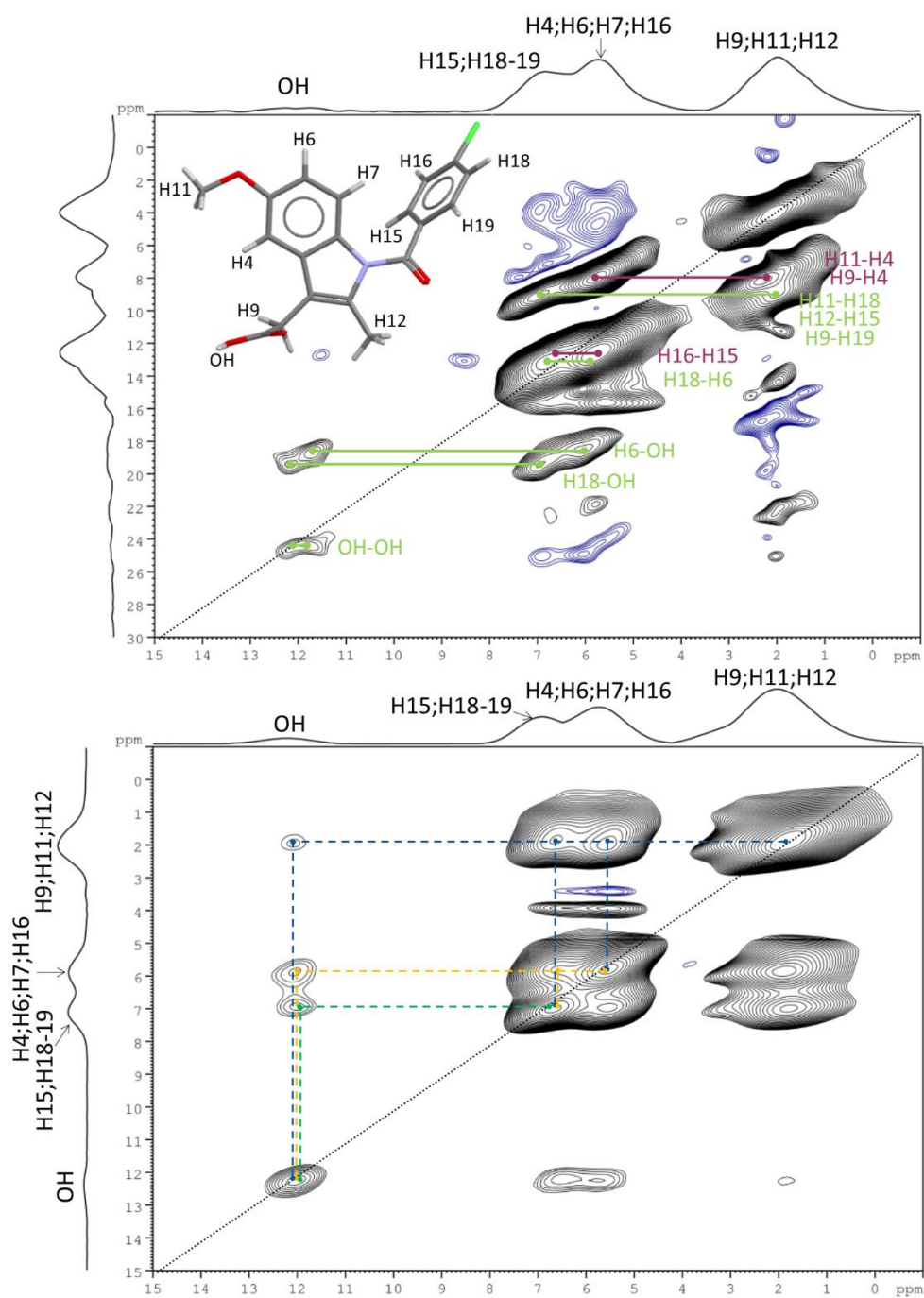
Figure 4-8. Top: ^{1}H-^{1}H SQ-DQ CRAMPS spectrum of γ-IMC (intramolecular short contacts are labelled in purple, while intermolecular short contacts are labelled in green). Bottom: ^{1}H-^{1}H CRAMPS NOESY spectrum of γ-IMC (cross-peaks between different ^{1}H sites are labelled with different colours). Both spectra were acquired at 9.4 T, at an MAS rate of 6.8 kHz for the best decoupling performance determined experimentally. Labelling of ^{1}H sites is based on GIPAW calculations and ^{1}H-^{13}C HETCOR experiment.

^{1}H-^{1}H SQ-DQ correlation spectroscopy is a powerful technique for structural studies, as it enables the determination of ^{1}H sites in close proximity (up to 3.5 Å). The ^{1}H SQ-^{1}H DQ spectrum of γ-IMC (Figure 4-8) is in an excellent agreement with the spectra published previously by Bradley *et al.* and Pham *et al.*[69,229] There are four resolved resonances; one aliphatic, two aromatic and one for -OH protons. Due to the low resolution of the spectra, it is not possible to extract all structural information without knowing the crystal structure. The only well separated peak of the OH group gives a DQ peak at δ_{DQ}=25.0 ppm corresponding to the formation of a centrosymmetric discrete carboxylic acid homodimer synthon with O-H⋯H-O proximity of 2.34 Å (for the geometry optimised structure). Two additional close intermolecular proximities of the OH group to H6 and H19 give DQ peaks at δ_{DQ}=19.8 ppm and 19.1 ppm, corresponding to the distances of 2.95 and 2.53 Å respectively. Other DQ correlations can be found at *ca.* δ_{DQ}=13.6 ppm, assigned to the intermolecular close contacts between aromatic protons H15 and H16 (2.43 Å) and H6 and H18 (2.29 Å) of neighbouring molecules. The most intense aliphatic ^{1}H peak at *ca.* δ_{DQ}=4 ppm is due to the close contact of the protons in two CH$_3$ groups (H11 and H12).

Complementary structural information can be extracted from the ^{1}H-^{1}H NOESY experiment in solid-state NMR, which correlates hydrogen atoms in close contacts up to 4 Å.[234] The spectral resolution is lower compared to the ^{1}H-^{1}H SQ-DQ correlation experiment, due to the lack of chemical shift spread for DQ frequency in the F1 dimension of the spectrum. For the -OH group, it is possible to distinguish three cross-peaks: two with aromatic protons (H18 and H6), which were also observed in the ^{1}H-^{1}H SQ-DQ experiment, and one with aliphatic protons. The ^{1}H-^{1}H NOESY spectrum also shows correlations between both aromatic peaks (H15 and H16, H7 and H15/H19) at 5.8 ppm (F1) and 6.9 ppm (F2), and further between aliphatic peak at 2.0 ppm (F1) and both aromatic peaks at 5.8 and 6.9 ppm (F2). These can be assigned based on the known structure of γ-IMC to intramolecular close contacts between H4 and H11 (2.37 Å) and H4 and one of the H9 hydrogens (2.55 Å), and intermolecular close contacts between hydrogens H11-H18; H12-H15 and H9-H19.

In summary, we have shown that the results of our combined computational and solid-state NMR methodology to study structure of γ-IMC is in agreement with previously published data.[156,228] Therefore, this approach was applied to investigate structural and conformational differences between other forms of IMC presented in further sections. The correlation between the position of the methoxy group (C11) and the chlorophenyl ring in known structures of IMC and chemical shifts of carbons and hydrogens sensitive to conformational changes was applied to elucidate structural information for IMC form IV and IMC form V. The analysis of both ^{13}C and ^{1}H chemical shifts in this study enabled us to gain structural information for systems with low crystallinity and Z'>1, where application of only ^{1}H NMR is difficult or not possible due to overlapping and broadening of the peaks.

4.2.1.4 Solid-state NMR of IMC methanol solvate

The IMC methanol solvate has one indomethacin molecule in the asymmetric unit alongside an additional methanol molecule, leading to the same number of peaks in the ^1H-^{13}C CP/MAS NMR spectrum as for γ-IMC, with one additional peak at 49.3 ppm arising from the methanol carbon (Figure 4-10). The conformation of IMC in the crystal structure of the IMC MeOH solvate differs significantly from that in the structure of γ-IMC (Figure 4-1B; γ-IMC in yellow; IMC MeOH solvate in green). These differences include (i) position of the chlorophenyl ring with respect to the C12 and C7 sites, (ii) position of the methoxy group (C13) with respect to the carbons (and hydrogens) C6 and C4 (H6 and H4) sites, and (iii) hydrogen bonding between the carboxylic acid motif involving the MeOH molecule and the carboxylic acid group of IMC. These structural changes can be deduced from the differences in the ^1H and ^{13}C chemical shifts between γ-IMC and IMC MeOH solvate (Figure 4-6 and Figure 4-10).
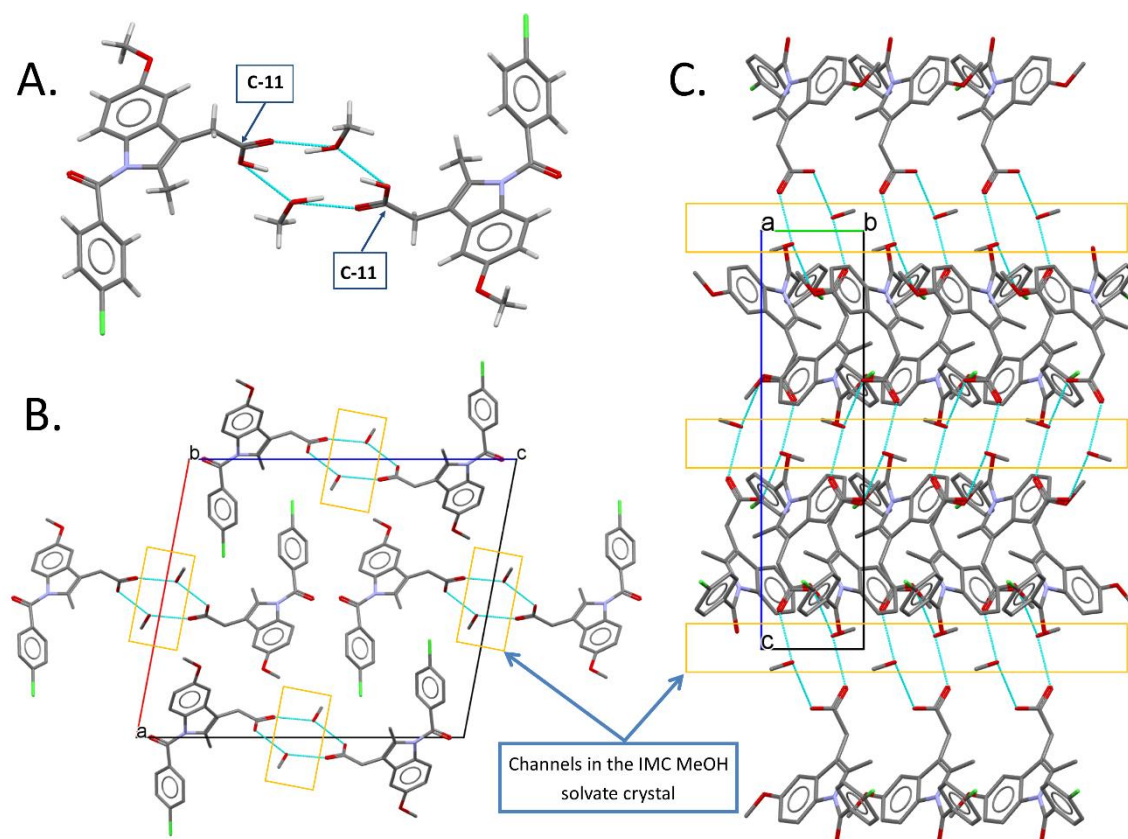

Figure 4-9. A. Hydrogen bonds between IMC MeOH solvate. **B.** View along crystallographic b axis. **C.** View along crystallographic c axis. Yellow boxes indicate channels in the structure.

Apart from the results of our recent studies there is no detailed structural or spectroscopic data on the IMC MeOH solvate.[88] The full assignment of the ^{1}H-^{13}C CP/MAS NMR spectrum was performed using the same method as for γ-IMC, using the BANMUZ[185] structure from the CCDC for CASTEP calculations (Figure 4-10, Table 4-3). Through acquisition of the ^{1}H-^{13}C CP/MAS NMR spectra at both 9.4 and 20.0 T, it was possible to distinguish and assign all the ^{13}C resonances, including a crowded aromatic region of the spectrum. The ^{1}H and ^{13}C chemical shifts calculated using GIPAW are in good agreement with the experimental data (Table 4-3). Compared to γ-IMC, the ^{1}H-^{13}C CP/MAS NMR spectrum of the IMC MeOH solvate shows several significant differences in the position of the ^{13}C peaks. The most pronounced change relates to the position of carbons C4 and C6, which undergo down- and upfield shifts of 7.5 and 6.9 ppm, respectively, compared to γ-IMC. Most likely, this is due to the change in the position of the methoxy group (C11) with respect to carbons C4 and C6. The differences between the conformation of the chlorophenyl ring with respect to the methyl group (C12) and carbon C7 were observed as a clear separation of the ^{13}C sites of the chlorophenyl ring in the IMC MeOH solvate structure but not in γ-IMC. The two most significant changes in the IMC MeOH spectrum as compared to the γ-IMC structure are related to the position of carbons C16 (upfield shift of 1.3 ppm) and C19 (downfield shift of 1.9 ppm). The change in the position of C16 may be related to the position of this site with respect to the chlorophenyl ring of neighbouring IMC molecule as discussed by Bradley et al.[156] The position of H16 (and C16) in the IMC MeOH solvate is still in close proximity to the centre of the chlorophenyl ring (3.39 Å), however the geometry of the interaction is significantly different. The downfield shift of C19 can be attributed to inter- and intramolecular close contacts of this site to carbonyl C13 (2.22 and 2.73 Å, respectively). This is further corroborated by changes in peak positions in the ^{1}H spectrum. The carboxylic acid carbon (C11) peak of the solvate undergoes three distinct changes: an upfield shift from 179.3 to 176.3 ppm, broadening, and decrease in intensity. The latter are most likely related to the close proximity of the methanol molecules in the solvate, forming the $R_4^4(12)$ ring motif, as shown in Figure 4-3.

Assignment of ^{1}H chemical shifts for the IMC MeOH solvate was carried out using the [1]H-^{13}C HETCOR spectrum and GIPAW chemical shifts calculations (Figure 4-12, Table 4-3). As solvent ^{1}H peaks can overlap with the ^{1}H spectrum of the drug, crystallisation of IMC from deuterated methanol was performed. The ^{1}H spectrum shows excellent separation of different ^{1}H sites at both fields (9.4 and 20.0 T, Figure 4-12). There are only two overlapping peaks in the ^{1}H spectrum acquired at 20.0 T (H16 and H18 at 6.0 ppm, and H4 and H15 at 6.9 (shoulder) and 6.6 ppm). The GIPAW calculated ^{1}H chemical shifts are also in excellent agreement with the experimental data (Table 4-3). The comparison of ^{1}H chemical shifts between IMC MeOH solvate and γ-IMC shows significant differences, again related to the different conformation of IMC molecules in each crystal structure.

In the GIPAW calculated ^{1}H chemical shifts of isolated molecules, there was one large chemical shift difference (of 2 ppm) for the H7 peak, shifting upfield from 7.8 ppm (IMC MeOH solvate) to 5.8 ppm (γ-IMC). This change is likely due to the CH-π interaction between H7 and centre of the chlorophenyl ring (2.93 Å) as previously described by Bradley et al.[156] and is further corroborated by the 0.6 ppm change in the calculated chemical shifts of H12 between both conformations. Similar effects of the aromatic ring on ^{1}H (and ^{13}C) chemical shifts are frequently observed in solution-state NMR spectroscopy of organic molecules and are used in structural studies of substituted aromatic molecules.[235–237] The effect of the electric current of the ring on the chemical shift can be calculated using density functional theory and it is known as nucleus-independent chemical shift (NICS, Figure 4-10).[238,239]

Table 4-3. Experimental (exp) and calculated (calc) ^{13C} and ^{1}H isotropic chemical shifts of IMC MeOH solvate. Nonquaternary carbons are labelled in blue.

^{13}C site	$δ_{exp}$	$δ_{calc}$	$δ_{mol}$	^{1}H site	$δ_{exp}$	$δ_{calc}$	$δ_{mol}$
C1	134.8	133.8	132.6				
C2	113.7	112.8	112.4				
C3	132.4	130.6	131.0				
C4	105.5	102.3	101.4	H4	6.9	6.8	6.4
C5	156.7	158.0	159.2				
C6	105.8	103.2	103.0	H6	5.3	5.3	6.4
C7	116.1	116.0	116.2	H7	8.4	8.3	7.8
C8	133.0	132.5	133.4				
C9	29.8	27.6	26.5	H9	3.0;3.9	3.1;4.1	3.4;3.7
C10	176.1	178.2	174.2				
C11	54.1	51.8	51.3	H11	2.2	2.3	3.5
C12	14.5	10.7	8.4	H12	0.8	1.1	1.5
C13	166.4	166.0	167.0				
C14	137.4	134.7	134.9				
C15	131.8	129.8	126.9	H15	6.6	6.5	7.1
C16	125.9	123.5	126.1	H16	6.0	5.8	6.7
C17	139.6	140.4	142.5				
C18	129.9	128.4	128.1	H18	6.0	6.0	6.8
C19	133.9	133.6	130.7	H19	8.7	8.4	6.8
MeOH	49.3	47.7	-	OH	11.8	13.0	7.9
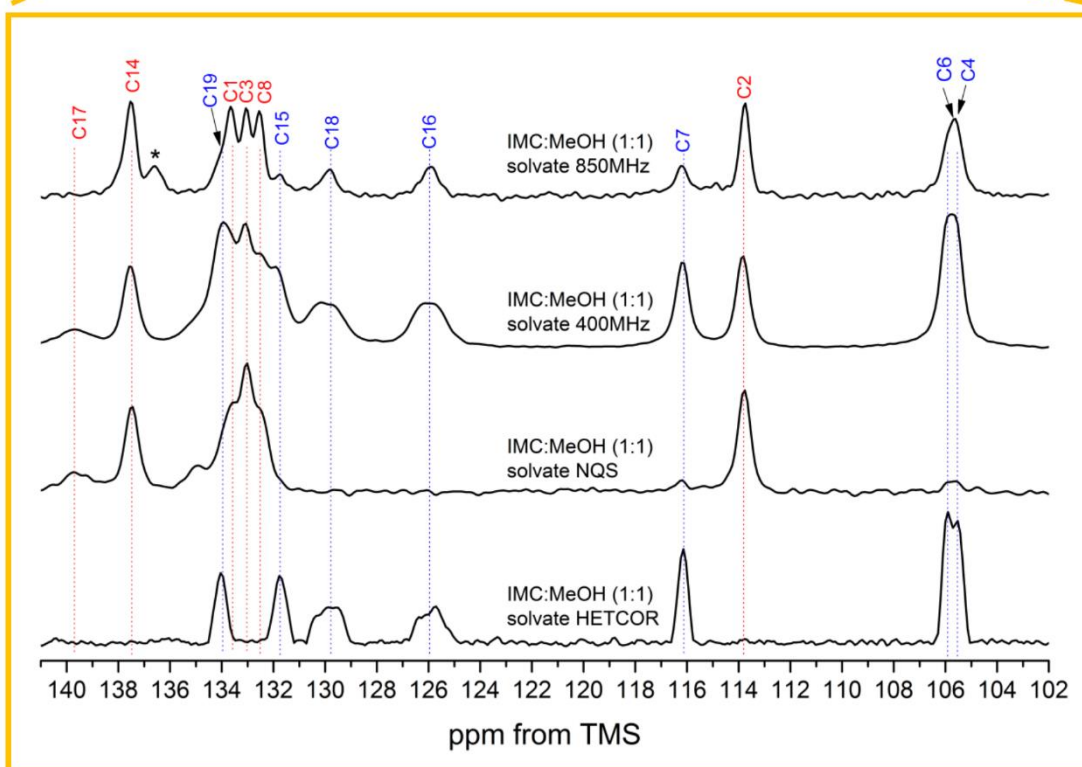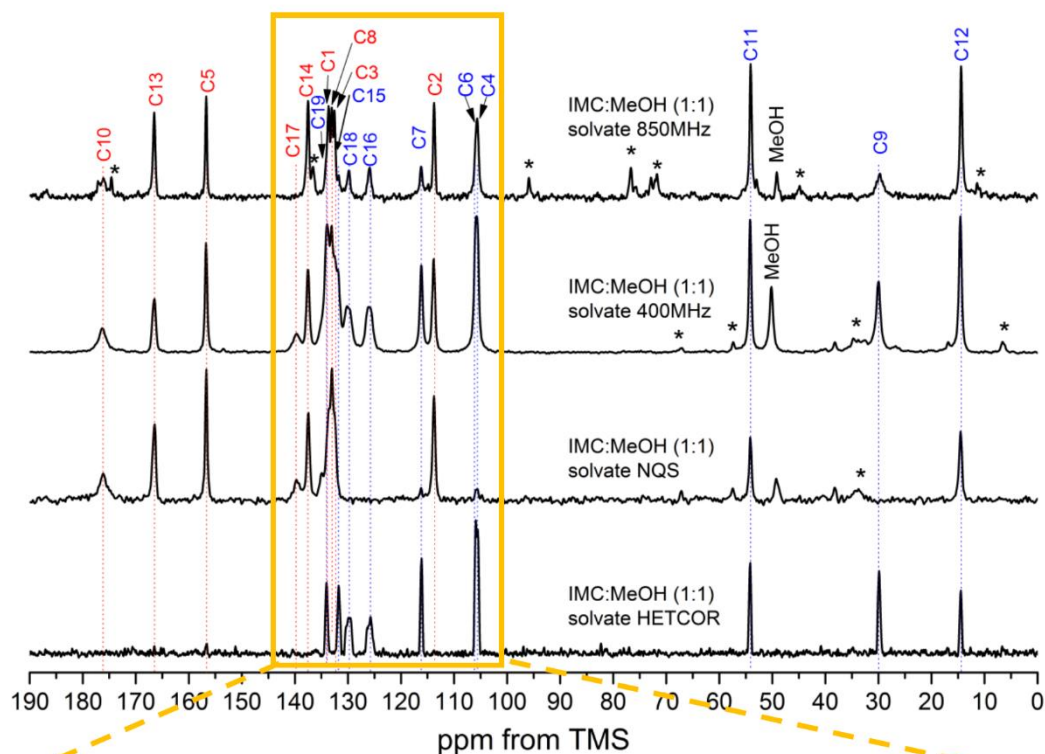
Figure 4-10. From the top: ^{1}H-^{13}C CP/MAS solid-state NMR spectra of IMC MeOH solvate acquired at 20.0 and 9.4 T, ^{1}H-^{13}C CP/MAS NQS and ^{13}C projection of ^{1}H-^{13}C HETCOR solid-state NMR spectra of IMC MeOH solvate (9.4 T). Spectra acquired at 10 kHz (9.4 T) and 13 kHz (20.0 T). Spinning sidebands are labelled with asterisks. Carbon labelling is based on GIPAW calculations (quaternary carbons are labelled in red and non-quaternary carbons are labelled in blue in agreement with scheme in Figure 4-1A).
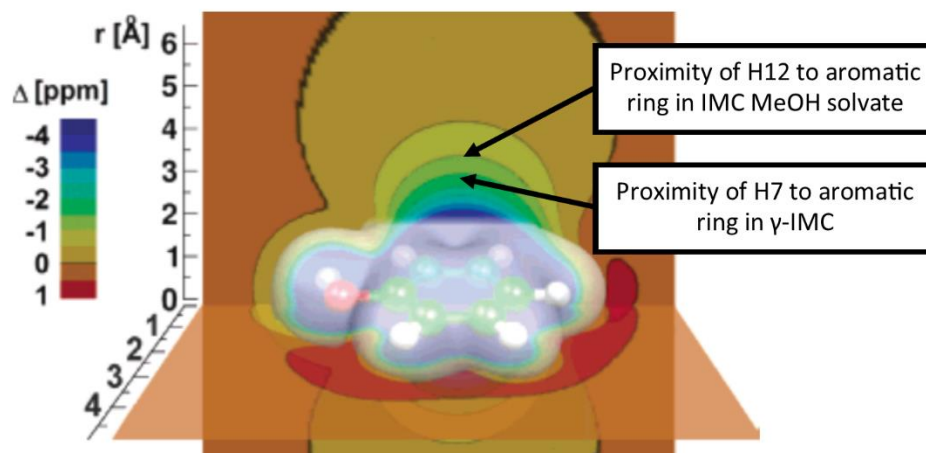
Figure 4-11. Nucleus-independent chemical-shift (NICS) map of a phenol. The colours reflect the chemical shift change of the nucleus, when placed in close proximity to the phenol ring. Different values are expected for IMC due to differences in the distribution of electronic cloud. Adapted from [239].

Although the effect of the aromatic ring current on the chemical shifts in ^{1}H solution-state NMR is well recognised, similar observations in solids are not frequently described. The examples include supramolecular assembles of dendritic polymers and intercalated polymers in aromatic nanochannels.[239,240] The shielding effect of the ring in the IMC MeOH solvate on H12 is less pronounced when compared to the same effect on H7 in γ-IMC conformation due to the larger distance of H12 in the IMC MeOH solvate to the centre of the ring (3.30 Å) and different geometry of the interaction. Another significant change was related to the position of the H6 peak, which undergoes a downfield shift in the BANMUZ conformation, relating to the change of position of the methoxy group (C11) with respect to hydrogen H6. Both trends (for H12 and H6 chemical shifts) were confirmed in further conformational calculations of chemical shifts for isolated α-IMC molecules, which have similar conformations to either γ-IMC or IMC MeOH solvate (see Table 4-5). A difference between the calculated ^{1}H chemical shifts for an isolated molecule and a molecule in the periodic crystal structure can be an indication of strong intermolecular interactions.[156]

The calculated chemical shifts of four hydrogens of the isolated molecule (H6, H11, H19 and OH site) differ significantly (by more than 1ppm) from experimental and calculated data for the crystalline structure, which can be explained through the hydrogen bonding between the OH groups of IMC and MeOH in the crystal structure. The downfield shift of H19 (of *ca.* 2 ppm) can be attributed to close contact interactions between H19 and the three neighbouring carbonyl groups in the crystal structure. Additionally, the upfield shifts of H11 (2.64 Å from the indole ring centre) and H6 may be due to the shielding effect of the indole ring and close proximity of two chlorophenyl rings, respectively, when compared to calculated ^{1}H chemical shifts for the isolated molecule.
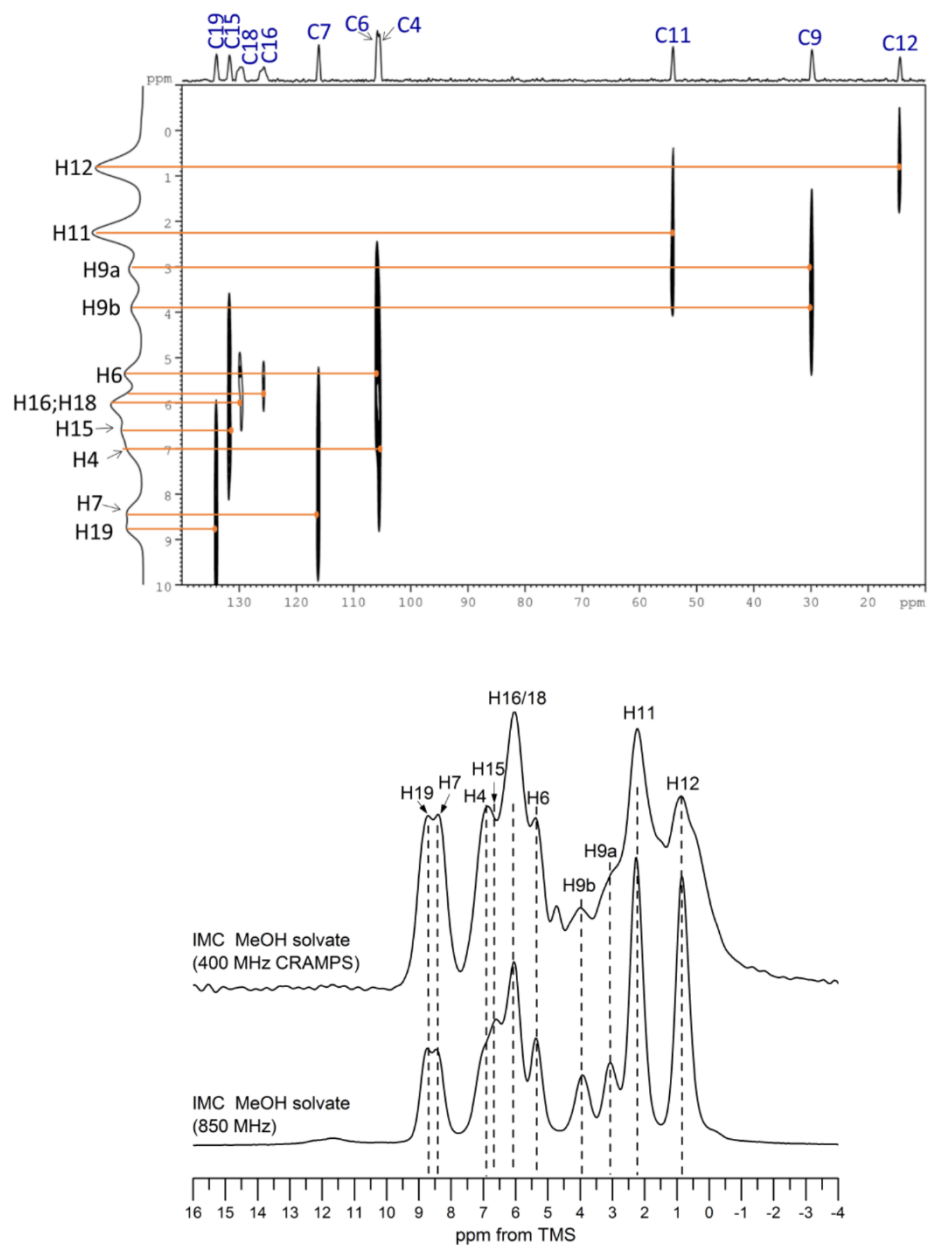
Figure 4-12. Top: ^1H-^{13}C HETCOR spectrum of IMC MeOH solvate; bottom: ^1H spectra of IMC MeOH solvate acquired at 20.0 T and an MAS rate 78 kHz and ^1H CRAMPS spectrum acquired at 9.4 T and an MAS rate of 6.8 kHz.
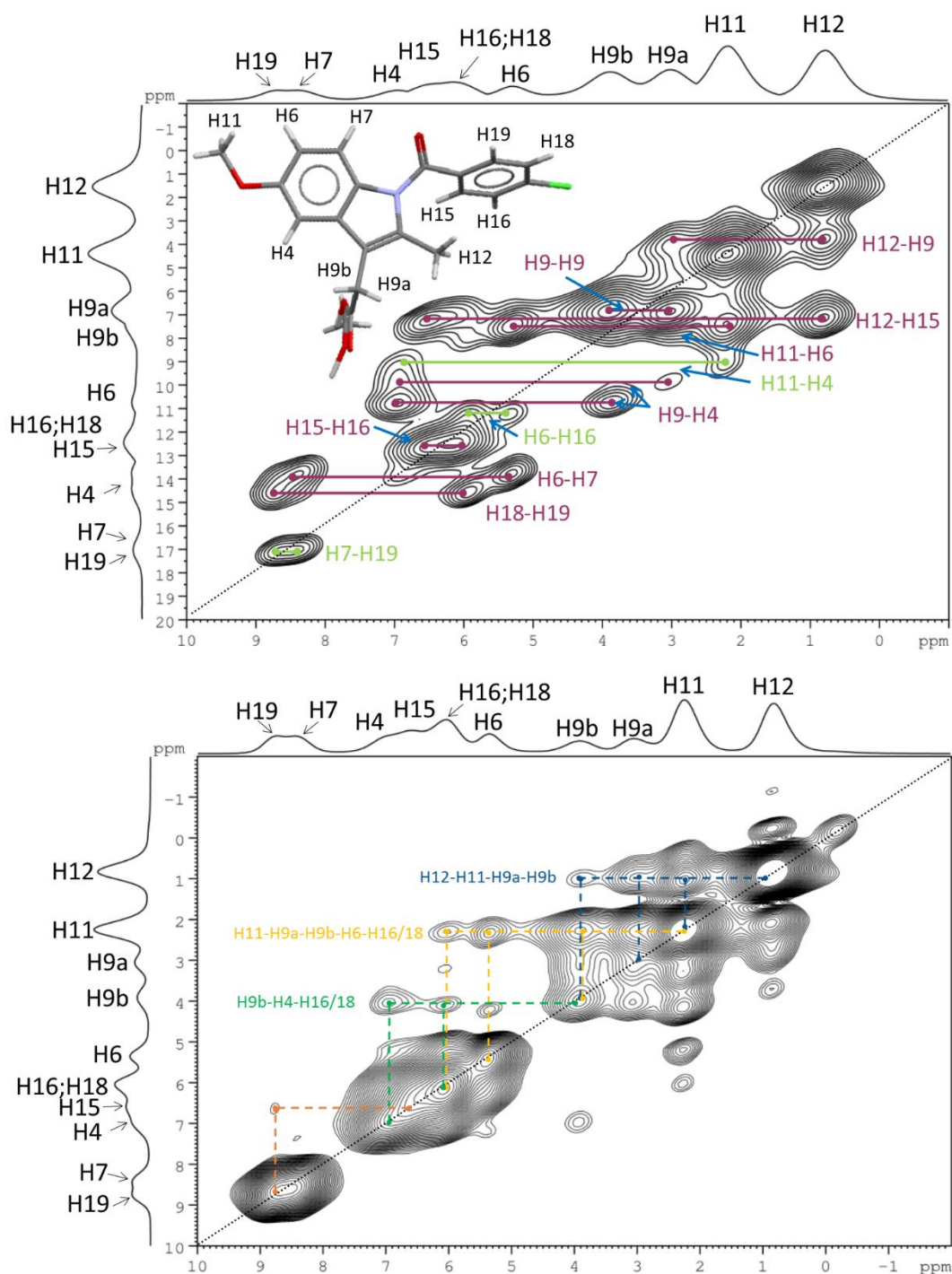
Figure 4-13. Top: ^{1}H-^{1}H SQ-DQ CRAMPS spectrum of IMC MeOH solvate (intramolecular short contacts are labelled in purple, while intermolecular short contacts are labelled in green). Bottom: ^{1}H-^{1}H CRAMPS NOESY spectrum of IMC MeOH solvate (cross-peaks between different ^{1}H sites are labelled with different colours). Both spectra were acquired at 20.0 T, at an MAS rate of 78 kHz. Labelling of ^{1}H sites is based on GIPAW calculations and ^{1}H-^{13}C HETCOR experiment.

^{1}H-^{1}H close contacts in the IMC MeOH solvate crystal structure were investigated further with ^{1}H-^{1}H SQ-DQ and ^{1}H-^{1}H NOESY experiments (Figure 4-13). The map of ^{1}H-^{1}H connectivity becomes especially important for further studies of IMC form V, as this structure is formed during the removal of MeOH from the channels of the IMC solvate. In the ^{1}H-^{1}H SQ-DQ spectrum of the IMC MeOH solvate, nine distinct ^{1}H sites were identified. However, due to the exchange of the OH hydrogens with deuterium (from deuterated methanol) correlations with the hydroxyl group were not visible in either the ^{1}H-^{1}H SQ-DQ or ^{1}H-^{1}H NOESY spectra (Figure 4-13). A distinct intermolecular correlation at δ_{DQ}=17.1 ppm (δ_{SQ}=8.7 + δ_{SQ}=8.4 : H7-H19) from three neighbouring IMC molecules in the close distance of *ca.* 3.1 Å was observed. Further intramolecular short contact interactions were seen for neighbouring protons of aromatic rings (H19- H18, δ_{DQ}=14.7 ppm; H6-H7, δ_{DQ}=13.7 ppm; H15- H16, δ_{DQ}=12.6 ppm). An interesting correlation was highlighted between H4 and both H9a and H9b sites at δ_{DQ}=10.8 ppm and δ_{DQ}=9.9 ppm, respectively, assigned to the intramolecular close contacts between H4 and H9b (2.50 Å) and between H4 and both H9a and H9b sites (2.73 Å and 3.10 Å, respectively). The H4 site was further correlated with the H11 site of a neighbouring molecule, indicated by a peak at δ_{DQ}= 9.1 ppm. Assignment of the two inequivalent H9 sites was made through correlation of one site with H12 at δ_{DQ}= 3.9 ppm, and further correlation between both H9 sites at δ_{DQ}=6.9 ppm. The position of the methoxy group in close proximity to H6 (2.23 Å) was confirmed by a distinct peak at δ_{DQ}=7.4 ppm. The conformation of the chlorophenyl ring with respect to H12 was confirmed through correlation between H12 and H15 at δ_{DQ}= 7.4 ppm due to intra- (2.61 Å) and intermolecular (2.56 Å) close proximities. Structural information gained from the ^{1}H-^{1}H SQ-DQ spectrum was further complemented by the ^{1}H-^{1}H NOESY spectrum (Figure 4-13). The low intensity cross-peak between H15 and H19 is due to overlay of the chlorophenyl rings of two neighbouring IMC molecules with both hydrogens almost parallel to each other, 3.83 Å apart. Further distinction between different H9 sites was made based on cross-peaks between H4 and H9b (in green) and H12 and H9a (in blue). The methoxy group hydrogens (H11) show several cross-peaks between H6, both H9 sites and overlapping aromatic protons H16/18. The intramolecular close contact between H11 and H6 explains only one of the correlations. The additional cross-peaks are most likely due to intermolecular close contacts of IMC molecules aligned antiparallel to each other (H11 to H18 = 3.34 Å; H11 to H9b = 3.48 Å). The ^{1}H-^{1}H NOESY spectrum is however less informative due to lower resolution in the F1 dimension, overlapping peaks, and the presence of artefacts.

4.2.1.5 Solid-state NMR of α-IMC

α-IMC is a frequently studied polymorph of IMC.[60,179,205,212,213,215,216,228,241] Partial assignment of the ^{13}C spectra was presented in initial solid-state NMR studies published by Masuda *et al*. and Ukmar *et al*.[205,228] To best of our knowledge, GIPAW computational studies of α-IMC have not been published due to the large number of atoms in the unit cell (246), which significantly increases computational time.[228] α-IMC has three molecules in the asymmetric unit (Molecule A, Molecule B and Molecule C - see Figure 4-3 and Figure 4-14 for details). The molecules A and B form a hydrogen-bonded carboxylic acid dimer; with molecule C forming a hydrogen bond between the carboxylic acid and the amide carbonyl (C13) of molecule B (Figure 4-3). All the three molecules are in different conformations. Molecule A follows a similar conformation to γ-IMC, whilst the conformation of molecule B is the same as the conformation found for the IMC MeOH solvate. The position of the methoxy group in the molecule C overlays with γ-IMC, but differs in the conformation of the chlorophenyl ring (see Figure 4-1 and Figure 4-14).

We firstly compared the calculated ^{1}H and ^{13}C chemical shifts of isolated molecule A and molecule B with previously calculated ^{1}H and ^{13}C chemical shifts of isolated γ-IMC and IMC MeOH solvate, respectively, due to the conformational similarities between them. Based on the chemical shift calculations and experimental spectra we concluded that the position of the methoxy group (C11) is highly correlated with the ^{13}C chemical shifts of C6 and C4. When the CH_3 group is in close contact (*ca.* 2.1 Å) with H4 (for molecule A, molecule C and γ-IMC), the shielding effect of this motif gives a calculated C4 peak position at 91-95 ppm. The C6 carbon in this conformation has a chemical shift in the range of 108-111 ppm (see Table 4-2, Table 4-3 and Table 4-4).
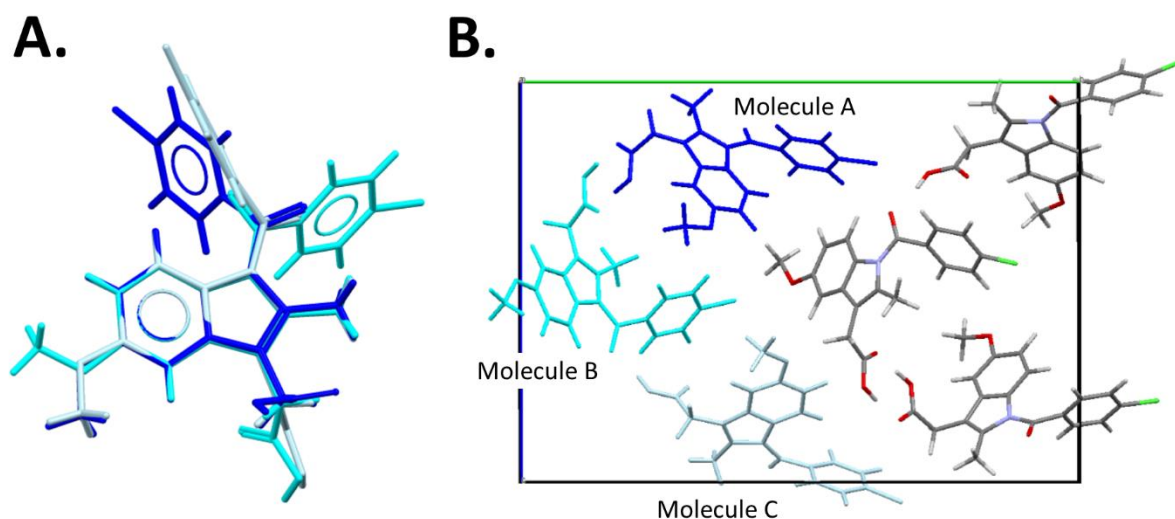

Figure 4-14. A. An overlay of molecule A, molecule B and molecule C forming crystal structure of α-IMC; **B.** packing of α-IMC (INDMET02[179]) – molecules forming asymmetric unit are labelled in different shades of blue.

If the CH$_3$ group (C11) is in close contact with C6 (*ca.* 2.1 Å) the calculated chemical shift of this site undergoes a dramatic upfield shift to 101-103 ppm with a concomitant shift of C4 by *ca.* 10 ppm to 101-103 ppm. Understanding the correlation between the conformation of the chlorophenyl ring and ^{13}C peak position changes is more challenging. The carbon sites which could be affected by close proximity of the ring (C12 and C7) do not show significant chemical shift differences between the conformations. However, the calculated chemical shift of C1 is sensitive to the position of the chlorophenyl ring: with molecule A and γ-IMC at *ca.* 138 ppm, molecule C at 143 ppm, and molecule B and BANMUZ conformations at a significant upfield shift of 132 ppm (see Table 4-2, Table 4-3 and Table 4-4). The conformational changes were correlated further with changes in the ^{1}H chemical shifts. The most pronounced difference was related to the position of H7. If H7 is in close contact (*ca.* 2.9 Å) with the centre of the chlorophenyl ring (molecules A and C, γ-IMC); the calculated value of the H7 chemical shift is 5.6-5.8 ppm. A significant downfield shift (of 2 ppm) is observed when the chlorophenyl ring is no longer in close contact with H7. In this conformation the ring is close (*ca.* 3.1 Å) to H12, manifested in an upfield shift of H12 of *ca.* 1 ppm (see Table 4-2, Table 4-3 and Table 4-5). As indicated by Bradley *et al.* these changes can be used as a direct measure of the CH-π interactions and can be further applied to obtain structural information in other systems where aliphatic and aromatic motifs can be present in close proximity. [156]

Changes in calculated ^{13}C and ^{1}H chemical shifts due to molecular flexibility can be used further to help assign the complex ^{1}H-^{13}C CP/MAS NMR spectrum of α-IMC. The acquired spectrum of α-IMC is in agreement with previously published spectra.[205,228] Three molecules in the asymmetric unit of α-IMC result in three peaks in the ^{13}C spectrum for each carbon atom (Figure 4-15). To distinguish between different molecules in the asymmetric unit, we used the following peak labelling system for ^{13}C sites: CX_Y, where X is the carbon number according to the labelling in Figure 4-1, and Y indicates molecule A, molecule B or molecule C according to the labelling in Figure 4-3 and Figure 4-14.

There are nine well resolved peaks from the three different molecules in the asymmetric unit in aliphatic region of the spectrum (0-60 ppm). The assignment of these sites were based on GIPAW calculations. Due to small differences in the calculated chemical shifts for carbon C11, it was not possible to distinguish clearly between the three different IMC molecules using calculated and experimental ^{13}C chemical shifts. In this case the ^{1}H-^{13}C HETCOR experiment alongside GIPAW calculated ^{1}H chemical shifts were used, and showed that H11_A site was shifted upfield (1.4 ppm) compared to H11_B and H11_C (2.1 ppm). The carbonyl region of the ^{1}H-^{13}C CP/MAS NMR spectrum (150-190 ppm) has only one overlapping peak, which was assigned to C10_C and C13_C. All peaks in this part of the spectrum are in good agreement with calculated chemical shifts for the INDMET02[179] crystal structure. There was a significant difference between the experimental

position of the carbonyl peaks of the crystalline material and calculated ^{13}C chemical shifts for isolated molecules. These changes are due to the formation of hydrogen bonds between a) the carboxylic motif (C10_A, C10_B), which shift downfield by 12 and 6 ppm, respectively, and b) C13_B, which shifts 6 ppm downfield due to hydrogen bonding with molecule C.

Table 4-4. Experimental (exp) and calculated (calc) ^{13}C isotropic chemical shifts of α-IMC and calculated ^{13}C chemical shifts of isolated molecules (mol) A, B and C. Non-quaternary carbons are labelled in blue.

^{13}C site	δ_{exp}			δ_{calc}			δ_{mol}		
	Mol A	Mol B	Mol C	Mol A	Mol B	Mol C	Mol A	Mol B	Mol C
C1	137.6	133.2	137.6	139.7	134.0	143.0	138.4	131.4	143.0
C2	110.5	115.5	111.8	113.3	118.0	114.5	113.8	116.5	113.7
C3	130.5	134.9	133.2	131.3	135.1	133.9	130.6	134.2	132.3
C4	97.1	105.8	97.8	95.7	105.5	96.5	95.1	103.4	92.0
C5	155.5	156.8	154.5	156.6	157.9	155.8	158.8	158.1	157.1
C6	111.2	104.7	110.5	110.5	101.4	106.9	111.3	101.3	107.9
C7	114.9	114.9	114.9	115.0	115.2	113.9	114.4	115.3	113.8
C8	130.5	130.5	130.5	129.1	132.0	132.9	128.0	133.2	131.9
C9	30.9	28.4	27.4	28.0	25.3	24.6	23.9	21.4	21.6
C10	179.1	180.3	166.0	176.6	183.3	168.0	167.1	174.0	163.5
C11	51.2	53.4	52.0	50.7	50.7	50.2	51.7	51.2	50.7
C12	12.9	11.2	13.6	9.0	8.4	11.2	6.9	8.5	8.7
C13	170.1	171.4	166.0	169.5	169.9	164.1	170.0	168.2	165.0
C14	133.2	133.2	136.4	134.2	135.0	137.8	136.1	138.3	138.8
C15	131.0	129.9	129.9	132.2	130.6	130.9	128.5	129.8	129.0
C16	129.5	128.6	128.7	129.6	127.7	128.9	127.8	126.9	127.5
C17	140.9	137.6	140.9	144.2	142.7	144.7	142.8	140.6	146.6
C18	127.7	129.9	131.5	127.6	130.4	134.5	127.4	128.4	131.6
C19	129.5	131.0	131.0	130.2	132.8	133.2	128.1	129.1	129.9

The most difficult region of the spectrum to assign is the crowded and highly overlapping aromatic part between 120 and 140 ppm. The peaks in this region describe 27 carbons from three different molecules making the assignment difficult. Better resolution was achieved in the aromatic part of the spectrum from 90 to 120 ppm, where it was possible to identify and assign the position of important carbons C6 and C4. The calculated ^{13}C chemical shifts for the crystalline structure are in agreement with the data for isolated molecules. Based on the conformational studies we were able to

distinguish two molecules (A and C) with the CH₃ group in close contact to C4 (H4) and one molecule (B) with the methoxy group in close proximity to C6 (H6) (Figure 4-15).
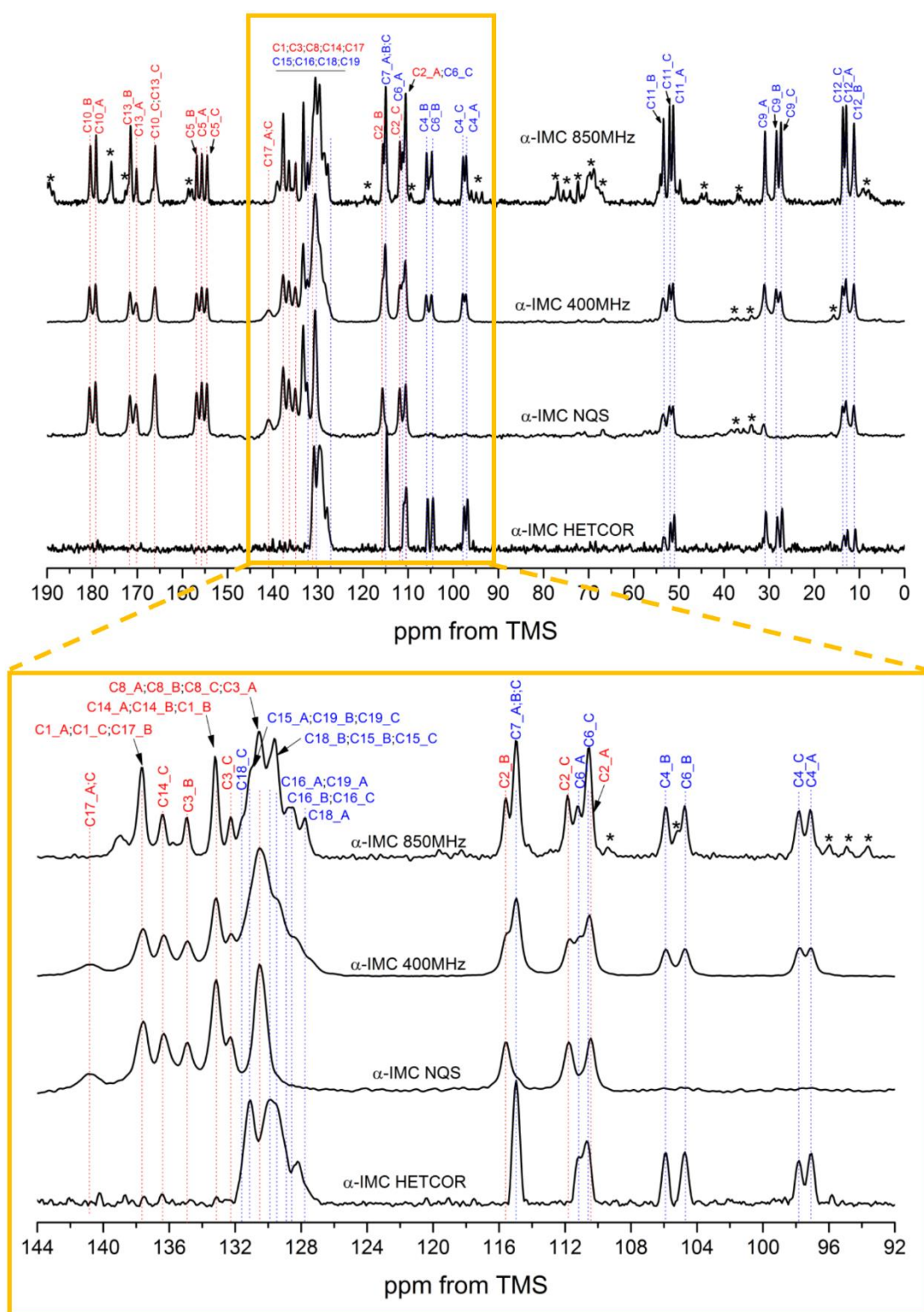

Figure 4-15. From the top: ¹H-¹³C CP/MAS solid-state NMR spectra of α-IMC acquired at 20.0 and 9.4 T, ¹H-¹³C CP/MAS NQS and ¹³C projection of ¹H-¹³C HETCOR solid-state NMR spectra of α-IMC (9.4 T). Spectra acquired at 10 kHz (9.4 T) and 13 kHz (20.0 T). Spinning sidebands are labelled with

asterisks. Carbon labelling is based on GIPAW calculations (quaternary carbons are labelled in red and non-quaternary carbons are labelled in blue in agreement with scheme in Figure 4-1A).
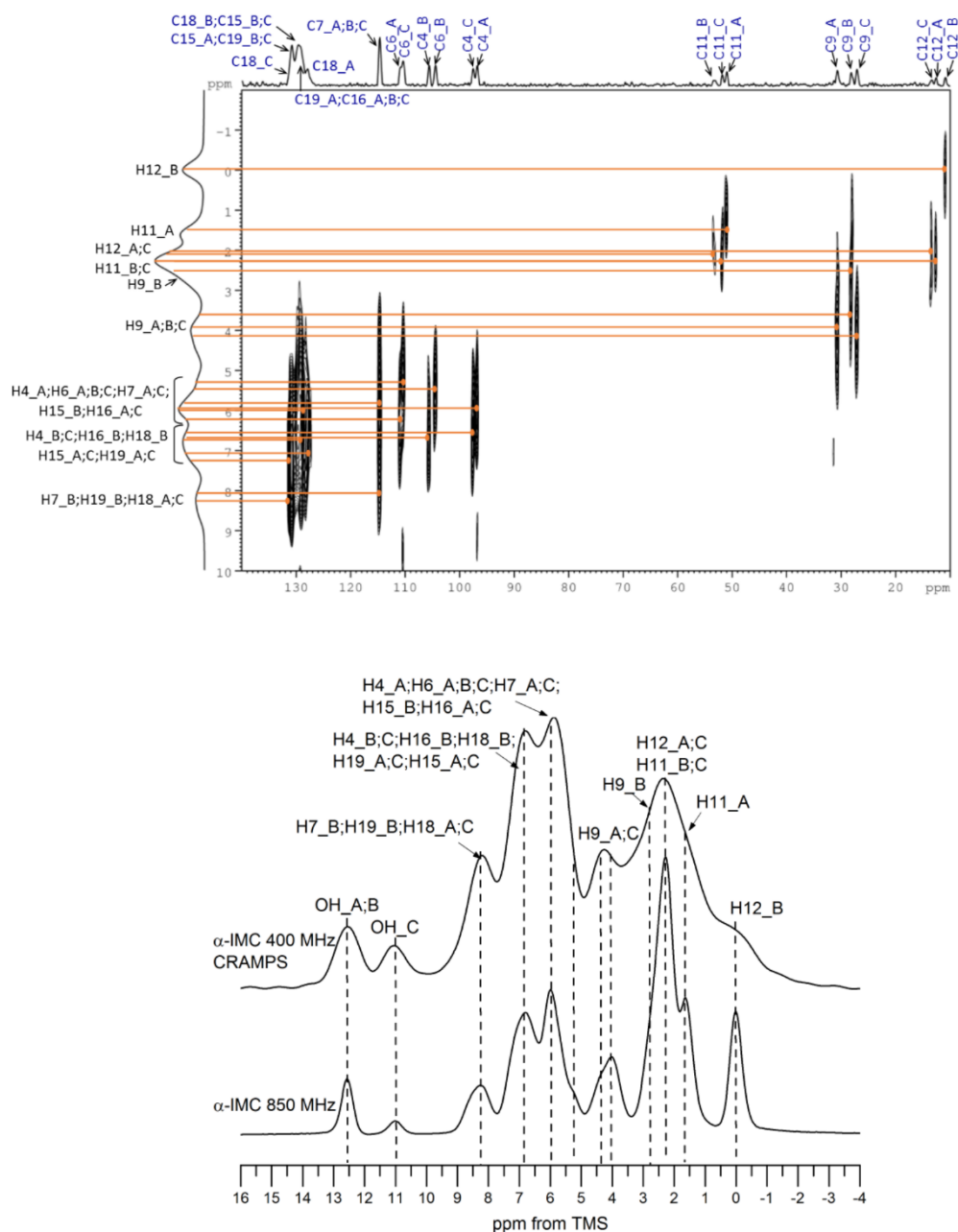
Figure 4-16. Top: ^1H-^{13}C HETCOR spectrum of α-IMC; bottom: ^1H spectra of α-IMC acquired at 20.0 T and spinning speed of 78 kHz and ^1H CRAMPS spectrum acquired at 9.4 T and spinning speed of 6.8 kHz. The assignment of proton spectra was made based on ^1H-^{13}C HETCOR spectrum of α-IMC and CASTEP calculations.

Assignment of the ^1H spectrum was based on the ^1H-^{13}C HETCOR experiment and GIPAW chemical shift calculations for α-IMC (Figure 4-16, Table 4-5). The calculated and experimental chemical shifts are in good agreement. There are nine peaks in the ^1H spectrum acquired at 20.0 T (78 kHz MAS rate), with a similar number of sites observed in the ^1H CRAMPS spectrum recorded at 9.4 T (6.8

kHz MAS rate). The majority of the peaks overlap but there is good separation for the OH groups indicating high sensitivity of ^{1}H solid-state NMR spectroscopy to different hydrogen bonding patterns. Separation of H12_B was achieved due to its close contact with the centre of the chlorophenyl ring leading to a significant (*ca.* 2 ppm) upfield shift of this site compared to molecules A and C. Further understanding of the α-IMC crystal packing was gained through the comparison of calculated and experimental ^{1}H chemical shift changes between isolated molecules and molecules forming a crystal (Table 4-5). Significant differences were found between calculated chemical shifts of the OH groups between isolated molecules and molecules in α-IMC structure (4.3-5.7 ppm), explained due to OH groups forming hydrogen bonds between IMC molecules in the crystal structure. Further differences were highlighted between hydrogens H19_B, H18_A and H18_B, (downfield shift of *ca.* 1 ppm as compared to the calculated ^{1}H chemical shifts for isolated molecules), due to short contact interactions with the electronegative oxygen from the neighbouring molecules. Similar changes were observed in the spectra of γ-IMC and IMC MeOH solvate. The differences between the calculated ^{1}H chemical shifts for H11 of isolated molecules and molecules forming the crystal structure can be related to the short contact (*ca.* 2.8 Å) interaction of the centre of the six carbon part of the indole ring with the CH_3 group. Interestingly, all three molecules in the unit cell show almost identical stacking interactions, where the C11 methoxy group is located below the six carbon part of the indole ring. Additionally, an upfield shift of 1.2 ppm (H12_B) when compared to the calculated ^{1}H chemical shift of the isolated molecule may be related to similar CH-π interactions, as this motif forms short contact interactions with the indole ring in the crystal structure.

Table 4-5. Experimental (exp) and calculated (calc) ^{1}H isotropic chemical shifts of α-IMC and molecules isolated from α-IMC crystal structure.

[1]H site	δ_{exp}			δ_{calc}			δ_{mol}		
	Mol A	Mol B	Mol C	Mol A	Mol B	Mol C	Mol A	Mol B	Mol C
H4	6.0	6.8	6.8	5.6	6.4	6.4	6.8	6.3	6.4
H6	6.0	6.0	6.0	4.8	5.2	5.6	5.8	6.4	5.7
H7	6.0	8.2	6.0	5.3	8.6	5.8	5.6	8.0	5.7
H9	4.0	4.0	4.4	3.7;4.0	2.7;3.7	3.9;4.3	3.1;3.6	3.3;3.5	3.5;3.7
H11	1.4	2.0	2.0	1.4	2.1	2.1	3.6	3.5	3.5
H12	2.3	0.0	2.3	2.3	-0.1	2.0	2.4	1.2	2.1
H15	6.8	6.0	6.8	6.6	5.7	6.5	6.5	6.6	6.6
H16	6.0	6.8	6.0	4.7	6.7	5.5	6.6	6.6	6.6
H18	8.2	6.0	8.2	7.8	6.1	7.9	6.9	6.8	7.0
H19	6.8	8.2	6.8	6.1	8.1	6.5	7.0	7.0	7.2
OH	12.5	12.5	11.0	14.5	13.5	12.0	6.8	7.3	6.7
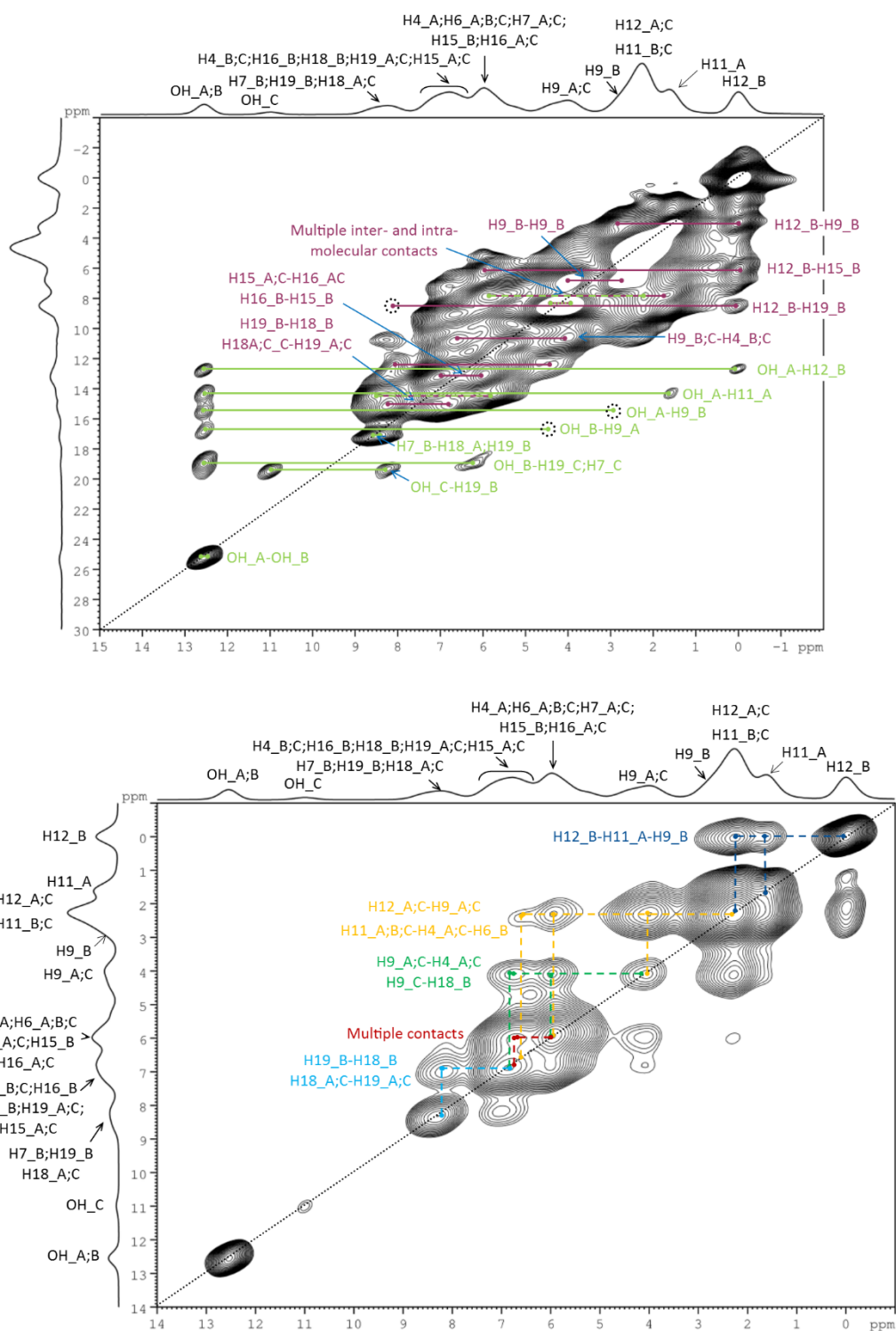
Figure 4-17. Top: ^{1}H-^{1}H SQ-DQ CRAMPS spectrum of α-IMC (intramolecular short contacts are labelled in purple, while intermolecular short contacts are labelled in green). Bottom: ^{1}H-^{1}H CRAMPS NOESY spectrum of α-IMC (cross-peaks between different ^{1}H sites are labelled with different colours). Both spectra were acquired at 20.0 T, at an MAS rate of 78 kHz. Labelling of ^{1}H sites is based on GIPAW calculations and ^{1}H-^{13}C HETCOR experiment.

Further structural analysis of α-IMC crystal packing was based on the ^{1}H-^{1}H SQ-DQ and ^{1}H-^{1}H NOESY experiments (Figure 4-17). It is possible to distinguish nine ^{1}H sites in the F2 dimension in the ^{1}H-^{1}H SQ-DQ spectrum, which shows good separation of the OH group of molecule C (δ_{SQ}=11.0 ppm) and OH groups from both molecules A and B (δ_{SQ}=12.5 ppm). Similarly to the ^{1}H-^{1}H SQ DQ spectrum of γ-IMC, correlations between both OH groups of molecule A and molecule B due to hydrogen-bonded carboxylic acid dimer were observed at δ_{DQ}=25.0 ppm.

Additional intermolecular correlations of both OH_A and OH_B hydroxyl groups were observed at δ_{DQ}=19.0 ppm (OH_B-H19_C;H7_C; *ca.* 3.2 Å), δ_{DQ}=16.8 ppm (OH_B-H9_A; 3.25 Å), δ_{DQ}=15.3 ppm (OH_A-H9_B; 2.85 Å), δ_{DQ}=14.3 ppm (OH_A-H11_A; 3.13 Å) and δ_{DQ}=12.8 ppm (OH_A-H12_B; 2.73 Å). The hydroxyl group of molecule C had only one clear correlation at δ_{DQ}=20.0 ppm, assigned to a short contact with hydrogen H19_B of the neighbouring IMC molecule. Two short intermolecular contacts of H7_B with H19_B (3.11 Å) and H18_A (2.69 Å) were observed at δ_{DQ}=17.1 ppm. The intramolecular interactions between aromatic ring hydrogens (H15, H16, H18, H19) are grouped in two correlated peaks at δ_{DQ}=15.1 and 13.1 ppm. An intramolecular short contact between H7_B and H6_B can be observed at δ_{DQ}=14.4 ppm. It is also possible to correlate hydrogens H18_A/C with H16_A/C of neighbouring molecules, which form stacked layers with chlorophenyl rings in close proximity (these inter- and intramolecular correlations overlap, hence they are labelled with dashed lines in Figure 4-17). The hydrogens of the H12_B form a well separated peak at δ_{SQ}=0.0 ppm, which has clear correlations with four other sites including the previously described OH_A peak. This correlation was used to confirm the position of one of the H9_B sites at δ_{SQ}=2.8 ppm, which is in agreement with the GIPAW calculated ^{1}H chemical shift (2.7 ppm). The close proximity of H12_B with the chlorophenyl ring hydrogens H15_B (2.75 Å) and H19_B (3.22 Å) is reflected in correlated peaks at δ_{SQ}=5.9 and δ_{SQ}=8.5 ppm, respectively; in agreement with calculated values. Based on the information from the H12_B correlations, we were able to confirm the position of the second H9_B site at δ_{SQ}=4.0, δ_{DQ}=6.8 ppm, and also H4_B site at δ_{DQ}=10.6 ppm, which is close to H9_B hydrogen (2.57 Å). The two peaks overlap with a correlated pair of hydrogens (H9_C and H4_C), which have very similar chemical shift values (Table 4-5). Similarly, the well separated peak of H11_A (δ_{SQ}=1.4 ppm) also confirms the conformation of the methoxy group with respect to H4_A at *ca.* δ_{DQ}=7 ppm, as this site overlaps with H12_A/C and H11_A/C, resulting in a broad peak centred at δ_{DQ}=7.8 ppm. Due to the highly overlapping aromatic part of the spectra centred at δ_{SQ}=6.0 and 6.8 ppm, it is not possible to unequivocally isolate correlations of all individual ^{1}H sites.

The ^{1}H-^{1}H NOESY spectrum recorded at relatively short mixing time (150 ms) is easier to interpret (Figure 4-17). Under these conditions, there were no hydroxyl cross-peaks. The cross-peak at δ= 8.1 ppm (F1) and δ=7.0 ppm (F2) between aromatic sites H19_B-H18_B and H18_A/C-H19_A/C (labelled in light blue) was similar to the ^{1}H-^{1}H SQ-DQ spectrum. Further short contacts between

aromatic protons were observed as a cross-peak at δ=6.7 ppm (F1) and δ=6.0 ppm (F2) (labelled in red). Intramolecular short contacts between hydrogens H9_A/C and H4_A/C were shown as a cross-peak at δ=4.1 ppm (F1) and δ=6.0 ppm (F2) and δ=6.7 ppm (F2), respectively. There was a strong correlation (cross-peak at δ=2.4 ppm (F1) and δ=4.0 ppm (F2)) between the aliphatic protons (H12_A/C, H11_A/C) and H9_A/C due to short intramolecular distances. The methyl protons showed two further correlations with aromatic sites at δ=6.0 ppm and δ=6.5 ppm (F2) due to intramolecular contacts with protons H4_A/C and H6_B, and several intermolecular contacts with neighbouring molecules. The separated H12_B site had two correlations, *i.e.*, an intramolecular cross-peak with one of the H9_B protons (2.09 Å) and an intermolecular correlation with H11_A site (2.87 Å) at δ=0.0 ppm (F1) and δ=1.6 ppm (F2).

In summary, we have presented for the first time detailed structural and computational studies for α-IMC. We proposed full assignment of ^{1}H and ^{13}C spectra based on the chemical shift calculations and ^{1}H-^{13}C HETCOR experiment. It needs to be emphasised that experimental identification of the ^{13}C peaks from independent molecules forming the structure is required to confirm the spectral assignment. This can be achieved using ^{13}C-^{13}C INADEQUATE experiment at natural abundance and will be a part of future work. Conformational studies of isolated molecules forming α-IMC using CASTP were in agreement with the results from γ-IMC and the IMC MeOH solvate. This enabled us to confirm the ^{1}H and ^{13}C sites in the IMC structure, which highly sensitive to the conformational changes.

4.2.1.6 Solid-state NMR of IMC form V

Careful desolvation of the IMC MeOH solvate yielded IMC form V. The solvent escaped from the crystal structure at room temperature over a period of a couple days or weeks depending on the sample size and desolvation conditions. The process can be accelerated at elevated temperatures, as described by Joshi *et al*.[180] Based on our experience, the desolvation at elevated temperatures often led to concomitant crystallisation of IMC form V alongside two other thermodynamically more stable forms (α- and γ-IMC). It was possible to monitor this process using solid-state NMR and hot stage microscopy. The room temperature transition of the IMC MeOH solvate to IMC form V occurred without an intermediate phase which was confirmed using ^{1}H-^{13}C CP/MAS NMR (Figure 4-18). New peaks of IMC form V appeared and the intensity of IMC MeOH solvate peaks decreased gradually, with decreasing solvent content.
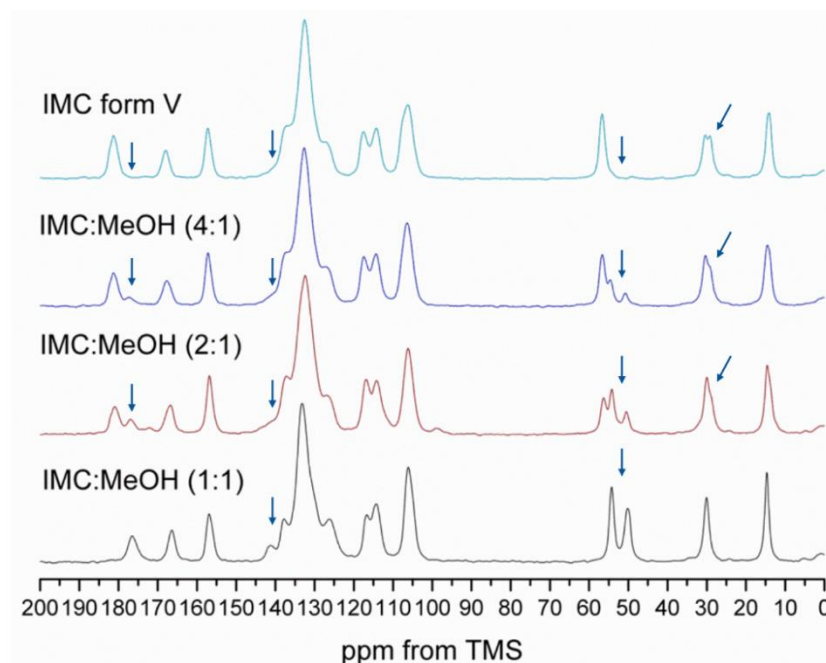
Figure 4-18. ^{1}H-^{13}C CP/MAS NMR spectra of IMC MeOH solvate recorded during desolvation at room temperature. The content of MeOH was measured using TGA analysis. Numbers in brackets indicate the stoichiometric ratio. Arrows indicate most pronounced changes in the spectrum.

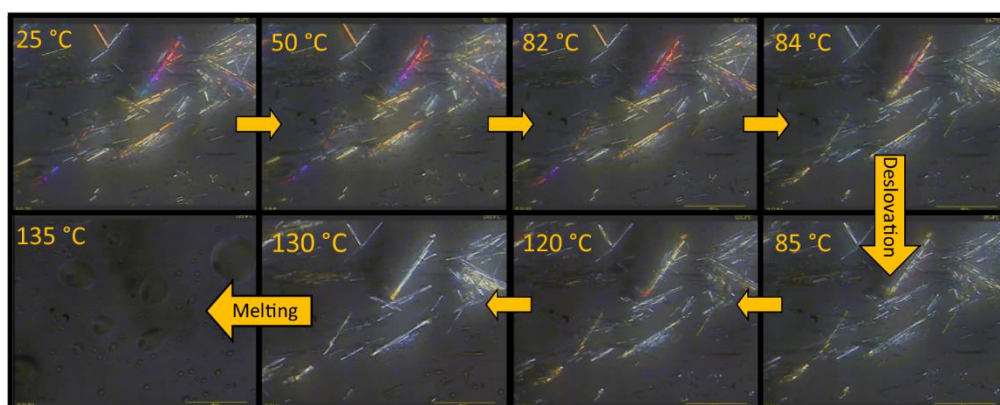**Figure 4-19.** A. Hot stage microscopy images and showing desolvation process of IMC MeOH solvate and formation of IMC form V.

Hot stage microscopy showed the presence of fine fine shiny needles of the IMC MeOH solvate, which upon desolvation became more opaque (Figure 4-19 A) and their melting at *ca.* 403-408 K, in line with the melting temperature of IMC form V.[88,180] Again, no other intermediate phase was detected.

As IMC form V is formed *via* desolvation of the IMC MeOH solvate, the ^{1}H and ^{13}C spectra of this polymorph will be discussed in comparison with the spectrum of the IMC MeOH solvate. There are several differences in the spectrum of IMC form V as compared to the IMC MeOH solvate. Firstly, the methanol carbon peak disappears and the C11 peak undergoes downfield shift from 54.1 to *ca.* 56 ppm. Secondly, splitting of different carbon sites indicates the presence of two molecules in the asymmetric unit, in agreement with the space group and unit cell parameters derived from PXRD data (Figure 4-20). C10, which is involved in the hydrogen bonding of the solvate, undergoes a downfield shift and splitting, indicating the presence of two magnetically non-equivalent carboxylic acid motifs. As shown above, the position of the C4 and C6 peaks are good indicators for the conformation of the methoxy group (C11) with respect to both C4 (H4) and C6 (H6) sites.

Table 4-6. Experimental (exp) ^{1}H and ^{13}C chemical shifts of IMC form V compared with experimental ^{1}H and ^{13}C chemical shifts of IMC MeOH solvate. Non-quaternary carbons are labelled in blue.

| [13]C site	δ_{exp} (MeOH)	δ_{exp} (form V)	[1]H site	δ_{exp} (MeOH)	δ_{exp} (form V)
C1	134.8	130-135			
C2	113.7	112.9;113.6			
C3	132.4	130-135			
C4	105.5	104.4;105.0	H4	6.9	6.1;7.1
C5	156.7	156.3;156.6			
C6	105.8	106.1;106.7	H6	5.3	5.0
C7	116.1	116.4	H7	8.4	8.4
C8	133.0	130-135			
C9	29.8	28.4;29.8	H9	3.0;3.9	2.2;2.7;3.8
C10	176.1	179.8;180.7			
C11	54.1	55.8;56.1	H11	2.2	2.2;2.7
C12	14.5	13.1;13.7	H12	0.8	0.6
C13	166.4	167.1;167.5			
C14	137.4	136.8			
C15	131.8	125-134	H15	6.6	6.1-8.4
C16	125.9	125-134	H16	6.0	6.1-8.4
C17	139.6	136.8			
C18	129.9	125-134	H18	6.0	6.1-8.4
C19	133.9	125-134	H19	8.7	6.1-8.4
MeOH	49.3	-	OH	11.8	12.4
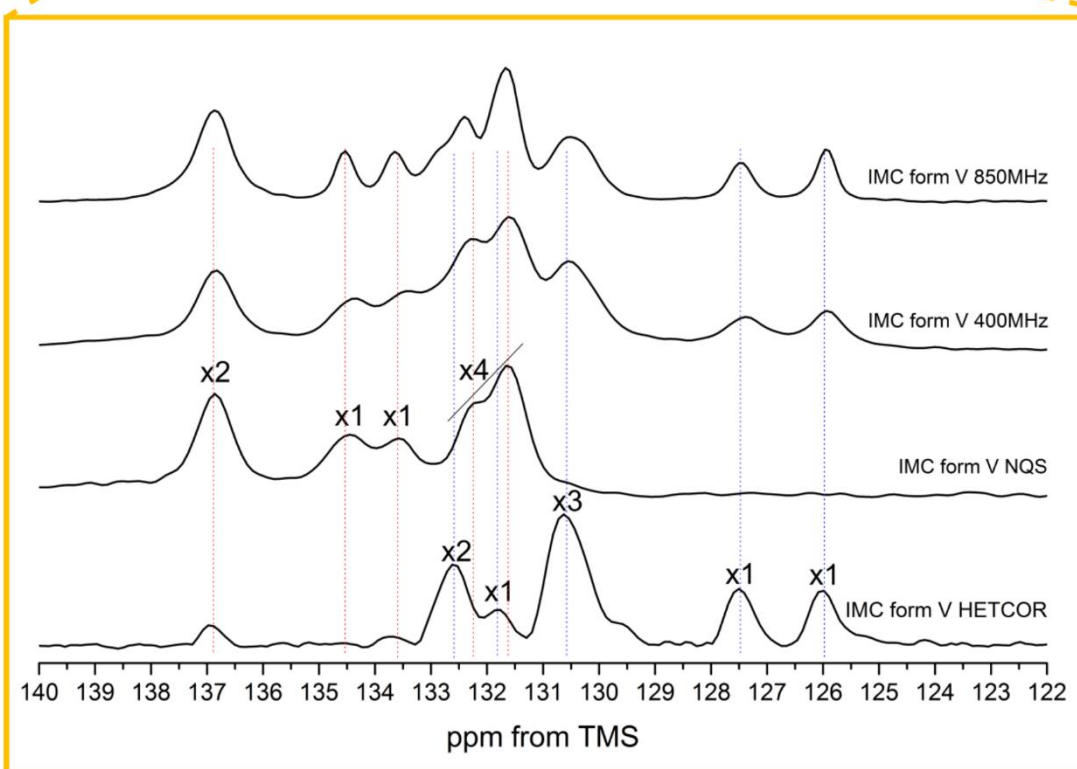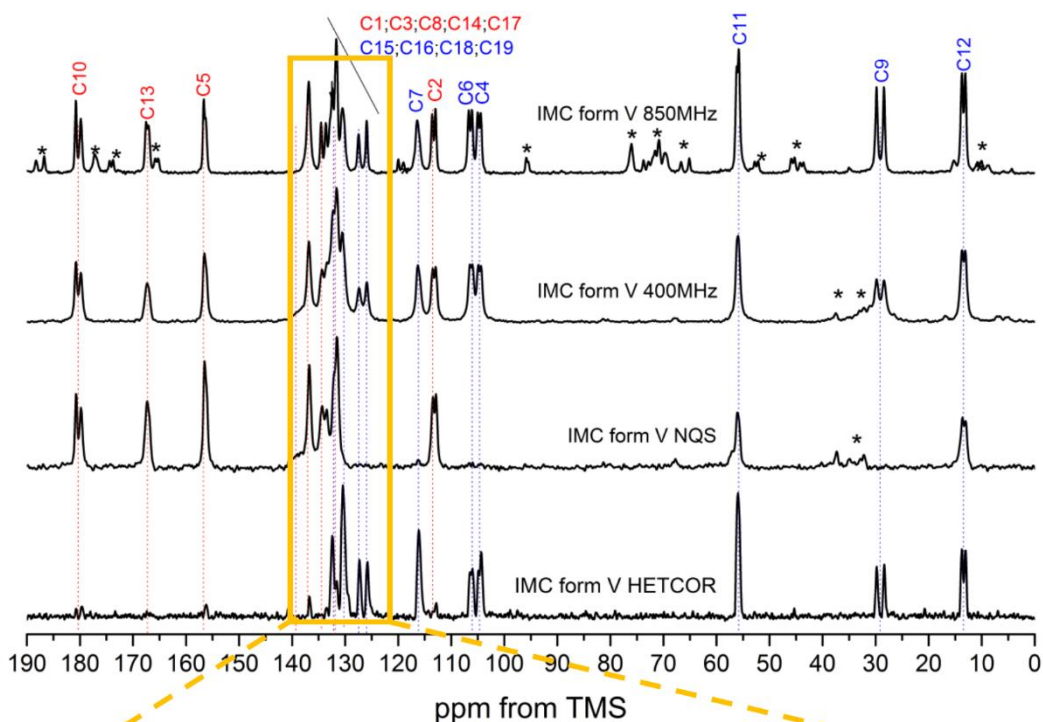
Figure 4-20. From the top: ^{1}H-^{13}C CP/MAS solid-state NMR spectra of IMC form V acquired at 20.0 and 9.4 T, ^{1}H-^{13}C CP/MAS NQS and ^{13}C projection of ^{1}H-^{13}C HETCOR solid-state NMR spectra of IMC form V (9.4 T). Spectra acquired at 10 kHz (9.4 T) and 13 kHz (20.0 T). Spinning sidebands are labelled with asterisks. Carbon labelling is based on similarities with previously assigned spectra of IMC polymorphs and MeOH solvate (quaternary carbons are labelled in red and non-quaternary carbons are labelled in blue in agreement with scheme in Figure 4-1A). The numbers in the zoomed region of the spectrum indicate integration of different ^{13}C sites.

The C4 peaks and C6 peaks at *ca.* 105 ppm and 106 ppm, respectively, indicate that the conformation of methoxy group (C11) does not change significantly upon desolvation and transition to IMC form V in both inequivalent molecules in the asymmetric unit. Although the considerably complex aromatic region of the ^{1}H-^{13}C spectrum (125 ppm to 140 ppm) could not be assigned fully, it was possible to distinguish between the non-quaternary carbons of the chlorophenyl ring (125-134 ppm), quaternary carbons of the indole ring and carbons C14 and C17 of the chlorophenyl ring (130-140 ppm).

Through assignment of the ^{1}H-^{13}C CP/MAS and ^{1}H-^{13}C HETCOR spectra it was possible to partly assign the ^{1}H spectrum of IMC form V (Figure 4-21). The ^{1}H spectrum of IMC form V shows nine peaks which are broadened in comparison to the ^{1}H spectrum of the IMC MeOH solvate, due to the presence of two inequivalent molecules in the asymmetric unit and low crystallinity of the material, leading to an increased distribution of ^{1}H sites. The peak positions are similar to those for the IMC MeOH solvate. There are several important features in the spectrum which enable the identification of the conformation of IMC molecules in the asymmetric unit. The highest sensitivity indicator for the position of the chlorophenyl ring with respect to H7 and H12 is the chemical shift value of H7 (and H12). The shielding effect of the chlorophenyl ring leads to a significant upfield shift of H7 if in close proximity. A similar, but less pronounced effect, is observed for the H12 site. Based on the ^{1}H-^{13}C HETCOR spectrum and similarities between the ^{1}H-^{13}C CP/MAS spectra of different IMC polymorphs, it was possible to assign the C7 site at 116.4 ppm and correlate it with the H7 site at *ca.* 8.4 ppm. The peak position of the H7 site in IMC form V was very similar to that of H7 in the ^{1}H spectrum of the IMC MeOH solvate indicating close proximity of the chlorophenyl ring to the methyl H12. This is further corroborated by only a minor shift of 0.2 ppm for the H12 peak towards a lower field in the ^{1}H spectrum of IMC form V as compared to IMC MeOH solvate ^{1}H spectrum (Figure 4-21).
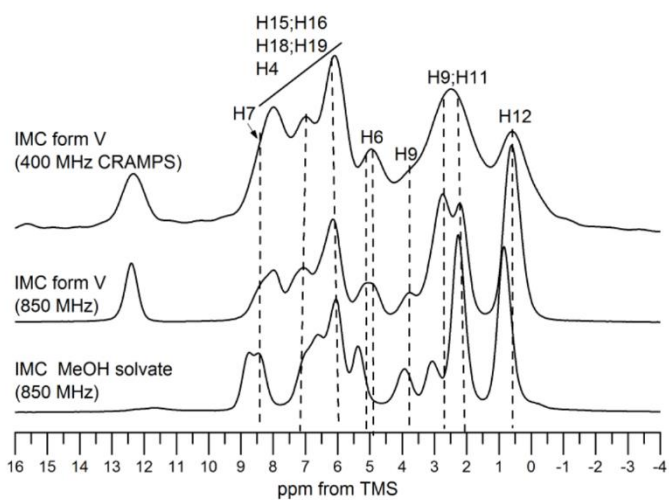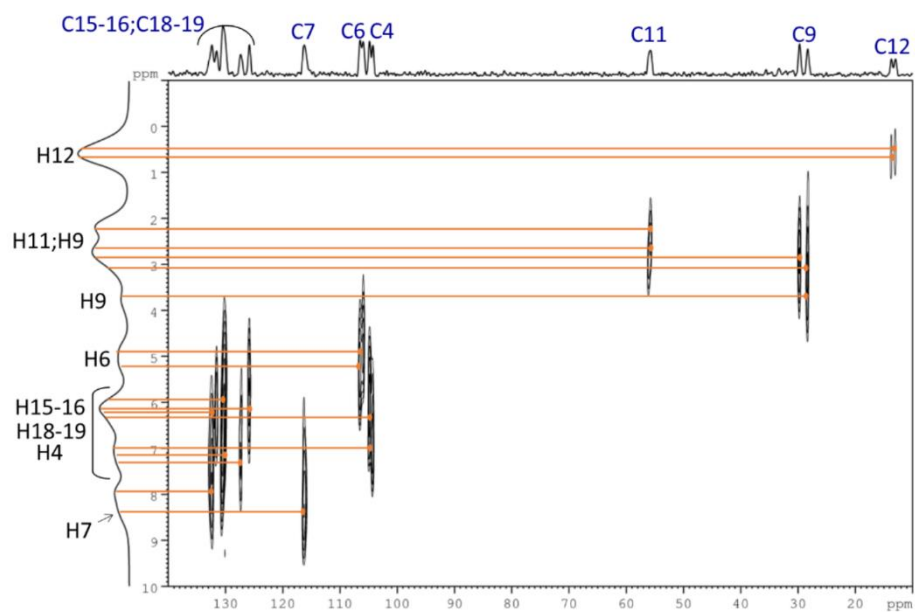
Figure 4-21. Top: ^1H-^{13}C HETCOR spectrum of IMC form V; bottom: ^1H spectra of IMC form V and IMC MeOH solvate acquired at 20.0 T and spinning speed of 78 kHz and ^1H CRAMPS spectrum of IMC form V acquired at 9.4 T and spinning speed of 6.8 kHz.
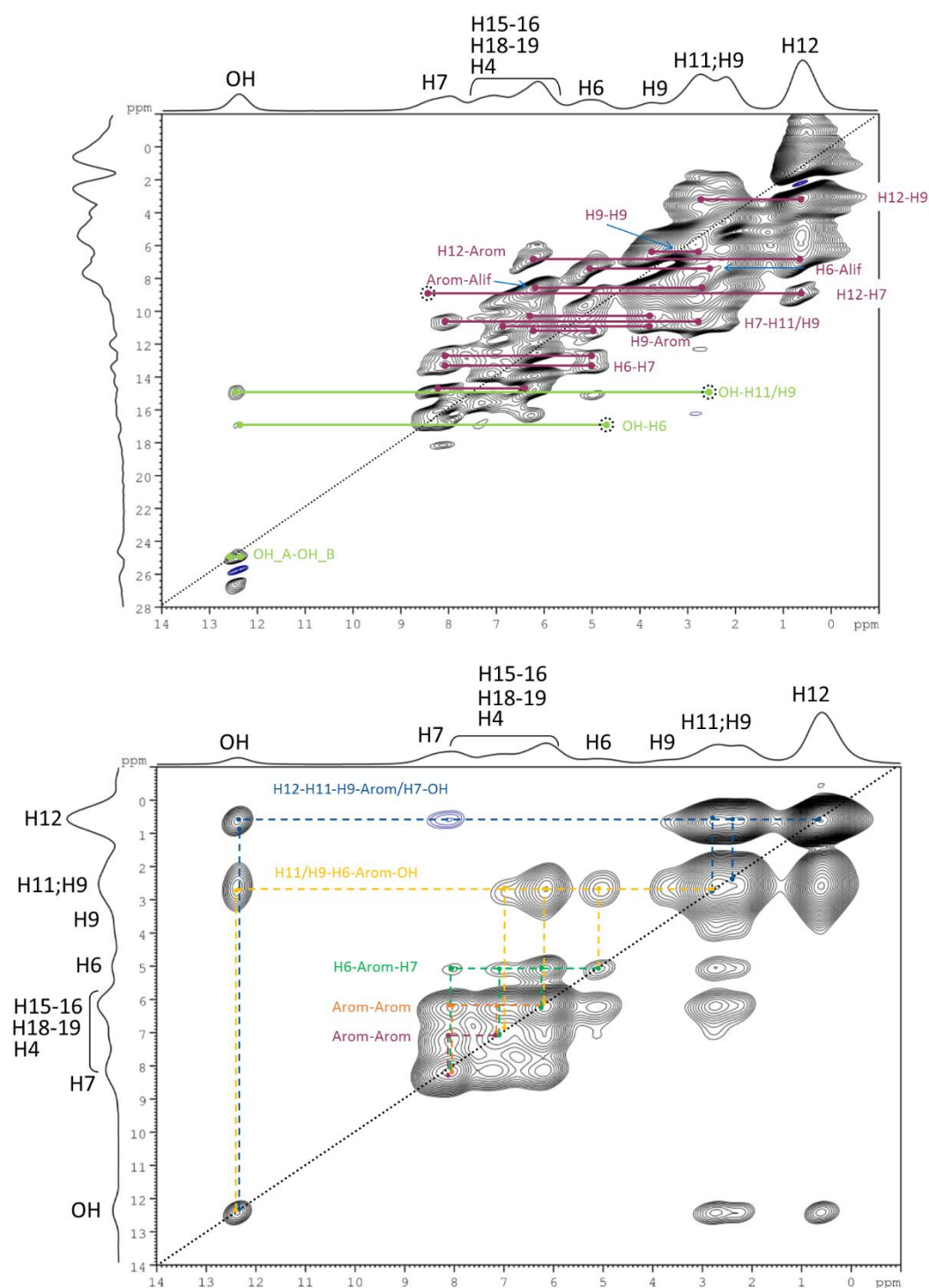
Figure 4-22. Top: [1]H-^{1}H SQ-DQ CRAMPS spectrum of IMC form V (intramolecular short contacts are labelled in purple, while intermolecular short contacts are labelled in green). Bottom: [1]H-^{1}H CRAMPS NOESY spectrum of IMC from V (cross-peaks between different ^{1}H sites are labelled with different colours). Both spectra were acquired at 20.0 T, at an MAS rate of 78 kHz. Labelling of ^{1}H sites is based on [1]H-^{13}C HETCOR experiment.

Additional information on the intra- and intermolecular close proximities for the IMC form V structure can be extracted from ^{1}H-^{1}H SQ-DQ and ^{1}H-^{1}H NOESY spectra (Figure 4-22). The ^{1}H-^{1}H SQ-DQ spectrum of IMC form V showed correlation between the OH groups at δ_{DQ}=24.8 ppm, which indicates that molecules in the crystal structure are stabilised by a carboxylic acid dimer similarly to the α- and γ-IMC structures. The OH site also showed two intermolecular close contacts between H6 and H9/H11 at *ca.* δ_{DQ}=17.4 ppm and δ_{DQ}=14.8 ppm, which were previously observed in the ^{1}H-^{1}H SQ-DQ spectra of α- and γ-IMC.

Clear correlation between neighbouring H6 and H7 sites were observed at δ_{DQ}=12.7 ppm and δ_{DQ}=13.3 ppm due to interactions with both methyl sites (H11 and H12 at δ_{DQ}=12.7 ppm and δ_{DQ}=13.3 ppm). The position of H6, and its close proximity to the H11 site, was confirmed by a correlation peak at δ_{DQ}=7.4 ppm. Three intramolecular close contacts of H9 were observed in the spectrum: H9 correlation with H12 at δ_{DQ}=3.25; correlation between inequivalent H9 (a and b) sites at δ_{DQ}=6.4 ppm; and correlation with aromatic protons (H4) at δ_{DQ}=10.3 and δ_{DQ}=11.0 ppm, which is in agreement with the position of two H4 sites determined using ^{1}H-^{13}C HETCOR. Further correlations between different aromatic sites in the highly overlapped region between 6.1 and 8.4 ppm were also found.

Two distinct correlations between the OH group and both methyl sites and H9 were observed in the ^{1}H-^{1}H NOESY spectrum (labelled in blue and yellow - Figure 4-22). The correlations may indicate further similarities between the desolvated crystal (IMC form V) and the IMC MeOH solvate; where the OH group is in close proximity to one of the H9 protons (3.16 Å), the two methyl protons H11 and H12 (2.93 and 3.41 Å) and the H12 motif. The H7 site had correlations between aromatic protons at 6.1 and 7.0 ppm, and one isolated correlation with H6 at 5.0 ppm. The H6 site was shown to be in intermolecular close contact with other aromatic hydrogens of the chlorophenyl ring through cross-peaks at 6.1 and 7.0 ppm. The correlation between H9/H11 sites with H6 site was also clearly visible in the ^{1}H-^{1}H NOESY spectrum providing further evidence of the conformation of the methoxy group in the structure. Additionally, the aliphatic H9/H11 site shows an intense cross-peak with the aromatic site at 6.1 ppm, and smaller shoulder at 7.0 ppm, which is likely due to intramolecular close contact of the H9 site with H4 and intermolecular close contacts of both H9/H11 with neighbouring molecules.

The solid-state NMR analysis of IMC form V indicates that there are two molecules in the asymmetric unit, which show similar conformations to the IMC MeOH solvate structure. The similarities between the ^{1}H-^{13}C CP/MAS spectra and ^{1}H MAS spectra of IMC form V and IMC MeOH solvate suggest the desolvation of the structure leads to changes in the packing of the molecules rather than changes in the molecular conformation. We were able to confirm the conformations of

the methoxy group C11 and the chlorophenyl ring through analysis of the position of C6 and C4 sites in the ^{1}H-^{13}C CP/MAS spectrum and the H7 site in ^{1}H MAS spectrum. Additionally, the ^{1}H-^{1}H SQ-DQ spectra enabled us to confirm the assignment of the ^{1}H spectrum through the dipolar correlations, and provided evidence for structure stabilisation through the hydrogen bonded carboxylic acid dimer, to α- and γ-IMC, as correlation between OH groups in the spectrum was observed.

4.2.1.7 Solid-state NMR of IMC form IV

To best of our knowledge the existence of IMC form IV has been reported only once in 1974 by Borka.[203] Form IV has been frequently confused with the already described IMC form V (δ) due to their similar melting points.

Table 4-7. Experimental (exp) ^{1}H and ^{13}C chemical shifts of IMC form IV compared with experimental ^{1}H and ^{13}C chemical shifts of γ-IMC. Non-quaternary carbons are labelled in blue.

| ^{13}C site	δ_{exp} (γ-IMC)	δ_{exp} (form IV)	^{1}H site	δ_{exp} (γ-IMC)	δ_{exp} (form IV)
C1	136.7	128.0-140.0			
C2	112.7	112.0;113.2			
C3	131.0	128.0-140.0			
C4	98.0	98.8	H4	5.4	4.7;6.1
C5	156.8	155.4			
C6	112.7	112.0;113.2	H6	5.9	4.7;5.4
C7	115.8	112.0;113.2	H7	6.1	4.7;5.4
C8	131.0	128.0-140.0			
C9	28.3	29.1;30.0	H9	1.8	2.1
C10	179.1	178.8;180.4			
C11	55.2	55.1;56.2	H11	2.4	3.1
C12	13.7	13.1;13.9	H12	2.1	0.7;1.3
C13	167.8	167.6;168.3			
C14	134.5	128.0-140.0			
C15	132.0	127.0-133.0	H15	7.2	4.7-7.2
C16	127.2	127.0-133.0	H16	5.7	4.7-7.2
C17	141.7	128.0-140.0			
C18	130.3	127.0-133.0	H18	7.1	4.7-7.2
C19	132.0	127.0-133.0	H19	7.2	4.7-7.2
		-	OH	12.8	12.0
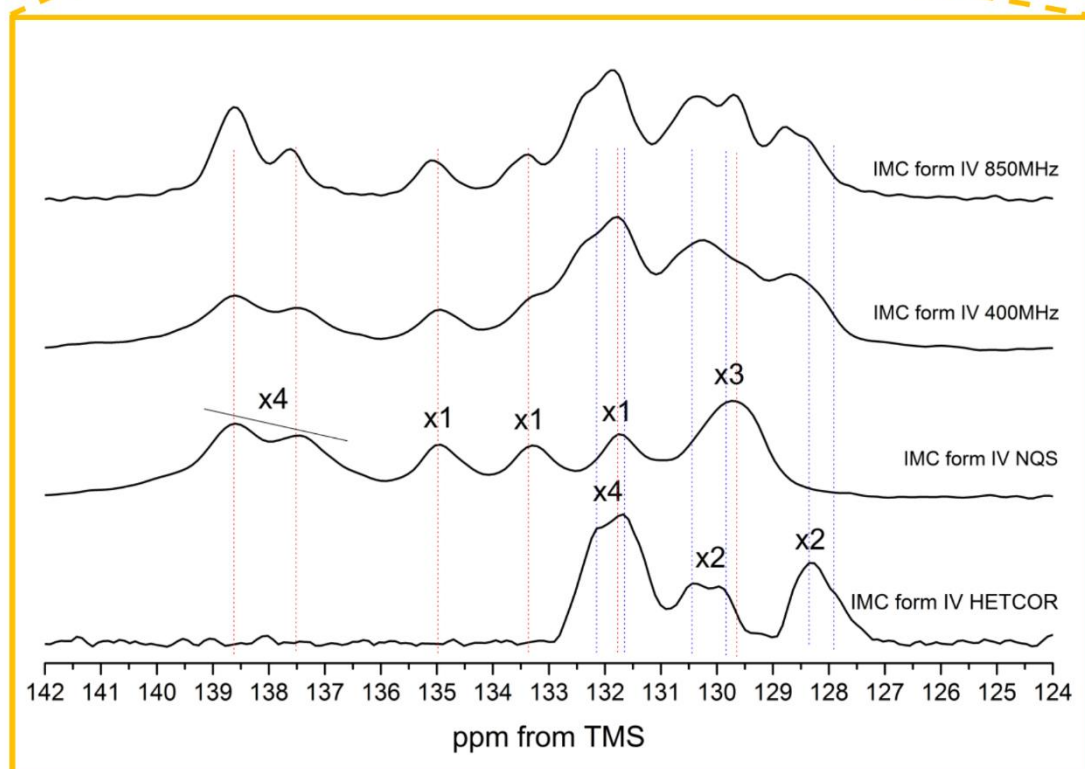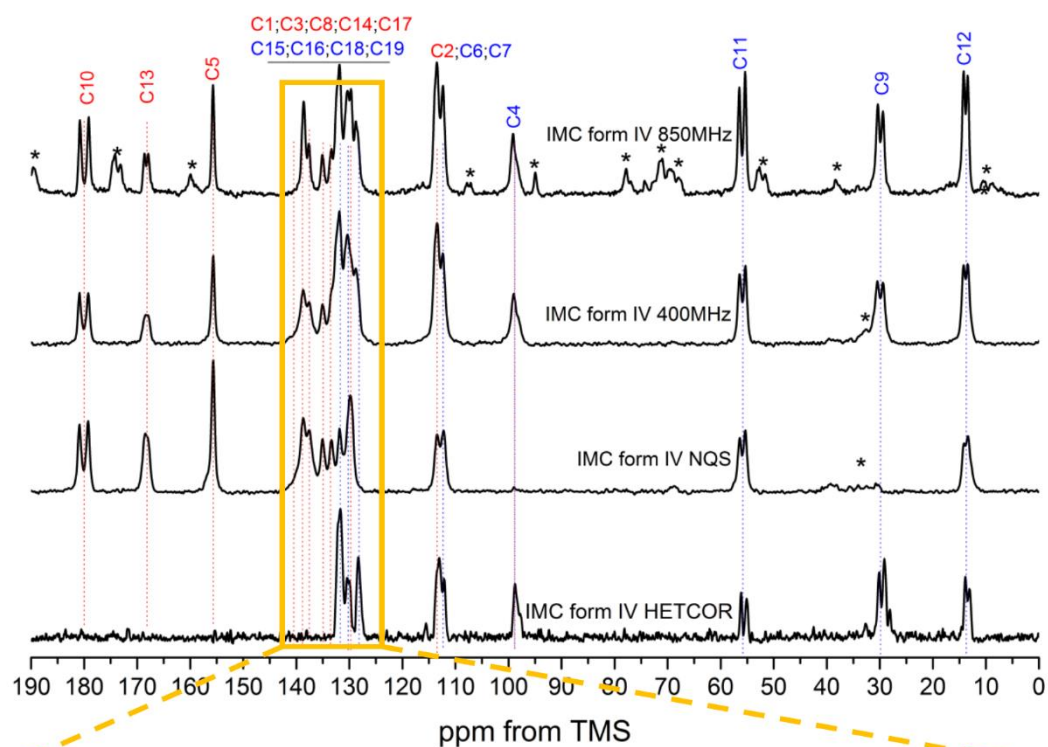
Figure 4-23. From the top: ^{1}H-^{13}C CP/MAS solid-state NMR spectra of IMC form IV acquired at 20.0 and 9.4 T, ^{1}H-^{13}C CP/MAS NQS and ^{13}C projection of ^{1}H-^{13}C HETCOR solid-state NMR spectra of IMC form IV (9.4 T). Spectra acquired at MAS rates of 10 kHz (9.4 T) and 13 kHz (20.0 T). Spinning sidebands are labelled with asterisks. Carbon labelling is based on similarities with previously assigned spectra of IMC polymorphs and MeOH solvate (quaternary carbons are labelled in red and non-quaternary carbons are labelled in blue in agreement with scheme in Figure 4-1A). The numbers in the zoomed spectra indicate integration of different ^{13}C sites.

Although we attempted to obtain the structural parameters of this form from PXRD data it was not possible to index the highly broadened PXRD pattern. However, we were able to obtain some structural information through solid-state NMR spectroscopy. The ^{1}H-^{13}C CP/MAS spectrum of IMC form IV showed two peaks for each carbon site indicating the presence of two non-equivalent molecules in the asymmetric unit. The close proximity of the methoxy group C11 to the carbon C4 was confirmed through the values of chemical shift of carbons C4 and C6 at *ca.* 99 and 112 ppm, respectively, which were similar to the C4 and C6 values for γ-IMC and molecules A and C of α-IMC (Figure 4-23, Table 4-7). The ^{13}C aromatic peaks of the chlorophenyl ring were in similar position compared to the position of the same motif in the γ-IMC, indicating further structural similarities (Figure 4-23, Table 4-7).

The assignment of different ^{1}H sites was conducted based on the ^{1}H-^{13}C HETCOR experiment (Figure 4-24). The ^{1}H spectrum of IMC form IV shows three distinct regions. Firstly, the aliphatic protons (H9, H12 and H11) are observed as a highly overlapping set of four peaks grouped between 0.8 and 3.5 ppm. The aromatic protons of the indole ring (H4, H6 and H7) have a broad peak between 4.5 and 5.5 ppm; and the chlorophenyl ring protons are grouped together as two peaks at *ca.* 6 ppm with two deshielded sites at *ca.* 7 ppm. The conformation of the chlorophenyl ring can be determined based on the chemical shift value of the H7 site.

As discussed previously, the CH-π shielding interactions between H7 and the chlorophenyl ring lead to a drastic upfield shift of the H7 peak from 8.4 ppm to *ca.* 5 ppm. The position of the H7 site for IMC form IV structure (as observed in the ^{1}H-^{13}C HETCOR experiment) indicated a close proximity between the chlorophenyl ring and H7 site.
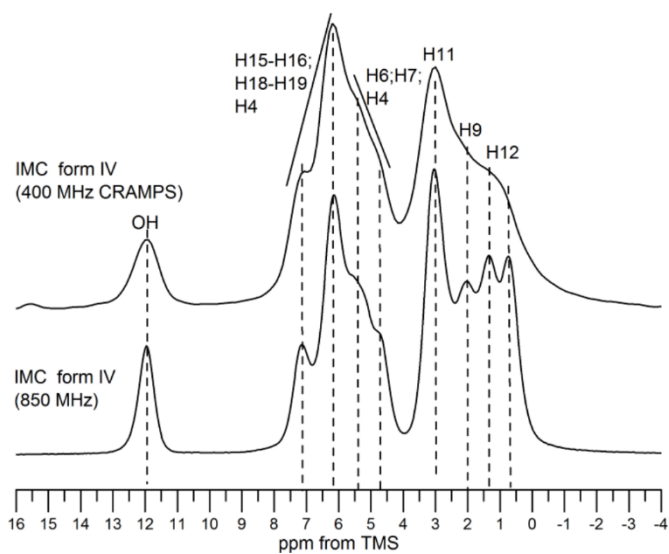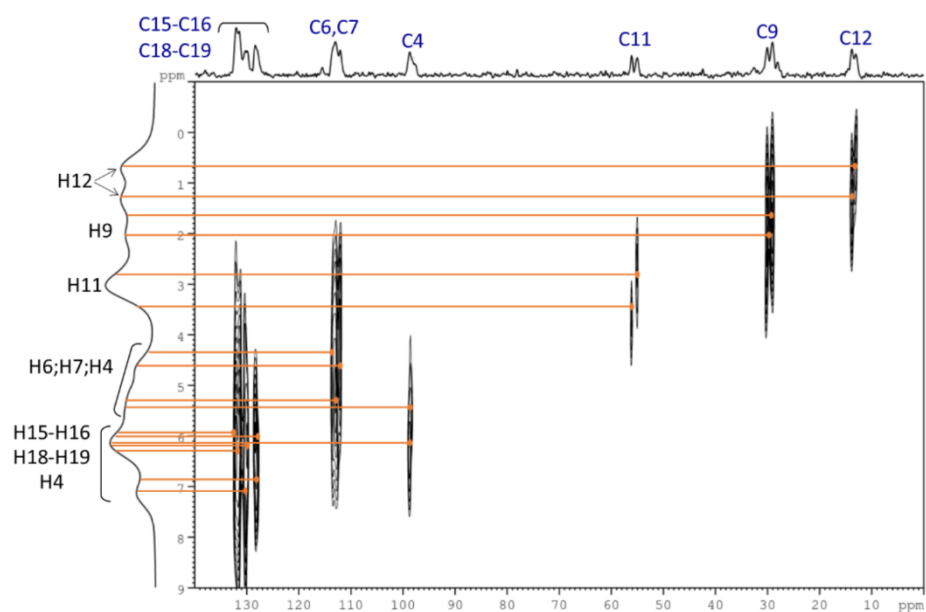
Figure 4-24. Top: ^1H-^{13}C HETCOR spectrum of IMC form IV; bottom: ^1H spectra of IMC form IV acquired at 20.0 T and spinning speed of 78 kHz and ^1H CRAMPS spectrum of IMC form IV acquired at 9.4 T and MAS rate of 6.8 kHz.
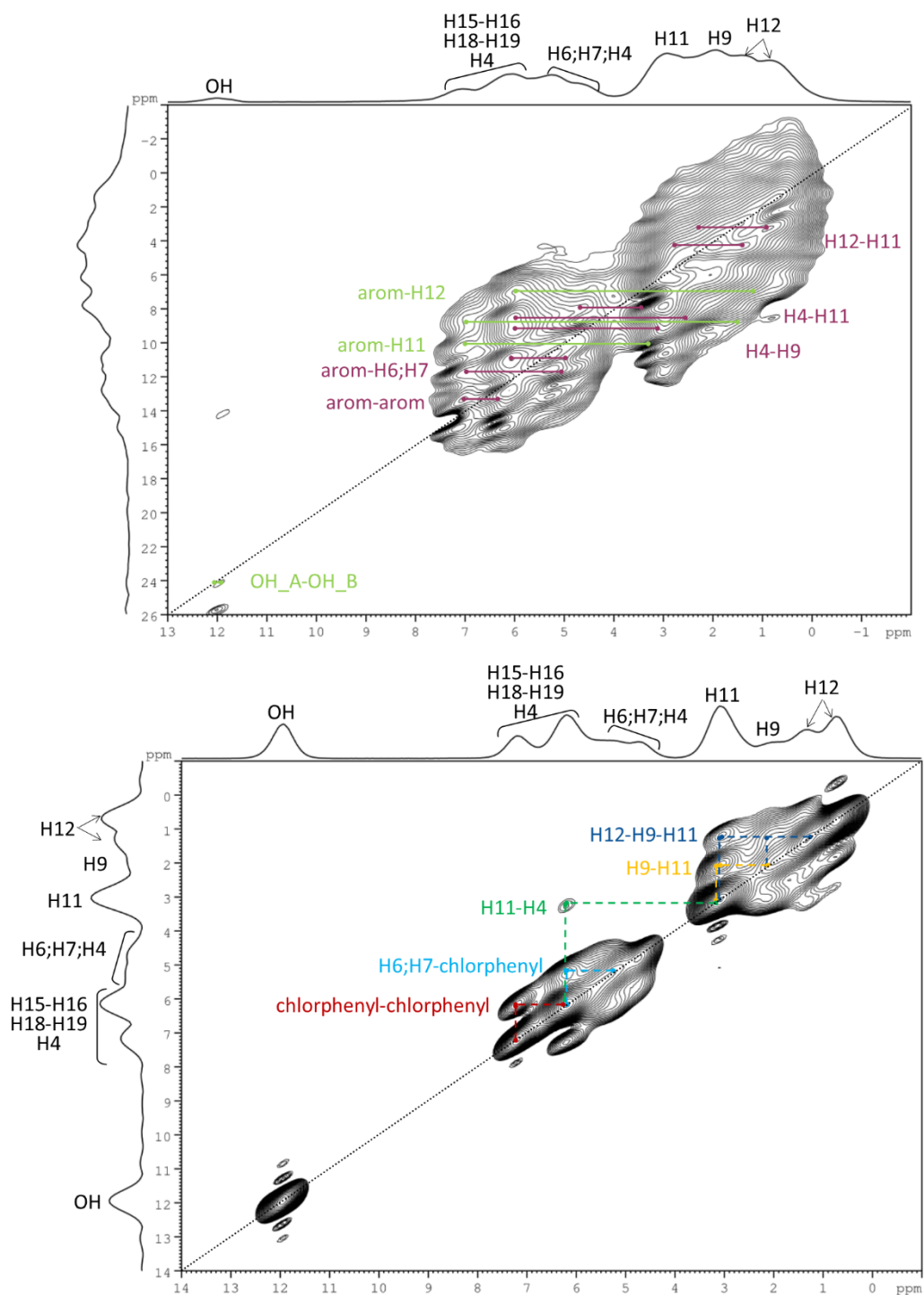
Figure 4-25. Top: ^{1}H-^{1}H SQ-DQ CRAMPS spectrum of IMC form IV (intramolecular short contacts are labelled in purple, while intermolecular short contacts are labelled in green). Bottom: ^{1}H-^{1}H CRAMPS NOESY spectrum of IMC from IV (cross-peaks between different ^{1}H sites are labelled with different colours). Both spectra were acquired at 20.0 T, at an MAS rate of 78 kHz. Labelling of ^{1}H sites is based on ^{1}H-^{13}C HETCOR experiment.

Unfortunately, little information could be extracted from the ^{1}H-^{1}H SQ-DQ and ^{1}H-^{1}H NOESY experiments due to overlapping peaks (Figure 4-25). The correlation peak between OH groups from two different molecules at δ_{DQ}=24.0 ppm indicates the formation of the carboxylic acid dimer, which may stabilise the structure in a similar way to γ-IMC. Splitting of the chlorophenyl ring protons into two peaks at *ca.* 6 and 7 ppm, as determined through ^{1}H-^{13}C HETCOR experiment, was confirmed by both the ^{1}H-^{1}H SQ-DQ correlation peak at δ_{DQ}=13.3 ppm and the distinct correlation in ^{1}H-^{1}H NOESY spectrum (labelled in red - Figure 4-25). The chlorophenyl ring was confirmed as being in close proximity to the H7 and H6 site, through correlation of these sites with aromatic protons at δ_{DQ}=11.8 and δ_{DQ}=11.0 ppm, and through the NOESY correlation peak at *ca.* 6 ppm (F2) and 5 ppm (F1) (labelled in light blue - Figure 4-25). Although the intramolecular correlation between H4 and H11 and H9 can be observed in both the ^{1}H-^{1}H SQ-DQ and ^{1}H-^{1}H NOESY spectra, it is also possible that other hydrogens in close proximity participate in the interaction due to overlapping peaks in both spectra.

The ^{13}C spectral analysis of IMC form IV suggests the presence of two IMC molecules in the asymmetric unit with similar conformation to γ-IMC. The chemical shifts of carbons C4 and C6 indicate close proximity of the methoxy group (C11) to C4, whilst chemical shift of hydrogen H7 to *ca.* 5 ppm confirmed its close proximity to the chlorophenyl ring. The highly overlapping ^{1}H spectrum of IMC form V was not very informative, however the visible correlation peak of both OH groups did indicate stabilisation of the structure *via* carboxylic acid dimer.

4.2.2   Summary of the solid-state NMR structural studies on IMC form IV and form V

IMC form V formed through the desolvation of the IMC MeOH solvate has been confused frequently in the scientific literature with IMC form IV, obtained by annealing of the amorphous glass, due to the similar melting temperature of both crystals at *ca.* 403 K. In our spectroscopic and diffraction studies significant differences between both structures have been demonstrated, unequivocally proving structural differences between both crystal forms. The combined use of computational and spectroscopic approaches for five different forms of IMC enabled significant understanding of the structures. Both molecules in the asymmetric unit of IMC form V were found to be closely related to the conformation of the IMC MeOH solvate. Methanol escaping from the crystal may induce some disorder. Changes in hydrogen bonding patterns and conformation of the carboxylic acid motif were reflected by significant differences in the position of both H9 and C10 peaks between the solvate and IMC form V. The presence of two molecules in the asymmetric unit, as determined with solid-state NMR, is in line with previous structural studies based on the PXRD.
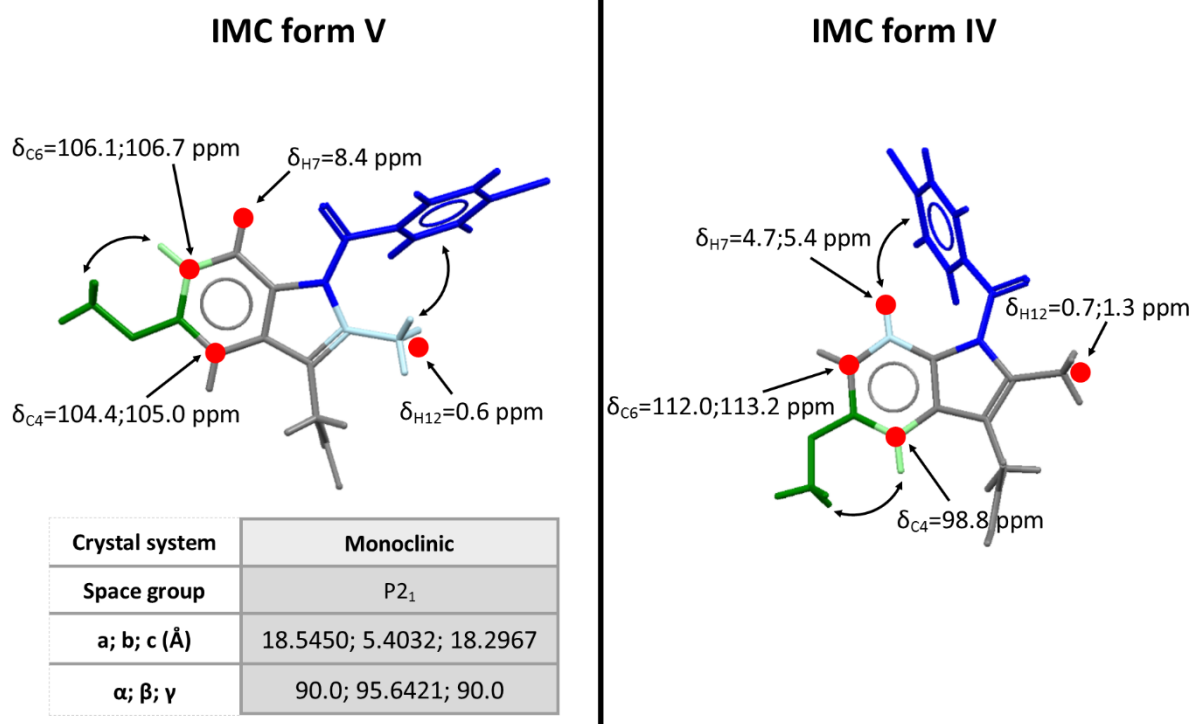
IMC form V

δ_{C6}=106.1;106.7 ppm δ_{H7}=8.4 ppm

δ_{C4}=104.4;105.0 ppm δ_{H12}=0.6 ppm

Crystal system	Monoclinic
Space group	P2$_1$
a; b; c (Å)	18.5450; 5.4032; 18.2967
α; β; γ	90.0; 95.6421; 90.0

IMC form IV

δ_{H7}=4.7;5.4 ppm

δ_{H12}=0.7;1.3 ppm

δ_{C6}=112.0;113.2 ppm

δ_{C4}=98.8 ppm

Figure 4-26. Summary of the conformational analysis of IMC form IV and IMC form V based on the combined experimental and computational ^{1}H and ^{13}C chemical shifts. Chemical shifts of different ^{1}H and ^{13}C sites sensitive to the conformation of chlorophenyl ring and methoxy group are labelled with red dots together with experimental chemical shift values.

IMC form IV has two molecules in the asymmetric unit which are related conformationally to γ-IMC. Both γ-IMC and IMC form IV can be obtained by annealing of the amorphous IMC glass. IMC form IV was formed by annealing of quenched, intact glass below 363 K: all other conditions lead to the formation of γ-IMC. This indicates that overcoming an energy barrier is required to form the thermodynamically most stable γ-IMC. Taking into account the crystallisation procedure of both IMC forms (γ-IMC and IMC form IV) from the amorphous state, it is not surprising that a) they are conformationally related and b) they are both stabilised through the formation of a carboxylic acid dimer. Detailed structural analysis of IMC polymorphs is of importance in a pharmaceutical field as IMC is frequently investigated model in crystallisation research. Furthermore, IMC is widely used as a model for poorly soluble compound in studies of amorphous solid dispersions. Due to this it is of importance to investigate possible crystallisation pathways of IMC from an amorphous state for better understanding of stability and nucleation processes in glassy solids.

4.2.3 Future work and concluding remarks

Although significant progress has been made towards understanding structures of IMC form IV and form V through the application of the combined computational and solid-state NMR approach

presented in this chapter, the ultimate goal of solving the crystal structures of both polymorphs is yet to be achieved. The mechanism of the IMC MeOH solvate desolvation and its effect on the decreased crystallinity of the material will be investigated further through the combined application of computational and experimental methods sensitive to local environment of atoms (solid-state NMR) and long range ordering (PXRD). This approach was recently demonstrated to be successful in investigation of structural disorder of orotic acid, which shows a significant decrease of crystallinity upon desolvation (DMSO solvate) and dehydration of the crystal.[242]

4.2.3.1 NMR studies

In order to fully assign IMC structures with Z'>1 it is essential to distinguish ^{13}C peaks from different molecules in the asymmetric unit. This can be achieved by correlating neighbouring carbon atoms through the use of J-couplings. In order to do that, it is possible to use INADEQUATE experiment in solid-state NMR, even at natural abundance.[146,243,244] Our attempt to record the INADEQUATE spectrum at UK 850 MHz Solid-State NMR Facility using a sample with natural abundance was not successful. This is likely due to fast decay of transverse magnetisation, which in turn is related to a short T_2 relaxation time. We are now in the process of applying for instrumental time at Nottingham DNP MAS NMR Facility in order to enhance the detection of ^{13}C-^{13}C J-coupling correlations at natural abundance, as was shown recently by Pinon *et al.*[245] The identification of ^{13}C signals from independent molecules in the IMC crystals with Z'>1 would enable complete assignment of the ^{13}C and ^1H spectra based on the combined experimental and computational approach and gain a detailed knowledge of the structure of IMC, which is an important model in crystallisation research. The detailed structural information would enable us to confirm that some parts of the IMC are highly sensitive towards conformational changes, which could have more general application in NMR crystallography.

4.2.3.1 Computational studies

In collaboration with Prof. Chris Pickard at Cambridge University we used AIRSS[246] (Ab Inition Random Structure Searching) methodology in order to find possible structures of IMC form V. 4000 structures were generated using as constraints space group and cell parameters obtained from indexed PXRD pattern, and IMC MeOH solvate without methanol molecules as a starting structure. The 20 lowest energy structures predicted using AIRSS, and geometry optimised with CASTEP, did not match any of the experimental PXRD patterns. Although the conformation of IMC in the predicted structures was in agreement with IMC conformation determined using NMR studies presented in this chapter, none of the structures was stabilised through the hydrogen-bonded carboxylic acid dimer. With structural information obtained from solid-state NMR and conformational studies and new developments in AIRSS, we expect to repeat structures search

using additional constraints. Additionally, in collaboration with Dr Doris Braun at University of Innsbruck, we are going to perform a crystal search using similar approach as presented for orotic acid. This is only possible due to the conformational information elucidated with solid-state NMR, as computations for flexible molecules in large unit cells and with Z'>1 are very expensive.

Through the application of structural information obtained from solid-state NMR we believe it will be possible to use CSP methods in order to find feasible structures for both IMC crystals. This in turn will enable us to explain in details the process of desolvation of IMC. This will be relevant to other systems, where new low crystallinity polymorphs are formed after desolvation.

Even more challenging is the explanation of nucleation processes in amorphous glasses, which, as was shown for IMC, lead to formation of either γ-IMC or IMC form IV depending on annealing conditions. Through the comparison of molecular packing and hydrogen bonding patterns in both IMC polymorphs (γ-IMC and IMC form IV), it might be possible to find spectral features in amorphous materials which would enable us to gain in depth understanding of this process.

Controlled crystallisation and stabilisation of IMC form V within MCF and CPG porous solids

Chapter 5

Findings from this chapter are published as:

5.1 Introduction

In the previous chapter we discussed polymorphism of a frequently used model drug IMC and its detailed structural and conformational flexibility using solid-state NMR spectroscopy. Furthermore, we proved structural differences between two metastable IMC polymorphs, *i.e.*, form IV and form V. In this work we have studied nano-crystallisation of IMC encapsulated within MCF and CPG porous solids via careful control of the confined structures from amorphous to crystalline states. With its well described polymorphism and phase transitions IMC is an excellent model compound for nano-crystallisation research.
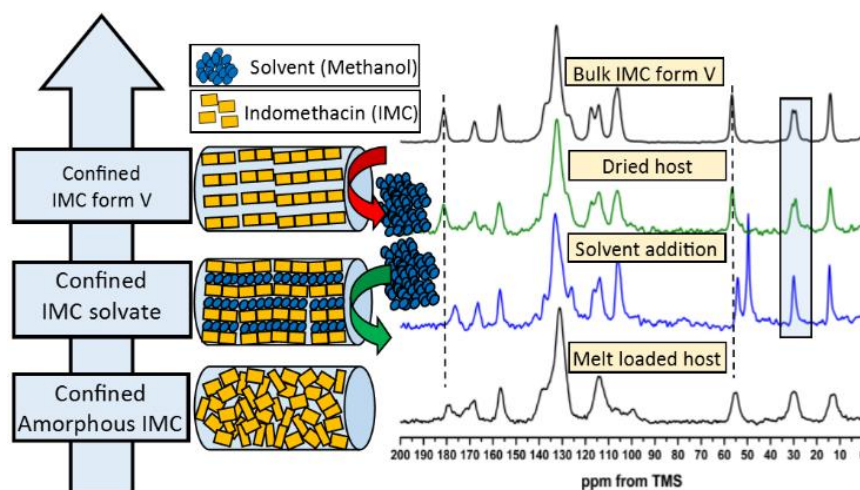

Figure 5-1. Multi-step phase transformation of confined IMC; from confined amorphous IMC to a stabilised metastable IMC form V, via a confined solvate.

Recently, SBA-15 mesoporous silica has been demonstrated to be a suitable host for the stabilisation of amorphous IMC loaded via an incipient wetness method.[41] An attempt to crystallise IMC 'inside' the pores of MCM-41 and SBA-15 materials was recently made by Ukmar *et al.*[86,87,247] Although the authors suggested selective crystallisation of one of the IMC polymorphs under mesoscopic confinement, the presented data show no decrease or broadening in the melting point of loaded drug, therefore cannot be described as confined crystallisation.[87] Moreover, the spectroscopic data are consistent with the presence of amorphous IMC in the pores, in agreement with Van Speybroeck *et al.*[41] In this work, for the first time we have shown multiple phase

transformations of the confined solids assuring in a critical and comprehensive way that all transitions take place inside the nanopores. Starting from confined amorphous IMC, through a confined IMC MeOH solvate, we show a novel method to crystallise and stabilise the rare and highly metastable IMC form V, a desolvation product.[180,185,220] We further demonstrate methods to control the drug phase through the effect of the pore size, loading procedure and guest content, which is of paramount importance for further industrial development.

5.2 Results and discussion

5.2.1 Loading efficiency and textural parameters of loaded materials

Several methods have been applied for loading drug molecules into the porous silica hosts, including impregnation, incipient wetness, rotary evaporation, immersion, spray drying and melt loading.[39,40,73,85,248,249] The studies of crystallisation in the confined space require accurate control of experimental protocols to prevent the loading of the drug outside the pores. Furthermore, it is important to note that distinguishing between the confined drug species and the bulk phase outside the pore space often presents a significant characterisation challenge. We used two loading methods, *i.e.*, incipient wetness and the melt loading method, for the encapsulation of indomethacin, and two different types of the silica hosts. The first one was the spherical (particle size 3-5 µm) MCF with ink-bottle like pores of 29.6 nm (Figure 5-2) in diameter interconnected by smaller windows (necks) of 11 nm as determined using nitrogen adsorption analysis (Figure 5-3). The second material was the commercially available unstructured CPG host with a mean pore size diameter of 55 nm and particle size of ca. 100-200 µm (Figure 5-2).
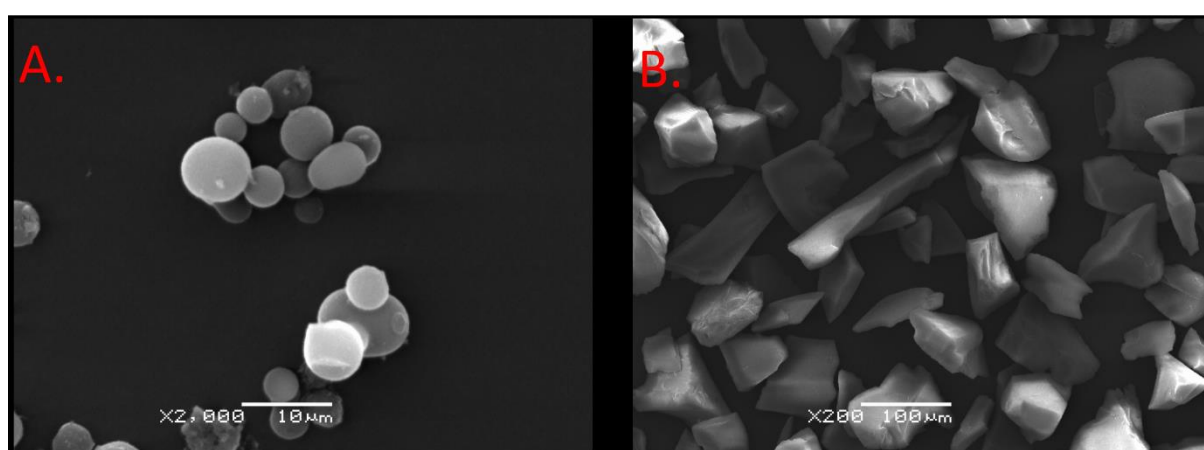

Figure 5-2. SEM images of A. MCF host and B. CPG host.

5.2.1.1 N_2 Adsorption-desorption isotherms

When the MCF silica host is loaded from the melt a gradual decrease of the total pore volume and surface area as a function of an increasing drug content are observed from nitrogen adsorption–desorption isotherms, indicating loading of the drug inside the pores. When the concentration of the embedded drug reaches 50 wt. % (MCF–IMC 50–50) the pores seem to be fully filled with the guest molecules (Figure 5-3, Table 5-1).
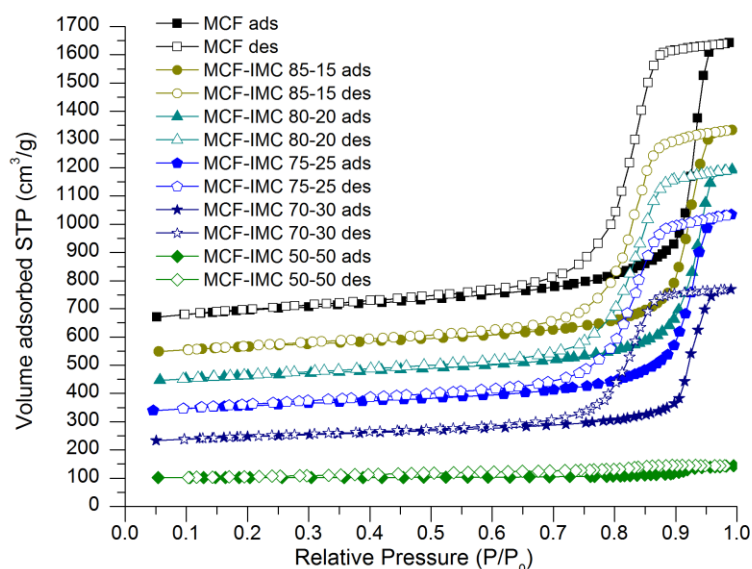

Figure 5-3. Nitrogen adsorption–desorption isotherms of MCF host loaded with different ratios of IMC using the melting method. The isotherms are offset by 100 cm^3 g^{-1}.

Table 5-1. Drug content in the MCF and CPG hosts and structural parameters of the hosts after melt loading. [a]

Host-guest composite	IMC (g g^{-1})	V_{total} [cm^3 g^{-1}]	d_{pore} [nm]	S_{BET} [$m^2 g^{-1}$]
MCF	N/A	1.613	29.6	333.2
MCF-IMC 85-15	0.151 ± 0.003	1.290	26.2	233.9
MCF-IMC 80-20	0.199 ± 0.010	1.225	30.0	220.1
MCF-IMC 75-25	0.243 ± 0.016	1.134	23.3	203.0
MCF-IMC 70-30	0.294 ± 0.010	0.880	25.8	167.8
MCF-IMC 50-50	0.494 ± 0.013	0.056	N/A	28.1
CPG	N/A	1.2[b]	55.0[b]	50.4
CPG-IMC 85-15	0.169 ± 0.010	-	-	30.4
CPG-IMC 80-20	0.218 ± 0.008	-	-	33.3
CPG-IMC 75-25	0.267 ± 0.018	-	-	33.7
CPG-IMC 70-30	0.285 ± 0.024	-	-	15.4
CPG-IMC 50-50	0.482 ± 0.032		-	N/A

[a] V_{total} – total pore volume calculated at P/P_0 of 0.99, d_{pore} – pore size diameter calculated from the adsorption branch using the BJH (Barrett–Jotyner–Halenda) method, S_{BET} – the BET specific surface area. [b] data from the manufacturer.

The CPG host with large pores of 55 nm in diameter can be classified as being on the boundary between mesoporous and macroporous silica materials. The combination of melting point depression (onset and heat of fusion) and changes in N_2 adsorption properties serve as a proof of the guest confinement. The loaded CPG silicas show some decrease of the BET specific surface area compared to the pure host (Table 5-1). However, the correlation between the drug content and decrease of surface area is not straightforward due to the relatively low value of the BET surface area of the host (*i.e.*, for the CPG material it is *ca.* 49.5 m^2 g^{-1} compared to 333.2 m^2 g^{-1} for the MCF host). The presence of crystalline guest embedded within the CPG host can be illustrated by the broadening and decrease of the IMC melting point, which is indicative of small crystals.[93,106,115]

5.2.2 Pore size diameter dependence of IMC recrystallisation from confined amorphous phase

The MCF and CPG hosts loaded using the melting method at different drug to host ratios do not show signs of a crystalline phase, only a broad 'halo' signifying the lack of long range order is visible in the PXRD patterns. These results are corroborated by the solid-state NMR spectra of confined IMC within both the MCF and CPG hosts (Figure 5-4). The broadening of the indomethacin peaks is due to the increased distribution of possible orientations and magnetically non-equivalent environments of carbon atoms, typical of amorphous solids. The significant broadening of the spectra from 160 to 180 ppm, corresponding to the carboxylic acid carbon, may be related to the presence of a variety of hydrogen bonding environments and orientations. This could also be related to an increased mobility.[74,77]
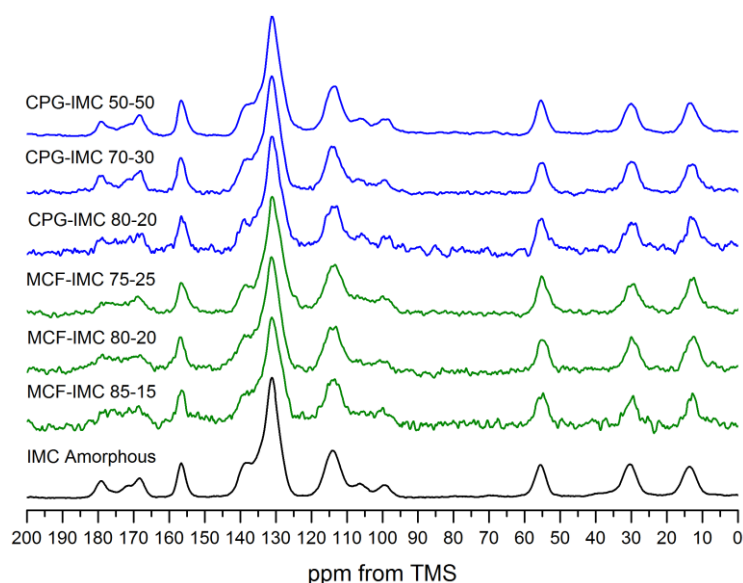

Figure 5-4. ^{1}H–^{13}C CP MAS NMR spectra of MCF and CPG hosts loaded with IMC using melting method at different host-drug ratios.

Although thermal properties and phase transitions of confined gases and liquids have been studied extensively, the effect of confinement on solids is still not understood fully. It is known that nano-size crystals show a decrease and broadening of the melting point and the melting enthalpy of confined crystals is smaller in comparison to the bulk phase.[106,110,114,115] Upon heating, bulk amorphous indomethacin shows a glass transition (T_g) at *ca.* 310 K followed by recrystallisation of α- and γ-IMC at 373-473 K and the melting of the latter two polymorphs.[59] DSC thermograms of the MCF host loaded with indomethacin using the melting method do not show any crystallisation and melting processes, proving it is in an amorphous state and the size of the pores of MCF (*ca.* 30 nm) prevents the thermally induced recrystallisation of indomethacin.
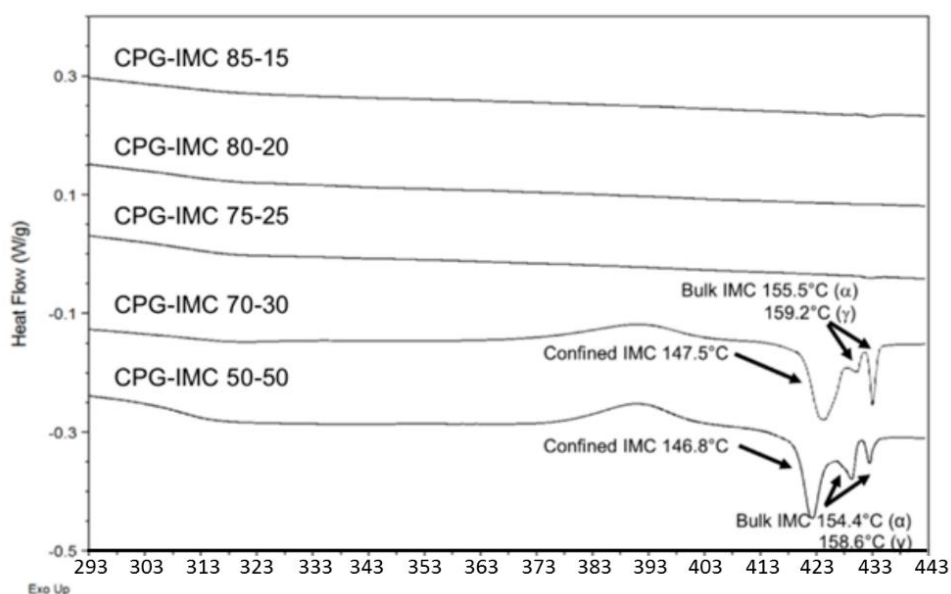

Figure 5-5. DSC thermograms of CPG host loaded with IMC using melting method at different host:drug ratios.

Interestingly, indomethacin confined within the larger pores of the CPG host (*ca.* 55 nm) shows a concentration dependent thermally induced crystallisation (Figure 5-5). No thermal transitions were observed at low concentrations of IMC (up to 25 wt. %). However, when the drug content reached 30 wt. %, recrystallisation of the amorphous indomethacin into both α- and γ-IMC is observed. Such recrystallisation occurs inside the pores, as confirmed by a decrease of the melting temperature and broadening of the melting peak (for CPG–IMC 70–30 T_m is 420.5 K, for CPG–IMC 50–50 T_m is 419.8 K). Nevertheless, the two other peaks present on the DSC thermogram for the materials loaded with IMC at concentrations of 30 and 50 wt. % indicate the presence of the bulk crystalline α- and γ-IMC, which again signifies the importance of the loading protocol on the crystallisation outcome.

5.2.3 Solvent driven recrystallisation of confined amorphous IMC and stabilisation of confined IMC form V

5.2.3.1 Changes in the textural properties of the host upon addition of the solvent

A substantial increase in the total pore volume and the surface area of the products loaded with high concentration of the drug (MCF–IMC 70–30 and MCF–IMC 50–50) was observed after addition of the solvent (Figure 5-6, Figure 5-7, Table 5-2). This may indicate dissolution and rearrangement of the confined amorphous phase prior to further crystallisation or some leakage of the drug from the pores as melting of bulk crystalline IMC was detected in DSC studies of the composites loaded with 30 and 50 wt. % IMC (see section 5.2.3.2.2 and related figures). It is important to mention that careful control over the solvent volume (lower than V_{total}) and total content of the drug within the pores is crucial to avoid leakage of the drug. Large volumes of solvent and high drug content increase the risk of the drug leakage leading to inhomogeneous composites. This is discussed in details in section 5.2.3.2.1.
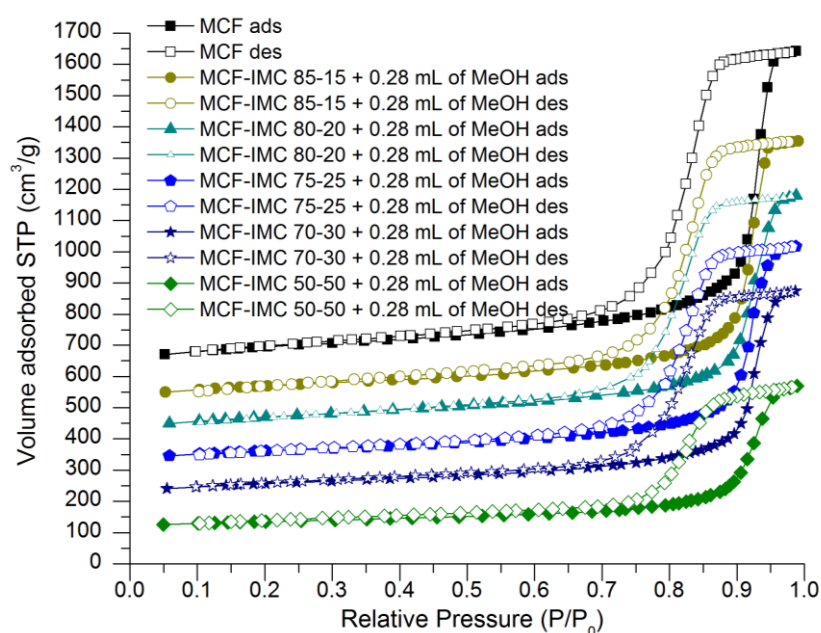

Figure 5-6. Nitrogen adsorption–desorption isotherms of MCF host loaded with different ratios of IMC using the melting method and subsequently treated with MeOH. The isotherms are offset by 100 cm^3 g^{-1}.

Table 5-2. Drug content in the MCF and CPG hosts and structural parameters of the hosts loaded using melting method and subsequently treated with MeOH. [a]

Host-guest composite	IMC (g g^{-1})	V$_{total}$ [cm^3 g^{-1}]	d$_{pore}$ [nm]	S$_{BET}$ [m^{2}g^{-1}]
MCF	N/A	1.613	29.6	333.2
MCF-IMC 85-15 + 0.28 mL MeOH	0.161 ± 0.012	1.322	26.1	251.2
MCF-IMC 80-20 + 0.28 mL MeOH	0.191 ± 0.070	1.206	23.1	260.0
MCF-IMC 75-25 + 0.28 mL MeOH	0.245 ± 0.041	1.109	26.1	214.3
MCF-IMC 70-30 + 0.28 mL MeOH	0.261 ± 0.027	1.042	26.0	204.8
MCF-IMC 50-50 + 0.28 mL MeOH	0.471 ± 0.073	0.725	23.1	126.7
CPG	N/A	1.2[b]	55.0[b]	50.4
CPG-IMC 85-15 + 0.28 mL MeOH	0.150 ± 0.001	-	-	38.4
CPG-IMC 80-20 + 0.28 mL MeOH	0.198 ± 0.003	-	-	22.4
CPG-IMC 75-25 + 0.28 mL MeOH	0.231 ± 0.002	-	-	35.3
CPG-IMC 70-30 + 0.28 mL MeOH	0.291 ± 0.003	-	-	29.1
CPG-IMC 50-50 + 0.28 mL MeOH	0.484 ± 0.012	-	-	3.3

[a] V$_{total}$ – total pore volume calculated at P/P$_0$ of 0.99, d$_{pore}$ – pore size diameter calculated from the adsorption branch using the BJH (Barrett–Jotyner–Halenda) method, S$_{BET}$ – the BET specific surface area. [b] data from the manufacturer.
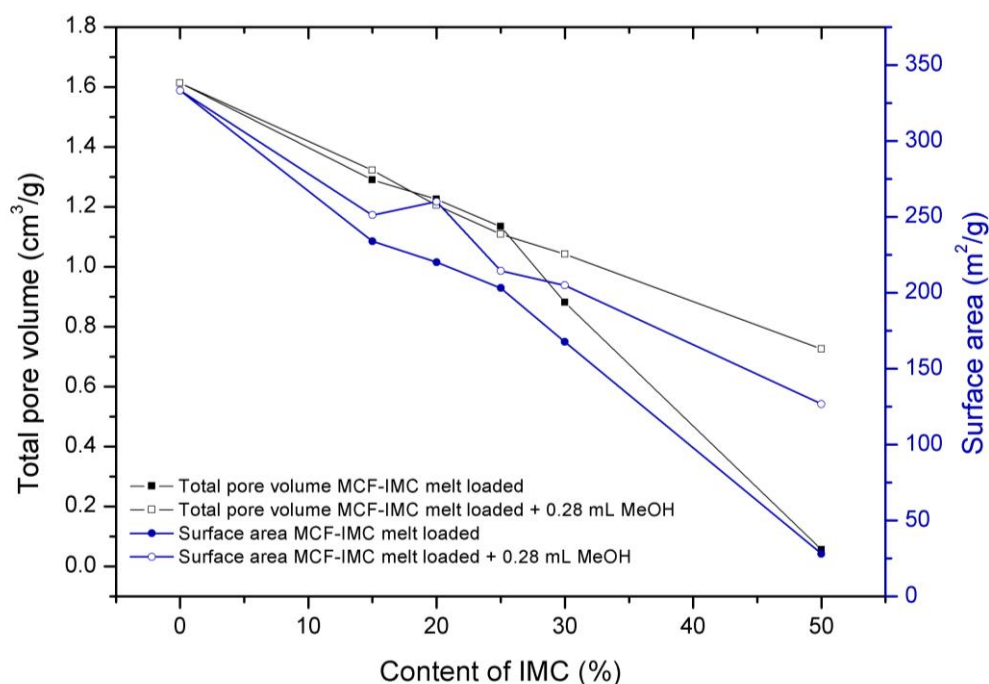

Figure 5-7. Total pore volume and BET surface area of MCF–IMC melt loaded samples before and after addition of the solvent. The total amount of IMC within the materials was determined using TG analysis.

5.2.3.2 Solvent induced amorphous to crystalline phase transition in confined space.

To drive indomethacin crystallisation from an amorphous phase embedded within the porous MCF and CPG hosts, three organic solvents, *i.e.*, methanol, ethanol and acetonitrile were used. It was reported previously that IMC crystallisation from acetonitrile always leads to the formation of γ-IMC, while crystallisation from ethanol may yield either the α- or the γ-polymorph depending on the supersaturation ratio.[203,206] Borka's first paper on indomethacin polymorphs indicated the formation of γ-IMC in a bulk acetonitrile solution and α-IMC on the walls of the crystallisation vial.[203] Crowley and Zografi reported the formation of IMC : methanol (1:1) solvate from hot methanol at a low supersaturation ratio.[212] As demonstrated by Joshi *et al.* and later by Surwase *et al.* this solvate may yield the metastable form V of IMC under careful desolvation. This form was reported to recrystallise subsequently into more stable polymorphs.[180,220] Using CPG host loaded with molten IMC at concentrations 15–25 % we were able to obtain exclusively γ-IMC after the addition of ethanol or acetonitrile as a crystallisation driving solvent. When methanol was used to drive IMC crystallisation, either pure IMC form V, with the methanol solvate as an intermediate, or a mixture of both γ-IMC and IMC form V were obtained (see next section 5.2.3.2.1).

5.2.3.2.1   Optimisation of volume and solvent addition to CPG melt loaded materials

To optimise the loading and phase transformation procedure we used the CPG porous host due to its previous application in crystallisation studies and commercial availability.[93,114,115,119,250] To investigate the impact of the solvent on the recrystallisation from an amorphous phase under confinement, we loaded the CPG material with indomethacin at the 85-15, 80-20 and 75-25 host:guest ratios, followed by the addition of three different solvents: methanol, ethanol and acetonitrile. After loading, the materials were dried under vacuum at 310 K for 2 hours. In the first series of experiments the volume of the solvent was adjusted to enable total filling of the pores *i.e.*, 1.4 mL g^{-1} of the material (*i.e.*, 0.28 mL of the solvent per 200 mg of the material used during the screening). The phase composition of the loaded indomethacin was assessed using PXRD. In the cases of using acetonitrile or ethanol as the crystallisation driving solvent, exclusive formation of γ-IMC was observed (Figure 5-8). In the case of using methanol as the crystallisation driving solvent we obtained the metastable IMC form V as confirmed during further studies (Figure 5-9).
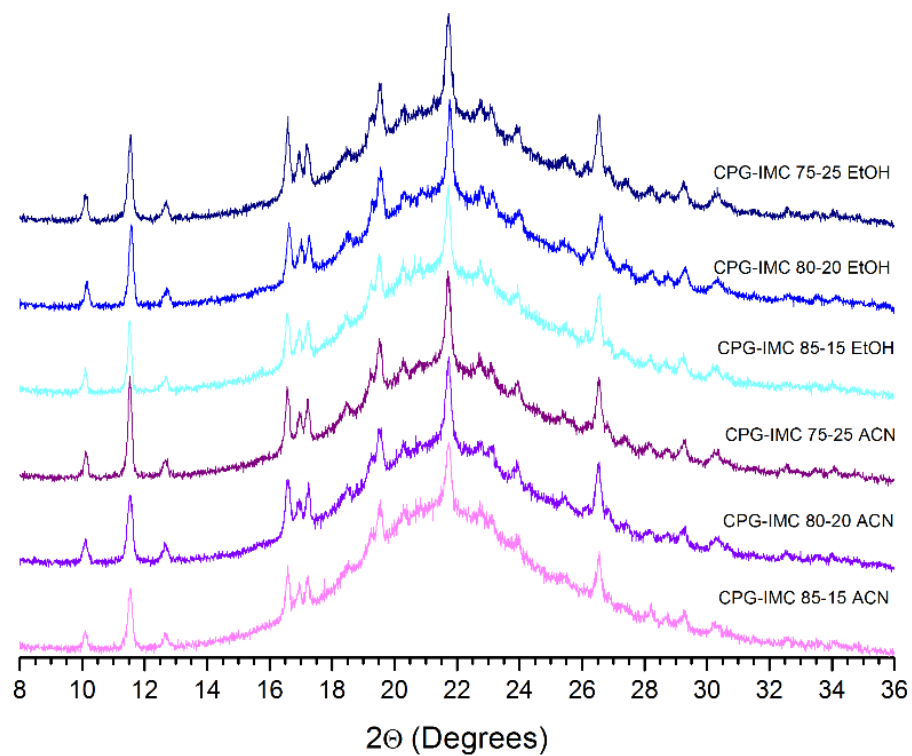
Figure 5-8. PXRD patterns of CPG material loaded with different ratios of indomethacin and subsequently treated with ethanol (EtOH) and acetonitrile (ACN).
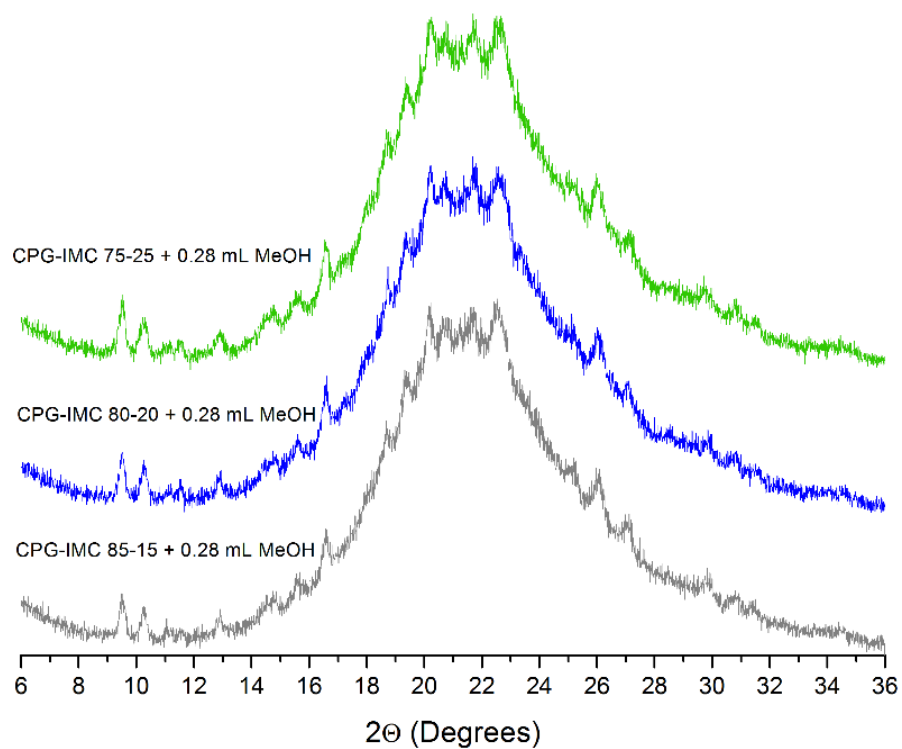

Figure 5-9. PXRD patterns of CPG material loaded with different amounts of indomethacin and subsequently treated with 0.28 mL of MeOH.

In the next step we optimised the volume of methanol required to form a pure crystalline phase of IMC form V in the pores. In this experiment, 0.140 or 0.560 mL of methanol were added to 200 mg of melt loaded CPG host. These volumes of the solvent were chosen to allow only a partial wetting of the pores (0.140 mL) and total overloading of the material with the solvent (0.560 mL). Both used volumes lead to the formation of the composites with two phases of indomethacin *i.e.*, γ-IMC and IMC form V. Only the host loaded with 20 % drug shows a PXRD pattern characteristic exclusively of the IMC form V after addition of 0.140 mL of methanol (Figure 5-10). Further confirmation of the concomitant crystallisation of γ-IMC and IMC form V was made using DSC analysis (Figure 5-11). It further confirmed partial leakage of IMC from the pores at high solvent volumes.
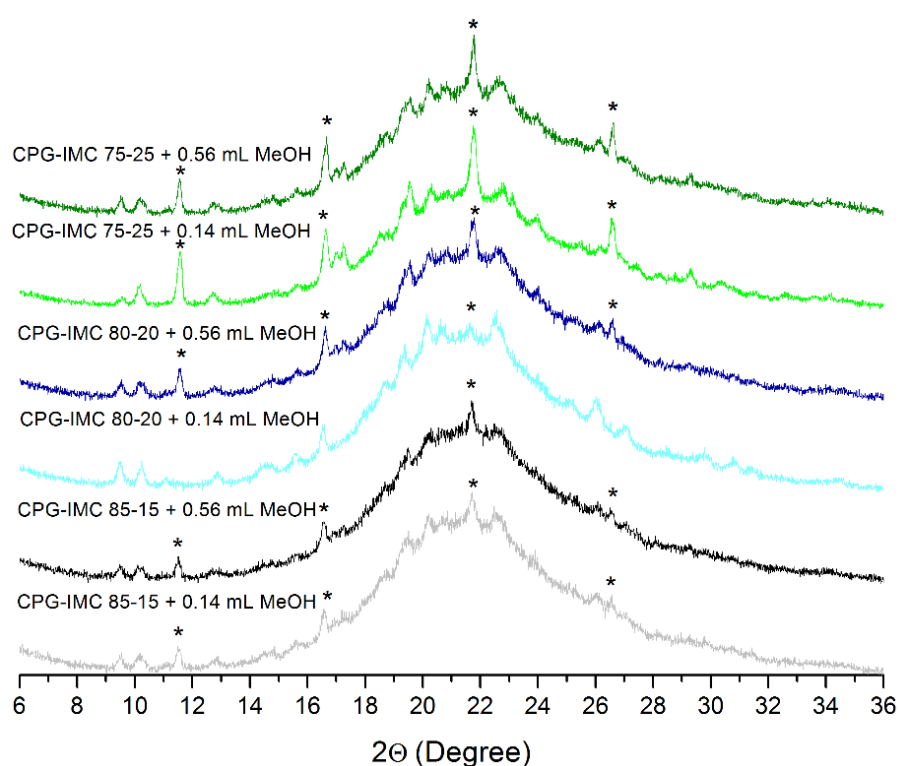

Figure 5-10. PXRD patterns of CPG material loaded with different ratios of indomethacin and subsequently treated with different volumes of methanol (peaks due to γ-IMC are indicated by asterisks).
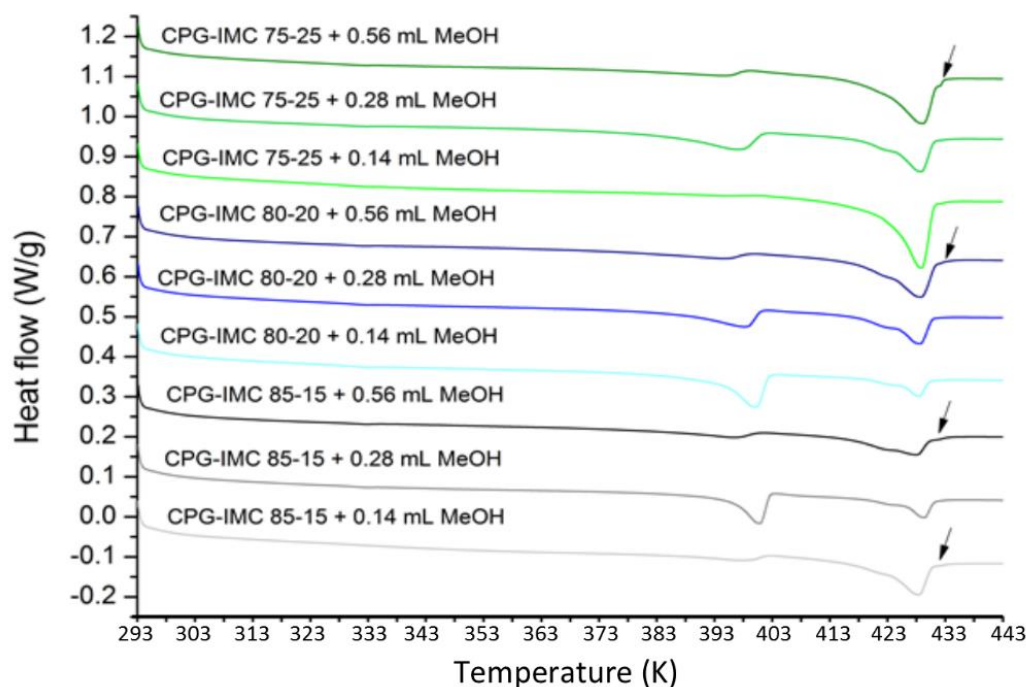
Figure 5-11. DSC thermograms of CPG material loaded with different ratios of indomethacin and subsequently treated with different volumes of methanol. The arrows indicate melting of bulk IMC outside the pores.

5.2.3.2.2   Deposition of indomethacin outside the pores of MCF and CPG composites at high drug loadings (30 and 50 %) after methanol addition

As shown in the Figure 5-5, the CPG host loaded with high drug contents of 30 and 50 wt. % shows thermally driven recrystallisation of IMC loaded outside the pores as confirmed by observation of the bulk melting temperature of both IMC polymorphs (α- and γ-). When IMC was loaded from the melt into the MCF host, no signs of drug loaded outside the pores could be detected using DSC, PXRD and solid-state NMR (Figure 5-4). The amorphous drug loaded within the MCF host at the concentration of 30 and 50 wt. % crystallises into a mixture of IMC phases after addition of methanol, which are partly loaded outside the pores. The DSC thermograms of both composites with the highest loadings show the melting peaks of bulk γ-IMC (Figure 5-12). This can be related to a leakage of the dissolved drug from the pores after addition of the solvent and recrystallisation on the external surface of the host, since the presence of the bulk crystalline phase in the highly concentrated samples could not be detected before the addition of the solvent. Similar findings regarding ibuprofen confined within MCM-41 were recently published by Skorupska *et al.*[79]

Figure 5-12. DSC thermograms of MCF and CPG hosts loaded with IMC using melting method at concentrations of 30 and 50 wt. % after the addition of methanol.
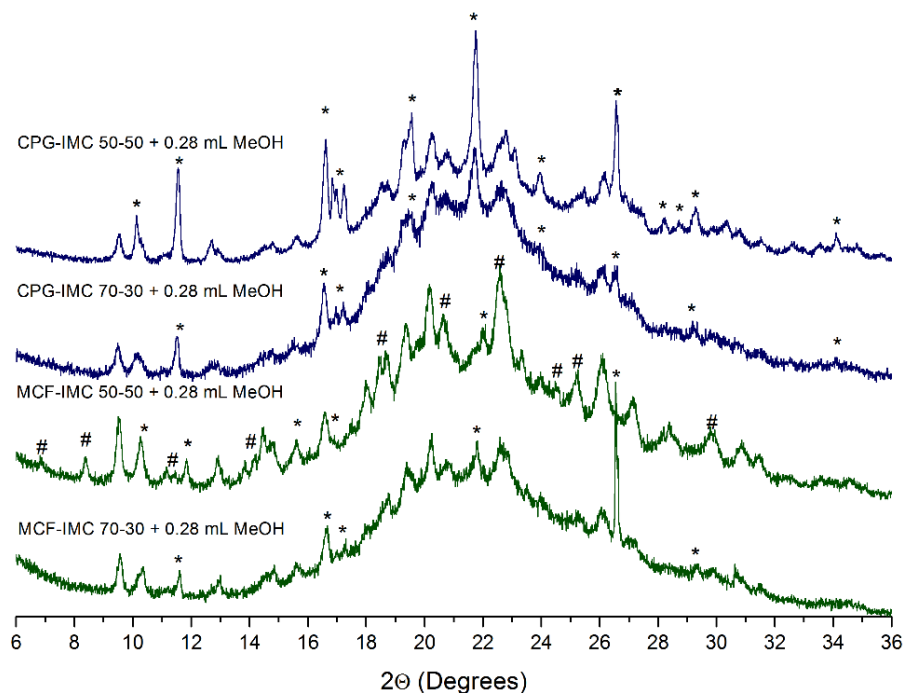
Figure 5-13. PXRD patterns of IMC loaded into MCF and CPG host from the melt at concentrations of 30 and 50 wt. % after addition of methanol (peaks showing the presence of γ-IMC are labelled with asterisks whereas peaks showing α-IMC are labelled with hash marks).

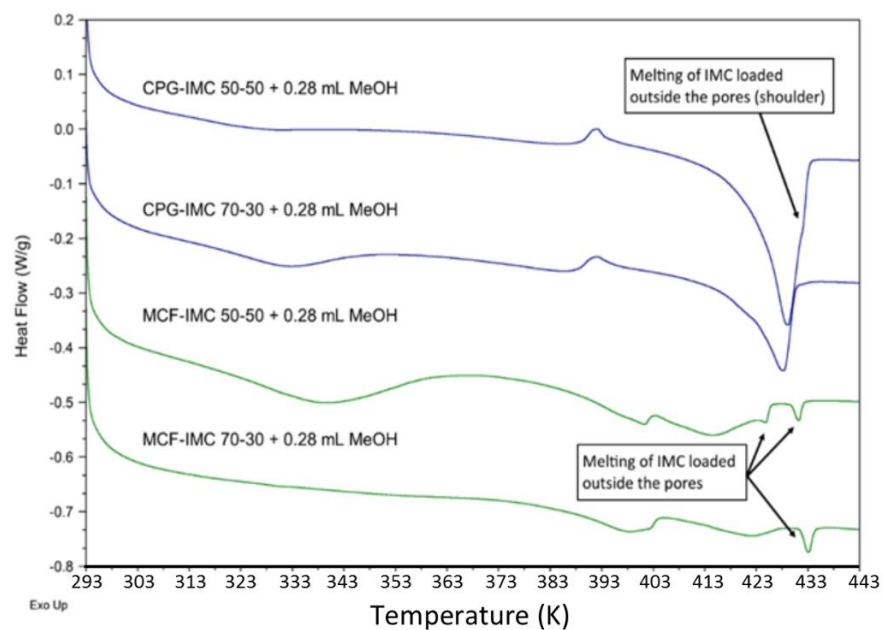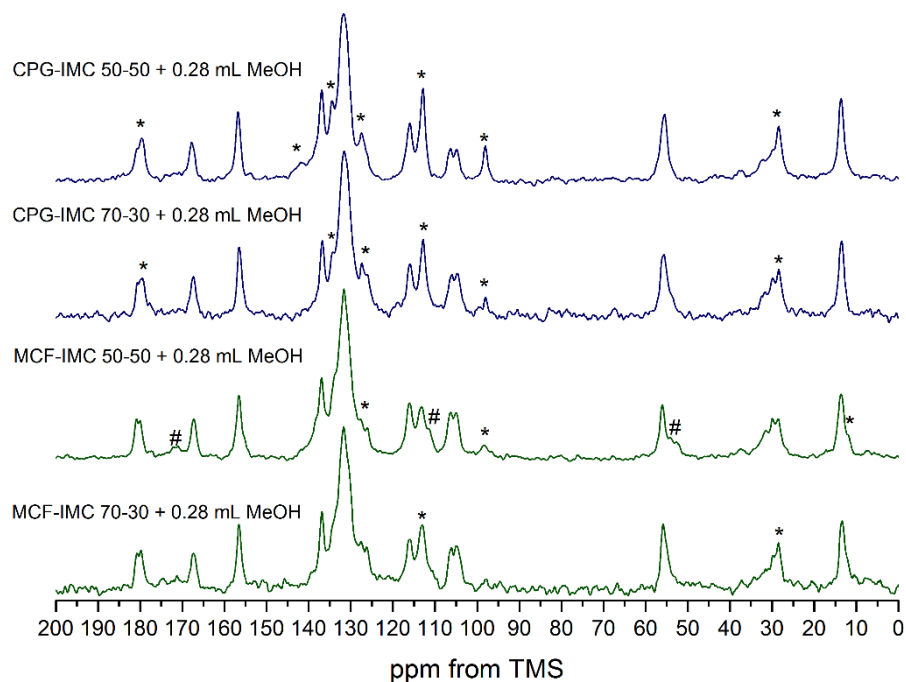**Figure 5-14.** ^{1}H-^{13}C CP/MAS solid-state NMR spectra of MCF and CPG hosts loaded with IMC using melting method at concentrations of 30 and 50 wt. % after addition of methanol (peaks showing the presence of γ-IMC are labelled with asterisks whereas peaks showing α-IMC are labelled with hash marks).

Solvent driven recrystallisation of the IMC loaded within MCF and CPG hosts at high IMC concentrations leads to a mixture of phases which are loaded inside and outside the pores. The presence of either α-, γ- and form V IMC was detected using PXRD and solid-state NMR (Figure 5-13, Figure 5-14), however, due to the complex thermal transitions it is difficult to state unequivocally which phase is formed due to the confinement or which is loaded outside the pores. Further investigation of concomitant crystallisation of non-confined systems is beyond the scope of this work.

5.2.3.2.3   Stabilisation of metastable IMC form V inside the pores of the MCF host

The DSC thermograms of IMC confined within the MCF pores show a decrease of the melting temperature and broadening of the melting peak indicating the presence of nanosize crystals (Figure 5-15).
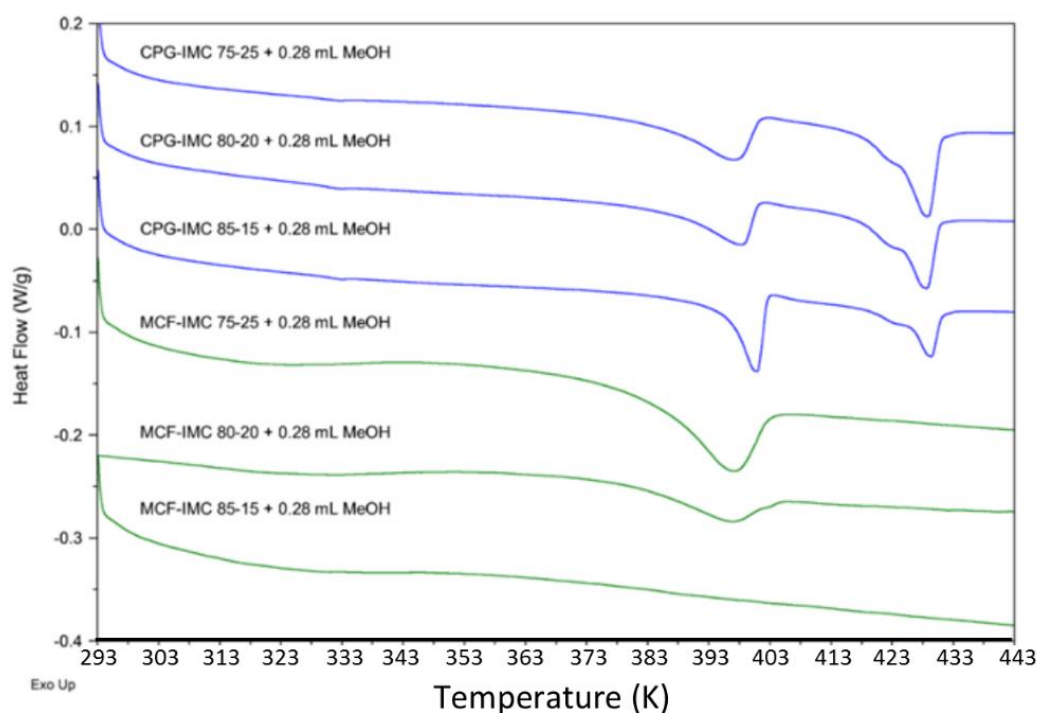
Figure 5-15. DSC thermograms of MCF and CPG hosts loaded with IMC from the melt after addition of methanol.

Table 5-3. Thermal transitions corresponding to confined IMC form V in MCF and CPG hosts loaded from the melt after addition of the solvent.

Host-guest composite	Melting onset (K)	ΔH_{fusion} (J g^{-1})
MCF-IMC 85-15 + 0.28 mL MeOH	-	-
MCF-IMC 80-20 + 0.28 mL MeOH	383.0 (form V)	18.3 (form V)[a]
MCF-IMC 75-25 + 0.28 mL MeOH	384.9 (form V)	35.8 (form V)
CPG-IMC 85-15 + 0.28 mL MeOH	395.6 (form V) 425.1 (γ-IMC)	31.6 (form V) 18.6 (γ-IMC)
CPG-IMC 80-20 + 0.28 mL MeOH	385.3 (form V) 423.1 (γ-IMC)	25.6 (form V)[b] 26.5 (γ-IMC)
CPG-IMC 75-25 + 0.28 mL MeOH	383.5 (form V) 422.6 (γ-IMC)	24.1 (form V)[b] 25.9 (γ-IMC)

[a] The lower measured heat of fusion value, compared to 'MCF–IMC 75–25 + 0.28 mL MeOH', indicates the presence of amorphous IMC. [b] Melting of form V and recrystallisation of α- and γ-IMC overlap, thus, the stated ΔH_{fusion} values are too low.

The host loaded with 15 wt. % of IMC shows no recrystallisation in the temperature range from 20 to 453 K confirming the presence of an amorphous phase, which is in agreement with the PXRD data (Figure 5-16). Increasing the guest loading to 20 % results in a mixture of amorphous and IMC form V. The composites loaded with 20 and 25 wt. % of IMC, after treatment with methanol, show a single melting point of form V IMC. This may indicate that spatial constraints of *ca.* 30 nm prevent the concomitant crystallisation of form V and other phase impurities (α- and γ-IMC). Thus, phase pure form V can be obtained.
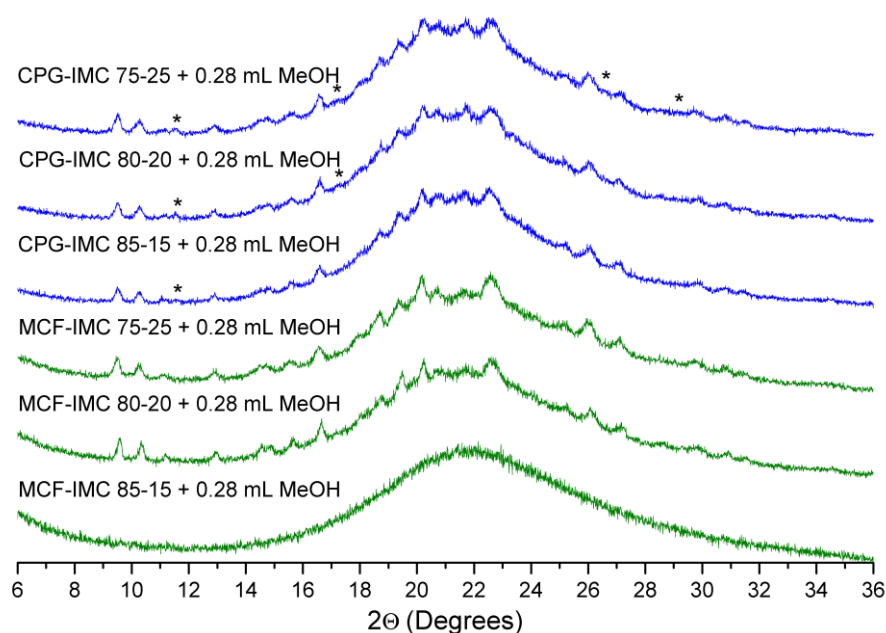
Figure 5-16. PXRD patterns of MCF and CPG hosts loaded with indomethacin using melting method and subsequently treated with methanol (peaks showing the presence of γ-IMC are labelled with asterisks).

The CPG–IMC composite loaded with 15 wt. % of IMC shows the PXRD pattern and solid-state NMR spectrum of the pure IMC form V (Figure 5-16, Figure 5-17). At host–guest ratio of the CPG–IMC 80–20 and the CPG–IMC 75–25, predominately indomethacin form V with a small amount of γ-IMC is formed (confirmed by the PXRD and solid-state NMR). Further increase of the IMC content to 30 and 50 wt. % leads to the increase of the proportion of the drug loaded outside the pores. The DSC thermograms of the CPG host loaded with IMC from the melt and subsequently treated with methanol show several thermal events, which may be assigned to the melting of IMC form V (below 398 K), recrystallisation of α- and γ-IMC, corresponding to the only exothermic event following the form V melting process, and finally the melting of α- (shoulder) and γ-IMC (*ca.* 430 K). Broadening

and decrease of the melting peaks of form V, as well as α- and γ-IMC, indicates that all observed phases are not bulk material, but are in the confined space (Figure 5-15, Table 5-3).

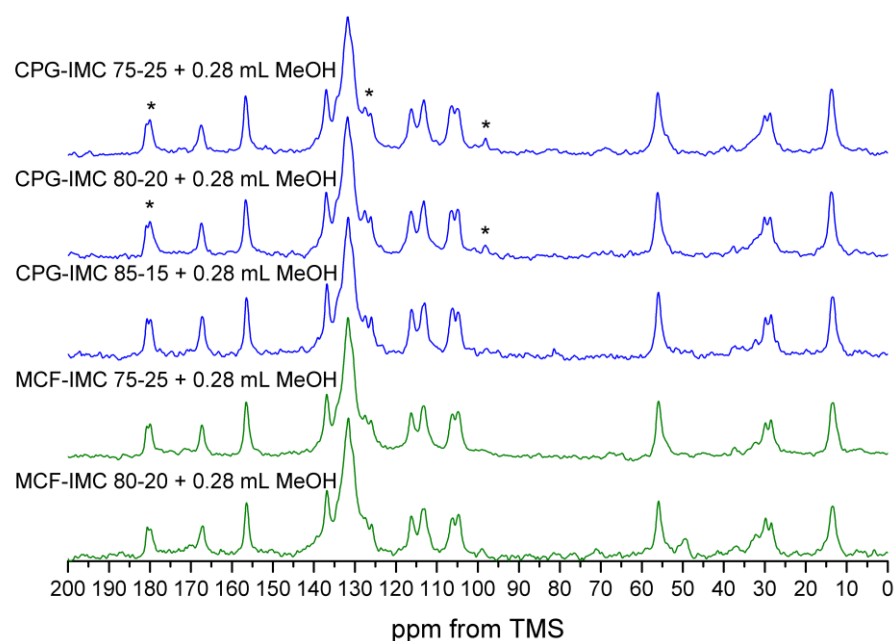**Figure 5-17.** $^1H–^{13}C$ CP/MAS NMR spectra of MCF and CPG hosts loaded with molten IMC at different host:drug ratios subsequently treated with methanol (peaks assigned to γ-IMC are labelled with asterisks).

Neither solid-state NMR nor PXRD indicated the formation of γ- or α-IMC within the CPG–IMC 85-15 composite after addition of methanol, suggesting that the presence of the melting peaks at 419.5 K (shoulder) and 425.1 K are due to recrystallisation of the α- and γ-IMC forms above the form V melting point. Seeds of γ- and α-IMC may be present below the PXRD and NMR detection limit and trigger the recrystallisation. A decrease of the melting peak onset temperature of IMC form V with increasing drug concentration in the CPG host is evident, indicating a decrease of the size of the crystals. Full understanding of the mechanism of thermal events in silica host loaded with large amounts of IMC is beyond the scope of this work.

5.2.3.2.4   IMC–silica composites obtained via incipient wetness method.

Indomethacin loaded using the incipient wetness method into both silica hosts shows different crystallisation products in comparison to melt loaded composites. The presence of metastable form V within loaded hosts was proven using PXRD, DSC and solid-state NMR. To investigate the impact of the added volume of the loading solution on the final composition of the loaded hosts we used 0.6 and 0.75 mL g^{-1} of a loading solution for the CPG and 0.8 mL g^{-1} for the MCF material. These

values were chosen taking into account the total pore volume of the CPG and the MCF hosts used in the study (1.18 and 1.61 cm^3 g^{-1} respectively).
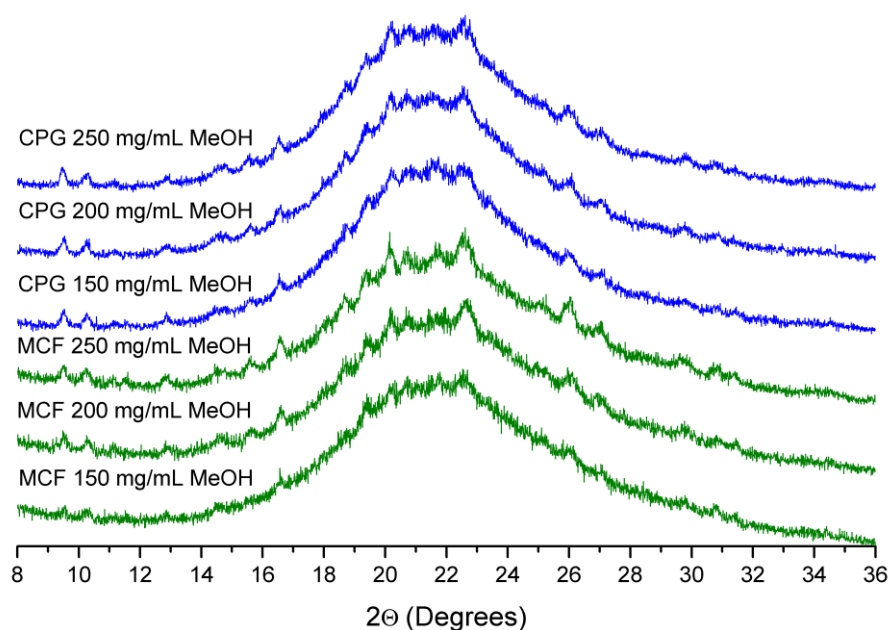

Figure 5-18. PXRD patterns of CPG host and MCF materials loaded with IMC using IW method with 0.6 mL g^{-1} of the solvent for CPG and 0.8 mL g^{-1} of the solvent for MCF.

PXRD patterns of the composites loaded with solutions of different indomethacin concentrations show peaks characteristic for IMC form V (and γ) (Figure 5-18). Due to overlapping and broadening of the peaks only traces of γ-IMC within the MCF composites can be detected, which is corroborated by DSC results. The DSC thermograms of CPG composites loaded using lower volumes (150 and 200 mg mL^{-1}) of the loading solution show a slightly broader melting endotherm of IMC form V and traces of bulk α- and γ-polymorphs of IMC (0.05–1.0 % as determined from melting point onset temperatures and heat of fusion). Furthermore, there is no exothermic recrystallisation event after the melting of IMC form V. This indicates the formation of confined IMC form V and the importance of the spatial constrains of silica walls in preventing the crystallisation of other IMC polymorphs in the temperature range 293 to 443 K. The 250 mg mL^{-1} sample shows a distinct γ-IMC melting peak. Loading from the solution with the highest concentration of IMC in methanol gives sharper form V melting peaks and a slightly lower decrease of the melting onset which may indicate that IMC form V is partly loaded outside the pores (Figure 5-19, Table 5-4).

The MCF host loaded with IMC from methanol using the IW method shows the presence of confined form V IMC, bulk γ-IMC and small amounts of α-IMC. Although the loading volume was much

smaller than the total pore volume of the MCF host, crystallisation outside the pores could not be avoided. Similarly to the CPG hosts loaded with higher volumes of loading solution (Figure 5-21), the DSC thermograms of MCF composites loaded with higher concentrations of IMC loading solution (200 and 250 mg mL^{-1} MeOH) show melting of form V IMC was preceded by a small endothermic event at *ca.* 358 K. This may be related to the presence of IMC methanol solvate (Figure 5-19). The endotherm below 353 K is related to the evaporation of water from the silica surface, as water sorption from the air may happen during sample preparation.
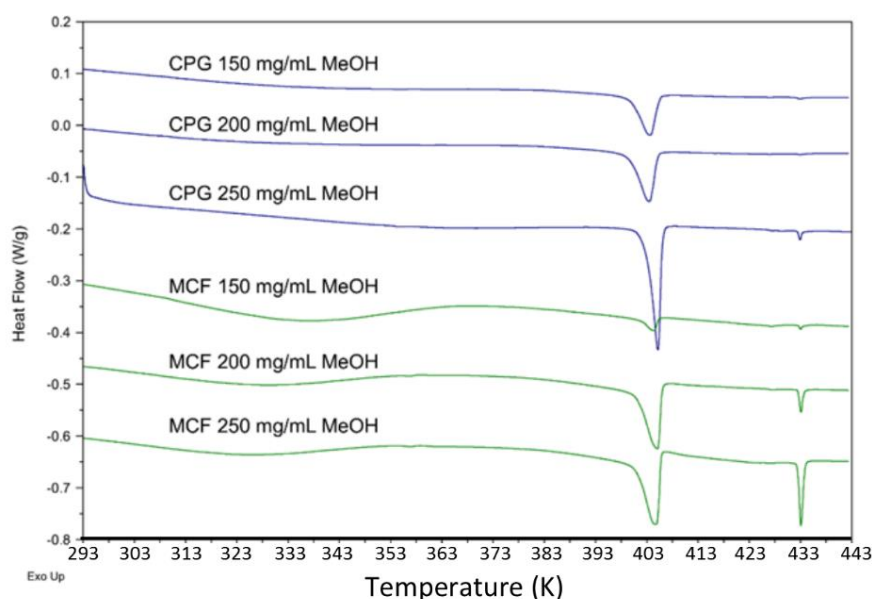
Figure 5-19. DSC thermograms of CPG and MCF hosts loaded with IMC using IW method.

Table 5-4. Thermal parameters of CPG and MCF hosts loaded using IW method from methanol.

Host-guest composite	Melting onset (K)	Melting peak (K)
CPG 150 mg mL^{-1} MeOH	399.9 (form V)	403.6
CPG 200 mg mL^{-1} MeOH	399.7 (form V)	403.4
CPG 250 mg mL^{-1} MeOH	402.9 (form V)	405.1
MCF 150 mg mL^{-1} MeOH	401.3 (form V)	404.4
	432.7 (γ-IMC)	433.1
MCF 200 mg mL^{-1} MeOH	400.6 (form V)	405.1
	432.5 (γ-IMC)	433.1
MCF 250 mg mL^{-1} MeOH	400.5 (form V)	404.7
	432.5 (γ-IMC)	433.1

Solid-state NMR spectra of both hosts loaded using the IW method at IMC concentration of 200 mg mL^{-1} in methanol are consistent with the presence of pure IMC form V within the composites. No peaks of other IMC crystalline phases could be detected, indicating that the presence of the γ-IMC peak at high loading concentrations of the MCF material is most likely due to temperature induced recrystallisation of the bulk drug phase loaded on the external surface of the host (Figure 5-19, Figure 5-20).
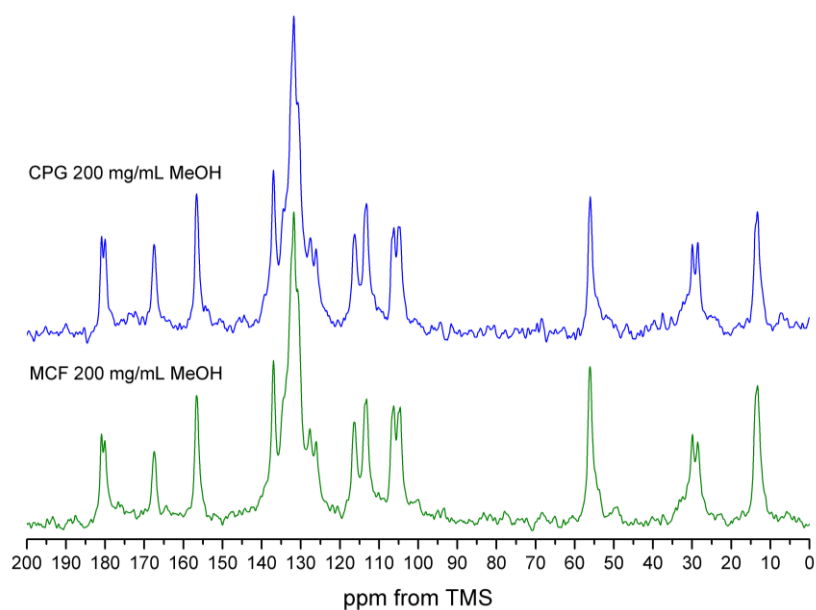
Figure 5-20. ^1H–^{13}C CP/MAS NMR spectra of CPG and MCF hosts loaded using IW method at indomethacin concentration in methanol of 200 mg mL^{-1}.

The outcome of the deposition of the drug on the external surface of the material is related to the concentration of the loading solution. A high concentration of the guest molecules in the loading solution (250 mg mL^{-1}) allows reaching reasonable API content within the composite. This, however, leads to the risk of some that the drug to be loaded outside the pores, as crystallisation of the supersaturated solution may start in contact with the external surface of silica.

CPG hosts loaded with a higher volume of the loading solution (0.75 mL g^{-1}) show distinct peaks of both crystalline phases (Figure 5-21). This is corroborated by DSC analysis, where thermograms show peaks of bulk crystalline phases of IMC (Figure 5-21).
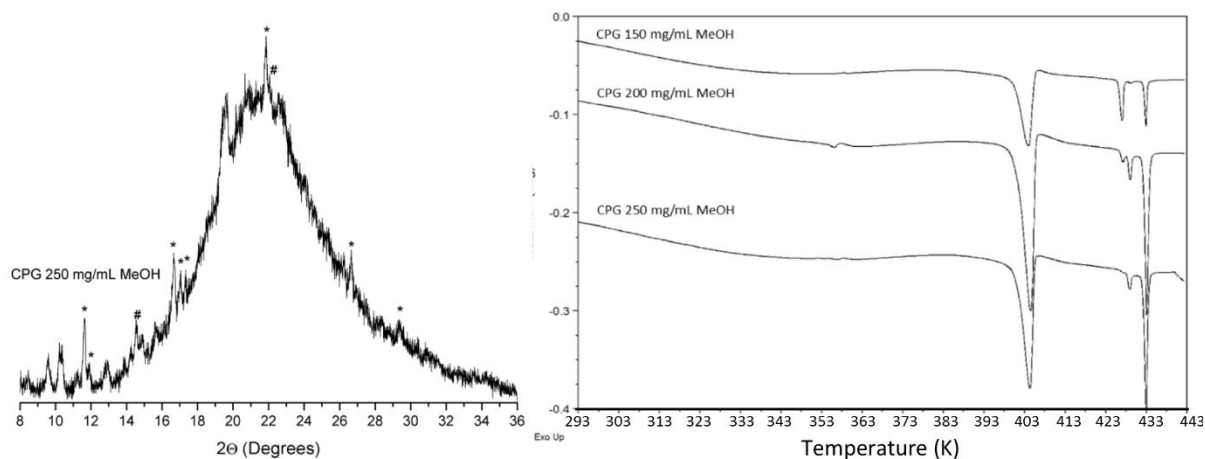
Figure 5-21. PXRD pattern (left) of the CPG material loaded with IMC using the IW method at the higher volume (0.75 mL g^{-1}) of loading solution. Asterisks and hash marks indicate peaks of the γ- and α-forms, respectively. DSC thermograms (right) of the CPG host loaded with IMC using the IW method with the higher volume (0.75 mL g^{-1}) of loading solution.

5.3   Summary

In this chapter we demonstrate the impact of mesoscopic confinement, loading method, drug content within the pores and subsequent solvent treatment of melt loaded composites on the formation of the nano-size crystals of the model pharmaceutical compound indomethacin (Scheme 1). It is possible to prevent the thermally induced recrystallisation of the amorphous indomethacin confined within the pores of the MCF host using a whole range of host guest ratios (up to 50 % of drug content).

Thermally induced recrystallisation of indomethacin confined within the CPG host was prevented at up to 30 wt. % drug content within the pores. This indicates an increased possibility for molecules to form different supramolecular assemblies within the pores, which can lead to polycrystalline composites.[87] Addition of methanol to the melt loaded MCF composites drives the crystallisation of the methanol solvate and upon vacuum drying IMC form V is obtained (at drug concentrations within the silica pores from 20 to 25 wt. %). Interestingly, confined form V does not show any recrystallisation upon heating, indicating that spatial constraints and the crystallisation method allowed us to readily produce phase pure methanol solvate and phase pure form V. Phase purity of the intermediate solvate and form V is crucial if one aims at preventing/slowing down the transformation to any of the other more stable IMC polymorphs.

The addition of the solvent to the MCF composite loaded with IMC at a concentration of 15 % does not drive crystallisation into any of crystalline forms of IMC. This may indicate both strong interactions between the drug and the silica walls and/or the insufficient number of drug molecules

to form nuclei large enough to form a crystal. Methanol driven crystallisation of amorphous indomethacin inside the larger pores of the CPG host shows the formation of a mixture of forms within the whole range of investigated host–guest ratios. However, a proportional preference towards the most stable γ-IMC with an increase in drug content is observed. The addition of either ethanol or acetonitrile to the melt loaded CPG composites leads to an exclusive recrystallisation into the most stable γ-IMC. This highlights the importance of both the nature of the confinement medium and the solvent on the formation of nanoscale confined crystals.

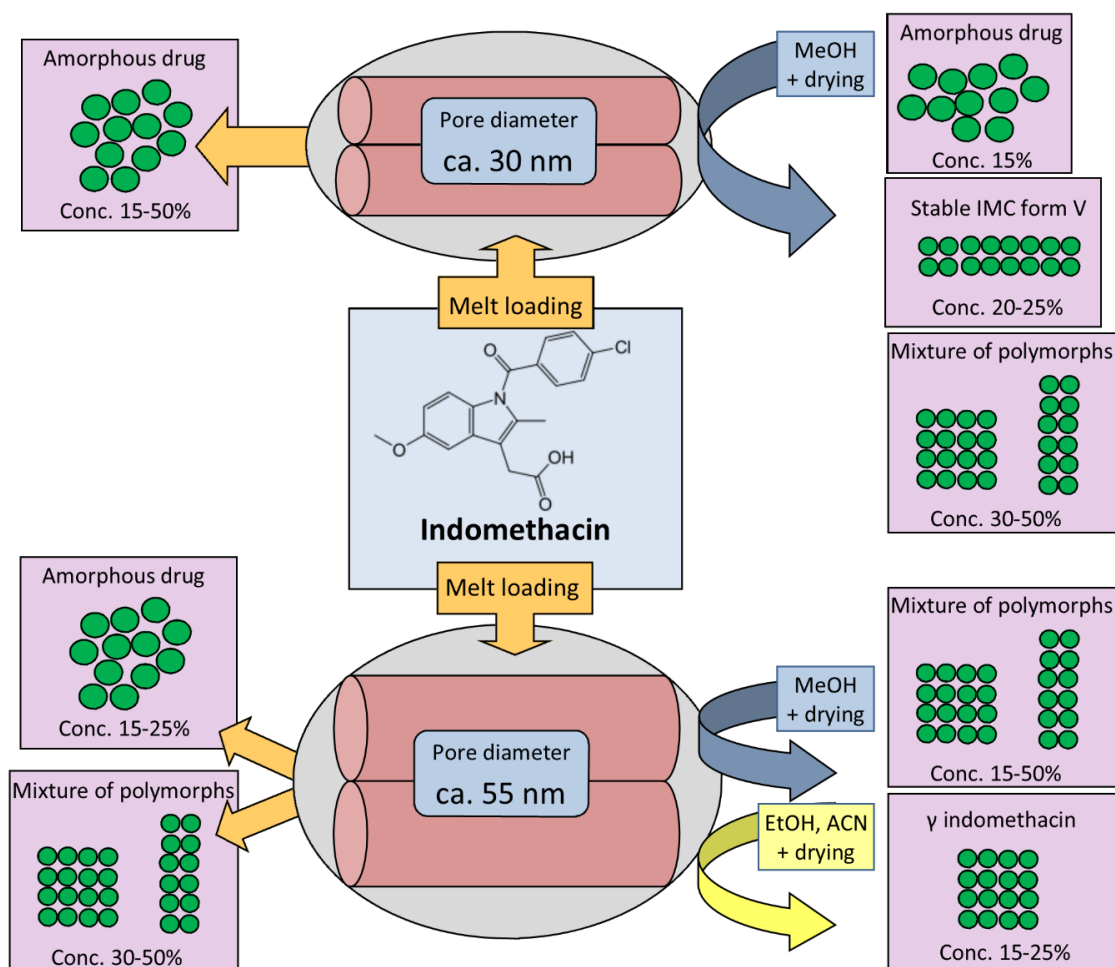**Figure 5-22.** Summary of possible amorphous to crystalline transformations of melt loaded indomethacin under confinement of MCF and CPG hosts.

The amount of guest molecules that can be successfully embedded within the silica hosts depends on a careful design of the loading procedure. The maximum loading capacity of the host might be overestimated due to the obstruction of the pores, especially when high drug loading is needed.

A uniform distribution of the drug within the host material during mixing helps to avoid the presence of drug rich domains which cannot be loaded fully into the pores by a capillary action and may lead to some drug being left on the external surface. Finally, the heating temperature needs to be sufficiently high to melt the guest, while avoiding its decomposition. The incipient wetness method is one of the solvent mediated methods for drug loading into the mesoporous silica hosts. However, it is much more difficult to control as increasing drug concentration within the loading solution increases risk of the spontaneous crystallisation of the supersaturated solution outside the pores. In the case of indomethacin, it can even lead to the formation of an elusive polymorph, IMC form V.

Mesoporous silica materials with pore diameters of up to 8 nm (MCM-41 and SBA-15) have been widely studied as drug delivery systems to stabilise amorphous phases. We have demonstrated that an increase in the pore size diameter of mesoporous silicas may lead to exciting changes in the crystallisation behaviour of a widely studied pharmaceutical compound indomethacin. Amorphous IMC can be stabilised when embedded within pores of *ca.* 30 nm using the melting method, whereas the CPG host with pores of *ca.* 55 nm can stabilise the amorphous phase only at low drug content within the composite. Furthermore, addition of a solvent to the melt loaded systems leads to the formation of nano-scale crystals inside the pores. The polymorphic phase formed under confinement depends on the pore size, embedded drug content and crystallisation solvent. Guest loading using the IW method leads directly to the formation of a crystalline phase. Thus, by choosing the right conditions it is possible to increase the solubility, which might be crucial for a poorly water soluble compound as indomethacin.

5.4   Conclusions

In this study, we have used a novel approach to investigate phase transitions inside silica based, nano-scale crystallisation chambers with well organised systems of pores, *i.e.*, MCF hosts. Combined application of nitrogen adsorption–desorption analysis, thermal and diffraction methods and solid-state NMR enabled much better control over the phase and transformations of the guest in the final products, which may lead to a better understanding of host guest interactions within drug delivery systems based on mesoporous silica composites. Furthermore, we have demonstrated a new method for the formation and stabilisation of IMC form V using mesopores to prevent recrystallisation into more stable IMC polymorphs. This should enable further studies of MCF based nano-crystalline drug delivery systems and highlights the importance of loading methods and laboratory procedures on the final product, which is of the interest for the pharmaceutical industry. ^{13}C solid-state NMR spectra of IMC methanol solvate and IMC form V were presented for the first time, highlighting the main structural changes related to the desolvation.

Mesoporous silicas with large pores are not only promising systems for nano-crystalline drug delivery systems, but are also well defined model materials for the investigation of early stages of crystallisation. Possible tailoring of the pore size diameter may enable effective control of the maximum size of critical nucleus during crystal formation. Furthermore, functionalisation of the internal surface of the silica host may target a particular hydrogen bonding motif on crystallisation outcome.

^{19}F NMR as a Highly Sensitive Probe Towards Understanding and Direct Monitoring of Confined Crystallisation within Nanoporous Materials

Chapter 6

6.1   Introduction

Incorporation of fluorine in the structure of pharmaceuticals has been an effective strategy for tuning their pharmacodynamic properties with more than 40 new drugs accessing the market in the last 15 years. In this context, ^{19}F NMR can be viewed as a useful probe for investigating the host-guest chemistry of pharmaceuticals in nanosize drug delivery systems. Although the interest in confined crystallisation, nanosize devices and porous catalysts is gradually increasing, understanding of the complex phase behaviour of organic molecules confined within nano-chambers or nano-reactors is still lacking. Using ^{19}F MAS NMR, we achieved detailed mechanistic insight into the crystallisation of flufenamic acid (FFA) in a confined environment of mesoporous silicas with different pore diameters (3.2 to 29 nm), providing a direct experimental proof of the formation of a molecular liquid-like layer in addition to the crystalline confined FFA form I.
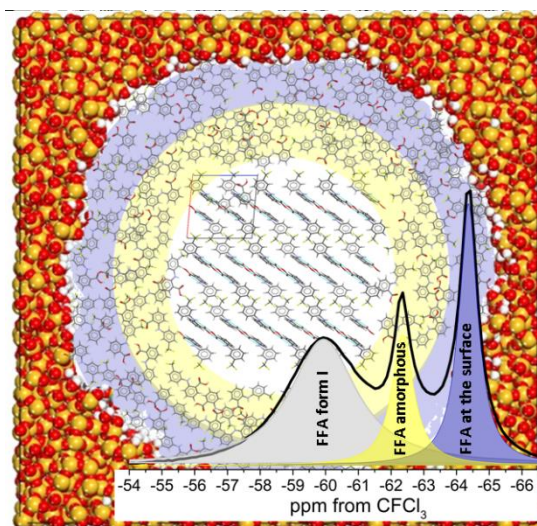
Figure 6-1. Schematic representation of FFA in three different molecular environments and mobility regimes from liquid-like species at the silica surface to confined nanocrystals as probed using ^{19}F MAS NMR.

The engineering of nanocrystals confined within nanosize chambers of controlled pore glasses has yielded new crystalline structures, stabilised metastable polymorphs or helped the formulation of amorphous drug delivery systems.[93,110,111,250] Although the number of studies aimed at new applications of porous silicas is rising, there is a considerable lack of molecular level understanding of the phenomena which govern the self-assembly in such systems. Thus, ibuprofen, benzoic acid and lauric acid confined within MCM-41 silicas (pore diameter *ca.* 3-4 nm) have been found in a highly mobile state, as liquid-like behaviour was observed with solid-state NMR.[74,75,77–79,251] The high mobility of confined ibuprofen (IBU) was confirmed indirectly with hyperpolarised [129]Xe NMR

spectroscopy and MAS-PFG NMR, where two different diffusion coefficients were observed for the guest.[78] Dielectric relaxation spectroscopy studies of the IBU/MCM-41 confirmed two different motional regimes for IBU, assigned to its populations in the pore voids and at the silica surface; this was corroborated with molecular dynamics simulations.[112] Detailed quantum mechanical modelling of the adsorption of clotrimazole and IBU in porous silicas confirmed very high mobility of these guests at silica surfaces, in good agreement with IR and solid-state NMR spectroscopic data.[80,81,252] As fluorinated pharmaceuticals are currently in the spotlight of drug discovery,[253] it is possible to take advantage of the high sensitivity of ^{19}F nuclei to changes in local environment and probe the nanoscale organisation of such molecules confined in porous hosts. In this work, we demonstrate that ^{19}F solid-state NMR can be used to detect the presence of confined molecules of the model pharmaceutical (flufenamic acid, FFA) in different environments and motional regimes. By encapsulation of FFA in three different silica scaffolds with pore diameters from 3.2 to 29 nm, we were able to fully control the confined crystallisation of FFA form I, gaining mechanistic insight of the self-assembly at different length scales. The combined use of ^{19}F MAS NMR and other characterisation tools enabled us to monitor the processes in the confined space *in situ*.

Using a variety of techniques (N_2 adsorption, PXRD, DSC, solid-state NMR and THz spectroscopy[254]) we have shown that FFA has been encapsulated inside the pores of the three silica scaffolds via the melt loading method. We gradually increased the guest loading to achieve gradual filling of the pores with different diameters. The materials are labelled as host:FFA X-Y, where the host is MCM-41, SBA-15 or MCF and X-Y is host:guest ratio in wt. %. It is important to note that stabilisation of the extremely unstable amorphous FFA (T_g = 286 K) was achieved for over a year inside the pores of the MCM-41 and SBA-15 hosts.

6.1.1   Polymorphism of Flufenamic acid

Flufenamic acid (FFA, 2-{[3-(Trifluoromethyl)phenyl]amino}benzoic acid) is a non-steroidal anti-inflammatory drug (NSAID) which up to date has the highest number of different crystalline structures reported in CCDC (The Cambridge Crystallographic Data Centre).[181] Based on a recent study by López-Mejías *et al.* nine polymorphs were proposed; eight structures elucidated with X-ray diffraction and a ninth elusive polymorph characterised with PXRD and Raman spectroscopy (Figure 6-3).[181] The high number of crystalline structures of FFA is not only of the interest from the pharmaceutical perspective, its supramolecular chemistry enabled authors to probe the concept of the polymorphophor in the group of fenamic acids.[181,255,256] In that case, a monocarboxylated diphenyl amine nucleus is a structural element, which promotes formation of multiple crystalline structures.[181]

The first crystal structure of FFA form III was published by McConnell in 1973 followed by the report on seven polymorphic forms of FFA by Krc and elucidation of the second well known polymorph, FFA form I, by Murthy *et al.* in 1982.[186,187,257] Although polymorphism of FFA has been known for the last 40 years, major progress in understanding the differences in structural conformations and transitions of FFA was made only recently.[1,4,5–11] Frequently occurring, commercially available, FFA form I crystallises as white needles in the $P2_1/c$ space group, while FFA form III forms yellow needles and crystallises in the $C2/c$ space group.[181,186,187,260,263] Both forms of FFA are enantiotropically related to each other with FFA form III being most stable below transition temperature at 315.5 K. [257,260,261,264] The phase transformation from form I to form III is faster for large crystals due to an increased number of surface defects in larger crystals.[260] Furthermore, it was demonstrated that FFA form I compared with form III shows an increased reactivity in the solid state with both ammonia gas and MgO due to packing differences leading to higher accessibility of the carboxylic acid motif in FFA form I.[258,261] Recently, Delaney *et al.* using periodic DFT analysis suggested that polymorphic order between FFA form I and FFA form III is the result of strong dipolar interactions related to presence of CF_3 motif in the structure.[263]

The presence of at least seven polymorphs of FFA was suggested by Krc in 1977 and only 35 years later López-Mejías *et al.* were able to obtain single crystals of the six new crystalline phases of FFA using polymer induced heteronucleation (Figure 6-3).[181] Lee *et al.* were able to stabilise FFA form V by addition of ammonium chloride.[182] Conformational analysis of FFA in different crystalline forms revealed that the main difference between building molecules lies in changes in the torsion angles τ_2 and τ_3 defined as planes connected by the biphenyl amine (Figure 6-2).[181]
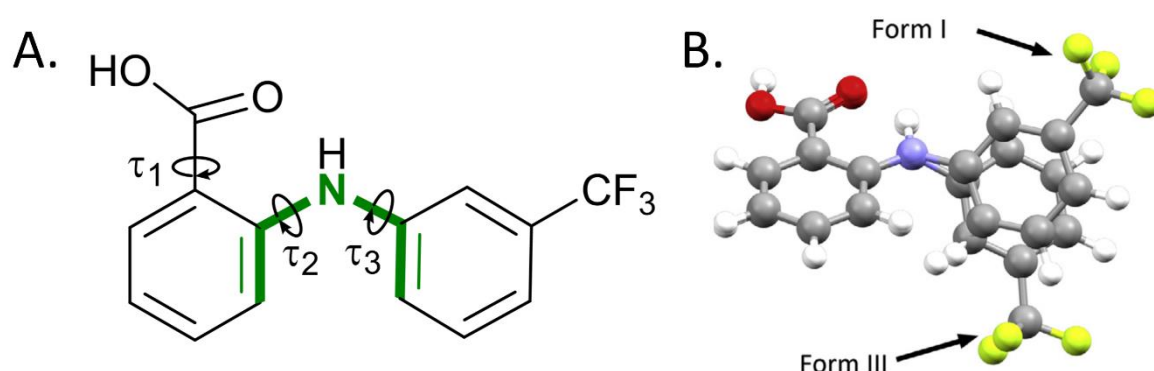
Figure 6-2 A. Structure of FFA with torsion angles τ_2 and τ_3 varying between the structures labelled in green. **B.** Example of conformational polymorphism between FFA form I and FFA form III (adapted from [181,263]).
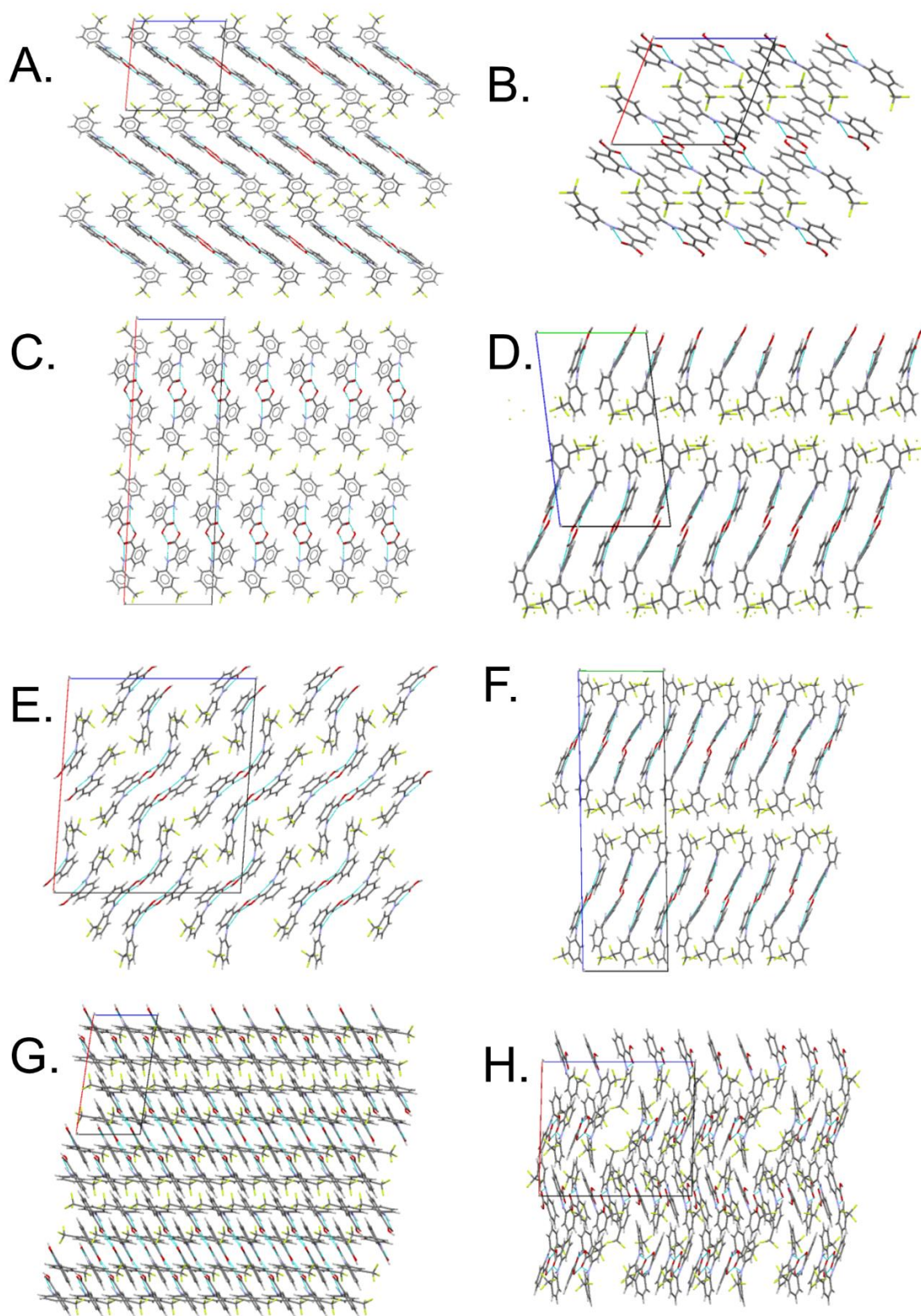
Figure 6-3. Molecular packing of FFA polymorphs. **A.** FFA form I (CSD ref. code FPAMCA11[186]), **B.** FFA form II (CSD ref. code FPAMCA17[181]), **C.** FFA form III (CSD ref. code FPAMCA[187]), **D.** FFA form IV (CSD ref. code FPAMCA15[181]), **E.** FFA form V (CSD ref. code FPAMCA16[181]), **F.** FFA form IV (CSD ref. code FPAMCA14[181]), **G.** FFA form VII (CSD ref. code FPAMCA12[181]), **H.** FFA form VIII (CSD ref. code FPAMCA13[181]). Forms I, II, III, V, VII and VIII are shown along b crystallographic axis, forms IV and VI are shown along a crystallographic axis.

Formation of intramolecular hydrogen bond between the carboxylic acid oxygen and the amino group in all conformers leads to a coplanar arrangement of the carboxylic group with the phenyl ring, hence small differences in the torsion angle τ_1 between the conformers.[181] Newly obtained forms II, V and VII of FFA similarly to FFA form I crystallise in the space group $P2_1/c$ with Z'=1, Z'=4 and Z'=2, respectively. Forms IV, VI and VIII crystallise in triclinic space group $P\bar{1}$ with 3, 6 and 9.5 molecules in the asymmetric unit, respectively. It is worth noting that there are less than 200 structures with Z'=6 reported in CSD and none of the reported structures has 9.5 molecules in an asymmetric unit.[181]

6.2 Results and discussion

6.2.1 Solid state characterisation of FFA form I and FFA form III

FFA form I is the commercially available form of FFA, while FFA form III was crystallised from ethanol. The experimental PXRD patterns of both investigated FFA polymorphs are in good agreement with simulated PXRD patterns based on the CSD reference structures FPAMCA11[186] (FFA form I) and FPAMCA[187] (FFA form III). FFA form I melts at 406.8 K while FFA form III melts at 399.2 K followed by its recrystallisation to the most stable form I.
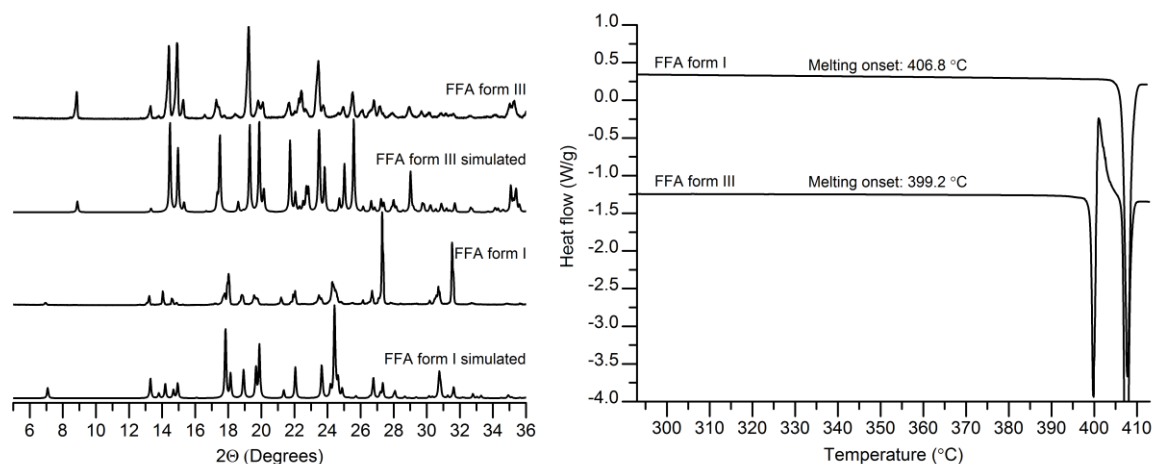
Figure 6-4. Simulated and experimental PXRD patterns of FFA form I (CSD ref. code FPAMCA11) and FFA form III (CSD ref. code FPAMCA) (left); DSC thermograms of FFA form I and FFA form III (right).
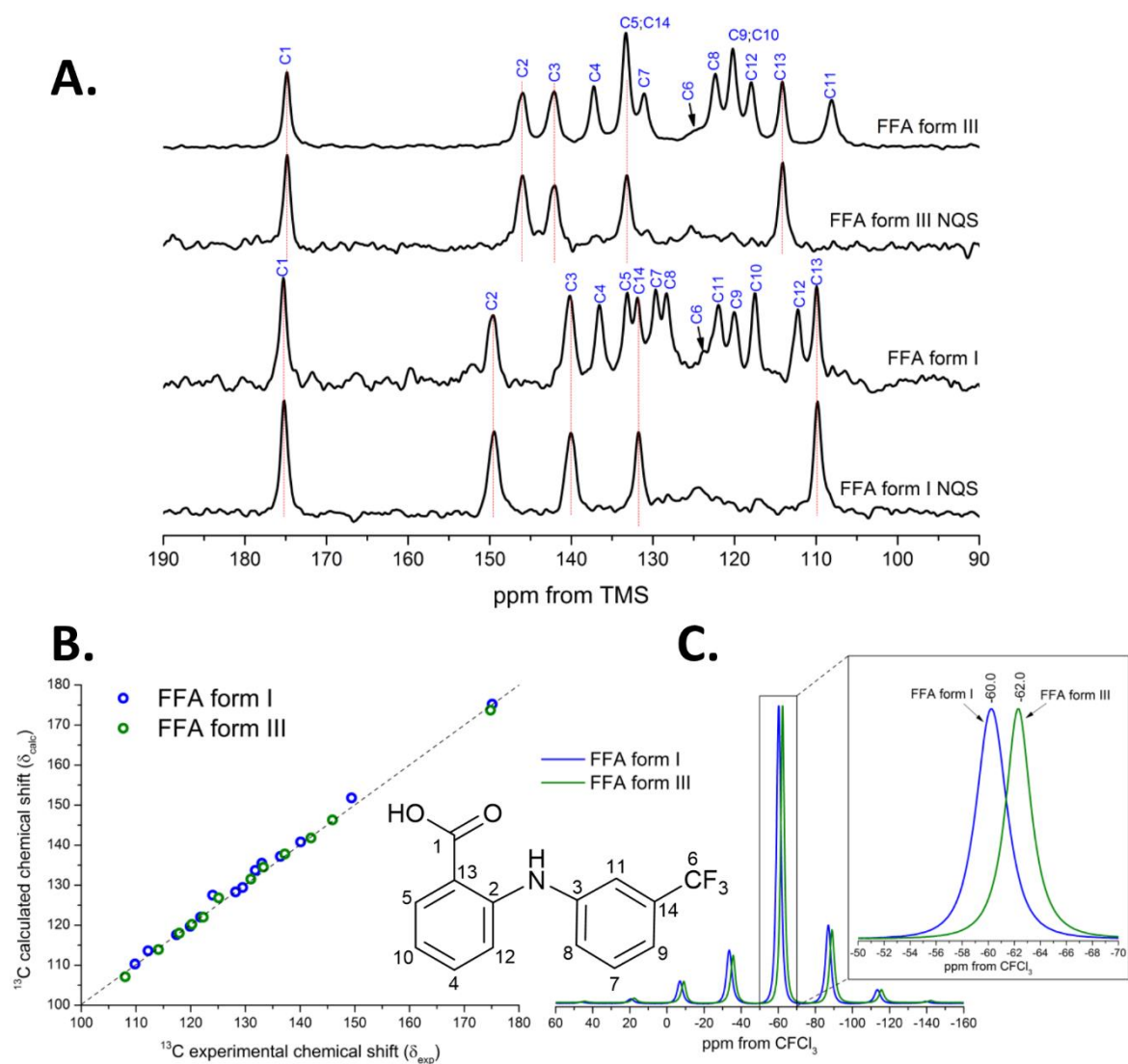
Figure 6-5. A. ^1H-^{13}C CP/MAS and ^1H-^{13}C CP/MAS NQS spectra of FFA form I and FFA form III recorded at 9.4 T; **B.** Experimental and CASTEP calculated ^{13}C chemical shifts of FFA form I (CSD ref. code FPAMCA11) and FFA form III (CSD ref. code FPAMCA); the dashed line shows perfect fit; **C.** ^{19}F MAS NMR spectrum of FFA form I and FFA form III recorded at 9.4 T. The ^{13}C numbering was made based on CASTEP calculations. The ^{13}C numbering is in agreement with the carbon numbers in the FFA structure presented in the figure.

The ^1H-^{13}C CP/MAS NMR spectra of FFA form I show 14 carbon peaks which can be assigned to all ^{13}C sites in the FFA structure indicating the presence of one molecule in the asymmetric unit (Figure 6-5 A.). The CASTEP calculated and experimental ^{13}C chemical shifts are in good agreement (Figure 6-5 B., Table 6-1). The assignment of the ^{13}C spectrum based on CASTEP calculations is further confirmed by ^1H-^{13}C CP/MAS NQS spectrum where only peaks from quaternary carbons can be observed. The low intensity of the carbon C6 peak is due to lack of ^1H in close proximity from which magnetisation could be gained during cross polarisation step in the ^1H-^{13}C CP/MAS NMR experiment.

Table 6-1. Comparison of experimental and CASTEP calculated ^{13}C chemical shifts of FFA form I and FFA form III. Non-quaternary carbons are labelled in blue.

^{13}C site	FFA form I		FFA form III	
	δ_{exp}	δ_{calc}	δ_{exp}	δ_{cal}
C1	175.1	175.2	174.8	173.7
C2	149.4	151.8	145.9	146.3
C3	140.1	140.8	142.0	141.8
C4	136.4	137.2	137.2	137.8
C5	133.0	135.5	133.3	134.5
C6	124.0	127.5	125.1	126.8
C7	129.5	129.4	131.0	131.5
C8	128.2	128.3	122.3	122.0
C9	119.9	119.7	120.2	120.2
C10	117.4	117.6	120.2	120.2
C11	121.8	122.0	108.0	107.1
C12	112.2	113.6	117.9	118.0
C13	109.8	110.3	114.1	113.9
C14	131.8	133.7	133.3	134.5

Similarly, the ^{1}H-^{13}C CP/MAS NMR spectrum of FFA form III indicates the presence of one molecule in asymmetric unit which is in agreement with crystallographic data. The ^{13}C spectrum shows 12 peaks with overlapping peaks for carbons C5, C14 and C9, C10. The CASTEP calculated ^{13}C chemical shifts are in excellent agreement with the experimental data (Figure 6-5 B., Table 6-1). Molecules in the asymmetric units of FFA form I and FFA form III structures are in very different conformations (Figure 6-2), leading to significant differences in the position of some ^{13}C peaks in the spectra. The torsion angles τ_2 and τ_3 of the FFA molecule differs significantly between both structures, *i.e.*, FFA form I: τ_2= 53.94°, τ_3 =1.76°, FFA form III τ_2= 8.72°, τ_3 =37.09°. These lead to very different conformations of the phenyl ring bearing fluoromethyl group in both structures. The differences are accompanied by significant changes in the positions of ^{13}C peaks C2 and C3 *i.e.*, up-field (C2) and down-field (C3) shift of both peaks by *ca.* 4 and 2 ppm, respectively. The most pronounced changes in the ^{13}C peak position can be observed for carbons C8, C11 and C12 as intramolecular interactions between these three sites are significantly different in both structures. Carbons C11 and C8 of FFA form I structure undergo significant up-field shift of *ca.* 14 and 5 ppm, respectively, in comparison to the peaks position in the FFA form III structure. In contrast, the C12 site in FFA form III undergoes down-field shift of *ca.* 5 ppm compared to the peak position in FFA form I structure.

One peak can be observed in the ^{19}F MAS NMR of FFA form I and FFA form III indicating all three fluorine atoms are in the same local environment. Sensitivity of fluorine to changes in the long-range electrostatic interactions enable the different FFA polymorphs to be distinguished, as FFA form I shows the ^{19}F MAS NMR peak at −60.0 ppm in comparison to −62.0 ppm for FFA form III (Figure 6-5 C.). To the best of our knowledge this is the first report of a full experimental and computational assignment of FFA form I and FFA form III ^{13}C solid-state NMR spectra.

6.2.2 Local structure of mesoporous silica hosts

The ^{29}Si solid-state NMR data show three characteristic peaks of silicon atoms in three different environments, *i.e.*, Q^4 site $Si(OSi)_4$ at *ca.* −110 ppm and two OH ended sites Q^2 $(HO)_2Si(OSi)_2$ and Q^3 $(HO)Si(OSi)_3$ at *ca.* −90 and −100 ppm, respectively. The degree of silica condensation determined as the ratio between 'surface' related sites (Q^2, Q^3) and bulk Q^4 (*i.e.*, Q^2+Q^3/Q^4) indicates similar population of the OH groups at the silica surface (Figure 6-6, Table 6-2).
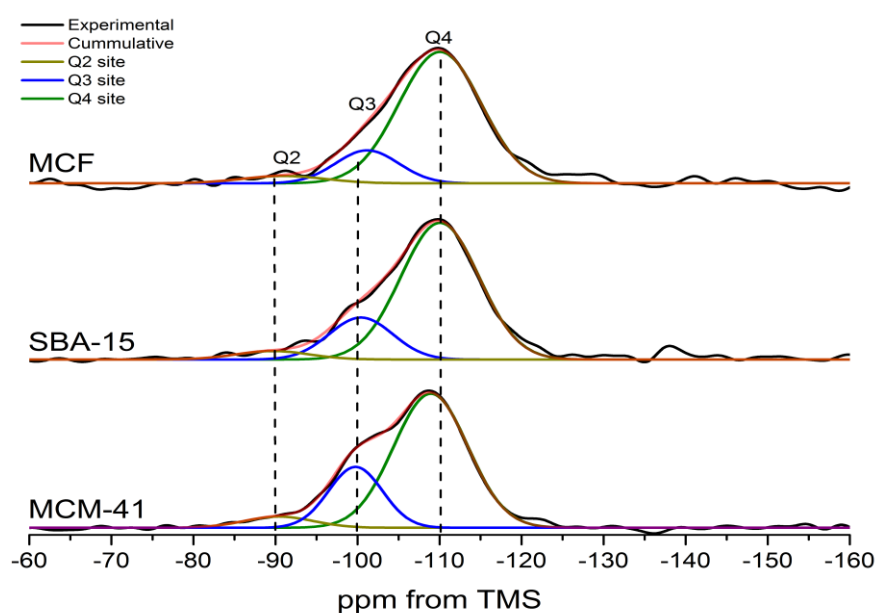
Figure 6-6. ^{29}Si MAS NMR spectra and deconvoluted peaks of mesoporous silica hosts MCM-41, SBA-15 and MCF.

Table 6-2. The deconvolution parameters of different silicon sites in the ^{29}Si MAS solid-state NMR spectrum and condensation parameter determined based on the integration of different Q sites.

Material	^2Q		^3Q		^4Q		R^2	$(^2Q+^3Q)/^4Q$
	Integral	FWHM	Integral	FWHM	Integral	FWHM		
MCM-41	0.82	9.93	3.51	7.7	10.67	10.7	0.997	0.41
SBA-15	0.67	10.5	2.85	9.1	11.43	11.2	0.991	0.31
MCF	0.96	11.5	2.79	9.1	11.53	11.6	0.983	0.33

Very similar population of OH bearing ^3Q and ^2Q silicon sites in the SBA-15 and MCF hosts suggests that the pore surfaces in such hosts are very similar. This is also confirmed by the ^1H-^{29}Si CP/MAS NMR spectra which in some publications are interpreted as more surface specific than ^{29}Si MAS NMR spectra (Figure 6-7).[5] Both MCF and SBA-15 silica hosts were synthesised using silica

condensation in acidic conditions hence both materials have very similar properties. The slightly higher value of the condensation parameter of a MCM-41 silica host may be related to differences in synthetic conditions, *i.e.*, basic conditions and different templating agent.
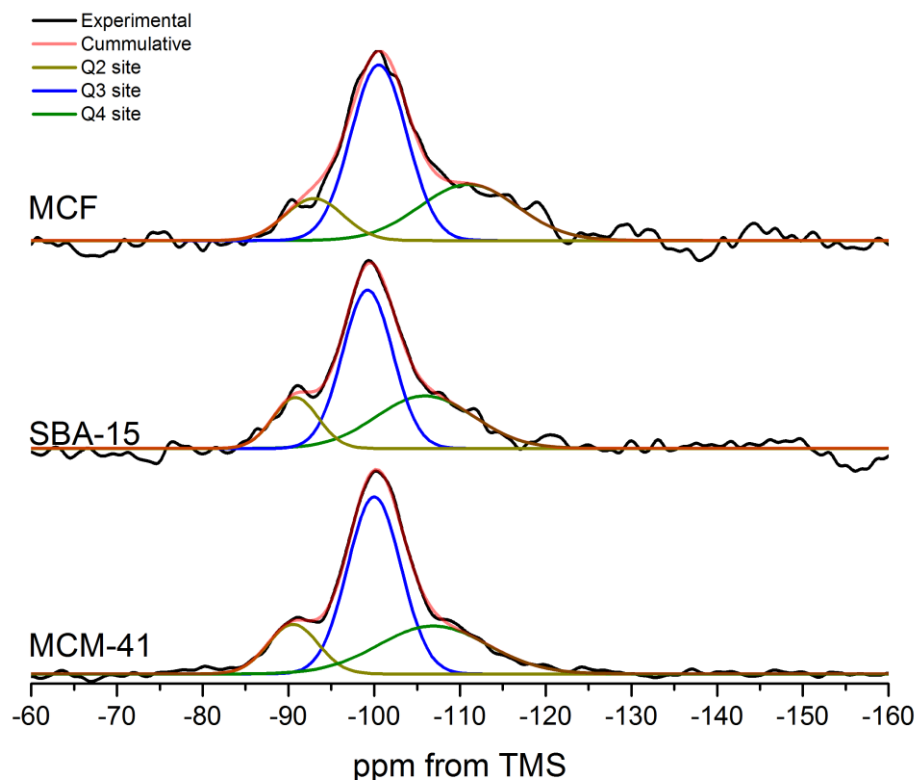
Figure 6-7. ^{1}H-^{29}Si CP/MAS NMR spectra and deconvoluted peaks of mesoporous silica hosts MCM-41, SBA-15 and MCF.

Several reports on the studies of surface in porous silicas assign different types of surface hydroxyls and water species depending on the density of silanols on the surface as manifested by the changes in ^{1}H chemical shifts.[265,266] The comparison of ^{1}H spectra reported for SBA-15 and MCM-41 hosts indicate that, in our hosts, the surface is dominated by regions with 3-4 Si-OH groups expected per nm^2 with ^{1}H chemical shifts in the range of 4.5-5.5 ppm. We also detected isolated very small amount of Si-OH species (*ca.* 2 ppm).[265,266] The similarity of ^{1}H spectra of FFA-loaded silicas supports our assumption of a similar level of OH-coverage between the three silica hosts.

6.2.3 Textural parameters of silica scaffolds and identification of FFA loaded outside the pores

Melt loading of FFA within mesoporous silicas resulted in a gradual decrease of the total pore volume and the BET surface area of the loaded composites as compared to unloaded porous scaffolds, consistent with the incorporation of the drug inside the pores of the hosts (Table 6-3, Figure 6-8 and Figure 6-9).

Table 6-3. FFA content within different hosts and structural parameters of the hosts after loading.

Host-guest composite	FFA (g g^{-1})	^{a}V$_{total}$ [cm^3 g^{-1}]	^{b}d$_{pore}$ [nm]	^{c}S$_{BET}$ [m^2 g^{-1}]
MCF	N/A	1.796	29.5 (14.9)	356.2
MCF-FFA 85-15	0.145	1.441	29.5 (15.0)	275.1
MCF-FFA 80-20	0.184	1.350	29.5 (14.0)	254.0
MCF-FFA 75-25	0.253	1.266	29.6 (11.7)	235.8
MCF-FFA 70-30	0.301	1.186	29.7 (13.8)	218.7
MCF-FFA 60-40	0.401	1.043	29.7 (13.0)	181.8
MCF-FFA 50-50	0.494	0.747	26.6 (13.1)	129.7
SBA-15	N/A	0.809	7.1	571.2
SBA-FFA 85-15	0.131	0.588	7.1	367.2
SBA-FFA 80-20	0.210	0.507	6.4	315.8
SBA-FFA 75-25	0.238	0.441	6.2	278.2
SBA-FFA 70-30	0.294	0.354	5.6	235.4
SBA-FFA 60-40	0.372	0.234	5.6	156.3
SBA-FFA 50-50	0.485	0.125	5.6	81.0
MCM-41	N/A	0.654	3.2	1370.4
MCM-FFA 85-15	0.145	0.434	3.2	872.7
MCM-FFA 80-20	0.214	0.341	3.1	715.4
MCM-FFA 75-25	0.259	0.277	3.2	563.8
MCM-FFA 70-30	0.309	0.178	3.1	361.6
MCM-FFA 60-40	0.399	0.162	3.2	306.6
MCM-FFA 50-50	0.525	0.056	3.2	89.1

^{a} V$_{total}$ – total pore volume calculated at P/P$_0$ of 0.99, ^{b} d$_{pore}$ – pore size diameter calculated from the adsorption branch of the isotherm using the BJH method, values in the brackets for MCF material indicate size of pores windows calculated using desorption branch of the isotherm, ^{c} S$_{BET}$ – the BET specific surface area
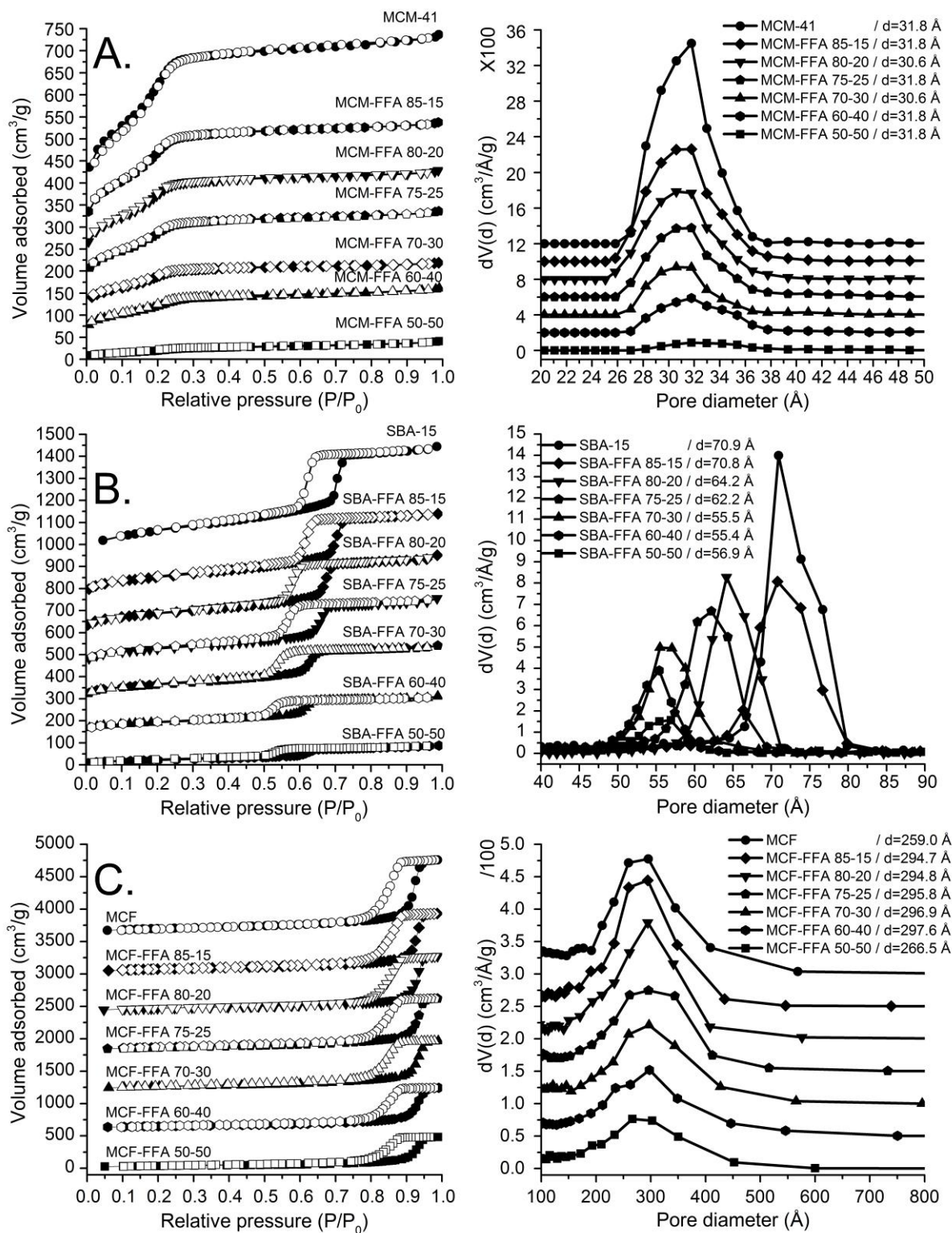
Figure 6-8. Nitrogen adsorption/desorption isotherms (left) and pore size distribution curves (right) of **A.** MCF, **B.** SBA-15, **C.** MCM-41 at different FFA loadings. Closed symbols indicate adsorption and open symbols indicate desorption of nitrogen. MCM-41 isotherms were offset by 50 cm^3 g^{-1}, SBA-15 isotherms are offset by 150 cm^3 g^{-1} and MCF isotherms are offset by 600 cm^3 g^{-1}.
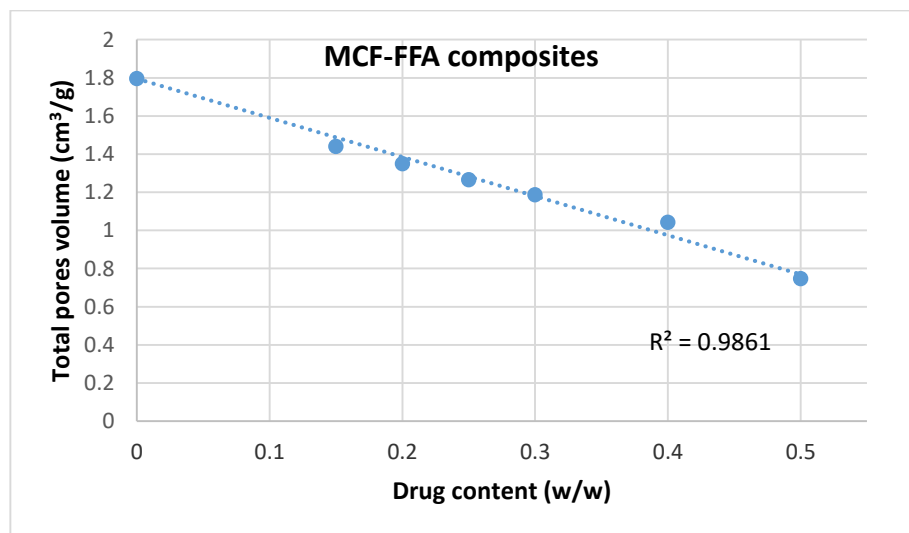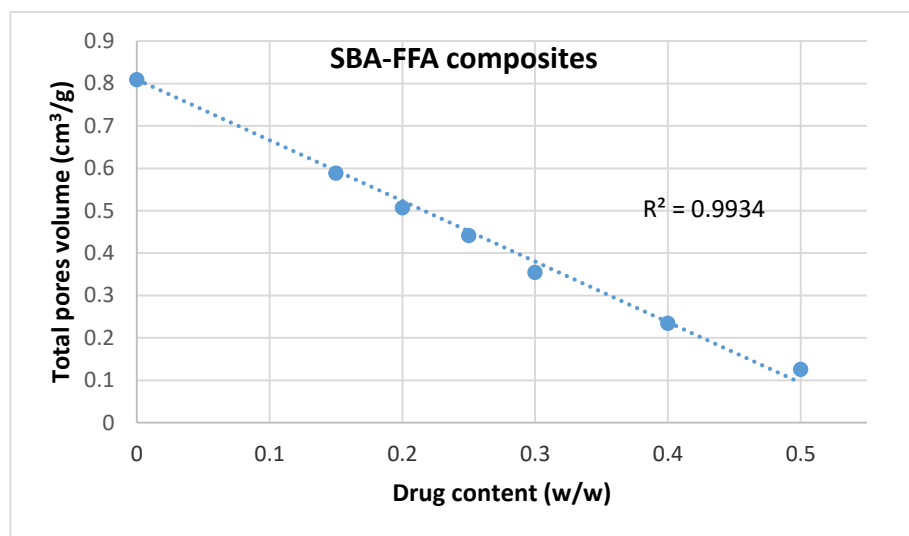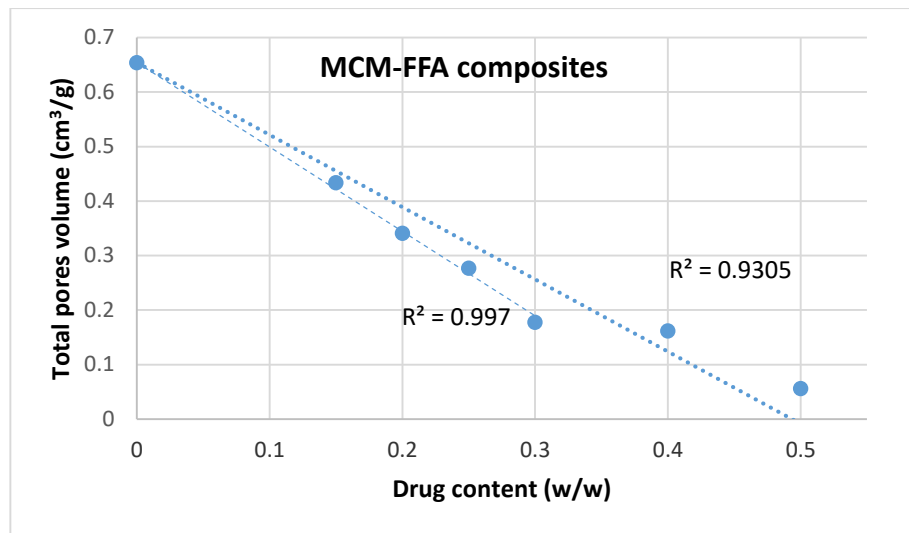
Figure 6-9. Linear relationship between the total pores volume and drug content in MCM-FFA, SBA-FFA and MCF FFA composites. Improved correlations can be observed for MCM-FFA composites, when the two last points (*i.e.*, when drug is loaded outside the pores) are excluded from the fit.
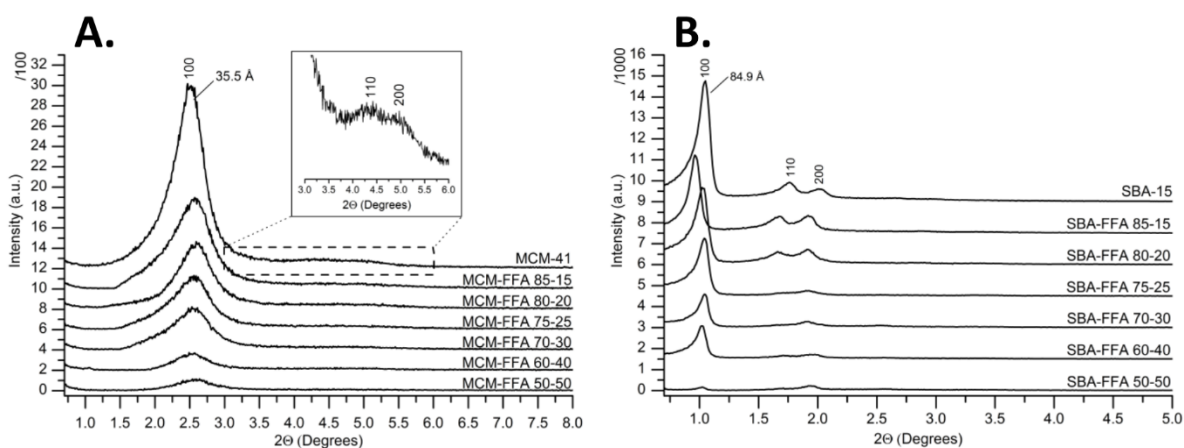
Figure 6-10. Low angle PXRD patterns of **A.** MCM-FFA and **B.** SBA-FFA (B) composites at different host:guest ratios (w/w).

A gradual decrease of the intensity of the [100] peak in the PXRD patterns of MCM-41 and SBA-15 materials loaded with FFA as compared to unloaded materials further corroborates the N_2 adsorption results and confirms the deposition of the loaded drug inside the pores of silica hosts.

6.3 Pore size dependent amorphous to crystalline transition of confined flufenamic acid

The encapsulation of organic guest molecules within the silica scaffolds leads to either the formation of confined crystals, or stabilisation of the confined amorphous phase, depending on the properties of the host (mainly pore size) and the guest molecules (size, flexibility and thermal behaviour).
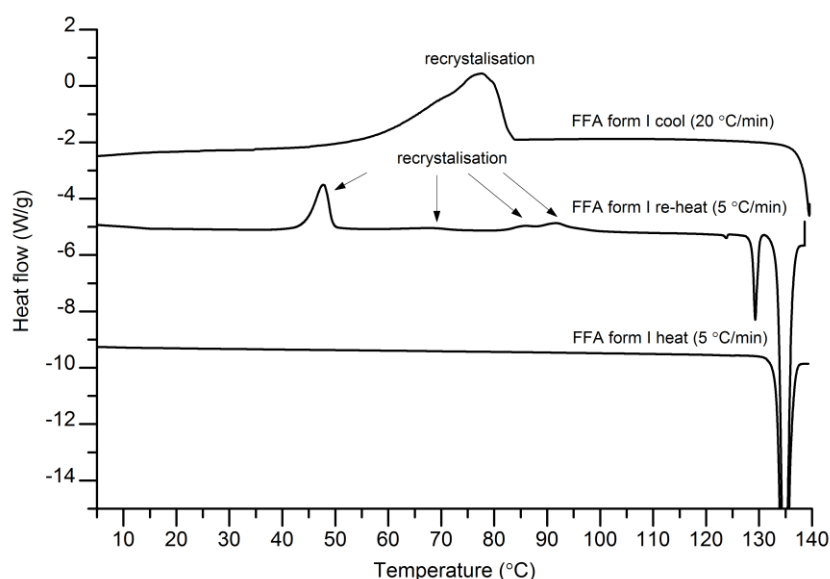
Figure 6-11. DSC thermogram of FFA form I during heat-cool-reheat cycle shows several transitions during cooling and subsequent reheating of the material indicating formation of mixture of different crystalline phases after melting and subsequent cooling.

As it is demonstrated in the previous chapter, it is of paramount importance in confined crystallisation research to ensure that all observed phases and transitions are due to confinement effect. As melting point depression is a good indicator of the formation of confined crystals, DSC analysis was carried out to identify non-uniformly loaded composites, where a bulk melting point is observed. FFA is highly unstable in the amorphous state (T_g = 286 K) and crystallises on cooling to a mixture of polymorphs (Figure 6-11).[267] DSC analysis enabled us to immediately identify the composites with FFA loaded outside the pores, due to the presence of melting points of the bulk FFA polymorphs (Figure 6-11).
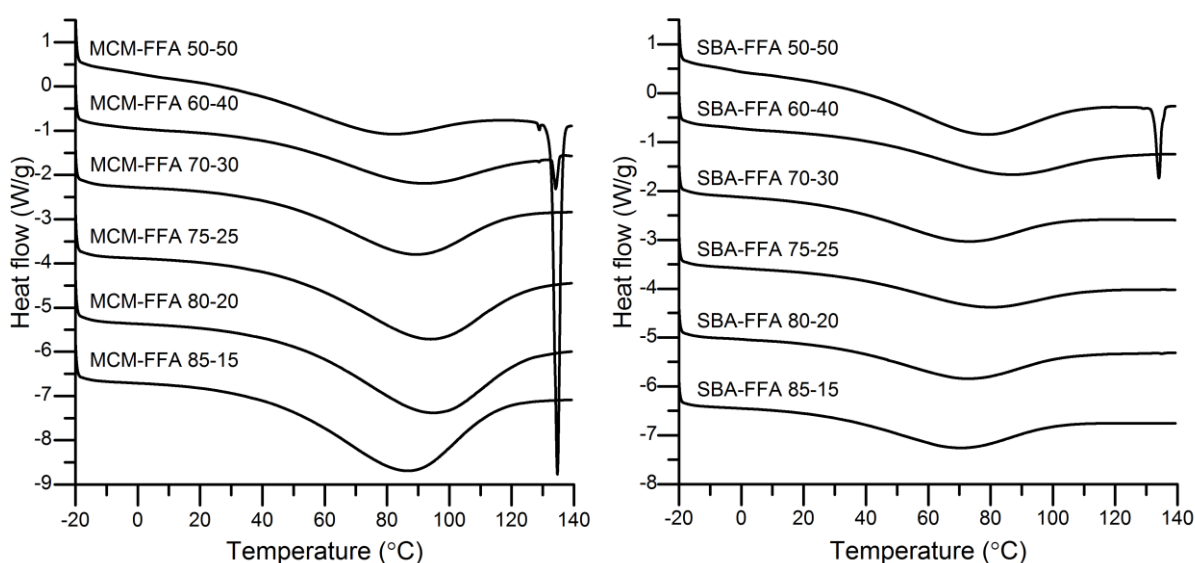
Figure 6-12. DSC thermograms of MCM-FFA and SBA-FFA composites at different host:guest ratios (w/w).

The two outcomes observed for confined FFA were directed primarily by silica pore size. Firstly, the encapsulation in MCM-41 (3.2 nm) or SBA-15 (7.1 nm) results in the stabilisation of amorphous FFA across all studied host:guest ratios. No melting point in the DSC thermograms and a broad 'halo' in the PXRD traces are characteristic of amorphous solids (Figure 6-12). The crystalline phase detected at high host:guest ratios can be assigned to FFA form I loaded outside the pores, as no decrease or broadening of the melting peak characteristic for confined crystals is observed in DSC.[93,106,110,115,116,250] The presence of the bulk FFA form I is corroborated by PXRD and solid-state NMR data (Figure 6-13, Figure 6-14) indicating a partial deposition of the drug outside the pores. This may be related to the complete filling of the available pore volume of the material as determined using N_2 adsorption measurements.
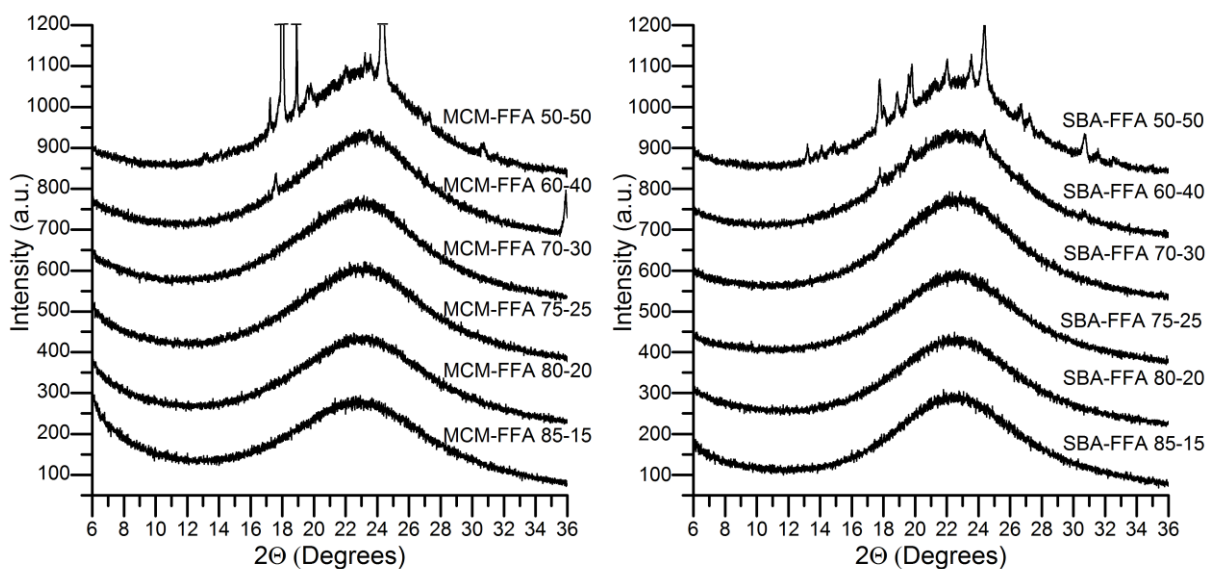
Figure 6-13. PXRD patterns of MCM-FFA and SBA-FFA composites at different host:guest ratios (w/w).

^{13}C solid-state NMR spectra of the MCM-FFA and SBA-FFA materials show very broad peaks and low signal intensity, especially at low guest contents (Figure 6-14). Such effects, characteristic of confined amorphous solids, can be attributed to the increased mobility of the guests, reducing the efficiency of ^{1}H-^{13}C cross-polarisation.[74,75,77,136]
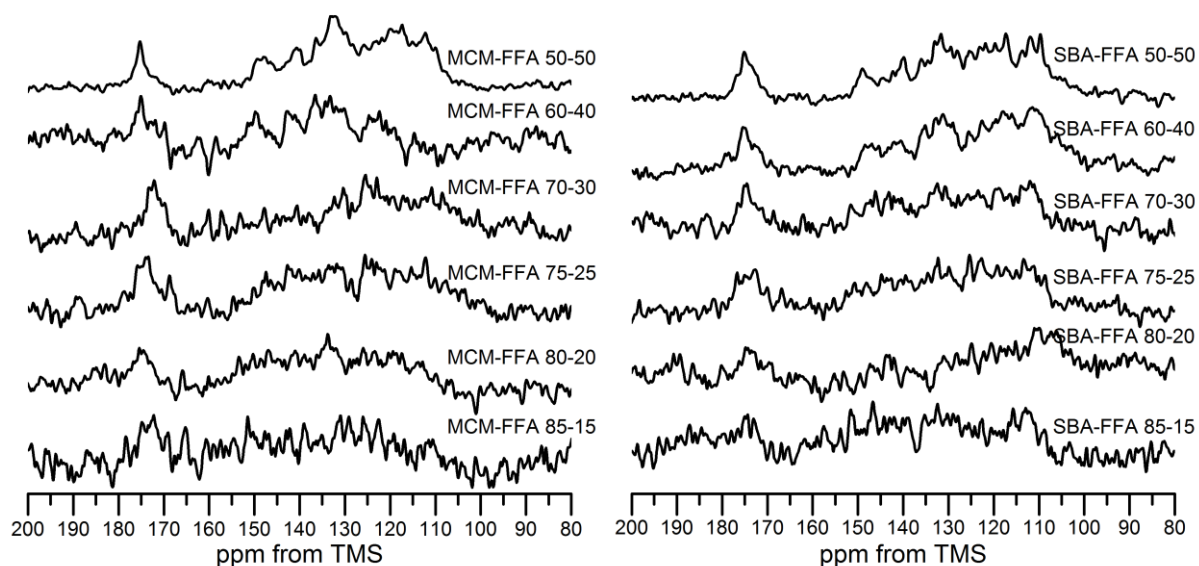
Figure 6-14. ^{1}H-^{13}C CP/MAS solid-state NMR spectra of MCM-FFA and SBA-FFA composites at different host:guest ratios (w/w).
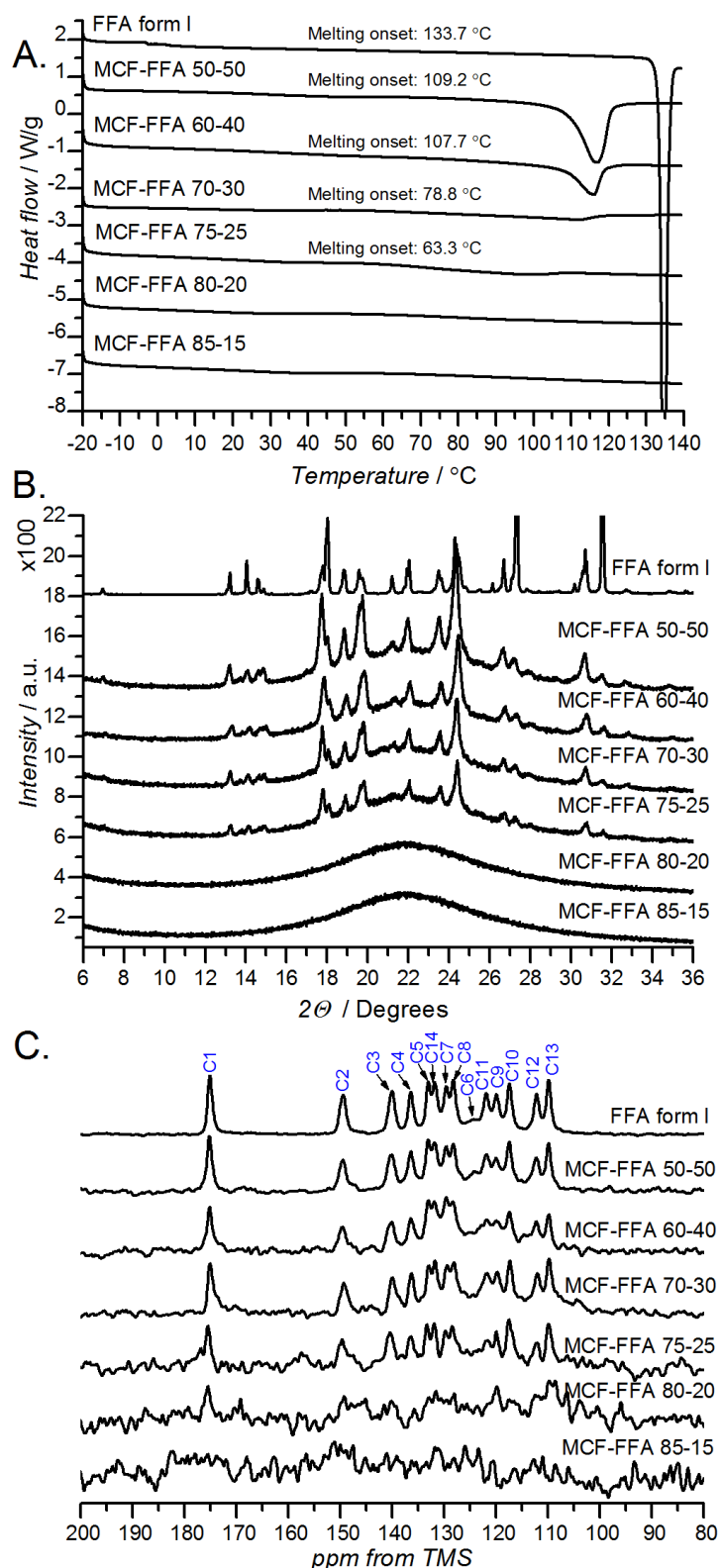
Figure 6-15. A. DSC thermograms, **B.** PXRD patterns and **C.** ^{1}H-^{13}C CP/MAS solid-state NMR spectra of MCF loaded with FFA at different host:drug ratios. Increase of the melting onset with increasing drug content (A.) indicates a gradual growth of the confined crystal in agreement with the Gibbs-Thomson relationship.[93,110] The samples are labelled accordingly with the host:FFA ratios (in wt. %).

In contrast to MCM-41 and SBA-15, the formation of crystalline FFA is observed in the pores of MCF silica (pore diameter *ca.* 29 nm). This effect was dependent on the loading level of FFA, with the drug remaining amorphous at low loadings (up to 20 wt. %) and crystallising into FFA form I at higher loadings. Crystallisation into FFA form I is confirmed by both PXRD and solid-state NMR. DSC thermograms show the broadening of the melting peak and lowering of the melting point of FFA form I, proving unequivocally the presence of the confined crystalline phase (Figure 6-15).
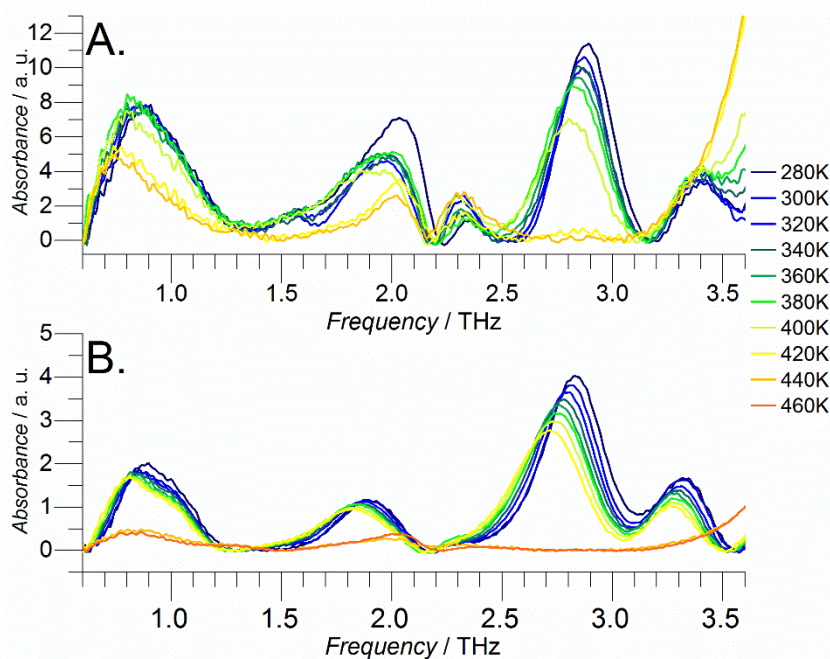
Figure 6-16. Variable temperature (VT) THz spectra of **A.** FFA form I confined within MCF (MCF-FFA 60-40) and **B.** FFA form I. Differences in peak positions and intensities between bulk and confined FFA form I can be observed for all spectral features. The peak at *ca.* 2.3 THz is due to the nano-porous silicas. Data acquired in collaboration with Dr Axel Zeitler and Dr Juraj Sibik.

Due to the high sensitivity of THz spectroscopy to molecular organisation in organic solids it can be used to show fine differences between bulk and confined FFA.[268,269] Changes in the peak positions and intensities can be observed in the VT THz spectra of both phases alongside peak broadening for the confined FFA compared to the bulk crystalline material (Figure 6-16). The blue shifts of the vibrational modes for spectra acquired at the same temperatures for FFA confined in MCF compared to the bulk FFA form I are in line with the previous observations using waveguide spectroscopy and can be viewed as a further signature of the confinement. The decreased melting point of the confined FFA form I is reflected in the loss of the THz signal between 400 and 420 K, which is in agreement with DSC data. The peak of FFA at 1.6 THz becomes attenuated upon loading FFA into nano-pores: this peak is distinct in the low temperature spectra of the pure crystalline FFA,

but is barely visible for the FFA confined in MCF (see Figure 6-28). This highlights the sensitivity of THz spectroscopy towards subtle changes in local ordering: it is exactly this feature that disappears completely upon heating, an effect which is indicative of an increased crystalline disorder, often due to intramolecular flexibility or rotator phases. It is not surprising that it is this spectral signature that exhibits the most pronounced difference between the bulk and confined FFA as the confinement will limit the degrees of freedom for the FFA molecule to form ordered domains.[269]

6.4 Directing the organisation of encapsulated flufenamic acid

Changes in the pore diameters upon encapsulation along with ^{19}F solid-state MAS NMR measurements indicate possible differences in the mechanism of drug encapsulation inside the pores of silica scaffolds, which depends on the size of the pore. The analysis of the changes in BET surface area and pore size distribution after loading FFA inside different silica scaffolds, along with the calculations of the expected surface area available for drug adsorption (Table 6-4), enabled us to postulate the loading and crystallisation mechanism illustrated in Figure 6-17. The values of available pore surface area and pore volume were calculated based on the N_2 adsorption isotherm data and the mass of the porous host used for drug loading (Table 6-4, see footnote for details). Similarly, the number of FFA molecules was calculated using the number of moles of FFA loaded inside the porous hosts. The suggested mechanism of the organisation of FFA molecules inside the hosts with different pore sizes is presented in Figure 6-17.

Table 6-4. Calculated surface area and pore volume available for FFA molecules, total volume of FFA molecules and maximum surface covered by FFA molecular monolayer. [a]

Mass (g)		Available pore surface (m²)			Available pore volume (cm³)			Surface covered by FFA monolayer (m²)	Total FFA volume (cm³)	Total box FFA volume (cm³)	Total cryst FFA volume (cm³)
host	drug	MCM-41	SBA-15	MCF	MCM-41	SBA-15	MCF				
0.085	0.015	116.4	48.5	30.3	0.0556	0.0688	0.1527	34.3	0.0072	0.0214	0.0101
0.080	0.020	109.6	45.7	28.5	0.0523	0.0647	0.1437	45.8	0.0097	0.0286	0.0135
0.075	0.025	102.7	42.8	26.7	0.0490	0.0607	0.1347	57.2	0.0121	0.0357	0.0169
0.070	0.030	95.9	40.0	24.9	0.0458	0.0566	0.1257	68.7	0.0145	0.0429	0.0203
0.060	0.040	82.2	34.3	21.4	0.0392	0.0485	0.1078	91.6	0.0193	0.0572	0.0270
0.050	0.050	68.5	28.5	17.8	0.0327	0.0404	0.0898	114.4	0.0242	0.0715	0.0338

[a] Surface area and pore volume were calculated based on the content of the material multiplied by the BET surface area and the total pore volume at P/P_0=0.99. The total pore volume is derived from the amount of vapour adsorbed at a relative pressure close to unity, by assuming that the pores are then filled with liquid adsorbate. Monolayer surface covered by FFA molecules was estimated based on the surface of the largest rectangle of single molecule as determined by the wrapping box tool in Olex^2 software (OlexSys Ltd, Durham, UK), *i.e.*, 12 Å × 8 Å and multiplied by theoretical number of molecules. Total FFA volume refers to an average van der Waals volume of a single FFA molecule multiplied by the theoretical number of molecules, total box FFA volume refers to an average volume of the wrapping box multiplied by theoretical number of molecules and total cryst volume refers to crystallographic volume of single FFA molecule in the FPAMCA11 structure (*i.e.*, unit cell volume/4 molecules). The realistic volume of the FFA molecules can be found between the box FFA volume (considered as maximum volume) and cryst FFA volume, as both values reflect the molecular flexibility, possible distances between molecules and packing density.

A. Flufenamic acid, FFA

surface

amorphous

crystal

8 Å
12 Å
6 Å

FFA content (%)
15 20 25 30   40   50
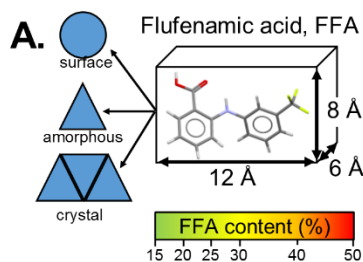
The average size of FFA was determined using the wrapping box tool in Olex[2] crystallographic software (OlexSys Ltd, Durham, UK) based on the Z'=1 crystalline structures of FFA reported in CCDC (structure code: FPAMCA, FPAMCA11, FPAMCA17). FFA encapsulated in silica scaffolds can be present in different environments including crystalline FFA form I, amorphous FFA or highly mobile molecules at the surface of the host—presented here in different shapes. The colour of the shape in the schemes below depends on the loading level of FFA in the material. All graphs (size of the pore and size of the molecule) were scaled 2500000:1 *i.e.*, 1Å = 0.025cm. In presented schemes we assume that molecules stick to the materials surface with the 12 Å × 8 Å plane.

B. MCM-41
1. Plug formation
30 Å
2. Growth
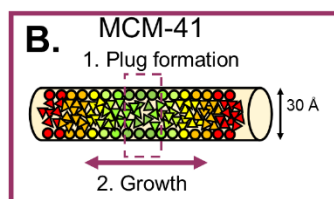
Loading of FFA into MCM-41 porous host with pore sizes of 3.2 nm results in decrease in total pore volume with negligible change in the pores size distribution (Figure 6-8). Two peaks in the ^{19}F NMR spectra at loadings above 15 wt. % indicate species in two different environments *i.e.*, highly mobile species of FFA and densely packed molecules forming amorphous plugs (Figure 6-18). A gradual increase in the intensity of both peak at *ca.* −62 ppm can be visualised as the gradual formation of the amorphous plug of FFA molecules along the pores with increasing drug content (Figure 6-21). No confined crystalline phase was detected in MCM-FFA composites at all drug loadings.

C. SBA-15
1. Surface saturation
70 Å
2. Plug formation and growth
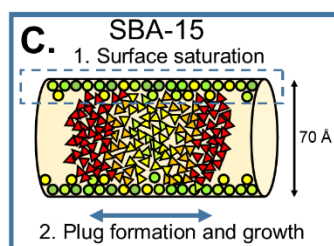
Loading of FFA into SBA-15 porous host with pore sizes of 7.1 nm results in a decrease of total pore volume and stepwise changes in the pore size distribution (Figure 6-8). Presence of only one peak at *ca.* −65 ppm in the ^{19}F NMR spectra at loadings up to 25 wt. % and gradual growth of the peak at *ca.* −62.3 ppm at higher loadings indicate stepwise mechanism of drug loading. A single layer of molecules (*ca.* 12 Å decrease in the PSD) is formed at the surface and highly mobile species are present in the pores void at loadings up to 25 wt. %. At higher drug content the amorphous plug of densely packed FFA molecules is formed gradually filling the pores void (Figure 6-21).

D. MCF
1. Surface saturation
150 Å
2. Nucleation and growth of a crystal
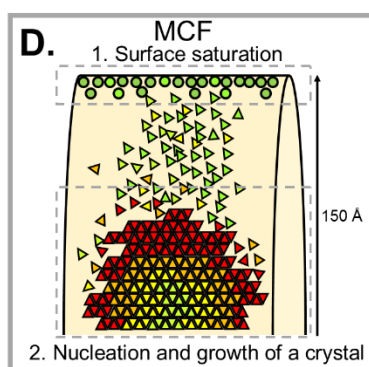
FFA loaded into MCF type of material with pore sizes of *ca.* 29 nm forms a crystalline phase at 25 wt. % loading level. The loading of the drug proceeds in several steps. Firstly, the deposition of the drug at internal pore surface is observed together with presence of highly mobile species in the pore voids (^{19}F NMR peak at −65 ppm). Secondly formation of the amorphous component in the pores void can be observed at drug loadings up to 20 wt. %, which further forms crystalline FFA form I inside the pores above 25 wt. % (^{19}F NMR peak at −60 ppm Figures 6-18; 6-21). It is important to note that the melting onset of confined FFA form I is increasing gradually with increasing drug content indicating growth of the crystals (Figure 6-15).

Figure 6-17. Proposed mechanism of drug loading and formation of confined crystalline phase based on the N$_2$ adsorption data, theoretical calculations and ^{19}F NMR analysis.
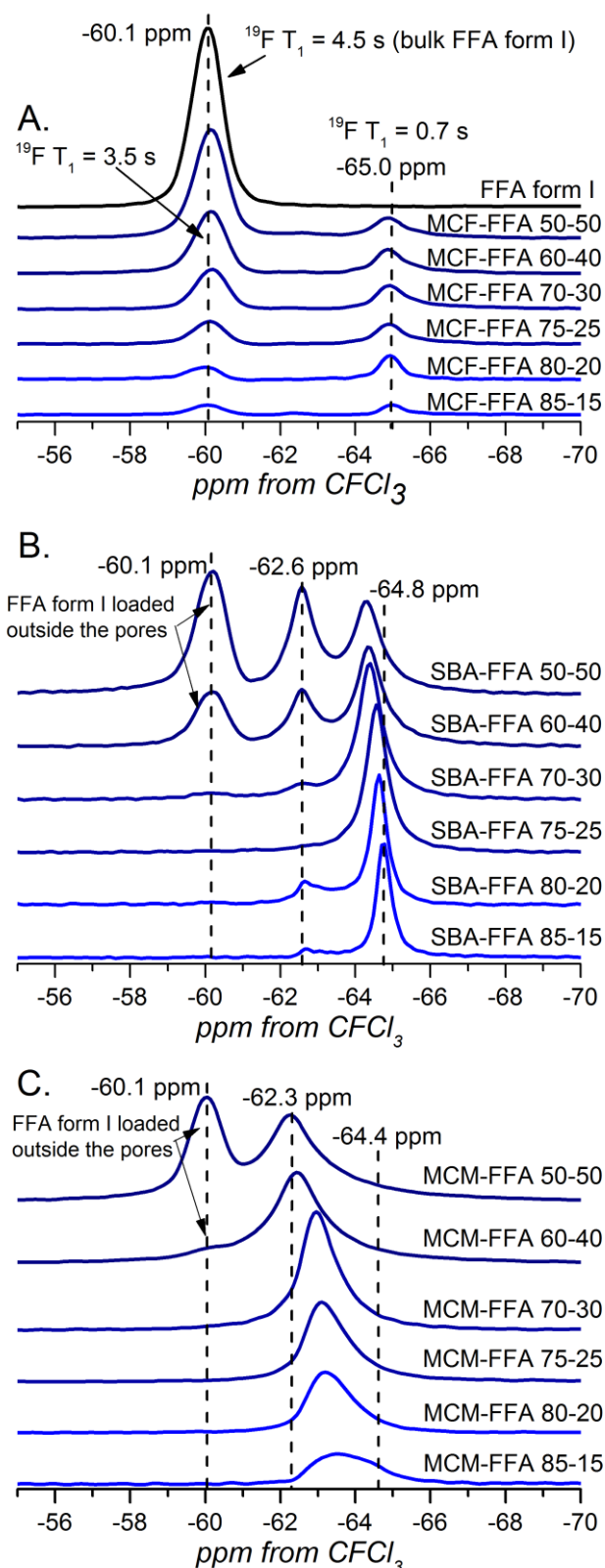
Figure 6-18. High-field ^{19}F{^{1}H} solid-state MAS NMR spectra (20.0 T) of **A.** MCF-FFA, **B.** SBA-FFA, **C.** MCM-FFA. The samples are labelled accordingly with the host:FFA ratios (in wt. %). Growth of the main peaks at −60, −62 and −64 ppm with FFA content is consistent with the pore loading pathways indicated in Figure 6-17. The high-field spectra are in full agreement with the data recorded at 9.4 T (Figure 6-23).

Molecules confined within mesopores of silicas can be present in several different environments, *i.e.*, confined crystals, amorphous aggregates and species interacting with the surface of the host. The 100 % natural abundance of ^{19}F and its high sensitivity to changes in the long-range electrostatic interactions[162] enabled us to detect the differences between these environments of FFA. Advantageously, crystalline FFA form I has one molecule in the asymmetric unit and three magnetically equivalent fluorine atoms in the structure, leading to a single peak at −60.1 ppm in the ^{19}F solid-state NMR spectra recorded both at 9.4 and 20.0 T (Figure 6-18, Figure 6-23).

^{19}F solid-state NMR spectra of FFA confined in the MCF host show that the guest species reside in two different environments with populations dependent on the host:guest ratios. A sharp peak at −65.0 ppm is present at the lowest loading. Increasing FFA content leads to the gradual growth of the broad peak at −60.1 ppm, attributable to FFA form I (Figure 6-18) which is also confirmed by ^{13}C NMR spectra (Figure 6-15). Two additional features of the peak at −65.0 ppm are important for further understanding of the spectra. Firstly, there are no spinning sidebands even at very slow MAS rates (1 kHz), indicating very low chemical shift anisotropy (Figure 6-25). This may be related to an increased molecular mobility for this population, which is further corroborated by ^{19}F T_1 relaxation times (Figure 6-19). Secondly, the intensity of this peak shows only minor changes across all host:guest ratios reaching saturation at 15 wt. % FFA. This is in agreement with the expected values for full surface coverage of the pores by a molecular monolayer. Linear increase of the intensity of the peak at *ca.* −60 ppm (FFA form I) with increasing content of FFA indicates a gradual growth of the crystalline phase inside the pores (Figure 6-18, Figure 6-21, Figure 6-23). Interestingly, it was possible to detect the confined crystalline phase using ^{19}F NMR at loadings as low as 15 wt. %, below the threshold of either DSC or PXRD. This may indicate formation of small nucleating clusters with only local ordering.

The presence of molecules in two distinct environments with different relaxation rates (^{19}F T_1 is *ca.* 3.5 s for the confined phase and 0.7 s for the liquid-like surface layer) supports the concept of a highly dynamic liquid-like molecular layer formed on the internal surface of the pores (Figure 6-19).[80,81,252] The presence of the liquid-like layer of FFA layer on the silica surface is not surprising, as host-guest interactions between the hydrophobic FFA guest and the silica surface of the host with a high content of ^{3}Q [((SiO)$_3$SiOH)] sites (see section 6.2.2) are expected to be weak. Similar phenomena have been suggested by the DFT and MD simulations of ibuprofen and clotrimazole encapsulated in MCM-41 and MSU silicas.[80,81,252] Importantly, these molecules share similar properties with FFA (*i.e.*, hydrophobicity and the presence of a carboxyl group for IBU).
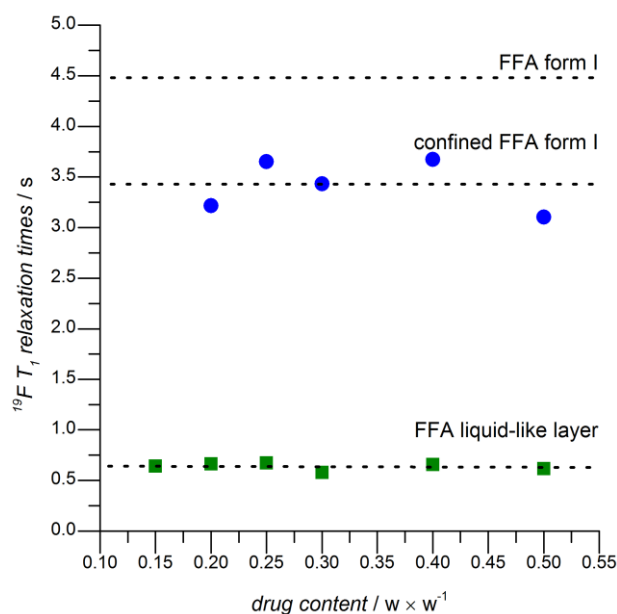
Figure 6-19. ^{19}F T_1 relaxation measurements of MCF-FFA composites at different drug loadings from 15-50 wt. %. The expected errors for the method are between 5 to 10 %.

Similarly to MCF-FFA materials, two different environments of FFA molecules can be detected when confined in MCM-41 and SBA-15. For SBA-FFA composites, a peak at −64.8 ppm is observed at low loading levels. The increasing FFA content leads to its downfield shift and the growth of a peak of confined amorphous drug at −62.6 ppm. ^{19}F NMR spectra of MCM-FFA composites show the two (merged) peaks at −63.5 and −64.4 ppm, which undergo a downfield shift with increasing drug content. The very low intensity of spinning sidebands in both SBA-FFA and MCM-FFA with up to 30 wt. % of FFA is consistent with the presence of a disordered amorphous guest phase along with the liquid-like layer of FFA, also confirmed by the ^{19}F T_1 relaxation times.

^{19}F T_1 relaxation measurements of confined FFA in both MCM-41 and SBA-15 hosts indicate the presence of highly mobile species, in a similar mobility regime to the amorphous/surface FFA confined in the MCF host (Figure 6-19). A gradual increase of the relaxation times with increasing drug content may indicate the formation of densely packed amorphous plugs of FFA with restricted mobility inside the pore voids. The presence of a distinct crystalline component (FFA form I) loaded outside the pores in MCM-FFA 50-50 composite affects the relaxation measurements significantly, leading to increased ^{19}F T_1 relaxation time.
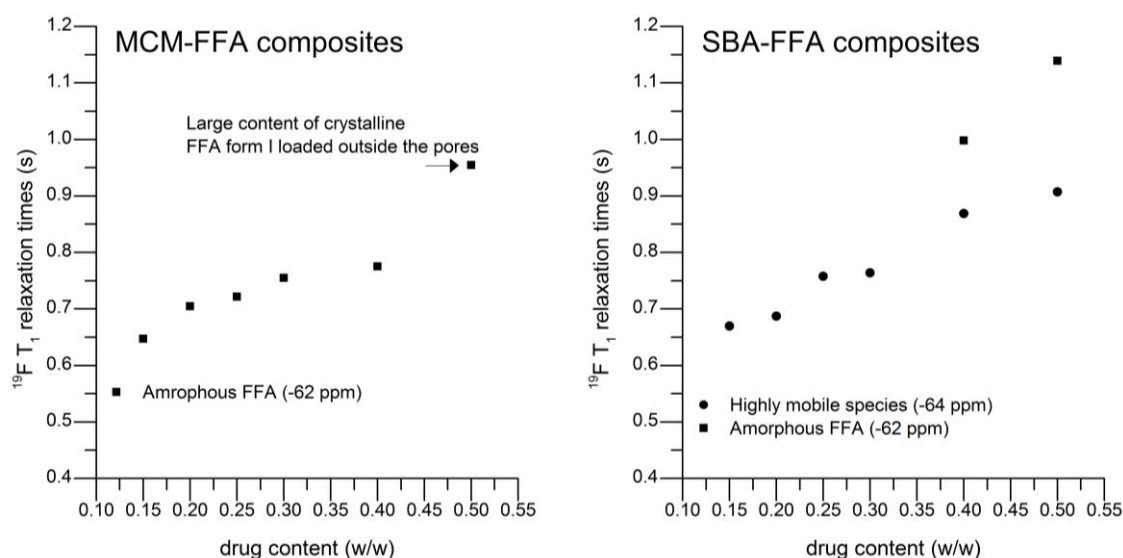
Figure 6-20. ^{19}F MAS NMR T_1 relaxation times of FFA confined inside MCM-41 (left) and SBA-15 (right) materials at different drug content. Presence of large crystalline component loaded outside the pores of MCM-FFA 50-50 significantly affects the ^{19}F T_1 relaxation time. The expected errors for the method are between 5 to 10 %.

The two distinct peaks observed in the ^{19}F MAS NMR spectra of SBA-FFA 60-40 and SBA-FFA 50-50 enable us to determine differences in the ^{19}F T_1 relaxation times of molecules in the high mobility regime; and the densely packed amorphous FFA molecules in the pore voids (Figure 6-20). The highly mobile species have relaxation times of *ca.* 0.85 and 0.9 s, whilst the amorphous plugs have relaxation times of 1.0 and 1.15 s for SBA-FFA 60-40 and SBA-FFA 50-50 composites, respectively. Furthermore, the presence of crystalline FFA loaded outside the pores (shoulder at *ca.* −60 ppm) may slightly increase the relaxation time of the FFA peak at *ca.* −62 ppm for SBA-FFA 50-50. The ^{19}F relaxation time measurements confirm the general model of pore loading, in which the presence of confined molecules in two different environments and motional regimes can be detected.

The ^{19}F spectra acquired at lower field (9.4 T) show sufficient resolution to identify FFA molecules in three different environment. Further deconvolution of different ^{19}F sites of the spectra acquired at lower field shows very good agreement with ^{19}F spectra acquired at 20.0 T proving sensitivity of ^{19}F NMR towards monitoring of confined crystallisation within nanoporous systems (Figure 6-23).

Figure 6-21. Deconvoluted ^{19}F MAS NMR spectra (recorded at 20.0 T) of **A.** MCM-FFA, **B.** SBA-FFA and **C.** MCF-FFA composites at different FFA loadings and evolution of the changes in deconvoluted peaks intensity (integration) for crystalline, amorphous and surface components.
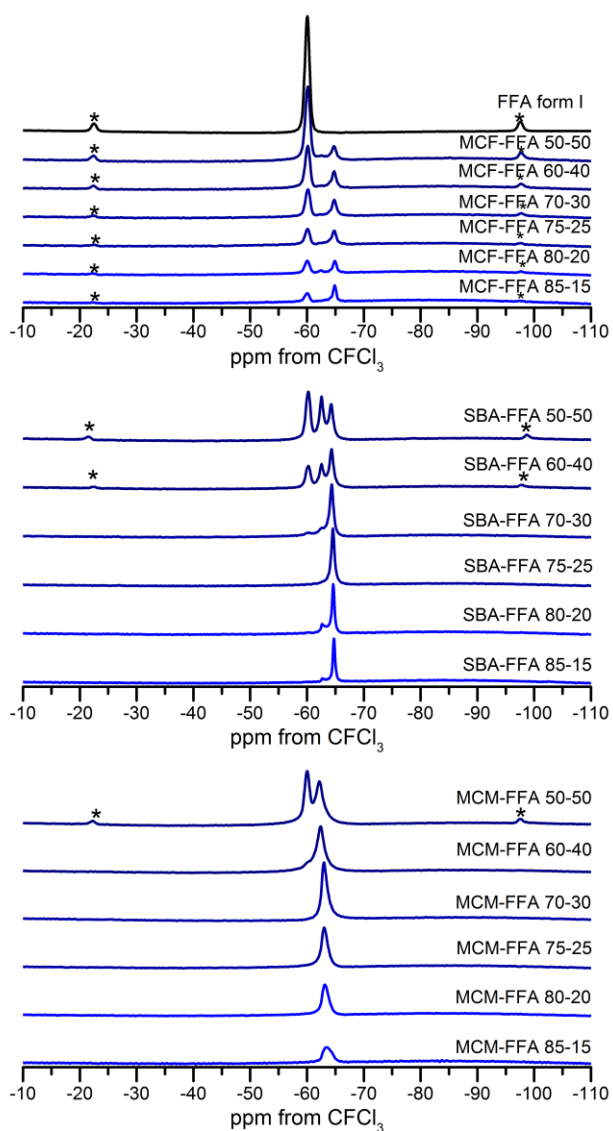
Figure 6-22. ^{19}F MAS NMR spectra (20.0 T) of **A.** MCM-FFA, **B.** SBA-FFA and **C.** MCF-FFA composites at different FFA loadings including the region of first spinning sidebands (labelled with asterisks). Spinning sidebands can be observed only from crystalline FFA form I.

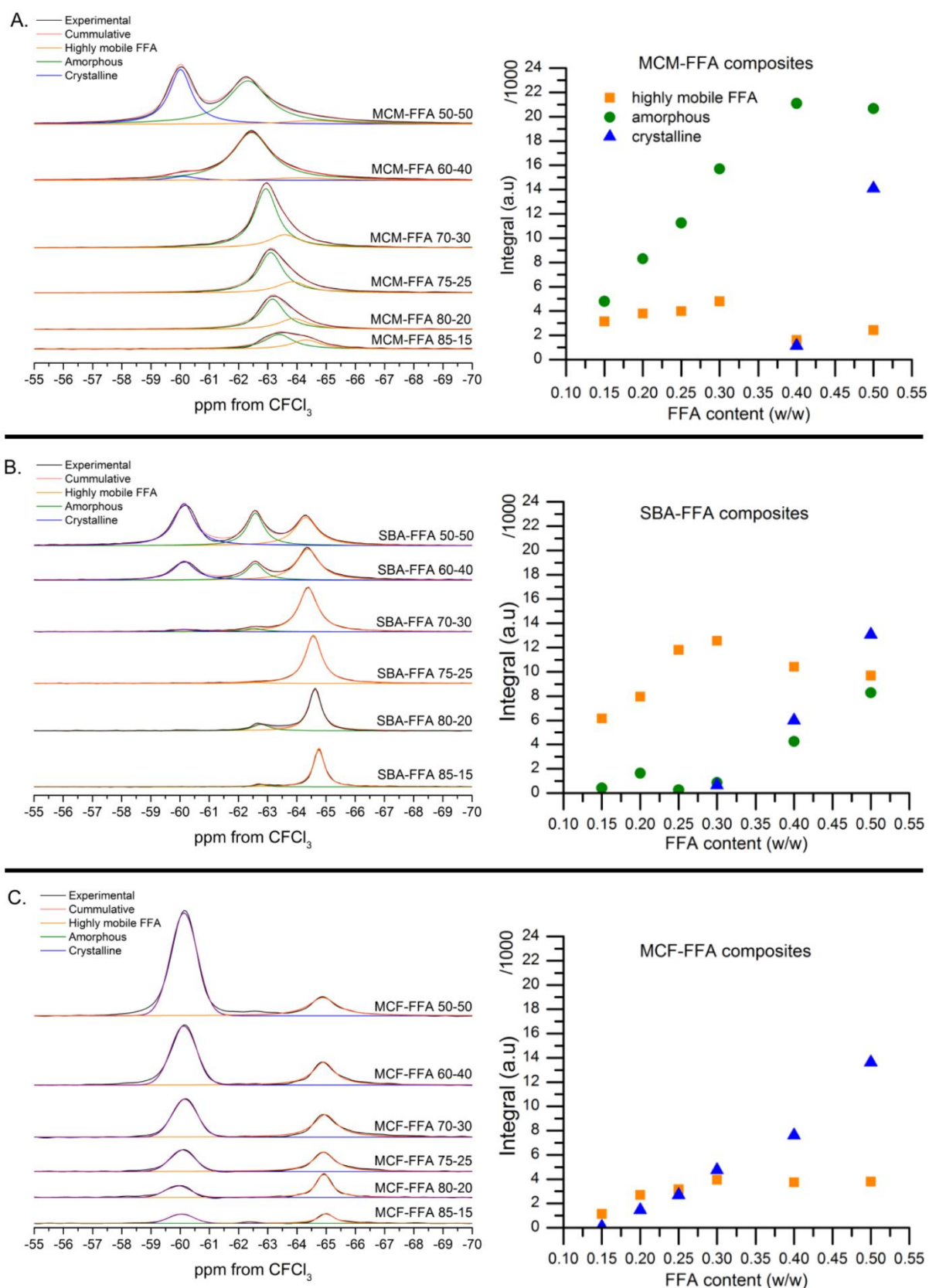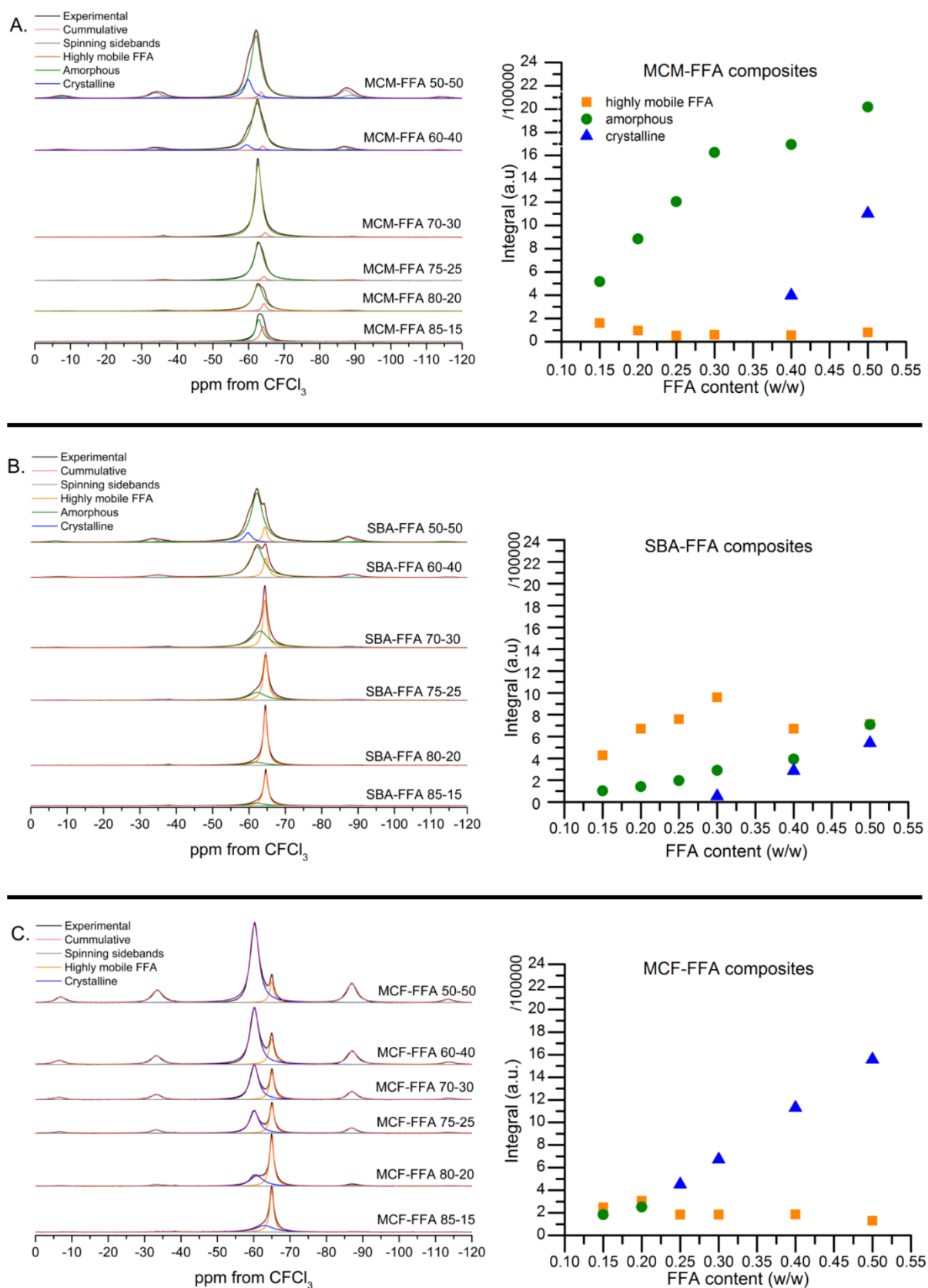**Figure 6-23.** Deconvoluted ^{19}F MAS NMR spectra (recorded at 9.4 T) of **A.** MCM-FFA, **B.** SBA-FFA and **C.** MCF FFA composites at different FFA loadings and evolution of the changes in deconvoluted peaks intensity (integration) for crystalline, amorphous and surface components.

The sideband pattern in the ^{19}F NMR spectra was used to estimate the ^{19}F CSA parameters using the SOLA Solid Lineshape Analysis software (version 2.2.3) implemented in the Topspin 3.2 (Bruker Biospin, Germany). For FFA form I, we used a single site model for data fitting. Due to the presence of the two peaks in the spectrum, *i.e.*, the peak of FFA form I at *ca.* −60 ppm and the isotropic peak of a highly mobile species at *ca.* −65 ppm, the fitting of the ^{19}F spectra of the FFA-MCF 60-40 composite required the use of a two site model. The strength of dipolar couplings was not included in the model, as ^{19}F nuclei in the CF_3 motif are not strongly coupled to ^{1}H nuclei due to spatial separation. This was confirmed by comparison of ^{19}F and $^{19}F\{^{1}H\}$ NMR spectra FFA form I spectra recorded at 20.0 T, which show no differences in linewidths between both spectra. Furthermore, the implementation of additional variables for each site may lead to non-comparable data.

We used Haeberlen conventions for shielding parameters, with the relation between them described as follows:

$$\text{Isotropic shielding: } \sigma_{iso} = (\sigma_{11} + \sigma_{22} + \sigma_{33})/3 \qquad (2)$$

$$\text{Anisotropy: } \zeta = \sigma_{33} - \sigma_{iso} \qquad (3)$$

$$\text{Asymmetry: } \eta = (\sigma_{22} - \sigma_{11})/\zeta \qquad (4)$$

The isotropic chemical shift, δ_{iso} is given by:

$$\delta_{iso} = -(\sigma_{iso} - \sigma_{ref}), \qquad (5)$$

where σ_{ref} is the shielding of a nucleus in a reference system as described by Yates *et al.*[270]

The three tensor components are given as follows:

$$|\sigma_{33} - \sigma_{iso}| \geq |\sigma_{11} - \sigma_{iso}| \geq |\sigma_{22} - \sigma_{iso}|. \qquad (6)$$
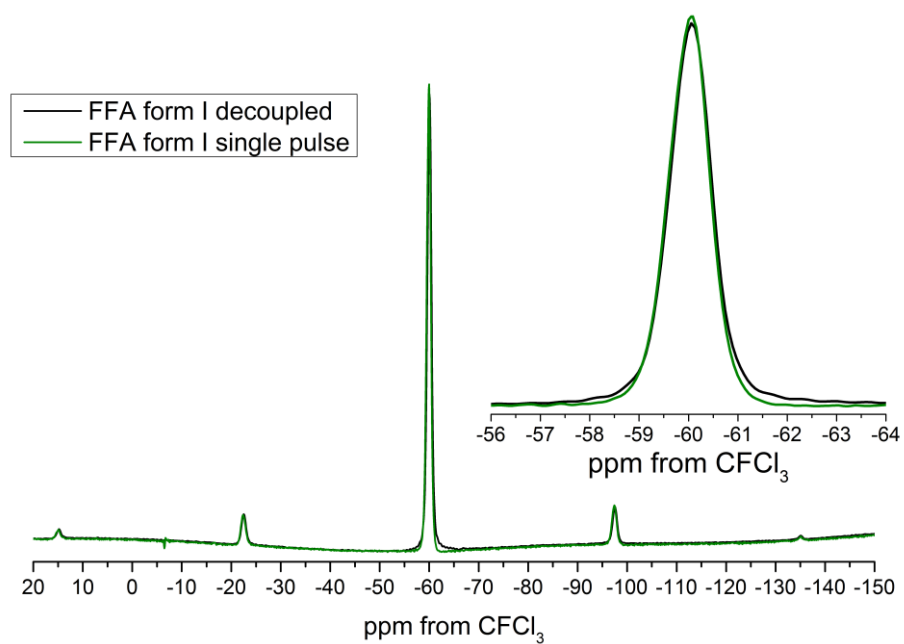
Figure 6-24. ^{19}F solid-state NMR spectra of FFA form I recorded at 20.0 T with and without ^{1}H decoupling. Spectra acquired at an MAS rate of 30 kHz.
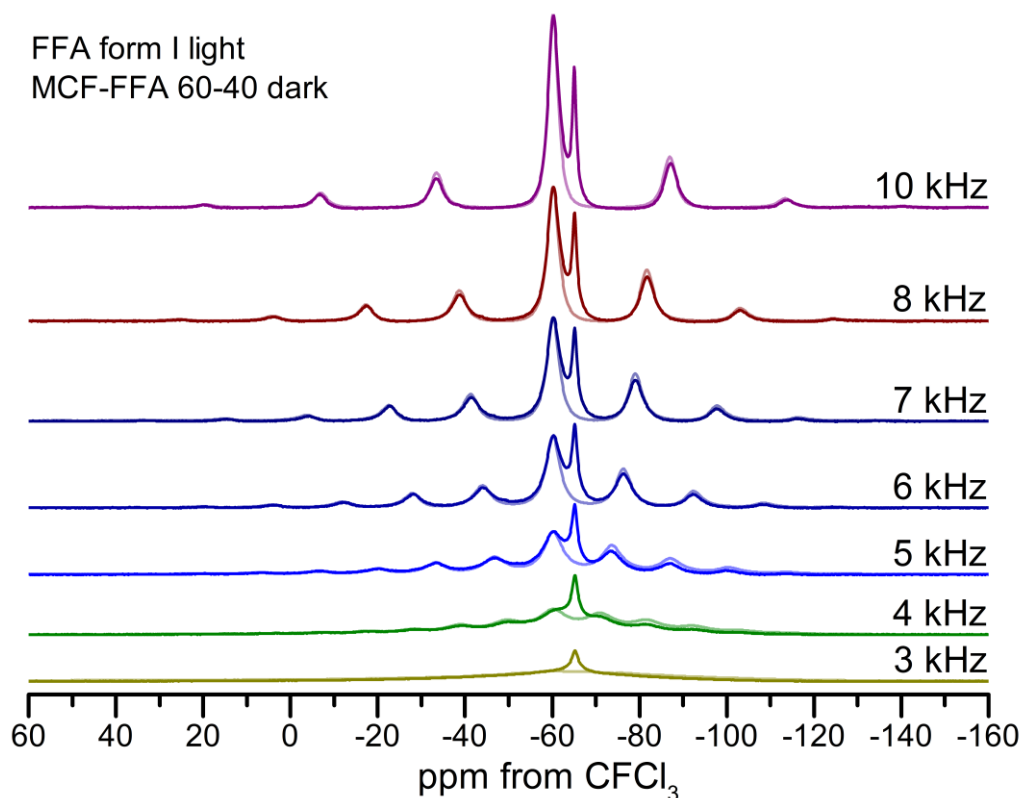
Figure 6-25. ^{19}F solid-state NMR spectra of FFA form I (spectra in light shade) and MCF-FFA 60-40 composite (spectra in dark shade) at different spinning speeds. Spectra at an MAS rate of 1 and 2 kHz are not shown for clarity.
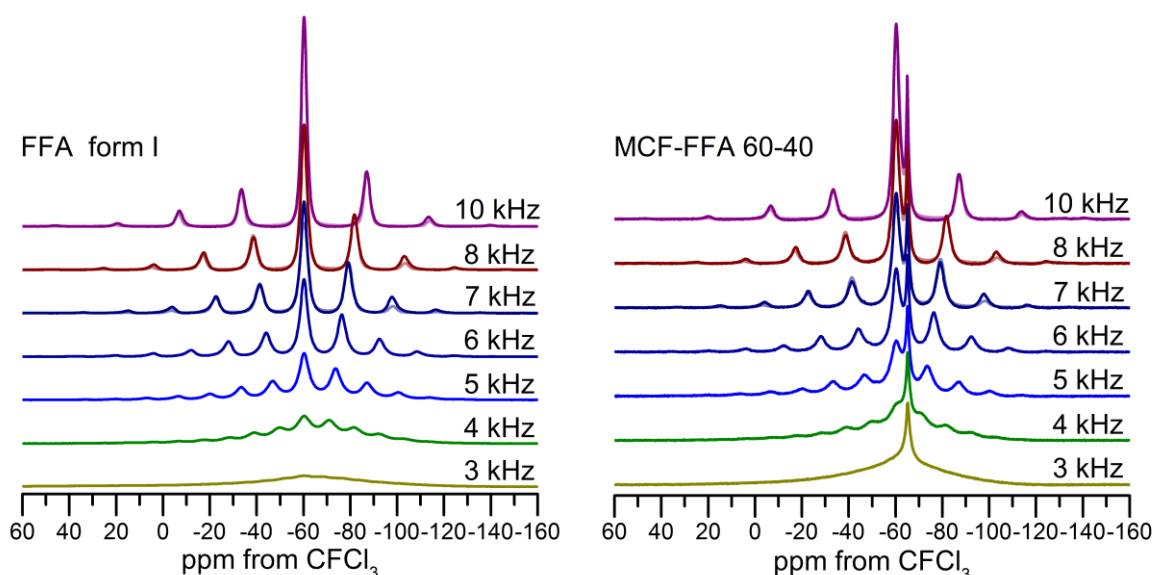
Figure 6-26. ^{19}F solid-state NMR spectra recorded at 9.4 T (dark shade) and fitted CSA models (light shade) of FFA form I and MCF-FFA 60-40 composite at an MAS rate of 10, 8 and 7 kHz.

Minor differences are observed in the spinning sideband patterns of the ^{19}F spectra for FFA form I in the bulk and confined nanocrystalline phases, which may be related to preferable growth of the confined crystal. Analysis of the CSA parameters shows slightly higher anisotropy of the bulk FFA form I as compared to the confined crystalline phase. Differences in anisotropy are followed by minor changes in asymmetry between the bulk and nanocrystalline FFA form I (Figure 6-24, Figure 6-26). The second component of the spectra of the MCF-FFA 60-40 composite at *ca.* −65 ppm (assigned to highly mobile FFA species) shows an absence of spinning sidebands and little broadening at spinning speeds as low as 3 kHz, indicating very small chemical shift anisotropy (Figure 6-25).

Table 6-5. Experimental ^{19}F NMR shielding tensor parameters for FFA form I as bulk and confined in MCF porous silica host. All parameters are referenced to $CFCl_3$ signal.

Spin rate	Material	$\lvert\sigma_{11}-\sigma_{ref}\rvert$	$\lvert\sigma_{22}-\sigma_{ref}\rvert$	$\lvert\sigma_{33}-\sigma_{ref}\rvert$	δ_{iso} [ppm]	ζ	η	Best fit[1]
10 kHz	FFA form I	31.7	12.6	44.3	-60.3	44.3	0.43	0.902
	MCF-FFA 60-40	30.1	11.1	41.2	-60.3	41.2	0.46	0.918
8 kHz	FFA form I	30.6	12.5	43.1	-60.2	43.1	0.42	0.908
	MCFFFA 6040	29.3	11.1	40.4	-60.3	40.4	0.45	0.912
7 kHz	FFA form I	29.7	12.4	42.2	-60.2	42.2	0.41	0.908
	MCFFFA 6040	28.9	10.9	39.8	-60.2	39.8	0.45	0.928

[1]Best overlap calculated as a difference between the experimental spectrum and the superimposed simulated spectra in the range of chemical shifts from 100 to -150 ppm.

6.5 Monitoring of confined crystallisation *in situ* using ^{19}F NMR

FFA loaded into the MCF host crystallises into FFA form I after a couple of hours. We prepared amorphous FFA inside the pores of the MCF scaffold and monitored the crystallisation of confined FFA form I between 293 and 333 K *in situ*. At 293 K two broad peaks are observed at *ca.* −65 and −62 ppm, indicating the presence of a highly mobile species of FFA alongside amorphous plugs of the drug in the pore voids. An Increase in temperature leads to the narrowing of both peaks due to increased mobility. At 323 K, the growth of an additional broad peak of crystalline FFA form I is observed at −60.0 ppm. The three different environments of FFA in the MCF host can be assigned as follows: confined crystalline FFA (form I) at −60.0 ppm; confined amorphous FFA at *ca.* −62.3 ppm; and highly mobile FFA adsorbed on the silica surface at *ca.* −65 ppm (Figure 6-27).

The intensity of the FFA form I peak (−60 ppm) during isothermal recrystallisation reached the maximum at 333 K after 60 minutes (Figure 6-27). Similarly, the intensity of the peak at −62.3 ppm (assigned to the confined amorphous FFA) reached a minimum and subsequently stabilised at the same temperature.

Interestingly, there was only a slight change to the intensity of the peak at *ca.* −65 ppm, which displayed only a minor change at the beginning of the experiment, indicating that the population of FFA molecules that are adsorbed at the silica surface is practically unaffected by crystallisation. At the end of the *in situ* crystallisation experiment at 333 K three different environments of FFA in the confined space were still observed. The spectrum acquired at room temperature following the whole recrystallisation experiment showed only two peaks - a broad peak at *ca.* −60 ppm (FFA form I) and a sharper peak at *ca.* -65 ppm (highly mobile FFA species).
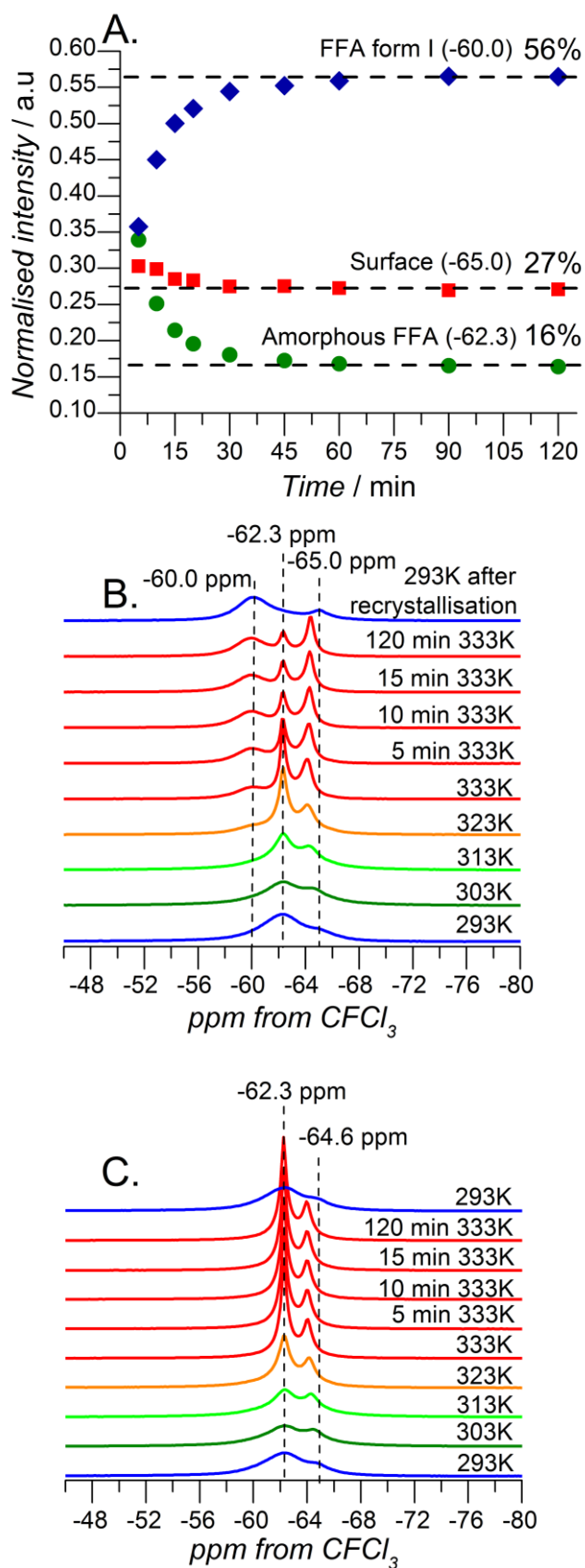
Figure 6-27. A. Kinetics (333 K) of confined crystallisation of FFA within MCF material at 60-40 host:guest ratio, ^{19}F solid-state NMR spectra (9.4 T) recorded at variable temperatures of FFA confined within **B.** MCF and **C.** SBA-15 porous hosts.
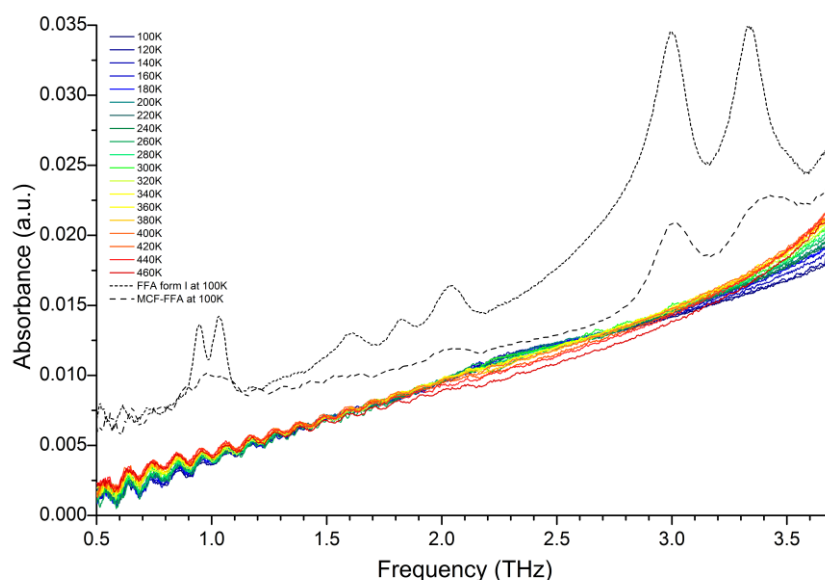
Figure 6-28. THz spectra of amorphous FFA confined in SBA-15 mesoporous silica at drug loading of 40 wt. % recorded at different temperatures. Lack of the peaks in the spectra reflects the amorphous nature of the analysed material. The THz spectra of crystalline FFA form I and FFA form I confined in the MCF material at 40 wt. % are shown for comparison (acquired at 100 K).

The amorphous SBA-FFA composite shows very different behaviour at elevated temperatures. Two ^{19}F NMR peaks are observed throughout the range of applied temperatures, which narrowed with increasing temperature. No crystallisation was observed during the experiment, indicating an efficient stabilisation of confined amorphous FFA (Figure 6-27). This was confirmed further using variable temperature THz spectroscopy, which is highly sensitive to the presence of crystalline phase within the material (Figure 6-28). It is interesting to note the significantly reduced baseline in the THz spectra of amorphous FFA molecules confined within SBA-15 material relative to the bulk drug. The reduction of the baseline has been reported previously for organic molecular crystals that were confined on the surface of single-mode metal parallel plate waveguide.[268] Given our observation of the spectra in SBA host we believe that this is a signature of molecular confinement, as the vibrational motions cannot be perturbed by disorder in the polycrystalline environment typically encountered in bulk transmission measurements, where the disorder at grain boundaries will have a significant effect on the complex motions that are observed in the far-infrared. We believe that the THz spectra of FFA in the SBA host are a result of a similar phenomenon, where the surface effects increase the global molecular mobility of the FFA.
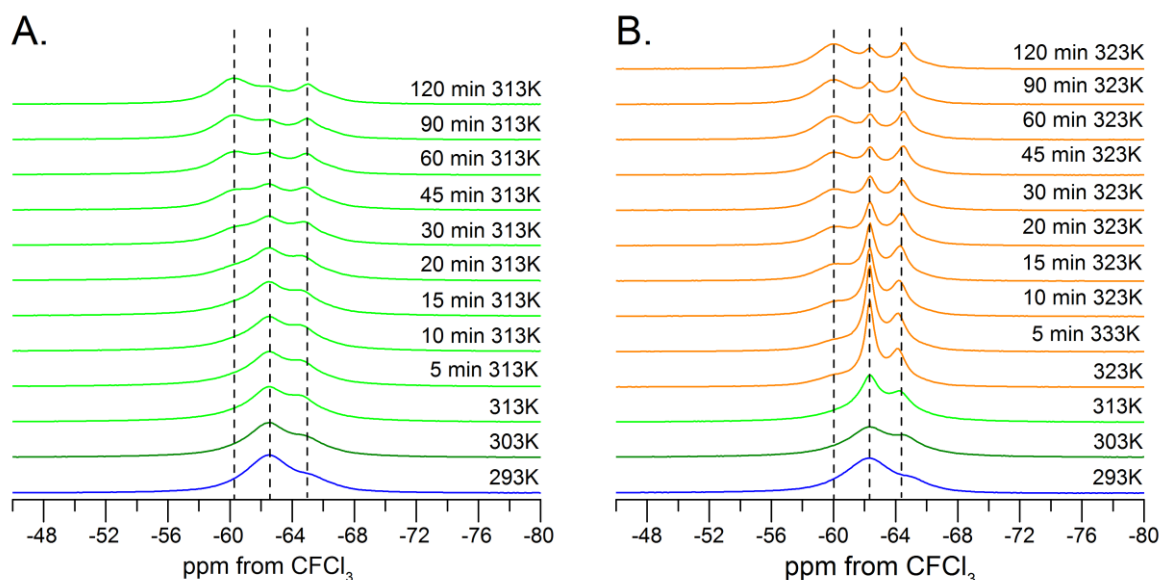
Figure 6-29. ^{19}F solid-state NMR spectra (9.4 T) recorded during isothermal crystallisation at **A.** 313 K and **B.** 323 K of FFA confined within MCF silica scaffold at 60:40 host:guest ratio.

To further investigate the distribution of FFA molecules in different environments we performed isothermal crystallisation of FFA confined within the MCF host at 313 and 323 K. Differences in the peak widths due to the changes in mobility and slower crystallisation rate was observed during crystallisation at lower temperatures (Figure 7-29). Similar distribution of the FFA molecules in three environments was observed for materials crystallised at 333 and 323 K. In the spectra of the material crystallised at 313 K, the induction period could be observed during first 15 minutes of the experiment where slow growth of FFA form I is observed. Furthermore, slight differences in the surface peak intensity (at *ca.* −65 ppm) between materials crystallised at different temperatures indicate dynamics of the highly mobile FFA molecules at the surface.
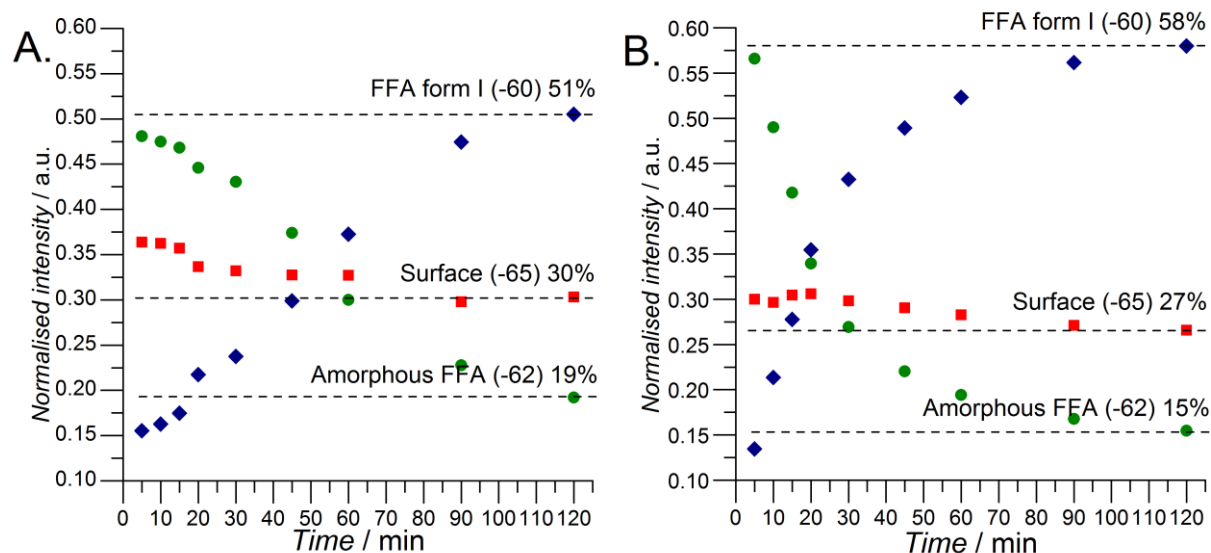
Figure 6-30. Kinetics of confined crystallisation of FFA within MCF material at 60-40 host:guest ratio at **A.** 313 and **B.** 323K.

6.6 Conclusion

In this work we demonstrated that ^{19}F NMR is a highly sensitive tool to probe the local environments of molecules confined within porous hosts. We were able to distinguish between molecules of the model pharmaceutical compound present in the pores as confined crystalline, confined amorphous and highly mobile species. The observation of the latter is consistent with the formation of a molecular liquid-like layer at the silica surface. To the best of our knowledge this is the first direct experimental proof of the presence of a liquid like layer of molecules on the silica surface. Simultaneous quantification of the three environments allowed us to use ^{19}F solid-state NMR to monitor the kinetics of confined crystallisation *in situ*. We have demonstrated that confined FFA (either amorphous in SBA-15 and MCM-41 or nano-crystalline in MCF) has very different dynamical properties as compared to bulk FFA form I. All the presented studies allow us to gain a better understanding of the fundamental processes of molecular aggregation at the nanoscale. Considering that 25 % of all marketed drugs are fluorinated molecules[253], these findings offer a fast and direct diagnostic tool for developing of novel nano-confined pharmaceutical formulations.

Controlled crystallisation, phase transitions and mobility of confined tolbutamide

Chapter 7

7.1 Introduction

Tolbutamide (1-butyl-3-(4-methylphenylsulfonyl) urea, TB) is an example of a sulfonylurea derivative, pioneer of the first-generation potassium channel blockers used in type II diabetes as an oral hypoglycaemic drug. Its flexible structure makes it an excellent model compound for studies of conformational polymorphism as up to date seven polymorphic forms of TB have been reported (including low temperature structures of TB form III[2] and high temperature TB form I[H]).[183,189,271–273]

In this chapter we begin with an introduction to TB polymorphism, followed by the characterisation of different TB polymorphs including TB form I, TB form IV and TB form V (confined in the MCM-41 scaffold). The ^{13}C NMR spectra of TB form V with full assignment based on the DFT calculations of chemical shifts using CASTEP code is presented for the first time, together with high-resolution ^1H CRAMPS spectra of TB forms I[L], I[H], IV and V. The NMR experiments are accompanied by computational studies of isotropic ^1H and ^{13}C NMR chemical shielding tensors of all investigated TB polymorphs using the CASTEP code. Through the acquisition of variable temperature ^1H-^{13}C CP/MAS NMR spectra and ^1H T_1, $T_{1\rho}$ and ^{13}C $T_{1\rho}$ relaxation measurements, we were able to investigate mobility of the aromatic ring of TB in both TB form I and TB form IV. Additionally, the new low temperature TB form IV with Z'>1 was observed using ^1H-^{13}C CP/MAS and ^1H CRAMPS NMR spectra below 283 K. The studies of TB polymorphism are followed by a structural and dynamical investigation of the drug encapsulated within the MCM-41 host at loading levels up to 50 wt. %, where selective crystallisation of TB form V was observed. We used ^1H-^{13}C CP/MAS NMR to monitor phase transitions of confined TB within the MCM-41 material *in situ*. Using ^1H-^{13}C CP/MAS NMR at low temperatures, we were able to prove TB is encapsulated as a solid, crystalline phase coexisting with highly mobile amorphous drug. To best of our knowledge, the encapsulation and crystallisation of TB molecules inside pores as small as *ca.* 3 nm has not been reported previously.

As the effect of humidity on drug molecules encapsulated within mesoporous silica based materials for drug delivery is poorly understood, in the last section, we present a set of NMR based methods designed to gain in-depth understanding of the physical state of confined TB using two model MCM-TB systems loaded at either low (20 wt. %) or high (50 wt. %) drug contents and different ^{13}C signal enhancement methods sensitive to molecular mobility.

The aim of this chapter is to understand crystallisation and phase transitions of the highly flexible TB molecule as a bulk drug, and encapsulated inside the small pores (3.2 nm) of a MCM-41 silica scaffold. The effect of storage conditions on the state of confined TB molecules was investigated extensively using a wide range of NMR methods alongside PXRD and DSC studies. Furthermore, through the application of NMR relaxation measurements we were able to gain better understanding of the molecular dynamics of the phenyl ring for a group of TB polymorphs.

7.1.1 Polymorphism of tolbutamide

Tolbutamide contains a rigid benzene ring and a highly mobile aliphatic chain with seven bonds that can rotate freely. The high flexibility of this structure has led to a large number of TB polymorphs reported in the CCDC (6 structures including a high Z' form III). Further understanding of TB polymorphism may serve as a base for structural studies of other (sulfonyl) urea derivatives, which are an important group of compounds in materials science, used frequently as low molecular weight gelators.[183,189,271,274]

The polymorphism of TB was firstly investigated in 1969, when three forms were reported by Kuhnert-Brandstätter and Wunsch[189,275]. Further investigation of TB crystal structures was carried out by Simmons et al. who obtained two TB structures – forms A and B.[189,276] The preparation of four forms of TB, i.e., forms I-IV (known as Burger's forms), was carried out by Burger in 1975.[189,277] Six years later the first structure of TB form I with atomic coordinates was reported independently by both Nirmala et al. and Donaldson et al. (CSD ref. codes ZZZPUS01, ZZZPUS02).[188,278] Thirty years later, the detailed structural analysis of four Burger's TB polymorphs was reported by Thirunahari et al. (CSD ref. codes: ZZZPUS04 (form I), ZZZPUS05 (form II), ZZZPUS06 (form III), ZZZPUS07 (form IV)).[189]

The temperature driven conformational changes within the TB form I were reported for the first time by Hasegawa et al. who identified that TB form I^L (low temperature TB form I) was stable below the transition temperature of ca. 310 K and TB form I^H (high temperature TB form I) was stable above ca. 310 K.[273] The identification of a low temperature (100 K) TB form III (known as TB form III^2) was carried out independently by both Nath et al. and Drebushchak et al. in 2011 (CSD ref. codes ZZZPUS08[183], ZZZPUS11[271]).[183,271] TB form III^2 was found to have three molecules in the asymmetric unit as compared to one molecule in TB form III. The reversible transition between form III and form III^2 is accompanied by the elongation of the b axis of the unit cell of TB form III and an increase in the unit cell volume from ca. 1439.2 to ca. 4155.2 $Å^3$ at 100 K.[183,271] Furthermore, Nath et al. reported a highly unstable (2 hours at room temperature) TB form V, which could only be prepared by recrystallisation from acidified methanol (CSD ref. code ZZZPUS10).[183] The structural parameters of the different TB polymorphs are listed in Table 7-1.
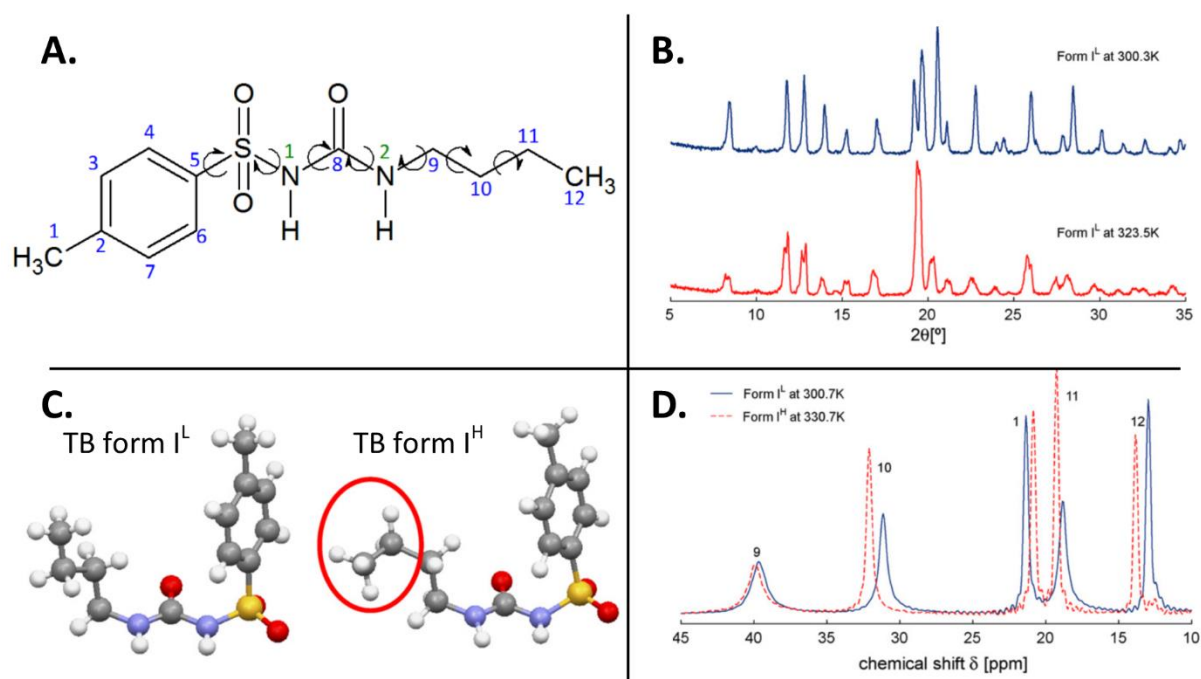
Figure 7-1. A. Numbering of carbon and nitrogen atoms; **B.** PXRD patterns of TB forms I^L and I^H; **C.** conformational changes in the structure of TB form I^L and TB form I^H; **D.** changes in the aliphatic region of TB form I^L upon heating and transition to TB form I^H. Adapted from [273].

Table 7-1. Crystallographic data of TB forms I-V reported by Thirunahari *et al.* and Nath *et al.*[183,189]

	Form I^L	Form I^H	Form II	Form III	Form III²	Form IV	Form V
Crystal habit	Prism		Plate	Needle	Needle	Needle	Plate
Colour	Colourless		Colourless	Colourless		White	Colourless
Crystal system	Orthorhombic	Orthorhombic	Monoclinic	Monoclinic	Monoclinic	Monoclinic	Orthorhombic
Temp. of structure determination (K)	153	363	153	153	100	298	298
Space group	$Pna2_1$	$Pna2_1$	Pc	$P2_1/n$	$P2_1/n$	$P2_1/c$	$Pbcn$
a (Å)	19.626(9)	20.8095(4)	9.087(8)	11.787(5)	11.5613(7)	10.091	15.851(6)
b (Å)	7.803(4)	7.9323(2)	17.228(3)	9.043(4)	27.189(4)	15.646	9.288(4)
c (Å)	9.058(4)	9.0610(2)	17.951(4)	13.955(6)	13.556(2)	9.261	19.691(8)
α (°)	90	90	90	90	90	90	90
β (°)	90	90	95.01(3)	104.644(7)	102.803(2)	100.49	90
γ (°)	90	90	90	90	90	90	90
V (Å³)	1387.3(11)	1494.67(5)	2799.8(10)	1439.2(10)	4155.2(11)	1438.9	2899.2(19)
Z/Z′	4/1	4/1	8/4	4/1	12/3	4/1	8/1
CSD ref. code	ZZZPUS04	N/A	ZZZPUS05	ZZZPUS06	ZZZPUS08	ZZZPUS07	ZZZPUS10
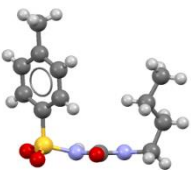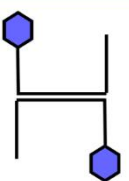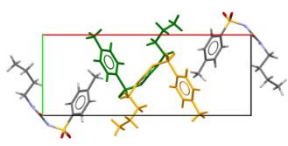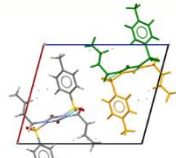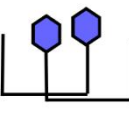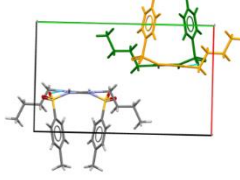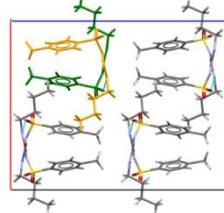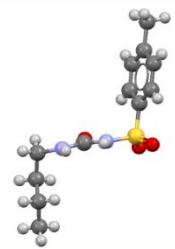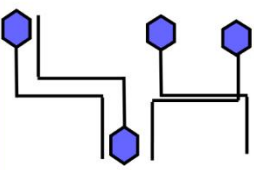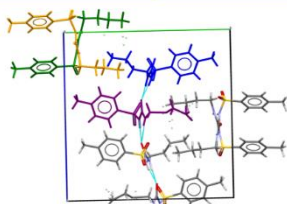
Conformation	Packing	Crystal structure	
		Form I	Form III
		Form IV	Form V
		Form II	

Figure 7-2. Conformations and packing arrangement of TB molecules in TB forms I-V based on the CSD structures ZZZPUS04 (form I), ZZZPUS05 (form II), ZZZPUS06 (form III), ZZZPUS07 (form IV), ZZZPUS10 (form V) (adopted from [189]).

Due to its high flexibility, TB adopts different conformations in different crystal forms and is therefore a representative example of conformational polymorphism. There are two types of conformations found within the crystalline structures of TB: the U-type and chair type. These conformations reflect the position of the phenyl ring and butyl tail with respect to the S-N1-C8-N2-C9 plane (Figure 7-2). In the U-type conformation the phenyl ring and the butyl chain are both at the same site of the S-N1-C8-N2-C9 plane, while in the chair type conformation the phenyl ring and the butyl tail are on the opposite sites of the sulfonylurea tape.[189] Based on the two conformation types, Thirunahari *et al.* proposed four packing schemes summarised in Figure 7-2. The proposed schemes take into account the relative orientation of the phenyl ring and butyl chain in adjacent molecules. For example, in the first packing scheme of TB forms I and III the two TB molecules lie on opposite sides of the urea tape bonding motif, while in the second packing scheme both the phenyl ring and the butyl chain are on the same side of the S-N1-C8-N2-C9 plane. Furthermore, similarly to other urea based compounds, the 'head-to-tail' (phenyl ring-to-butyl chain) packing mode is dominant in all TB polymorphs and stabilised by the bifurcated N-H···O hydrogen bonding synthon formed between two NH hydrogen donors and carbonyl acceptor.[183,189]

7.2 Results and discussion

7.2.1 Thermal, spectroscopic and computational studies of TB polymorphs

Variable temperature ^1H-^{13}C CP/MAS NMR studies of the phase transition between TB forms I^L and I^H were begun by Dr Lucy Hawarden as a part of her PhD program. Significant broadening of the aromatic carbon peaks was observed upon cooling of TB form I^L, however, due to time constrains this was not investigated further. In this section we aim to elucidate the motional processes within TB polymorphs (form I^L, form IV and confined forms I^L and form V). We made several attempts to crystallise pure TB forms II and III, but these forms were consistently obtained concomitantly with other structures. Using the method described by Nath *et al.* (crystallisation of form V from acidified methanol), we obtained colourless highly unstable crystals, which only formed on the vial walls, and quickly recrystallised to TB form I^L when scratched for analysis. In our experiments, TB form V was obtained inside the pores of the MCM-41 host (pores of *ca.* 2.6 nm in diameter - see section 7.2.3). Interestingly, in a control experiment (crystallisation from methanol without nitric acid), we always obtained fine white needles of TB form IV on the vial walls. These polymorphs were identified using a combination of PXRD, DSC and solid-state NMR (Figure 7-3, Figure 7-4).
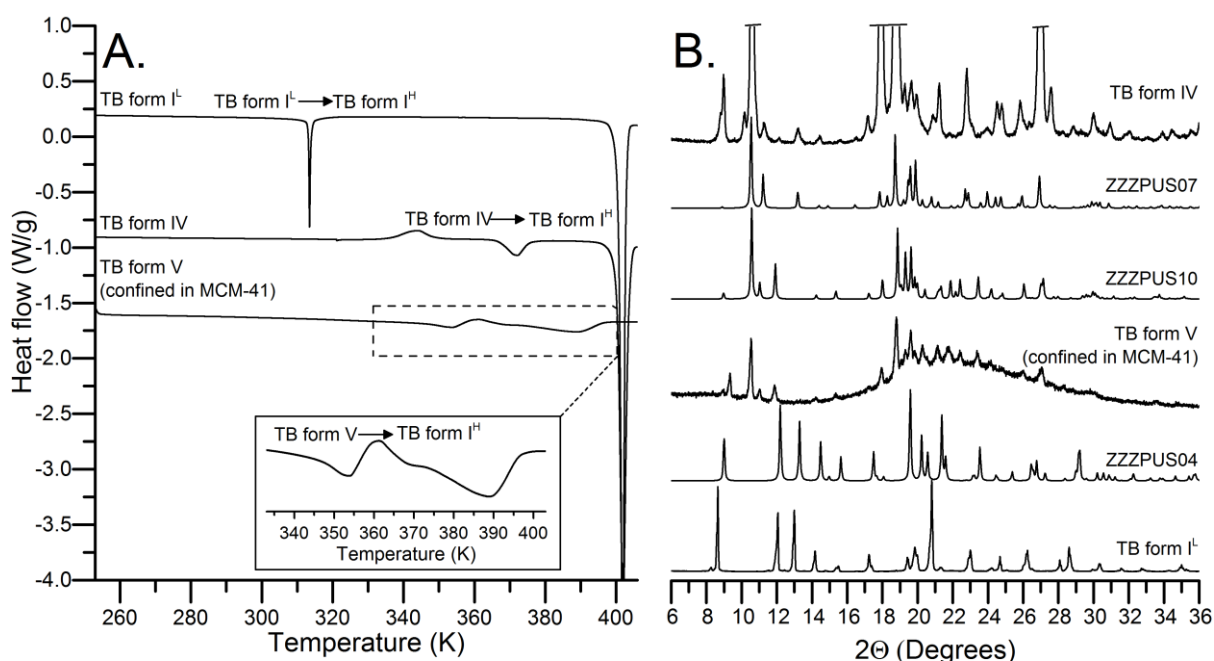
Figure 7-3. A. DSC thermograms; **B.** experimental and simulated PXRD patterns of TB form I (CSD ref. code ZZZPUS04[189]), form IV (CSD ref. code ZZZPUS07[189]) and form V (CSD ref. code ZZZPUS10[183]).

The PXRD patterns of TB forms used in this study (TB forms I, IV and V) were in good agreement with simulated PXRD patterns for CSD structures ZZZPUS04[189] (TB form I), ZZZPUS07[189] (TB form IV) and ZZZPUS10[183] (TB form V). The TB form IV crystallises as very fine, white needles which, even after grinding, displayed preferred orientation in PXRD patterns, manifested as strong intensity peaks with d(110) = 10.65 Å and d(210) = 18.72 Å. The stability order of TB polymorphs has been discussed separately by Burger, Kimura *et al.* and Thirunahari *et al.*[189,274,277] Although the latest comprehensive thermodynamic stability analysis by Thirunahari *et al.* showed TB form II to be the most stable form below *ca.* 353 K and TB form I^H the most stable form above *ca.* 353 K, we did not detect formation of TB form II at any stage of our studies. The analysed materials either recrystallised to TB form I^L when stored below *ca.* 315 K, or to TB form I^H upon heating. Based on our DSC studies, the clear transition of TB form I^L to TB form I^H was observed at *ca.* 315 K followed by melting of TB form I^H at *ca.* 399 K. TB form IV shows two transitions on heating – an exothermic transition with onset at 336 K followed by an endothermic transition with onset at 366.8 K. The VT solid-state NMR spectra of this material indicate that these changes could be related to a phase transition of TB form IV to TB form I^H (see section 7.2.2). There are some discrepancies between the DSC thermograms published by Thirunahari *et al.* and Kimura *et al.* which may be related to the analysis conditions, which are not fully specified by Kimura *et al.*[189,274] The DSC thermograms presented in this chapter were measured on multiple occasions using either crystallisation from methanol or the method described by Thirunahari *et al.* (crystallisation from acetonitrile).[189] The TB form V was formed from the melt inside the pores of MCM-41 material (see section 7.2.3). The PXRD pattern of TB form V shows a broad 'halo' peak of amorphous silica walls and slightly broadened peaks of TB form V due to size constraints for the confined crystals. There are no DSC data published on TB form V due to its thermodynamic instability. TB form V as a confined crystal shows an endothermic transition at *ca.* 333 K followed by melting of confined TB form I^H at *ca.* 373 K, proving the formation of confined crystals (see section 7.2.4).
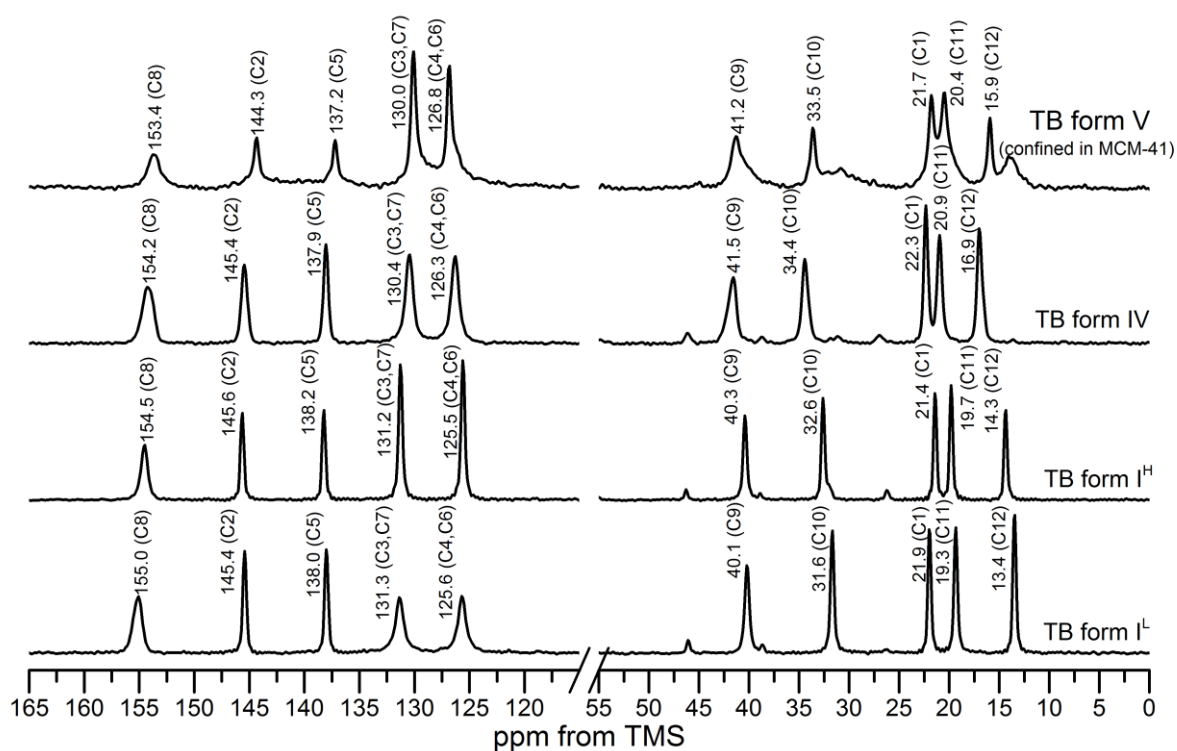
Figure 7-4. ^1H-^{13}C CP/MAS NMR spectra of TB forms I^L, I^H, IV and form V confined within MCM-41 pores (spectra acquired at 298 K).

^1H-^{13}C CP/MAS solid-state NMR spectra of TB forms I^L, I^H IV and V show 10 peaks for 12 carbon atoms in the TB structure grouped in 2 regions (aromatic and aliphatic). The number of peaks in the spectra indicates the presence of one molecule in the asymmetric unit, in agreement with crystallographic data. There are five well-separated peaks in the aliphatic region of the spectra between 10 and 45 ppm, while the aromatic and carbonyl carbons are grouped into the spectral region between 120 to 160 ppm as five separate peaks. The aromatic carbons C3/C7 and C4/C6 overlap to give a single peak at *ca.* 130 (C3/C7) and 126 (C4/C6) ppm, respectively (Figure 7-4). The ^{13}C chemical shifts (listed in Table 7-2) are in excellent agreement with the ^{13}C chemical shifts published by Kimura *et al.* for form I^L and form IV and Hasegawa *et al.* for forms I^L and I^H.[273,274] The presented ^1H-^{13}C CP/MAS NMR spectra are also in agreement with the spectra published by Thirunahari *et al.*[189] The phase transition between TB forms I^L and TB form I^H is detected by the changes in the ^{13}C peaks positions of the spectra recorded at 283 K and 333 K, in agreement with the ^1H-^{13}C CP/MAS spectra published by Hasegawa *et al.*[273] Additionally, a substantial narrowing of the peaks at 131.2 and 125.5 ppm is observed upon heating, which has not been previously discussed in any of the published papers and will be discussed in detail from a dynamical perspective in section 7.2.2.

The ^1H-^{13}C CP/MAS solid-state NMR spectrum of TB form V is shown in Figure 7-4 for the first time. As discussed in the previous chapters, the confined crystalline phase is usually present together

with confined amorphous species, therefore both components are observed in the spectrum. The ^{13}C spectrum of TB form V is composed of sharp resonances of the crystalline phase superimposed on slightly broadened peaks of the disordered species. There is an extra peak of amorphous TB present at *ca.* 12 ppm, observed previously in our group during analysis of amorphous solid dispersions of TB in a polymer matrix (Figure 7-4).[49]

The carbon peaks were assigned based on the papers of Kimura *et al.*, Thirunahri *et al*. and Hasegawa *et al.* Independently, we performed calculations of chemical shifts using CASTEP code for the TB structures reported in the CSD by Thirunahari *et al.* and Nath *et al.* (structures ZZZPUS04[189] (TB form I), ZZZPUS07[189] (TB form IV), ZZZPUS10[183] (TB form V)). The calculated ^{13}C chemical shifts are in very good agreement for all the three structures (Table 7-2; Figure 7-5). Contrary to the assignment proposed by Kimura *et al.,* the peak at *ca.* 130 ppm was assigned to sites C3/C7 and the peak at *ca.* 125 ppm was assigned to carbons C4/C6 based on the CASTEP results.

Table 7-2. Experimental and CASTEP calculated ^{13}C and ^{1}H chemical shifts of different TB polymorphs. [13]C experimental chemical shifts are compared to these published by Kimura *et al*. for TB form I[L] and IV and Hasegawa *et al*. for TB form I[H].

[13]C site	TB form I[L]			TB form I[H]		TB form IV			TB form V	
	δ_{exp}	δ_{exp}[274]	δ_{calc}	δ_{exp}	δ_{exp}[273]	δ_{exp}	δ_{exp}[274]	δ_{calc}	δ_{exp}	δ_{cal}
C1	21.9	21.8	19.6	21.4	20.9	22.3	22.1	19.5	21.7	19.7
C2	145.4	145.8	149.2	145.6	145.1	145.4	144.8	148.5	144.3	147.9
C3	131.3	126.2	133.9	131.2	125.1	130.4	127.2	133.4	130.0	133.3
C4	125.6	131.8	127.0	125.5	130.7	126.3	130.4	126.6	126.8	129.3
C5	138.0	138.1	140.8	138.2	137.8	137.9	137.5	141.8	137.2	139.5
C6	125.6	131.8	127.0	125.5	130.7	126.3	130.4	126.6	126.8	129.3
C7	131.3	126.2	133.9	131.2	125.1	130.4	127.2	133.4	130.3	133.3
C8	155.0	155.0	152.0	154.5	154.2	154.2	154.0	153.8	153.6	153.9
C9	40.1	40.1	37.3	40.3	40.0	41.5	41.5	39.9	41.2	40.0
C10	31.6	31.8	29.5	32.6	32.2	34.4	33.8	33.8	33.5	33.0
C11	19.3	19.4	15.5	19.7	19.3	20.9	20.7	18.3	20.4	18.7
C12	13.4	13.6	8.8	14.3	13.9	16.9	16.1	15.5	15.9	15.0

[1]H site	TB form I[L]		TB form IV	
	δ_{exp}	δ_{cal}	δ_{exp}	δ_{cal}
H1	1.9	2.1	1.9	2.2
H3;H7	7.6;7.6	7.7	6.1;6.6	6.5
H4;H6	7.2;7.4	7.3	6.3;6.9	6.5
H9a;b	2.5;3.2	3.1	3.5;3.5	3.3;3.3
H10a;b	0.0;1.3	0.4;0.8	1.1	0.7;0.8
H11a;b	1.4	1.3	1.1;1.9	1.0;1.5
H12	0.0	-0.4	0.2	0.1
NH1	10.8	11.3	10.2	11.3
NH2	7.6	7.9	7.7	7.8
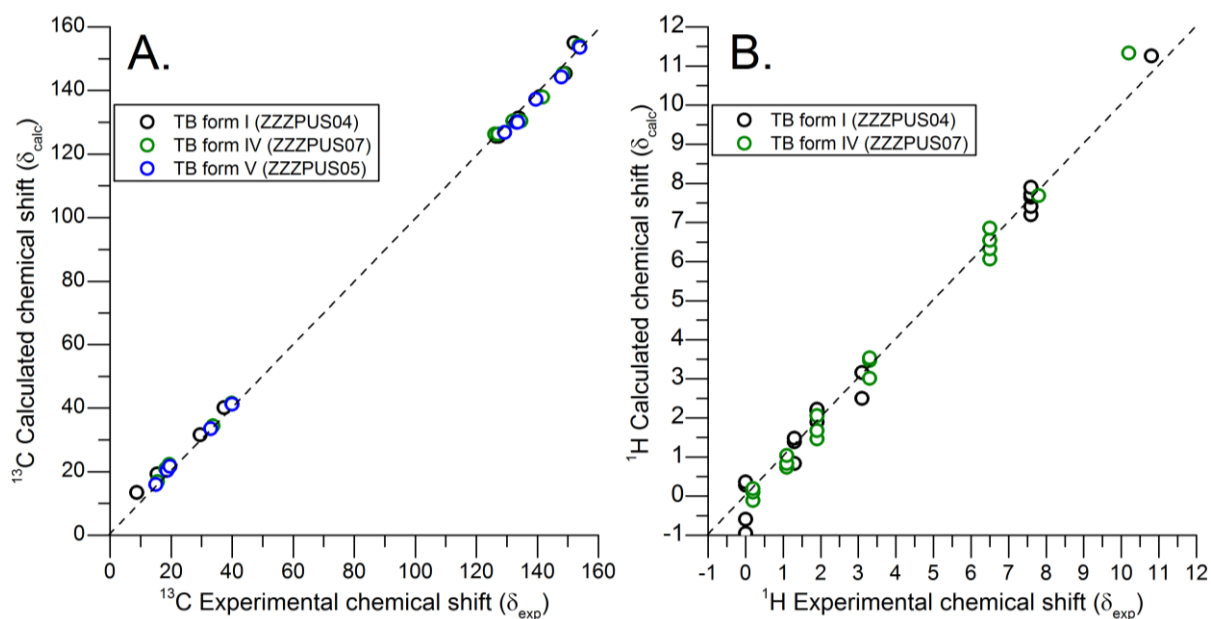
Figure 7-5. Comparison of experimental and CASTEP calculated **A.** ^{13}C and **B.** ^{1}H chemical shifts; the dashed line shows the perfect fit.
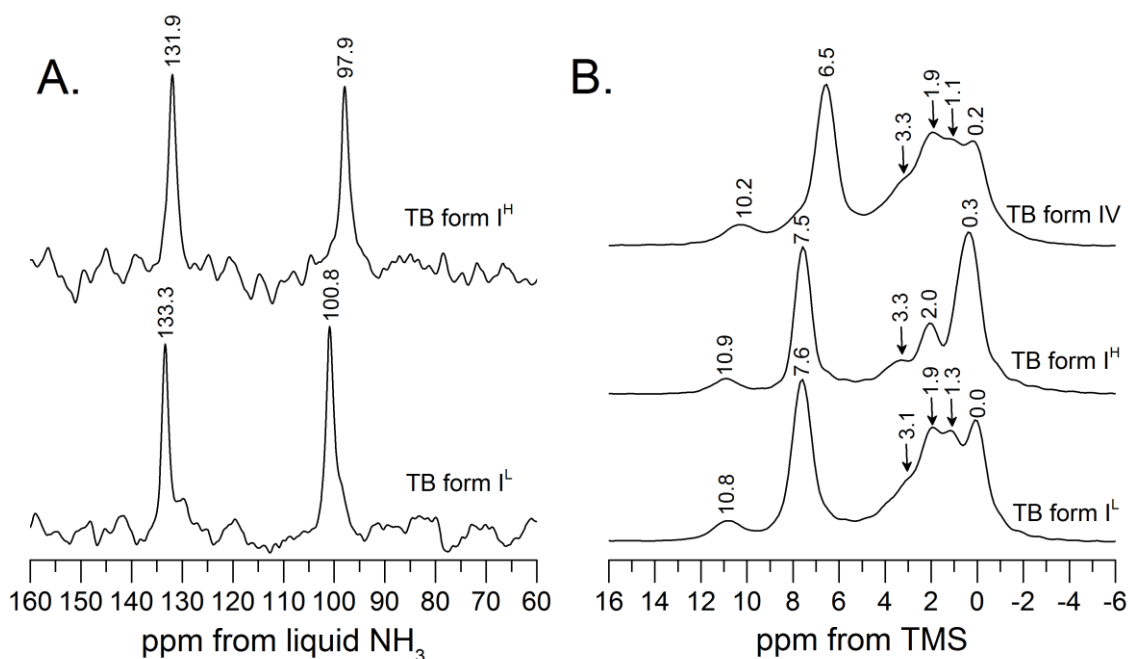
Figure 7-6. A. ^{1}H-^{15}N CP/MAS NMR spectra of TB forms I^L and I^H; **B.** ^{1}H CRAMPS spectra of TB forms I^L, I^H and TB form IV; the spectra were recorded at an MAS rate of 6.8 kHz.

The structural differences between TB form I^L and I^H can be visualised using ^{1}H-^{15}N CP/MAS spectra and ^{1}H CRAMPS spectra (Figure 7-6). The two ^{15}N sites in the TB structure result in two peaks in the ^{1}H-^{15}N CP/MAS spectra of TB form I^L at 100.8 ppm (N2) and 133.3 ppm (N1). Both peaks undergo an up-field shift of *ca.* 3 and 2 ppm, respectively, upon heating to 333 K due to the transition to TB

form I[H]. The assignment of both nitrogen sites was based on CASTEP calculations. The differences between TB polymorphs were investigated further using ^{1}H CRAMPS spectroscopy. The aromatic hydrogens of TB form I[L] were observed as a single peak at 7.6 ppm, while the aliphatic hydrogens lead to at least four peaks between 0 and 4 ppm. The conformational differences due to the TB form I[L] → TB form I[H] phase transition were reflected by a change in the aliphatic part of the spectrum, where three resonances can be seen. Although the U-shape conformation of TB form IV is similar to the conformation of TB form I[L] and TB form I[H], the differences in the packing scheme (see Figure 7-2) are highlighted by *ca.* 1 ppm up-field shift of the aromatic peak from 7.6 ppm in TB forms I[L] and I[H] to 6.5 ppm in TB form IV. All three structures show a similar urea tape hydrogen bonding pattern, reflected in only a slight up-field shift of the NH1 hydrogen peak (0.6 ppm) in the TB form IV spectrum compared to TB I[L] spectrum. The NH$_2$ proton peak is observed as a part of the aromatic peak in the spectra of both TB form I[L] and TB form I[H], appearing as a small shoulder peak in the TB form IV spectrum at *ca.* 7.6 ppm. All peaks observed in the ^{1}H CRAMPS spectra of TB form I[L] and form IV are in good agreement with CASTEP calculations of ^{1}H chemical shifts.

7.2.2 Variable temperature solid-state NMR studies of TB form I and TB form IV

NMR spectroscopy is a powerful and unique tool to study molecular dynamics over a wide range of timescales from 10^1 to 10^{-10} s, due to the sensitivity of magnetic interactions for molecular motions.[139,140,279] The possible molecular motions observed in solids include conformational changes, fluxionality, molecular reorientation and pseudorotations, and can be divided into slow < 10^3 Hz, intermediate $10^3 - 10^6$ Hz and fast > 10^6 Hz.[139,140,279] These are manifested as changes in NMR relaxation properties and NMR parameters sensitive to motional averaging, including CSA and dipolar interactions.[279] Importantly, some of the molecular motions detected using NMR spectroscopy are undetectable using diffraction based techniques, unless they lead to positional disorder.[279] This is due to differences in the timescale of diffraction processes, which are very fast (10^{-18} s) compared to the broad timescale of interactions which are possible to analyse using NMR spectroscopy.[279] Detailed studies of TB form I were started recently in our group due to the detection of unusual dynamic behaviour of the phenyl carbons C3/C7 and C4/C6 in the ^{1}H-^{13}C CP/MAS NMR spectra at low temperatures (Figure 7-7). These changes could be explained as either thermally induced disorder around the aromatic part of TB or dynamics of the aromatic ring, which at lower temperatures may be manifested as loss of structural equivalence of different aromatic carbon sites leading to distribution of ^{13}C chemical shifts.[49]
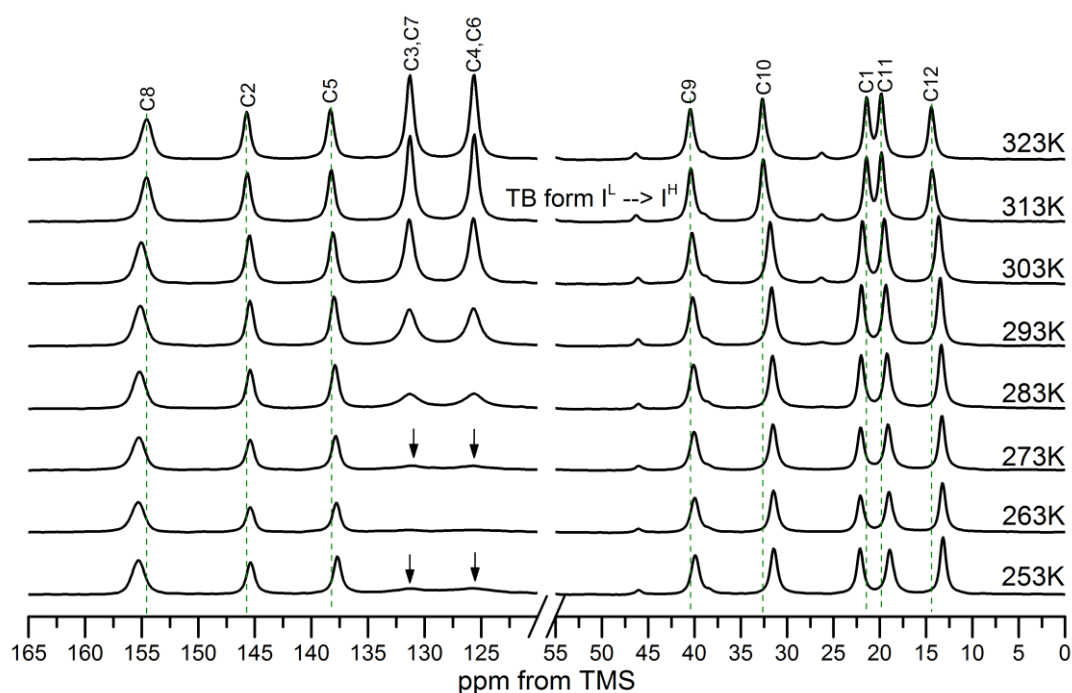
Figure 7-7. ^{1}H-^{13}C VT CP/MAS NMR spectra of TB form I^L (all spectra acquired at an MAS rate of 10 kHz).

It was shown recently by Nath *et al*. and Drebushchak *et al.* using diffraction studies that TB form III undergoes structural changes at temperatures below 150 K, where one of the cell parameters *(b)* triples, leading to a structure with Z'=3 compared to Z'=1 structure at room temperature.[183,271] Furthermore, room temperature TB form III shows a significant disorder of the butyl chain. Based on this result, Drebushchak *et al.* performed a similar study for TB form I and TB form II. As reported by these authors, the two forms do not change upon cooling to 100 K.[271] In relation to the crystallographic data from Drebushchak *et al.*, the gradual broadening and loss of intensity of aromatic carbons observed in our ^{1}H-^{13}C CP/MAS spectra of TB form I is unlikely to be a result of major structural rearrangements within the crystal. Thirunahari *et al.* described significant changes in the calculated and experimental PXRD patterns of TB form I at room temperature and at 153 K, which were explained by thermal effects on the lattice parameters and anisotropy of the lattice contractions at low temperature. The redetermination of the crystal structure at room temperature revealed slight torsional changes in the butyl chain of TB, while the aromatic part of the molecule was not affected.[189]

Substantial broadening and loss of signal intensity of phenyl carbons undergoing a 180° reorientation or 'flip' motions in ^{1}H-^{13}C CP/MAS NMR spectra were observed for several crystalline penicillin salts, ibuprofen-Na salt and L-phenylalanine HCl salt (Figure 7-8).[139,279–281] Such dynamics of the phenyl ring lead to equivalence of *ortho* (C3/C7) and *meta* (C4/C6) carbon peaks in the fast limit on the broadening-exchange timescale, while carbons in the *ipso* (C2) and *para* (C5) positions are unaffected by this motion.[279] The possible mechanisms of line broadening in the ^{1}H-^{13}C CP/MAS

NMR spectra under MAS and ^{1}H decoupling were investigated in details by Vanderhart *et al.* who indicated that molecular motions in solids at the frequencies of the ^{1}H decoupling can cause line broadening due to enhanced relaxation for transverse ^{13}C magnetisation.[282] Rothwell and Waugh showed that the temperature dependence of the broadening enables determination of the rates and types of rotational motions in solids using examples of hexamethylbenzene, hexamethyletane and adamantane.[283] The mechanism of broadening was explained to be due to enhanced relaxation of S spins in the presence of molecular motions (incoherent averaging), which reduces the efficiency of *rf* decoupling (coherent averaging), particularly when both processes are on the same timescale.[283] It was further shown by Long, Bowen and Griffin that molecular motions may interfere with particular frequencies of the pulse trains and *rf* fields leading to 'disappearing lines'. This was shown for labelled alanine using VT ^{1}H spectra under CRAMPS decoupling and [15]N{[1]H} under CW decoupling.[284] The interference of the TB phenyl ring motions with [1]H-^{13}C dipolar decoupling frequencies (here *ca.* 80 kHz) resulted in substantial broadening of the aromatic peaks C3/C7 and C4/C6 in the spectra. [279,280] This indicates motion of the phenyl ring in the crystal structure in the range of kHz or tens of kHz.[139]
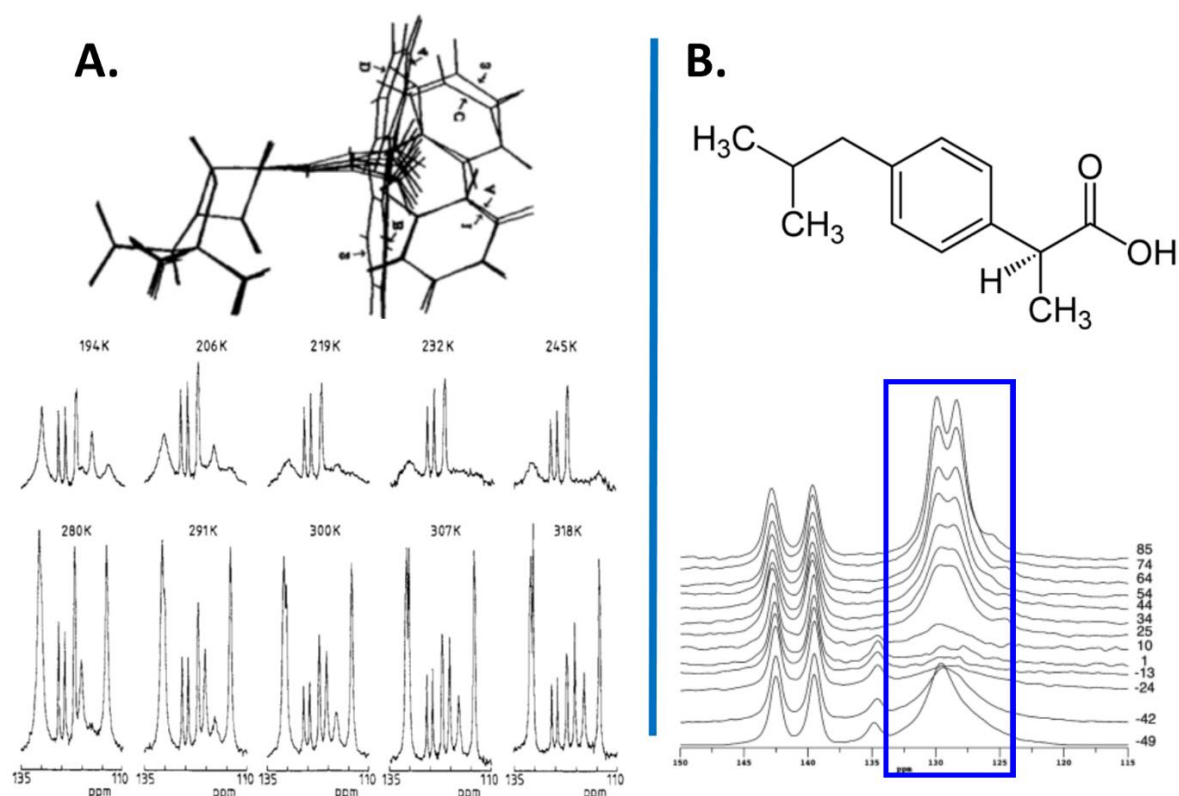
Figure 7-8. A. An overlay of different potassium penicillin salt structures, which undergo dynamical interchange and effect of motion on the aromatic region of VT [1]H-^{13}C CP/MAS spectra. **B.** Structure of ibuprofen and an effect of aromatic ring motions on VT [1]H-^{13}C CP/MAS spectra. Adapted from [139,279].

Very recently (June 2016) Drebushchak *et al*. published detailed structural analysis of the TB I^L→ TB I^H phase transition, which was described as single crystal to single crystal conformation transformation between two phases using variable temperature single crystal X-ray studies.[285] The authors solved the crystal structure of TB form I^H, which is now deposited in CSD database. The unit cell parameters and the space group of newly solved structure is in agreement with the data published previously by Hasegawa *et al.* if taking into account the thermal expansion. Based on the recent structural studies by Drebushchak *et al.,* the ordered aliphatic tail of TB form I^L is disordered in the TB form I^H, split between two positions. The size of thermal ellipsoids of carbons C10 and C12 increases significantly, while the position of carbon C11 is split into two ellipsoids with occupancies of 0.59(3) and 0.41(3) (Figure 7-9). Despite of the disorder of the alkyl tail, the space group remains unchanged and molecular pacing and hydrogen bonding is largely unaffected by the TB form I^L→TB form I^H polymorphic transformation.[285]

TB form I^L 100 K   TB form I^L 200 K   TB form I^L 295 K   TB form I^H 330 K
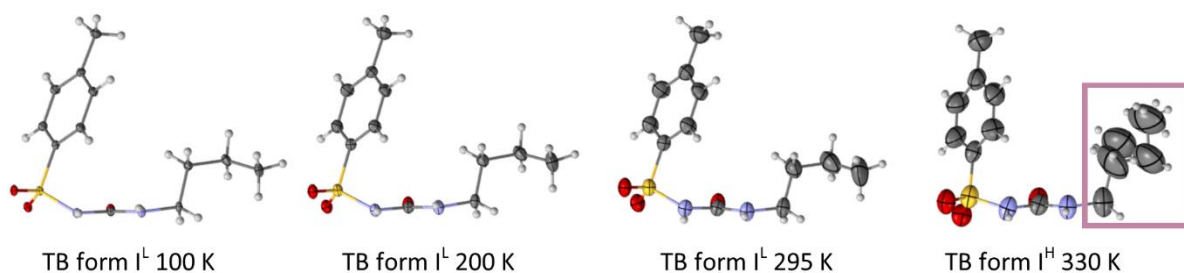
Figure 7-9. The asymmetric unit of TB form I at different temperatures. The displacement ellipsoids are drawn with 50 % probability. The disordered aliphatic tail at 330 K is highlighted in the box. Adapted from [285].

The structural studies of Drebushchak *et al*. highlight that, as observed by our group, the disappearance of the aromatic ^{13}C peaks in the VT ^{1}H-^{13}C CP/MAS experiment is not related to the structural disorder in the aromatic part of the molecules, but as discussed previously it is likely due to the mobility of the aromatic ring interfering with the *rf* field of heteronuclear dipolar decoupling. The structural disorder of the aliphatic part of the molecule above the TB form I^L→TB form I^H phase transition may explain the differences in the ^{1}H T$_{1\rho}$ and ^{1}H T$_1$ times above the phase transition temperature, which are likely to be related to the molecular motions being dominated by the dynamics of aliphatic tail of the molecule (Figure 7-11, Figure 7-12).
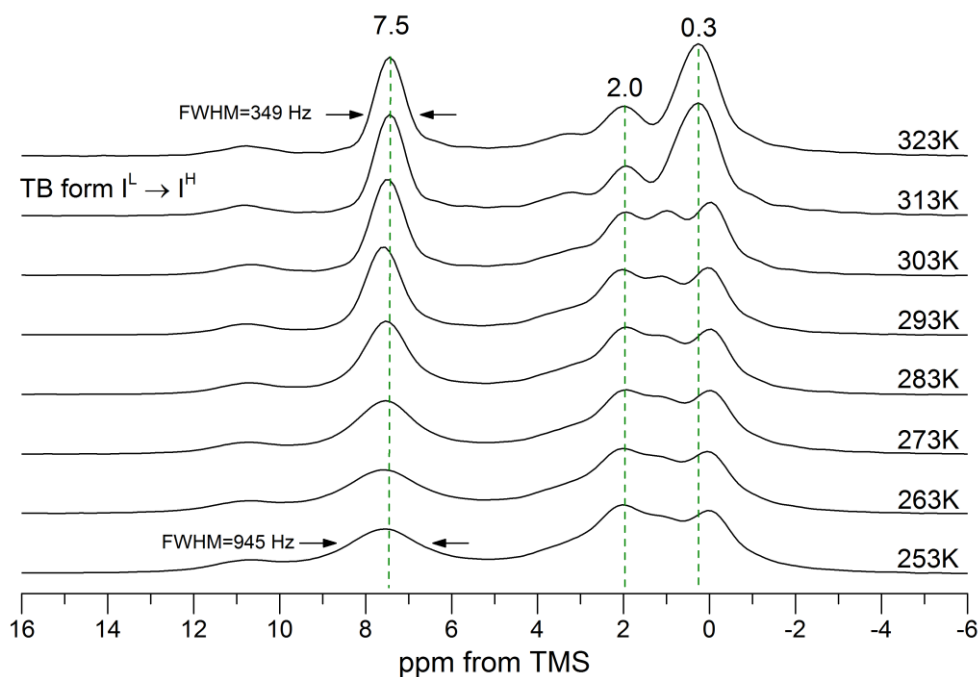
Figure 7-10. ^{1}H VT CRAMPS spectra of TB form I^L (all spectra acquired at 6.8 kHz).

The phase transition of TB form I^L to TB form I^H and broadening of the aromatic carbons C3/C7 and C4/C6 in the ^{1}H-^{13}C CP/MAS spectra are corroborated by VT ^{1}H CRAMPS spectra (Figure 7-10). Significant broadening (FWHM = 945 Hz) of the aromatic peak of the spectrum at *ca.* 7.5 ppm was observed at 253 K as compared to the spectrum recorded at 323 K (FWHM = 349 Hz). The broadening of the peak may indicate an increased distribution of possible ^{1}H chemical shifts of the hydrogens H3/H7 and H4/H6 due to the loss of equivalence between different proton sites due to slowing the motion of the aromatic ring. The aliphatic component of the spectra broadens to a much lesser extent with decreasing temperature, indicating only minor structural changes in the butyl chain of TB at low temperatures. In contrast to this, an increase in temperature above the phase transition of TB form I^L →TB form I^H results in the merging of two peaks at 0.0 ppm and 1.9 ppm in a one broad resonance at 0.3 ppm in the ^{1}H CRAMPS spectra, related to conformational changes of the butyl chain between TB form I^L and TB form I^H.

Variable temperature measurements of ^{1}H T_1 and ^{1}H $T_{1\rho}$ relaxation times of the TB form I were started in our group by Dr Lucy Hawarden and highlighted the differences in dynamics between TB form I^L and TB form I^H.[49] Here we have continued this work by performing the measurements for TB form IV and expanding the temperature scale of the experiments for TB form I. ^{1}H relaxation is dominated by homonuclear dipolar interactions, averaging T_1 and $T_{1\rho}$ relaxation times of different protons to a single value.[139,140]
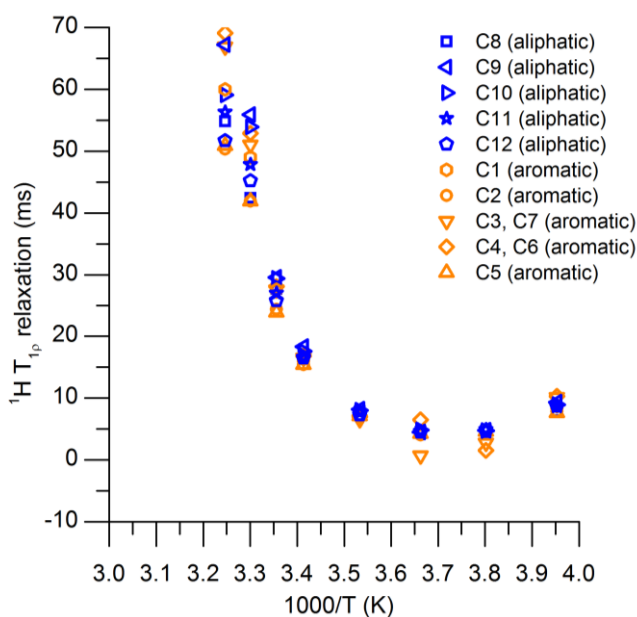
Figure 7-11. Variable temperature ^1H $T_{1\rho}$ times of TB form I^L. The expected errors for the method are between 5 to 10 %.

VT ^1H $T_{1\rho}$ relaxation time measurements of TB form I show two types of behaviour. Below the phase transition at 313 K, single values of ^1H $T_{1\rho}$ times were observed for all proton sites, with a clear minimum at *ca.* 263 K. Above the phase transition, a substantial increase in distribution of the ^1H $T_{1\rho}$ relaxation times was observed, with values too long to be determined accurately (above 70 ms).[139,140,279] The parameters of the motions calculated previously in our group indicate a τ_c of 5.6×10^{-4} s with an activation energy of 56.6 kJ mol^{-1}.[49] The substantial differences in the ^1H $T_{1\rho}$ relaxation times between TB form I^L and TB form I^H indicate that both structures have very different dynamic behaviour despite their structural similarities.
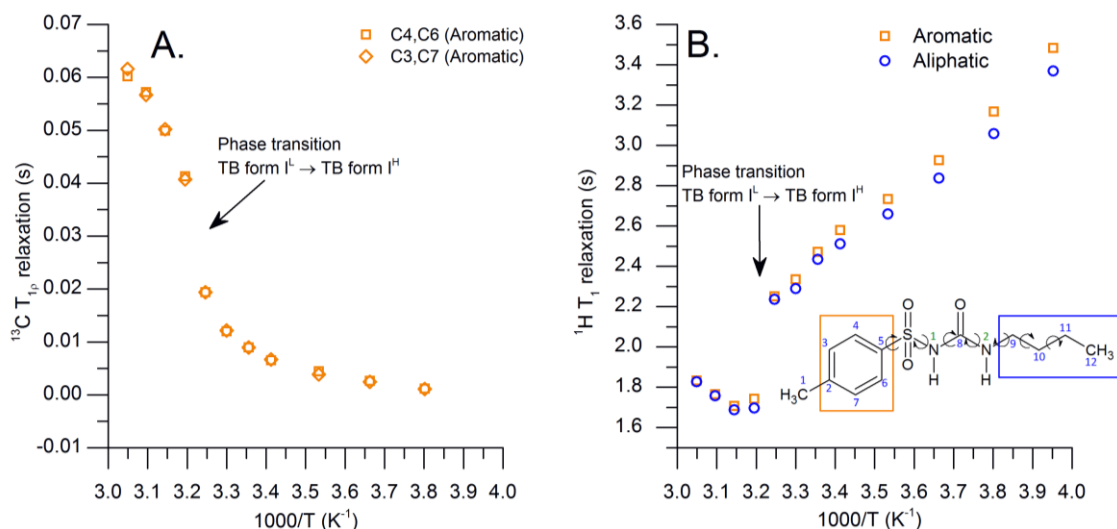
Figure 7-12. Variable temperature **A.** ^{13}C $T_{1\rho}$ times and **B.** ^1H T_1 times of TB form I^L. The expected errors for the method are between 5 to 10 %.

The VT ^{1}H T_1 relaxation times show slight differences between aromatic and aliphatic hydrogens in the temperature range from 253 to 293 K which may indicate that both sites are in slightly different motional regimes. The ^{1}H T_1 relaxation times measured as a function of increasing temperature show a substantial drop in the relaxation times values from *ca.* 2.2 s to 1.7 s around the TB form I^L → TB form I^H transition temperature at *ca.* 313 K. This indicates a dramatic change in the dynamics of TB form I^L above its phase transition temperature. The ^{1}H T_1 relaxation times for both aromatic and aliphatic sites are equal above the phase transition temperature, indicating a sufficient averaging of the relaxation times through the spin diffusion phenomenon. The ^{1}H T_1 relaxation time minimum at *ca.* 318 K, slightly above the phase transition temperature, describes molecular motions of TB on the MHz timescale, which are likely to be dominated by the movement of butyl tail. The activation energy of this motion was previously calculated to be 6.77 kJ mol^{-1}.[49]

The interpretation of ^{13}C $T_{1\rho}$ relaxation (^{13}C $T_{1\rho}^{exp}$) times is not straightforward, as it does not only represent a purely dynamical contribution from the spin-lattice relaxation in the rotating frame (^{13}C $T_{1\rho}^{dyn}$), but it can also be affected by spin-spin interactions between thermally coupled ^{13}C and ^{1}H spins (T_{CH}^{D}). Furthermore, the ^{1}H-^{13}C dipolar interaction (T_{CH}^{D}) relaxes to the lattice with the time constant T_{1D}, hence the observed ^{13}C $T_{1\rho}^{exp}$ relaxation times includes contributions from T_{CH}^{D}, T_{1D} and the heat capacity of proton dipolar reservoir.[140,286]

Both aromatic ^{13}C sites (C3/C7 and C4/C6) have relatively short (up to 70 ms) and similar ^{13}C $T_{1\rho}$ relaxation times as compared to other ^{13}C sites, which show a wide distribution of experimental ^{13}C $T_{1\rho}$ relaxation times. The temperature dependence of the ^{13}C $T_{1\rho}$ relaxation times of both aromatic carbon sites showed a broad minimum at 253-263 K (due to the low resolution of the spectra acquired at 253 K, the ^{13}C $T_{1\rho}$ times could not be measured accurately) and a substantial increase in the ^{13}C $T_{1\rho}$ relaxation times above the TB form I^L→TB form I^H phase transition temperature. Interestingly, the substantial increase in relaxation times of both aromatic carbon sites was observed above the phase transition temperature at *ca.* 313 K. This is another proof of drastic change in dynamic properties between TB form I^L and TB form I^H, which is likely due to the structural disorder of the aliphatic tail for TB form I^H as compared to TB form I^L. The structural changes observed by Drebushchak *et al.* using single crystal X-ray diffraction may indicate the dynamics of TB above the phase transition temperature (*ca.* 313 K) is dominated by the fast motions of the aliphatic part of the molecule, which is expected to be on the MHz timescale.[285] The increased disorder of the butyl tail at room temperature was also observed by the same group for TB form III.
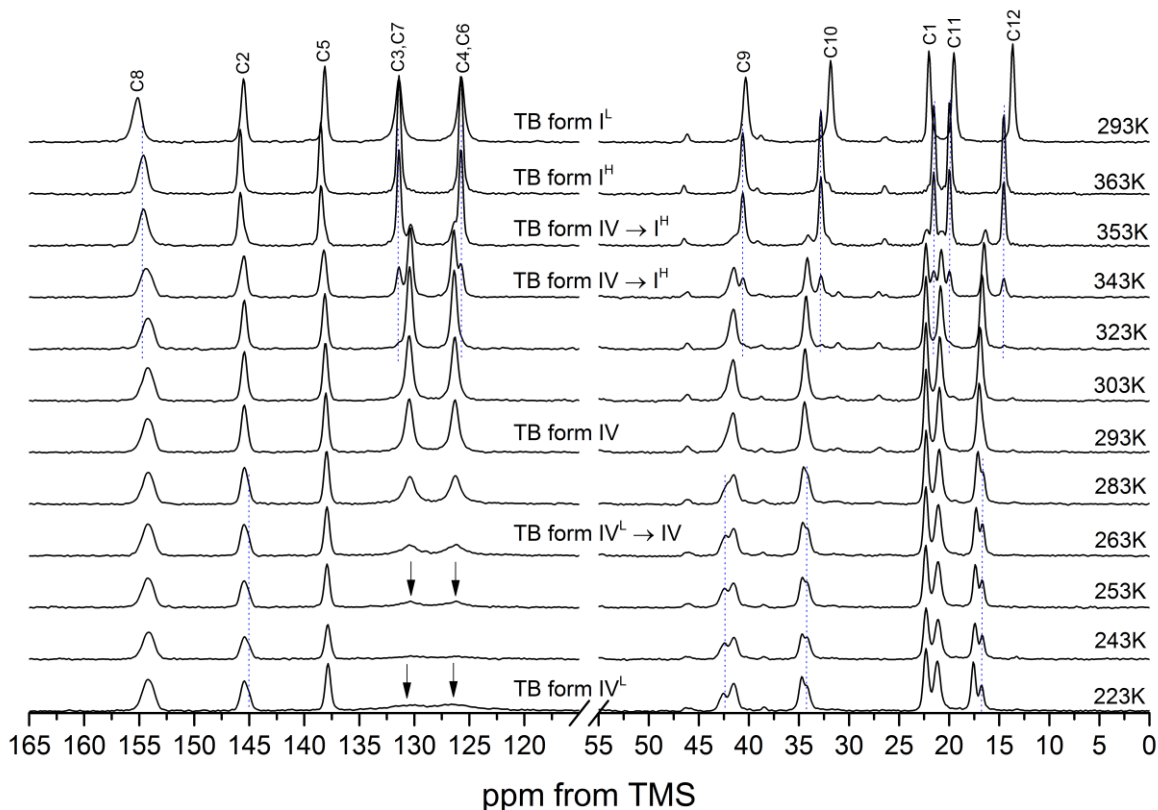
Figure 7-13. ^{1}H-^{13}C VT CP/MAS NMR spectra of TB form IV (all spectra acquired at an MAS rate of 10 kHz).

As at least two TB polymorphs (TB form I and TB form III) show unusual structural and dynamic behaviour at low temperatures, we decided to expand the VT solid-state NMR studies to include TB form IV.[183,271,273] It is known that TB form IV undergoes a phase transition to TB form I^H in the range of temperatures between 343 and 373 K.[61,189,287] These changes were monitored using ^{1}H-^{13}C CP/MAS NMR spectra at 343 and 353 K, where peaks from TB form IV and TB form I^H are observable (Figure 7-13). Following cooling of the sample back to room temperature, the spectrum attributable to TB form I^L was obtained, indicating that the phase transition from TB form IV →TB form I^H is irreversible. This is in agreement with previous reports, as TB form I^H is the most stable form above *ca.* 343 K.[189] During the gradual cooling of TB form IV to 223 K, significant broadening and a decrease of the intensity of the aromatic carbons C3/C7 and C4/C6 peaks was observed, with a minimum at *ca.* 243 K (20 K below the minimum observed in the spectra of Tb form I^L). Additionally, line broadening (C8, C2, C1, C11) or growth of new carbon peaks (C9, C10, C12) were observed in the spectra below 283 K, indicating a loss of chemical equivalence of TB molecules in the crystal structure. This is likely due to a low temperature phase transition of TB form IV below 283 K. The TB form IV→TB form IV^L transition may be similar the TB form III→TB form III^2 at low temperatures, where the translational symmetry changes due to the changes in the conformation of every third molecule leading to Z'=3 structure with two molecules in a gauche conformation and one molecule

with a trans conformation of the butyl tail. As this is the first observation of TB form IV undergoing structural changes at low temperatures, we will refer to it as low temperature TB form IV: TB form IV^L.
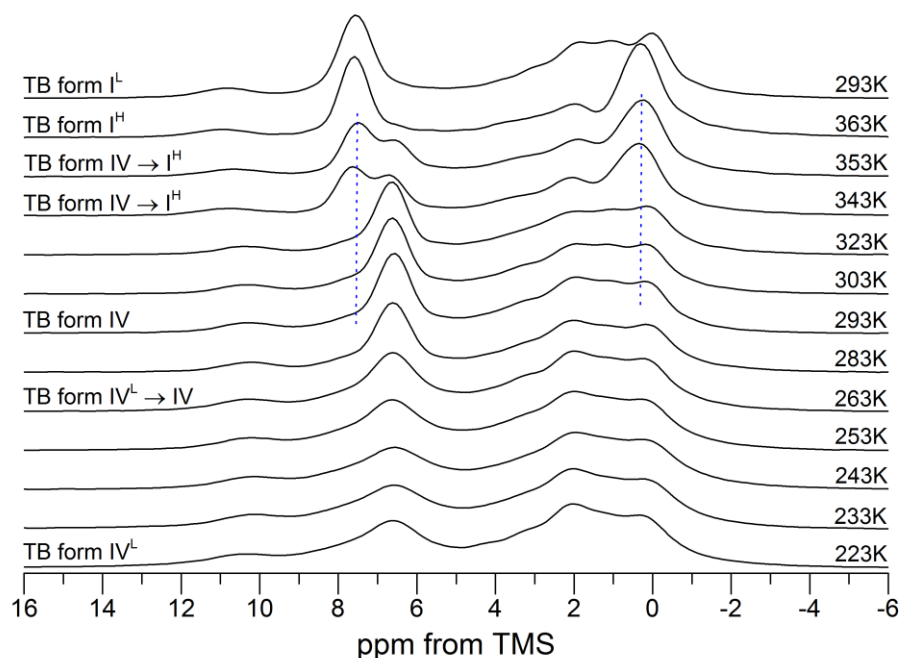
Figure 7-14. ^{1}H VT CRAMPS spectra of TB form IV (all spectra acquired at an MAS rate of 6.8 kHz).

The structural changes observed in the ^{1}H-^{13}C CP/MAS spectra are corroborated by VT ^{1}H CRAMPS spectra. Firstly, the phase transition between TB form IV and TB form I^H was successfully monitored using ^{1}H CRAMPS. The substantial differences in the aromatic region of the spectra are observed between 343 and 353 K, where the two aromatic peaks at *ca.* 6.5 ppm (TB form IV) and *ca.* 7.5 ppm (TB form I^H) indicate the simultaneous presence of both TB forms. The low temperature transition, clearly observed in the ^{13}C spectra is not so evident in the ^{1}H CRAMPS spectra. At temperatures below 283 K, the broadening of all ^{1}H sites may indicate structural changes displayed as a distribution of ^{1}H chemical shifts of different hydrogen sites. Additional broadening of the aromatic peak in the spectrum may be related to the dynamics of aromatic ring, as observed previously for TB form I^L.
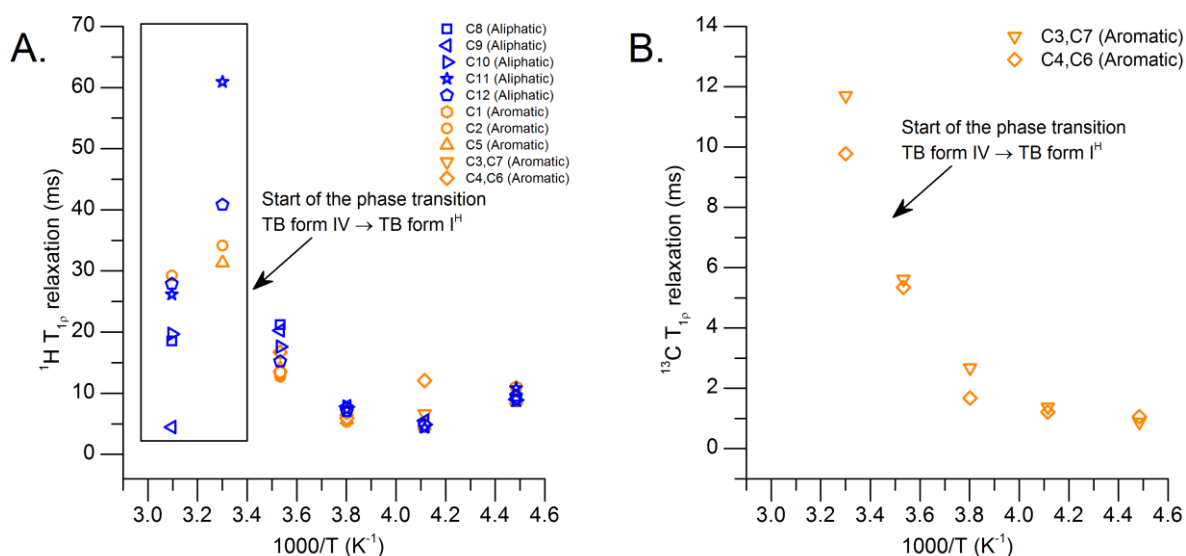
Figure 7-15. Variable temperature ^1H $T_{1\rho}$ and ^{13}C $T_{1\rho}$ times of TB form IV (left) and zoomed temperature region (right) with uniform relaxation times for all ^1H sites. The expected errors for the method are between 5 to 10 %.

The VT ^1H $T_{1\rho}$ measurements of TB form IV showed averaged relaxation times across all ^1H sites with a clear minimum at *ca.* 243 K, which is 20 K lower than the minimum observed for VT ^1H $T_{1\rho}$ times for TB form I^L. The distribution of measured ^1H $T_{1\rho}$ relaxation times for all ^1H sites is evident at temperatures above 303 K. This is indicative of the start of TB form IV → TB form I^H phase transition as small peaks of TB form I^H are displayed in the ^1H-^{13}C CP/MAS spectrum acquired at 323 K. The VT ^{13}C $T_{1\rho}$ times of aromatic carbons C3/C7 and C4/C6 of TB form IV show the start of a broad minimum at *ca.* 223-243 K, with an increase in relaxation times with increasing temperature, similar to the effects observed for TB form I^L. The ^{13}C $T_{1\rho}$ relaxation times for other carbon sites of TB form IV showed very long values, with a wide distribution of relaxation times, hence were not used for comparison. The ^{13}C $T_{1\rho}$ relaxation is driven mostly by heteronuclear dipolar interactions, therefore relaxation processes of quaternary carbons are complex and cannot be assessed accurately using simple models. In the case of the aliphatic carbons of TB, their relaxation is dominated by the fast motions of the aliphatic part of molecule (MHz timescale) therefore cannot be measured through ^{13}C $T_{1\rho}$ relaxation measurements.

The structural and dynamical studies of two TB polymorphs, *i.e.*, TB form I and TB form IV, using VT ^1H CRAMPS and ^1H-^{13}C CP/MAS solid-state NMR spectroscopy and relaxation measurements have shown the molecular motions at low temperatures are likely to be dominated by dynamics of the aromatic ring in both TB structures. To fully understand the motions of the phenyl ring of crystalline TB, it is important to use more sophisticated solid-state NMR methods including observation of ^2H nuclei, 2D exchange or CODEX experiments.[125,126,281]

Solid-state ^{2}H NMR (I = 1) is a widely used method to probe dynamics in the solids due to relatively small (*ca.* 250 kHz) first-order quadrupolar coupling interaction, which allows probing molecular motions in a timescale between 10^{-4} and 10^{-7} s.[126,288] The appearance of the ^{2}H NMR static spectrum is affected by molecular motions due to partial averaging of the ^{2}H quadrupolar interactions and changes in the line shapes. Furthermore, the quadrupolar coupling in ^{2}H NMR is highly sensitive to internal molecular motions with respect to the external magnetic field. Therefore, the analysis of static lineshapes enables an insight into the mechanism and timescale of atomic and molecular motions in solids. In addition to quadrupolar couplings, ^{2}H T_1 relaxation measurements may be used to calculate the rate of molecular motions.[125,126,289,290] ^{2}H MAS NMR has gained much interest in the last decade due to its increased sensitivity and resolution based on the distinct chemical shift of different ^{2}H sites and possibility to probe the motions on the microsecond timescale.[266,288,291,292] The solid-state ^{2}H NMR was applied successfully to probe molecular motions of the ring in poly(L-phenylalanine),[290] dynamics of polymers,[289] hydrated clays[288,291] and encapsulated molecules within the porous solids.[91,266,289,292–294]

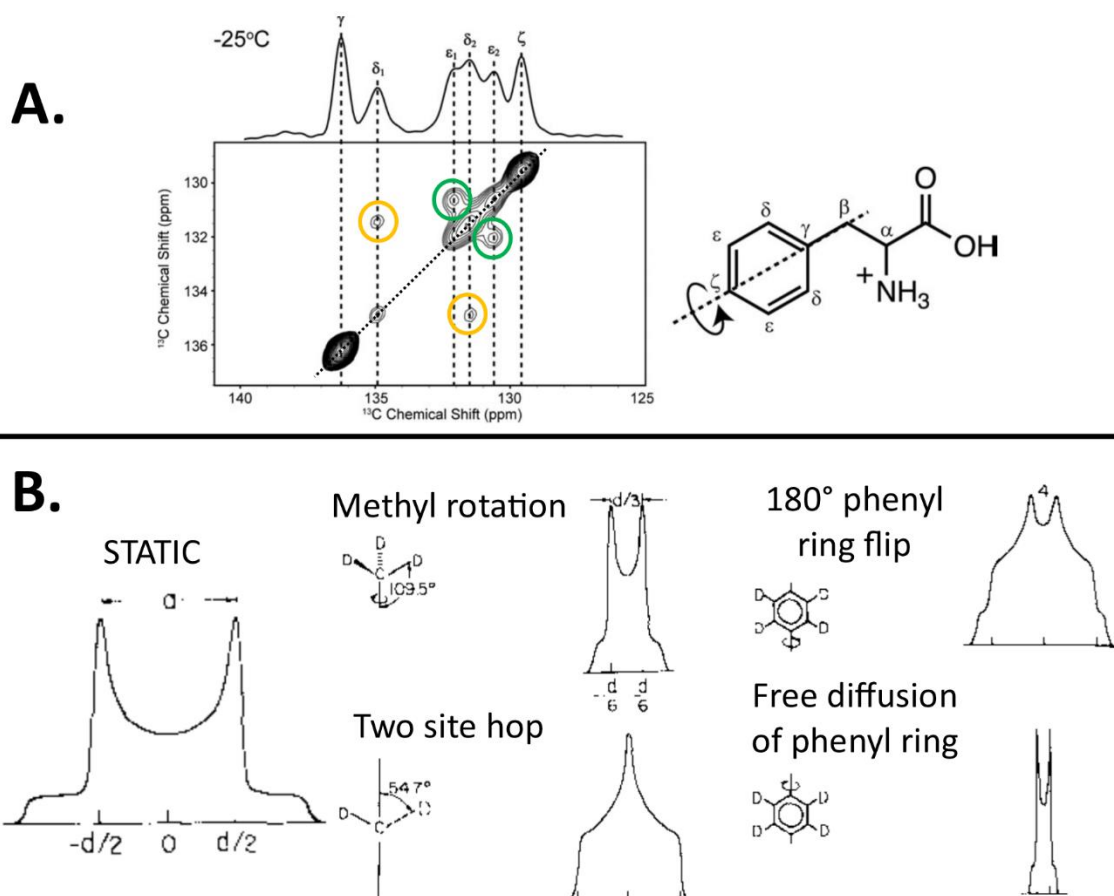**Figure 7-16. A.** 2D exchange spectrum of ^{13}C sites in phenylalanine – two sites undergoing 180° flip exchange are shown as cross peaks circled in yellow and green. **B.** Calculated ^{2}H solid-state NMR line shapes for static carbon-deuterium pair or undergoing different motions. Adapted from [281,289].

The dynamics of different sites of the molecule can be probed using 2D exchange experiment. Although this method enables the identification of the motional model and calculation of motion rates, its full evaluation requires chemical shift separation between exchanging sites and large amount of spectrometer time for acquisition of multiple 2D spectra.[281] As an alternative, the 1D centerband-only detection of exchange (CODEX) experiment was proposed, which enables to determine both the exchange rate and amplitude of motion on the ms to s timescale. CODEX uses anisotropic interactions (chemical shift anisotropy or heteronuclear dipolar interactions) to encode the molecular orientation and monitor the ability to refocus the spatially dependent interaction as a function of mixing time.[281,295,296] Examples of NMR methods to probe molecular motions are highlighted in Figure 7-16.

The low temperature TB form IV^L with Z' > 1 was detected below 283 K using VT ^{1}H-^{13}C CP/MAS experiments. Although the peak splitting observed may indicate this structure has two molecules in the asymmetric unit, relative intensities between different ^{13}C sites suggest the Z' = 3 structure is also possible. To answer this question, it would be necessary to perform additional experiments at higher magnetic field, to achieve a better resolution in the ^{1}H-^{13}C CP/MAS spectrum and acquire single pulse ^{13}C spectra below the transition temperature for precise quantification of different ^{13}C sites. Full proof of this transition is the subject of further research using VT PXRD and VT IR studies in collaboration with Dr Doris Braun at the University of Innsbruck and VT THz studies in collaboration with Dr J. Axel Zeitler at Cambridge University. PXRD would unequivocally prove changes in the long-range ordering of the TB form IV crystal at low temperatures. Furthermore, both vibrational spectroscopies, frequently used in the characterisation of pharmaceutical polymorphism, may provide additional information on changes in hydrogen bonding and changes in lattice vibrations upon cooling, which could be correlated with the dynamics of phenyl ring.[297–299]

In summary, it was shown using VT ^{1}H-^{13}C CP/MAS, ^{1}H CRAMPS, ^{1}H T1 and ^{1}H $T_{1\rho}$ relaxation measurements that two different polymorphs of tolbutamide TB form I and TB form IV have similar dynamics of the aromatic ring, which was found to be on the kHz timescale. The molecular motions below the temperature of the TB form I^L→TB form I^H and TB form IV→TB form I^H phase transitions are dominated by the ring dynamics in both TB crystals, as minima in the temperature dependence of ^{1}H $T_{1\rho}$ were detected for both phases. The disorder of the butyl tail in TB form I^H reported recently by Drebushchak *et al*. may explain the drastic change in the dynamics of the system above the phase transition temperature, which is dominated by fast motions, observed as a minimum at *ca.* 313 K in the temperature dependence of ^{1}H T_1 relaxation times. Additionally, we reported new low temperature phase of TB form IV (TB form IV^L), detected below 283 K, which will be the subject of further structural studies.

7.2.3 Formation of nano-crystalline metastable TB form V within mesoporous MCM-41 material

7.2.3.1 Textural properties of TB loaded materials

Synthesised sub-micrometre spherical particles of the MCM-41 host with pore size diameter of *ca.* 3.2 nm were loaded with tolbutamide using the melting method (Figure 7-17). Loaded composites analysed with nitrogen adsorption/desorption isotherms showed a gradual decrease of the total pore volume and surface area with increasing drug content (Figure 7-18, Table 7-3).
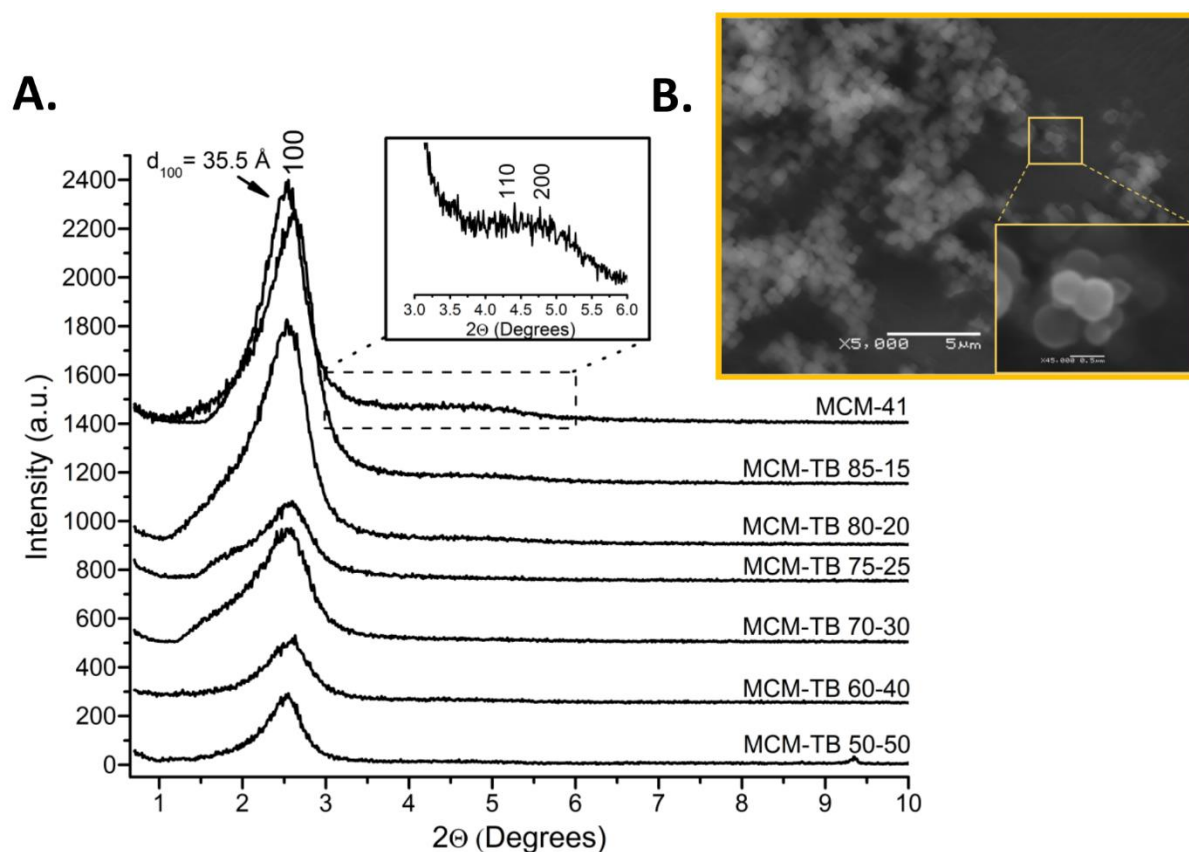
Figure 7-17. A. Low angle PXRD patterns of MCM-TB composites at different loading levels. **B.** SEM micrograph of MCM-41 particles.

These results are corroborated by low angle PXRD, where a gradual decrease of the d[100] peak intensity was observed with increasing drug content (Figure 7-17), indicating a gradual deposition of the drug molecules within the pores of the MCM-41 host. Thermogravimetric analysis of the drug-SiO$_2$ composites confirmed that the expected drug content was achieved during loading (Table 7-3). It is important to mention that the water content of the final composites was *ca.* 1-2 %, as determined by TGA (see section 7.2.6 for detailed studies of water effects on the drug phase inside the pores of silica).
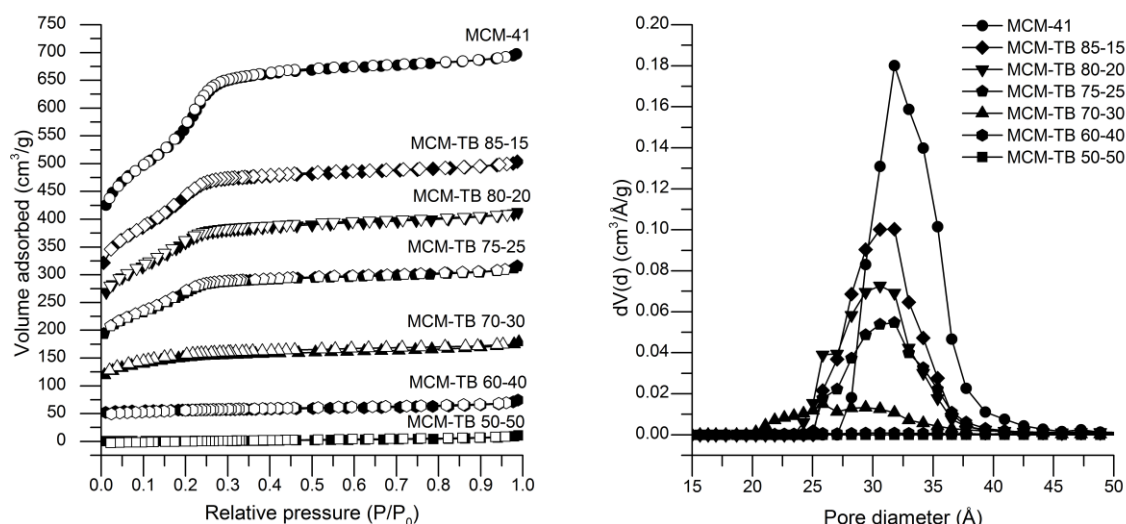
Figure 7-18. Nitrogen adsorption-desorption isotherms (left) and pores size distribution curves (right) of MCM-TB composites at different drug loadings (the isotherms are offset by 50 cm^3 g^{-1}).

Table 7-3. Drug content and structural parameters of MCM-41 host and loaded composites.

Host-guest composite	TB (g g^{-1})	V_{total} [cm^3 g^{-1}]	d_{pore} [Å]	S_{BET} [m^2 g^{-1}]
MCM-41	N/A	398	31.8	1277.1
MCM-TB 85-15	0.163	254	31.8	780.3
MCM-TB 80-20	0.211	213	30.6	614.4
MCM-TB 75-25	0.254	166	30.6	484.6
MCM-TB 70-30	0.317	78.8	28.2	176.2
MCM-TB 60-40	0.420	24.5	N/A	34.6
MCM-TB 50-50	0.504	10.6	N/A	2.1

7.2.3.2 Powder X-ray diffraction and differential scanning calorimetry results

Amorphous tolbutamide has a low glass transition temperature (T_g = 277 K) and is included in the first class of glass forming agents based on the classification system implemented by Taylor *et al.*[267] Compounds in this class recrystallise during cooling from the undercooled melt state, regardless of cooling rate, and therefore the crystallisation process is dominated by thermodynamics.[61,267] Based on the results reported by Kawakmi *et al.,* amorphous TB recrystallises to form IV on cooling with a further recrystallisation to form III observed during subsequent heating.[61] Tolbutamide encapsulated inside the silica scaffolds using the melting method displayed a very different behaviour compared to the bulk drug cooled from the melt. We found that TB remained amorphous at loading levels up to 30 wt. %, with crystallisation into the highly metastable TB form V occurring at higher drug loadings (40-50 wt. %), confirmed using a combination of PXRD, DSC and solid-state NMR.
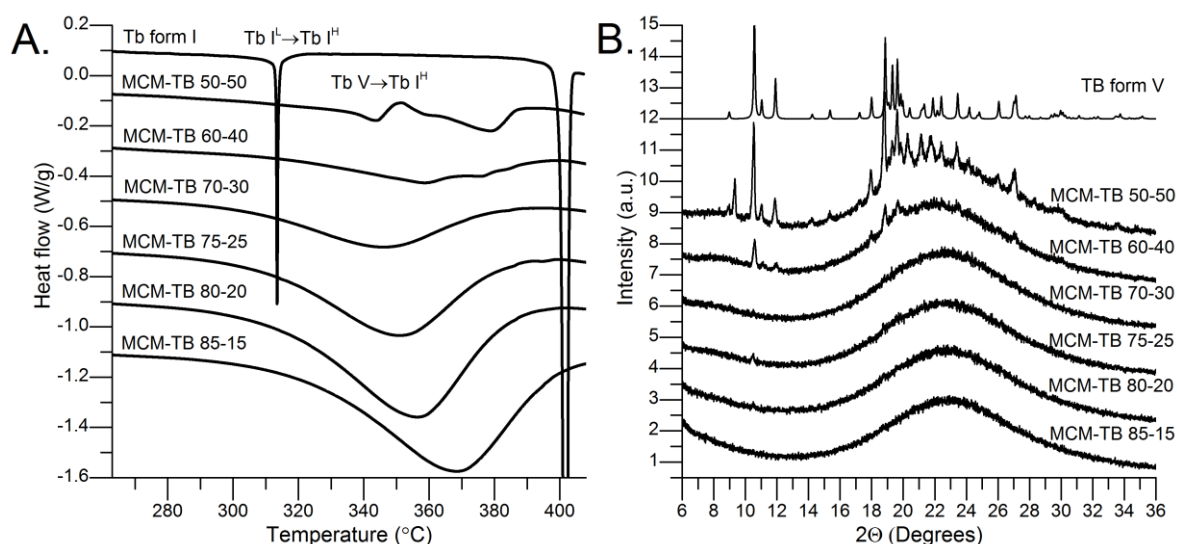
Figure 7-19. DSC thermograms and PXRD patterns of MCM-TB composites at different drug loadings. The PXRD pattern of TB form V was simulated using ZZZPUS10[183] CSD structure.

PXRD patterns (Figure 7-19) show a broad 'halo' peak due to the presence of amorphous MCM-TB composites at drug concentrations up to 30 wt. %. The small reflection at d = 8.39 Å observed for composites loaded with TB at 20 and 25 wt. % may indicate the confined guest is a mixture of amorphous and partially crystalline TB form V. The PXRD patterns of the host loaded at 40 and 50 wt. % are in agreement with the simulated PXRD pattern of the highly unstable crystalline TB form V, which has only previously been formed through crystallisation from acidified methanol.[183]

DSC analysis (Figure 7-19) of MCM-TB composites with drug content up to 30 wt. % does not show the melting peaks characteristic of TB polymorphs. The broad endotherm observed here may be related to the evaporation of loosely bound surface water as this is a frequently reported phenomenon for mesoporous silica based drug delivery systems.[41] At drug loadings of 40 and 50 wt. %, a broad melting endotherm of confined TB form V was observed at 339.9 K followed by recrystallisation and melting of TB form I^{H} at 364.2 K. Due to the broadening and decrease of the melting point expected with confined crystalline material, TB form I^{H} was identified only using variable temperature ^{13}C solid-state NMR spectroscopy (see section 7.2.4). This method enabled us to provide additional information on the supramolecular organisation of tolbutamide in the pores, and to monitor the phase transition of confined drug *in situ* (Figure 7-22).

7.2.3.3 Solid-state NMR studies
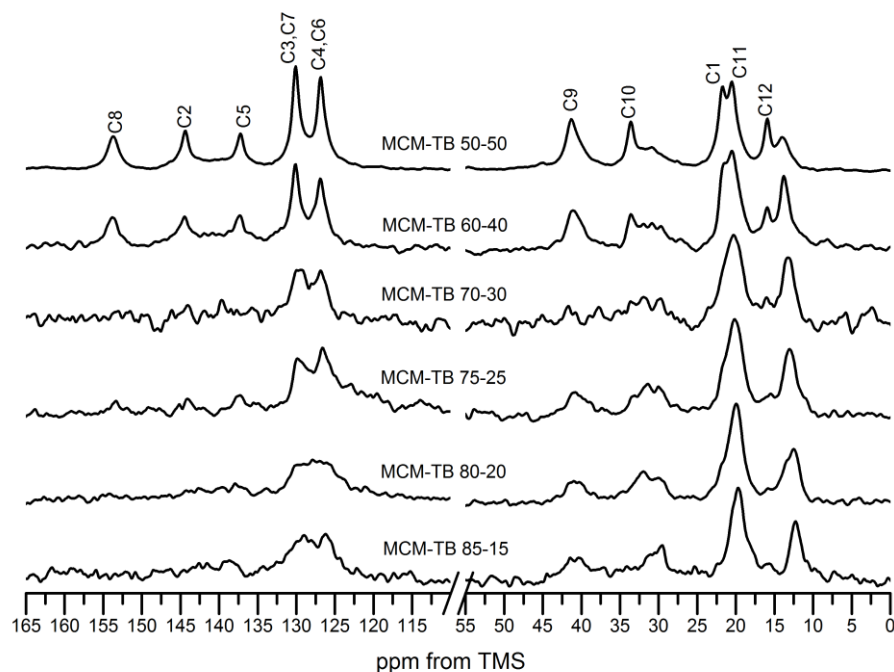
Figure 7-20. ^{1}H-^{13}C CP/MAS solid-state NMR spectra of MCM-TB composites with different drug loadings.

^{1}H-^{13}C CP/MAS NMR spectra of confined tolbutamide indicate the presence of amorphous drug at drug loading up to 30 wt. % (Figure 7-20). The peak broadening is due to the presence of magnetically non-equivalent environments of the carbon atoms alongside increased distribution of possible orientations, typical of amorphous solids. At the higher drug content of 40 and 50 wt. %, much sharper ^{13}C peaks are observed, which indicates the presence of crystalline TB form V confined within the porous MCM-41 host, in agreement with PXRD data. The ^{1}H-^{13}C CP/MAS NMR spectrum of TB form V confined within MCM-41 is in agreement with the ^{13}C chemical shifts calculated with CASTEP, based on the ZZZPUS10[183] structure reported in the CSD (see section 7.2.1). Additionally, a decrease in the peak intensity of the amorphous TB (6144 transients averaged) as compared to crystalline TB (1024 transients averaged) may indicate increased mobility of the confined amorphous drug, resulting in the inefficient transfer of magnetisation during the cross-polarisation. This explanation was corroborated by ^{1}H T_1 relaxation measurements of confined crystalline and amorphous TB/MCM-41 composites compared to bulk crystalline TB. In the ^{1}H-^{13}C CP/MAS spectra of MCM-TB 50-50 composite it was possible to observe, not only the peaks of TB form V, but also broad peaks of the confined amorphous species at *ca.* 12 and 30 ppm. The broadening of the base of the aromatic peaks of carbons C3/C7 and C4/C6, together with the slight asymmetry of the C9 peak, provide a further proof of both the presence of amorphous and crystalline species confined within the pores of MCM-41.
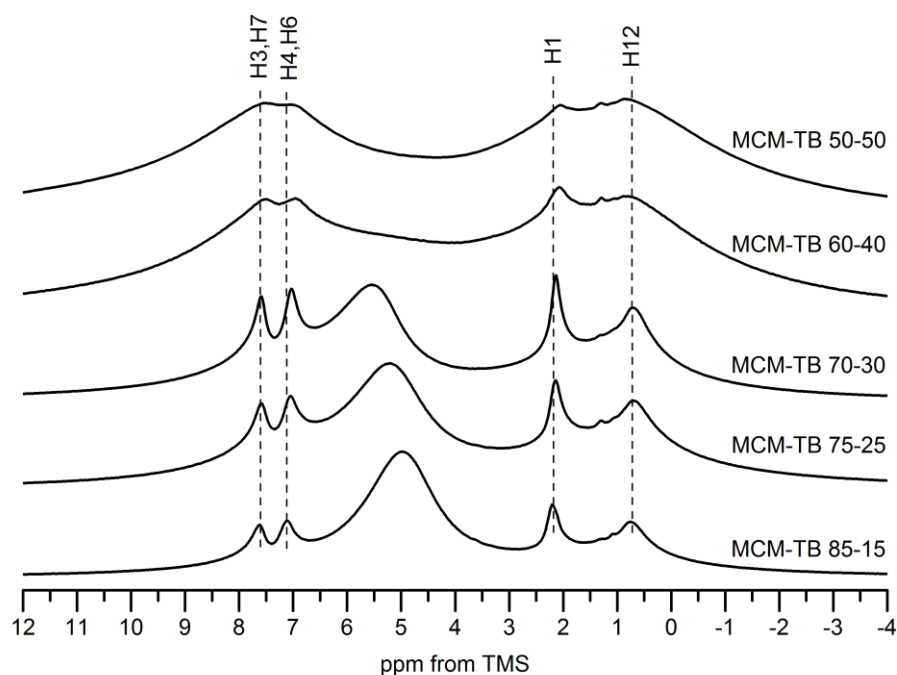
Figure 7-21. ^{1}H MAS NMR spectra of MCM-TB composites with different drug loadings. Spectra acquired at an MAS rate of 10 kHz.

^{1}H MAS NMR spectra of rigid solids usually show very broad peaks due to the presence of strong homonuclear [1]H-^{1}H dipolar interactions. To partially overcome these interactions in ^{1}H solid-state NMR, fast MAS (up to 120 kHz) and/or [1]H-^{1}H homonuclear decoupling sequences are used.[133–135] In the case of confined TB at drug contents up to 30 wt. %, five different proton sites were identified, indicating that the confined drug is in a highly dynamic state. These sites were assigned to the protons of aromatic ring (H4, H7 and H3, H6) and to two CH_3 groups (H1 and H12). The assignment was carried out based on both ^{1}H solution NMR spectra of TB, and CASTEP calculations. Further increase of the drug content within the material (40-50 wt. % drug loading) lead to crystallisation of TB inside the pores. This was confirmed by the broadening of the ^{1}H peaks, consistent with the presence of enhanced [1]H-^{1}H dipolar interactions, which are expected for rigid crystalline solids (**Figure 7-21**).

7.2.4 Solid-state NMR *in situ* monitoring of TB form V phase transformation under confinement

The investigation of phase transitions of confined solids is a considerable analytical challenge due to decrease and broadening of the melting peak in DSC and broadening of PXRD peaks for nano-size crystals.[93,106,110] In such cases, full understanding of the phase transitions in confinement requires application of methods sensitive to the local environment of atoms, therefore solid-state NMR is essential to probe both structure and dynamics.
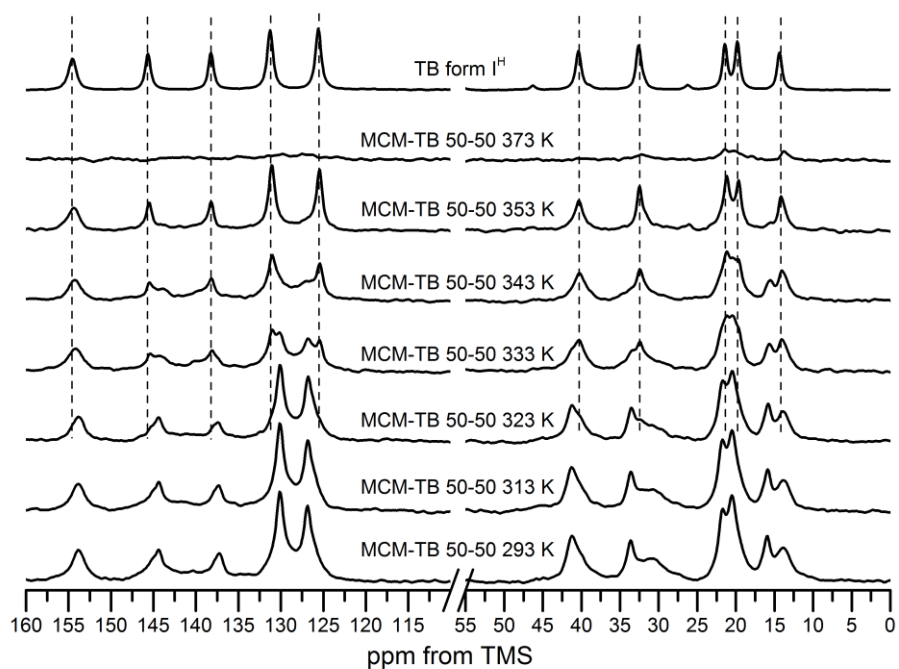
Figure 7-22. ^1H-^{13}C VT CP/MAS NMR spectra of MCM-TB 50-50 composite with confined TB form V.

At temperatures up to 333 K there was no change observed in the spectra of the MCM-TB 50-50 composite, which is in agreement with DSC analysis. At 333 K peak splitting was detected, which indicated the presence of two crystalline phases. This agrees well with DSC results, where the first transition onset was observed at *ca.* 339 K. With increasing temperature further (up to 343 K) recrystallisation was observed through growth of the peaks associated with form I^H, resulting in only one phase being detected by 353 K, as the confined metastable TB form V underwent a phase transition to TB form I^H. This transition was in agreement with the DSC data, which demonstrated that there is a narrow temperature range at which TB form I^H can be present before it melts at 366 K. When the temperature reached 373 K, the confined drug melted. This was confirmed firstly by a loss of the CP efficiency observed as a substantial decrease of the peaks intensity in the ^1H-^{13}C CP/MAS spectrum (Figure 7-22), and secondly by the significant narrowing of lines in the ^1H spectrum at 373 K, due to an increased mobility (Figure 7-23). To the best of our knowledge, this is the first attempt to monitor the crystallisation of a confined pharmaceutical molecule within the mesopores of MCM-41 scaffold.
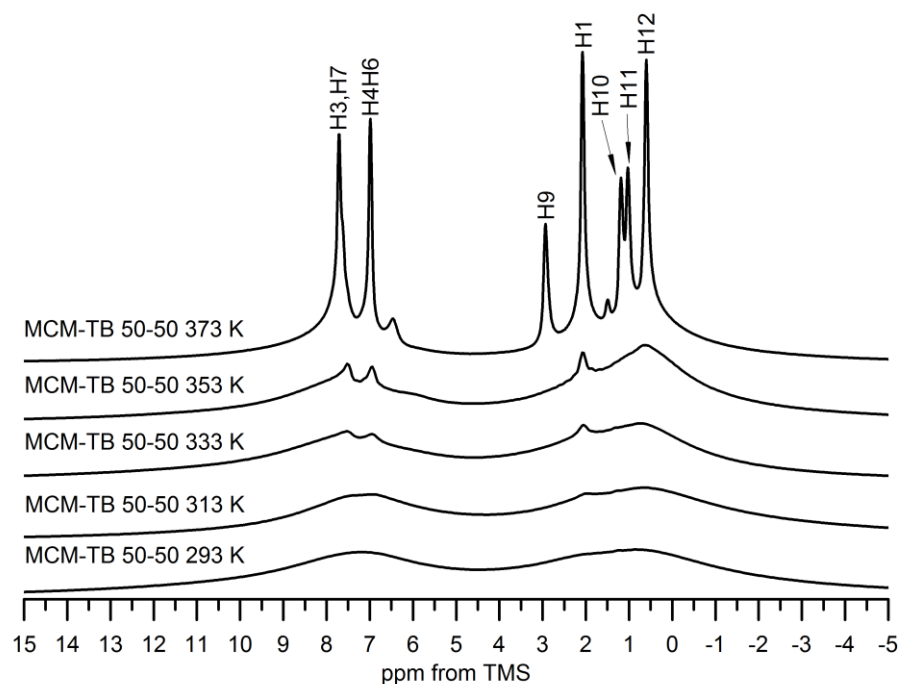
Figure 7-23. ^{1}H VT MAS NMR spectra of MCM-TB 50-50 composite with confined TB form V.

The VT ^{1}H MAS spectra of the MCM-TB 50-50 composite with confined TB form V showed a gradual narrowing of proton peaks H1, H3, H4, H6 and H7 with increasing temperature. The gradual narrowing of the peaks was attributed to increased dynamics of the aromatic ring of tolbutamide with increasing temperature. This is not unexpected as all TB polymorphs are stabilised through the rigid sulfonylurea bonding motif, hence the aromatic ring of tolbutamide may be in a different motional regime compared to the aliphatic part of the molecule.

7.2.5 Structure and dynamics of TB form I confined within MCM-41 host: NMR studies

7.2.5.1 Preparation of confined TB form I^L

Confined TB form I^L was obtained by heating the MCM-TB 50-50 composite loaded with confined TB form V above its phase transition to TB form I^H at *ca.* 333-343 K *in situ* within the spectrometer, followed by subsequent cooling of the sample to 293 K. The rotor with the converted material was removed from the spectrometer and stored at room temperature in a desiccator for a week to allow further recrystallisation of residual amorphous drug to TB form I^L.

7.2.5.2 Variable temperature solid-state NMR studies

The ^{1}H-^{13}C CP/MAS NMR spectrum of the MCM-TB 50-50 composite loaded with TB form I^L, acquired at 293 K, shows peaks of TB form I^L built on the broad peaks of amorphous TB. The presence of the disordered phase inside the pores becomes more evident upon gradual cooling,

which results in a gradual increase of ^1H-^{13}C dipolar interactions leading to an increased CP efficiency.
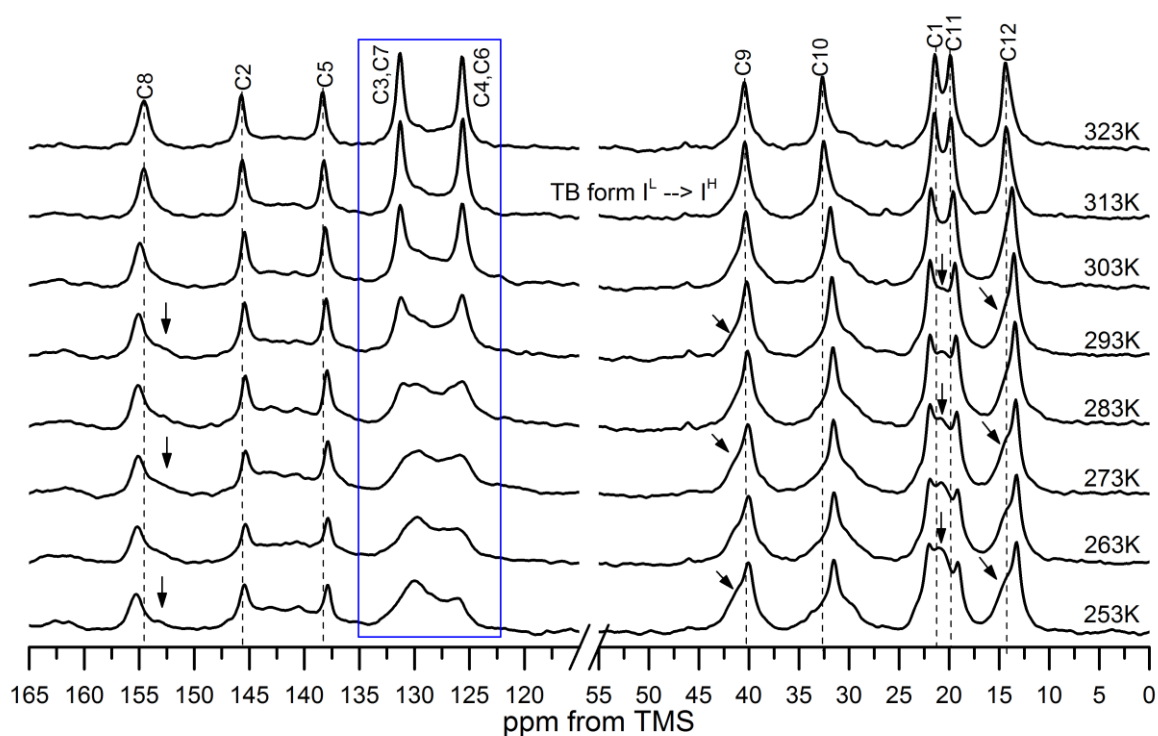
Figure 7-24. ^1H-^{13}C VT CP/MAS NMR spectra of MCM-TB 50-50 composite with confined TB form I. Amorphous TB peaks are indicated by arrows.

In this regime, the broad amorphous TB peaks, (indicated by arrows in Figure 7-24) present either as a shoulder (C8, C9, C12) or as a broad base (C2, C5, both aromatic peaks, C9, C1, C11), were observed under the sharper peaks of crystalline TB form I^L. The substantial decrease and broadening of both aromatic peaks (carbons C3/C7 and C4/C6) of TB form I^L was observed in the spectra below 283 K, in agreement with data for bulk TB form I^L. Interestingly, the aromatic peaks (C3/C7 and C4/C6) of confined amorphous TB display a very different behaviour when compared to the crystalline material. The presence of both aromatic peaks of amorphous TB at decreased temperatures may indicate substantial differences in the mobility of the confined amorphous drug as compared to crystalline TB form I^L. The absence of the peaks of amorphous TB in the ^1H-^{13}C CP/MAS spectra at increased temperatures may indicate it is in liquid like state, similarly to ibuprofen confined in MCM-41 as reported by Azais *et al.* and Skorupska *et al.* The decrease in the temperature may result in vitrification of liquid like TB into a glassy state observed as broad peaks in ^1H-^{13}C CP/MAS spectra. Similar observation was made by Azais *et al.* for confined ibuprofen at 223 K (discussed further in General discussion chapter). The differences in the dynamics between

confined amorphous and crystalline drug are corroborated by measurements of relaxation time (Figure 7-26, Figure 7-27). Gradual heating of the material from 293 to 303 K led to a decrease in the peak intensity of confined amorphous TB, and narrowing of the peaks of confined TB form I^L. This is particularly well illustrated for both aromatic carbons of TB highlighted in the blue box in Figure 7-24. The confined TB form I^L undergoes a phase transition to TB form I^H above *ca.* 313 K, close to the transition temperature of bulk TB form I^L (indicated by dashed lines in Figure 7-24).

The ^{1}H CRAMPS spectra of the MCM-TB 50-50 composite loaded with confined TB form I^L indicate the presence of two superimposed components. This was highlighted by the asymmetry of the aromatic peak at temperatures below 283 K and a shoulder peak (shown by arrows in Figure 7-25) at temperatures of 303 K and above, due to increased distribution of ^{1}H chemical shifts.
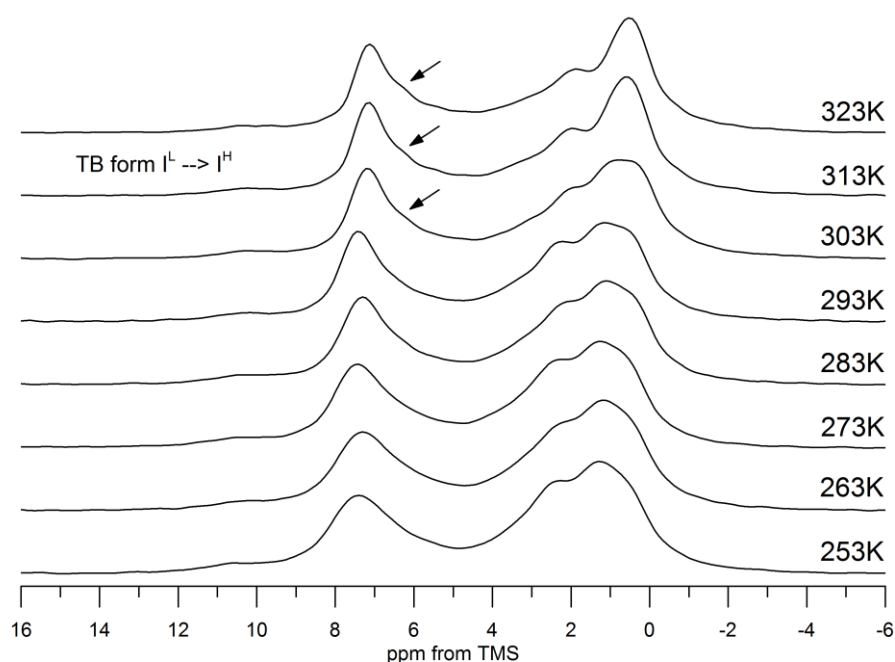
Figure 7-25. ^{1}H CRAMPS VT MAS NMR spectra of MCM-TB 50-50 composite with confined TB form I. The arrows indicate a shoulder peak, which suggests the presence of more than one component in the spectrum.

This is in agreement with the broadening of the aliphatic part of the ^{1}H CRAMPS spectra of the confined TB form I^L. The spectrum of bulk drug is composed of four distinguishable peaks (see Figure 7-6 for comparison), while the spectra of confined TB form I^L acquired at 303 K and below show only two broad resonances. The changes in the aliphatic part of the spectra between 303 and 313 K indicate the presence of confined TB form I^L to TB form I^H, highlighting the sensitivity of this method towards subtle structural changes in crystalline/amorphous composite systems.

7.2.5.3 Relaxation time measurements of confined TB form I^L within MCM-TB 50-50 composite

Substantial differences were observed in the VT ^{1}H T_1 and ^{1}H $T_{1\rho}$ relaxation times of confined TB form I^L in comparison to bulk drug. The temperature dependence of the ^{1}H $T_{1\rho}$ values shows a clear minimum at *ca.* 263 K, which is likely to be related to the dynamics of the aromatic ring of TB form I^L. Interestingly, the values of ^{1}H $T_{1\rho}$ times for carbons C3/C7 and C4/C6 at temperatures below 283 K are slightly longer compared to the values for other hydrogens of confined TB. These differences could be the result of a decreased intensity of the peaks for carbons C4/C6 and C3/C7 at temperatures below 283 K, alongside an increased intensity of the peaks of the amorphous component in the spectra. Therefore, the measured ^{1}H $T_{1\rho}$ times for the aromatic carbons represents a mixture of relaxation times of the two components (crystalline and amorphous TB). The ^{1}H $T_{1\rho}$ relaxation time of amorphous TB incorporated in the PVP-VA polymer matrix was measured previously as *ca.* 12 ms (at 263 K)[49], which is in agreement with data presented for amorphous TB encapsulated in the MCM-41 scaffold and significantly longer (3 times) than for the crystalline TB form I^L at 263 K.
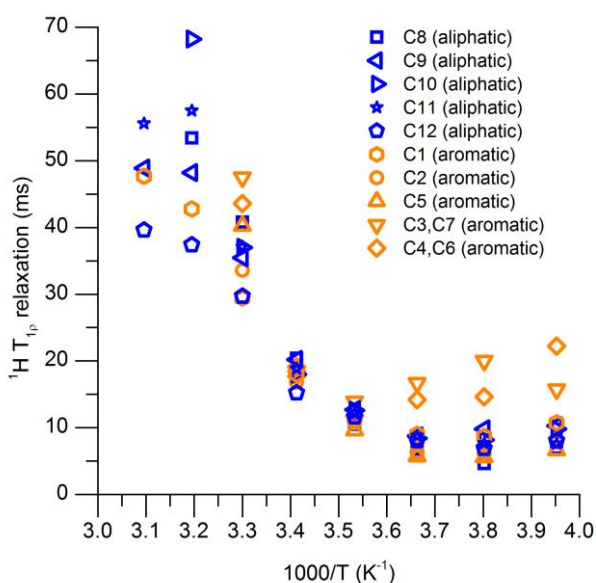
Figure 7-26. Variable temperature ^{1}H $T_{1\rho}$ data of MCM-TB 50-50 composite with confined TB form I. The expected errors for the method are between 5 to 10 %.

At temperatures close to the TB form I^L → TB form I^H phase transition (*ca.* 313 K) the separation of ^{1}H $T_{1\rho}$ relaxation times becomes pronounced. A similar phenomenon was observed for bulk TB form I, but to greater extent as ^{1}H $T_{1\rho}$ relaxation times well above 70 ms could not be measured accurately. This is either due to the differences in dynamics of confined crystalline TB form I in comparison to bulk, or to the presence of two components with very different dynamics inside the pores.
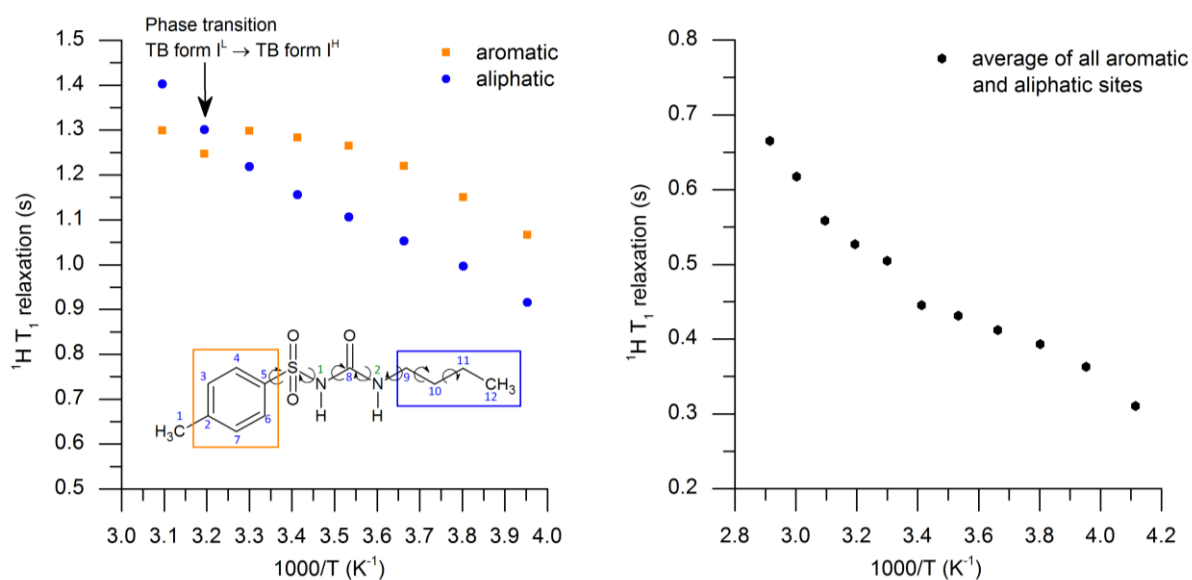
Figure 7-27. Variable temperature ^1H T_1 data of MCM-TB 50-50 composite with confined TB form I. The expected errors for the method are between 5 to 10 %.

The analysis of the VT ^1H T_1 times recorded for the MCM-TB 50-50 composite with confined TB form I^L shows a very different behaviour as compared to bulk TB form I. There was a clear minimum observed in the temperature dependence of the ^1H T_1 values for bulk TB form I, centred at the phase transition temperature at *ca.* 313 K (Figure 7-12), while an increase in the ^1H T_1 relaxation times with increasing temperature was observed for confined TB form I^L. Further differences were observed between the relaxation times for aromatic and aliphatic peaks of TB with increasing temperature. While the ^1H T_1 values for the aliphatic hydrogens increase almost linearly with increasing temperature, the ^1H T_1 values for aromatic hydrogens increase linearly up to 283 K, then plateau and go through a local minimum at *ca.* 313 K (the phase transition temperature between TB form I^L and TB form I^H). As confined TB in the MCM-TB 50-50 composite has both the crystalline and amorphous drug, we measured ^1H T_1 relaxation times for only amorphous drug confined within the MCM-41 pores at 20 wt. % (Figure 7-27). An almost linear increase in the ^1H T_1 relaxation times was observed with increasing temperature with absolute ^1H T_1 values being significantly smaller than those observed for the MCM-TB 50-50 composite. Additionally, the measured values of ^1H T_1 relaxation for amorphous confined TB are unlikely to be affected by the ^1H T_1 relaxation of the population of silanol protons, which were determined by Hansen *et al.* and Overloop *et al.* as equal to 3 and 4 s, respectively.[300] Furthermore, the linear increase of the ^1H T_1 relaxation time with increasing temperature was observed by Aksnes and co-workers for cyclohexane and cylopentane[301,302] and Hansen *et al.* for silanol protons of the MCM-41 pore wall.[300] A similar observation was made by the Navrotsky group for organic solid N,N,N-trimethyl-1-adamantammonium iodide confined within silica scaffolds with pore sizes between 0.8 and 20 nm.[303]

An increase in the ^{1}H T_1 values was observed by Aksnes and co-workers with increasing content of confined organic liquids (cyclohexane and cyclopentane). This observation was explained due to the increased contribution of the 'bulk' liquid in the middle of the pore to the overall ^{1}H T_1 relaxation time of the surface species. These were measured to have six times lower ^{1}H T_1 relaxation time compared to the 'bulk' species located in the pores centre. Porion *et al*. reported similar findings for T_1 relaxation of confined water, where ^{1}H T_1 relaxation times were increasing with increasing water content.[304] This observation is in agreement with our ^{1}H T_1 relaxation studies for confined TB at 20 wt. % and 50 wt. % and earlier ^{19}F T_1 relaxation times of FFA-MCM and FFA-SBA composites at different loading levels.[301,302]

In summary, significant differences in mobility between bulk and confined TB crystals have been observed using ^{1}H T_1 and ^{1}H $T_{1\rho}$ measurements. The observed changes in the dynamics of bulk and confined TB form I may be the result of the biphasic nature of the confined drug molecules. As it was indicated throughout this section using VT NMR studies, the TB molecules are present inside the pores as both confined crystals and confined amorphous species, both shown to be in two different motional regimes. The observed ^{1}H MAS spectrum was an average of all TB molecules present in all different environments and motional regimes, therefore the measured ^{1}H T_1 values are likely to be an overall average of different motional processes of confined TB molecules.

The equation for the calculation of the average T_1 of confined water was established for macroporous solids and further applied for organic liquids, assuming the molecules reside either at the surface of the pores, with particular relaxation time T_{1S}, or in the pore void, with relaxation time equal T_{1B}.[305] Therefore, if the two-site fast exchange model for relaxation is still valid for the system, the overall relaxation time is expressed as:

$$\frac{1}{T_1} = \frac{x}{T_{1S}} + \frac{(1-x)}{T_{1B}}, \qquad \text{(Eq. 7-1)}$$

Where x is the fraction of molecules present at the surface sites. This model was applied successfully for cyclohexane and cyclopentane confined within the MCM-41 host to determine the thickness of the molecular layer of highly mobile species at the pores surface.[301] Our results were in agreement with the model assuming the material is dominated by amorphous species (x = 0.8), and T_{1S} = 0.36 s at 253 K and T_{1B} = 3.42 s for confined amorphous TB at 20 wt. % loading and bulk TB, respectively. The mechanism of increased dipolar relaxation of the surface species was explained by both translational diffusion at the surface or bulk-mediated surface diffusion through the Levy walk mechanism of desorption and readsorption of the surface species.[305]

7.2.6 Changes of the structure and dynamics of confined tolbutamide during storage at dry and humid conditions (75 % RH)

Understanding the changes to the structure and dynamics of confined pharmaceuticals upon storage is of paramount importance from an industrial and regulatory perspective. Recently we have shown that the crystallisation of FFA can be inhibited inside the pores of MCM-41 and SBA-15 (pore size diameters *ca.* 3 and 8 nm, respectively), whilst FFA form I is formed inside the pores of MCF (pore size diameter *ca.* 29 nm).[306] In another study we have shown that IMC crystallisation can be driven inside the pores through the addition of organic solvents (MeOH, EtOH or ACN). These findings enable the prediction of the material's performance during pharmaceutical processing such as wet granulation, coating or spray drying.[88]

The effect of water on the mesoporous silica-drug composites is very poorly understood and is rarely addressed in the scientific literature. To date, there is only one study by Skorupska *et al.* showing a molecular level understanding of water and ethanol effects on confined ibuprofen loaded inside the pores of MCM-41 material at high drug contents (50 and 60 wt. %).[79] The study presented in this section was developed based on two observations regarding MCM-TB composites. Firstly, at low drug contents (for amorphous materials), the ^{1}H and ^{13}C MAS NMR spectra differed for the same sample depending on the storage conditions: narrowing of the ^{1}H peaks and substantial decrease of the ^{1}H-^{13}C CP/MAS NMR signal were observed during the analysis performed at high ambient humidity. Secondly, the formation and stability of TB form V confined within MCM-41 scaffolds was affected by residual water content and storage conditions. This is not surprising as Nath *et al*. have highlighted decreased stability of bulk TB form V under increased humidity.[183] In the following study we chose two model MCM-TB composites loaded with 20 and 50 wt. % of the drug to show the effect of water on the structural and dynamical properties of confined molecules. We further showed application of different NMR methods to gain a better understanding of the structure and mobility of confined tolbutamide.

7.2.6.1 Effect of storage conditions on the state of amorphous TB confined within MCM-41 silica scaffold loaded at 20 wt. % using melting method

The MCM-41 material loaded with 20 wt. % of TB yields amorphous composite as determined by the broad 'halo' in the PXRD pattern and absence of melting endotherm in the DSC thermogram (week 0 - Figure 7-28).
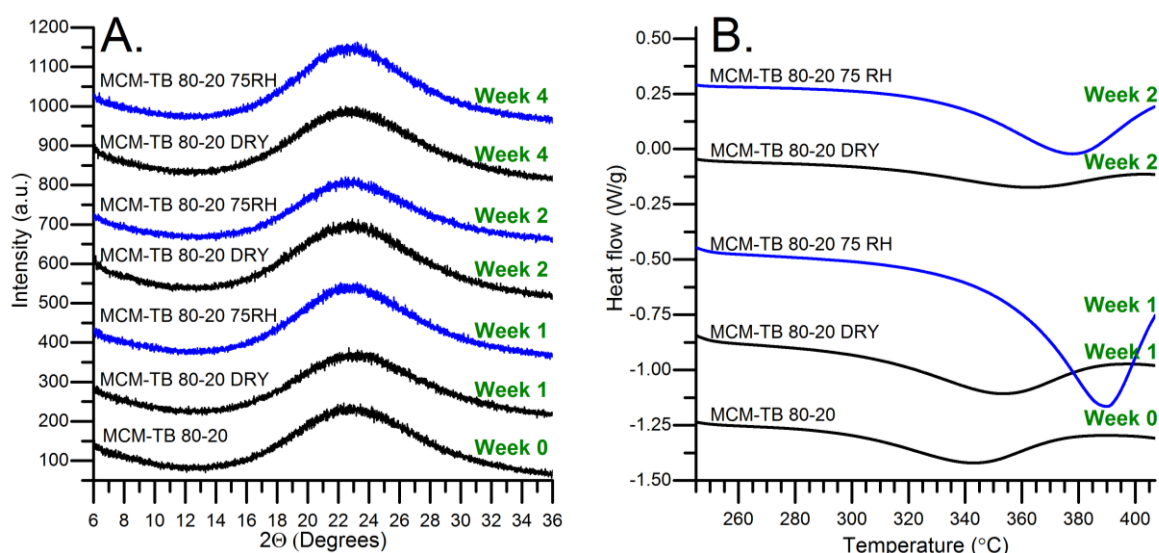
Figure 7-28. A. PXRD patterns and **B.** DSC thermograms of MCM-TB 80-20 composite stored at dry and humid (75 % RH) conditions over a period of four weeks.

The material stored over a period of 4 weeks in either dry or humid conditions remained amorphous as determined using PXRD and DSC analysis (Figure 7-28). The DSC thermograms of the material stored at 75 % RH show a broad endotherm in the temperature range from *ca.* 323 to 403 K, which may be related to the evaporation of loosely adsorbed water during storage. These endotherms are less pronounced and centred between 300-370 K for the composite stored at dry conditions (Figure 7-28).

DSC and PXRD methods could only confirm that the TB confined within the MCM-41 host at low loading levels (20 wt. %) remained amorphous over a period of four weeks, regardless of the storage conditions. Additional information on the state of the drug confined within the nanopores was obtained using solid-state NMR. The ^{1}H MAS NMR spectra of the composite stored at dry conditions show three broad peaks attributable to aromatic (at *ca.* 8 ppm) and aliphatic (at *ca.* 1 and 2 ppm) hydrogens of TB (Figure 7-29) and did not change over a period of four weeks. In contrast, the ^{1}H MAS NMR spectra of the material stored at 75 % RH showed substantial narrowing of the peaks after one week of storage.

The spectra show eight peaks, assigned to both aromatic sites (H3/H7 and H4/H6) at 7.6 and 7.0 ppm, intense water peak at 5.2 ppm, H9 site at 2.9 ppm, and intense H1 methyl peak at 2.1 ppm (Figure 7-29). Interestingly, the H12 site has two peaks (0.6 and 0.8 ppm), which is evident from the HSQC spectrum (Figure 7-30) and hydrogens H10 and H11 were observed as a broad shoulder centred at 1.1 ppm. The two peaks for the H12 site, with an integral equal to an integral of H1 methyl site along with the broadening of the H9-H11 protons of butyl tail, may indicate that the flexible aliphatic part of tolbutamide is present in more than one conformation inside the pores of MCM-41.
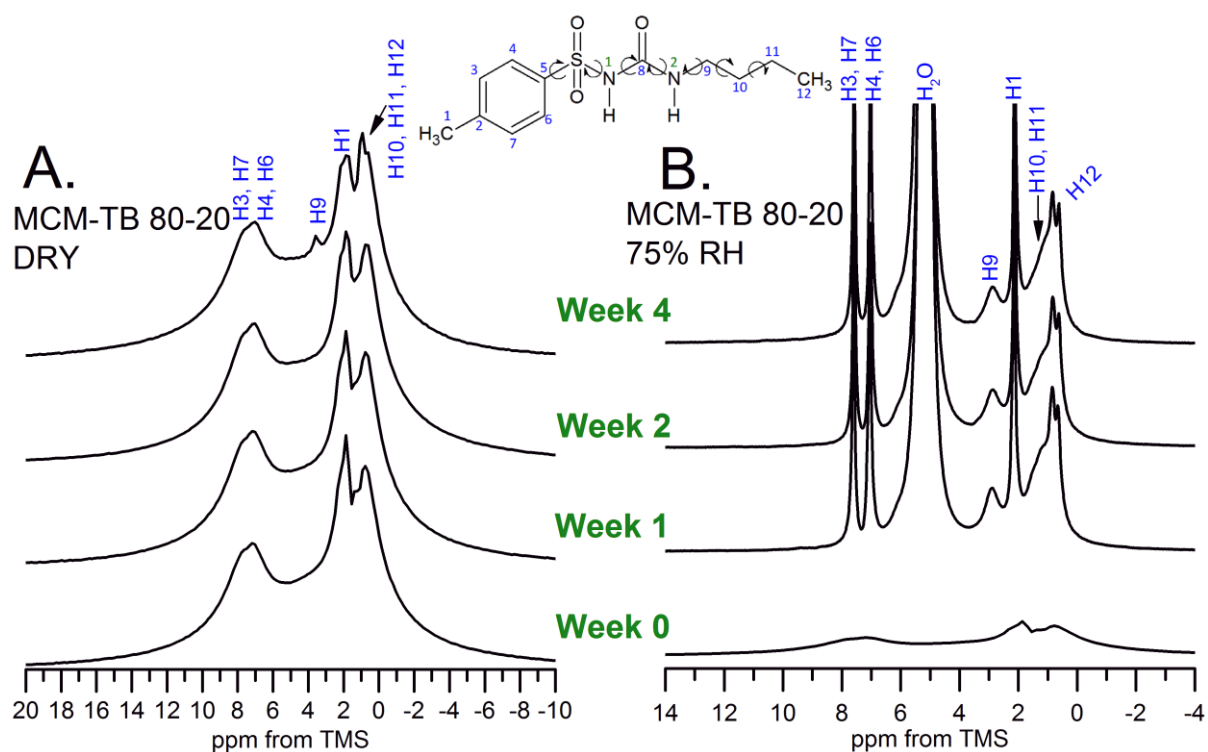
Figure 7-29. ¹H MAS solid-state NMR spectra of MCM-TB 80-20 composite stored at **A.** dry and **B.** humid (75 % RH) conditions over four weeks.
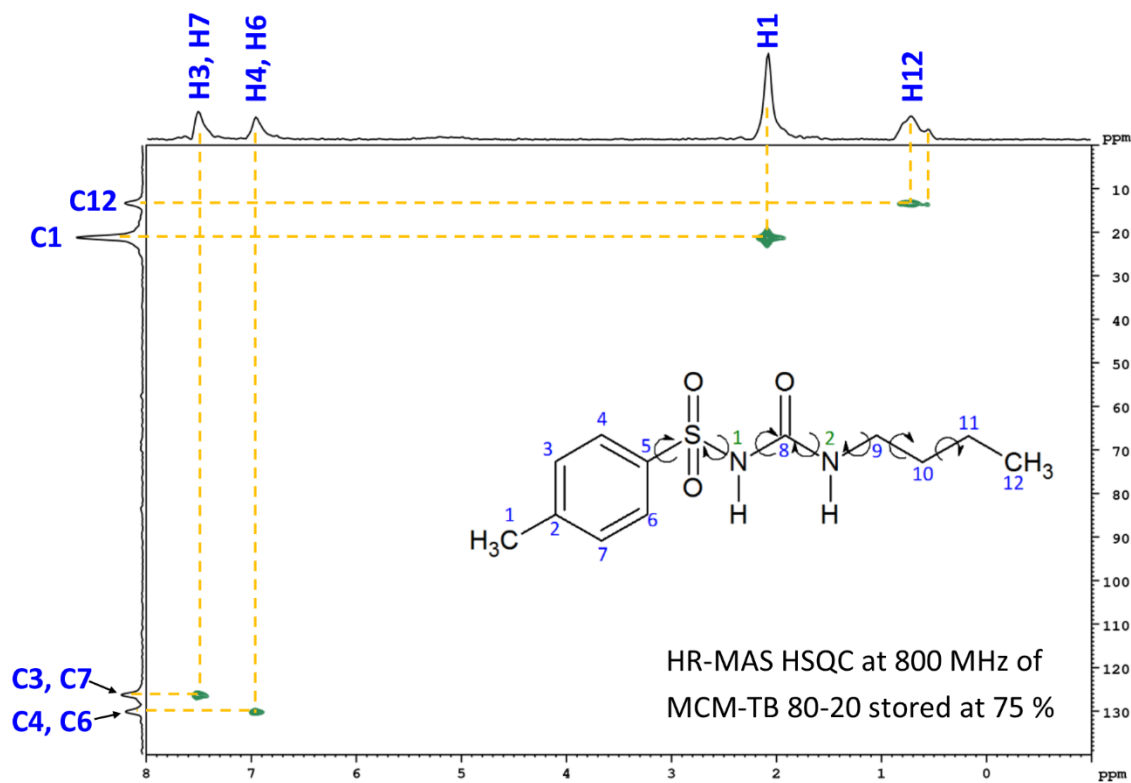
Figure 7-30. ¹H-¹³C HR-MAS HSQC spectrum of MCM-TB 80-20 after a week of storage at 75 % RH acquired at 18.8 T using MAS rate of 8 kHz.

The ^{1}H-^{13}C CP/MAS NMR spectrum of the MCM-TB composite loaded with 20 wt. % shows five broad low intensity peaks, indicating the presence of amorphous TB inside the pores. The ^{1}H-^{13}C CP spectra of the material stored in dry conditions did not change over four weeks. However, the formulation stored at 75 % RH showed significant narrowing, and substantial decrease in peak intensity as compared to the starting material (week 0) after the first week of storage. Decrease in signal intensity in CP/MAS spectra was previously observed by Azais *et al.* and Skorupska *et al.* for small organic molecules (ibuprofen, benzoic acid, lauric acid) and can be a result of an increased mobility of confined TB stored in humid conditions.[74,75,77,79] Furthermore, eight different resonances were identified in the ^{1}H-^{13}C CP/MAS spectra of the materials stored in humid conditions compared to the five resonances for the compound stored in dry conditions. These are the carbons with directly bonded hydrogens including aromatic carbons C3/C7 and C4/C6 at 130.1 and 126.7 ppm, respectively, and aliphatic carbons C1, C9-C12 in the range from 13.9 to 40.7 ppm. Interestingly there are two peaks at 29.8 and 32.1 ppm, which can be assigned to carbon C10 in the material stored at 75 % RH. The methyl C12 can be found in at least two different environments in the starting material at 12.5 and 13.9 ppm and has relatively low intensity in the spectra of the TB-MCM-41 stored at 75 % RH. This is in agreement with the ^{1}H MAS NMR spectra (Figure 7-29) and J-MAS-INEPT (Figure 7-32) spectra, indicating that the butyl chain of TB could be present in more than one conformation. This hypothesis is based on recent single crystal X-ray studies by Drebushchak *et al.* for TB form I^{L} and I^{H}, where substantial disorder in the aliphatic tail was observed with site C11 being present in two different positions.[285] The disorder of the aliphatic part of TB was also observed earlier by the same group for TB form III above 150 K or freezing of the molecules below 150 K in either gauche or trans conformation of the butyl tail in TB form III^{2} structure.[271]
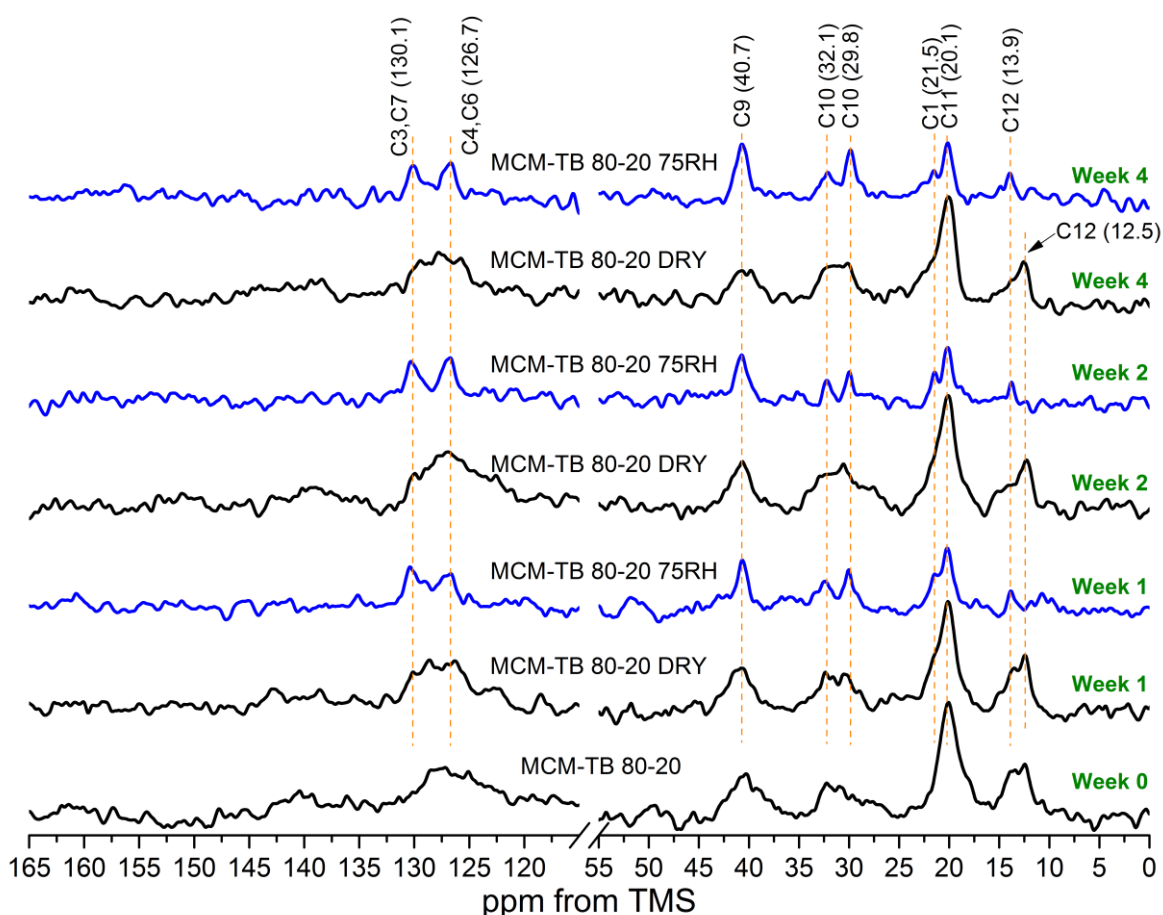
Figure 7-31. ^{1}H-^{13}C CP/MAS NMR spectra of MCM-TB 80-20 composite stored at dry and humid (75 % RH) conditions over four weeks**.**

The application of [1]H-^{13}C INEPT experiments in 'true' solids is limited due to the rapid decay of ^{1}H transverse magnetisation coherences. As MAS does not average [1]H-^{1}H dipolar couplings fully, [125,126] the effective transverse dephasing times are very short, therefore the application of multi-pulse homonuclear decoupling sequences is required during the polarisation transfer times in the INEPT pulse sequence.[198] Application of solution-state INEPT pulse sequence (without proton decoupling) under MAS conditions has been reported only for poorly coupled nuclei of inorganic solids or mobile systems such as inorganic gels and drugs or surfactants confined in MCM-41 silica scaffold.[74,77,197,199,307] In the latter case, there are only two model systems studied using J-MAS-INEPT (ibuprofen and benzoic acid confined in MCM-41 material).[74,75,77,79] It important to note that ibuprofen has a low melting temperature (351 K), hence it is expected to be present in the liquid state in confined media due to the effect of melting point depression related to confinement.[74,75,77,79]
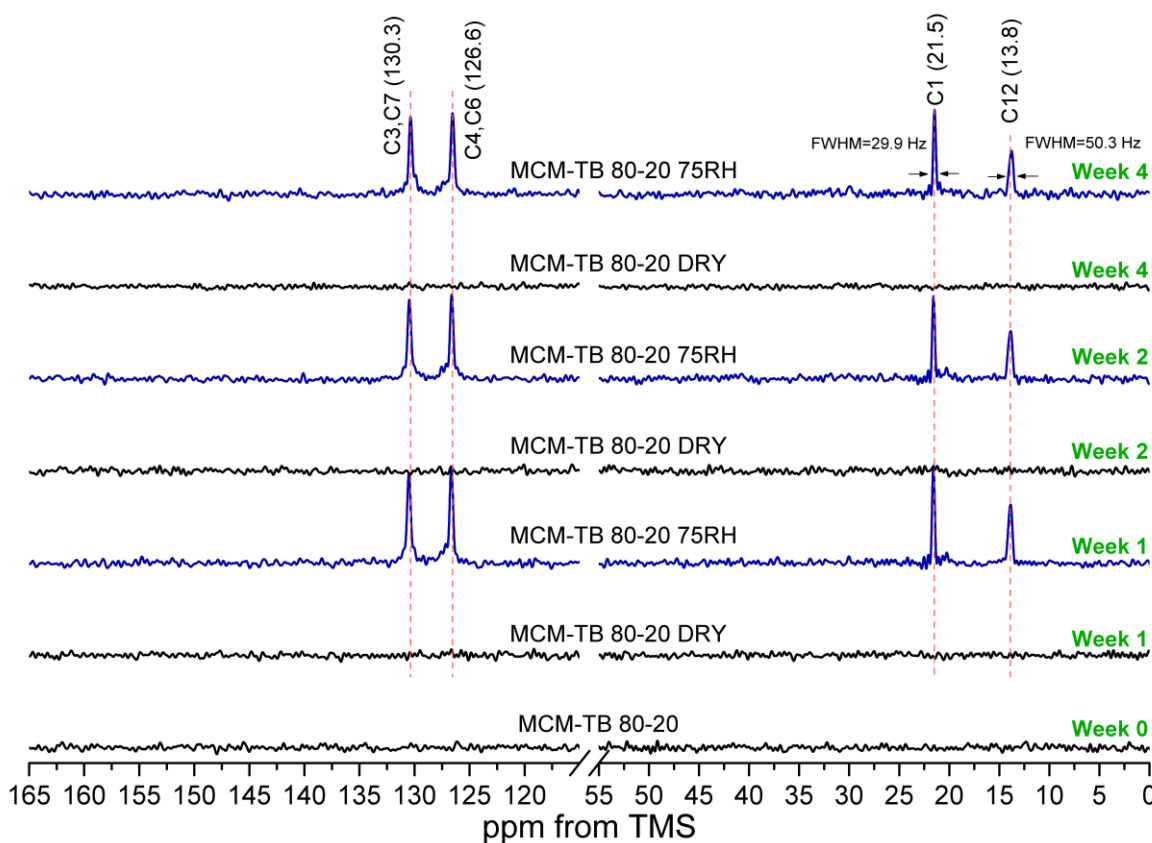
Figure 7-32. ^{13}C J-MAS-INEPT spectra of TB-MCM 80-20 composite stored at dry and humid (75 % RH) conditions over a period of four weeks.

The starting material loaded with 20 wt. % of TB did not show any peaks in the ^{13}C J-MAS-INEPT spectrum, indicating the inefficiency of the polarisation transfer through the scalar couplings. Similarly, there was no signal in the ^{13}C J-MAS-INEPT spectra of the materials stored in dry conditions over four weeks due to formation of amorphous TB inside the pores (Figure 7-32). The TB-MCM-41 stored at 75 % RH showed four resonances in the ^{13}C J-MAS-INEPT spectra, which can be assigned to aromatic carbons (C3/C7 at 130.3 ppm and C4/C6 at 126.6 ppm) and methyl sites (C1 at 21.5 ppm and C12 at 13.8 ppm). There are two interesting features in these ^{13}C J-MAS-INEPT spectra. Firstly, the intensity of the methyl C12 is around half that of the methyl C1, and the C12 site is almost twice as broad as the C1 site. Secondly, there are no CH_2 resonances present in the spectra (Figure 7-32). The broadening and decrease of the intensity of the C12 peak could be another proof of the aliphatic chain being present in more than one conformation in confined TB, due to increased distribution of possible orientations of the C12, which resulted in peak broadening. The absence of CH_2 peaks was observed in the ^{13}C J-MAS-INEPT and ^{1}H-^{13}C HSQC spectra, both recorded at different fields. It is known that CH_2 groups in solid state have very short ^{1}H to ^{13}C transverse coherence lifetimes and are difficult to decouple.[198] In our case, all ^{1}H peaks (H9-H11) of the three CH_2 groups were broadened in the ^{1}H MAS spectra, indicating reduced mobility, which may explain the lack of CH_2 peaks in the J-MAS-INEPT spectra.
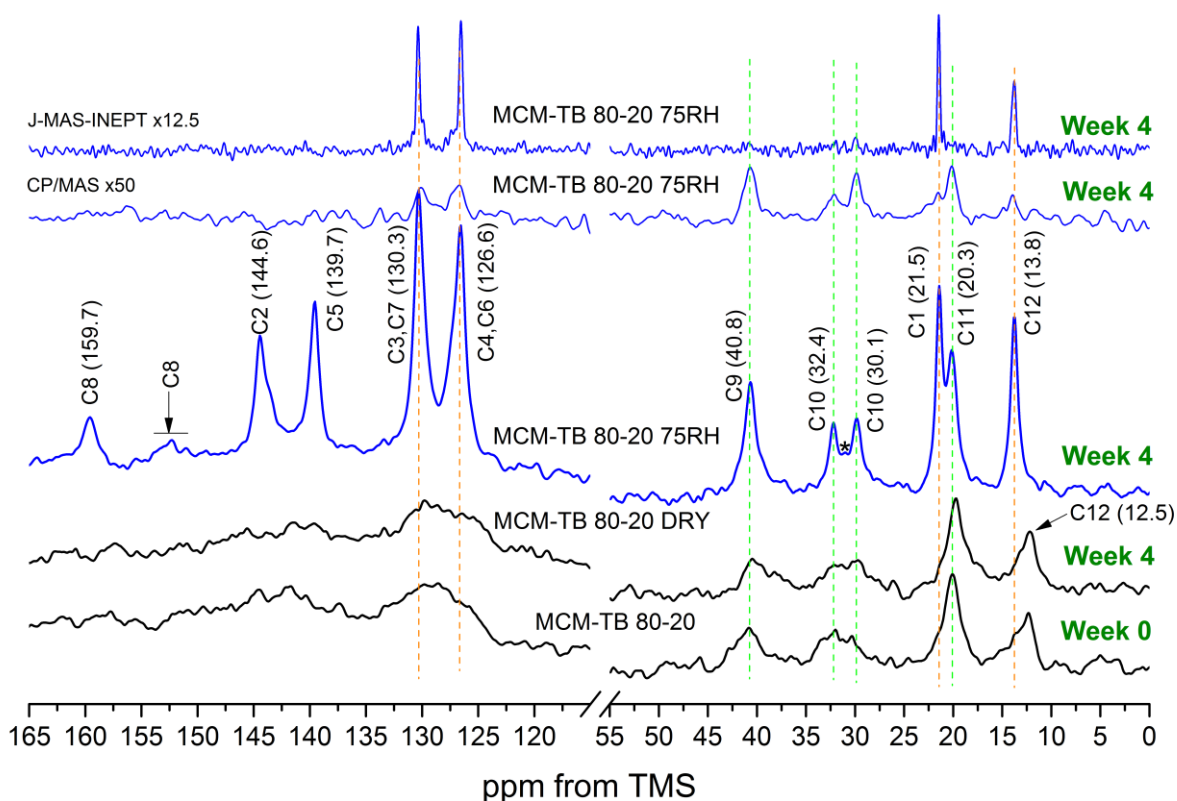
Figure 7-33. $^{13}C\{^1H\}$ MAS NMR spectra of MCM-TB 80-20 at week 0 and after 4 weeks of storage at dry and humid conditions (75 % RH); the J-MAS-INEPT and CP/MAS spectra of MCM-TB 80-20 after 4 weeks of storage at 75 % RH conditions are added on the top for comparison. The orange dashed lines indicate peaks present in both J-MAS-INEPT and $^{13}C\{^1H\}$ spectra, while green dashed lines indicate peaks present in both CP/MAS and $^{13}C\{^1H\}$ spectra.

In the last set of experiments, we recorded $^{13}C\{^1H\}$ MAS NMR spectra, which in principle should provide information on all the TB species confined in the MCM-41 scaffold (Figure 7-33). The spectrum of the starting material (week 0) shows four broad resonances in the aliphatic region, and two very broad peaks covering the full aromatic and carbonyl spectral range from 120 to 165 ppm. An almost identical spectrum was measured after four weeks of storage in dry conditions. The $^{13}C\{^1H\}$ MAS NMR spectrum of the MCM-TB 80-20 composite stored at 75 % RH shows substantial differences as compared to the spectrum of the material stored in dry conditions and the starting material. Here we observed all 11 resonances of the different TB carbon sites. The aromatic region showed a peak for each carbon site C2, C5, C4/C6 and C3/C7, similarly to the spectrum of crystalline TB. The carbonyl carbon C8 underwent an unusual downfield shift of *ca.* 5 ppm as compared to the spectra of the TB polymorphs. Additionally, the peak intensity was half of the other peaks, which may indicate broadening of the peak at *ca.* 152 ppm (indicated by arrow), possibly assigned to an additional C8 site. The aliphatic region of the spectrum shows four peaks (for sites C1, C9, C11 and C12) and again two peaks at 30.1 and 32.4 ppm (for carbon C10). The carbon C12 of the material

stored at increased humidity underwent down-field shift of *ca.* 1 ppm compared to the starting material. Furthermore, the asymmetry of the C12 peak in the spectrum of the starting material may indicate the presence of two C12 sites of TB in the silica pores. Similarly, splitting of C10 carbon indicates it is present in two different environments.
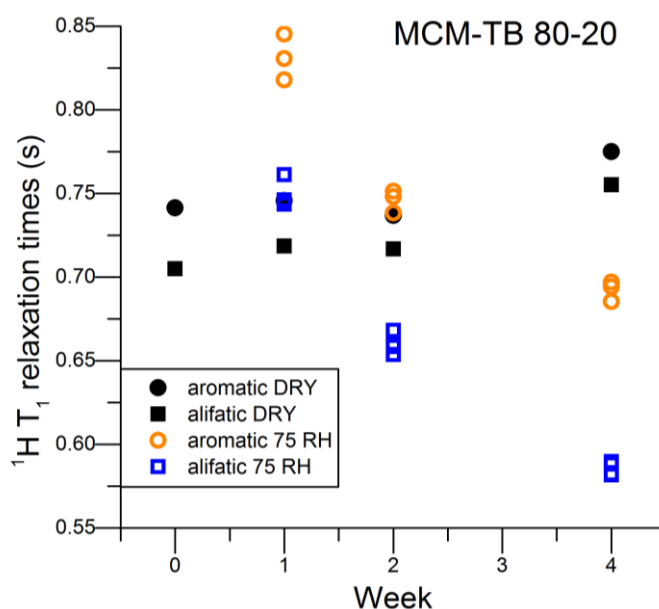
Figure 7-34. ^{1}H T_1 relaxation times for MCM-TB 80-20 composite stored in dry and humid conditions over a period of four weeks. The expected errors for the method are between 5 to 10 %.

The ^{1}H T_1 relaxation times (Figure 7-34) highlight differences in the mobility of MCM-TB 80-20 composite stored in either dry or humid conditions. Clear separation between ^{1}H T_1 relaxation times of the aliphatic and aromatic ^{1}H sites in the material stored at 75 % RH highlights differences in mobility across both parts of the molecule. A gradual decrease in ^{1}H T_1 relaxation times with storage was observed for this material, which may be related to progressing dissolution and/or increasing content of water inside the pores. The material stored in dry conditions does not show significant differences in ^{1}H T_1 values over the four weeks of storage as shown in Figure 7-34.

7.2.6.2 Effect of storage conditions on the TB confined within MCM-41 silica scaffold loaded at 50 wt. % using melting method

TB loaded into the MCM-41 silica host at 50 wt. % underwent complex phase transitions upon storage at room temperature in both dry and humid conditions. It is important to emphasise that TB form V described previously can only be formed by slow crystallisation under dry conditions at 277 K. When the MCM-TB 50-50 composite was stored at RT and above, a mixture of phases, or only TB form I, was formed. The ^{1}H-^{13}C CP/MAS spectrum of the MCM-TB 50-50 composite (week 0) shows broad resonances of amorphous drug inside the pores (Figure 7-35).
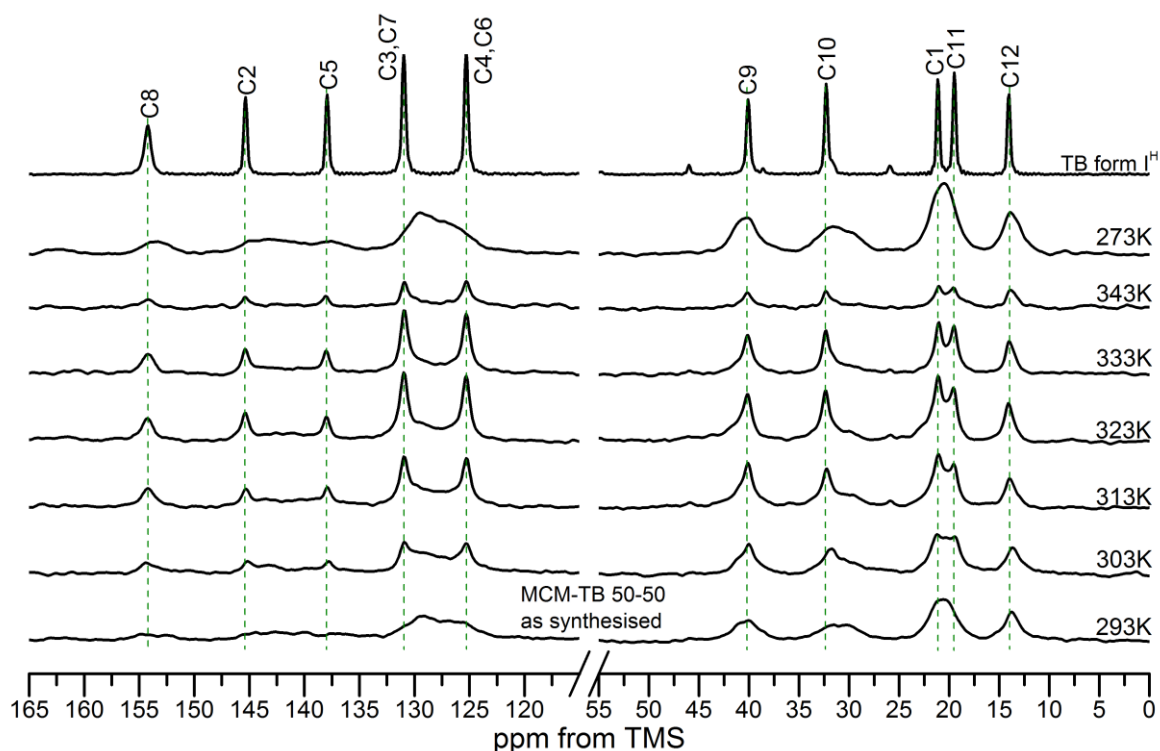
Figure 7-35. Variable-temperature ^{1}H-^{13}C CP/MAS spectra of as synthesised MCM-TB 50-50 composite and TB form I^H. The spectra show growth of TB form I^H followed by its melting at 343K and formation of amorphous confined TB after cooling to 273 K.

Gradual *in situ* heating of the MCM-TB 50-50 composite led to an increased population of TB form I^H as significant narrowing of the ^{13}C peaks was observed in the VT ^{1}H-^{13}C CP/MAS spectra (Figure 7-35). The decrease of the peak intensity in the spectrum acquired at *ca.* 343 K indicates melting of confined TB form I^H. The increased mobility of molten drug leads to a decrease in the CP efficiency, resulting in decreased peak intensity (Figure 7-35). When the sample was cooled to 273 K, broad peaks of confined amorphous TB, formed after melting at 343 K, were observed.

Although the ^{1}H-^{13}C CP/MAS NMR spectrum of the freshly loaded material (week 0) indicated formation of amorphous TB inside the pores, the PXRD pattern of this composite shows four broad peaks, which do not match any of the known TB polymorphs (Figure 7-36 A). The PXRD peaks display significant narrowing upon storage at both the dry and 75 % RH conditions, indicating a growth of the confined crystallites (Figure 7-36). The PXRD peaks may be due to the formation of an intermediate disordered phase, which upon heating transforms directly into stable TB form I^H, as confirmed with VT ^{1}H-^{13}C NMR studies. The DSC thermogram of the starting material (MCM-TB 50-50, week 0) showed a single melting peak at *ca.* 353 K (Figure 7-36). This endotherm displayed the melting of TB form I^H in agreement with melting of this form observed through VT ^{1}H-^{13}C

CP/MAS spectra (Figure 7-35). It is important to note the depression of the melting point of confined TB form I^H by *ca.* 40 K compared to the bulk drug. Furthermore, a lack of the transition peak at *ca.* 313 K indicates there was no confined TB form I^L in the starting material (Figure 7-36).
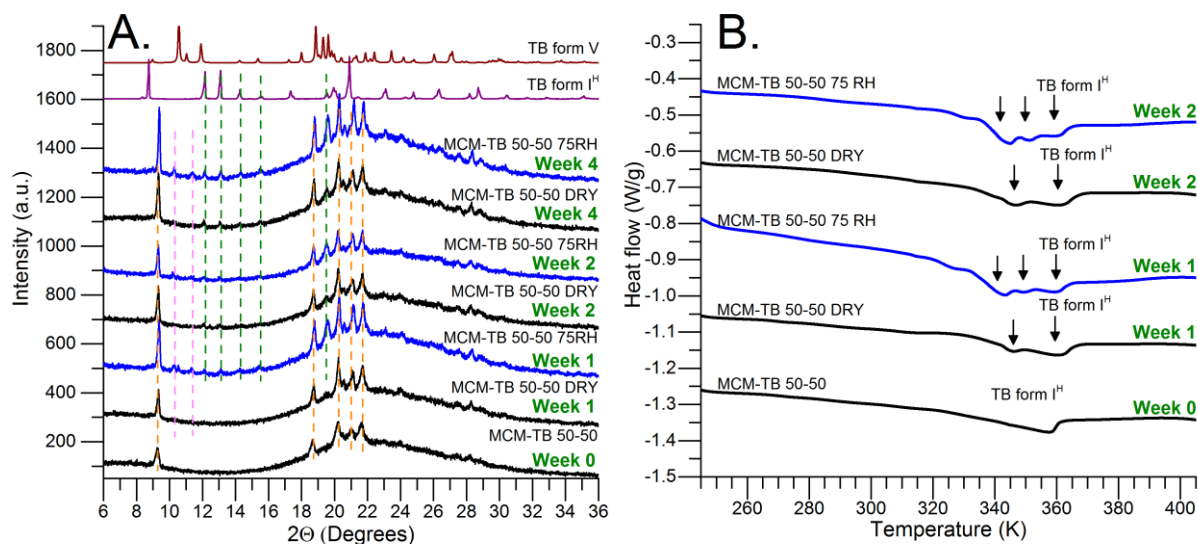
Figure 7-36. A. PXRD patterns and **B.** DSC thermograms of MCM-TB 50-50 composite stored at dry and humid (75 % RH) conditions over a period of four weeks. The PXRD patterns of TB form IL and form V are shown for comparison. Different phases are indicated by dashed lines in green (TB form I^L), orange and pink.

The phase stability of TB confined inside the pores of the MCM-41 silica host at 50 wt. % was highly affected by storage conditions. The accelerated growth of crystalline phases, including TB form I^L in the materials stored at 75 % RH was demonstrated using PXRD, DSC and solid-state NMR spectroscopy (Figure 7-36, Figure 7-37). Three distinct endothermic transitions were seen in the DSC thermograms of the materials stored at increased humidity, indicating the presence of three phases inside the pores of the silica host (Figure 7-36, indicated by arrows). This is in agreement with PXRD data, where three different phases were indicated. Due to similarities in PXRD patterns and overlapping of the peaks, it was difficult to state unequivocally which phases were present within the material. Only TB form I^L could be recognised easily based on the PXRD pattern of the reference material (indicated by green dashed lines). In contrast, the DSC thermograms of the material stored in dry conditions showed only two distinct endotherms indicating the presence of only two phases inside the pores. The DSC data is in good agreement with the PXRD patterns, which show only two distinct phases labelled with orange and green (TB form I^L) dashed lines in Figure 7-36.
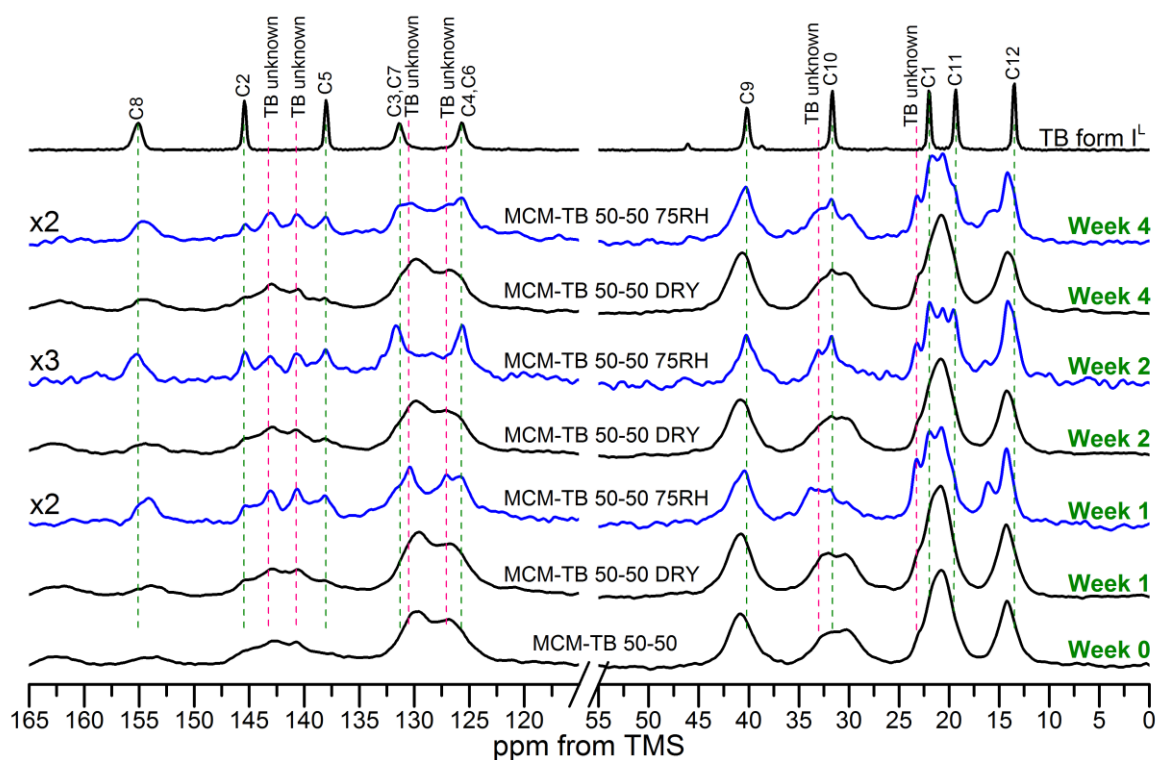
Figure 7-37. ^{1}H-^{13}C CP/MAS solid-state NMR spectra of MCM-TB 50-50 composite stored at dry and humid (75 % RH) conditions over four weeks.

The ^{1}H-^{13}C CP/MAS NMR spectra of the material stored in dry conditions were dominated by broad peaks characteristic of amorphous disordered TB (Figure 7-37). The significant distribution of the ^{13}C chemical shifts of the aromatic carbons in the spectra of amorphous TB (stored at dry conditions) led to only two broad peaks of the six aromatic carbons in the spectrum. The presence of a crystalline component was detected by the presence of sharper peaks superimposed with the broad component of the spectrum. The peaks in the spectra of the MCM-TB composite stored at 75 % RH had 2-3 times lower intensity compared to the spectra of the MCM-TB 50-50 composite stored in dry conditions. Additionally, significant narrowing of multiple peaks in the spectra indicates the presence of more than one crystalline phase. TB form I^L was identified in the spectra of the materials stored at increased humidity (Figure 7-37), labelled with green dashed lines, in agreement with the PXRD patterns. An additional crystalline component identified in the spectra has been labelled with pink dashed lines, but could not be assigned to any of the referenced TB polymorphs described in this chapter. The broadening of the peaks indicated that amorphous TB was still present inside the pores of the material stored at increased humidity. Furthermore, the ^{1}H MAS spectra of the MCM-TB 50-50 composite stored at 75 % RH were also indicative of the presence of multiple components in the material, as substantial broadening of the peaks was observed (Figure 7-38).
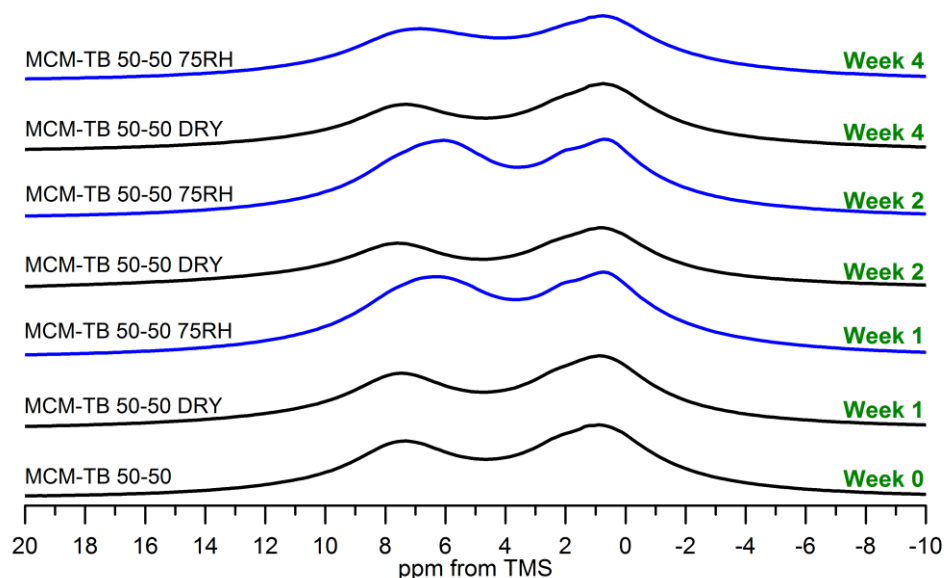
Figure 7-38. ^{1}H MAS solid-state NMR spectra of MCM-TB 50-50 composite stored at **A.** dry and **B.** humid (75 % RH) conditions over four weeks**.**
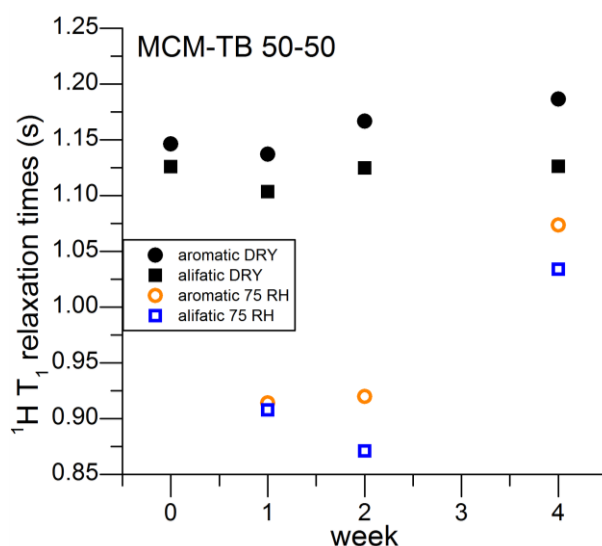
Figure 7-39. ^{1}H T_1 relaxation times for MCM-TB 50-50 composite stored in dry and humid conditions over a period of four weeks. The expected errors for the method are between 5 to 10 %.

The slight increase in mobility of confined TB loaded within the MCM-41 silica scaffold at 50 wt. % stored at 75 % RH was evident from the ^{1}H T_1 relaxation measurements. The ^{1}H T_1 relaxation times of the MCM-TB 50-50 composite stored in dry conditions remained constant (at *ca.* 1.15 s) throughout the four weeks, whilst decrease of TB relaxation times (*ca.* 0.9 s) was observed for the material stored at 75 % RH (Figure 7-39). The substantial differences (*ca.* 0.4 s) in the ^{1}H T_1 relaxation times between the confined TB loaded at 20 wt. % and 50 wt. % indicate increased mobility of the amorphous TB species loaded inside the pores at 20 wt. %, compared to the

crystalline/amorphous composites loaded at 50 wt. %. This may be due to the presence of the free space available for reorientation of TB molecules at lower loadings compared to the densely packed molecules within the pores at 50 wt. % loading. The small changes in the ^{1}H T_1 relaxation times of MCM-TB 50-50 composites compared to the distinct changes in dynamics of TB confined within MCM-TB 80-20 host may be related to the differences in filling of the pores. As seen from the nitrogen adsorption analysis (Figure 7-18) at 20 wt. % drug loading, there is still enough space within the pores for water vapour to enter and dissolve the drug molecules. However, at 50 wt. % loading, pores seem to be completely filled with drug molecules, seen through the almost flat nitrogen adsorption isotherm (type II isotherm) (Figure 7-18), which is characteristic of nonporous solids. Therefore, most of the drug molecules encapsulated deeper within the pores are not accessible for water due to limited penetration.

The ^{1}H T_1 relaxation times of both MCM-TB 50-50 and MCM-TB 80-20 composites stored in dry conditions indicate a higher mobility of TB molecules in fully amorphous composites (MCM-TB 80-20) compared to the silica host loaded with crystalline drug. Similar differences were demonstrated in materials stored at 75 % RH humidity, where composites loaded at 20 wt. % displayed lower ^{1}H T_1 relaxation times (Figure 7-34) compared to MCM-TB scaffolds loaded at 50 wt. % (Figure 7-39). These differences may be due to packing density of TB within the pores: as TB loaded at 20 wt. % has more space for reorientation, it undergoes faster motions, compared to the more densely packed crystalline TB encapsulated inside mesopores of MCM-41 at higher loading level.

To summarise, we have demonstrated that the state of encapsulated TB depends on the drug content within the pores and relative humidity storage conditions. We were able to distinguish TB confined in the pores of MCM-41 material in different local environments with different dynamics using both ^{1}H and ^{13}C NMR experiments. The application of different ^{13}C signal enhancement methodologies, sensitive to either solid or liquid like environments, enabled us to distinguish both rigid and highly mobile components of the confined TB at low loading levels. TB loaded at 20 wt. % within the MCM-41 silica host and stored at 75 % RH was found to reside in more than one environment, as highly mobile liquid like species. The composites stored in dry conditions remained amorphous and did not change over a period of four weeks, as demonstrated using PXRD, DSC and solid-state NMR. The materials loaded with 50 wt. % of TB and stored at 75 % RH displayed accelerated crystallisation towards two TB polymorphs including TB form I^L as compared to the predominately amorphous material stored in dry conditions. These findings have implications for the pharmaceutical industry regarding the effect of storage conditions on the phase stability of encapsulated drug molecules. In depth, understanding of such processes is of paramount importance from an industrial perspective, as it enables knowledge-based design of drug delivery systems.

7.3   Conclusions

In this chapter we gained in-depth understanding of possible phase transitions of the flexible molecule TB encapsulated inside very small pores of MCM-41 silica host (*ca.* 2.6 nm).

Firstly, we focused on the detailed characterisation of model TB polymorphs (forms I^L, I^H, IV and V) and detected dynamics of the TB phenyl ring in three different crystalline forms using VT solid-state NMR studies. We further have identified low temperature phase transition of TB form IV (TB form IV^L). The dynamics of the phenyl ring may be linked with the relative phase stability order and transitions between different TB forms. The new TB form IV^L and ring dynamics in a series of TB crystals will be the subjects of further structural and spectroscopic studies.

Detailed investigation of TB confined within MCM-41 pores enabled us to develop a new method to crystallise highly unstable TB form V inside the mesopores of *ca.* 2.6 nm. The crystallisation of the relatively large model pharmaceutical TB (270.35 g mol^{-1}) is very unusual in small pores and to the best of our knowledge this is the first report of such a phenomenon. We believe this may be related to the flexibility of the molecule, which enables it to be packed more efficiently in confined geometries. For comparison, flufenamic acid (281.23 g mol^{-1}) can be crystallised only in ten times larger pores[306]. The *in situ* monitoring of the confined phase transitions of TB form V → Tb form I^H and TB form I^L→TB form I^H was demonstrated for the first time. By application of VT ^{1}H-^{13}C CP/MAS NMR studies we have proven that at high drug loadings, TB molecules are present as both confined crystals and amorphous drug molecules.

Finally, confined TB loaded at 20 wt. % was shown to undergo dissolution inside the silica pores when exposed to 75 % RH. The dissolved molecules were in at least two different environments, detected through the application of different ^{13}C NMR methods. In contrast, at 50 wt. % drug loading, accelerated crystallisation into the more stable TB polymorphs was detected. In these studies, we developed an experimental approach towards molecular level understanding of dissolution processes of drug delivery systems using NMR based methods.

General discussion and conclusions

Chapter 8

8.1 Knowledge based design of mesoporous silica based systems for drug delivery – from amorphous to nano-crystalline composites

In formulation science it is of paramount importance to prepare uniformly loaded composites, which are physically stable over a storage time. To design the mesoporous silica based composites for drug delivery one needs to consider several factors affecting the final state of the confined drug. These factors are:

A. Structure of the drug and its physicochemical properties;
B. Type of mesoporous silica – pore diameter, total pore volume and surface area, pores architecture;
C. Loading method and desired drug content within the pores.

These three main factors affect the expected phase of confined drug, which in turn may affect important pharmaceutical properties including dissolution or phase stability. Herein we present general approach for the design of silica-drug scaffolds based on our findings in context of other work published to date.

8.1.1 Structure of the loaded drug and its physicochemical properties

In our study, we used three model drugs (FFA, TB, IMC), which differ in molecular size, flexibility and physicochemical properties. Both FFA and TB have similar glass forming ability *i.e.*, they recrystallise on cooling from the melt and are difficult to stabilise in an amorphous state due to low T_g (*ca.* 278 K for TB and *ca.* 290 K for FFA). Additionally, both are of similar size but differ in molecular flexibility; as FFA has a more rigid structure with only three bonds that can differ between the conformers whilst TB has a flexible structure with seven bonds that can rotate freely. IMC has significantly higher T_g (*ca.* 323 K) and it is known to stay amorphous for at least 36 h when stored at 303 K prior to crystallisation to its thermodynamically most stable form γ-IMC.[59,204] The core of the IMC molecule is an indole ring which has three flexible motifs attached to it: a chlorophenyl ring, a methoxy group and an acetic acid motif and the position of these three components with respect to the indole ring differs between the crystal structures (Figure 8-1).

In order to make sure that the drug is loaded inside the pores of the silica host, the size of the molecule needs to be smaller than the size of the pores. This is not difficult to achieve for small pharmaceutical molecules, with the longest dimension usually shorter than 20 Å, however for delivery of peptides or small proteins size constraints need to be considered.

Figure 8-1. Top. Size of FFA, TB and IMC determined using the bounding box tool in Olex2 software. **Bottom:** comparison of physicochemical properties of TB, FFA and IMC.
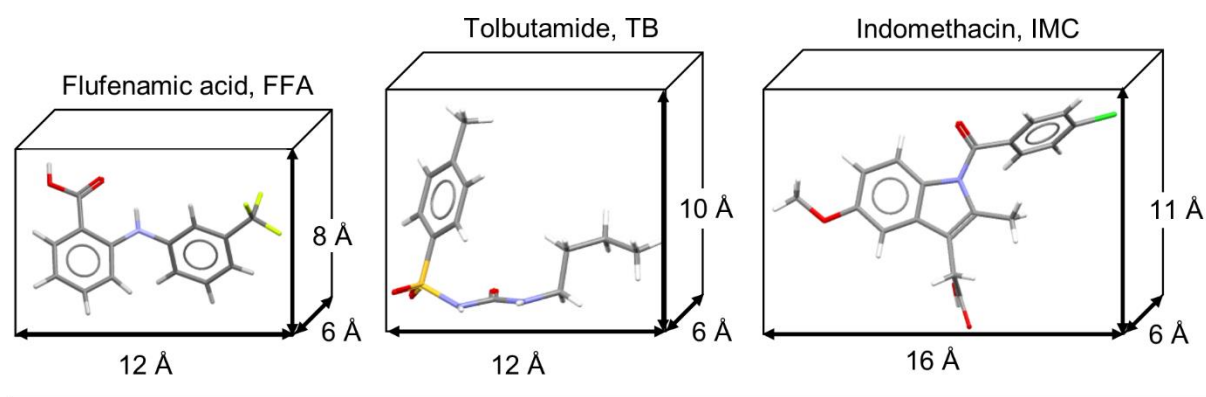
Properties	Flufenamic acid	Tolbutamide	Indomethacin
Molecular weight	281.2	270.4	357.8
Glass transition temperature (K)	290	278	323
Melting point (K)	407 – Form I	400 – Form I^H	433 – γ-IMC
Molecular volume (Å^3)	211	227	283
Number of polymorphs	9	6	>5

Molecular size is also important for the phase prediction of the loaded drug, as critical nucleus size (r*) needs to be achieved for crystallisation to occur. If the nucleus size is smaller than r*, it will dissolve spontaneously; whilst nuclei larger than r* will grow spontaneously.[93,308] The critical nucleus size is considered to be on the nm scale, however the absolute values for r* are related to the solid/liquid interfacial energy and the difference between the Gibbs free energy per unit volume of solids and liquids. It is therefore not surprising that different critical nucleus sizes are expected for different molecules. For example, it was shown by Pradzynski et al. that a cluster of 275 water molecules was required to form an ice crystal [309] which represents an 18 × 18 × 18 Å cube, which is in excellent agreement with the critical size of an ice nucleus (12 – 18 Å) as determined by Cooper and co-workers.[310] Davey et al. (2013) gave examples of experimentally determined 20 nm sized nucleating clusters in solution for alanine and citric acid.[308] Much smaller sizes of 1-3 nm were reported by Ginde and Myerson for glycine, citric acid and urea.[308,311] This agrees with the results of Ward and co-workers who crystallised β-glycine inside 7.5 nm CPG pores.[250] In recent work, Navrotsky et al. showed that for the confined crystallisation of N,N,N-trimethyl-1-adamantammonium iodide within porous silicas, the volume of one unit cell size was sufficient for molecules to crystallise.[303]

We showed that molecular size, structural flexibility and glass forming ability are all important factors to consider for the prediction of crystallisation outcome inside porous hosts. In our studies, we used the melting method to incorporate drug molecules inside the pores. This method was successfully used by Beiner *et al.* to load paracetamol into CPG hosts with different pore size diameters. Additionally, it allowed direct differentiation between the bulk and confined species based on the melting point depression for compounds which recrystallise on cooling, or subsequent reheating.[114] For relatively large IMC (MW=357.8 g/mol), which forms a well-documented amorphous solid, we did not observe crystallisation inside the pores of MCM-41 and SBA-15 materials (pore size *ca.* 3 and 8 nm respectively). This was in agreement with data published by Lehto[85] and Van den Mooter[41]. We only observed the thermal recrystallisation of IMC at high drug contents inside the large pores of the CPG host (*ca.* 55 nm), while inside the pores of the slightly smaller MCF host (*ca.* 30 nm), thermal recrystallisation of IMC was again supressed. Crystallisation to either γ-IMC or the IMC MeOH solvate was only driven by the addition of organic solvents into the IMC loaded MCF hosts, indicating the enhanced structural rearrangement of the confined species, likely due to increased mobility following solvent addition.

TB and FFA were used as model compounds as they are both unstable in the amorphous state, recrystallising quickly following cooling. When FFA was confined inside the pores of MCM-41 and SBA-15 hosts, it remained amorphous during heating. The thermally induced recrystallisation of this compound was only observed inside the 30 nm pores of the MCF host at loadings above 20 wt. %. In contrast, the highly flexible TB molecule crystallised inside the 3 nm pores of MCM-41. Our results therefore suggest that it is not only the molecular size, but also structural flexibility which is important in predicting the phase of the confined drug, as the presence of multiple freely rotating bonds plays an important role in confined crystallisation.

Finally, it is important to discuss our results in the context of other low melting point compounds described in the literature (ibuprofen, IBU T_m = 351 K, fenofibrate, FEN T_m = 353 K and coumarin, COU T_m = 345 K) (Figure 8-2). Ibuprofen is a well known model drug used in nanoconfinement research.[75,79,112] It is relatively small (MW = 206 g/mol) and highly unstable in the amorphous state (T_g = 228 K). Therefore, we can expect IBU to crystallise inside the small pores of MCM-41 in a similar way to TB. IBU loaded inside MCM-41 scaffolds (*ca.* 3-4 nm) was investigated by both Azais *et al*. and Skorupska *et al.*[77,79] Azais *et al.* showed that confined IBU stayed in a highly mobile liquid-like state at room temperature and vitrified at 223 K, using solid-state NMR spectroscopy.[77,79] The lack of crystallisation was thought to be due to spatial constraints, preventing nucleation of the confined drug.[77] Conversely, Skorupska *et al.* observed peaks due to both crystalline and amorphous drug in the ^{13}C spectra and explained that amorphous IBU was formed inside the pores, whilst crystalline drug was present outside the pores.[79] Unfortunately, both studies lacked DSC and PXRD data, and

therefore it is difficult to state unequivocally whether the crystalline species observed by Skorupska *et al.* was due to bulk drug loaded outside the pores, or confined crystalline IBU. When IBU was loaded inside the large pores of MCM-41 (*ca.* 12 nm), Azais *et al.* observed crystallisation of the drug at 223 K, well below its bulk melting point.[77] The confined crystallisation of IBU inside porous silicon was observed by Lehto *et al.*[312] Although the size of the pores was not specified by the authors, the presence of a hysteresis loop at a high relative pressure in the N_2 adsorption/desorption data indicates they used pore sizes of 20-30 nm.[312]
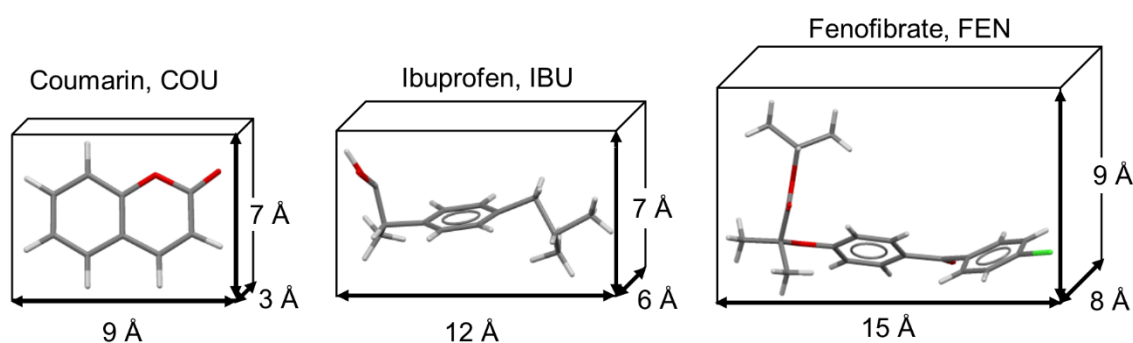
Properties	Coumarin	Ibuprofen	Fenofibrate
Molecular weight	146.2	206.3	360.8
Glass transition temperature (K)	NA	228	253
Melting point (K)	345	351	354
Molecular volume ($Å^3$)	123	190	297
Number of polymorphs	2	2	3

Figure 8-2. Top. Size of COU, IBU and FEN determined using the bounding box tool in Olex2 software. **Bottom:** comparison of physicochemical properties of COU, IBU and FEN.

Fenofibrate has a similar molecular weight to IMC (MW = 360.8 g/mol), but due to its linear structure, it is more flexible than IMC. Recently, Myerson *et al.* showed that FEN crystallised inside *ca.* 20 nm pores when loaded from solution, whilst further decrease of pore size to *ca.* 13 nm led to stabilisation of the amorphous drug.[111] These findings are in agreement with our results for IMC, as we observed the formation of crystalline drug inside 29 nm pores. The additional degree of structural flexibility for FEN enabled the formation of confined crystals inside smaller 20 nm pores, but as with IMC, its large molecular size prevented the formation of a critical nucleus inside the 13 nm pores.[111]

Coumarin is small rigid compound (MW = 146.2 g/mol) used frequently in perfumes and its derivatives are known as laser dyes.[115] It crystallises as α-coumarin in the orthorhombic *Pca*2_1 space group with four molecules in the unit cell (Z'=1).[313,314] Ward and co-workers obtained a new polymorphic form of COU (β-coumarin) inside the pores of a CPG host (pore size less than 23 nm) using the melting method for encapsulation.[115] The group identified both α and β COU inside 7.5 nm CPG pores using PXRD, which were measured at 278 K due to the partial melting of COU crystals at room temperature.[115] The photo-physical and photo-luminescence properties of COU derivatives encapsulated in *ca.* 4 nm MCM-41 hosts using the melting method were investigated by Li *et al.* and Zhao *et al.*[315,316] Based on the absorption, emission[315] and fluorescence[316] spectra, both groups stated that encapsulated COU derivatives formed a monomolecular dispersion.[315,316] These findings are in agreement with the results of the Ward group, as due to the decrease of the melting point (due to encapsulation), COU would be expected to remain as a liquid inside the 4 nm pores of the MCM-41 host.

In summary, to predict the phase of drug molecules confined within mesoporous silica based scaffolds, it is important to consider both the size and structural flexibility of the molecule of interest, as these parameters influence the resulting phase of loaded drug. Other important predictors are T_g and T_m, as these can also determine whether the loaded drug will crystallise, remain amorphous or form a highly mobile liquid-like species at room temperature. For the design of mesoporous silica based DDS, it is additionally necessary to know the properties of the silica scaffold and required drug loading level within the pores. These factors are discussed in section 8.1.2.

8.1.2   Type of mesoporous silica – pore diameter, total pore volume and surface area, pores architecture

In this section, I will highlight the properties of mesoporous silicas, which can be synthetically tailored to provide unique features required for the encapsulation of the pharmaceutical molecule of interest.

For standard sol-gel synthesis of ordered mesoporous silicas, the pore size determines the available scaffold surface and volume. Hosts with small pores will have a large surface area and relatively small pore volume (per mass unit). This is important for the adsorption of drug molecules, as the encapsulation process inside the pores of such hosts (*e.g.*, SBA and MCF) begins on the pore surface and proceeds after the saturation of the surface: a plug of drug molecules is formed in the pore void, which subsequently grows along the pores, filling the available pore volume (Figure 8-3). This mechanism was suggested by Ukmar *et al.* for IMC encapsulation in SBA-15[87] and was recently proven by our group using ^{19}F NMR and FFA as a model compound.[306]
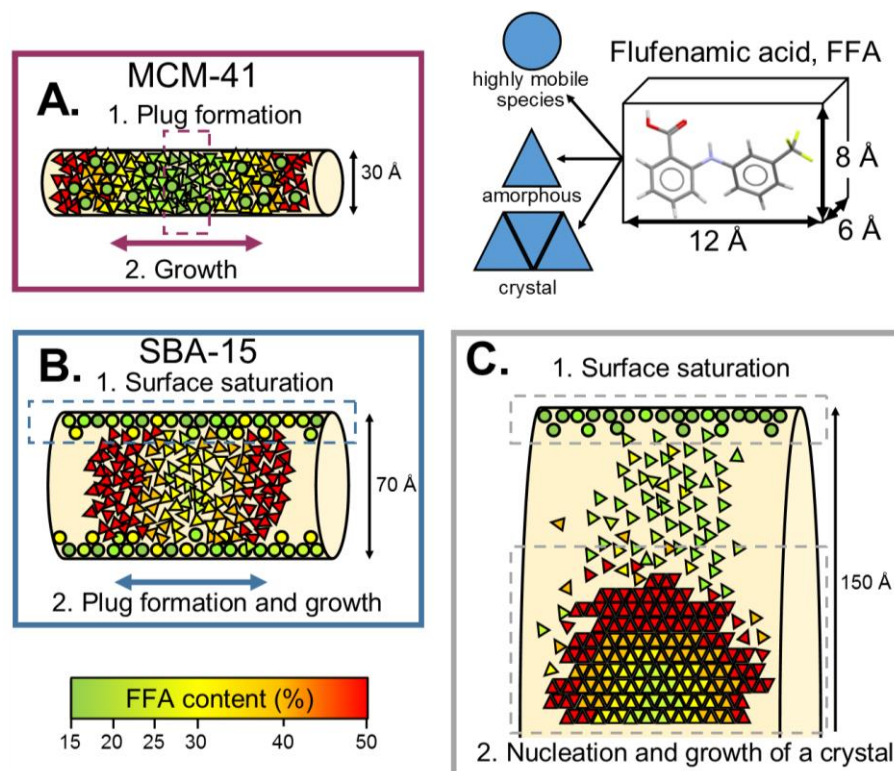
Figure 8-3. Top right: Average dimensions of the FFA molecule and the three different states of FFA species inside the pores. **A)** and **B)** Different mechanisms for FFA adsorption and stabilization of the amorphous state. **C)** Mechanism of the formation of crystalline FFA form I in MCF (for a detailed description, see Chapter 6). Adapted from [306].

To understand how differences in the surface area of the porous host can affect the final state of confined drug, both size and molecular flexibility of the drug must be considered alongside the required drug loading level and material properties. For a system of a small MW drug encapsulated in pores larger than 7 nm with a drug loading below 25 wt. %, we expect only the presence of species adsorbed at the pore surface. Crystallisation of the drug in this case would be unlikely, as sufficiently large nuclei of drug molecules cannot be formed in the pore void. Based on our studies, the encapsulation mechanism is different for systems with small pores (MCM-41, *ca.* 3 nm) as compared to systems with larger pores (SBA-15 and MCF), as the plug of drug inside the pores is formed even at low drug loadings. The crystallisation is the effect of molecular properties, including flexibility (important for efficient packing) and minimal size of nucleus (r*) required for crystal growth.

Total pore volume is another parameter that determines the maximum loading capacity of the host. The total pore volume for mesoporous silicas synthesised using standard sol-gel procedures increases with increasing pore size diameter. Therefore, loading capacity of large pore scaffolds is higher compared to hosts with smaller pores (*e.g.,* V_{total} MCF = 1.8 cm^3/g, V_{total} MCM-41 = 0.65

cm^3/g). This parameter is a crucial consideration for larger drug molecules, or when high drug loading needs to be achieved. We have shown for FFA that exclusive drug loading within the pores of MCF was achieved at 50 wt. %, whilst for scaffolds with smaller pores (MCM-41 and SBA-15), crystallisation outside the pores was detected above 40 wt. % drug loading.

8.1.3   Loading method and desired drug content within the pores

There are two frequently used methods for loading pharmaceutical molecules into mesoporous silicas: the impregnation method and the melting method. For efficient loading from the solvent, high concentration of the solute in the loading solution must be achieved, and impregnation is required to be repeated three to four times, to obtain sufficient drug content within the pores. This procedure often leads to the deposition of the loaded drug on the external surface of the silica particles, therefore additional washing of the material is required.[74,317] The maximum drug loading using the impregnation method does not usually exceed 30 wt. %, with many reported systems not reaching 20 wt. %.[39,40] The loading efficiency can be solvent dependent, therefore the correct choice of solvent is important to achieve the desired drug loading.

We used the impregnation method to load IMC into the MCF and CPG scaffolds (pore size of *ca.* 30 and 55 nm respectively).[88] We used concentrated IMC in MeOH solutions (150, 200 and 250 mg/mL) with a lower solvent volume than the available pore volume, in order to obtain reasonable drug loading and avoid deposition of the drug outside the pores of the silica hosts. The obtained drug loading did not exceed 15 wt. % and crystallisation of IMC form V (and γ-IMC) was observed within all composites. Deposition of the drug outside the pores was evident for the materials loaded from the solution of highest concentration (250 mg/mL), due to fast recrystallisation of IMC upon contact with the silica surface. Additionally, if the volume of loading solution exceeded the pore volume, a significant increase if the population of bulk IMC crystals was observed with PXRD and DSC.[88] We tried solvent mediated loading for two other model APIs (TB and FFA), however due to the formation of heterogeneous composites with crystalline drug loaded outside the pores we decided to focus on the more reliable melting method for drug encapsulation.

There is very little data in the literature describing the effect of the solvent impregnation method on confined crystallisation. For the majority of the published systems, where either MCM or SBA silicas were used, the confined drug was amorphous, or not described.[41,70,83,89] Myerson and co-workers used solvent impregnation to incorporate model compounds (IBU, FEN, IMC and griseofulvin) into large pores (40 nm) of commercially available silica (AEROPERL® 300 Pharma). A loading efficiency below 10 wt. % was achieved after washing the drug from the external surface. The presence of a crystalline phase was only detected for FEN and griseofulvin using solid-state NMR, with PXRD not detecting crystalline material. However, due to the low signal intensity for

CP/MAS experiments, the solid-state NMR required 80 000 scans (4.5 days of spectrometer time) for one sample.[317] The same group investigated the confined crystallisation of FEN loaded using the impregnation method for a broad range of CPG scaffolds (pore sizes between *ca.* 13 and 300 nm). A drug content of *ca.* 25-30 wt. % was achieved, with crystallisation of FEN form I detected inside pores of 20 nm and larger.[111] Wang *et al.* used MCF (pore size diameter *ca.* 28 nm) to load two large drugs: simvastatin (SIM, MW = 418.6 g/mol) and telmisartan (TEL, MW = 514.6 g/mol) by soaking the porous scaffold in concentrated ethanol and acetic acid solutions respectively.[249,318] Amorphous composites were obtained at lower drug loadings, but at drug loadings above 40 wt. %, crystalline component loaded outside the pores was detected using both PXRD and DSC.[249,318]

In this work we extensively used the melting method to load model pharmaceuticals (TB, FFA and IMC) into different mesoporous silica scaffolds, achieving a high level of control over the drug phase, distribution and its loading level within the pores. Compared to the impregnation method, the melting method enabled much better control over drug loading level within the pores, as a physical mixture of the drug and the silica scaffold was prepared prior to loading. The main drawback of this procedure was the requirement for the loaded compound to be thermally stable at the loading temperature, which was around 5-10 K higher than the melting point of the drug. We found that amorphous composites were likely to be formed at low drug loadings (below 20-25 wt. %), whilst crystallisation of the API was observed at higher drug loadings. The melting method has been applied successfully in other literature studies for loading paracetamol into CPG glasses and AAO (anodic aluminum oxide) membranes,[113,114,117,119] ibuprofen and itraconazole into MCM-41 scaffolds and porous silicon[79,83,84,312] and dicarboxylic acids and coumarin into CPG glasses and polymeric monoliths.[115,118] Recently, Skorupska *et al.* used the melting method for the encapsulation of benzoic acid/fluorinated benzoic acid and naproxen/picolinamide co-crystals into MCM-41 and SBA-15 materials.[91,92]

It is important to choose the correct encapsulation method to ensure phase control of the resulting solid. We showed that the melting method enables sufficient phase control of encapsulated API. Firstly, we were able to obtain the highly unstable TB form V by encapsulation within the MCM-41 scaffold using the melting method. Previously, this polymorph had only been crystallised from acidified methanol.[183] We were also able to stabilise metastable IMC form V within *ca.* 30 nm pores of MCF using a hybrid approach for crystallisation. We encapsulated amorphous IMC within the silica pores using the melting method, then drove the crystallisation of encapsulated drug into the metastable IMC form V through the addition of methanol.[88] Furthermore, through careful choice of pore size of the silica hosts, and manipulation of the drug content within the pores, we were able to stabilise amorphous FFA within MCM-41 and SBA-15 scaffolds, amorphous TB within MCM-41 at

low drug loadings and amorphous IMC within both MCF and CPG porous hosts at loading levels below 25 wt. %.[88,306]

The use of the melt loading method for encapsulation and formation of crystalline organic molecules confined within nanoporous materials has also been described by other authors. It was shown by Beiner and co-workers that it was possible to obtain usually inaccessible paracetamol form III within a CPG host with pore sizes between 22 and 103 nm, when crystallising form the melt.[114] The same group reported stabilisation of amorphous paracetamol inside 10 nm pores of CPG and significant depression of T_g of the confined drug (*ca.* 20 K) in comparison to bulk paracetamol, which indicates increased mobility of confined drug.[114,117] Unfortunately, the loading level of the drug inside the pores was not specified by the authors.
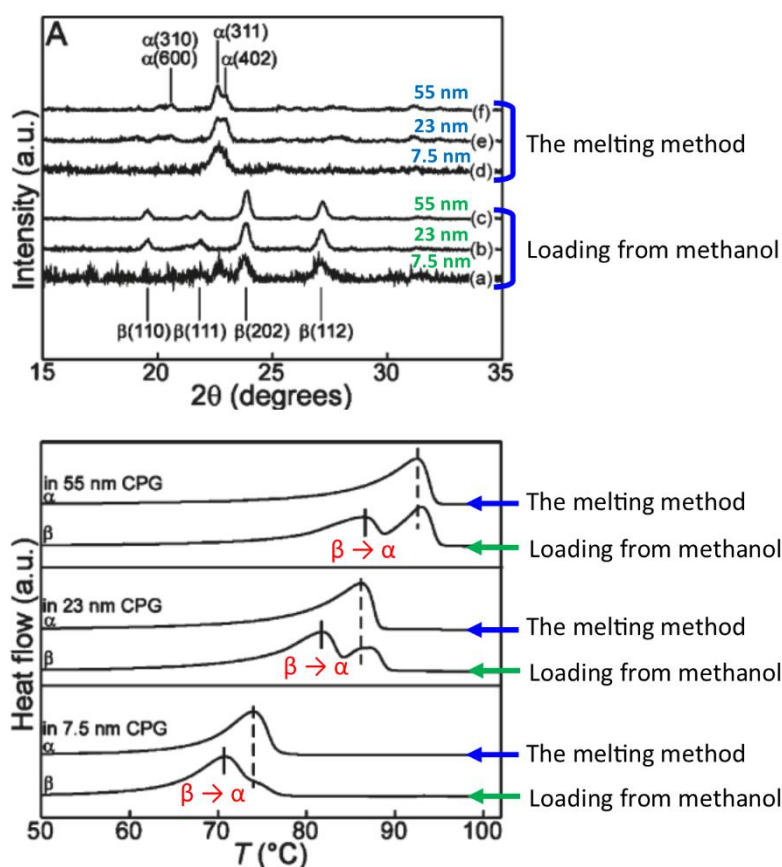
Figure 8-4. PXRD patterns (top) and DSC thermograms (bottom) for glutaric acid loaded within the CPG pores of 7.5, 23, and 55 nm using the melting method and methanol solution. The vertical dashed lines indicate the melting of α-glutaric acid, and the vertical solid lines indicate the β → α phase transition. Adapted from [115].

Ward and co-workers performed crystallisation of dicarboxylic acids inside CPG hosts loaded using both melting and solvent based methods.[115] They achieved much higher drug loading with the

melting method, as compared to solvent mediated loading. Furthermore, the observed crystallisation outcome was found to be dependent on the loading method. For example, it was shown that glutaric acid formed a mixture of α and β polymorphs when crystallised from a methanol solution within the CPG scaffolds, but when using the melt loading method only the metastable α polymorph was observed, and remained stable within the CPG pores for months (not specified).[115]

The melting method was also used by Skorupska *et al.* for loading IBU and two model co-crystals (benzoic acid/fluorinated benzoic acid and naproxen/picolinamide) into MCM-41 and SBA-15 hosts.[79,91,319] The authors demonstrated that although high drug loadings of IBU and co-crystals could be achieved using the melting method, part of the drugs remained in their crystalline phase outside the pores, highlighting the importance of optimisation of drug loading capacity within the mesoporous scaffolds.[79,92,319] Interestingly, the authors demonstrated that for the naproxen/picolinamide system it was possible to overcome the limitations of thermal instability of the drug (in this case naproxen) through the formation of co-crystals, which had a lower melting point compared to bulk drug prior its loading using the melting method.[319]

In summary, we have demonstrated the importance of several parameters that need to be taken into account to design mesoporous silica based materials for drug delivery. Efficient drug encapsulation and control over the physical state of confined molecules is a balancing act between molecular and host properties, alongside experimental protocols for drug encapsulation *i.e*., the loading method. It is important to emphasise that small and flexible molecules tend to crystallise inside the silica pores more easily as compared to relatively large drugs. Nevertheless, the drug content within the pores is of importance, as a sufficiently large and densely packed plug of molecules inside the pore void must be formed for crystal nuclei to grow. Finally, as it is possible to tailor the properties of the silica scaffolds synthetically, the materials can be designed for a particular molecule or a group of compounds.

8.2 Probing structural heterogeneities in confined pharmaceutical systems – the role of solid state NMR

The investigation of the structure of multicomponent materials is a significant challenge, frequently requiring the use of several analytical techniques to gain molecular level understanding of heterogeneous solids. Pharmaceuticals encapsulated within mesoporous silicas are one example of a multicomponent solid, where the drug molecules are confined within the pores of the porous silica scaffold, or loaded outside the pores. We have shown throughout this work that drug molecules can reside in more than one physical state within the pores, ranging from highly mobile liquid-like species to rigid nano-crystalline solids. This section highlights the importance of solid-state NMR in the structural studies of amorphous and amorphous/crystalline composite materials.

Solid-state NMR spectroscopy is a powerful method for the analysis of amorphous solids, as it enables molecular level structural information to be gained through the analysis of the local environment of atoms in solids. Pharmaceutical formulations are frequently developed as amorphous systems, due to the improved dissolution of API as compared to crystalline drugs. A detailed structural and dynamical investigation of drug/polymer amorphous solid dispersions was recently carried out by Dr Lucy Hawarden[49]. Here we present a structural and dynamical investigation of amorphous/nanocrystalline mesoporous silica-drug composites, using similar methods

Although PXRD and DSC are often used to assess the crystallinity of materials, or determine the glass transition temperature of amorphous solids, they have very limited use in detailed structure elucidation of non-crystalline materials. In this work we have shown several examples of seemingly identical amorphous systems (determined using DSC and PXRD), which through analysis with solid-state NMR, were shown to be structurally and dynamically heterogeneous. The amorphous MCM-FFA and SBA-FFA composites were shown to have very different distributions of confined molecules within the pores of silica scaffolds, and significantly different drug loading mechanisms (Figure 8-3). Using ^{19}F MAS NMR, FFA loaded within the 29 nm pores of the MCF scaffold was proven to be present inside the pores as both a crystalline solid and a highly mobile amorphous species, likely located at the pore surface. Additionally the high sensitivity of ^{19}F MAS NMR enabled us to differentiate between crystalline, amorphous and surface species during the *in situ* crystallisation experiment.[306]

The simultaneous presence of a highly mobile species located at the silica surface and amorphous, or nanocrystalline plugs in the pore voids has been postulated by several research groups, and was recently confirmed by our group using ^{19}F MAS NMR.[78,87,110,112,117,303,306] Interestingly, very similar behaviour for the confined mixture of amorphous benzoic acid/fluorinated benzoic acid within a SBA-15 host was shown by the Potrzebowski group using ^{19}F NMR (Figure 8-5).[91]
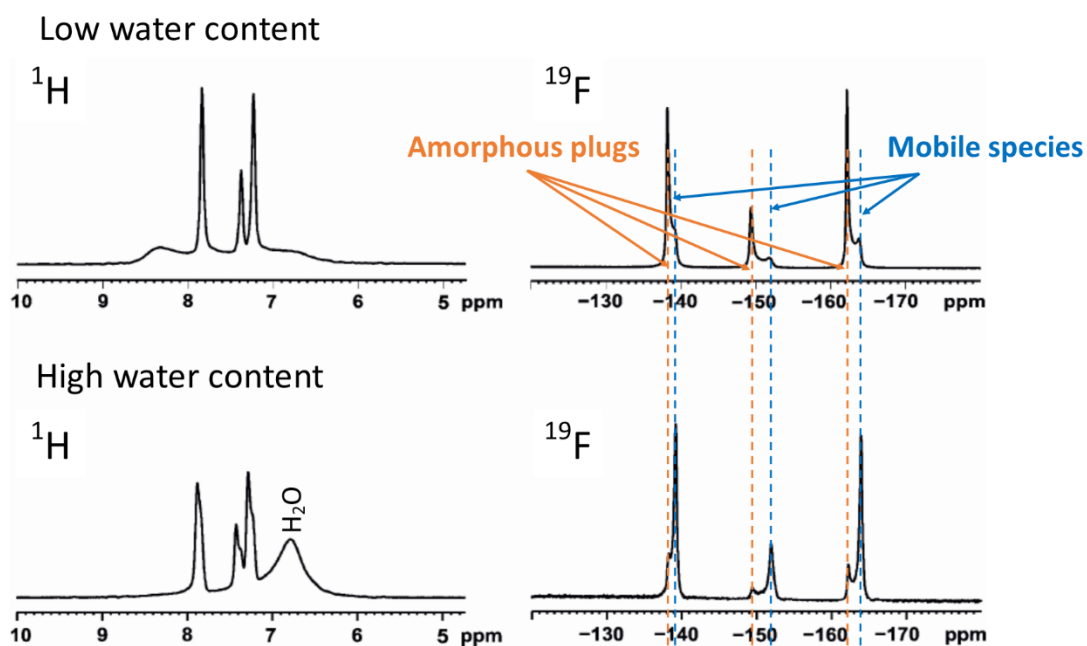
Figure 8-5. ^1H and ^{19}F MAS NMR spectra of benzoic acid/fluorinated benzoic acid confined within SBA-15 with **(Top)** small water content and **(Bottom)** large water content. Adapted from [91].

Two distinct ^{19}F peaks were observed for each fluorine site of fluorinated benzoic acid and the relative population of both peaks was shown to change upon exposure to water.[91] Although this phenomenon was not investigated in detail, and not fully explained by the authors, it does corroborate our findings for the presence of confined molecules in different local environments inside the silica pores.

The identification of species in different environments and motional regimes becomes more complex for molecules that do not contain ^{19}F, or similar high sensitivity nuclei. One of the examples used in this study was confined TB, which was shown to be present in different environments and motional regimes using ^1H T_1 and $T_{1\rho}$ relaxation time measurements alongside with ^1H and ^{13}C NMR methods sensitive to dynamics on different timescales.

Confined TB loaded within MCM-41 at 20 wt. % and stored at 75 % RH was shown to be amorphous using PXRD and DSC. However, solid-state NMR spectroscopy identified a highly mobile liquid-like species inside the silica pores, using ^1H MAS NMR, ^1H-^{13}C J-MAS-INEPT and ^1H-^{13}C HSQC HR/MAS experiments. The presence of ^{13}C NMR peaks in INEPT based experiments without ^1H decoupling between the pulses indicates the presence of a highly mobile liquid-like species, as these have sufficiently long T_2 relaxation for efficient polarisation transfer through the j-couplings. In contrast, in the CP/MAS experiment, using ^1H-^{13}C dipolar couplings for polarisation of ^{13}C signal is not efficient for highly mobile systems, as increased mobility decreases the strength of dipolar couplings, leading to inefficient magnetisation transfer, therefore only rigid components of the material are observed.

The combined application of NMR methods sensitive to different mobility regimes enabled us to identify the co-existence of both highly mobile and rigid TB inside the silica pores.

Confined TB at high drug loadings (50 wt. %) formed confined crystals inside the pores, identified using PXRD, DSC and ^{1}H-^{13}C CP/MAS NMR. The application of the ^{1}H-^{13}C J-MAS-INEPT experiment for this composite did not successfully identify mobile TB species confined within the pores, most likely due to the viscous/rubbery state of the API, which was too rigid to be observed with J-MAS-INEPT. In order to detect the amorphous drug in an intermediate mobility regime (between rigid and liquid states), we re-introduced dipolar interactions by decreasing the temperature during acquisition of ^{1}H-^{13}C CP/MAS spectra, which highlighted broad peaks of non-crystalline TB species alongside crystalline peaks of TB form I^L. The similar use of different ^{13}C excitation methods was described by other authors for the low melting point drug IBU confined within 3.5 and 11.6 nm MCM-41 silica hosts (Figure 8-6).[77]
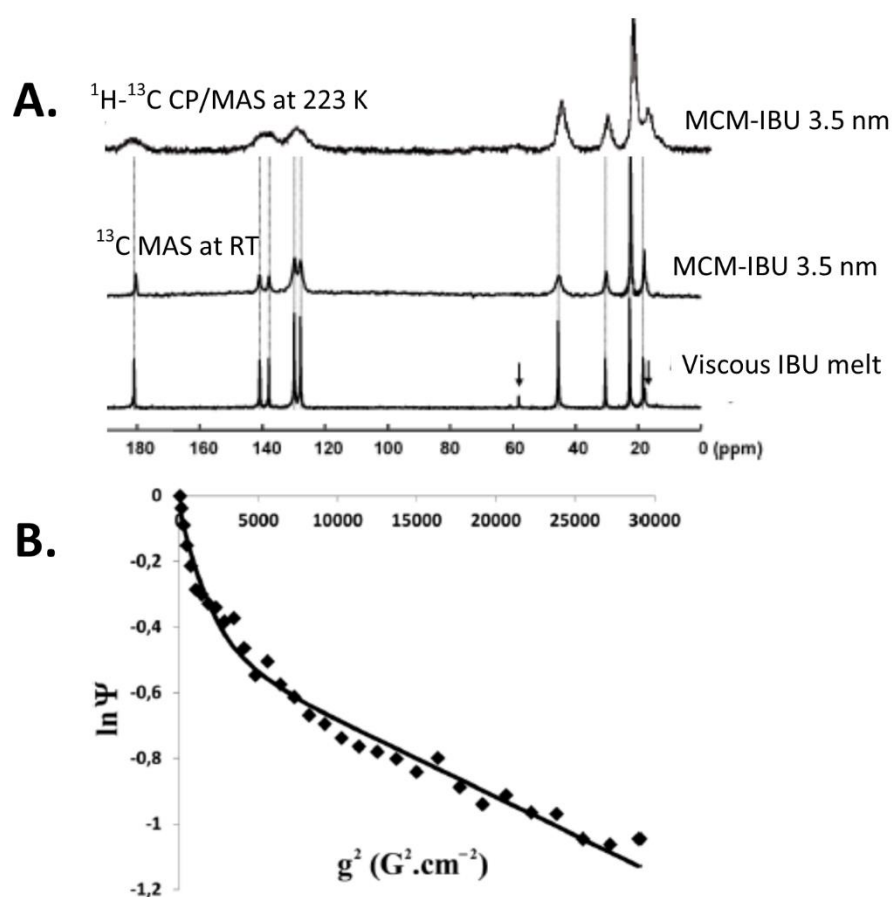
Figure 8-6. A. ^{1}H-^{13}C CP/MAS and ^{13}C MAS spectra of viscous IBU melt and IBU confined within the MCM-41 host at different temperatures; **B.** PFG-MAS ^{1}H NMR echo attenuation curve for IBU confined within the large pores MCM-41 scaffold (ca. 12 nm). The solid line represents bimodal fit to the experimental data. Adapted from [77,78].

Babonneau *et al* identified confined IBU in 3.5 nm MCM-41 scaffolds as either liquid-like species or vitrified drug using ^{13}C NMR (Figure 8-6). Narrow peaks in the ^{13}C MAS NMR spectrum were observed for confined IBU at room temperature, assigned to the presence of a liquid-like species, corroborated by the substantial decrease of signal in ^{1}H-^{13}C CP/MAS NMR, and sharp peaks in the ^{1}H-^{13}C J-MAS-INEPT due to increased mobility and decreased strength of dipolar couplings. At 223 K, significant broadening of the ^{13}C peaks characteristic for amorphous drug was observed using ^{1}H-^{13}C CP/MAS, due to decreased mobility of the drug at low temperatures, corroborated by the gradual broadening of ^{1}H peaks with decreasing temperature.[77] Low temperature crystallisation of IBU confined within the large pores of MCM-41 (11.6 nm) was also observed by Babonneau and co-workers using ^{1}H-^{13}C CP/MAS NMR. The authors observed the coexistence of amorphous and crystalline species through the presence of sharp ^{13}C NMR peaks of crystalline IBU superimposed on the broad peaks of amorphous component (Figure 8-7 A).[77] Additionally, the application of ^{1}H MAS PFG NMR for the amorphous IBU-MCM system with large pores (11.6 nm) revealed the presence of confined molecules in two different motional regimes, assigned again to species at the silica surface and in the pore void.[78]
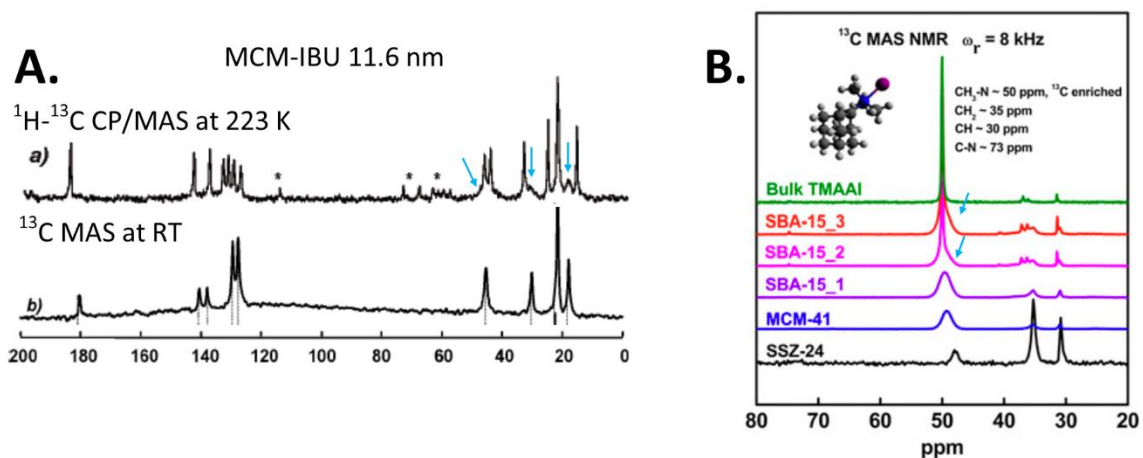
Figure 8-7. A. Crystallisation of IBU within the 11.6 nm pores of the MCM-41 host at 223 K; **B.** Formation of amorphous and crystalline species of the TMAAI inside the pores of different silica frameworks. The arrows indicate the presence of amorphous component. Adapted from [77,303].

The group of Navrotsky investigated in depth host-guest interactions of N,N,N-trimethyl-1-adamantammonium iodide (TMAAI) encapsulated within porous silica scaffolds with pore sizes between 0.8 to 20 nm.[303] The authors observed crystallisation of the TMAAI inside the SBA-15 pores larger than 12 nm, while encapsulation within the smaller pores resulted in the formation of amorphous systems. Using selective ^{13}C labelling, the authors identified the coexistence of

amorphous and crystalline species inside the pores larger than 12 nm (Figure 8-7 B). Using the Scherrer formula, the size of the confined crystals was determined as 11.6 nm for the 12.8 nm pore size of SBA-15, and 18.3 nm for the 20.0 nm pore size of SBA-15, indicating the single nanocrystal filled the pore. Based on these results, and further calculations with Gibbs-Thomson equation, the authors indicated the presence of a molecular layer of a disordered species at the silica surface and a single crystal in or close to the pore centre. This hypothesis is in agreement with our findings from ^{19}F MAS NMR of confined FFA, alongside low temperature ^{1}H-^{13}C CP/MAS NMR studies of confined crystalline TB, where the presence of both amorphous and crystalline species were identified.

The structural investigation of heterogeneous composite materials is analytically challenging due to the presence of multiple components, which could be either an integral part of the structure or phase contamination, which does not carry real structural information for the system. Therefore, for complex materials, it is important to rely on more than one complementary analytical method for structure elucidation, which differ between the confined and bulk species e.g. melting point depression for confined crystals or differences in the relaxation times between bulk and confined species.

For heterogeneous composites of FFA confined within both MCM-41 and SBA-15 silica scaffolds at high drug loadings, we observed a substantial increase in the ^{19}F T_1 relaxation times due to the presence of crystalline FFA species loaded outside the pores with significantly longer ^{19}F T_1 relaxation times. Here, differences in the mobility between the confined and bulk species were used to determine whether the formation of a crystalline phase occurred within the silica pore or outside the pore as bulk crystallisation.

The mobility based approach was used by Potrzebowski and co-workers to distinguish between crystalline IBU loaded outside the pores and a highly mobile species of the drug confined within the MCM-41 pores with the application of variable contact time CP/MAS NMR and dipolar dephasing experiments (Figure 8-8 A).[79]
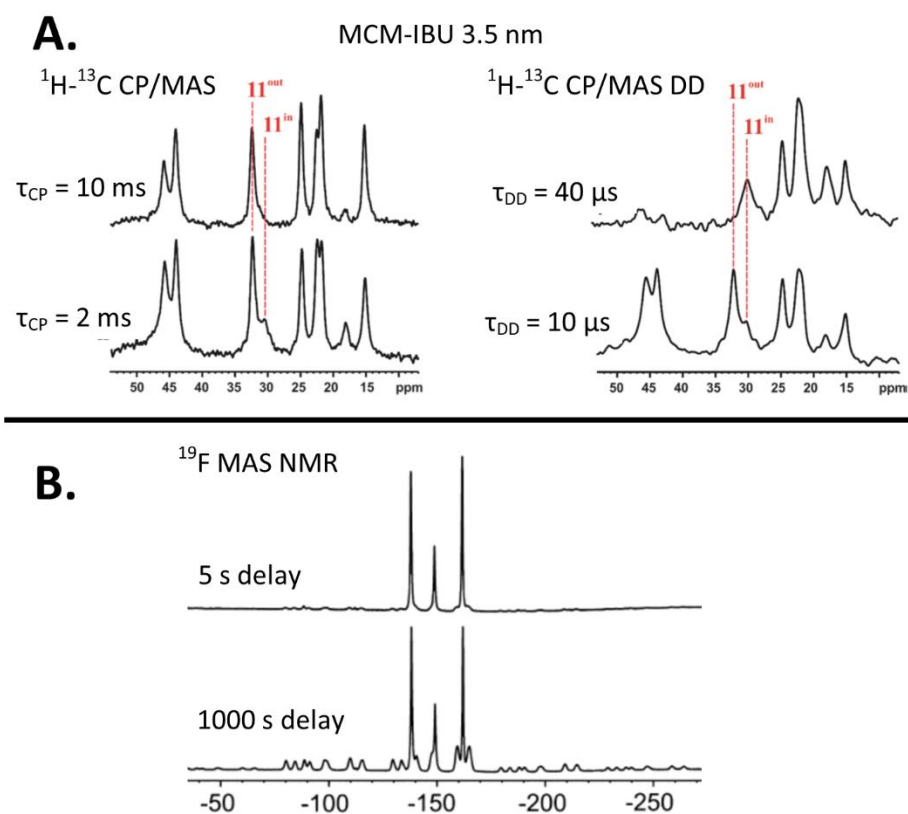
Figure 8-8. A. Variable contact time ^1H-^{13}C CP/MAS spectra and dipolar dephasing (DD) spectra of IBU confined within MCM-41 at high drug loadings – the peaks of the species located inside and outside the silica pores re labelled with red dashed lines; **B.** ^{19}F MAS NMR spectra of fluorinated benzoic acid confined within the MCM-41 host at different recycle delay times. The sharp isotropic peaks indicate highly mobile species confined within the MCM-41 pores while low intensity peaks are due to crystalline species loaded outside the pores. Adapted from [79,91].

In the CP/MAS experiment with 10 ms contact time, the highly mobile species had lower peak intensity compared to the rigid component due to shorter relaxation times. On the other hand, in the dipolar dephasing experiment, the highly mobile drug molecules had intense peaks, due to decreased strength of ^1H-^{13}C dipolar couplings. The rigid species loaded outside the pores disappeared in the spectrum due to enhanced relaxation through the dipolar interactions during the dephasing delay in the pulse program. In another example, the authors used a ^{19}F MAS T_1 filter to distinguish between fluorinated benzoic acid species loaded within the pores of MCM-41, and a crystalline species present outside the pores (Figure 8-8 B).[91] The sharp isotropic ^{19}F peaks of the loaded compound with much faster relaxation times were observed after a 5 s recycle delay, while the broader peaks of the crystalline component were only present after a recycle delay of 1000 s.[91]

In summary, solid-state NMR spectroscopy enabled us to gain an insight into the molecular level structure of fully amorphous composites, identifying molecules in different local environments and motional regimes. The application of this method for heterogeneous crystalline/amorphous

composites is not straightforward, as it requires the distinction between crystalline species loaded inside or outside the pores. For these materials, it is extremely important to apply a multi-technique approach using a combination of DSC, PXRD and N_2 physisorption analysis prior to NMR investigation, as the combined use of these methods enable to confirm that all the observed phenomena are due to the molecules confined within the pores.

8.3 Confined crystallisation from the amorphous state

In-depth understanding of nucleation and crystallisation from the amorphous state is a significant challenge in academic and industrial research, as it ultimately enables control over the structure of the resulting solid. The application of nanoscale confinement offers a unique opportunity to gain insight into the early stages of crystallisation, where small crystalline species have high surface-to-volume ratio.[117] As indicated by Beiner and co-workers the main difference between the crystallisation model based on mesoporous silica and the formation of nano-crystals in the bulk melt is the nature of the interface.[117] The authors suggest that the presence of a layer of amorphous drug molecules at the silica surface is similar to the bulk nanocrystal/melt interface, with the only difference being the mobility and density of the amorphous drug interface.[117] Mesoporous materials are attractive models, which can be used to gain insight into the transient structure of the nucleus and the origin of the crystal/melt interface. There are several open questions that need answering in order to fully understand confined crystallisation. These questions concern: the effect of the pore surface on the spatial distribution of molecules inside the pore; the different molecular environments of confined amorphous molecules, the thickness of the amorphous layer at the pore surface and how the amorphous layer and the pore directs the crystallisation process or the growth of the crystal.

In this work we demonstrated that confined FFA and TB molecules can be present as either fully amorphous or a mixture of amorphous and crystalline forms inside the silica pores. The confined non-crystalline API can be further divided into either highly-mobile surface species, or amorphous species forming a plug in the pore centre. The mechanism of confined crystallisation is not straightforward and depends on the space accessible for the formation of critical nuclei. We showed for all three investigated APIs confined within pores of different sizes that it is not only the size of the pores which are important in confined crystallisation, but also the content of the drug and its distribution within the pores. For example, the thermally induced crystallisation of confined amorphous IMC inside the 29 nm pores of MCF was suppressed up to 50 wt. % drug loading, whilst recrystallisation inside the 55 nm pores of CPG was observed at 30 and 50 wt% loadings.[88] The recrystallisation of confined FFA inside the 29 nm pores of the MCF host detected at drug loadings of 25 wt. % and above, whilst FFA remained amorphous at 15 and 20 wt. % loadings.[306] Similarly,

we were able to crystallise confined TB inside a 3.2 nm MCM-41 silica host, but only at drug loadings of 40 and 50 wt. %. These findings proved the deposition of the drug species at the pore surface prior to the plug formation in the pore void.
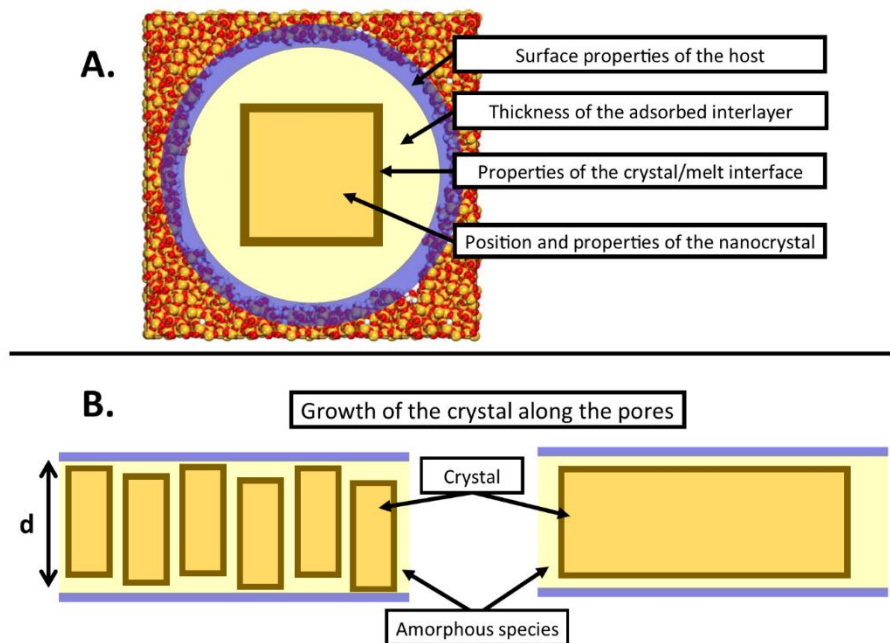
Figure 8-9. A. Summary of the fundamental questions for fully understanding the confined crystallisation from the amorphous state; B. Two possibilities for the crystal growth along the pores of the material.

Beiner and co-workers demonstrated that it was possible to estimate the critical size of the pores (d*) inside which the crystallisation was suppressed, due to the higher surface energy contribution as compared to the energetically advantageous release of internal energy upon crystallisation. The critical pore size is described as follows:

$$d^* = \frac{4\sigma_{cl}T_m^\infty}{(T_m^\infty - T)\Delta H_m \rho_c},$$
(Eq. 8-1)

where σ_{cl} is surface energy between crystal and melt, T_m^∞ is the bulk melting temperature, ΔH_m is the heat of melting and ρ_c is the density of the crystal. This model assumes the pores are fully filled with drug, therefore for systems with low drug loadings, crystallisation might not be observed due to the distribution of the drug molecules at the silica surface.
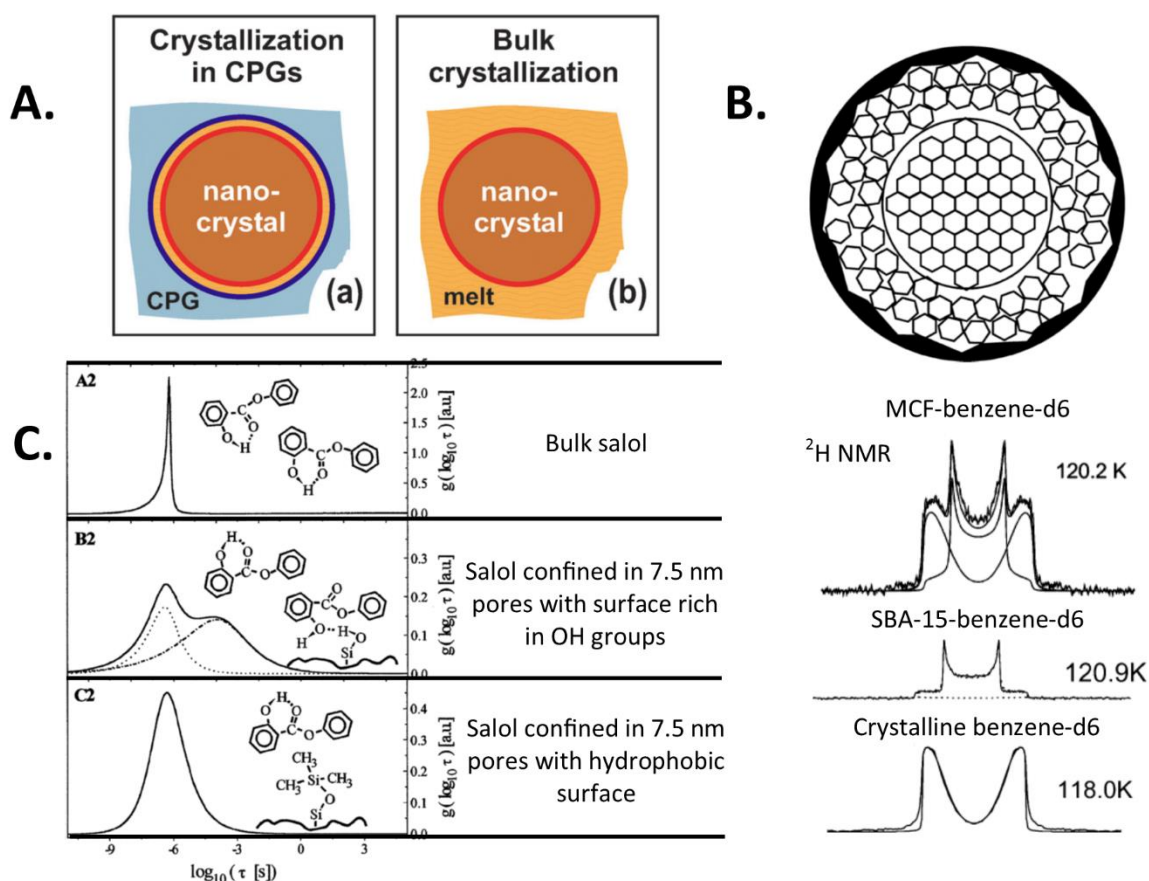
Figure 8-10. A. Similarities between early stages of crystallisation within the melt loaded CPG porous hosts and in the bulk. The red circle represents the nanocrystal/melt interface, dark blue circle represents the hydroxyl terminated silica interface, orange represents amorphous drug and light blue represents the silica wall; **B.** The model of benzene confined within a 30 nm MCF scaffold and ^{2}H NMR spectra of benzene-d6 loaded within MCF silica host showing the presence of crystalline and glassy benzene inside the pores; the spectra of bulk crystalline and glassy (confined in SBA-15) benzene are given for comparison; **C.** The relaxation time distribution g[log$_{10}$(τ)] corresponding to different relaxational processes; an interfacial relaxation process is present for salol confined in the 7.5 nm pores with surface rich in OH groups. Adapted from [117,293,320–322]

The presence of confined molecules distributed at both the silica surface and in the pore void has been proposed in the literature by many authors.[112,117,293,303,306,320] Nevertheless, it is not fully understood: what directs the molecules towards the silica surface; what is the thickness of the adsorbed molecular layer; are the surface/drug interactions characteristic for particular systems? Based on both the ^{19}F NMR and nitrogen physisorption, we were able to determine the thickness of the liquid-like drug layer at the surface of SBA-15 porous host prior to the drug deposition in the pore void (*ca.* 12 Å).[306] We observed similar phenomenon for drug deposition in the MCF scaffold, prior to its crystallisation in the pore void. Using ^{2}H NMR, Buntkowsky and co-workers identified two amorphous solid components for benzene confined in SBA-15 material,[321] and highly mobile and crystalline benzene confined in a 30 nm MCF silica host.[320] The authors determined that the

surface phase had an average thickness of 2-3 molecular layers of benzene.[320] Aksnes *et al.* determined the thickness of cyclohexane and cyclopentane adsorbed onto MCM-41 as 0.65 and 0.51 nm respectively.[301] Navrotsky and co-workers indirectly determined the thickness of the surface phase of confined TMAAI as 1.2-1.6 nm through the determination of the nanocrystal size using the Scherrer formula.[303] Based on the above examples it could be hypothesised that the formation of a highly mobile molecular layer at the silica surface is a general phenomenon for nanoencapsulation within silica pores. However, as the majority of the reports investigated adsorption onto the surfaces rich in silanol groups this could still be a system specific phenomenon. Kremer *et al.* elegantly showed the effect of the surface properties (hydrophilic or hydrophobic) on the adsorption of salol at the pore surface. The authors observed two populations of molecules assigned to the surface species, and molecules in the pore void upon confinement inside the OH group rich material. When salol was confined inside the material with a hydrophobic surface, functionalised with $(CH_3)_3Si-$ groups only one population of molecules assigned to the species distributed in the pore centre was observed.[322]

In summary, the confined crystallisation from the amorphous state is a complex process dependent on the size of the pores, nature of confined molecules, properties of the silica surface and interfacial interactions as shown in Figure 8-9 and Figure 8-10. Despite the complexity of the systems, and the several remaining unanswered questions, mesoporous silicas remain attractive models which can be used to gain molecular level insight into the early stages of crystallisation. Recent developments in solid-state NMR methods for probing the local environment of confined species including ^{2}H NMR (widely used by the Buntkowsky group), selective ^{13}C labelling (used by Navrotsky and co-workers) and mobility sensitive ^{1}H-^{13}C NMR experiments, together with ^{19}F NMR (used in this work) will help to answer some of the questions regarding confined crystallisation and the nature of the critical nucleus.

8.4   NMR insight into structural reorganisation of pharmaceuticals

This project focussed on the application of NMR spectroscopy, supported by complementary techniques (PXRD, DSC, microscopy) and DFT calculations, in understanding the structural reorganisation of pharmaceuticals, in particular confine nanocrystalline and amorphous species present in mesoporous silicas. We were particularly interested in understanding the structural reorganisation in pharmaceutical crystalline solids, including solvates and co-crystals, and identifying the discrete intermediate phases, which are important in so called 'spontaneous reactions' in the solid state. Therefore, the findings from previously published research on co-crystallisation processes[323,324] and disordered crystals[242] have been discussed here.

The importance of co-crystals in pharmaceutical drug delivery is gradually increasing, as these novel materials show promise in providing improved stability, increased dissolution rates and bioavailability compared to the parent crystalline drug. There are several methods for co-crystals formation including crystallisation from solvents, melting, crystallisation through spray drying or mechanical treatment. Some co-crystals can form 'spontaneously' in a physical mixture of each compounds, but sometimes this process is activated with pre-grinding of the physical mixture.[323] The 'spontaneity' of co-crystallisation is frequently related to the presence of intermediate phases or reactions, which are difficult to investigate using standard research procedures.
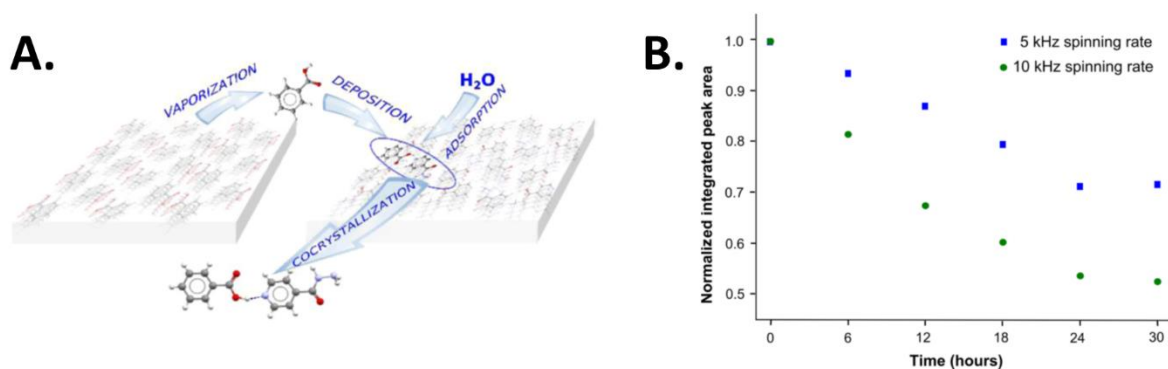
Figure 8-11. A. The schematic mechanism of benzoic acid : isoniazid co-crystallisation reaction; **B.** Normalized intensity of the benzoic acid carbonyl peak during co-crystallisation under 5 and 10 kHz MAS spinning rates.

The isoniazid-benzoic acid co-crystal is an example of a solid, which forms spontaneously from the physical mixture of the compounds. This reaction is accelerated by elevated temperature and humidity or mechanochemical activation.[323] To gain a molecular level understanding of the co-crystallisation process, we used solid-state NMR to support the hypothesis that the crystallisation process is driven by the deposition of highly volatile benzoic acid on the soft surface of hydrophilic isoniazid. In agreement with the results from other methods, we observed no changes in the spectra for the simple physical mixtures of the compounds over an experiment time of 18 h. However, for mechanochemically activated samples, a substantial increase in the reaction rate was observed due to the 10 kHz MAS rate during spectral acquisition. These findings were further confirmed at a slower MAS rate of 5 kHz, where relatively slower conversion was observed.[323] The effect of sample spinning on the material properties is frequently discussed in the literature for fragile samples analysed under fast MAS conditions. Here the increase of sample temperature due to frictional heating and heating through the high power *rf* irradiation can change the temperature inside the rotor.[325–327] We presented direct evidence that fast sample spinning

can accelerate the co-crystallisation reaction rate and therefore significantly alter reaction conditions, likely due to increased frictional forces. Similar observations were made by Harris and co-workers, who noted that fast sample rotation (7 kHz) under MAS conditions can alter the dehydration process of sodium acetate trihydrate, and consequently the polymorphic product of dehydration.[328]
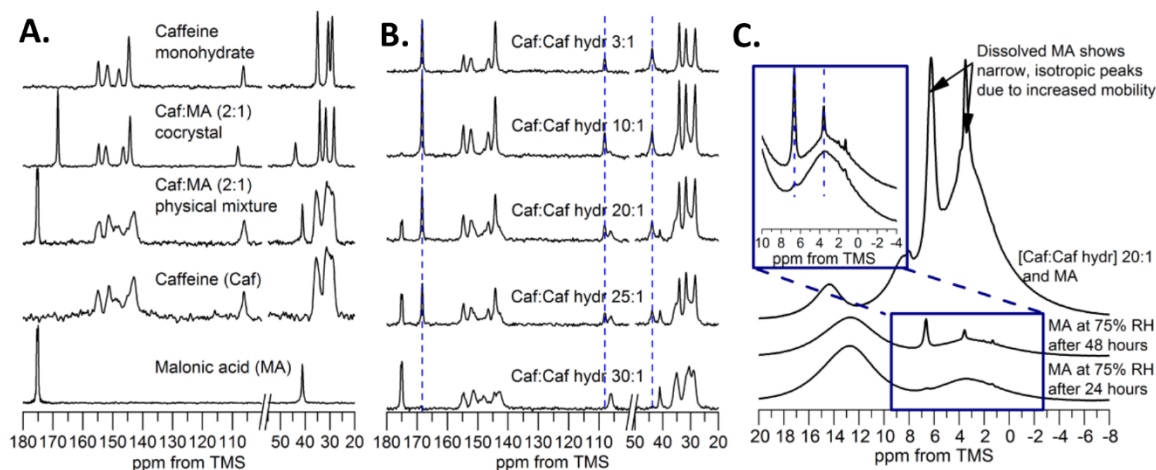
Figure 8-12. A. ^{1}H-^{13}C CP/MAS solid-state NMR spectra of malonic acid, caffeine anhydrous, caffeine monohydrate, caffeine:malonic acid physical mixture and caffeine:malonic acid co-crystal; **B.** ^{1}H-^{13}C CP/MAS NMR spectra showing the effect of water on the rate of formation of the caffeine:malonic acid co-crystal; **C.** ^{1}H MAS NMR spectra of malonic acid after 24 and 48 hours of storage at 75 % RH and [caffeine:caffeine hydrate] 20 : 1 mixture with malonic acid.

The accelerating effect of water on the spontaneity of the co-crystallisation process of caffeine and malonic acid was investigated by our group using solid-state NMR. We outlined that it was possible to tune the kinetics of spontaneous co-crystal formation through the control of water content in the sample. The mechanism of the reaction was understood with the aid of ^{1}H MAS NMR, as we observed sharp ^{1}H peaks of a highly mobile species of malonic acid after storage of the compound at 75 % RH and in the mixture of the reacting compounds, which was assigned to the dissolved species at the crystal surface.[324]

The effect of solvents on the crystallisation is of high importance in materials science, as it can drive structural reorganisation of solids towards materials with new properties. We demonstrated that water dissolved TB confined in MCM-41 material, and that the addition of methanol to IMC loaded MCF silica hosts led to the formation of IMC form V through the intermediate phase of the IMC MeOH solvate.[88]. Through the application of different pulse programs and detection schemes it is possible to distinguish between mobile and rigid species. CLASSIC NMR (Combined Liquid- And

Solid-State In-situ Crystallization NMR) is a recent development in the field introduced by Harris *et al.*.[329–331] This method enables *in-situ* monitoring of the evolution of the crystallisation process through by alternating between two pulse sequences (^{1}H-^{13}C CP/MAS and ^{13}C MAS or ^{1}H-^{31}P CP/MAS), simultaneously probing both the solid component of the mixture and changes in the solution spectra during crystallisation.[329] Using CLASSIC NMR, the authors reported new transient polymorphs during crystallisation of the 1,10-dihydroxydecane-(urea)$_2$ co-crystal and new phases of methyldiphenylphosphine oxide.[331]

The difficulty of producing sufficiently large crystals for single crystal X-ray diffraction studies and the formation of disordered pharmaceutical polymorphs unsuitable for PXRD studies signifies the importance of NMR crystallography in the field of pharmaceuticals. We demonstrated an in depth understanding of order-disorder phenomena in orotic acid crystals formed upon solvent removal.[242] Through the application of multiple analytical techniques, together with CSP and chemical shift calculations, we proposed a mechanism for the structural reorganisation of orotic acid hydrate by the formation of a disordered anhydrous phase upon removal of water. Based on analysis of the changes in the ^{1}H, ^{13}C and ^{15}N chemical shifts between the structures, we were able to identify the sites most affected by solvent removal, and use this information to gain molecular level understanding of the formation of stacking faults in the structure. Interestingly, it was possible to use line widths in ^{13}C NMR spectra to distinguish between anhydrous orotic acid structures with different level of ordering, and aditionally we were able to identify the sites affected by solvent removal by identification of the presence of local disorder by peak broadening.[242] The importance of pharmaceutical hydrates from an industrial perspective makes structural analysis, understanding of hydration/dehydration mechanisms and the prediction of hydrate formation a vital topic in crystallography.[242,332,333] Due to the application of CSP alongside advanced solid-state NMR methods and chemical shift calculations, it is now possible to gain molecular level understanding of the role of water in crystal formation.

In summary, we have shown that solid-state NMR can be successfully used to gain mechanistic insight into structural reorganisation during phase transitions or crystallisation, as it is possible to simultaneously monitor the changes in the liquid and solid phases. Additionally, the combined application of solid-state NMR together with CSP and robust DFT codes, enable identification the structures of low crystallinity materials, which are not suitable for X-ray diffraction studies.

8.5 Overall conclusions

1. Mesoporous silica/pharmaceutical composites were successfully prepared using three model APIs (IMC, FFA and TB) with different structural and physicochemical properties and four model porous scaffolds with pores sizes between 3 and 55 nm at different host:guest ratios. It was possible to determine and correlate maximum loading capacity of the silica host with the structural parameters of the drug (molecular weight, molecular volume and three dimensional size). The combined application of complementary analytical techniques, including DSC, PXRD, nitrogen adsorption analysis and TGA, allowed successful investigation of the structure and mobility of confined molecules. The combined application of multiple analytical techniques was essential for full understanding of complex composite materials and to distinguish between the bulk and confined species.

2. Based on the chosen model compounds and silica systems we developed a general strategy for knowledge based design of mesoporous silica based drug delivery systems. We have demonstrated the importance of several parameters in order to ensure either the stabilisation of the amorphous drug inside the silica pores or to obtain nanocrystalline composites. It was identified that small flexible molecules (*e.g.* TB) tend to crystallise inside 3 nm sized pores of the silica scaffolds, while more rigid (*e.g.* FFA) or larger compounds (*e.g.* IMC) require more space for the formation of sufficiently large critical nuclei for spontaneous growth. It was shown that at low drug loadings (15-20 wt. %), the formation of confined crystals is less likely as compared to high drug loadings (25-50 wt. %), due to preferential drug distribution at the surface of the pores of the silica scaffold, prior to filling of the pore void and formation of the nuclei in the pore centre.

3. Through the application of ^{19}F MAS NMR and ^{1}H-^{13}C CP/MAS NMR experiments at low temperatures, it was proven that confined molecules are present inside the silica pores in multiple local environments. It was demonstrated through the application of ^{19}F T_1, ^{1}H T_1 and ^{1}H $T_{1\rho}$ that highly mobile amorphous species, likely localised at the silica surface, are formed at low drug loading levels inside the pores, whilst at higher loadings, the molecules begin to form densely packed plugs in the centre of the pore, which eventually may achieve the size of critical nucleus and spontaneously grow as a nanocrystal. The highly mobile species are present alongside the densely packed amorphous or nanocrystalline phase likely forming an interface between the centre of the pore and the hydroxyl terminated silica walls.

4. It was proven through the application of multiple NMR experiments sensitive to molecular dynamics, that water moisture may dissolve the confined species, which displayed liquid-like behaviour and increased mobility. The dissolved confined molecules may reside in more than

one conformation indicated through the application of multiple ^{13}C experiments. The water moisture was shown to accelerate recrystallisation of the confined molecules loaded at high drug contents, however the penetration into the pores was restricted. The addition of organic solvents to the materials loaded with drug molecules in amorphous state enabled us to obtain and stabilise metastable IMC form V.

5. The combined application of solid-state NMR together with computational conformational studies of known crystal structures of IMC enabled us to gain molecular insight into the structure of two low crystallinity Z' = 2 polymorphs of IMC (IMC form IV and IMC form V). Through the application of conformational analogies and comparison between experimental and calculated ^{1}H and ^{13}C chemical shifts of IMC molecules isolated from different crystal structures, we were able to identify spectral features sensitive to the conformational changes. The structural information about two IMC polymorphs (form IV and form V) obtained in this investigation will be used in further computational studies using CSP methods to gain mechanistic insight and better understanding of desolvation processes, which may lead to discoveries of new polymorphs.

6. A detailed understanding of crystallisation processes was achieved through the application of methods sensitive to the local environment of molecules. Advanced NMR methods helped us to explain the molecular processes in the early stages of crystal formation due to its sensitivity towards both solid and liquid species. Furthermore, the effect of water moisture on the physical state of confined TB enabled us to gain an insight into drug dissolution and identification of liquid-like and solid species inside the silica pores. These findings are of importance for further understanding of the APIs release mechanisms from mesoporous silica based drug delivery systems.

References:

[1]   J. Y. Ying, C. P. Mehnert, M. S. Wong, *Angew. Chemie Int. Ed.* **1999**, *38*, 56–77.

[2]   S. Giret, M. Wong Chi Man, C. Carcel, *Chemistry* **2015**, *21*, 13850–65.

[3]   S. Wang, *Microporous Mesoporous Mater.* **2009**, *117*, 1–9.

[4]   Y. Han, S. S. Lee, J. Y. Ying, *Chem. Mater.* **2007**, *19*, 2292–2298.

[5]   N. E. Fauré, P. J. Halling, S. Wimperis, *J. Phys. Chem. C* **2014**, *118*, 1042–1048.

[6]   J. T. A. Jones, C. D. Wood, C. Dickinson, Y. Z. Khimyak, *Chem. Mater.* **2008**, *20*, 3385–3397.

[7]   M. G. Rimoli, M. R. Rabaioli, D. Melisi, A. Curcio, S. Mondello, R. Mirabelli, E. Abignente, *J. Biomed. Mater. Res. Part A* **2008**, *87A*, 156–164.

[8]   P. Horcajada, C. Serre, M. Vallet-Regí, M. Sebban, F. Taulelle, G. Férey, *Angew. Chemie* **2006**, *118*, 6120–6124.

[9]   Y. Xu, S. Jin, H. Xu, A. Nagai, D. Jiang, R. M. Barrer, R. Fricke, H. Kosslick, G. Lischke, M. Richter, et al., *Chem. Soc. Rev.* **2013**, *42*, 8012.

[10]   A. Corma, **1997**, DOI 10.1021/CR960406N.

[11]   T. H. Elmer, in *Eng. Mater. Handb.*, ASM International, Materials Park, Ohio, **1992**, pp. 427–432.

[12]   S. H. Hakim, B. H. Shanks, *Chem. Mater.* **2009**, *21*, 2027–2038.

[13]   M. Thommes, K. Kaneko, A. V. Neimark, J. P. Olivier, F. Rodriguez-Reinoso, J. Rouquerol, K. S. W. Sing, *Pure Appl. Chem.* **2015**, *87*, 1051–1069.

[14]   T. Čendak, E. Žunkovič, T. U. Godec, M. Mazaj, N. Z. Logar, G. Mali, *J. Phys. Chem. C* **2014**, *118*, 6140–6150.

[15]   V. Meynen, P. Cool, E. F. Vansant, *Microporous Mesoporous Mater.* **2009**, *125*, 170–223.

[16]   R. Amorim, N. Vilaça, O. Martinho, R. M. Reis, M. Sardo, J. Rocha, A. M. Fonseca, F. Baltazar, I. C. Neves, *J. Phys. Chem. C* **2012**, *116*, 25642–25650.

[17]   I. Braschi, G. Paul, G. Gatti, M. Cossi, L. Marchese, G. Domagk, B. A. Hemstreet, A. K. Sarmah, M. T. Meyer, A. B. Boxall, et al., *RSC Adv.* **2013**, *3*, 7427.

[18]   I. Braschi, G. Gatti, G. Paul, C. E. Gessa, M. Cossi, L. Marchese, *Langmuir* **2010**, *26*, 9524–9532.

[19]   N. Vilaça, R. Amorim, A. F. Machado, P. Parpot, M. F. R. Pereira, M. Sardo, J. Rocha, A. M. Fonseca, I. C. Neves, F. Baltazar, *Colloids Surfaces B Biointerfaces* **2013**, *112*, 237–244.

[20]   P. Horcajada, C. Serre, G. Maurin, N. A. Ramsahye, F. Balas, M. Vallet-Regí, M. Sebban, F. Taulelle, G. Férey, *J. Am. Chem. Soc.* **2008**, *130*, 6774–6780.

[21]   C.-Y. Sun, C. Qin, X.-L. Wang, G.-S. Yang, K.-Z. Shao, Y.-Q. Lan, Z.-M. Su, P. Huang, C.-G. Wang, E.-B. Wang, et al., *Dalt. Trans.* **2012**, *41*, 6906.

[22]   J.-S. Qin, D.-Y. Du, W.-L. Li, J.-P. Zhang, S.-L. Li, Z.-M. Su, X.-L. Wang, Q. Xu, K.-Z. Shao, Y.-Q. Lan, et al., *Chem. Sci.* **2012**, *3*, 2114.

[23]   A. C. McKinlay, R. E. Morris, P. Horcajada, G. Férey, R. Gref, P. Couvreur, C. Serre, *Angew. Chemie Int. Ed.* **2010**, *49*, 6260–6266.

[24]   C. T. Kresge, M. E. Leonowicz, W. J. Roth, J. C. Vartuli, J. S. Beck, *Nature* **1992**, *359*, 710–712.

[25]   J. S. Beck, J. C. Vartuli, W. J. Roth, M. E. Leonowicz, C. T. Kresge, K. D. Schmitt, C. T. W. Chu, D. H. Olson, E. W. Sheppard, *J. Am. Chem. Soc.* **1992**, *114*, 10834–10843.

[26]   V. Paul, Novel Sol-Gel Materials for Advanced Glass Products: Structure, Dynamics and Stability, **2012**.

[27]   J. C. Vartuli, K. D. Schmitt, C. T. Kresge, W. J. Roth, M. E. Leonowicz, S. B. McCullen, S. D. Hellring, J. S. Beck, J. L. Schlenker, *Chem. Mater.* **1994**, *6*, 2317–2326.

[28]   J. S. Beck, J. C. Vartuli, G. J. Kennedy, C. T. Kresge, W. J. Roth, S. E. Schramm, *Chem. Mater.* **1994**, *6*, 1816–1821.

[29]   A. Steel, S. W. Carr, M. W. Anderson, J. S. Beck, J. C. Vartuli, W. J. Roth, M. E. Leonowicz, C. T. Kregse, K. D. Schmitt, C. T.-W. Chu, et al., *J. Chem. Soc. Chem. Commun.* **1994**, *114*, 1571.

[30]   A. Monnier, F. Schüth, Q. Huo, D. Kumar, D. Margolese, R. S. Maxwell, G. D. Stucky, M. Krishnamurty, P. Petroff, A. Firouzi, et al., *Science (80-.).* **1993**, *261*.

[31]   C.-Y. Chen, S. L. Burkett, H.-X. Li, M. E. Davis, *Microporous Mater.* **1993**, *2*, 27–34.

[32]   E. Davies, M. J. Duer, S. E. Ashbrook, J. M. Griffin, *J. Am. Chem. Soc.* **2012**, *134*, 12508–12515.

[33]   G. J. d. A. A. Soler-Illia, E. L. Crepaldi, D. Grosso, C. Sanchez, *Curr. Opin. Colloid Interface Sci.* **2003**, *8*, 109–126.

[34]   Susan M. De Paul, † Josef W. Zwanziger, Ralph Ulrich, *,‡ and Ulrich Wiesner, H. W. Spiess*, **1999**, DOI 10.1021/JA984389Q.

[35]   D. Zhao, *Science (80-.).* **1998**, *279*, 548–552.

[36]   M. K. and, M. Jaroniec*, C. H. K. and, R. Ryoo, **2000**, DOI 10.1021/CM000164E.

[37]   * Pascal Van Der Voort, and Mina Benjelloun, E. F. Vansant, **2002**, DOI 10.1021/JP0261152.

[38]   P. Schmidt-Winkel, W. W. Lukens, P. Yang, D. I. Margolese, J. S. Lettow, J. Y. Ying, G. D. Stucky, *Chem. Mater.* **2000**, *12*, 686–696.

[39]   M. Manzano, M. Colilla, M. Vallet-Regí, *Expert Opin. Drug Deliv.* **2009**, *6*, 1383–400.

[40]   M. Vallet-Regí, F. Balas, D. Arcos, *Angew. Chem. Int. Ed. Engl.* **2007**, *46*, 7548–58.

[41]   M. Van Speybroeck, V. Barillaro, T. Do Thi, R. Mellaerts, J. Martens, J. Van Humbeeck, J. Vermant, P. Annaert, G. Van den Mooter, P. Augustijns, *J. Pharm. Sci.* **2009**, *98*, 2648–58.

[42]   C. Argyo, V. Weiss, C. Bräuchle, T. Bein, *Chem. Mater.* **2014**, *26*, 435–451.

[43]   G. Cavallaro, P. Pierro, F. S. Palumbo, F. Testa, L. Pasqua, R. Aiello, *Drug Deliv.* **n.d.**, *11*, 41–6.

[44]   M. Vallet-Regí, L. Ruiz-González, I. Izquierdo-Barba, J. M. González-Calbet, *J. Mater. Chem.* **2006**, *16*, 26–31.

[45]   T. Asefa, Z. Tao, *Chem. Res. Toxicol.* **2012**, *25*, 2265–2284.

[46]   H. A. Santos, J. Salonen, L. M. Bimbo, V.-P. Lehto, L. Peltonen, J. Hirvonen, *J. Drug Deliv. Sci. Technol.* **2011**, *21*, 139–155.

[47]   M. Manzano, M. Vallet-Regí, R. Langer, M. Vallet-Regí, F. Balas, D. Arcos, L. L. Hench, J. Wilson, M. Vallet-Regí, L. Ruiz-González, et al., *J. Mater. Chem.* **2010**, *20*, 5593.

[48]   W. Xu, J. Riikonen, V.-P. Lehto, *Int. J. Pharm.* **2013**, *453*, 181–97.

[49]   L. E. Hawarden, Polymer Drug Dispersions: Understanding Structure and Dynamics, University of East Anglia, **2015**.

[50]   C. A. Angell, *Proc. Natl. Acad. Sci. U. S. A.* **1995**, *92*, 6675–82.

[51]   J. F. Willart, M. Descamps, *Mol. Pharm. 5*, 905–20.

[52]   "http://www.oxforddictionaries.com/definition/english/crystal," **n.d.**

[53]   L. Smart, E. Moore, *Solid State Chemistry : An Introduction*, CRC Press, **2012**.

[54]   Y. Kawabata, K. Wada, M. Nakatani, S. Yamada, S. Onoue, *Int. J. Pharm.* **2011**, *420*, 1–10.

[55]   J. S. LaFountaine, J. W. McGinity, R. O. Williams, III, *AAPS PharmSciTech* **2016**, *17*, 43–55.

[56]   L. Yu, *Adv. Drug Deliv. Rev.* **2001**, *48*, 27–42.

[57]   J. D. Mullins, T. J. Macek, *J. Am. Pharm. Assoc. (Scientific ed.)* **1960**, *49*, 245–248.

[58]   E. Fukuoka, M. Makita, S. Yamamura, *Chem. Pharm. Bull. (Tokyo).* **1986**, *34*, 4314–21.

[59]   M. Yoshioka, B. C. Hancock, G. Zografi, *J. Pharm. Sci.* **1994**, *83*, 1700–5.

[60]   P. Karmwar, K. Graeser, K. C. Gordon, C. J. Strachan, T. Rades, *Int. J. Pharm.* **2011**, *417*, 94–100.

[61]   K. Kawakami, T. Harada, K. Miura, Y. Yoshihashi, E. Yonemochi, K. Terada, H. Moriyama, **2014**.

[62]   Y. Yoshihashi, H. Iijima, E. Yonemochi, K. Terada, *J. Therm. Anal. Calorim.* **2006**, *85*, 689–692.

[63]   M. Tobyn, J. Brown, A. B. Dennis, M. Fakes, Q. Gao, J. Gamble, Y. Z. Khimyak, G. McGeorge, C. Patel, W. Sinclair, et al., *J. Pharm. Sci.* **2009**, *98*, 3456–68.

[64]   K. Löbmann, R. Laitinen, H. Grohganz, K. C. Gordon, C. Strachan, T. Rades, *Mol. Pharm.* **2011**, *8*, 1919–28.

[65]   A. Shayanfar, A. Jouyban, *J. Pharm. Innov.* **2013**, *8*, 218–228.

[66]   A. Paudel, M. Geppi, G. Van den Mooter, *J. Pharm. Sci.* **2014**, *103*, 2635–2662.

[67]   Y. Aso, S. Yoshioka, T. Miyazaki, T. Kawanishi, *Chem. Pharm. Bull. (Tokyo).* **2009**, *57*, 61–64.

[68]   Y. Song, X. Yang, X. Chen, H. Nie, S. Byrn, J. W. Lubach, *Mol. Pharm.* **2015**, *12*, 857–866.

[69]   T. N. Pham, S. A. Watson, A. J. Edwards, M. Chavda, J. S. Clawson, M. Strohmeier, F. G. Vogt, *Mol. Pharm.* **2010**, *7*, 1667–91.

[70]   * M. Vallet-Regi, A. Rámila,   and R. P. del Real, J. Pérez-Pariente, **2000**, DOI

10.1021/CM0011559.

[71] B. Muñoz, A. Rámila, J. Pérez-Pariente, and I. Díaz, M. Vallet-Regí*, **2002**, DOI 10.1021/CM021217Q.

[72] A. Rámila, B. Muñoz, J. Pérez-Pariente, M. Vallet-Regí, *J. Sol-Gel Sci. Technol.* **2003**, *26*, 1199–1202.

[73] C. Charnay, S. Bégu, C. Tourné-Péteilh, L. Nicole, D. A. Lerner, J. M. Devoisselle, *Eur. J. Pharm. Biopharm.* **2004**, *57*, 533–40.

[74] T. Azais, G. Hartmeyer, S. Quignard, G. Laurent, F. Babonneau, *J. Phys. Chem. C* **2010**, *114*, 8884–8891.

[75] T. Azaïs, G. Hartmeyer, S. Quignard, G. Laurent, C. Tourné-Péteilh, J.-M. Devoisselle, F. Babonneau, *Pure Appl. Chem.* **2009**, *81*, 1345–1355.

[76] F. Babonneau, L. Yeung, N. Steunou, C. Gervais, A. Ramila, M. Vallet-Regi, *J. Sol-Gel Sci. Technol.* **2004**, *31*, 219–223.

[77] T. Azaïs, C. Tourné-Péteilh, F. Aussenac, N. Baccile, C. Coelho, J.-M. Devoisselle, F. Babonneau, *Chem. Mater.* **2006**, *18*, 6382–6390.

[78] F. Guenneau, K. Panesar, A. Nossov, M.-A. Springuel-Huet, T. Azaïs, F. Babonneau, C. Tourné-Péteilh, J.-M. Devoisselle, A. Gédéon, *Phys. Chem. Chem. Phys.* **2013**, *15*, 18805–8.

[79] E. Skorupska, A. Jeziorna, P. Paluch, M. J. Potrzebowski, *Mol. Pharm.* **2014**, *11*, 1512–9.

[80] M. Delle Piane, M. Corno, A. Pedone, R. Dovesi, P. Ugliengo, *J. Phys. Chem. C* **2014**, *118*, 26737–26749.

[81] M. Delle Piane, S. Vaccari, M. Corno, P. Ugliengo, *J. Phys. Chem. A* **2014**, *118*, 5801–7.

[82] M. van Speybroeck, R. Mellaerts, T. Do Thi, J. A. Martens, J. Van Humbeeck, P. Annaert, G. Van den Mooter, P. Augustijns, *J. Pharm. Sci.* **2011**, *100*, 4864–76.

[83] R. Mellaerts, J. A. G. Jammaer, M. Van Speybroeck, H. Chen, J. Van Humbeeck, P. Augustijns, G. Van den Mooter, J. A. Martens, *Langmuir* **2008**, *24*, 8651–9.

[84] P. Kinnari, E. Mäkilä, T. Heikkilä, J. Salonen, J. Hirvonen, H. A. Santos, *Int. J. Pharm.* **2011**, *414*, 148–56.

[85] T. Limnell, T. Heikkilä, H. A. Santos, S. Sistonen, S. Hellstén, T. Laaksonen, L. Peltonen, N. Kumar, D. Y. Murzin, M. Louhi-Kultanen, et al., *Int. J. Pharm.* **2011**, *416*, 242–51.

[86] T. Ukmar, T. Čendak, M. Mazaj, V. Kaučič, G. Mali, *J. Phys. Chem. C* **2012**, *116*, 2662–2671.

[87] T. Ukmar, A. Godec, O. Planinšek, V. Kaučič, G. Mali, M. Gaberšček, *Phys. Chem. Chem. Phys.* **2011**, *13*, 16046–54.

[88] K. P. Nartowski, J. Tedder, D. E. Braun, L. Fábián, Y. Z. Khimyak, *Phys. Chem. Chem. Phys.* **2015**, DOI 10.1039/c5cp03880d.

[89] A. Kiwilsza, B. Milanowski, K. Drużbicki, L. E. Coy, M. Grzeszkowiak, M. Jarek, J. Mielcarek, J. Lulek, A. Pajzderska, J. Wąsicki, *J. Porous Mater.* **2015**, *22*, 817–829.

[90] A. Kiwilsza, A. Pajzderska, J. Mielcarek, J. Jenczyk, J. Wąsicki, *Chem. Phys.* **2016**, *475*, 126–130.

[91] E. Skorupska, P. Paluch, A. Jeziorna, M. J. Potrzebowski, *J. Phys. Chem. C* **2015**, *119*, 8652–8661.

[92] E. Skorupska, A. Jeziorna, M. J. Potrzebowski, *J. Phys. Chem. C* **2016**, acs.jpcc.6b05302.

[93] B. D. Hamilton, J.-M. Ha, M. A. Hillmyer, M. D. Ward, *Acc. Chem. Res.* **2012**, *45*, 414–23.

[94] J. W. Steed, J. L. Atwood, *Supramolecular Chemistry*, Wiley, **2009**.

[95] W. C. McCrone, in *Phys. Chem. Org. Solid State,* (Eds.: M.M.L.. Fox, A. Weissberger), Wiley Interscience, New York, **1965**, pp. 725–767.

[96] J. Bernstein, *Polymorphism in Molecular Crystals*, Oxford University Press, **2007**.

[97] J. O. Henck, J. Bernstein, A. Ellern, R. Boese, *J. Am. Chem. Soc.* **2001**, *123*, 1834–41.

[98] H. G. Brittain, *J. Pharm. Sci.* **2012**, *101*, 464–84.

[99] B. Moulton, M. J. Zaworotko, *Chem. Rev.* **2001**, *101*, 1629–58.

[100] J. Haleblian, W. McCrone, *J. Pharm. Sci.* **1969**, *58*, 911–929.

[101] H. G. Brittain, *Polymorphism in Pharmaceutical Solids, Second Edition*, CRC Press, **2009**.

[102] E. H. Lee, *Asian J. Pharm. Sci.* **2014**, *9*, 163–175.

[103] J. Bauer, S. Spanton, R. Henry, J. Quick, W. Dziki, W. Porter, J. Morris, *Pharm. Res.* **2001**, *18*,

859–66.

[104] S. L. Morissette, S. Soukasene, D. Levinson, M. J. Cima, O. Almarsson, *Proc. Natl. Acad. Sci. U. S. A.* **2003**, *100*, 2180–4.

[105] C. Jackson, G. McKenna, *J. Non. Cryst. Solids* **1991**.

[106] M. Alcoutlabi, G. B. McKenna, *J. Phys. Condens. Matter* **2005**, *17*, R461–R524.

[107] H. K. Christenson, T. W, E. R. and M. B. M. U, E. R, B. R. W. and F. A. G, P. I. B. A. and E. D. H. Defay R, R. H. and W. I. B, L. A. Q. J. F. and E. C. Brun M, L. A. Q. J.-F. and E. C. Brun M, D. B. V, et al., *J. Phys. Condens. Matter* **2001**, *13*, R95–R133.

[108] C. Alba-Simionesco, G. Dosseh, E. Dumont, B. Frick, B. Geil, D. Morineau, V. Teboul, Y. Xia, *Eur. Phys. J. E - Soft Matter* **2003**, *12*, 19–28.

[109] C. Alba-Simionesco, B. Coasne, G. Dosseh, G. Dudziak, K. E. Gubbins, R. Radhakrishnan, M. Sliwinska-Bartkowiak, *J. Phys. Condens. Matter* **2006**, *18*, R15-68.

[110] Q. Jiang, M. D. Ward, *Chem. Soc. Rev.* **2014**, *43*, 2066–79.

[111] L. M. Dwyer, V. K. Michaelis, M. O'Mahony, R. G. Griffin, A. S. Myerson, *CrystEngComm* **2015**, DOI 10.1039/C5CE01148E.

[112] A. R. Brás, E. G. Merino, P. D. Neves, I. M. Fonseca, M. Dionísio, A. Schönhals, N. T. Correia, *J. Phys. Chem. C* **2011**, *115*, 4616–4623.

[113] G. T. Rengarajan, D. Enke, M. Beiner, *Open Phys. Chem. J.* **2007**, *1*.

[114] M. Beiner, G. T. Rengarajan, S. Pankaj, D. Enke, M. Steinhart, *Nano Lett.* **2007**, *7*, 1381–5.

[115] J.-M. Ha, B. D. Hamilton, M. A. Hillmyer, M. D. Ward, *Cryst. Growth Des.* **2009**, *9*, 4766–4777.

[116] J.-M. Ha, J. H. Wolf, M. A. Hillmyer, M. D. Ward, *J. Am. Chem. Soc.* **2004**, *126*, 3382–3.

[117] G. T. Rengarajan, D. Enke, M. Steinhart, M. Beiner, E. Mitscherlich, E. Mitscherlich, W. Ostwald, B. C. Hancock, M. Parks, G. P. Johari, et al., *Phys. Chem. Chem. Phys.* **2011**, *13*, 21367.

[118] J.-M. Ha, B. D. Hamilton, M. A. Hillmyer, M. D. Ward, *Cryst. Growth Des.* **2012**, *12*, 4494–4504.

[119] G. Graubner, G. T. Rengarajan, N. Anders, N. Sonnenberger, D. Enke, M. Beiner, M. Steinhart, *Cryst. Growth Des.* **2014**, *14*, 78–86.

[120] P. J. Hore, *Nuclear Magnetic Resonance*, Oxford University Press, **1995**.

[121] R. K. (Robin K. Harris, *Nuclear Magnetic Resonance Spectroscopy : A Physicochemical View*, Longman Scientific & Technical, **1987**.

[122] J. Keeler, *Understanding NMR Spectroscopy*, John Wiley And Sons, **2010**.

[123] A. E. Derome, *Modern NMR Techniques for Chemistry Research*, Pergamon Press, **1987**.

[124] T. D. W. Claridge, *High-Resolution NMR Techniques in Organic Chemistry*, Elsevier, **2009**.

[125] D. D. Laws, H.-M. L. Bitter, A. Jerschow, *Angew. Chem. Int. Ed. Engl.* **2002**, *41*, 3096–129.

[126] M. J. Duer, Ed. , *Solid-State NMR Spectroscopy Principles and Applications*, Blackwell Science Ltd, Oxford, UK, **2001**.

[127] Andrew, E. R. Andrew, *Nature* **1958**, *182*, 1659–1659.

[128] J.-P. Demers, V. Chevelkov, A. Lange, *Solid State Nucl. Magn. Reson.* **2011**, *40*, 101–113.

[129] F. Bloch, *Phys. Rev.* **1956**, *102*, 104–135.

[130] A. E. Bennett, C. M. Rienstra, M. Auger, K. V. Lakshmi, R. G. Griffin, *J. Chem. Phys.* **1995**, *103*, 6951.

[131] B. M. Fung, A. K. Khitrin, K. Ermolaev, *J. Magn. Reson.* **2000**, *142*, 97–101.

[132] M. Lee, W. I. Goldburg, *Phys. Rev.* **1965**, *140*, A1261–A1271.

[133] A. Bielecki, A. C. Kolbert, M. H. Levitt, *Chem. Phys. Lett.* **1989**, *155*, 341–346.

[134] M. Leskes, P. K. Madhu, S. Vega, *Chem. Phys. Lett.* **2007**, *447*, 370–374.

[135] D. Sakellariou, A. Lesage, P. Hodgkinson, L. Emsley, *Chem. Phys. Lett.* **2000**, *319*, 253–260.

[136] W. Kolodziejski, J. Klinowski, *Chem. Rev.* **2002**, *102*, 613–628.

[137] A. Jones, James, Thomas, Synthesis and Characterization of Porous Organic/ Inorganic Hybrid Materials, **2009**.

[138] R. K. Harris, *Solid State Sci.* **2004**, *6*, 1025–1037.

[139] E. Carignani, S. Borsacchi, M. Geppi, *J. Phys. Chem. A* **2011**, *115*, 8783–90.

[140] E. Carignani, S. Borsacchi, M. Geppi, *ChemPhysChem* **2011**, *12*, 974–981.

[141] S. E. Ashbrook, D. McKay, *Chem. Commun.* **2016**, *52*, 7186–7204.

[142] C. Bonhomme, C. Gervais, F. Babonneau, C. Coelho, F. Pourpoint, T. Azaïs, S. E. Ashbrook, J. M. Griffin, J. R. Yates, F. Mauri, et al., *Chem. Rev.* **2012**, *112*, 5733–79.

[143] R. K. Harris, P. Hodgkinson, C. J. Pickard, J. R. Yates, V. Zorin, *Magn. Reson. Chem.* **2007**, *45*, S174–S186.

[144] D. C. Apperley, A. H. Forster, R. Fournier, R. K. Harris, P. Hodgkinson, R. W. Lancaster, T. Rades, *Magn. Reson. Chem.* **2005**, *43*, 881–92.

[145] A. BURGER, K. T. KOLLER, *Sci. Pharm.* **n.d.**, *64*, 293–301.

[146] R. K. Harris, S. A. Joyce, C. J. Pickard, S. Cadars, L. Emsley, *Phys. Chem. Chem. Phys.* **2006**, *8*, 137–43.

[147] R. K. Harris, P. Y. Ghi, R. B. Hammond, C.-Y. Ma, K. J. Roberts, *Chem. Commun.* **2003**, *0*, 2834.

[148] P. J. Chu, M. J. Potrzebowski, A. I. Scott, Y. Gao, *J. Am. Chem. Soc.* **1990**, *112*, 881–883.

[149] S. Mohamed, D. A. Tocher, S. L. Price, *Int. J. Pharm.* **2011**, *418*, 187–198.

[150] S. L. Price, *Chem. Soc. Rev.* **2014**, *43*, 2098–2111.

[151] T. Friščić, D. G. Reid, G. M. Day, M. J. Duer, W. Jones, *Cryst. Growth Des.* **2011**, *11*, 972–981.

[152] P. Hohenberg, W. Kohn, *Phys. Rev.* **1964**, *136*, B864–B871.

[153] W. Kohn, L. J. Sham, *Phys. Rev.* **1965**, *140*, A1133–A1138.

[154] J. P. Perdew, K. Burke, M. Ernzerhof, *Phys. Rev. Lett.* **1996**, *77*, 3865–3868.

[155] C. J. Pickard, F. Mauri, *Phys. Rev. B* **2001**, *63*, 245101.

[156] J. P. Bradley, S. P. Velaga, O. N. Antzutkin, S. P. Brown, *Cryst. Growth Des.* **2011**, *11*, 3463–3471.

[157] S. (Sally) L. Price, *Acc. Chem. Res.* **2009**, *42*, 117–126.

[158] G. M. Day, *Crystallogr. Rev.* **2011**, *17*, 3–52.

[159] E. Salager, G. M. Day, R. S. Stein, C. J. Pickard, B. Elena, L. Emsley, *J. Am. Chem. Soc.* **2010**, *132*, 2564–6.

[160] M. Baias, J.-N. Dumez, P. H. Svensson, S. Schantz, G. M. Day, L. Emsley, *J. Am. Chem. Soc.* **2013**, *135*, 17501–7.

[161] E. Salager, R. S. Stein, C. J. Pickard, B. Elena, L. Emsley, *Phys. Chem. Chem. Phys.* **2009**, *11*, 2610–21.

[162] J. W. Emsley, L. Phillips, *Prog. Nucl. Magn. Reson. Spectrosc.* **1971**, *7*, 1–520.

[163] F. Piana, D. H. Case, S. M. Ramalhete, G. Pileio, M. Facciotti, G. M. Day, Y. Z. Khimyak, J. Angulo, R. C. D. Brown, P. A. Gale, et al., *Soft Matter* **2016**, *12*, 4034–4043.

[164] M. Baias, A. Lesage, S. Aguado, J. Canivet, V. Moizan-Basle, N. Audebrand, D. Farrusseng, L. Emsley, *Angew. Chem. Int. Ed. Engl.* **2015**, *54*, 5971–6.

[165] R. E. Dinnebier, S. J. L. Billinge, Eds. , *Powder Diffraction*, Royal Society Of Chemistry, Cambridge, **2008**.

[166] P. Pecharsky, Vitalij, Zavalij, *Fundamentals of Powder Diffraction and Structural Characterization of Materials, Second Edition*, Springer, Boston, MA, **2009**.

[167] K. S. W. Sing, *Pure Appl. Chem.* **1985**, *57*, 603–619.

[168] M. Thommes, *Chemie Ing. Tech.* **2010**, *82*, 1059–1073.

[169] G. Leofanti, M. Padovan, G. Tozzola, B. Venturelli, *Catal. Today* **1998**, *41*, 207–219.

[170] S. Brunauer, P. H. Emmett, E. Teller, *J. Am. Chem. Soc.* **1938**, *60*, 309–319.

[171] E. P. Barrett, L. G. Joyner, P. P. Halenda, *J. Am. Chem. Soc.* **1951**, *73*, 373–380.

[172] D. Q. M. Craig, M. Reading, *Thermal Analysis of Pharmaceuticals*, CRC Press/Taylor & Francis, **2007**.

[173] M. Grün, K. K. Unger, A. Matsumoto, K. Tsutsumi, *Microporous Mesoporous Mater.* **1999**, *27*, 207–216.

[174] R. Ryoo, S. Jun, *J. Phys. Chem. B* **1997**, *101*, 317–320.

[175] C. Li, Y. Wang, Y. Guo, X. Liu, Y. Guo, Z. Zhang, Y. Wang, G. Lu, *Chem. Mater.* **2007**, *19*, 173–178.

[176] W. Haller, *Nature* **1965**, *206*, 693–696.

[177] W. Haller, *J. Chem. Phys.* **1965**, *42*, 686.

[178] T. J. Kistenmacher, R. E. Marsh, *J. Am. Chem. Soc.* **1972**, *94*, 1340–5.

[179] X. Chen, K. R. Morris, U. J. Griesser, S. R. Byrn, J. G. Stowell, *J. Am. Chem. Soc.* **2002**, *124*, 15012–9.

[180] V. Joshi, K. R. Morris, S. R. Byrn, M. T. Carvajal, *Cryst. Growth Des.* **2009**, *9*, 3359–3366.

[181] V. López-Mejías, J. W. Kampf, A. J. Matzger, *J. Am. Chem. Soc.* **2012**, *134*, 9872–5.

[182] E. H. Lee, S. X. M. Boerrigter, A. C. F. Rumondor, S. P. Chamarthy, S. R. Byrn, *Cryst. Growth Des.* **2008**, *8*, 91–97.

[183] N. K. Nath, A. Nangia, *CrystEngComm* **2011**, *13*, 47–51.

[184] S. J. Clark, M. D. Segall, C. J. Pickard, P. J. Hasnip, M. I. J. Probert, K. Refson, M. C. Payne, *Zeitschrift für Krist.* **2005**, *220*, 567–570.

[185] Y. M. Stowell, J.G., Byrn S.R., Zografi G., *Crystallogr. Data Centre, 12 Union Road, Cambridge, England,* **2002**.

[186] H. M. Krishna Murthy, T. N. Bhat, M. Vijayan, *Acta Crystallogr. Sect. B Struct. Crystallogr. Cryst. Chem.* **1982**, *38*, 315–317.

[187] J. F. McConnell, *Cryst. Struct. Commun.* **1973**, *2*, 459–461.

[188] J. D. Donaldson, J. R. Leary, S. D. Ross, M. J. K. Thomas, C. H. Smith, *Acta Crystallogr. Sect. B Struct. Crystallogr. Cryst. Chem.* **1981**, *37*, 2245–2248.

[189] S. Thirunahari, S. Aitipamula, P. S. Chow, R. B. H. Tan, *J. Pharm. Sci.* **2010**, *99*, 2975–90.

[190] D. Vanderbilt, *Phys. Rev. B* **1990**, *41*, 7892–7895.

[191] J. R. Yates, C. J. Pickard, F. Mauri, *Phys. Rev. B* **2007**, *76*, 24401.

[192] W. W. Lukens, P. Schmidt-Winkel, D. Zhao, J. Feng, G. D. Stucky, *Langmuir* **1999**, *15*, 5403–5409.

[193] L. Duvillaret, F. Garet, J.-L. Coutaz, *IEEE J. Sel. Top. Quantum Electron.* **1996**, *2*, 739–746.

[194] J. Peng, S. Peng, A. Jiang, J. Wei, C. Li, J. Tan, *Anal. Chim. Acta* **2010**, *683*, 63–8.

[195] P. Bertani, J. Raya, B. Bechinger, *Solid State Nucl. Magn. Reson.* **2014**, *61–62*, 15–18.

[196] G. A. Morris, R. Freeman, *J. Am. Chem. Soc.* **1979**, *101*, 760–762.

[197] C. A. Fyfe, K. C. Wong-Moon, Y. Huang, H. Grondey, *J. Am. Chem. Soc.* **1995**, *117*, 10397–10398.

[198] B. Elena, A. Lesage, S. Steuernagel, A. Böckmann, L. Emsley, *J. Am. Chem. Soc.* **2005**, *127*, 17296–302.

[199] C. Coelho, T. Azaïs, L. Bonhomme-Coury, G. Laurent, C. Bonhomme, *Inorg. Chem.* **2007**, *46*, 1379–87.

[200] B.-J. van Rossum, H. Förster, H. J. M. de Groot, *J. Magn. Reson.* **1997**, *124*, 516–519.

[201] D. . Burum, A. Bielecki, *J. Magn. Reson.* **1991**, *94*, 645–652.

[202] S. P. Brown, A. Lesage, B. Elena, L. Emsley, *J. Am. Chem. Soc.* **2004**, *126*, 13230–1.

[203] L. Borka, *Acta Pharm. Suec.* **1974**, *11*, 295–303.

[204] M. Otsuka, N. Kaneniwa, *Chem. Pharm. Bull. (Tokyo).* **1988**, *36*, 4026–32.

[205] K. Masuda, S. Tabata, H. Kono, Y. Sakata, T. Hayase, E. Yonemochi, K. Terada, *Int. J. Pharm.* **2006**, *318*, 146–53.

[206] S. Lohani, I. V. Nesmelova, R. Suryanarayanan, D. J. W. Grant, *Cryst. Growth Des.* **2011**, *11*, 2368–2378.

[207] B. Legendre, Y. Feutelais, *J. Therm. Anal. Calorim.* **2004**, *76*, 255–264.

[208] P. Karmwar, J. P. Boetker, K. A. Graeser, C. J. Strachan, J. Rantanen, T. Rades, *Eur. J. Pharm. Sci.* **2011**, *44*, 341–50.

[209] N. Hamdi, Y. Feutelais, N. Yagoubi, D. de Girolamo, B. Legendre, *J. Therm. Anal. Calorim.* **2004**, *76*, 985–1001.

[210] J.-B. Guilbaud, L. Cummings, Y. Z. Khimyak, *Macromol. Symp.* **2007**, *251*, 41–46.

[211] S. S. Dalal, M. D. Ediger, *J. Phys. Chem. Lett.* **2012**, *3*, 1229–33.

[212] K. J. Crowley, G. Zografi, *J. Pharm. Sci.* **2002**, *91*, 492–507.

[213] V. Andronis, G. Zografi, *J. Non. Cryst. Solids* **2000**, *271*, 236–248.

[214] V. Andronis, G. Zografi, *Pharm. Res.* **1998**, *15*, 835–42.

[215] J. M. Aceves-Hernandez, I. Nicolás-Vázquez, F. J. Aceves, J. Hinojosa-Torres, M. Paz, V. M. Castaño, *J. Pharm. Sci.* **2009**, *98*, 2448–63.

[216] V. Andronis, M. Yoshioka, G. Zografi, *J. Pharm. Sci.* **1997**, *86*, 346–51.

[217] P. A. Slavin, D. B. Sheen, E. E. . Shepherd, J. N. Sherwood, N. Feeder, R. Docherty, S. Milojevic, *J. Cryst. Growth* **2002**, *237–239*, 300–305.

[218] S. Hellstén, H. Qu, M. Louhi-Kultanen, *Chem. Eng. Technol.* **2011**, *34*, 1667–1674.

[219] P. J. Cox, P. L. Manson, *Acta Crystallogr. Sect. E Struct. Reports Online* **2003**, *59*, o1189–o1191.

[220] S. A. Surwase, J. P. Boetker, D. Saville, B. J. Boyd, K. C. Gordon, L. Peltonen, C. J. Strachan, *Mol. Pharm.* **2013**, *10*, 4472–80.

[221] P. Karmwar, K. Graeser, K. C. Gordon, C. J. Strachan, T. Rades, *Int. J. Pharm.* **2011**, *417*, 94–100.

[222] P. Karmwar, K. Graeser, K. C. Gordon, C. J. Strachan, T. Rades, *Eur. J. Pharm. Biopharm.* **2012**, *80*, 459–64.

[223] M. C. Etter, J. C. MacDonald, J. Bernstein, *Acta Crystallogr. B.* **1990**, *46 (Pt 2)*, 256–62.

[224] L. Carpentier, L. Bourgeois, M. Descamps, *J. Therm. Anal. Calorim.* **n.d.**, *68*, 727–739.

[225] A. J. Markvardsen, W. I. F. David, J. C. Johnson, K. Shankland, *Acta Crystallogr. Sect. A Found. Crystallogr.* **2001**, *57*, 47–54.

[226] W. I. F. David, K. Shankland, J. van de Streek, E. Pidcock, W. D. S. Motherwell, J. C. Cole, *J. Appl. Crystallogr.* **2006**, *39*, 910–915.

[227] F. H. Allen, *Acta Crystallogr. B.* **2002**, *58*, 380–8.

[228] T. Ukmar, V. Kaučič, G. Mali, *Acta Chim. Slov.* **2011**, *58*, 425–33.

[229] J. P. Bradley, C. J. Pickard, J. C. Burley, D. R. Martin, L. P. Hughes, S. D. Cosgrove, S. P. Brown, *J. Pharm. Sci.* **2012**, *101*, 1821–30.

[230] K. Eichele, R. E. Wasylishen, J. S. Grossert, A. C. Olivieri, *J. Phys. Chem.* **1995**, *99*, 10110–10113.

[231] M. Strohmeier, A. M. Orendt, D. W. Alderman, D. M. Grant, *J. Am. Chem. Soc.* **2001**, *123*, 1713–1722.

[232] M. J. Willans, B. A. Demko, R. E. Wasylishen, *Phys. Chem. Chem. Phys.* **2006**, *8*, 2733–2743.

[233] S. Sturniolo, T. F. G. Green, R. M. Hanson, M. Zilka, K. Refson, P. Hodgkinson, S. P. Brown, J. R. Yates, *Solid State Nucl. Magn. Reson.* **2016**, DOI 10.1016/j.ssnmr.2016.05.004.

[234] D. Neuhaus, M. P. Williamson, *The Nuclear Overhauser Effect in Structural and Conformational Analysis*, Wiley, **2000**.

[235] C. S. Wannere, P. von R. Schleyer, *Org. Lett.* **2003**, *5*, 605–608.

[236] R. D. Vernet, V. Boekelheide, *Proc. Natl. Acad. Sci. U. S. A.* **1974**, *71*, 2961–4.

[237] R. H. Levin, J. D. Roberts, *Tetrahedron Lett.* **1973**, *14*, 135–138.

[238] P. von R. Schleyer, C. Maerker, A. Dransfeld, H. Jiao, N. J. R. van E. Hommes, *J. Am. Chem. Soc.* **1996**, *118*, 6317–6318.

[239] A. Rapp, I. Schnell, D. Sebastiani, S. P. Brown, V. Percec, H. W. Spiess, *J. Am. Chem. Soc.* **2003**, *125*, 13284–97.

[240] P. Sozzani, A. Comotti, S. Bracco, R. Simonutti, G. R. Desiraju, I. W. Hamley, S. Förster, T. Plantenberg, C. M. Dobson, A. Šali, et al., *Chem. Commun.* **2004**, *35*, 768–769.

[241] M. Savolainen, A. Heinz, C. Strachan, K. C. Gordon, J. Yliruusi, T. Rades, N. Sandler, *Eur. J. Pharm. Sci.* **2007**, *30*, 113–23.

[242] D. E. Braun, K. P. Nartowski, Y. Z. Khimyak, K. R. Morris, S. R. Byrn, U. J. Griesser, *Mol. Pharm.* **2016**, *13*, 1012–1029.

[243] A. Lesage, C. Auger, S. Caldarelli, L. Emsley, *J. Am. Chem. Soc.* **1997**, *119*, 7867–7868.

[244] R. K. Harris, S. Cadars, L. Emsley, J. R. Yates, C. J. Pickard, R. K. R. Jetti, U. J. Griesser, *Phys. Chem. Chem. Phys.* **2007**, *9*, 360–8.

[245] A. C. Pinon, A. J. Rossini, C. M. Widdifield, D. Gajan, L. Emsley, *Mol. Pharm.* **2015**, *12*, 4146–4153.

[246] C. J. Pickard, R. J. Needs, *Phys. Rev. Lett.* **2006**, *97*, 45504.

[247] T. Ukmar, U. Maver, O. Planinšek, A. Pintar, V. Kaučič, A. Godec, M. Gaberšček, *J. Mater. Chem.* **2012**, *22*, 1112–1120.

[248] A. Kiwilsza, J. Mielcarek, A. Pajzderska, J. Wąsicki, *J. Microencapsul.* **2013**, *30*, 21–7.

[249] Y. Zhang, T. Jiang, Q. Zhang, S. Wang, *Eur. J. Pharm. Biopharm. Off. J. Arbeitsgemeinschaft*

für Pharm. Verfahrenstechnik e.V **2010**, *76*, 17–23.

[250]   B. D. Hamilton, M. A. Hillmyer, M. D. Ward, *Cryst. Growth Des.* **2008**, *8*, 3368–3375.

[251]   F. Babonneau, L. Yeung, N. Steunou, C. Gervais, A. Ramila, M. Vallet-Regi, *J. Sol-Gel Sci. Technol.* **2004**, *31*, 219–223.

[252]   A. Gignone, M. Delle Piane, M. Corno, P. Ugliengo, B. Onida, *J. Phys. Chem. C* **2015**, *119*, 13068–13079.

[253]   J. Wang, M. Sánchez-Roselló, J. L. Aceña, C. del Pozo, A. E. Sorochinsky, S. Fustero, V. A. Soloshonok, H. Liu, *Chem. Rev.* **2014**, *114*, 2432–506.

[254]   E. Parrott, J. Zeitler, T. Friscic, G. Day, M. Pepper, W. Jones, L. Gladden, **2008**.

[255]   K. M. Lutker, Z. P. Tolstyka, A. J. Matzger, *Cryst. Growth Des.* **2008**, *8*, 136–139.

[256]   K. M. Lutker, A. J. Matzger, *J. Pharm. Sci.* **2010**, *99*, 794–803.

[257]   J. J. Krc, *Microscope* **1977**, *25*, 31–45.

[258]   X. Chen, T. Li, K. R. Morris, S. R. Byrn, *Mol. Cryst. Liq. Cryst.* **2002**, *381*, 121–131.

[259]   E. H. Lee, S. X. M. Boerrigter, S. R. Byrn, *Cryst. Growth Des.* **2010**, *10*, 518–527.

[260]   H. Li, H. Wen, J. G. Stowell, K. R. Morris, S. R. Byrn, *J. Pharm. Sci.* **2010**, *99*, 3839–48.

[261]   X. Chen, J. G. Stowell, K. R. Morris, S. R. Byrn, *J. Pharm. Biomed. Anal.* **2010**, *51*, 866–74.

[262]   E. H. Lee, S. R. Byrn, *J. Pharm. Sci.* **2010**, *99*, 4013–22.

[263]   S. P. Delaney, T. M. Smith, T. M. Korter, *J. Mol. Struct.* **2014**, *1078*, 83–89.

[264]   Y. Hu, J. K. Liang, A. S. Myerson, L. S. Taylor, *Ind. Eng. Chem. Res.* **2005**, *44*, 1233–1240.

[265]   J. Trébosc, J. W. Wiench, S. Huh, V. S.-Y. Lin, M. Pruski, *J. Am. Chem. Soc.* **2005**, *127*, 3057–68.

[266]   T. Amitay-Rosen, S. Vega, *Phys. Chem. Chem. Phys.* **2010**, *12*, 6763–73.

[267]   J. A. Baird, B. Van Eerdenbrugh, L. S. Taylor, *J. Pharm. Sci.* **2010**, *99*, 3787–806.

[268]   J. S. Melinger, S. S. Harsha, N. Laman, D. Grischkowsky, *J. Opt. Soc. Am. B* **2009**, *26*, A79.

[269]   N. Y. Tan, J. A. Zeitler, *Mol. Pharm.* **2015**, *12*, 810–5.

[270]   J. R. Yates, S. E. Dobbins, C. J. Pickard, F. Mauri, P. Y. Ghi, R. K. Harris, *Phys. Chem. Chem. Phys.* **2005**, *7*, 1402.

[271]   T. N. Drebushchak, N. A. Pankrushina, E. V. Boldyreva, *Dokl. Phys. Chem.* **2011**, *437*, 61–64.

[272]   K. Kimura, F. Hirayama, H. Arima, K. Uekama, *Pharm. Res.* **n.d.**, *16*, 1729–1734.

[273]   G. Hasegawa, T. Komasaka, R. Bando, Y. Yoshihashi, E. Yonemochi, K. Fujii, H. Uekusa, K. Terada, *Int. J. Pharm.* **2009**, *369*, 12–8.

[274]   K. Kimura, F. Hirayama, K. Uekama, *J. Pharm. Sci.* **1999**, *88*, 385–91.

[275]   M. Kuhnert-Brandstätter, S. Wunsch, *Mikrochim. Acta* **1969**, 1297–307.

[276]   Simmons, D. L. Simmons, *Can. J. Pharm. Sci.* **1972**, *7*.

[277]   Burger, A. Burger, *Sci. Pharm.* **1975**, *43*.

[278]   K. A. Nirmala, D. S. Sake Gowda, *Acta Crystallogr. Sect. B Struct. Crystallogr. Cryst. Chem.* **1981**, *37*, 1597–1599.

[279]   J. Fattah, J. M. Twyman, S. J. Heyes, D. J. Watkin, A. J. Edwards, K. Prout, C. M. Dobson, *J. Am. Chem. Soc.* **1993**, *115*, 5636–5650.

[280]   M. Wendeler, J. Fattah, J. M. Twyman, A. J. Edwards, C. M. Dobson, Stephen J. Heyes, K. Prout, **1997**, *119*, 9793–9803.

[281]   W. Li, A. E. Mcdermott, *Concepts Magn. Reson. Part A* **2013**, *42A*, 14–22.

[282]   D. . Vanderhart, W. L. Earl, A. . Garroway, *J. Magn. Reson.* **1981**, *44*, 361–401.

[283]   W. P. Rothwell, J. S. Waugh, *J. Chem. Phys.* **1981**, *74*, 2721.

[284]   J. R. Long, B. Q. Sun, A. Bowen, R. G. Griffin, *J. Am. Chem. Soc.* **1994**, *116*, 11950–11956.

[285]   T. N. Drebushchak, V. A. Drebushchak, N. A. Pankrushina, E. V. Boldyreva, A. J. Cruz-Cabeza, J. Bernstein, A. Nangia, J.-P. Brog, C.-L. Chanez, A. Crochet, et al., *CrystEngComm* **2016**, *18*, 5736–5743.

[286]   K. Akasaka, S. Ganapathy, C. A. McDowell, A. Naito, *J. Chem. Phys.* **1983**, *78*, 3567–3572.

[287]   K. Kimura, F. Hirayama, H. Arima, K. Uekama, *Chem. Pharm. Bull. (Tokyo).* **2000**, *48*, 646–50.

[288]   J. M. Griffin, A. J. Miller, A. J. Berry, S. Wimperis, S. E. Ashbrook, M. Kitamura, S. Kondoh, N. Morimoto, G. H. Miller, G. R. Rossman, et al., *Phys. Chem. Chem. Phys.* **2010**, *12*, 2989.

[289]   L. W. Jelinski, *Annu. Rev. Mater. Sci.* **1985**, *15*, 359–377.

[290] T. Hiraoki, A. Kogame, N. Nishi, A. Tsutsumi, *J. Mol. Struct.* **1998**, *441*, 243–250.

[291] M. Cutajar, S. E. Ashbrook, S. Wimperis, *Chem. Phys. Lett.* **2006**, *423*, 276–281.

[292] T. Amitay-Rosen, S. Kababya, S. Vega, *J. Phys. Chem. B* **2009**, *113*, 6267–6282.

[293] G. Buntkowsky, H. Breitzke, A. Adamczyk, F. Roelofs, T. Emmler, E. Gedat, B. Grünberg, Y. Xu, H.-H. Limbach, I. Shenderovich, et al., *Phys. Chem. Chem. Phys.* **2007**, *9*, 4843.

[294] R. Eckman, A. J. Vega, *J. Am. Chem. Soc.* **1983**, *105*, 4841–4842.

[295] W. Li, A. McDermott, *J. Magn. Reson.* **2012**, *222*, 74–80.

[296] A. Krushelnitsky, D. Reichert, K. Saalwächter, *Acc. Chem. Res.* **2013**, *46*, 2028–2036.

[297] G. M. Day, J. A. Zeitler, W. Jones, T. Rades, P. F. Taday, *J. Phys. Chem. B* **2006**, *110*, 447–56.

[298] J. A. Zeitler, D. A. Newnham, P. F. Taday, T. L. Threlfall, R. W. Lancaster, R. W. Berg, C. J. Strachan, M. Pepper, K. C. Gordon, T. Rades, *J. Pharm. Sci.* **2006**, *95*, 2486–98.

[299] R. K. Gilpin, W. Zhou, *J. Pharm. Biomed. Anal.* **2005**, *37*, 509–15.

[300] E. W. Hansen, R. Schmidt, M. Stoecker, D. Akporiaye, *J. Phys. Chem.* **1995**, *99*, 4148–4154.

[301] D. W. Aksnes, K. Førland, M. Stöcker, *Microporous Mesoporous Mater.* **2005**, *77*, 79–87.

[302] L. Gjerdåker, D. W. Aksnes, G. H. Sørland, M. Stöcker, *Microporous Mesoporous Mater.* **2001**, *42*, 89–96.

[303] D. Wu, S.-J. Hwang, S. I. Zones, A. Navrotsky, *Proc. Natl. Acad. Sci.* **2014**, *111*, 1720–1725.

[304] P. Porion, A. . Faugère, P. Levitz, H. Van Damme, A. Raoof, J. . Guilbaud, F. Chevoir, *A NMR Investigation of Adsorption/desorption Hysteresis in Porous Silica Gels*, **1998**.

[305] P. J. Barrie, *Annu. Reports NMR Spectrosc.* **2000**, *41*, 265–316.

[306] K. P. Nartowski, D. Malhotra, L. E. Hawarden, J. Sibik, D. Iuga, J. A. Zeitler, L. Fábián, Y. Z. Khimyak, *Angew. Chemie Int. Ed.* **2016**, DOI 10.1002/anie.201602936.

[307] B. Alonso, D. Massiot, *Multi-Scale NMR Characterisation of Mesostructured Materials Using 1H→13C through-Bond Polarisation Transfer, Fast MAS, and 1H Spin Diffusion*, **2003**.

[308] R. J. Davey, S. L. M. Schroeder, J. H. ter Horst, *Angew. Chem. Int. Ed. Engl.* **2013**, *52*, 2166–79.

[309] C. C. Pradzynski, R. M. Forck, T. Zeuch, P. Slavíček, U. Buck, M. Kulmala, L. Delzeit, D. Blake, R. Zhang, A. Khalizov, et al., *Science* **2012**, *337*, 1529–32.

[310] J. Liu, C. E. Nicholson, S. J. Cooper, *Langmuir* **2007**, *23*, 7286–7292.

[311] R. M. Ginde, A. S. Myerson, *J. Cryst. Growth* **1992**, *116*, 41–47.

[312] V.-P. Lehto, K. Vähä-Heikkilä, J. Paski, J. Salonen, *J. Therm. Anal. Calorim.* **2005**, *80*, 393–397.

[313] E. Gavuzzo, F. Mazza, E. Giglio, IUCr, *Acta Crystallogr. Sect. B Struct. Crystallogr. Cryst. Chem.* **1974**, *30*, 1351–1357.

[314] P. Munshi, T. N. Guru Row, *J. Phys. Chem. A* **2005**, *109*, 659–672.

[315] D. Li, W. Zhao, X. Sun, J. Zhang, M. Anpo, J. Zhao, *Dye. Pigment.* **2006**, *68*, 33–37.

[316] W. Zhao, D. Li, B. He, J. Zhang, J. Huang, L. Zhang, *Dye. Pigment.* **2005**, *64*, 265–270.

[317] X. Yang, T. C. Ong, V. K. Michaelis, S. Heng, J. Huang, R. G. Griffin, A. S. Myerson, *CrystEngComm* **2014**, *16*, 9345–9352.

[318] Y. Zhang, J. Zhang, T. Jiang, S. Wang, *Int. J. Pharm.* **2011**, *410*, 118–24.

[319] E. Skorupska, A. Jeziorna, M. J. Potrzebowski, *J. Phys. Chem. C* **2016**, *120*, 13169–13180.

[320] †,‡ Wlodzimierz Masierak, † Thomas Emmler, † Egbert Gedat, § Andreas Schreiber, § and Gerhard H. Findenegg, † Gerd Buntkowsky*, **2004**, DOI 10.1021/JP047348R.

[321] † E. Gedat, ‡ A. Schreiber, † J. Albrecht, † Th. Emmler, † I. Shenderovich, ‡ G. H. Findenegg, † and H.-H. Limbach, †,§ G. Buntkowsky*, **2002**, DOI 10.1021/JP012391P.

[322] M. Arndt, R. Stannarius, H. Groothues, E. Hempel, F. Kremer, *Phys. Rev. Lett.* **1997**, *79*, 2077–2080.

[323] I. Sarceviča, L. Orola, K. P. Nartowski, Y. Z. Khimyak, A. N. Round, L. Fábián, *Mol. Pharm.* **2015**, *12*, 2981–2992.

[324] K. P. Nartowski, Y. Z. Khimyak, D. J. Berry, *CrystEngComm* **2016**, *18*, 2617–2620.

[325] K. R. Thurber, R. Tycko, *Measurement of Sample Temperatures under Magic-Angle Spinning from the Chemical Shift and Spin-Lattice Relaxation Rate of 79Br in KBr Powder*, **2009**.

[326] G. Neue, C. Dybowski, *Determining Temperature in a Magic-Angle Spinning Probe Using the Temperature Dependence of the Isotropic Chemical Shift of Lead Nitrate*, Academic Press,

1997.

[327] L. C. M. van Gorkom, J. M. Hook, M. B. Logan, J. V. Hanna, R. E. Wasylishen, *Magn. Reson. Chem.* **1995**, *33*, 791–795.

[328] M. X. and, K. D. M. Harris*, **2005**, DOI 10.1021/JA052668P.

[329] C. E. Hughes, P. A. Williams, K. D. M. Harris, *Angew. Chemie Int. Ed.* **2014**, *53*, 8939–8943.

[330] C. E. Hughes, P. A. Williams, V. L. Keast, V. G. Charalampopoulos, G. R. Edwards-Gau, K. D. M. Harris, B. Kahr, J. M. McBride, J. D. Dunitz, R. J. Davey, et al., *Faraday Discuss.* **2015**, *179*, 115–140.

[331] C. E. Hughes, P. A. Williams, T. R. Peskett, K. D. M. Harris, *J. Phys. Chem. Lett.* **2012**, *3*, 3176–3181.

[332] M. K. Dudek, T. Pawlak, P. Paluch, A. Jeziorna, M. J. Potrzebowski, *Cryst. Growth Des.* **2016**, *16*, 5312–5322.

[333] M. K. Dudek, A. Jeziorna, M. J. Potrzebowski, F. Mallamace, C. Corsaro, D. Mallamace, S. Vasi, C. Vasi, H. E. Stanley, S.-H. Chen, et al., *CrystEngComm* **2016**, *18*, 5267–5277.